

UNIVERSITY OF
BIRMINGHAM

ULTRASONIC ASSISTED CREEP FEED GRINDING AND DRESSING OF ADVANCED AEROSPACE ALLOYS

by

DEBAJYOTI BHADURI

A thesis submitted to
The University of Birmingham
for the degree of
DOCTOR OF PHILOSOPHY

School of Mechanical Engineering
College of Engineering and Physical Sciences
The University of Birmingham
April 2014

UNIVERSITY OF
BIRMINGHAM

University of Birmingham Research Archive

e-theses repository

This unpublished thesis/dissertation is copyright of the author and/or third parties. The intellectual property rights of the author or third parties in respect of this work are as defined by The Copyright Designs and Patents Act 1988 or as modified by any successor legislation.

Any use made of information contained in this thesis/dissertation must be in accordance with that legislation and must be properly acknowledged. Further distribution or reproduction in any format is prohibited without the permission of the copyright holder.

ABSTRACT

The novelty of the present research was in developing a 'hybrid' ultrasonic vibration assisted machining process for creep feed grinding of advanced aerospace alloys including Inconel 718 and CMSX-4 nickel based superalloys (typically used in turbine discs and blades respectively) as well as gamma titanium aluminide (γ-TiAl), the latter having the potential to replace some of the former in aeroengines due to its higher specific strength and ability to withstand elevated temperatures compared to conventional α/β Ti-6Al-4V alloy.

Following a detailed literature review on the use of ultrasonic vibration when grinding various workpiece materials including ceramics, glass, stainless/alloyed steels and aluminium alloys, three main phases of experimental work were undertaken involving ultrasonic assisted grinding (UAG) of nickel based superalloys (Inconel 718 and CMSX-4) and a gamma γ-TiAl together with a limited number of tests on ultrasonic assisted dressing (UAD) of a conventional silicon carbide (SiC) wheel.

The majority of published work on UAG has involved surface grinding operations with a depth of cut typically limited to ≤0.3 mm, with relatively few papers addressing UAG under a creep feed configuration (depths of cut ≥1 mm). The typical frequency range was 20 to 25 kHz with corresponding amplitudes of vibration varying from 0.5 to 32 μm. Vibration was applied either to the grinding wheel or workpiece using piezoelectric transducers (a minority of papers reported use of magnetostrictive transducers). However, even less information is available concerning UAG of advanced aerospace alloys such as nickel based superalloys or γ-TiAl.

Preliminary feasibility trials were carried out using a low power ultrasonic generator (250 W) and a conical horn attached to the workpiece when grinding Inconel 718 with a conventional SiC wheel, however the set-up was found to be unsuitable for creep feed grinding (CFG) operations. A bespoke transducer-booster-table sonotrode assembly with a high power ultrasonic generator (1 kW) was evaluated for the mainstream UAG trials on Inconel 718 and CMSX-4 using conventional alumina wheels (POROS2 and VORTEX) with variations in wheel speed, table feed, depth of cut and amplitude of vibration. In general, grinding forces decreased with the application of ultrasonic actuation (~20 to 60%), while conversely, radial wear increased (corresponding deterioration in G-ratio by 30 to 60%). Additionally, surfaces produced by UAG typically exhibited higher roughness values with greater smearing, side flow/ploughing and overlapping grit marks. Sub-surface

microhardness typically increased by ~5-10% following UAG compared to the specimens ground by conventional CFG.

While evaluating UAG on γ-TiAl using a conventional SiC and single layer diamond superabrasive (D252) wheels, the effects of ultrasonic vibration were more apparent in comparison to the nickel based superalloys. Reductions in grinding forces (up to 35%) and improvement in wheel G-ratios (30-75% for SiC and 100-800% for diamond) were observed when γ-TiAl workpieces were subject to ultrasonic assisted mode. In contrast to nickel based superalloys, lower workpiece roughness (R_a reduced by ~3-10%) was also recorded when UAG of γ-TiAl using SiC wheels.

The primary advantage of employing ultrasonic vibration in CFG was the reduction in grinding forces for both nickel based superalloys and γ-TiAl, with superior performance observed in the latter in terms of lower radial wheel wear and workpiece surface roughness. While surface defects in the majority of conventional CFG trials were found to be minimal, US assisted grinding typically produced damage-free surfaces.

LIST OF PUBLICATIONS

- **Papers published**

  - **D. Bhaduri**, S.L. Soo, D.K. Aspinwall, D. Novovic, P. Harden, S. Bohr, D. Martin, A study on ultrasonic assisted creep feed grinding of nickel based superalloys, Procedia CIRP 1 (**2012**) 376-381.

  - **D. Bhaduri**, S.L. Soo, D. Novovic, D.K. Aspinwall, P. Harden, C. Waterhouse, S. Bohr, A.C. Mathieson, M. Lucas, Ultrasonic assisted creep feed grinding of Inconel 718, Procedia CIRP 6 (**2013**) 616-621.

- **Refereed Conferences/Presentation**

  - **D. Bhaduri**, S.L. Soo, D.K. Aspinwall, D. Novovic, Ultrasonic assisted creep feed grinding and dressing of advanced aerospace alloys, Talk in CIRP January Meeting–HybP-1-(Cross Track 1/Track 2), 25th - 28th January, **2011**, Paris, France.

- **Papers under preparation**

  - **D. Bhaduri**, S.L. Soo, D.K. Aspinwall, D. Novovic, P. Harden, S. Bohr, D. Martin, Ultrasonic assisted grinding: A literature review, *to be submitted in International Journal of Machine Tools and Manufacture*.

  - **D. Bhaduri**, S.L. Soo, D. Novovic, D.K. Aspinwall, S. Bohr, P. Harden, C. Waterhouse, Effects of ultrasonic vibration when creep feed grinding Inconel 718 with an open structured alumina wheel, *to be submitted in International Journal of Advanced Manufacturing Technology*.

  - **D. Bhaduri**, S.L. Soo, D. Novovic, D.K. Aspinwall, S. Bohr, P. Harden, C. Waterhouse, Ultrasonic assisted creep feed grinding of a cast nickel based superalloys, *to be submitted in Journal of Materials of Processing Technology*.

  - **D. Bhaduri**, S.L. Soo, D.K. Aspinwall, D. Novovic, P. Harden, S. Bohr, D. Martin, A study on ultrasonic assisted creep feed grinding of a gamma titanium aluminide, *to be submitted in Intermetallics*.

ACKNOWLEDGEMENTS

I take this opportunity to express my earnest gratitude to my academic supervisors Dr. Sein Leung Soo (Senior Lecturer and Head of the Machining Research Group) and Prof. David Aspinwall for their guidance, encouragement and enthusiasm throughout the course of current work. I am also indebted to my industrial collaborators for providing technical as well as financial support, special thanks are due to Dr. Donka Novovic from Rolls Royce Plc, Dr. Stefan Bohr and Mr. David Balshaw from Saint-Gobain Abrasives, Mr. David Martin, Mr. Chris Waterhouse and Mr. John McTernan from Hardinge Group and Dr. Peter Harden formerly from Element Six.

I would also like to express my sincere gratitude to Mr. Richard Fasham and Mr. Andrew Loat (Machining Research Group Technician) for their assistance with experimental work and associated samples preparation. Special thanks are also due to Dr. Richard Hood (Lecturer, School of Mechanical Engineering) for sharing his knowledge and expertise throughout the duration of the project.

My sincere gratitude also goes to my colleagues within the Machining Research Group, special thanks are for Mr. Maojun Li, Mr. Raul Munoz, Mr. Alex Kuo, Mr. Mohamed El-Hofy, Mr. Ali Abdelhafeez, Dr. Rattachanai Rattanakit, Dr. Sarmad Ali Khan and Dr. Saad Mahmoud.

Last but not the least, I wish to express my love and deepest gratitude to my family and friends especially Mr. Nilanjan Das Chakladar, Mr. Abhishek Das, Mr. Arnab Palit, Mr. Supratik Mukhopadhyay and Ms. Paranjayee Mandal for their endless encouragement and support throughout my doctoral work.

CONTENTS

ABSTRACT **i**

LIST OF PUBLICATIONS **iii**

ACKNOWLEDGEMENTS **iv**

LIST OF FIGURES **x**

LIST OF TABLES **xxiii**

LIST OF NOMENCLATURES **xxiv**

1. INTRODUCTION **1.1-1.3**

1.1 Background to the project **1.1**

1.2 Aims and objectives of the project **1.2**

1.3 Industrial collaborators and funding **1.3**

2. LITERATURE REVIEW **2.1-2.63**

2.1 Ultrasonic machining (USM) **2.1**

2.1.1 Introduction 2.1

2.1.2 Mechanics of USM 2.3

2.1.3 Process parameters 2.5

2.1.4 Equipment/machine tools 2.8

2.2 Ultrasonic assisted machining **2.9**

2.2.1 Introduction 2.9

2.2.2 Ultrasonic assisted grinding (UAG) 2.12

2.2.2.1 Application of US vibration to grinding tool/wheel 2.15

2.2.2.2 Application of US vibration to the workpiece 2.23

2.2.3 Ultrasonic assisted dressing (UAD) 2.41

2.3 Creep feed grinding **2.42**

2.3.1 Introduction 2.42

2.3.2 Mechanics 2.44

2.3.3 Applications 2.46

2.3.4 Grinding wheel wear 2.48

2.4 Nickel based superalloys **2.51**

2.4.1 Introduction 2.51
2.4.2 Compositions 2.52
2.4.3 Applications 2.54
2.4.4 Grindability 2.55

2.5 Gamma titanium aluminide intermetallic alloys **2.57**

2.5.1 Introduction 2.57
2.5.2 Properties 2.58
2.5.3 Applications 2.59
2.5.4 Grindability 2.60

2.6 Workpiece surface integrity **2.61**

3. EXPERIMENTAL WORK 3.1-3.25

3.1 Workpiece materials **3.1**

3.2 Grinding wheels **3.4**

3.3 Test and analysis equipment **3.5**

3.3.1 Machine tool, wheel dressing and cooling/cleaning arrangement 3.5
3.3.2 Ultrasonic vibration systems 3.7
3.3.3 Grinding/dressing forces and power 3.10
3.3.4 Radial wheel wear and G-ratio 3.10
3.3.5 Surface roughness/topography 3.11
3.3.6 Microhardness and microstructure analysis 3.12
3.3.7 Optical and scanning electron microscopy 3.14

3.4 Experimental procedure and test arrays **3.14**

3.4.1 Phase 1A: UAG experiments using Flexiskills ultrasonic system 3.14
3.4.2 Phase 1B: Initial UAG trials of Inconel 718 with a VORTEX 80 mesh wheel using the MPI ultrasonic system 3.15
3.4.3 Phase 1C: Initial experiments on ultrasonic assisted dressing 3.17
3.4.4 Phase 2A: Identification of process parameters for UAG of Inconel 718 3.18

3.4.5 Phase 2B and 2C: Evaluation of UAG on Inconel 718 using POROS2 and VORTEX 60 mesh wheels 3.19
3.4.6 Phase 2D: Assessment of UAG on CMSX-4 using POROS2 wheel 3.21
3.4.7 Phase 2E: Effects of depth of cut and vibration amplitude when UAG of Inconel 718 3.22
3.4.8 Phase 3A: Assessment of UAG on γ-TiAl using conventional SiC abrasive wheel 3.23
3.4.9 Phase 3B: Investigation of UAG on γ-TiAl with electroplated diamond superabrasive wheel 3.24

4. RESULTS AND DISCUSSION 4.1-4.115

4.1 Initial trial experiments on ultrasonic assisted grinding and dressing 4.1

4.1.1 Phase 1A: UAG experiments using Flexiskills ultrasonic system 4.1

4.1.2 Phase 1B: Initial UAG trials of Inconel 718 with a VORTEX 80 mesh wheel using the MPI ultrasonic system 4.2

4.1.3 Phase 1C: Initial experiments on ultrasonic assisted dressing 4.6
4.1.3.1 Dressing and grinding forces 4.6
4.1.3.2 Workpiece surface topography and quality 4.8
4.1.3.3 Wear of PCD insert and wheel condition following grinding 4.10

4.2 Ultrasonic assisted grinding of nickel based superalloys 4.11

4.2.1 Phase 2A: Identification of process parameters for UAG of Inconel 718 4.11

4.2.2 Phase 2B: Evaluation of UAG on Inconel 718 using POROS2 wheel 4.16
4.2.2.1 Grinding forces 4.16
4.2.2.2 Radial wheel wear and G-ratio 4.19
4.2.2.3 Workpiece surface topography and quality 4.21
4.2.2.4 Grinding wheel surface evaluation 4.26
4.2.2.5 Microhardness and workpiece microstructure 4.32

4.2.3 Phase 2C: Evaluation of UAG on Inconel 718 using VORTEX 60 mesh wheel 4.36
4.2.3.1 Grinding forces 4.36
4.2.3.2 Radial wheel wear and G-ratio 4.39

4.2.3.3 Workpiece surface topography and quality 4.40
4.2.3.4 Grinding wheel surface evaluation 4.44
4.2.3.5 Microhardness and workpiece microstructure 4.48

4.2.4 Phase 2D: Assessment of UAG on CMSX-4 using POROS2 wheel 4.52
4.2.4.1 Grinding forces 4.52
4.2.4.2 Radial wheel wear and G-ratio 4.55
4.2.4.3 Workpiece surface topography and quality 4.56
4.2.4.4 Grinding wheel surface evaluation 4.60
4.2.4.5 Microhardness and workpiece microstructure 4.65

4.2.5 Phase 2E: Effects of depth of cut and vibration amplitude when UAG of Inconel 718 4.70
4.2.5.1 Grinding forces 4.70
4.2.5.2 Radial wheel wear and G-ratio 4.73
4.2.5.3 Workpiece surface topography and quality 4.75
4.2.5.4 Grinding wheel surface evaluation 4.77
4.2.5.5 Microhardness and workpiece microstructure 4.80

4.3 Ultrasonic assisted grinding of gamma titanium aluminide (γ-TiAl) intermetallic alloys 4.84

4.3.1 Phase 3A: Assessment of UAG on γ-TiAl using conventional SiC abrasive wheel 4.84
4.3.1.1 Grinding forces 4.84
4.3.1.2 Radial wheel wear and G-ratio 4.87
4.3.1.3 Workpiece surface topography and quality 4.89
4.3.1.4 Grinding wheel surface evaluation 4.94
4.3.1.5 Microhardness and workpiece microstructure 4.99

4.3.2 Phase 3B: Investigation of UAG on γ-TiAl with electroplated diamond superabrasive wheel 4.104
4.3.2.1 Grinding forces 4.104
4.3.2.2 Radial wheel wear and G-ratio 4.105
4.3.2.3 Workpiece surface topography and quality 4.107
4.3.2.4 Grinding wheel surface evaluation 4.111
4.3.2.5 Microhardness and workpiece microstructure 4.112

5. CONCLUSIONS 5.1-5.10

6. RECOMMENDATIONS FOR FUTURE WORK 6.1

7. REFERENCES 7.1-7.16

APPENDICES **A.1-A.21**

Appendix A1: Collaborators contact details **A.1**

Appendix A2: Survey of commercial ultrasonic equipment suppliers **A.2**

Appendix A3: Measurement of amplitude of vibration **A.3**

Appendix A4: Phase 2C: Evaluation of UAG on Inconel 718 using VORTEX 60 mesh wheel **A.7**

Appendix A5: Phase 2D: Assessment of UAG on CMSX-4 using POROS2 wheel **A.9**

Appendix A6: Phase 2E: Effects of depth of cut and vibration amplitude when UAG of Inconel 718 **A.10**

Appendix A7: Phase 3A: Assessment of UAG on γ-TiAl using conventional SiC abrasive wheel **A.16**

Appendix A8: Phase 3B: Investigation of UAG on γ-TiAl with electroplated diamond superabrasive wheel **A.17**

LIST OF FIGURES

Figure No.	Illustrations	Page No.
2.1.1	Basic elements of USM head (Thoe et al., 1998)	2.2
2.1.2	(a) Schematic diagram of rotary ultrasonic machining, (b) Ultrasonically machined holes (Churi et al., 2007)	2.3
2.1.3	Schematic representation of the material removal mechanisms in USM (Khairy, 1990)	2.3
2.1.4	Material removal characteristics with variation in frequency of vibration (Ghosh and Mallik, 1985)	2.6
2.1.5	Relationship between penetration rate and amplitude of vibration (Kazantsev, 1966)	2.6
2.1.6	Variation of MRR with (a) Feed force, (b) Work to tool hardness ratio (Ghosh and Mallik, 1985)	2.7
2.1.7	Variation of MRR with abrasive concentration in slurry (Ghosh and Mallik, 1985)	2.7
2.2.1	Principal vibration directions during ultrasonically assisted turning (Babitsky et al., 2003)	2.10
2.2.2	Principle of inclined ultrasonic assisted cutting method (Jin and Murakawa, 2001)	2.11
2.2.3	Thrust force in drilling under various combinations of vibration amplitude and frequency (Liao et al., 2007)	2.12
2.2.4	A schematic design showing radially vibrating grinding wheel (Anon, 1963)	2.13
2.2.5	(a) Effect of ultrasonic treatment applied to the grinding wheel periphery, (b) Comparison between workpiece surfaces ground with a normally worn wheel and ultrasonically treated wheel (Kalizer and Limb, 1968)	2.14
2.2.6	(a) Ultrasonically treated, (b) Non-ultrasonically treated working surfaces of the grinding wheel (Sakamoto et al., 2006)	2.14
2.2.7	(a) Ultrasonic grinding attachment, (b) Reduction of grinding force in US-grinding (Suzuki et al., 1988)	2.15
2.2.8	(a) Schematic diagram of the principle of grinding with a non-rotational tool, (b) Samples of recesses with sharp inner corners formed on alumina (Suzuki et al., 1993)	2.16

2.2.9	Examples of fabricated microtools (a) Without and (b) With ultrasonic vibration (Onikura et al., 2000)	2.17
2.2.10	Specific normal force with regard to bond system and ultrasonic amplitude (Uhlmann and Sammler, 2010)	2.18
2.2.11	(a) Truing and dressing, (b) Truing force Vs vibration amplitude (Nomura et al., 2007)	2.19
2.2.12	(a) Illustration of constant depth of cut UAG, (b) Non-ultrasonically dressed wheel, (c) Ultrasonically dressed wheel (Nomura et al., 2007)	2.20
2.2.13	(a) Schematic of ultrasonically assisted face grinding, (b) Drawing of electroplated tool, (c) Topography of tool end face following grinding with and without ultrasonic vibration (Hara et al., 2008)	2.21
2.2.14	Tool topography and top 10 μm diamond grains using (a) AF, (b) WLI, (c) CLSM (Ismail et al., 2010)	2.22
2.2.15	Model prediction for cutting forces with variations in amplitude and grain density respectively (Qin et al., 2009)	2.22
2.2.16	Experimental results for cutting forces with variations in diamond grain size and federate respectively (Qin et al., 2009)	2.23
2.2.17	Relative motion of single grain diamond (Uhlmann, 1998)	2.24
2.2.18	Scratches on different ceramics with and without ultrasonics (Uhlmann, 1998)	2.24
2.2.19	Different mechanisms of surface formation showing increase in mechanical but decrease in thermal load during UAG (Uhlmann, 1998)	2.25
2.2.20	Influence of ultrasonic grinding on (a) Surface roughness, (b) Surface quality of workpiece (Denkena et al., 2003)	2.26
2.2.21	Effect of feed rate and wheel speed on surface roughness (Zheng and Xu, 2006)	2.27
2.2.22	(a) Kinematic path of single abrasive particle (V_w=0.1 m/s, f=20 kHz, A=B=15 μm), (b) Contact model between abrasive particle and workpiece (Yan et al., 2009)	2.28
2.2.23	SEM of nano-ZrO_2 after (a) conventional grinding, (b) TDUAG (Yan et al., 2009)	2.29
2.2.24	Principle of ultrasonic elliptical vibration shoe centreless grinding (Wu et al., 2004b)	2.30
2.2.25	Experimental set-up (a) Schematic drawing, (b) Photograph (Liang et al., 2010)	2.30

2.2.26	Topography of abrasive grain in the wheel surface following grinding of sapphire: (a) Conventional grinding, (b) Elliptic ultrasonic assisted grinding (Liang et al., 2012)	2.31
2.2.27	Surface condition of polysilicon when ground: (a) With ultrasonic elliptical vibration, (b) Without ultrasonic elliptical vibration (Peng et al., 2011)	2.32
2.2.28	SEM of scratches: (a) Scratch without ultrasonication, (b) Scratch with parallel ultrasonication, (c) Scratch with normal ultrasonication (Peng et al., 2012b)	2.33
2.2.29	(a) 3D model of acoustic head, (b) Amplitude Vs frequency from harmonic analysis in 3D modelling (Azarhoushang and Tawakoli, 2011)	2.33
2.2.30	The experimental set up (Azarhoushang and Tawakoli, 2011)	2.34
2.2.31	(a) Experimental set up for ultrasonic assisted dry grinding, (b) Graph for specific grinding forces Vs feed rate (Tawakoli and Azarhoushang, 2008)	2.35
2.2.32	(a) Photograph of ground workpiece surfaces, (b) Specific normal grinding forces as a function of depth of cut, (c) Surface roughness values R_a and R_z as a function of depth of cut (Tawakoli et al., 2009a)	2.36
2.2.33	Grinding model for ultrasonic assisted grinding (UAG): (a) Schematic of the motion of a grit on the workpiece surface, (b) Path generation of a grit by UAG (Tawakoli et al., 2009b)	2.37
2.2.34	Ultrasonic set up attached to the workpiece (Nik et al., 2012)	2.39
2.2.35	Ground Ti-6Al-4V surfaces following dry grinding: (a) Without and (b) With ultrasonic assistance (Nik et al., 2012)	2.39
2.2.36	Experimental grinding forces Vs feed rate at depths of cut of 25 and 50 µm: (a) Vertical forces, (b) Horizontal forces (Abdullah et al., 2012)	2.40
2.2.37	Reduction in (a) Horizontal, (b) Vertical force when UAG (Abdullah et al., 2013)	2.40
2.2.38	Reduction in grinding forces and increase in workpiece roughness following ultrasonic assisted dressing with form roller, A_{US}: amplitude of vibration, a_{ed}: dressing depth of cut (Tawakoli et al., 2011)	2.42
2.3.1	Comparison between (a) Reciprocating surface grinding and (b) Creep feed grinding (Andrew et al., 1985)	2.43
2.3.2	Surface burn when creep feed grinding of burn-resistant titanium alloy (BuRTi) (Soo et al., 2011b)	2.44
2.3.3	Schematic diagram of grinding process showing different process variables (Bianchi et al., 2001)	2.45

2.3.4	Radial wheel wear measured (RWW) Vs cutting speed at different feed rates (Abdullah et al., 2007)	2.47
2.3.5	(a) Crack on the machined surface, (b) Sub-surface crack shown on the cross-sectional view (Hood et al., 2007a)	2.48
2.3.6	Three types of wheel wear: A-Attritious wear, B-Grain fracture, C-Bond fracture (Malkin and Cook, 1971)	2.49
2.3.7	Attritious wear on (a) An electroplated diamond grit (Hwang et al., 2000), (b) A brazed cBN grit (Bhaduri et al., 2011a)	2.49
2.3.8	Schematic diagram showing wheel-workpiece-chip interactions in: (a) Brazed wheel, (b) Electroplated wheel (Ghosh and Chattopadhyay, 2007a)	2.50
2.3.9	Various grain failures in a single-layer electroplated wheel: (a) Grit pull-out, (b) Breakage at bond level, (c) Fracture above bond level, (d) Micro-fracture at the tip (Bhaduri et al., 2011b)	2.51
2.4.1	Comparison of microstructures of (a) Eqiaxed, (b) Directionally solidified, (c) Single crystal superalloys (Rolls Royce plc., 1992)	2.52
2.4.2	Development of various nickel based superalloys over a period of ~70 years (Reed, 2006)	2.54
2.4.3	Material usage and corresponding aeroengine temperatures (Soo et al., 2011a)	2.55
2.4.4	(a) Profiled cBN grinding points, (b) Machining of one side of the blade root slot (Soo et al., 2002)	2.56
2.4.5	SEM micrographs of grain pull out from a B91 cBN wheel (Aspinwall et al., 2007)	2.56
2.5.1	Microstructures of Ti-47Al-3.7(Nb, Cr, Mn, Si)-0.5B (at.%): (a) Coarse near lamellar microstructure of the ingot, (b) Equiaxed, T = 1300°C, (c) Duplex, T = 1340°C, (d) Near-lamellar microstructure, T = 1360°C (Apple et al., 2000)	2.58
2.5.2	A γ-TiAl made turbocharger for a passenger vehicle (Tetsui, 1999)	2.59
2.5.3	Cross-sectional microstructures of γ-TiAl surfaces (Hood et al., 2007b)	2.60
2.6.1	Surface damages following machining: (a) BUE, (b) Grooves and cracks, (c) Side flow, (d) Tearing generated by broken carbide particles (Zhou et al., 2012)	2.62
2.6.2	Various surface damages when drilling CFRP: (a) Delamination, (b) Edge chipping/fracture, (c) Fuzzing and spalling (Shyha et al., 2009)	2.63
3.1.1	Microstructure of (a) Inconel 718, and (b) CMSX-4 workpiece material	3.1

3.1.2	EDX area mapping and spot analysis of etched Inconel 718 sample confirming the presence of different compositions	3.2
3.1.3	(a) Microstructure of gamma titanium aluminide, (b) Regions for spot EDX analysis, (c) EDX data obtained for spectrum 1, (d) EDX data obtained for spectrum 2	3.3
3.2.1	Conventional abrasive wheels (a) SiC (GC601J45VKRNN), (b) VORTEX Al_2O_3 (IPA60EH20VTX), and (c) POROS2 (25A601I74VPMCNN)	3.4
3.2.2	(a) Electroplated diamond superabrasive wheel, (b) Distribution of diamond grits on the wheel surface	3.5
3.3.1	Bridgeport FGC1000 flexible grinding centre	3.6
3.3.2	(a) Diamond roller dresser, (b) Arrangement of cooling and cleaning jet nozzles	3.6
3.3.3	(a) Flexiskills Ltd. 250 W ultrasonic generator, (b) 20 kHz ultrasonic transducer-booster-horn assembly	3.7
3.3.4	(a) Top view of the table sonotrode, (b) Rear view	3.8
3.3.5	Ultrasonic system with workpiece mounted on the table sonotrode	3.8
3.3.6	Response curves during tuning of the transducer (a) Without load, (b) With load	3.9
3.3.7	Screenshot of ultrasonic parameter control settings in LABVIEW software	3.9
3.3.8	Kerry 150 W ultrasonic generator	3.10
3.3.9	Photographic view of Taylor Hobson Form Talysurf 120L	3.11
3.3.10	(a) Buehler mould mounting equipment, (b) Buehler grinder-polisher	3.12
3.3.11	Mitutoyo HM-124 microhardness tester	3.13
3.3.12	(a) Leica DMLM microscope, (b) JEOL 6060 scanning electron microscope	3.14
3.4.1	On-machine configuration of workpiece-horn-booster-transducer assembly (a) Front view, (b) Top view	3.15
3.4.2	(a) On-machine configuration of wheel-workpiece-sonotrode assembly, (b) Clamping arrangement of workpiece and dummy	3.16
3.4.3	On-machine configuration of wheel-dressing tool-dynamometer assembly	3.18
3.4.4	Set-up for (a) Phase 2B, (b) Phase 2C	3.20

3.4.5	(a) CMSX-4 workpiece clamped on to the block sonotrode (b) On-machine configuration	3.21
3.4.6	Set-up for UAG of γ-TiAl trials with SiC wheel	3.24
3.4.7	Set-up for UAG of γ-TiAl with electroplated D252 diamond wheel	3.25
4.1.1	Force traces when grinding (a) Without and (b) With ultrasonic vibration	4.1
4.1.2	Forces due to ultrasonic vibration (zero load) at varying amplitude levels	4.2
4.1.3	Maximum forces recorded during grinding of Inconel 718	4.3
4.1.4	Radial wheel wear and corresponding G-ratio of VORTEX 80 mesh wheel	4.3
4.1.5	Images of workpiece surfaces ground at a depth of cut of 0.5 mm	4.4
4.1.6	A typical 2D surface profile showing the depth of deformation	4.4
4.1.7	Images of workpiece surfaces ground at depths of cut of (a) 1.0 mm and (b) 1.5 mm	4.5
4.1.8	SEM micrographs of Inconel 718 workpiece ground at a depth of cut of 1.0 mm without vibration (Test 7) at (a) Start of cut, (b) End of cut	4.5
4.1.9	Maximum dressing forces recorded when dressing with single point PCD insert	4.6
4.1.10	Average dressing forces recorded when dressing with single point PCD insert	4.7
4.1.11	Average grinding forces following dressing with roller dresser and single point PCD dressing tool	4.8
4.1.12	Influence of dressing operation on ground workpiece surface roughness	4.9
4.1.13	Optical micrographs of ground surfaces following conventional dressing (without ultrasonic vibration) under dry environment	4.9
4.1.14	SEM micrographs of ground surfaces following (a) and (b) Conventional dressing under wet environment, (c) and (d) Ultrasonic assisted dressing under wet environment	4.10
4.1.15	Wear of PCD insert following dressing	4.10
4.1.16	Condition of grinding wheel surface following (a) Wet conventional dressing (Test 1), (b) Wet ultrasonic assisted dressing (Test 3)	4.11
4.2.1	Ground Inconel 718 workpieces showing depression marks at various operating conditions: (a) Tests 1 and 2, (b) Tests 3 to 6	4.12
4.2.2	Ground Inconel 718 workpieces showing depression marks as well as damage-free surfaces in: (a) Tests 8 and 9, (b) Tests 10 and 11	4.12

4.2.3	Ground Inconel 718 workpieces showing depression marks as well as damage-free surfaces in: (a) Tests 12 to 15, (b) Tests 16 and 17	4.13
4.2.4	Ground Inconel 718 workpieces showing depression marks as well as damage-free surfaces in: (a) Tests 18 to 21, (b) Tests 22 to 24	4.14
4.2.5	Grinding force graphs obtained in (a) Test 11: V_C=30 m/s, V_W=200 mm/min, a_e=1.5 mm, Pressure=15 bar (b) Test 21: V_C=40 m/s, V_W=400 mm/min, a_e=1.0 mm, Pressure=28 bar	4.15
4.2.6	Vertical (F_v) and horizontal (F_h) forces under different grinding conditions	4.16
4.2.7	Main effects and interaction plots for vertical grinding force	4.17
4.2.8	Main effects and interaction plots for horizontal grinding force	4.18
4.2.9	Typical force traces when grinding at V_C=35 m/s, V_W=200 mm/min, a_e=1 mm, (a) Without and (b) With ultrasonic vibration	4.19
4.2.10	Radial wheel wear and G-ratio under different grinding conditions	4.20
4.2.11	Main effects and interaction plots for wheel G-ratio	4.20
4.2.12	Images of Inconel 718 workpiece surfaces ground at different operating conditions	4.21
4.2.13	Representative 3D topographies of ground surfaces produced (a) With ultrasonics and (b) Without ultrasonics	4.22
4.2.14	Surface roughness (R_a) of ground Inconel 718 workpiece surfaces	4.22
4.2.15	Main effects and interaction plots for 2D surface roughness (R_a) of ground workpieces	4.23
4.2.16	3D topographical parameters of ground Inconel 718 workpiece surfaces	4.24
4.2.17	SEM micrographs of ground workpiece surfaces (a) Test 3: V_C=30 m/s, V_W=250 mm/min, US OFF, (b) Test 4: V_C=30 m/s, V_W=250 mm/min, US ON, (c) Test 10: V_C=35 m/s, V_W=250 mm/min, US ON	4.25
4.2.18	Presence of NbC on the ground surface	4.26
4.2.19	Typical 3D topographies of wheel surfaces measured from graphite replicas (negative) following grinding (a) With ultrasonics and (b) Without ultrasonics	4.27
4.2.20	Surface topography parameters (2D and 3D) from graphite (negative) replicas of the grinding wheel	4.27
4.2.21	Main effects and interaction plots for 2D surface roughness (R_a) of graphite (negative) replicas of the grinding wheel	4.28

4.2.22	Typical 3D topographies of wheel surfaces measured from resin replicas (positive) following grinding; (a) With ultrasonics (b) Without ultrasonics	4.29
4.2.23	3D topographical parameters of resin (positive) replicas of the grinding wheel	4.29
4.2.24	Main effects and interaction plots for 3D surface parameter (S_a) of resin (positive) replicas of the grinding wheel	4.30
4.2.25	Main effects and interaction plots for 3D surface parameter (S_{ds}) of resin (positive) replicas of the grinding wheel	4.31
4.2.26	SEM micrographs of selected wheel surface resin replicas following (a) Roller dressing, (b) Test 5:V_C=30 m/s, V_W=300 mm/min, US OFF, (c) Test 6:V_C=30 m/s, V_W=300 mm/min, US ON	4.32
4.2.27	Microhardness depth profile of Inconel 718 samples ground at V_W=200 mm/min; measurements taken along transverse feed direction	4.33
4.2.28	Microhardness depth profile of Inconel 718 samples ground at V_W=200 mm/min; measurements taken along longitudinal feed direction	4.33
4.2.29	Microstructure of Inconel 718 on longitudinal feed plane showing deformation/bending of grains (Test 7)	4.34
4.2.30	Microstructures of Inconel 718 on transverse feed plane ground at V_C = 35 m/s, V_W = 200 mm/min, d = 1.0 mm, (a) US OFF, (b) US ON	4.34
4.2.31	Vertical (F_v) and horizontal (F_h) forces under different grinding conditions	4.36
4.2.32	Main effects and interaction plots for vertical grinding force	4.37
4.2.33	Main effects and interaction effects plots for horizontal grinding force	4.38
4.2.34	Radial wheel wear and G-ratio under different grinding conditions	4.39
4.2.35	Main effects and interaction plots for wheel G-ratio	4.40
4.2.36	Images of Inconel 718 workpiece surfaces ground at different operating conditions	4.41
4.2.37	2D roughness parameter (R_a) of ground Inconel 718 workpiece surfaces	4.42
4.2.38	Main effects and interaction plots for 2D roughness (R_a) of ground workpieces	4.42
4.2.39	SEM micrographs of ground workpiece surfaces (a) Test 5: V_C=30 m/s, V_W=300 mm/min, US OFF, (b) Test 17: V_C=40 m/s, V_W=300 mm/min, US OFF, (c) Test 6: V_C=30 m/s, V_W=300 mm/min, US ON, (d) Test 12: V_C=35 m/s, V_W=300 mm/min, US ON	4.43

4.2.40	2D and 3D surface parameters of graphite (negative) replicas of grinding wheel	4.44
4.2.41	Main effects and interaction plots for 2D surface roughness (R_a) of graphite (negative) replicas of the grinding wheel	4.45
4.2.42	3D topographical parameters of resin (positive) replicas of VORTEX wheel	4.46
4.2.43	Main effects and interaction plots for 3D surface parameter (S_a) of resin (positive) replicas of the VORTEX wheel	4.47
4.2.44	Main effects and interaction effects plots for 3D surface parameter (S_{ds}) of resin (positive) replicas of the VORTEX wheel	4.47
4.2.45	SEM micrographs of (a) VORTEX wheel surface (Anon. 2005), (b) wheel resin replicas taken after Test 13: V_C=40 m/s, V_W=200 mm/min, US OFF, (c) Test 17: V_C=40 m/s, V_W=300 mm/min, US OFF, (d) Test 18: V_C=40 m/s, V_W=300 mm/min, US ON	4.48
4.2.46	Microhardness depth profile of Inconel 718 samples ground at V_W=200 mm/min; measurements taken in transverse feed direction	4.49
4.2.47	Microhardness depth profile of Inconel 718 samples ground at V_W=200 mm/min; measurements taken in longitudinal feed direction	4.50
4.2.48	SEM micrographs of microstructures of Inconel 718 on (a) Transverse feed plane, (b) Longitudinal feed plane; ground at V_C = 40 m/s, V_W = 300 mm/min, d = 1.0 mm, US ON	4.50
4.2.49	Vertical (F_v) and horizontal (F_h) forces under different grinding conditions	4.52
4.2.50	Main effects and interaction plots for vertical grinding force	4.53
4.2.51	Main effects and interaction plots for horizontal grinding force	4.54
4.2.52	Radial wheel wear and G-ratio of the POROS2 wheel when grinding CMSX-4 under different operating conditions	4.55
4.2.53	Main effects and interaction plots for wheel G-ratio	4.56
4.2.54	Images of CMSX-4 workpiece surfaces ground at different operating conditions	4.57
4.2.55	2D roughness parameter (R_a) of ground CMSX-4 workpiece surfaces	4.57
4.2.56	3D topographical parameters of ground CMSX-4 workpiece surfaces	4.58
4.2.57	Main effects and interaction plots for 2D surface roughness (R_a) of ground CMSX-4 workpieces	4.59

4.2.58	SEM micrographs of ground workpiece surfaces (a) Test 3: V_C=30 m/s, V_W=400 mm/min, US OFF, (b) Test 7: V_C=30 m/s, V_W=600 mm/min, US OFF, (c) Test 4: V_C=30 m/s, V_W=400 mm/min, US ON, (d) Test 6: V_C=30 m/s, V_W=500 mm/min, US ON, (e) Test 8: V_C=30 m/s, V_W=600 mm/min, US ON, (f) Test 16: V_C=40 m/s, V_W=600 mm/min, US ON	4.60
4.2.59	2D and 3D surface parameters of graphite (negative) replicas of grinding wheel	4.61
4.2.60	Main effects and interaction plots for 2D surface roughness (R_a) of graphite (negative) replicas of the POROS2 wheel	4.62
4.2.61	3D topographical parameters of resin (positive) replicas of grinding wheel	4.63
4.2.62	Main effects and interaction plots for 3D surface parameter (S_a) of resin (positive) replicas of the POROS2 wheel	4.63
4.2.63	Main effects and interaction plots for 3D surface parameter (S_{ds}) of resin (positive) replicas of the POROS2 wheel	4.64
4.2.64	SEM micrographs of POROS2 wheel resin replicas taken after (a) Test 11: V_C=30 m/s, V_W=300 mm/min, US OFF, (b) Test 2: V_C=30 m/s, V_W=300 mm/min, US ON, (c) Test 7: V_C=30 m/s, V_W=600 mm/min, US OFF, (d) Test 10: V_C=40 m/s, V_W=300 mm/min, US ON	4.65
4.2.65	Microhardness depth profile of CMSX-4 samples ground at V_C=40m/s; measurements taken in the transverse feed direction	4.66
4.2.66	Microhardness depth profile of CMSX-4 samples ground at V_C=40m/s;measurements taken along longitudinal feed direction	4.67
4.2.67	Microstructure of CMSX-4 on longitudinal feed plane showing deformation/bending of γ’ phase	4.67
4.2.68	Microstructures of CMSX-4 on transverse feed plane ground at V_C = 30 m/s, V_W = 400 mm/min, d = 1.0 mm, (a) US OFF, (b) US ON	4.68
4.2.69	Microstructure of CMSX-4 on transverse feed plane showing typical grit marks	4.68
4.2.70	Vertical (F_v) and horizontal (F_h) forces under different grinding conditions	4.70
4.2.71	Main effects and interaction plots for vertical grinding force	4.71
4.2.72	Grinding power measured under conventional and ultrasonic assisted conditions	4.72
4.2.73	Grinding forces measured when conventional and ultrasonic assisted grinding with varying amplitude of vibration	4.73

4.2.74	Radial wheel wear and G-ratio under different grinding conditions	4.74
4.2.75	Main effects and interaction plots for wheel G-ratio	4.74
4.2.76	Images of Inconel 718 workpiece surfaces ground at different operating conditions	4.75
4.2.77	Surface roughness (R_a) of ground Inconel 718 workpieces	4.75
4.2.78	3D topographical parameters of ground Inconel 718 workpiece surfaces	4.76
4.2.79	SEM micrographs of ground workpiece surfaces (a) Test 9: V_C=30 m/s, V_W=300 mm/min, US OFF, (b) Test 17: V_C=40 m/s, V_W=300 mm/min, US OFF, (c) Test 6: V_C=30 m/s, V_W=300 mm/min, US ON, (d) Test 12: V_C=35 m/s, V_W=300 mm/min, US ON	4.77
4.2.80	Surface topography parameters (2D and 3D) from graphite (negative) replicas of the grinding wheel	4.78
4.2.81	3D topographical parameters of resin (positive) replicas of grinding wheel	4.78
4.2.82	SEM micrographs of POROS2 wheel surface following: (a) Roller dressing, (b) Grinding without vibration, (c) With vibration at 'High' amplitude, (d) With vibration at 'Low' amplitude	4.80
4.2.83	Microhardness depth profile of Inconel 718 samples ground at a_e=1.0 mm; measurements taken in the transverse feed plane	4.81
4.2.84	Microhardness depth profile of Inconel 718 samples ground at a_e=0.5 mm; measurements taken in the transverse feed plane	4.81
4.2.85	Microstructure of Inconel 718 on longitudinal feed plane showing elongation/deformation of grains	4.82
4.2.86	Microstructure of Inconel 718 on transverse feed plane showing typical grit marks	4.82
4.3.1	Vertical (F_v) and horizontal (F_h) forces under different grinding conditions	4.84
4.3.2	Main effects and interaction effects plots for vertical grinding force	4.85
4.3.3	SEM micrographs of ground γ-TiAl surface at (a) Test 1: V_C = 15 m/s, V_W = 150 mm/min, d = 1.0 mm, US OFF, (b) Test 5: V_C = 30 m/s, V_W = 150 mm/min, d = 1.0 mm, US OFF	4.86
4.3.4	Main effects and interaction plots for horizontal grinding force	4.87
4.3.5	Radial wheel wear and G-ratio under different grinding conditions	4.88
4.3.6	Main effects and interaction effects plots for wheel G-ratio	4.89
4.3.7	Photographic views of ground γ-TiAl workpiece surfaces	4.90

4.3.8	SEM micrographs of ground γ-TiAl surface at (a) and (b) Test 5: V_C = 15 m/s, V_W = 150 mm/min, d = 1.0 mm, US OFF, (c) Test 4: V_C = 15 m/s, V_W = 600 mm/min, d = 1.0 mm, US ON, (d) Test 6: V_C = 30 m/s, V_W = 150 mm/min, d = 1.0 mm, US ON	4.91
4.3.9	2D roughness parameter (R_a) of ground γ-TiAl workpiece surfaces	4.92
4.3.10	3D topographical parameters of ground γ-TiAl workpiece surfaces	4.92
4.3.11	Main effects and interaction plots for 2D surface roughness (R_a) of ground γ-TiAl workpieces	4.93
4.3.12	3D surface parameters of graphite (negative) replicas of SiC wheel	4.95
4.3.13	Main effects and interaction plots for 3D surface roughness (S_a) of graphite (negative) replicas of the SiC wheel	4.95
4.3.14	3D topographical parameters of resin (positive) replicas of SiC wheel	4.96
4.3.15	Main effects and interaction plots for 3D surface parameter (S_a) of resin (positive) replicas of the SiC wheel	4.97
4.3.16	Main effects and interaction plots for 3D surface parameter (S_{ds}) of resin (positive) replicas of the SiC wheel	4.97
4.3.17	SEM micrographs of selected wheel surface resin replicas: (a) After roller dressing, (b) Grinding at V_C=30 m/s, V_W=150 mm/min, US OFF, (c) Grinding at V_C=30 m/s, V_W=150 mm/min, US ON, (d) Micro-fracture at cleavage planes of grains subject to vibration	4.98
4.3.18	Microhardness depth profile of γ-TiAl samples ground at V_C=30m/s; measurements taken in the transverse feed direction	4.99
4.3.19	Microhardness depth profile of γ-TiAl samples ground at V_C=30m/s; measurements taken in the longitudinal feed direction	4.100
4.3.20	SEM micrograph of the microstructure of γ-TiAl in the longitudinal feed plane showing deformation/bending of lamellae (ground at V_C = 15 m/s, V_W = 150 mm/min, d = 1.0 mm, US ON)	4.101
4.3.21	Microstructures of γ-TiAl samples on (a), (b) Transverse feed planes, (c), (d) Longitudinal feed planes	4.102
4.3.22	Vertical (F_v) and horizontal (F_h) forces under different grinding conditions	4.104
4.3.23	Radial wheel wear and G-ratio under different grinding conditions	4.106
4.3.24	Optical micrographs of wheel surfaces following grinding at (a)V_C=30 m/s, V_W=150 mm/min, US OFF, (b) V_C=30 m/s, V_W=150 mm/min, US ON	4.107
4.3.25	Images of the ground γ-TiAl workpiece surfaces	4.108

4.3.26	Surface roughness parameter (R_a) of ground γ-TiAl workpiece surfaces	4.109
4.3.27	3D topographical parameters of ground γ-TiAl workpiece surfaces	4.109
4.3.28	SEM micrographs of ground γ-TiAl surface at (a) Test 1: V_C = 30 m/s, V_W = 150 mm/min, d = 1.0 mm, US OFF, (b) Test 3: V_C = 30 m/s, V_W = 150 mm/min, d = 1.0 mm, US OFF	4.110
4.3.29	SEM micrographs of ground γ-TiAl surface at (a) and (b) Test 2: V_C = 30 m/s, V_W = 150 mm/min, d = 1.0 mm, US ON, (c) Test 5: V_C = 40 m/s, V_W = 600 mm/min, d = 1.0 mm, US OFF, (d) Test 6: V_C = 40 m/s, V_W = 600 mm/min, d = 1.0 mm, US ON	4.111
4.3.30	2D and 3D surface parameters of graphite (negative) replicas of EP D252 wheel	4.112
4.3.31	Microhardness depth profile of γ-TiAl samples after 1st and 2nd pass; measurements taken in the longitudinal feed direction	4.113
4.3.32	Microhardness depth profile of γ-TiAl samples after 5th and 6th pass; measurements taken in the longitudinal feed direction	4.113
4.3.33	Microstructure of γ-TiAl on the transverse feed plane: (a) After 1st pass, (b) After 6th pass	4.114
4.3.34	Microstructure of γ-TiAl on the longitudinal feed plane showing deformation/bending of lamellae	4.114

LIST OF TABLES

Table No.	Description	Page No.
2.5.1	Comparison of properties of γ-TiAl with other materials (Dimiduk, 1999, Hood, 2010, Sharman et al., 2001b)	2.59
2.6.1	Different levels of surface integrity (SI) data set (Field et al., 1972)	2.61
3.1.1	Elemental compositions (% weight) of nickel based superalloys under investigation	3.1
3.2.1	Grinding wheels and corresponding workpiece materials employed in different experimental phases	3.5
3.3.1	Grinding and polishing conditions for Inconel 718 and CMSX-4 workpieces	3.12
3.3.2	Grinding and polishing conditions for γ-TiAl workpieces	3.13
3.4.1	List of trials carried out in Phase 1B	3.16
3.4.2	List of trials carried out in Phase 1C	3.17
3.4.3	List of trials carried out in Phase 2A	3.19
3.4.4	Full factorial experimental array used in Phase 2B and 2C	3.20
3.4.5	Full factorial experimental array used in Phase 2D	3.22
3.4.6	Full factorial experimental array used in Phase 2E	3.23
3.4.7	Full factorial experimental array used in Phase 3A	3.23
3.4.8	Full factorial experimental array used in Phase 3B	3.24
4.1.1	Grinding forces recorded without and with ultrasonic assistance	4.1
4.2.1	Percentage contribution ratios of factors with respect to different response measures (Phase 2B)	4.18
4.2.2	Percentage contribution ratios of factors with respect to different response measures (Phase 2C)	4.38
4.2.3	Percentage contribution ratios of factors with respect to different response measures (Phase 2D)	4.54
4.2.4	Percentage contribution ratios of factors with respect to different response measures (Phase 2E)	4.72
4.3.1	Percentage contribution ratios of factors with respect to different response measures (Phase 3A)	4.86

LIST OF NOMENCLATURES

2D	Two dimensional
3D	Three dimensional
A	Amplitude of vibration (μm)
a_e	Wheel depth of cut (mm)
Al_2O_3	Aluminium oxide
ANOVA	Analysis of Variance
BUE	Built-up edge
BuRTi	Burn resistant titanium
c	Active cutting point density (number/mm^2)
cBN	Cubic boron nitride
CFG	Creep feed grinding
D	Grinding wheel diameter (mm)
EDM	Electro discharge machining
EDX	Energy dispersive X-ray spectroscopy
EP	Electroplated
EUAG	Elliptical ultrasonic assisted grinding
F_h	Horizontal component of grinding force (N)
F_v	Vertical component of grinding force (N)
G-ratio	Grinding ratio
h	Convective heat transfer coefficient
HAZ	Heat affected zone
$HK_{0.025}$	Knoop hardness at 25 g load
h_m	Undeformed chip thickness (mm)
HSM	High speed machining
H_w	Brinell hardness
K	Thermal conductivity of the workpiece material
l_g	Contact length
MRR	Material removal rate
PCD	Polycrystalline diamond
PCR	Percentage contribution ratio
Q	Volume rate of work material removed (mm^3/s)

q	Heat flux applied by the source
R_a	Roughness parameter, arithmetic mean deviation of the assessed profile (µm)
R_t	Roughness parameter, total height of the profile in the evaluation length (µm)
R_z	Roughness parameter, ten point height of the roughness profile (µm)
S_a	Areal surface parameter, arithmetic mean deviation of the surface (µm)
S_{ds}	Areal surface parameter, density of summits of the surface (peaks/mm^2)
SEM	Scanning electron microscopy
SiC	Silicon carbide
S_p	Areal surface parameter, maximum surface summit height (µm)
S_{sk}	Areal surface parameter, skewness of the surface
S_t	Areal surface parameter, total height of the surface (µm)
S_v	Areal surface parameter, maximum surface valley depth (µm)
S_z	Areal surface parameter, ten point height of the surface (µm)
T	Workpiece temperature in creep feed grinding
TDUAG	Two dimensional ultrasonic assisted grinding
UAD	Ultrasonic assisted dressing
UAG	Ultrasonic assisted grinding
UAT	Ultrasonic assisted turning
USM	Ultrasonic machining
v	Volume of work material dislodged per impact (mm^3)
V_C	Wheel speed (m/s)
V_W	Table feed (mm/min)
XRD	X-Ray diffraction
α	Semi-included angle for the undeformed chip cross-section (degree)
γ	Gamma phase
γ'	Gamma prime precipitate
γ''	Gamma double prime precipitate
δ	Delta phase
κ	Thermal diffusivity of the workpiece material
λ	Ratio of the flow stress developed in the tool to that in the workpiece
μ	Proportional constant
ν	Frequency (number of cycles per unit time) (kHz)

1. INTRODUCTION

1.1 Background to the project

Grinding of advanced aerospace materials such as nickel based superalloys and titanium alloys is a key production process in the manufacture of turbine and compressor blades and discs, nozzle guide vanes etc. The operation can however cause adverse workpiece surface integrity issues such as the generation of a heat affected zone (HAZ), cracks (Hood et al., 2007b), laps, tears and thermal fatigue problems due in-part to workpiece material properties such as low thermal conductivity, chemical reactivity and a greater tendency for built-up-edge (BUE) formation at elevated cutting temperatures etc (Ezugwu et al., 1999). In addition, abrasive wheel loading and inefficient fluid delivery due to a characteristic air barrier operating around the grinding wheel, can significantly reduce productivity and increase costs.

The use of ultrasonic vibration (~20 kHz frequency) during cutting to aid machinability has been known since the 1950's (Balamuth, 1966). Ultrasonic machining (USM) has been routinely combined in a hybrid arrangement with conventional metal removal processes such as turning, drilling, milling, broaching as well as non-conventional machining operations such as electro discharge machining (EDM) and wire electro discharge machining (WEDM) etc. Some of the earliest work relating to ultrasonic assisted grinding (UAG) dates back to the mid-1950's and highlighted benefits in terms of reduced grinding temperature and workpiece residual stresses (Colwell, 1956). Despite comprehensive research on UAG of various workpiece materials such as ceramics, glass, alloyed steel etc over the past ~60 years, work on UAG of nickel based superalloys such as Inconel 718 (typically used for turbine discs) and advanced titanium alloys such as gamma titanium aluminide (γ-TiAl) is extremely limited. Additionally, UAG has been mainly associated with surface grinding configurations with the depth of cut typically limited to ≤0.3 mm (Tawakoli et al., 2009a), relatively few papers have reported UAG in creep feed mode with the depth of cut ≥1 mm. The majority of published work has disclosed results relating to grinding force, wheel wear (G-ratio) and workpiece surface roughness, with minimal details of surface integrity issues such as microhardness and microstructure (for locating recast layer, HAZ, crack, lap, tear etc). There is also little or no information available on the effects of ultrasonic vibration on the abrasive grains. These suggest that there is substantial scope and potential for investigating the effects of ultrasonic vibration in creep feed grinding of nickel based superalloys etc with regard to grinding productivity, wheel wear, cutting forces, workpiece surface roughness and integrity.

The use of ultrasonic vibration in dressing of grinding wheels has been recently cited with benefits reported such as a reduction in subsequent grinding forces (Tawakoli et al., 2011). However this area of research has also potential for further/in-depth work to determine the effects of vibration on wheel wear and ground workpiece surface roughness following dressing etc.

1.2 Aims and objectives of the project

The overall aim of the project was to develop a 'hybrid' process involving ultrasonic vibration of the workpiece material when creep feed grinding (CFG) of advanced aeroengine alloys, in particular two nickel based superalloys (Inconel 718 and CMSX-4) and a γ-TiAl. The effects of ultrasonic assistance were investigated on grinding forces, radial wheel wear (G-ratio), workpiece surface topography/quality and grinding wheel surface topography. It was also intended to research ultrasonic assisted dressing of conventional wheels to evaluate the effects of vibration on dressing as well as grinding forces, workpiece surface roughness etc. Specific objectives were to:

- Carry out a comprehensive literature review of ultrasonic assisted machining operations with particular emphasis on grinding and dressing.
- Undertake preliminary feasibility study on ultrasonic assisted grinding of Inconel 718 using an ultrasonic system involving a conical horn.
- Undertake a preliminary feasibility study on UAG of Inconel 718 using an ultrasonic system involving a specially designed table sonotrode.
- Identify appropriate creep feed grinding parameters (wheel velocity, feed rate, depth of cut and cutting fluid pressure) for mainstream UAG trials.
- Undertake mainstream UAG experiments on Inconel 718 and CMSX-4 with conventional abrasive grinding wheels (alumina and silicon carbide) involving full factorial experimental designs using the table sonotrode-ultrasonic system and evaluate the effects of process parameters (wheel velocity, feed rate, depth of cut, the presence of vibration as well as amplitude of vibration) on grinding forces, radial wheel wear (G-ratio), 2D and 3D surface parameters of the ground workpieces as well as graphite and resin replicas of post-grinding wheel surfaces together with workpiece microhardness and microstructure.
- Undertake UAG of γ-TiAl with conventional (silicon carbide) as well as single layer superabrasive (electroplated diamond) wheels using the table sonotrode-ultrasonic system and investigate the effects of wheel velocity, feed rate and presence of

vibration on grinding forces, radial wheel wear (G-ratio), the surface parameters of ground workpieces as well as graphite and resin replicas of wheel surfaces together with the workpiece microhardness and microstructure.

- Carry out ultrasonic assisted dressing of a conventional grinding wheel (silicon carbide) with a single point diamond (PCD) dresser and study the effects of vibration and cutting fluid on dressing and grinding forces, ground workpiece surface roughness and quality.

1.3 Industrial collaborators and funding

The project involved four collaborating companies:

- Rolls Royce plc supplied CMSX-4 and γ-TiAl workpiece materials together with financial support of £60,000.
- Hardinge-Bridgeport provided a Bridgeport FGC1000 flexible grinding centre.
- Saint-Gobain Abrasives supplied conventional (alumina and silicon carbide) and superabrasive (electroplated diamond) grinding wheels.
- Element Six (E6) supplied diamond grit material to Saint-Gobain to produce the superabrasive grinding wheel.
- In addition, the School of Mechanical Engineering, University of Birmingham, UK awarded a scholarship of £38,400 which covered the cost of tuition fees over a 3 year period.

Details of company contacts etc can be found in Appendix A1.

2. LITERATURE REVIEW

2.1 Ultrasonic machining (USM)

2.1.1 Introduction

The use of ultrasonic actuation to aid material removal was first proposed in a paper by R.W. Wood and Alfred L. Loomis in 1927 (Wood and Loomis, 1927, Neppiras, 1956), where glass plates were etched and drilled rapidly by using strong ultrasonic vibration of glass rod tools in an oil bath. About ten years later, Kinoshita and Yoshioka also succeeded in engraving glass by transmitting ultrasonic waves through an oil medium via a small glass rod bonded to one end of a steel rod which in turn was fixed to a conical horn (Nishimura et al., 1954). One of the first patents in this area was issued to Lewis Balamuth in 1945 (Balamuth, 1945), since when the technology has been variously termed as 'ultrasonic machining' (USM), 'impact grinding' or 'slurry drilling' (Graff, 1975). By the early 1950's ultrasonic machining began to emerge as one of the prominent industrial applications of ultrasonics, especially in the USA, Japan and England (Nishimura et al., 1954).

The basic USM process (also known as conventional USM according to Neppiras (1972)) utilises the imposition of high frequency vibration (≥ 20 kHz) on cutting tools (Astashev et al., 2009) with an amplitude of 5-50 μm. The tool is generally fed towards the workpieces by a controlled static uniform force, while the small gap between the tool and the work surface is flushed with a continuous flow of abrasive slurry comprising a mixture of abrasive material such as silicon carbide or boron carbide etc suspended in water or oil (Thoe et al., 1998). Figure 2.1.1 shows the basic elements of an USM set up using either a magnetostrictive or piezoelectric transducer with brazed and screwed tooling.

Historically, USM has mainly been associated with the machining of non-conductive hard but brittle materials (Singh and Khamba, 2006) such as inorganic glass, silicon nitride, and other engineering ceramics (Vogt, 2002) etc. Thoe and Aspinwall (1996) studied ultrasonic machining of hot isostatically pressed (HIPed) silicon nitride (Si_3N_4) and synthetic ruby with silver steel, diamond electroplated steel and SYNDITE polycrystalline diamond (PCD) tools operating in a boron carbide slurry. Higher tool wear occurred when machining Si_3N_4 with the silver steel and the diamond electroplated steel as compared to that with SYNDITE PCD. Ultrasonic drilling (USD) of alumina and alumina based engineering ceramics was carried out by Zhang et al. (2000) and Jadoun et al. (2009) respectively. The machining

mechanism of USD ceramics was modelled and the effect on material removal rate (MRR) measured. The test results were in accordance with the model and showed that an increase in any of the operating parameters such as amplitude of vibration, applied static load, rotational speed of the drilling tool and abrasive grit size, resulted in an increase in MRR (Zhang et al., 2000).

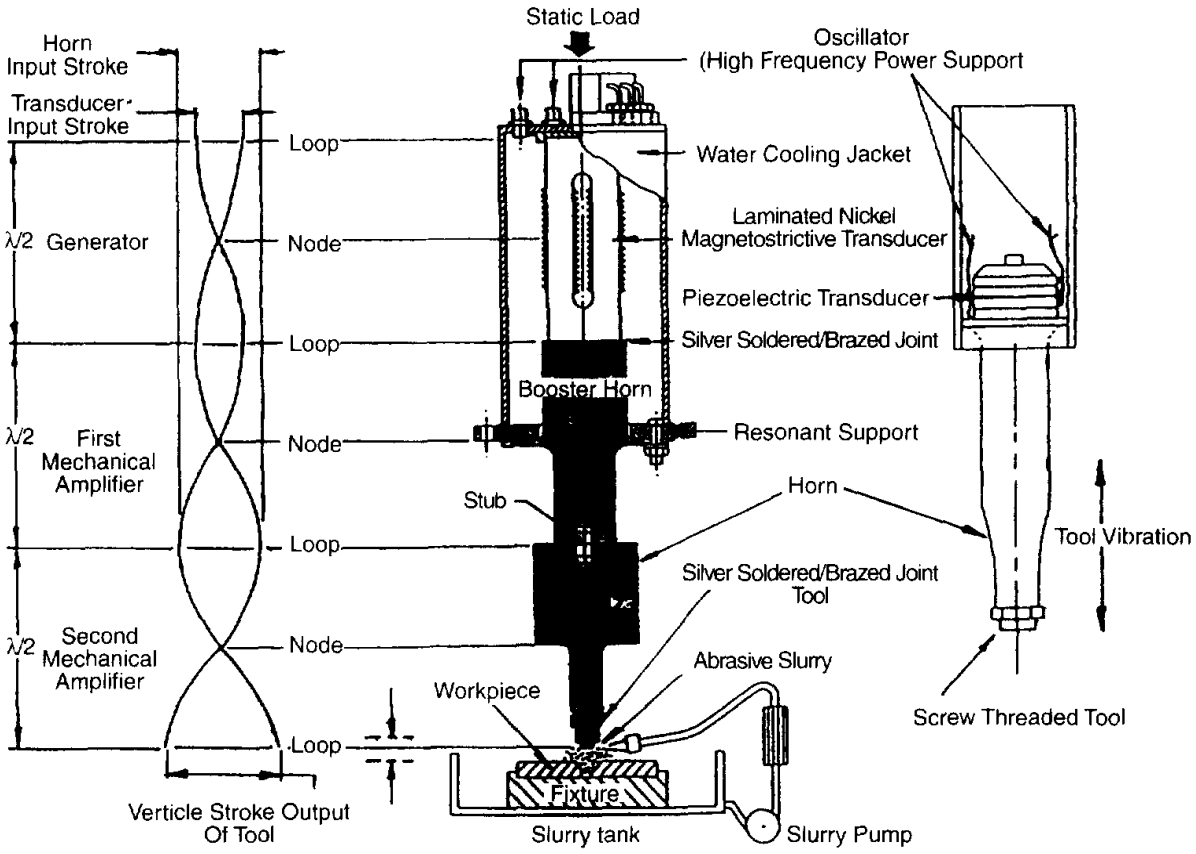
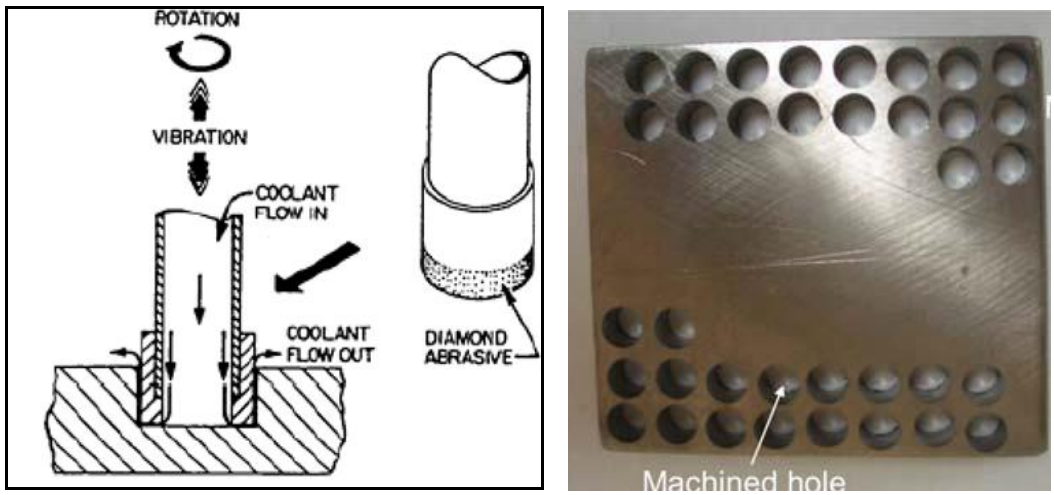


Fig. 2.1.1 Basic elements of USM head (Thoe et al., 1998)

Over the past ~15 years, research on USM has been further extended to machining metallic materials such as nickel/titanium alloys (Aspinwall et al., 2001a) and even ductile materials like aluminium and steel (Neugebauer and Stoll, 2004). In the former work, ultrasonic machining of gamma titanium aluminide (γ-TiAl) was undertaken using solid or hollow SYNDITE PCD tools to produce holes without causing excessive surface integrity damage albeit at the cost of extremely low productivity. A detailed study on the effects of machining variables and tool variables on rotary ultrasonic drilling of Ti-6Al-4V was carried out by Churi et al. (2006) and Churi et al. (2007) respectively. A schematic diagram of rotary ultrasonic machining is detailed in Fig. 2.1.2(a) while ultrasonically machined holes are shown in Fig. 2.1.2(b). Recent investigations on ultrasonic assisted drilling of aluminium alloys identified a 30-50% reduction in drilling force and moment (Neugebauer and Stoll, 2004). The work also revealed enhanced chip breakage and better chip removal.



(a) (b)

Fig. 2.1.2 (a) Schematic diagram of rotary ultrasonic machining, (b) Ultrasonically machined holes (Churi et al., 2007)

2.1.2 Mechanics of USM

Material removal mechanisms during USM are shown in Fig. 2.1.3 and are listed below (Ghosh and Mallik, 1985, Thoe et al., 1998):

1. Mechanical abrasion by direct hammering of the abrasive particles against the work surface (Shaw, 1956, Rozenberg et al., 1964);
2. Micro chipping by impact of the free moving abrasive particles (Rozenberg et al., 1964);
3. The erosion due to cavitation (Rozenberg et al., 1964, Kremer et al., 1981);
4. Chemical action associated with the fluid used (Shaw, 1956).

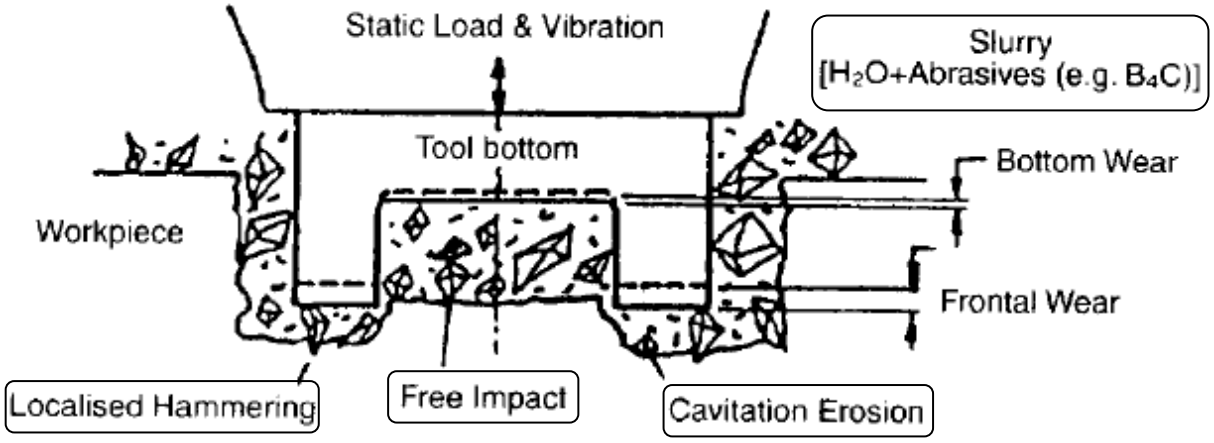


Fig. 2.1.3 Schematic representation of the material removal mechanisms in USM (Khairy, 1990)

A number of past researchers have tried to develop theories to predict the characteristics of USM. The model proposed by M.C. Shaw (1956) is generally well-accepted and despite its

limitations, explains the material removal process reasonably well. In this model, the direct impact of the tool on the grains in contact with the workpiece is taken into consideration as this is primarily responsible for the major portion of the material removal. The assumptions associated with this model are:

1. The rate of work material removal is proportional to the volume of work material per impact;
2. The rate of work material removal is proportional to the number of particles making impact per cycle;
3. The rate of work material removed is proportional to the frequency (number of cycles per unit time);
4. All impacts are identical;
5. All abrasive grains are identical and spherical in shape (however in reality their shapes are irregular).

Using the model, the rate of the volume of work material removed is expressed in Eqn. 2.1.

$$Q \propto v Z \nu \qquad \ldots 2.1$$

where,

Q: rate of the volume of work material removed (mm^3/s)

v: volume of work material dislodged per impact (mm^3)

Z: number of particles making impact per cycle

ν: frequency (number of cycles per unit time) (kHz)

The expression for Q can be further extended in terms of the known parameters as shown in Eqn. 2.2.

$$Q \propto \frac{A^{3/4} d^{1/4} F^{3/4} C^{1/4}}{H_w^{3/4}} \nu \qquad \ldots 2.2$$

where,

A: Amplitude of vibration of the tool (μm)

d: Mean diameter of the spherical abrasive grains (μm)

F: Mean static feed force applied to the tool (N)

C: Concentration of abrasive grains in the slurry (vol%)

H_w: Brinell hardness of the work material

Although Eqn. 2.2 indicates that the rate of material removal is proportional to $d^{1/4}$, it is actually proportional to d. This discrepancy between the theoretical prediction and the observed fact is due to the fact that the actual shape of an abrasive grain is not spherical, rather it has projections of average diameter d_1 which is observed to be proportional to the square of the nominal diameter of the grain (d).

$$d_1 = \mu d^2 \qquad \ldots 2.3$$

μ: proportional constant

Using the expression for d_1, Eqn. 2.2 can be reformulated as:

$$Q \propto \frac{dA^{3/4}F^{3/4}C^{1/4}}{H_w^{3/4}(1+\lambda)^{3/4}}\nu \qquad \ldots 2.4$$

where,

λ: Ratio of the flow stress developed in the tool to that in the workpiece

The model proposed by Shaw has a number of limitations. For example, it does not correctly predict the effects of variation of d, A, F and ν on MRR. In practice, MRR decreases after an increase in the above parameter values either due to excessive slurry concentration or crushing of abrasive grains under heavy load (Thoe et al., 1998).

2.1.3 Process parameters

The various process parameters which affect the USM process are:

1. Frequency of vibration;
2. Amplitude of vibration;
3. Static loading (feed force);
4. Hardness ratio of the tool and the workpiece;
5. Grain size;
6. Grain hardness
7. Abrasive slurry concentration.

Although according to Shaw (1956) MRR is directly proportional to the frequency of vibration (ν) (Eqn. 2.4), some past researchers have reported that at constant amplitude, MRR varied with a square of the frequency up to 400 Hz (Neppiras, 1956). With a further increase in frequency up to 5 kHz, a linear relation between MRR and frequency was found. Above an upper threshold value, the MRR fell off rapidly where MRR $\propto \nu^{1/2}$ (Neppiras and Foskett,

1957). Figure 2.1.4 shows theoretical and actual trends of MRR with the variation in frequency.

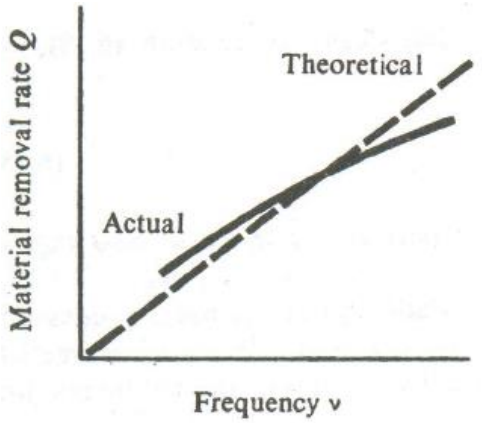


Fig. 2.1.4 Material removal characteristic with variation in frequency of vibration (Ghosh and Mallik, 1985)

With an increase in amplitude of vibration, MRR is expected to increase according to Eqn. 2.4, however the actual response is again somewhat different from the theoretically predicted one. The main discrepancy stems from the fact that the duration of penetration of the abrasive grains is calculated based on the average velocity of the particles which is quite different from their actual oscillatory velocity. Figure 2.1.5 shows that there exists an amplitude level at which MRR starts to decrease.

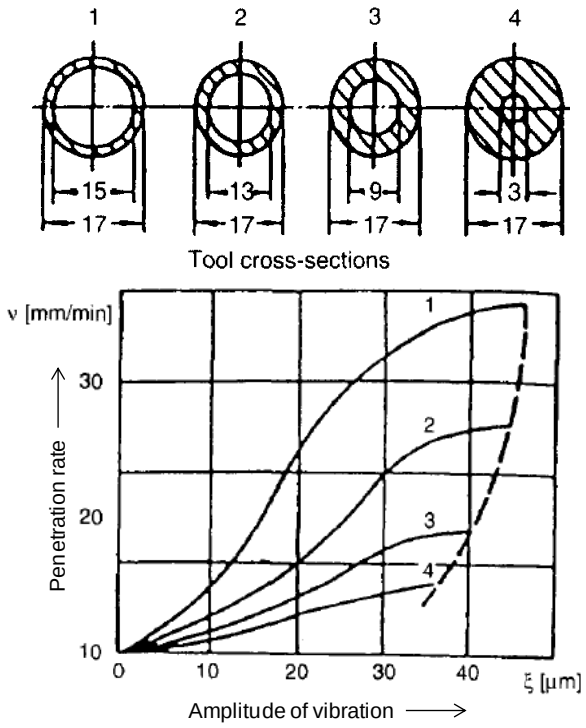


Fig. 2.1.5 Relationship between penetration rate and amplitude of vibration (Kazantsev, 1966)

An increase in static load leads to an increase in MRR, however in practice, beyond a critical value of force MRR decreases as the abrasive grains are crushed. The variation of MRR with feed force for different values of amplitude is detailed in Fig. 2.1.6(a). The ratio of workpiece hardness and tool hardness significantly affects MRR as shown in Fig. 2.1.6(b). Although USM can be used for both hard and soft workpiece materials, brittle materials are preferable (Neppiras, 1956). Hard materials are cut by brittle fracture as opposed to plastic shear in the case of softer ductile materials. In such cases, abrasive grits tend to embed themselves into the workpiece (Neppiras, 1964).

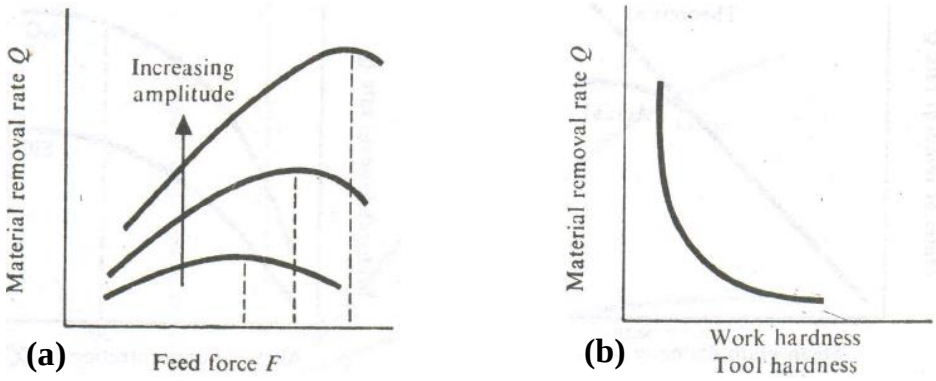


Fig. 2.1.6 Variation of MRR with (a) Feed force, (b) Work to tool hardness ratio (Ghosh and Mallik, 1985)

Equation 2.4 indicates that the MRR should proportionally increase with the mean grain diameter (d), however when d becomes too large and approaches the magnitude of amplitude A, the crushing tendency increases leading to a fall in MRR. The concentration of abrasive slurry directly controls the number of grains impacting per cycle as well as the magnitude of each impact. The variation in MRR with the slurry concentration is detailed in Fig. 2.1.7, which shows that MRR falls at concentrations above 30% (Neppiras, 1956, Pentland and Ektermanis, 1965). Apart from the foregoing process parameters, the physical properties of the fluid used for the slurry, such as viscosity, also affect the MRR. Past researches have reported a drop in the MRR with an increase in the viscosity (Ghosh and Mallik, 1985).

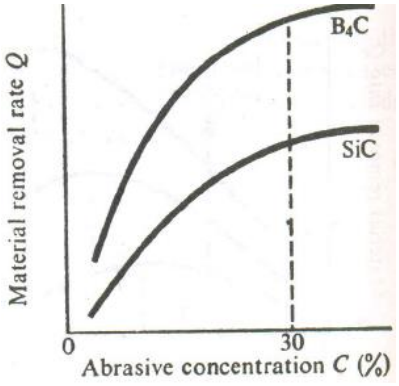


Fig. 2.1.7 Variation of MRR with abrasive concentration in slurry (Ghosh and Mallik, 1985)

Although MRR is the major factor in judging USM performance, tool wear and surface finish/integrity are also important response measures. Both tool wear and MRR increase when harder and coarser abrasives are used. Tool wear is also affected by the hardness as well as the toughness of the workpiece. Workpiece surface finish, on the other hand, depends mainly on the size of the abrasive grains. A decrease in the abrasive grain size during USM leads to lower R_a values with improved accuracy of the machined hole (Thoe et al., 1998).

2.1.4 Equipment/machine tools

The main elements of an ultrasonic machining unit are:

1. Acoustic head
2. Feeding unit
3. Tool/horn
4. Abrasive slurry and pump unit
5. Work table and body of the machine

The function of the acoustic head is to produce vibration in the tool. It consists of a generator for supplying a high frequency electric current, which is converted into a high frequency mechanical vibration with the help of a transducer. The acoustic head also comprises a concentrator to mechanically amplify the vibration while transmitting it to the tool. Traditionally, tuning of the horn and tool to the generator system was achieved by adjusting their dimensions to attain resonance. However, over the past ~15 years, resonance following generators have become available which automatically adjust the output frequency to match the exact resonant frequency of the horn/tool assembly (Thoe et al., 1998).

Transducers can be either magnetostrictive (Nishimura et al., 1954) made of laminated nickel sheets (Balamuth, 1966) or piezoelectric (Shaw, 1956) using ceramic elements sandwiched under compressive strain between metal plates. They vibrate in a longitudinal or transverse mode. Magnetostrictive transducers allow vibration to be transmitted over a wide range of frequency (e.g. 17-23 kHz for a 20 kHz generator). They also provide greater flexibility in the design of horns and can accommodate tool wear. Despite all these advantages, the major drawbacks of magnetostrictive transducers are their high electrical losses (e.g. eddy current loss) and low energy efficiency (~55%). These losses transform into heat, therefore the transducer has to be air/water cooled, which makes the transducer bulky. In contrast, the piezoelectric transducers are much smaller in size with high energy efficiencies (~90-96%) and they do not undergo heat damage, thus do not require any cooling. They also

appear to be more easily adaptable for rotary operations (Legge, 1966) and more easily constructed (Thoe et al., 1998).

The objective of the feed mechanism is to apply the working force during the machining operation. An instrument showing the movement of the tool indicates the depth achieved. The different types of feed mechanisms include counterweight, spring, pneumatic, hydraulic and motor type etc.

The tool in ultrasonic machining is generally made of a ductile metal. It should also possess high wear resistance, good elastic and fatigue strength properties and optimum level of toughness and hardness. Generally stainless steel and low carbon steels are used for making tools as they wear much less faster than aluminium and brass tools. Polycrystalline diamond (PCD) has also been introduced over the past ~20 years for the machining of hard work materials such as hot isostatically pressed silicon nitride (Thoe et al., 1995).

The most common abrasives are boron carbide (B_4C), silicon carbide (SiC), corundum (Al_2O_3), diamond, boron silicarbide etc. Boron carbide is the most common and efficient amongst the abrasives however it is expensive. Silicon carbide is used on glass, germanium and some ceramics, although it is 20-40% less efficient than B_4C in terms of the machining time. The cutting time for corundum is 3-4 times more than that for B_4C. Diamond dust is usually employed for cutting diamonds and rubies. Water is the most commonly used fluid in the slurry, however benzene, glycerol and oils are also utilised (Ghosh and Mallik, 1985).

Typical examples of ultrasonic machine manufacturers include DMG/Mori Seiki, Sonic-Mill, Chengdu Wolfni Technology Co. Ltd., Unitech Allied Automation with average price for small machining units ranging from ~$2000 to 12000.

2.2 Ultrasonic assisted machining

2.2.1 Introduction

The purpose of employing a hybrid machining process (HMP) is to make use of the mutually enhanced advantages of two or more complimentary cutting techniques and to reduce some of their individual adverse effects (Rajurkar et al., 1999). HMPs can be broadly classified under two categories, firstly, processes in which all constituent processes are directly involved in the material removal and secondly, those in which only one of the participating processes directly removes material while the others only assists in removal by changing conditions of machining in a ‘positive’ manner from the point of view of improving the capability of machining (Kozak and Rajurkar, 2000, Lauwers, 2011). Vibration (frequency

≤10 kHz) or ultrasonic (frequency ≥20 kHz) assisted machining falls under the latter category. Over the past ~60 years, conventional ultrasonic machining has been combined with other specialised machining operations, notably electrolytic erosion and spark erosion to gain the advantages of both techniques (Neppiras, 1964). Ultrasonic machining has been routinely coupled with EDM (Kremer et al., 1989, Kremer et al., 1991) and wire-EDM (Guo et al., 1997a, Guo et al., 1997b) in order to obtain improvements in productivity (Enache et al., 1990, Zhixin et al., 1997, Thoe et al., 1999, Lin et al., 2000, Chen and Lin, 2009), through enhanced removal of debris (Enache et al., 1990), and greater process stability (Thoe et al., 1999, Lin et al., 2000) while providing machined surface quality benefits (Chen and Lin, 2009) etc. The scope of ultrasonic assisted machining has been further expanded by combining it with conventional metal machining operations, such as turning (Sharman et al., 2001a), milling, shaping, broaching, grinding etc (Balamuth, 1966). It is also worth mentioning that there exist a number of instances where ultrasonic vibration has been employed in metal forming operations e.g. press forming, tube drawing (Buckley and Freeman, 1970), deep drawing (Jimma et al., 1998) etc., where the reduced friction exhibited faster operation with lower stress levels. Applications of industrial macrosonics can be further found in the areas of cleaning, plastic and metal welding, chemical processing (Neppiras, 1972) etc.

Turning and drilling are areas where ultrasonic assisted machining has seen widespread application over the past ~40 years. In ultrasonic assisted turning (UAT) vibration of the cutting tool (see Fig. 2.2.1) can be employed in the feed direction (Skelton, 1969), the direction of cutting velocity (or tangential direction) (Moriwaki and Shamoto, 1991) and in the radial direction.

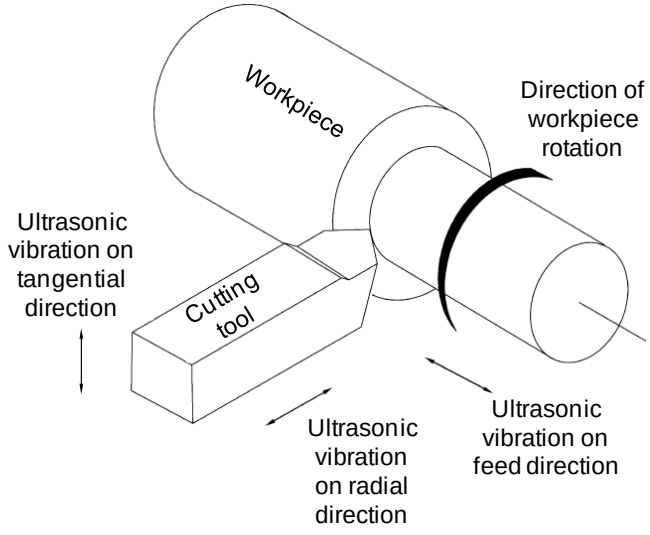


Fig. 2.2.1 Principal vibration directions during ultrasonically assisted turning (Babitsky et al., 2003)

Work involving ultrasonic assisted turning has highlighted improvements over conventional turning in terms of chip production, elimination of built-up edge (BUE), reduction in cutting forces together with improvement in tool life and surface finish. Skeleton (1969) reported a 20% reduction in the radial component of cutting force when ultrasonic vibration was used in the feed direction using a magnetostrictive transducer with a frequency and amplitude of 12.4 kHz and 25.4 μm respectively during turning of mild steel. The approach has been further modified by applying vibration simultaneously in two directions (in an elliptical fashion) (Brehl and Dow, 2008) in order to reduce cutting forces and chip thickness. Moriwaki et al. (1996) highlighted reductions in peak cutting force by ~14% and average forces by more than 4% when using elliptical ultrasonic vibration in turning of JIS SKD61 alloy steel. Ultrasonic assisted turning is not limited to machining steel; it has also been employed in the turning of brittle materials such as optical glass under a ductile-regime cutting mode with an ultrasonic frequency and amplitude of 40 kHz and ~3 μm respectively (Klocke and Rübenach, 2000, Rübenach, 2003). More recently, UAT was successfully implemented in turning of aviation material Inconel 718 (Babitsky et al., 2003, Babitsky et al., 2004). Ultrasonic aided cutting is reported to improve the machined surface roughness by 9.10-51.61% as well as reducing cutting forces by 24.47-32.34% in comparison to conventional turning of Inconel 718 (Hsu et al., 2008). Ultrasonic assisted turning has also been utilised when turning gamma titanium aluminide, which is a promising aerospace alloy with a potential to replace some nickel based superalloys in gas turbines. It was observed that an increase in cutting speed typically resulted in longer tool life when cutting was assisted with ultrasonic vibration, due to reduced non-contact time producing lower fatigue stresses on the tool edge (Sharman et al., 2001b). In order to prevent edge chipping of the cutting tool during conventional UAT, an inclined ultrasonic assisted cutting method was introduced by Jin and Murakawa (2001), a schematic diagram of the set up is shown in Fig. 2.2.2.

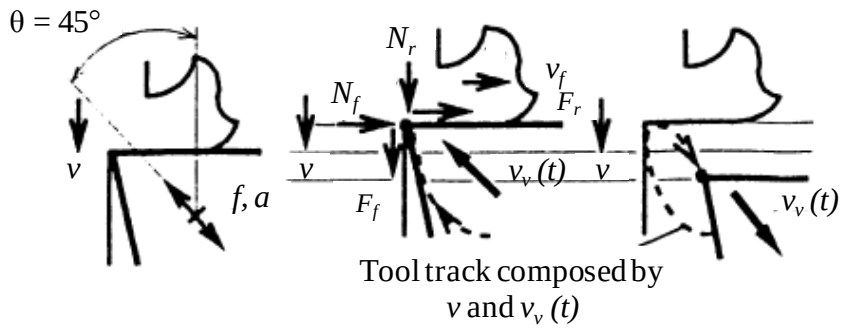


Fig. 2.2.2 Principle of inclined ultrasonic assisted cutting method (Jin and Murakawa, 2001)

With regard to ultrasonic assisted drilling, different researchers have reported significant reductions in thrust force (up to ~30-50%), burr size (up to ~85%), noise and surface roughness (up to ~60%) when drilling different workpiece materials such as glass fibre-reinforced plastic (Takeyama and Kato, 1991), fibre-reinforced composite materials (FRCMs) (Zhang et al., 2001), aluminium-silicon alloys (Chang and Bone, 2004, Neugebauer and Stoll, 2004), Inconel 738LC (Azarhoushang and Akbari, 2007), Ti-6Al-4V (Pujana et al., 2009) and stainless steel 3J1 (Zhang et al., 2010). A 60% improvement in surface roughness and hole circularity was reported when drilling Inconel 738-LC superimposed with ultrasonic vibration (Azarhoushang and Akbari, 2007). Ultrasonic assisted drilling of Inconel 718 produced smaller chips and an increase in the proportion of segmented chips. Ultrasonic assisted drilling has also been shown to reduce thrust force, stabilise torque results and increase drill life (Liao et al., 2007). It was also suggested that a smaller amplitude (<12 μm) and a higher frequency (~31.8 kHz) were more appropriate for vibration assisted drilling of Inconel 718 (Fig. 2.2.3).

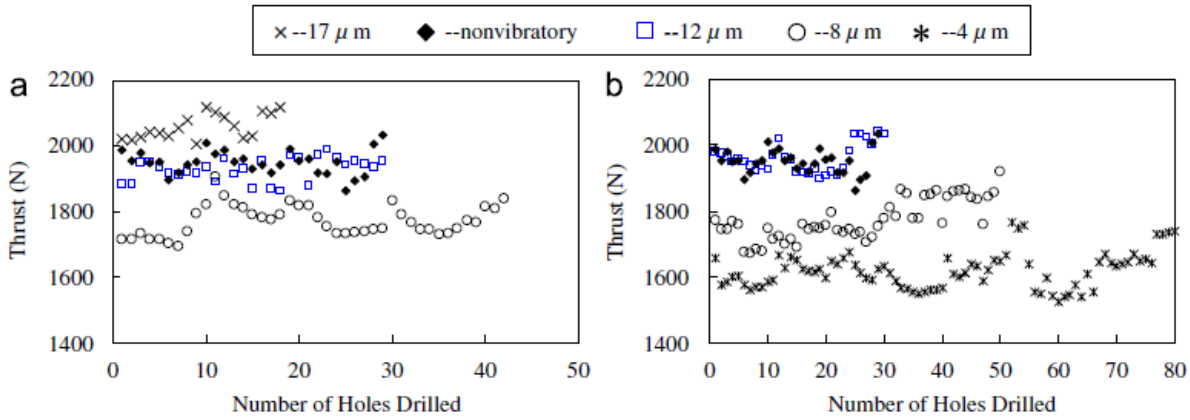


Fig. 2.2.3 Thrust force in drilling under various combinations of vibration amplitude and frequency (Liao et al., 2007)

2.2.2 Ultrasonic assisted grinding (UAG)

The earliest reference to the assistance of ultrasonic vibration in grinding can be found in the work by Colwell (1956) in the mid-1950's. Here the workpiece was mounted on a magnetostrictive transducer and vibrated axially at a frequency of 10-18 kHz with an amplitude of 25.4 μm. The benefits highlighted were a reduction in grinding temperature and workpiece tensile residual stresses; albeit at a cost of lower G-ratios due to a greater degree of wheel breakdown. Several years later, a project undertaken by the United States Air Force reported work on excitation of the grinding wheel in a radial direction by attaching the

transducer to a half-wave bar (the wheel hub). This resulted in alternate swelling and shrinking of the wheel, see Fig. 2.2.4 (Anon, 1963). Internal grinding of Armco's PH 15-7 Mo stainless steel, external grinding of Rene 41 and surface grinding of H-11 hot work tool steel as well as Ti-6Al-4V, were carried out with standard vitrified bonded alumina wheels vibrated at a frequency of 20 kHz with amplitudes up to ~40 µm. Increasing amplitude resulted in reduced spindle power, temperature and chip load coupled with an increase in G-ratio, however, there were optimum levels of amplitude, above or below which, negative effects were observed.

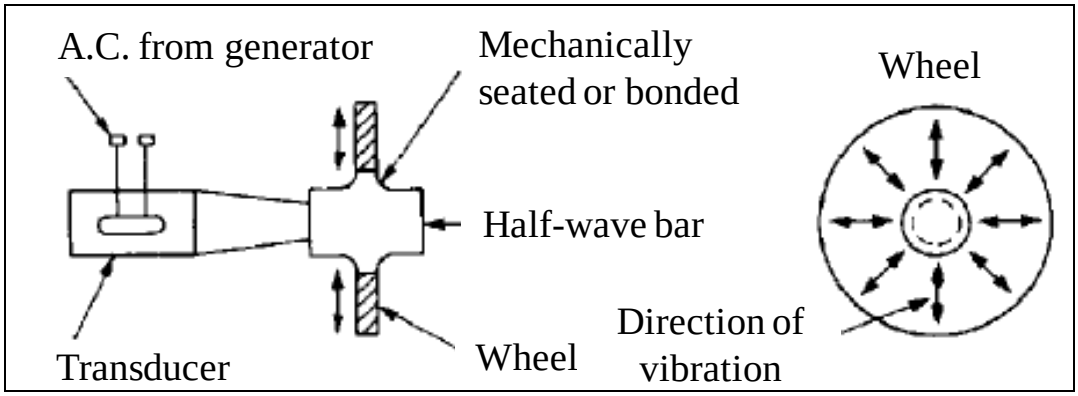


Fig. 2.2.4 A schematic design showing radially vibrating grinding wheel (Anon, 1963)

The majority of published work on UAG over the past ~30 years can be broadly classified into two sub-categories, depending on whether the vibration was applied to the grinding wheel or workpiece as detailed in the following sections. Additionally there are a few publications where ultrasonics have been utilised in maintaining a cleaner grinding wheel (Balamuth, 1966) through use of a high frequency (20 kHz) activator to effect low amplitude oscillation along the fluid jet axis (Kalizer and Limb, 1968, Barker et al., 1967-68). The wheels exhibited higher permeability, higher G-ratio and less chatter vibration in comparison to the non-ultrasonically treated wheels. Figure 2.2.5(a) shows two parts of a grinding wheel before and after ultrasonic treatment. The bottom part of the wheel is fully covered with metal particles whereas the ultrasonically treated top part appears freshly dressed.

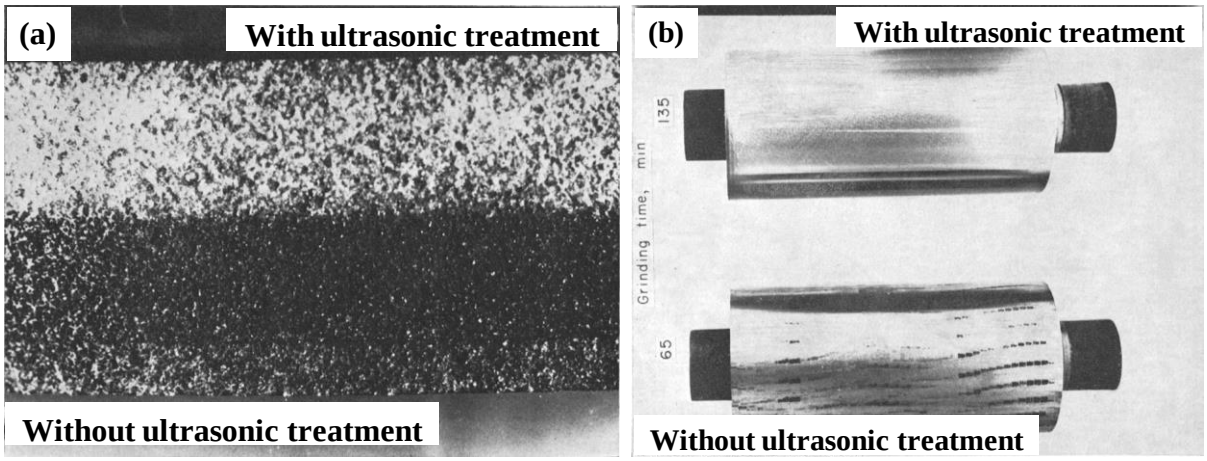


Fig. 2.2.5 (a) Effect of ultrasonic treatment applied to the grinding wheel periphery, (b) Comparison between workpiece surfaces ground with a normally worn wheel and ultrasonically treated wheel (Kalizer and Limb, 1968)

Figure 2.2.5(b) shows workpiece surfaces ground with a normally worn wheel and a wheel cleaned with ultrasonically activated cutting fluid. The surface ground with the ultrasonically treated wheel showed a much better finish after 135 min of grinding than a similar workpiece machined conventionally after a grinding time of only 65 min (Kalizer and Limb, 1968). Recently, Sakamoto et al. (2006) developed an ultrasonically activated coolant technique operating at a much higher frequency (3 MHz), in order to improve performance when cylindrical grinding hardened chromium-molybdenum steel SCM440 (HRc>50). The special coolant delivery system suppressed loading and wear of the grinding wheel. Figure 2.2.6 shows the working surface of the wheel following grinding with and without ultrasonic treatment. The high vibration acceleration additionally increased the kinetic energy of the coolant stream, which resulted in more efficient ingress of the cutting fluid in the grinding zone by overcoming the air-barrier generated around the wheel due to its rotation. The ultrasonically cleaned wheel produced ground surfaces with 30.6-39.8% lower R_z than those generated by a conventionally cleaned wheel.

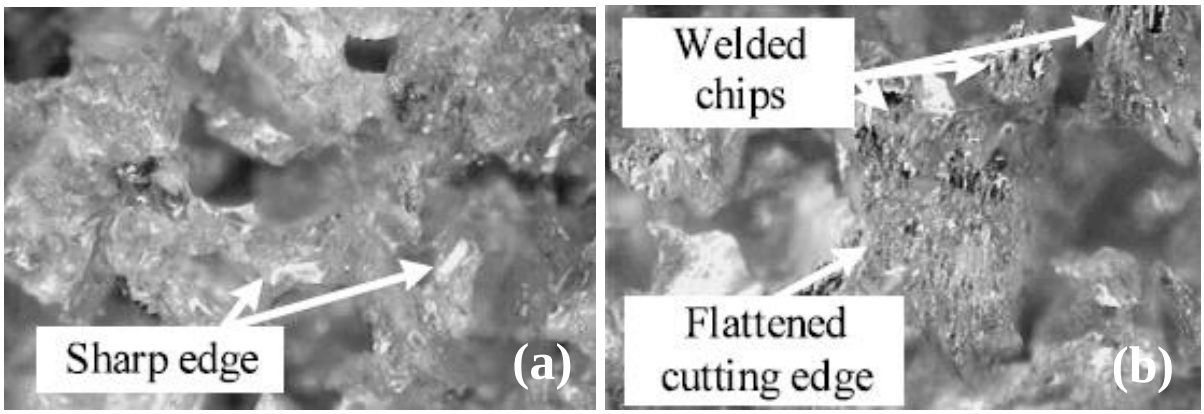


Fig. 2.2.6 (a) Ultrasonically treated, (b) Non-ultrasonically treated working surfaces of the grinding wheel (Sakamoto et al., 2006)

2.2.2.1 Application of US vibration to grinding tool/wheel

(a) Ceramic and glass workpieces

Ceramics are possibly the most widely used workpiece materials ground with the assistance of ultrasonic vibration not least because the primary machining mechanism is brittle fracture. Early work on US assisted ceramic grinding was carried out by Nakagawa et al. (1988) and Suzuki et al. (1988), where a grinding centre based on an NC turning centre was developed with an ultrasonic attachment mounted on the spindle, see Fig. 2.2.7(a). Alumina, silicon nitride and tungsten carbide workpieces were ground with a cast iron fibre bonded diamond wheel vibrating along its axis at a frequency of 20 kHz. The results showed that larger depths of cut (120 μm) were possible leading to higher material removal rates (320 mm^3/s) and improved dimensional accuracy, together with a 60-70% reduction in normal grinding force (Nakagawa et al., 1988). Figure 2.2.7(b) shows a decrease in normal grinding force (F_z) by more than 50% when grinding alumina with a cup-shaped wheel (Suzuki et al., 1988). Further reduction of force was observed by combining both ultrasonic vibration and electro discharge machining with grinding (Ultrasonic-Electro-Discharge Grinding or US-ED-G) when machining TiB_2, sintered carbide, boride ceramics and Sialon etc. (Suzuki et al., 1988).

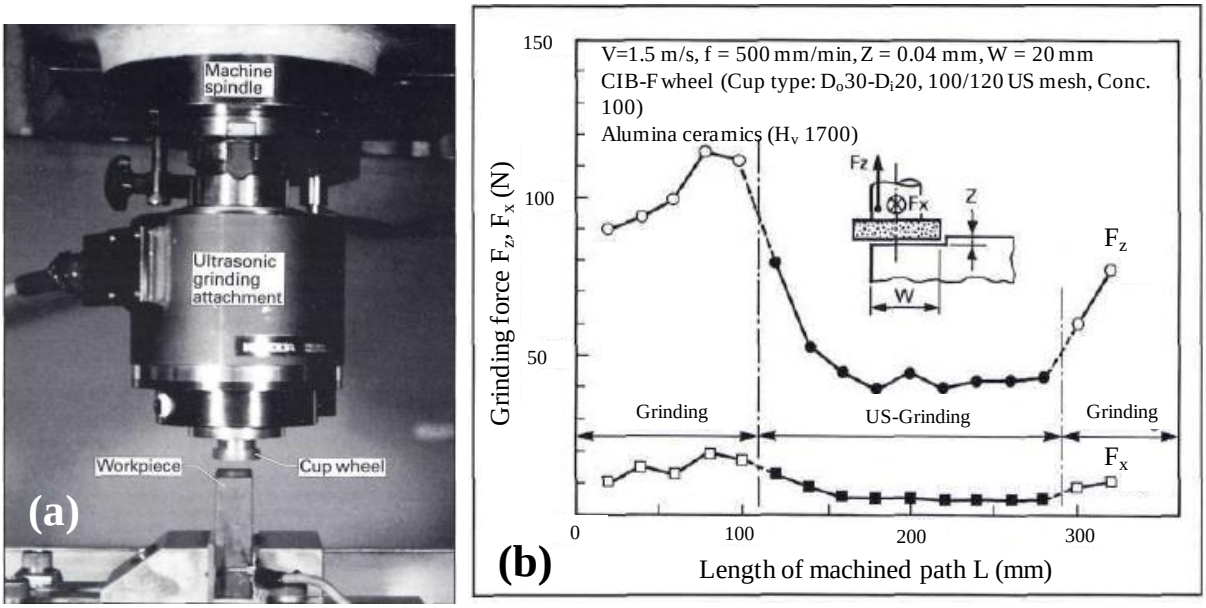


Fig. 2.2.7 (a) Ultrasonic grinding attachment, (b) Reduction of grinding force in US-grinding (Suzuki et al., 1988)

Suzuki et al. (1992) further studied the grinding of green alumina ceramic bodies having sharp inside corners with a blade-like metal bonded diamond tool actuated with simultaneous bending and longitudinal vibrations (using a biaxial ultrasonic vibrating transducer), at frequencies of 19 and 28 kHz and amplitudes of 12 and 20 μm respectively. The investigation extended to the grinding of alumina, sintered and semi-sintered tungsten carbide and optical glass with a non-rotational, non-circular square/triangular bottom electroplated diamond tool, which was vibrated either longitudinally, torsionally or simultaneously in both directions (complex mode), see Fig. 2.6.8(a) (Suzuki et al., 1993). The frequencies and amplitudes of vibration along longitudinal and torsional directions were 29.4 kHz, 6 μm and 19.4 kHz, 32 μm respectively. The vertical and horizontal forces in complex vibration mode were found to be ~30% of the values obtained in the longitudinal vibration mode when machining sintered alumina ceramics. By using this method, grooves or holes with sharp inner corners, which were impossible to produce with conventional rotational grinding wheels, were successfully generated, see Fig. 2.2.8(b).

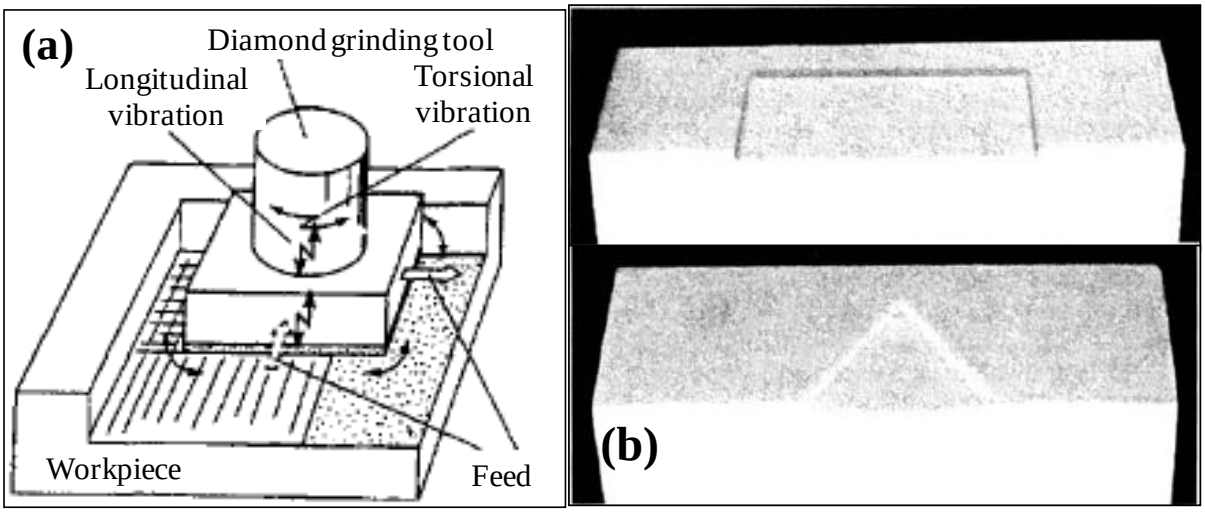
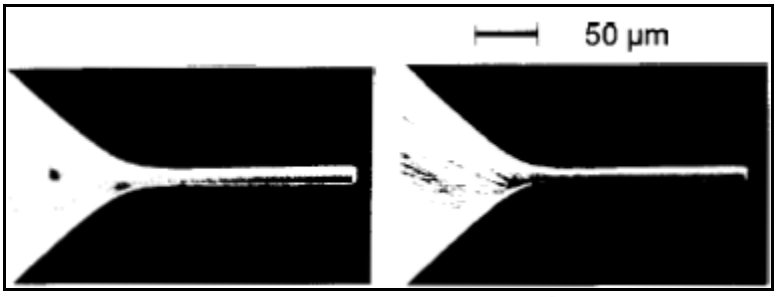


Fig. 2.2.8 (a) Schematic diagram of the principle of grinding with a non-rotational tool, (b) Samples of recesses with sharp inner corners formed on alumina (Suzuki et al., 1993)

The effects of grinding wheel rotational speed, the contact pressure between the wheel and the workpiece and amplitude of vibration were examined by Spur and Holl (1996) when face grinding alumina with a diamond grinding wheel (D126 BZ 335 C75) vibrating at a frequency of 20-25 kHz with amplitudes of 11 and 13 μm. The results showed that the material removal rate increased by up to ~3 times with an increase in rotational speed and contact pressure when the amplitude remained constant. The reasons for this were attributed to larger scratch lengths per grit engagement and longer effective contact between the grit and the workpiece respectively.

A new method of machining cold-pressed zirconia was proposed by Doutsu et al. (1996) where an ultrasonic frequency of 40 kHz was used instead of a conventional 20 kHz frequency. The ceramic specimens were grooved with 7 mm dia. end-milling diamond tools vibrated along their axis at an amplitude of 25 μm. The machining forces when using ultrasonic assistance were found to be 3 to 5 times lower than those obtained without vibration. The maximum depth of cut could also be increased to 0.4 mm during ultrasonic operation which was much higher than the depth of 0.1 mm used in conventional machining, however the quality of the machined surface was inferior with vibration assistance. Three other ceramics were also machined along with zirconia and the ease of machining appeared as alumina > silicon carbide > zirconia > silicon nitride.

Cutting and grinding have been shown to be effective methods in fabricating micro mechanical parts, cutting involving single crystal diamond and cemented carbide tool materials. In making these tools, EDM and grinding are usually employed, EDM providing negligible machining force but suffering from poor productivity. Grinding renders a higher machining rate, however it is necessary to reduce the grinding forces. With this in mind, Onikura et al. (2000) developed an ultrasonic assisted method of fabricating micro cutting tools such as drills or end mills with diameters less than 100 μm using cup-shaped diamond wheels fed axially (Z-direction) at constant speed towards an ultra-fine grain (JIS: Z01) cemented carbide cylindrical workpiece and then transversely (X-direction) whilst vibrating in the axial direction at a frequency of 75 kHz and an amplitude of 0.5 μm. Ultrasonic actuation provided lower wheel loading as well as fabrication of workpieces with a 10-20% smaller diameter (Fig. 2.2.9) and 50% larger aspect ratio. Brecher et al. (2010) used finite element analysis (FEA) to design cup-shaped diamond wheels for use in US-assisted grinding and validated the simulation result through actual grinding of optical glass (NBK-7). The wheel was vibrated longitudinally at a frequency of 20 kHz with an amplitude of 13 μm; the effect of which was a reduction of process forces by 47%.



(a) (b)

Fig. 2.2.9 Examples of fabricated microtools (a) Without and (b) With ultrasonic vibration (Onikura et al., 2000)

Uhlmann and Sammler (2010) commented that the ultrasonic amplitude must be larger than the maximum kinematic chip thickness in order to ensure that the contact between tool and workpiece is intermittently broken by the vibrations. In their study, a vibration amplitude of 2 µm was used when grinding alumina with multilayer bonded diamond pins. Three different types of bond in the grinding pins were tested for a grain size of D64. Figure 2.2.10 shows that the maximum reduction in specific normal force was observed for the sintered brazed bond, although a general decrease in the grinding forces was noted.

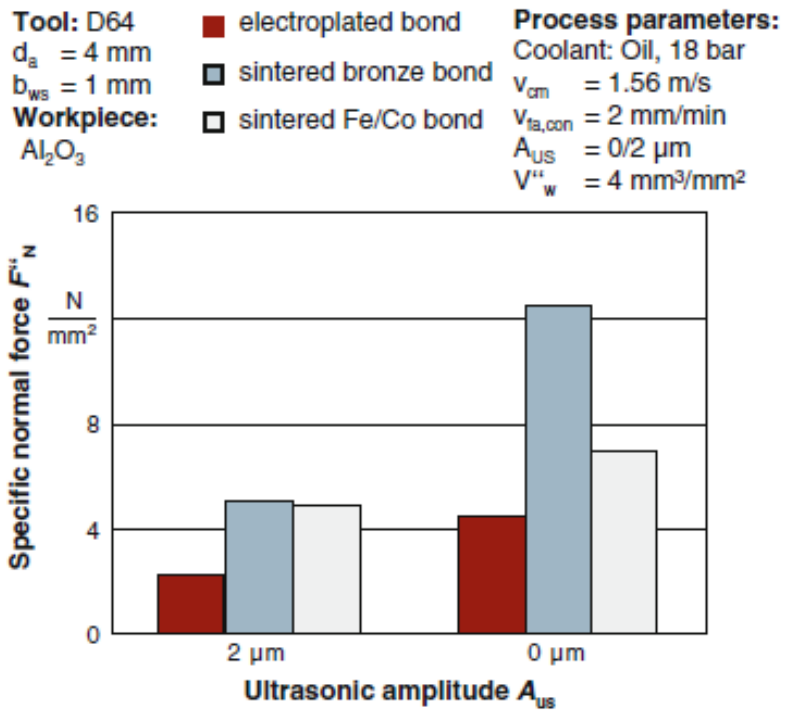
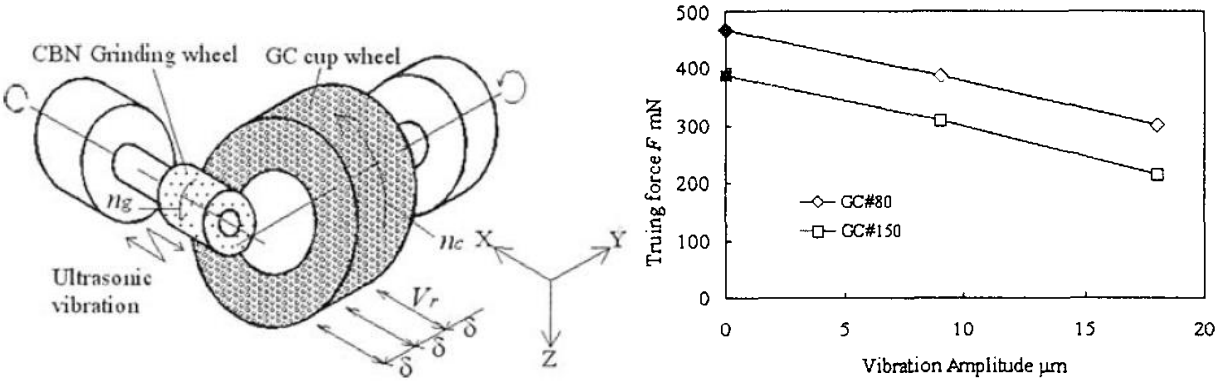


Fig. 2.2.10 Specific normal force with regard to bond system and ultrasonic amplitude (Uhlmann and Sammler, 2010)

(b) Steel workpieces

Stainless steel and hardened tool steel comprise the second most frequently assessed materials after ceramics with regard to ultrasonic assisted grinding. In order to explore the mechanism behind the reduction of grinding force in UAG, Wu et al. (2004a) developed a mathematical model describing the cutting trace of an abrasive grain and established an equation relating the grinding force with process parameters such as frequency and amplitude of vibration, grinding wheel speed etc. The theoretical predictions were verified through actual tests where SUS440C stainless steel specimens were ground with a miniature cBN wheel, screwed onto the end face of a spindle and vibrating axially at a frequency of 19.2 kHz and amplitudes of 9, 18 and 21 µm. Both theoretical and experimental results showed that the

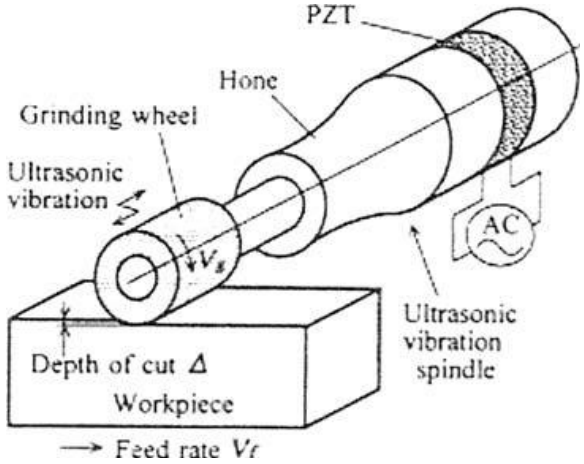
decrease in grinding force with US assistance was due to thinner and more fractured grinding chips. The drop in force was greater at higher vibration amplitude and lower wheel speed. The study was further extended by Nomura et al. (2007) using small cBN wheels (diameter Φ5 mm with mesh sizes of #100, #400) vibrated at a frequency of 19.2 kHz and amplitudes of 9 and 18 μm during truing and dressing with rotary cup wheels (GC #80, #150, #600), see Fig. 2.2.11(a). The truing force was found to decrease with an increase in vibration amplitude, the maximum reduction being more than 22%, see Fig. 2.2.11(b). The run-out of the wheel also decreased from a value of 1.1 μm in conventional grinding to that of 0.8 μm in hybrid mode.



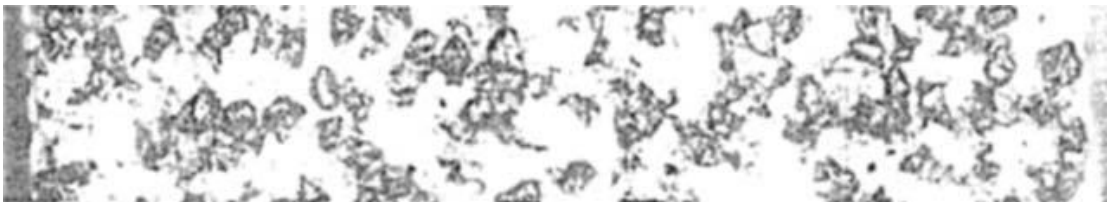
(a) (b)

Fig. 2.2.11 (a) Truing and dressing, (b) Truing force Vs vibration amplitude (Nomura et al., 2007)

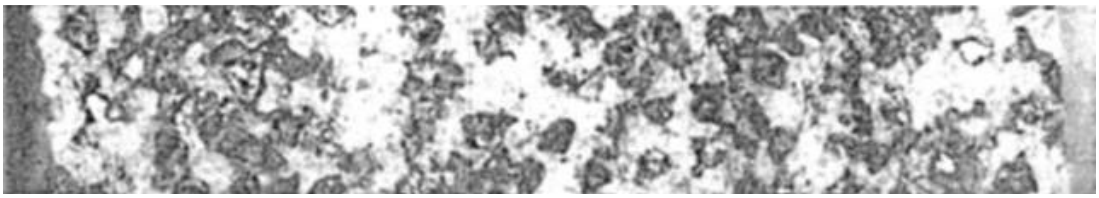
In subsequent UAG at constant depth of cut on SUS440C, see Fig. 2.2.12(a), Nomura et al. (2007) showed that the 400 mesh cBN wheel produced reductions in normal and tangential grinding forces by more than 20% and 24% respectively with workpiece surface roughness R_a around 18% lower. The reasons were attributed to improved grain sharpness, grain protrusion and increased abrasive grain density with US assistance (see Fig. 2.2.12(b) and (c)).



(a)



(b)



(c)

Fig. 2.2.12 (a) Illustration of constant depth of cut UAG, (b) Non-ultrasonically dressed wheel, (c) Ultrasonically dressed wheel (Nomura et al., 2007)

Hara et al. (2008) demonstrated that it was possible to produce mirror surfaces when face grinding die steel (NAK80) with diamond electroplated tools (diameter Φ2 mm, average grain diameter 150 μm) vibrating axially at a frequency of 60 kHz and an amplitude of 4μm, see Fig. 2.2.13(a) and (b) for the schematic diagrams of set-up and electroplated tool. Grinding of ferrous alloys with diamond tools is generally not recommended and in conventional grinding without ultrasonic vibration, severe abrasive wear and 'drop out' of the diamond grains was visible, see Fig. 2.2.13(c), along with a poor material removal rate. With US grinding, the mirror surfaces (roughness R_z 0.40–0.84 μm) were capable of reflecting characters.

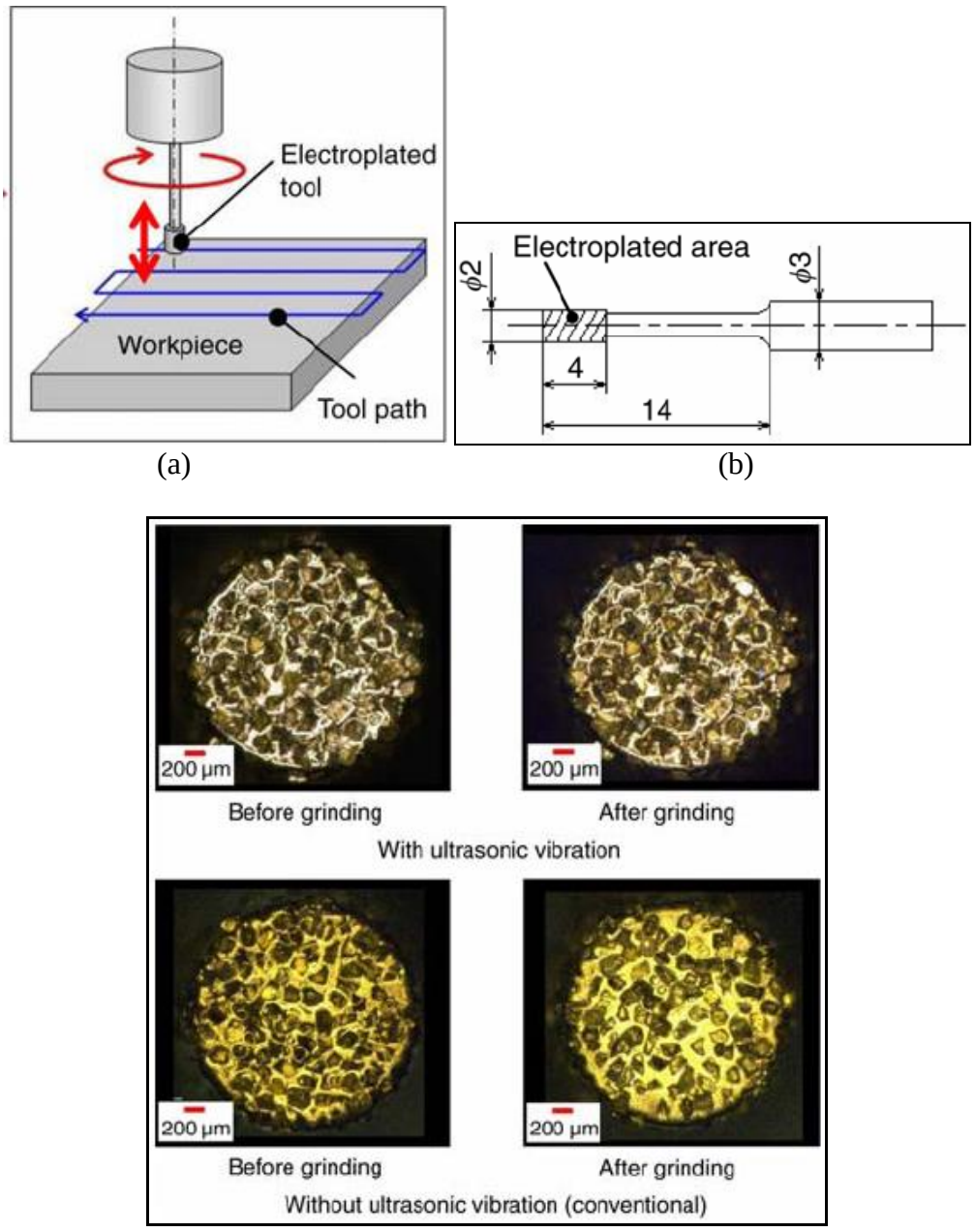


Fig. 2.2.13 (a) Schematic of ultrasonically assisted face grinding, (b) Drawing of electroplated tool, (c) Topography of tool end face following grinding with and without ultrasonic vibration (Hara et al., 2008)

In order to assess the geometrical properties of electroplated diamond wheels, Ismail et al. (2010) used different characterisation equipment including a confocal laser scanning microscope (CLSM), point auto focus microscope (AF) and white light interferometer (WLI) following grinding of NAK80 steel workpiece. The grinding tool was vibrated at a frequency of 60 kHz and an amplitude of 0.5 µm. Figure 2.2.14 shows images of tool topography and diamond grains in the top 10 µm of the surface using AF, WLI and CLSM respectively.

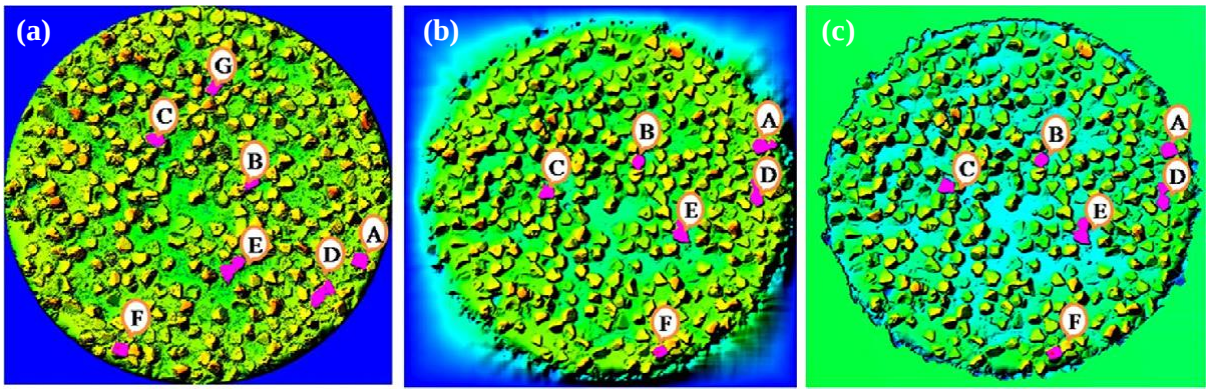


Fig. 2.2.14 Tool topography and top 10 µm diamond grains using (a) AF, (b) WLI, (c) CLSM (Ismail et al., 2010)

(c) Aerospace alloys

Published research on UAG of advanced aerospace materials, such as nickel or titanium alloys, is extremely limited. Qin et al. (2009) detailed ultrasonic assisted grinding of titanium alloy Ti-6Al-4V using rotary diamond tools vibrating along the spindle axis. A predictive cutting force model was developed and the model was validated by actual experiment. The vibration frequency and amplitude were 20 kHz and 10-50 µm respectively. The model predicted that the cutting forces would reduce with an increase in vibration frequency or amplitude or cutting speed, however forces would increase with an increase in diamond grain density or grain size or work feed rate (see examples in Fig. 2.2.15). The experimental results generally agreed well with the estimated trends with the exception of that of the diamond grain size. This was due to the assumption that the other parameters remained unchanged when only the grain size varied, which in reality was not the case. Some representative graphs obtained from the experimental trials are shown in Fig. 2.2.16.

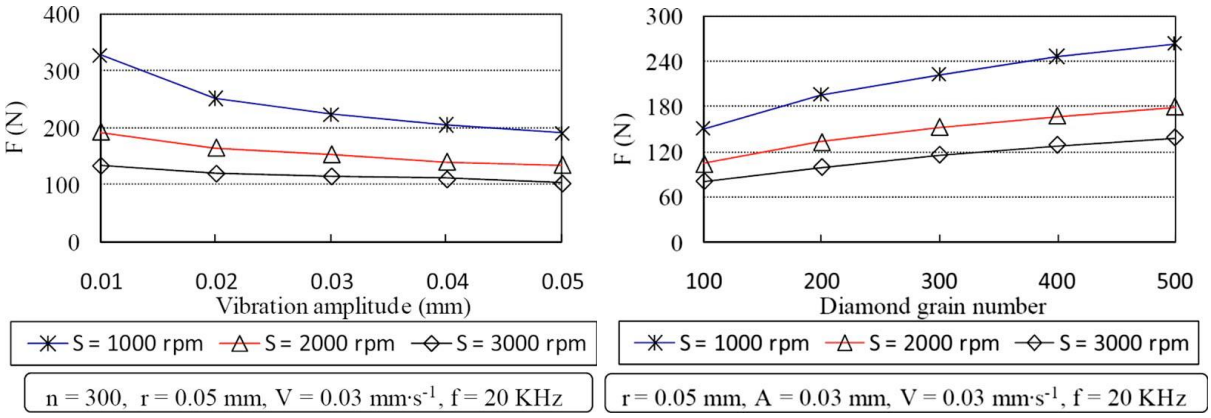


Fig. 2.2.15 Model prediction for cutting forces with variations in amplitude and grain density respectively (Qin et al., 2009)

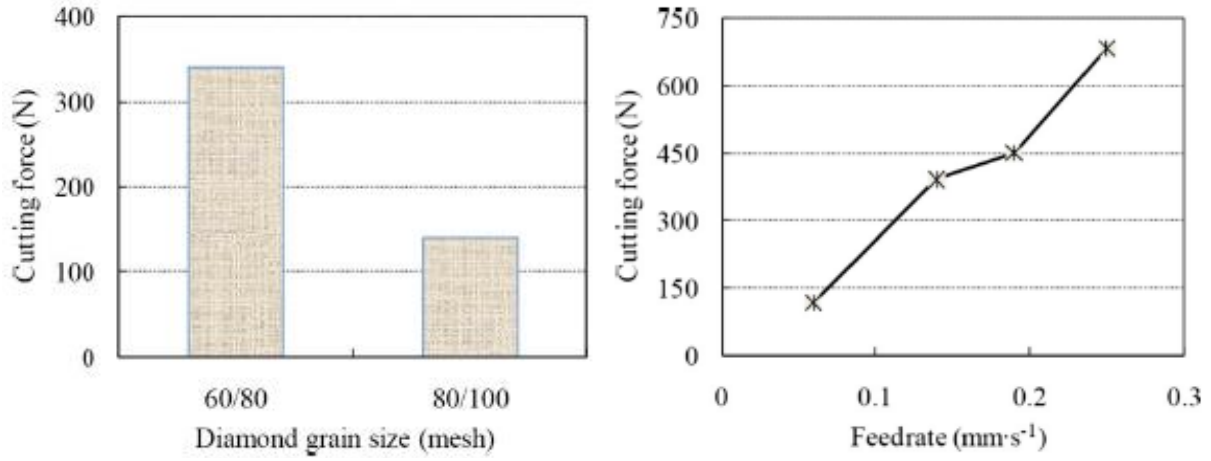


Fig. 2.2.16 Experimental results for cutting forces with variations in diamond grain size and federate respectively (Qin et al., 2009)

2.2.2.2. Application of US vibration to the workpiece

(a) Ceramic and glass workpieces

There are several limitations of transmitting vibration through the grinding tool/wheel as this requires consideration of special bearing designs, restrictions on the weight and size of the grinding wheel, the direction of the applied vibration etc. Therefore, research involving vibration of the workpiece has been more extensive, mainly due to the comparatively simpler experimental setup. In the majority of past studies, workpiece vibration was achieved by gluing the material to be machined on the top of a nickel stack or by screw clamping it to the end of an ultrasonic horn. Ceramics and glass were the main focus of attention.

Jixian et al. (1996) studied deep hole grinding of a silicon carbide (SiC) workpiece with a diamond wheel while the workpiece was vibrated at a frequency of 20-23 kHz and an amplitude of 6-15 μm. The grinding pressure and thermal stress were reduced with ultrasonic assistance. Additionally the R_a of the surface and roundness of the hole decreased from 1.6 μm and 5.56 μm (in conventional grinding) to 0.16 μm and 1.2 μm respectively in hybrid mode. In another study on cut-off grinding of alumina ceramics, the workpieces were vibrated in the table feed direction at a frequency and amplitudes of 30 kHz and 0.45-2.75 mm respectively (Hanasaki et al., 1996). The volume of wheel wear was found to reduce in the vibratory mode. Results were compared with those obtained during the cut-off grinding of high speed steel (SKH51), which exhibited a reverse trend as wheel wear was larger with the hybrid arrangement. An improvement in the flatness of the cut-off surface and prevention of burn marks and burrs also ensued with the assistance of vibration.

A detailed study of the mechanism of material removal during ultrasonic assisted grinding of different ceramic materials, such as sintered silicon nitride (SSN), alumina, SiC and ZrO_2 was carried out by Spur and Holl (1997) and Uhlmann (1998). In order to clarify the active mechanisms, analogy tests were conducted by single grain scratching. This involved mounting of single grit diamonds on the circumference of a metal grinding wheel which was moved over the ceramic workpiece materials with constant wheel speed and feed speed in down cut mode. The workpices were vibrated in the radial (normal) direction at a frequency and amplitude of 22 kHz and 4 µm respectively. This imparted additional relative motion between the diamond grain and the workpiece surface (shown schematically in Fig. 2.2.17), thereby leading to an interrupted cutting action of the grits, see Fig. 2.2.18.

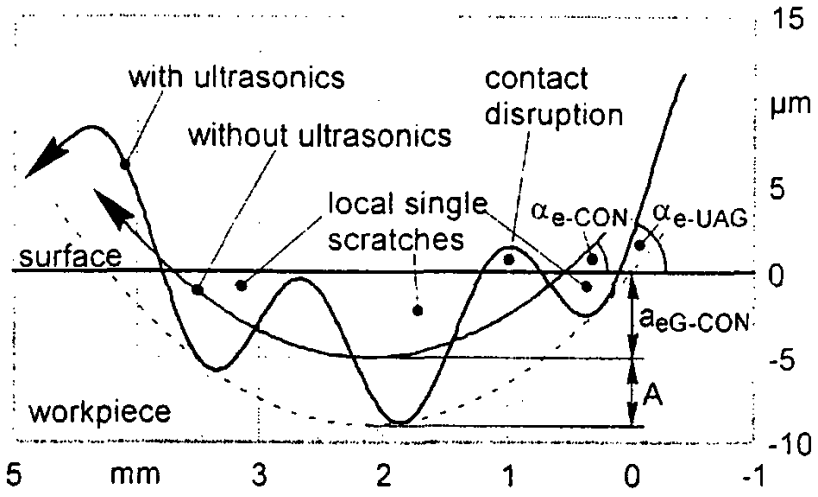


Fig. 2.2.17 Relative motion of single grain diamond (Uhlmann, 1998)

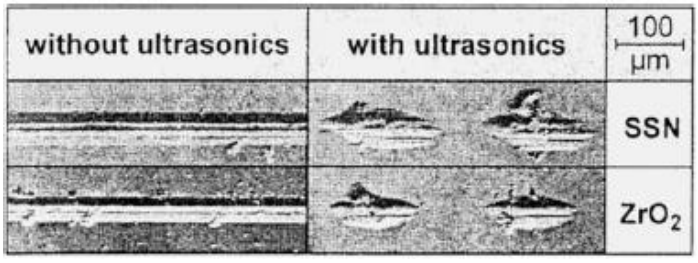


Fig. 2.2.18 Scratches on different ceramics with and without ultrasonics (Uhlmann, 1998)

The superimposition of ultrasonic vibration resulted in larger angles of grit engagement with the work surface, shorter length of chip, and higher depths of indentation, thus exposing both the diamond grits and the material to higher mechanical loads. The impulse-like load and load relieving phases on the single cutting edges led to larger micro-splintering and reduced grit flattening of the diamond grits. As a result, the number of active cutting edges increased

and the phenomenon of graphitisation diminished. Friction effects on the active areas were also reduced leading to a significant decrease in thermal load and a reduction in process forces. The increase in mechanical load but decrease in thermal load on the workpiece during UAG is outlined in Fig. 2.2.19 (Uhlmann, 1998).

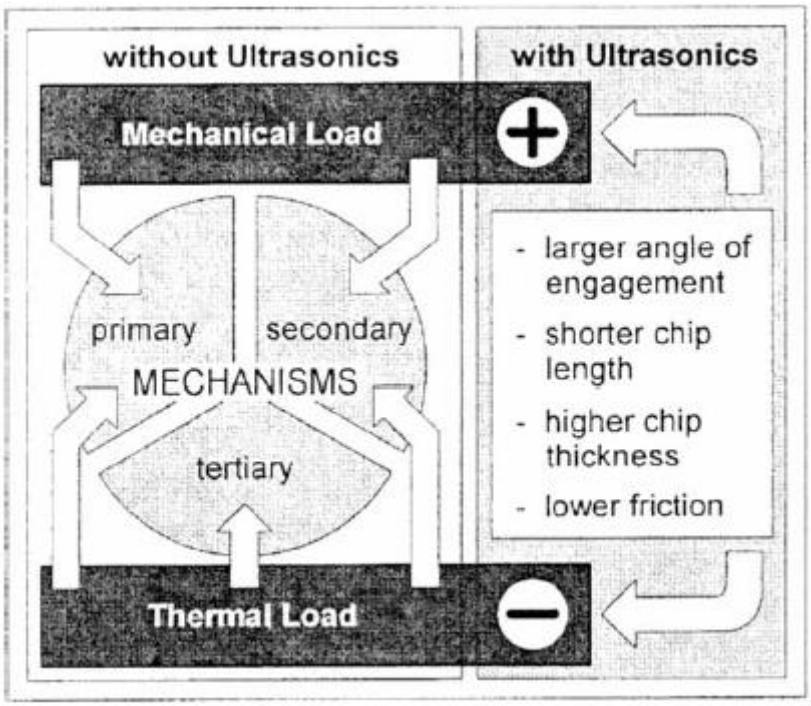


Fig. 2.2.19 Different mechanisms of surface formation showing increase in mechanical but decrease in thermal load during UAG (Uhlmann, 1998)

A sub-surface analysis of the machined surface showed compressive residual stresses parallel to the grinding direction close to the surface, with higher values measured for ultrasonic assistance, however bending strengths were found to be higher with conventional grinding. It was concluded that ultrasonic assisted grinding could offer the potential for a significant increase in material removal rate without causing proportionately higher sub-surface damage (Uhlmann, 1998).

An attempt was made to reduce subsurface damage and increase material removal rate in grinding of ceramics with ultrasonic assistance by Qu et al. (2000). An indentation damage model was first simulated, the output of which was then validated by single-grit scratch tests on Pyrex glass. The progress of lateral cracks during unloading exhibited a shielding effect on the propagation of median cracks during loading. Modelled data suggested a damage depth when using ultrasonic assistance of 176 μm at a maximum depth of cut of 20 μm, however with the same depth of cut, the average damage depth was 231 μm when operating without ultrasonic assistance. An increase in depth of cut by 50% resulted in an average damage depth

of 240 μm. Experimental results produced a 62% increase in MRR with almost no increase in the depth of damage and a decrease of 24% in the depth of damage with almost the same MRR when grinding was employed with US vibration.

In order to achieve high surface quality in micro manufacturing of alumina ceramic (Al_2O_3+Ti(C,N) parts, Denkena et al. (2003) superimposed ultrasonic vibration when grinding. The workpieces were vibrated at a frequency of ~22 kHz and an amplitude of 10 μm. As seen in Fig. 2.2.20(a), ultrasonic assistance produced surface roughness (R_a = 20 nm and R_z = 180 nm) results which were three times lower than when compared to that in conventional grinding (R_a = 75 nm and R_z = 600 nm). Figure 2.2.20(b) represents the ground surface topography measured by atomic force microscopy. The generated surface in conventional peripheral grinding was characterised by long and straight grinding grooves. The dimensions of these grooves were significantly bigger than those in ultrasonic assisted grinding. The overlapping grit marks due to the influence of ultrasonics are evident in Fig. 2.2.20(b).

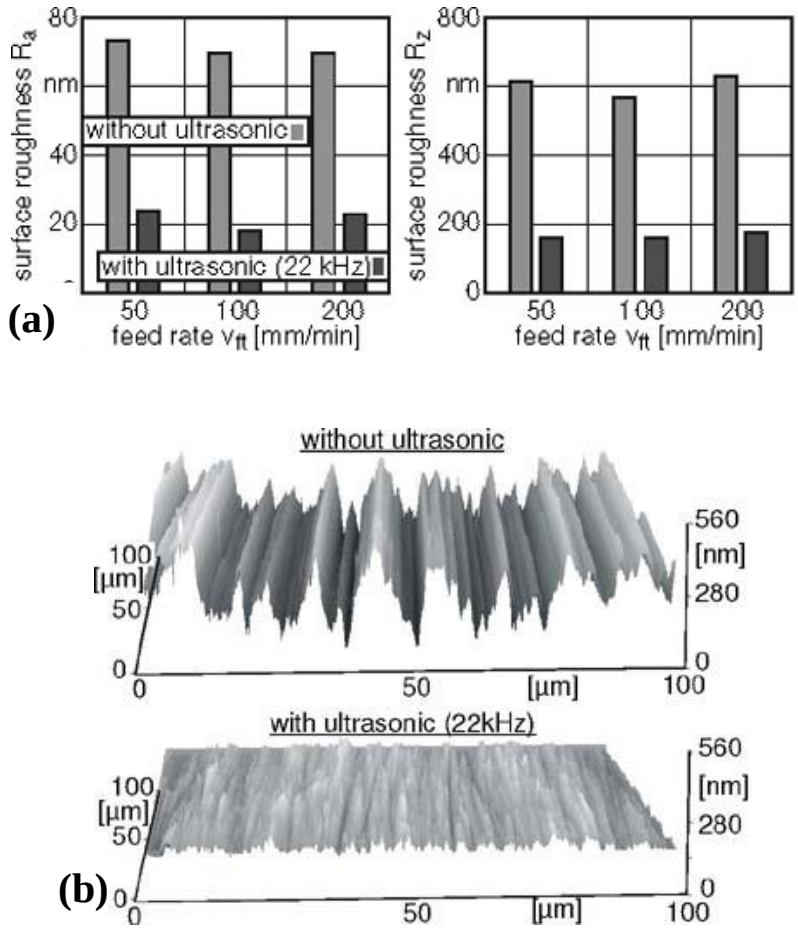


Fig. 2.2.20 Influence of ultrasonic grinding on (a) Surface roughness, (b) Surface quality of workpiece (Denkena et al., 2003)

Zhong and Yang (2004) reported that the direction of applied vibration had a significant effect on the surface finish of silicon workpieces following US assisted grinding with resin bonded diamond wheels. Roughness was reduced by 45 to 50% when vibration was transmitted in the cross-feed direction, whereas it was only reduced by 33 to 48% when ultrasonic actuation occurred in the table feed direction. This observation is at odds with that obtained by Zheng and Xu (2006) when creep feed grinding alumina with electroplated diamond wheels. The workpiece was vibrated along two different directions separately: creep feed and normal to the creep feed. UAG produced higher surface roughness values in comparison to mechanical grinding when the direction of the vibration was normal to that of the feed motion. Roughness marginally reduced under ultrasonic mode when the vibration was parallel to the direction of creep feed (R_a=5.146 μm) however, this exceeded the surface roughness values recorded under conventional creep feed grinding (R_a=5.078 μm) when V_C increased up to 5.682 m/s, see Fig. 2.2.21.

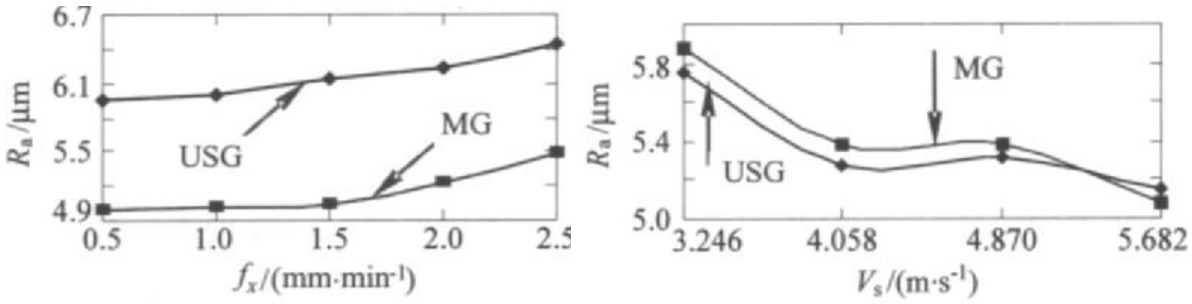


Fig. 2.2.21 Effect of feed rate and wheel speed on surface roughness (Zheng and Xu, 2006)

An extensive study was carried out by a group of researchers on modelling the working locus of abrasive particle and mechanics of surface formation under two dimensional ultrasonic assisted grinding (TDUAG), with actual tests performed on nano-zirconia (nano-ZrO_2) workpiece (Zhao et al., 2006b, Yan et al., 2006, Yan et al., 2009). The motion path of a particle during TDUAG is shown in Fig. 2.2.22(a) which is a series of ellipses along a spiral line. The contact model between abrasive particle and the machining material in one cycle during TDUAG is represented in Fig. 2.2.22(b). The moving locus varied with the feed of the grinding wheel and the amplitudes and frequencies of ultrasonic vibration. The contact area between the abrasive particles and workpiece altered continuously with time, and the contact line changed along the route A–B–C–D in a vibration cycle. This led to an increase in interference along the machining loci of abrasive particles, and an improved quality of finished surface (Zhao et al., 2006b). Grinding tests were carried out with resin bonded diamond wheels (mesh size #270) with the nano-ZrO_2 workpieces vibrated in tangential and

axial wheel directions at frequencies and amplitudes of 19.356 kHz-10.22 μm and 20.168 kHz-11.98 μm respectively (Yan et al., 2009). Figure 2.2.23(a) shows SEM micrographs of the workpieces in different zones on the same grinding surface after conventional grinding, whereas Fig. 2.2.23(b) shows surfaces after TDUAG. The elliptical machining locus and rotating cutting characteristic of TDUAG produced improved surface quality and increased the life of the diamond wheel. The grooves obtained with TDUAG were smoother, wider and shallower as well as cleaner with much less burring. At a depth of cut (DOC) of 1 μm, R_a was improved from 0.162 μm in conventional grinding (CG) to 0.081 μm in TDUAG. With the DOC set at 3 μm roughness was reduced from a value of 0.225 μm (CG) to 0.126 μm with TDUAG.

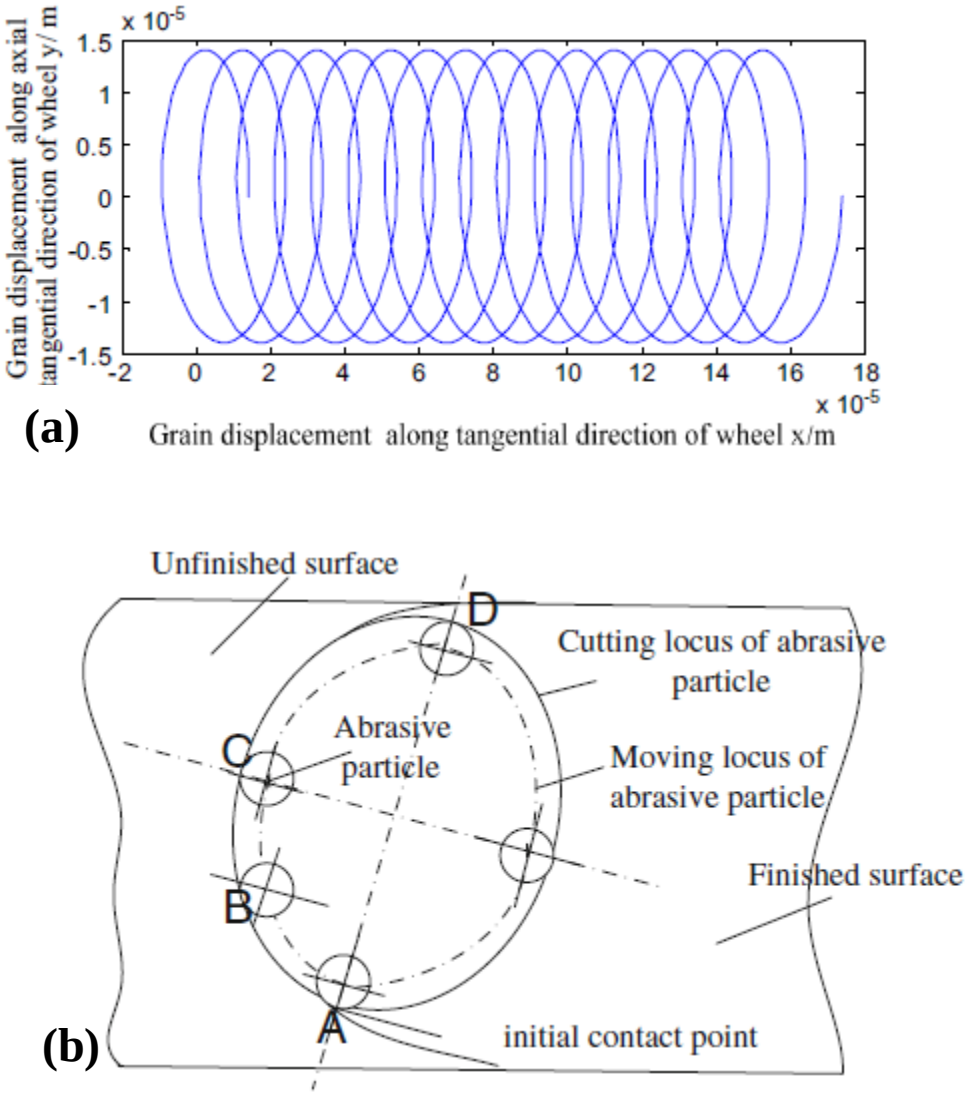


Fig. 2.2.22 (a) Kinematic path of single abrasive particle (V_w=0.1 m/s, f=20 kHz, A=B=15 μm), (b) Contact model between abrasive particle and workpiece (Yan et al., 2009)

Similar observations on the surface characteristics of nano-ZrO_2 were also noted by Gao et al. (2009) when grinding was carried out with a diamond wheel (grain size #350), the workpiece being vibrated in a single direction at a frequency of 20 kHz and amplitudes of 10-12 μm. The material removal mechanism changed from a fracture regime in conventional grinding to a ductile regime in ultrasonic grinding. The surfaces obtained with ultrasonic assistance were free from any burrs and built-up edges. The critical ductile grinding depth in US grinding also increased by around 30% compared to that in conventional grinding (Gao et al., 2009, Zhao et al., 2006a). The coarse blocky grinding chips of width 8-10 μm and thickness 5-7 μm, obtained in conventional grinding, changed to micro-powder with ultrasonic assisted grinding (Zhao et al., 2006a).

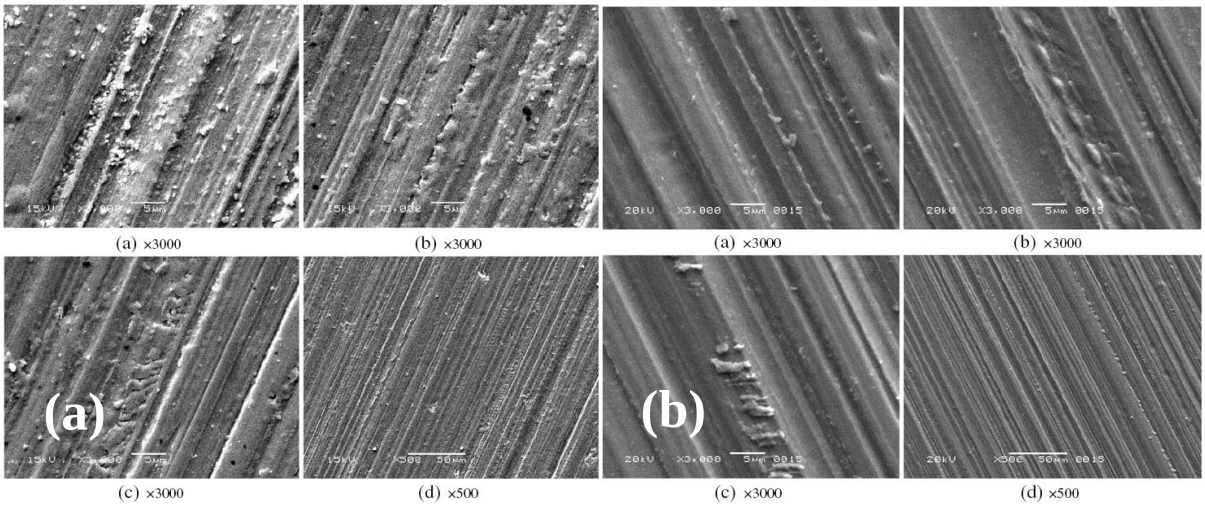


Fig. 2.2.23 SEM of nano-ZrO_2 after (a) conventional grinding, (b) TDUAG (Yan et al., 2009)

Wu et al. (2004b) and Wu et al. (2005) developed a new centreless grinding technique which involved an ultrasonic elliptical vibration shoe to support the workpiece and control its rotation instead of employing a regulating wheel as in conventional centreless grinding. The shoe was constructed by bonding a piezoelectric ceramic device (PZT) having four separated electrodes onto a stainless steel plate (SUS304) and made to vibrate along bending and longitudinal directions simultaneously, which created an elliptical motion on the end-face of the metal plate (Fig. 2.2.24). Efforts were made in improving the roundness of the cylindrical workpieces made from SK4 steel (Wu et al., 2004b, Wu et al., 2005), tungsten carbide (Wu et al., 2006), TH10 (Xu et al., 2010) etc. A similar kind of vibrator, see Fig. 2.2.25, was used in grinding monocrystalline silicon, the vibrator being actuated with two alternating current voltages (Liang et al., 2010). A phase difference of 0° or 180° was capable of producing axial or vertical vibrations respectively. Compared with conventional grinding (CG), axial vibration led to improved surface quality as well as a reduction in grinding forces by 20%, which

further decreased by 50% with vertical vibration. Combined elliptical ultrasonic vibration contributed to a decrease in surface roughness by 10% and a reduction in grinding forces by 30% compared with CG. The decrease in surface roughness was attributed to axial vibration while that of the grinding force was thought to be due to vertical vibration.

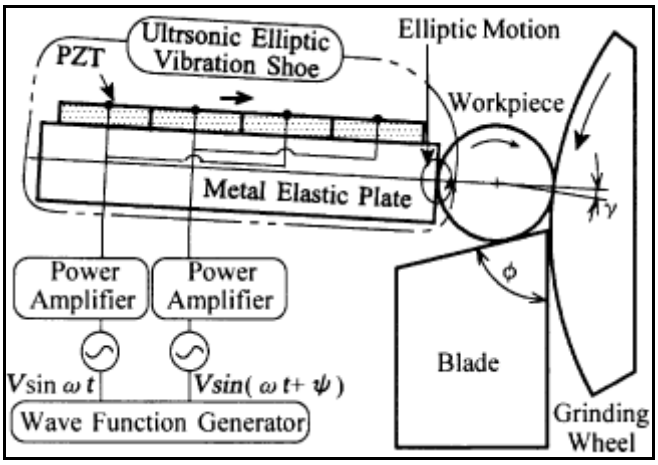


Fig. 2.2.24 Principle of ultrasonic elliptical vibration shoe centreless grinding (Wu et al., 2004b)

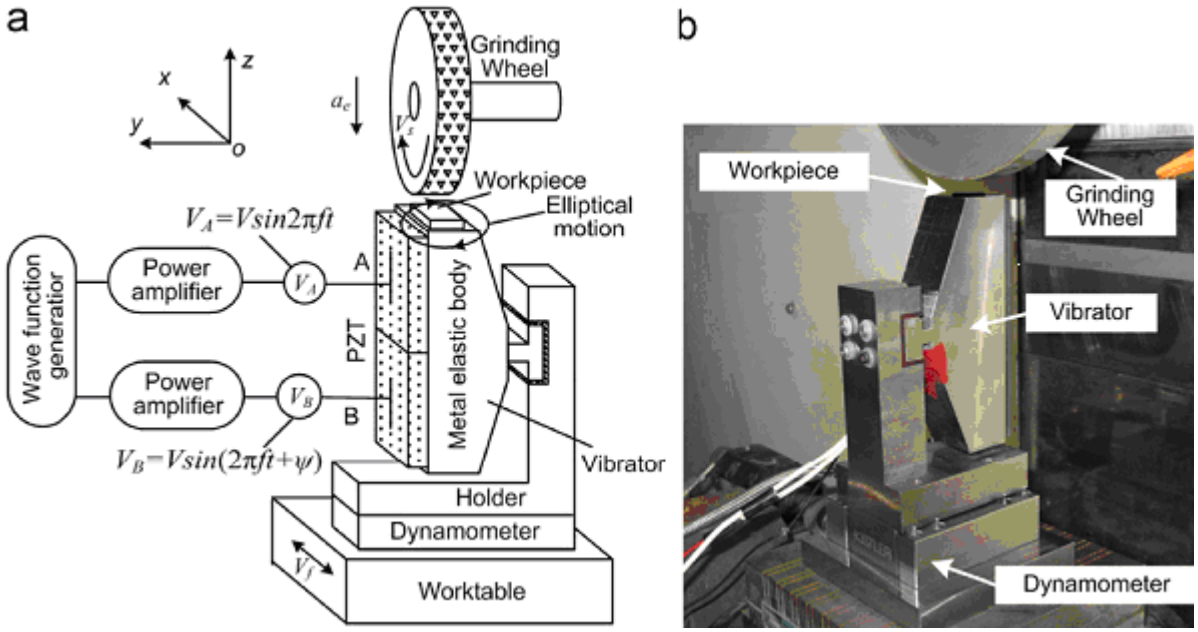


Fig. 2.2.25 Experimental set-up (a) Schematic drawing, (b) Photograph (Liang et al., 2010)

Elliptical ultrasonic assisted grinding (EUAG) also helped to increase the steady process region during grinding by 20% compared with conventional machining, indicating that the grinding wheel had a longer sharp cutting period in EUAG. Figure 2.2.26(a) shows that the main wear mechanisms in conventional grinding were macro-fracture and generation of wear flats, whereas micro-fracture and cleavage of abrasive grains were the dominating wear

mechanisms during EUAG as seen from Fig. 2.2.26(b). This had a positive effect, producing better grinding performance with lower grinding forces, force ratio, wheel loading and a smoother work-surface (Liang et al., 2012).

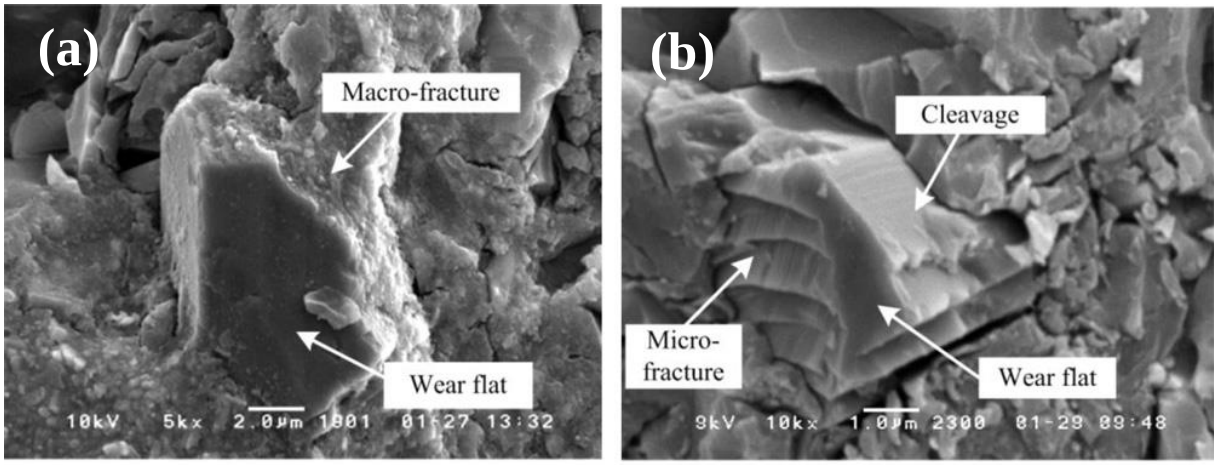


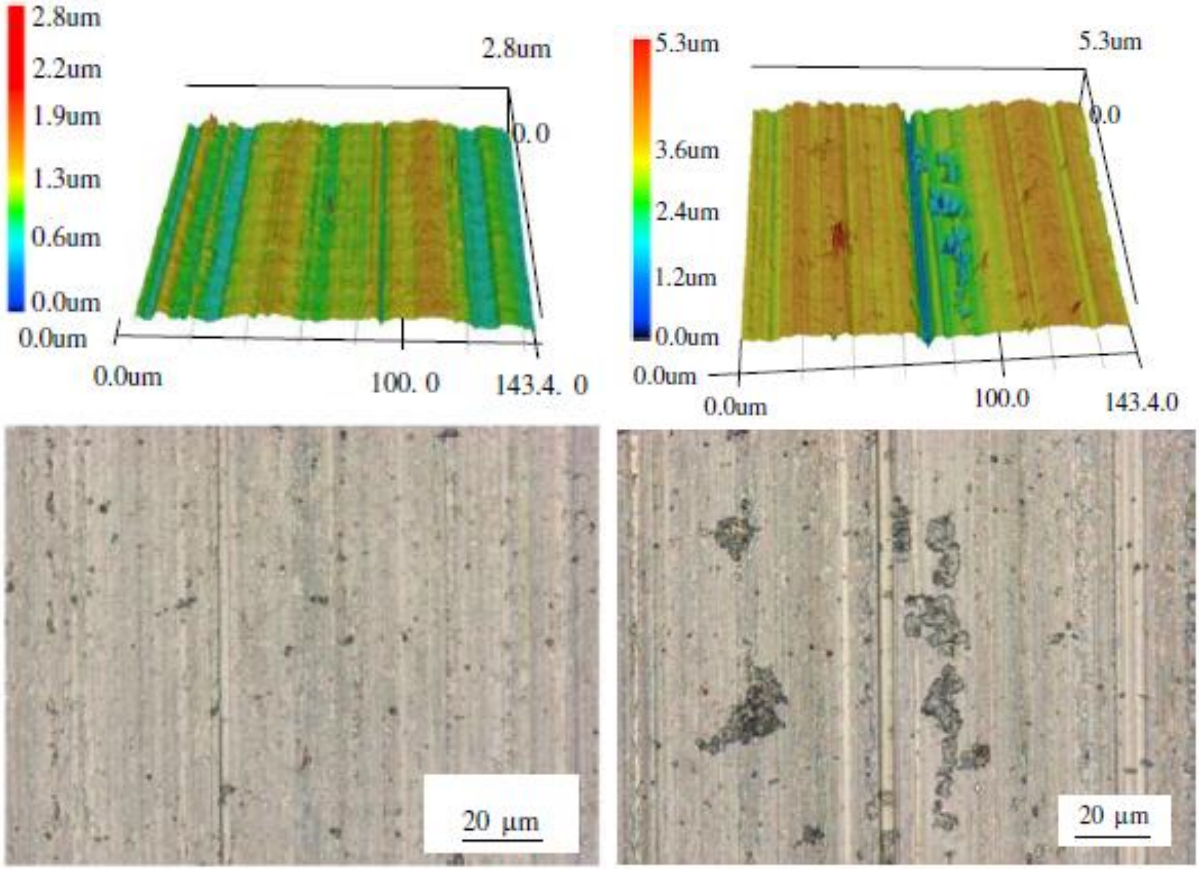
Fig. 2.2.26 Topography of abrasive grain in the wheel surface following grinding of sapphire: (a) Conventional grinding, (b) Elliptic ultrasonic assisted grinding (Liang et al., 2012)

The same ultrasonic elliptical vibration system was utilised in dry grinding of polysilicon by Peng et al. (2011), where the workpiece was vibrated in the longitudinal and vertical directions simultaneously at frequencies of 21.871 and 21.885 kHz and amplitudes of 0.5 and 0.2 μm respectively. The approach produced lower grinding forces along with an improvement in surface finish by 15-26% compared with results in conventional grinding. Workpiece surfaces exhibited smaller grooves, fewer brittle cracks and a much smoother appearance (Fig. 2.2.27). The material removal mechanism transformed from brittle fracture to a ductile grinding regime under the action of vibration and produced continuous chips (Peng et al., 2012a).

Using the EUAG system developed by Wu et al. (2004b), Peng et al. (2012b) further tested vibration assisted scratching on polysilicon with a diamond scriber. The approach was detailed as elliptical ultrasonic vibration assisted cutting or EUVAC and operated at a frequency of 21.9 kHz with amplitudes of 0.8 and 0.6 μm along the two axes of the ellipse respectively. The scratch marks under different cutting conditions are shown in Fig. 2.2.28. The plastic flow of the material under ductile material removal in EUVAC is apparent from the SEM micrographs. The interrupted cutting action in EUVAC decreased the tool wear as well as the cutting time of the diamond tool.

Wu et al. (2009) further developed a rotary ultrasonic spindle consisting of two rotary bearings and their housings to hold the spindle, eight electromagnets and their supporters for the generation of a fluctuating electromagnetic force, and a base plate. Its performance was

investigated for different machining conditions. The results showed that an ultrasonic vibration with a sub-micron amplitude was generated on the spindle and that the applied electromagnetic force affected the spindle performance significantly.



(a) (b)

Fig. 2.2.27 Surface condition of polysilicon when ground: (a) With ultrasonic elliptical vibration, (b) Without ultrasonic elliptical vibration (Peng et al., 2011)

In order to grind difficult-to-machine ceramic matrix composites (CMC), Azarhoushang and Tawakoli (2011) developed a block sonotrode using a perforated plate and demonstrated multi-resonant frequency behaviour. The 3D model of the acoustic head and the amplitude versus frequency from the 3D modelling of harmonic analysis are shown in Fig. 2.2.29(a) and (b) respectively. In experimental work, two different ceramic matrix composites, C/SiC-I and C/SiC-II, were used as the workpiece materials, vibrating parallel to the feed direction at a frequency of 20 kHz and an amplitude of 8 μm. The effects of process variables, such as feed speed, cutting speed, and the influence of workpiece material and the grinding process on wheel wear, grinding forces, workpiece surface roughness, and debris, were investigated. The experimental set up is detailed in Fig. 2.2.30. Results showed a significant reduction in grinding forces (up to 20%) and surface roughness (up to 30%), together with lower radial

wheel wear and higher G-ratio for the metal bonded diamond wheel, when grinding with superimposed ultrasonic vibration.

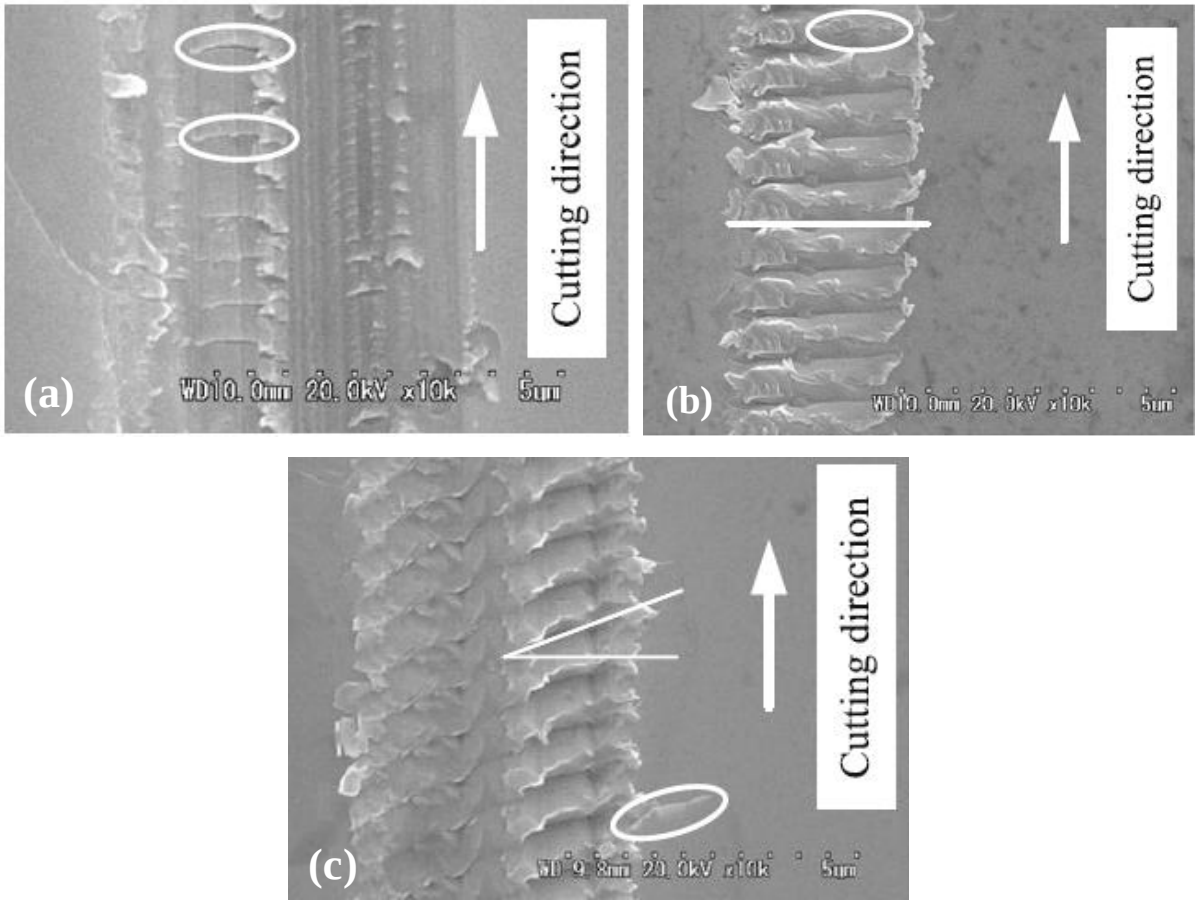
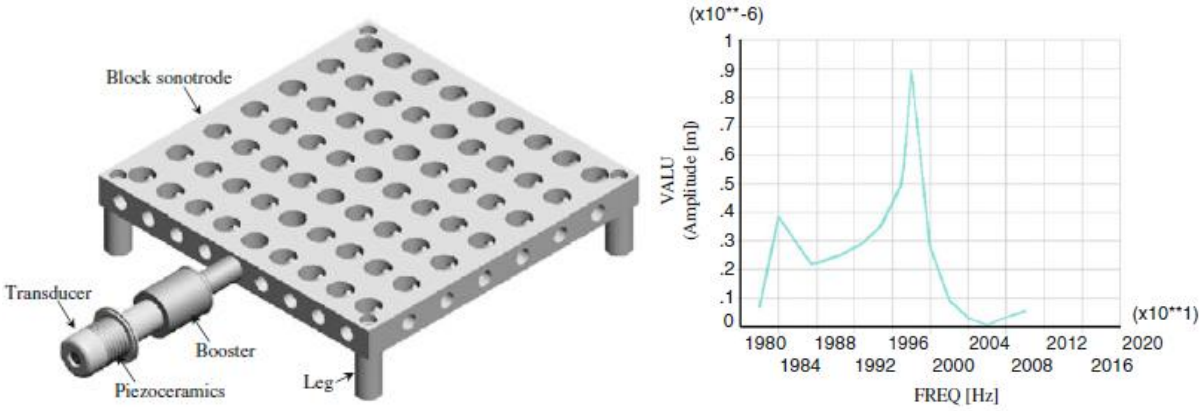


Fig. 2.2.28 SEM of scratches: (a) Scratch without ultrasonication, (b) Scratch with parallel ultrasonication, (c) Scratch with normal ultrasonication (Peng et al., 2012b)



(a) (b)

Fig. 2.2.29 (a) 3D model of acoustic head, (b) Amplitude Vs frequency from harmonic analysis in 3D modelling (Azarhoushang and Tawakoli, 2011)

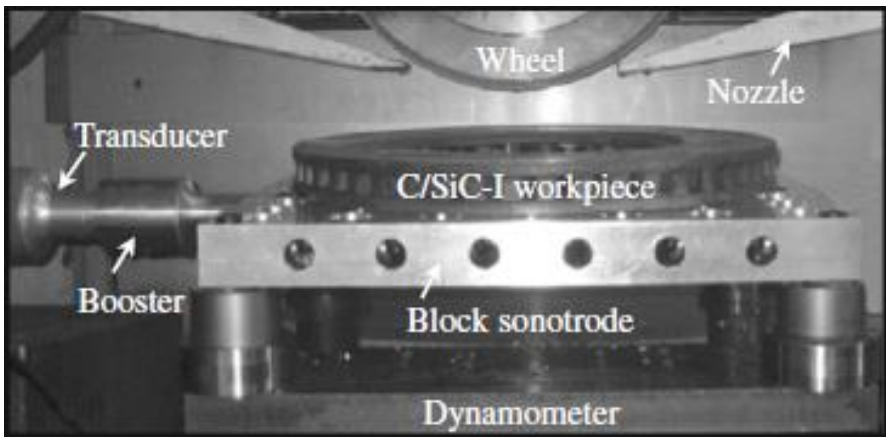


Fig. 2.2.30 The experimental set up (Azarhoushang and Tawakoli, 2011)

(b) Steel workpieces

Some of the earliest work relating to ultrasonic assisted grinding was carried out on AISI 1020 and AISI 52100 steel with workpieces mounted on a nickel stack (magnetostrictive transducer) and vibrated at a frequency of 10-18 kHz and an amplitude of 25.4 µm (Colwell, 1956). A maximum reduction in surface roughness of 60% was observed when grinding the 52100 steel. Microscopic examination of the grinding swarf and visual observation of the spark stream showed a smaller percentage of globules and thinner chips, thereby indicating lower temperature as a result of induced vibration. The vibration produced uniform breakdown of the wheel surface, thus avoiding abnormal wear and higher temperatures from those portions of a grinding wheel duller than the average. Residual stress measurements were carried out on ultrasonically and non-ultrasonically ground SAE X 4340 steel specimens, the former case producing lower tensile stress levels. Despite such advantages, vibration caused higher wheel breakdown resulting in a lowering of G-ratio when grinding 52100 steel. The paper by Colwell (1956) also highlighted advantages of US assistance when grinding Ti 150A titanium and Carboloy 78B tungsten carbide (WC). While generally not recommended for tungsten carbide, it was possible to produce thermally crack-free WC inserts with aluminium oxide (Corundum) wheels.

The critical speed of a single abrasive grit in tangential ultrasonic assisted grinding (TUAG) was formulated using mathematical modelling by Zhang and Zhang (2009). The expression not only contained the amplitude and frequency of US vibration but also included the grinding velocity and inter-grit spaces. Experimental trials on grinding of AISI 1045 steel were subsequently carried out with a metal bonded cBN wheel while the workpiece was vibrated tangentially to the wheel velocity at a frequency of 22.1 kHz and an amplitude of 4 µm. Significant reductions in both normal and tangential forces were observed when the

workpiece feed speed was below the critical speed, however the forces in TUAG approximated to those in conventional grinding (CG) as the value of feed speed approached that of the critical speed.

Tawakoli and Azarhoushang (2008) and Tawakoli et al. (2009a and 2009b) undertook a detailed study to investigate the feasibility of ultrasonic assisted dry grinding (UADG) of soft steels in an attempt to minimise/eliminate the need for coolant. A vitrified bonded alumina wheel was utilised to grind 100Cr6 (82 HRB) workpiece material which was vibrated in the feed direction at a frequency of 23 kHz and an amplitude of 10 µm (Tawakoli and Azarhoushang, 2008). The set up configuration is detailed in Fig. 2.2.31(a). The results showed reductions in the normal and tangential forces by up to 70% and 50% respectively when employing ultrasonic assistance compared with conventional dry grinding (CDG) (see Fig. 2.2.31(b)).

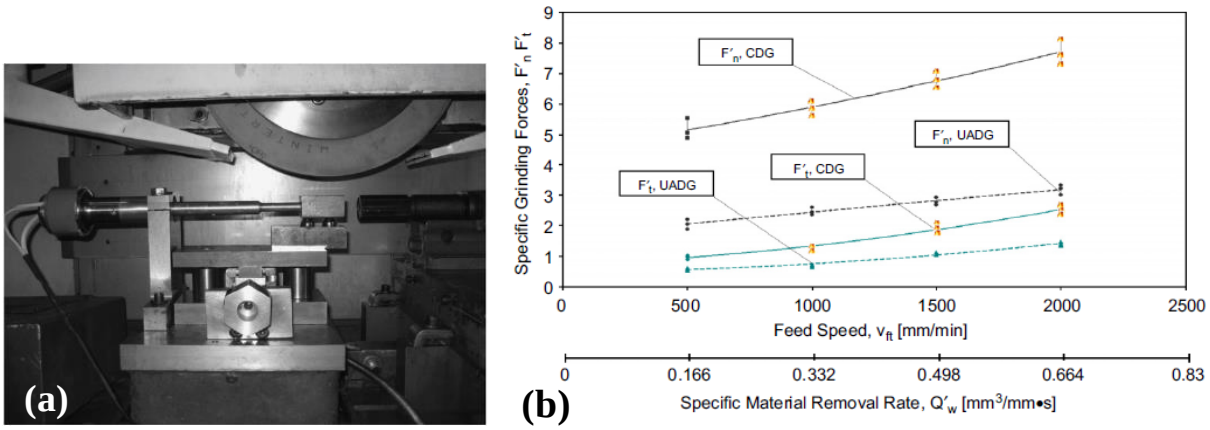


Fig. 2.2.31 (a) Experimental set up for ultrasonic assisted dry grinding, (b) Graph for specific grinding forces Vs feed rate (Tawakoli and Azarhoushang, 2008)

Ultrasonic actuation also limited thermal damage/grinding burn on the workpiece surface, thereby improving workpiece surface finish. Ultrasonic assisted dry grinding rendered a higher G-ratio and smaller grinding swarf in comparison to CDG. Similar benefits were obtained when the wheel and workpiece were utilised in a wet environment (Tawakoli et al., 2009d). In a different study, a vitrified bonded cBN wheel was employed in grinding 100Cr6 material with (Tawakoli et al., 2009a and 2009c) and without grinding fluid (Tawakoli et al., 2009a) when the workpiece was vibrated in the transverse-feed direction at a frequency and amplitude of 21 kHz and 10 µm respectively. The grinding burn was absent under both wet and dry conditions (Fig. 2.2.32(a)) when operating with ultrasonic assistance, which also contributed in reducing the grinding forces and workpiece surface roughness (R_z in particular) by 30-50% (Fig. 2.2.32(b) and 2.2.32(c)).

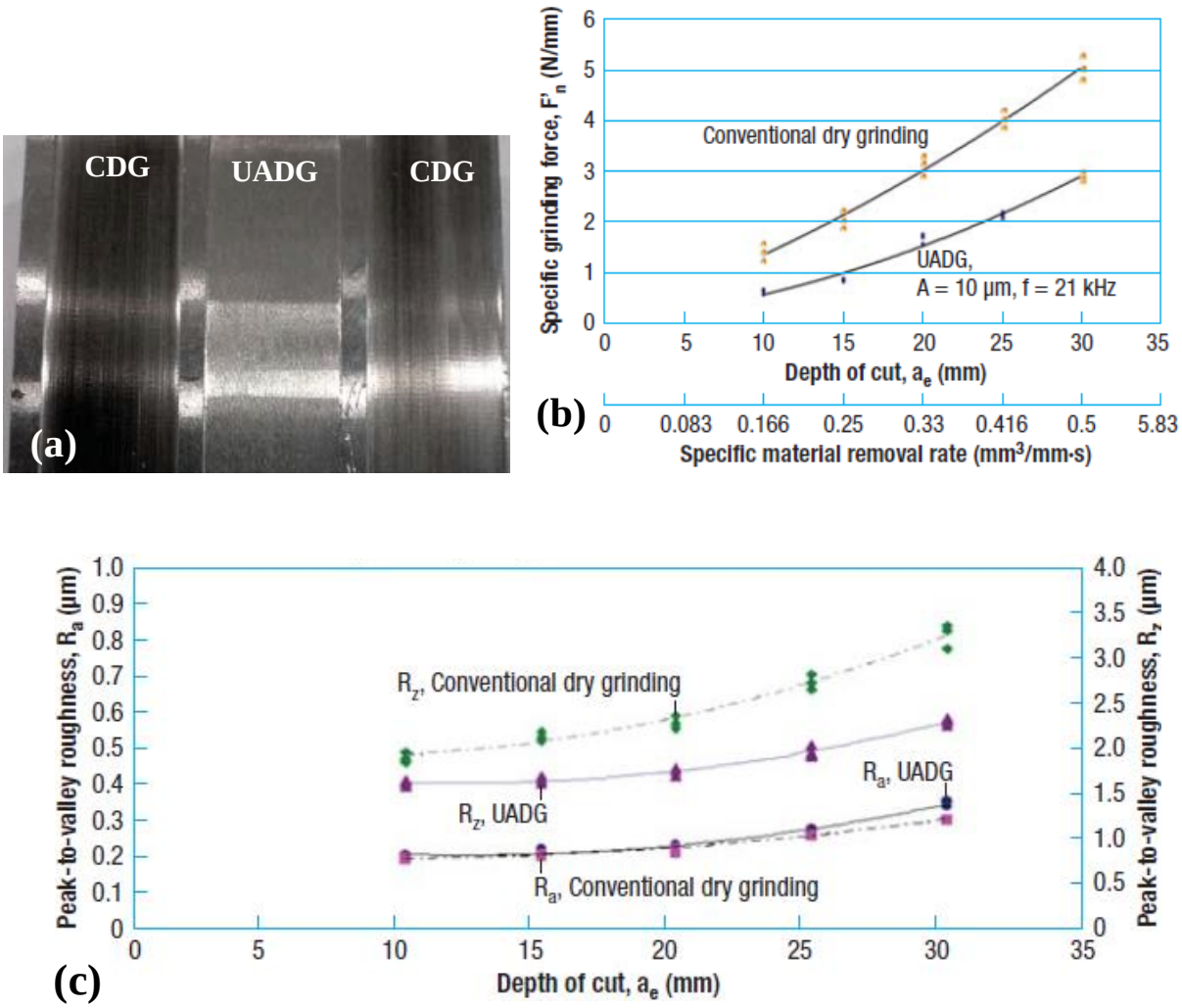


Fig. 2.2.32 (a) Photograph of ground workpiece surfaces, (b) Specific normal grinding forces as a function of depth of cut, (c) Surface roughness values R_a and R_z as a function of depth of cut (Tawakoli et al., 2009a)

Similar results were observed when a vitrified cBN wheel was used in dry grinding 42CrMo4 (85 HRB), the workpiece being vibrated in the cross-feed direction at a frequency of 21 kHz and an amplitude of 10 µm (Tawakoli et al., 2009b). A subsequent study on kinematic aspects of UDAG showed that the nature of the cutting process changed in UADG, to involve multiple-impact interaction between the tool and the formed chip (shown in Fig. 2.2.33), resulting in interrupted cutting and reduced grinding forces, frictional effects and the plastic deformation zone.

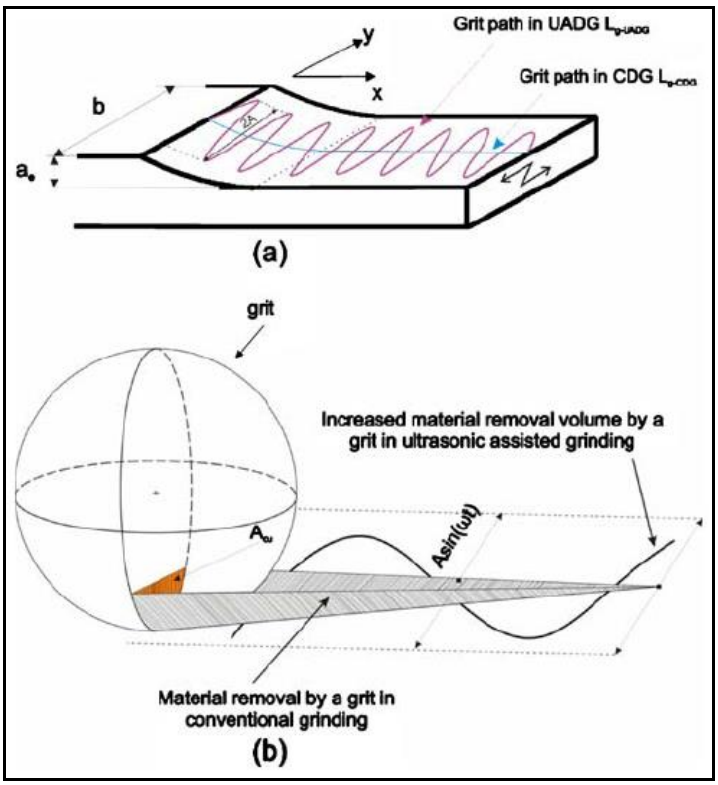


Fig. 2.2.33 Grinding model for ultrasonic assisted grinding (UAG): (a) Schematic of the motion of a grit on the workpiece surface, (b) Path generation of a grit by UAG (Tawakoli et al., 2009b)

Following the use of a conical horn for ultrasonic assisted grinding, Azarhoushang and Tawakoli (2012) further employed the specially designed block sonotrode, mentioned previously, for grinding 100Cr6 (60 HRC) with a vitrified bonded cBN wheel (B126C125V). The acoustic head exhibited a multi-resonant frequency behaviour with one of the resonant frequencies at ~20 kHz. New multi-frequency multi-mode modulated (MMM) technology, developed by MP Interconsulting, Switzerland, was utilised in designing the ultrasonic generator which was capable of synchronously producing many vibrating modes in order to generate uniform and repeatable multimode vibrations with high intensity, while avoiding the creation of stationary and standing waves. The MMM generator was also able to produce variable frequency sweeping oscillations around a central operating frequency, and contained an amplitude-modulated output signal. During the grinding trials (Azarhoushang and Tawakoli, 2012), the set frequency and amplitude for the workpiece vibration were 22 kHz and 10 μm respectively. Comparative experiments demonstrated reductions in grinding force by up to 25% for the workpieces machined with superimposed ultrasonic vibration. Some of the conventionally ground workpieces exhibited thermal damage such as grinding cracks and burns due to the high cutting forces and temperatures in the contact zone however, with UAG thermal damage was reduced as was wheel wear due to lower grinding forces and

temperatures. It was also found that UAG led to significant improvements in R_z, which was possibly due to the longer interaction between the grit and the workpiece surface under the influence of ultrasonic actuation. Similar reductions in the values of R_a and R_t by up to 20% when ultrasonically grinding AISI 1045 steel using aluminium oxide wheels (99A120K8V) were reported by Chen et al. (2013).

Although in the majority of papers a vibration frequency of ~20 kHz was utilised, Tsiakoumis and Batako (2012) applied a much lower frequency of 275 Hz when dry grinding three different steel workpieces viz. mild steel (BS970 080440, HRB 90.1), hardened En31 (BS534A99, HRC 64.5) and M2 tool steel (BS BM2, HRC 62) with medium grade semi-friable alumina (454A 601 L 7G V3) and Altos long grain friable wheels. The ultrasonic actuation did not reduce grinding forces when grinding the mild steel. The reason was attributed to the soft and ductile nature of mild steel, which deformed elastically without actual fracture under the action of vibration. In contrast, reductions in normal and tangential grinding forces by up to 10% were observed for the other two workpieces under hybrid operation. The trend in the force values was similar with the Altos wheel; a 23.6% reduction in tangential forces was noted when grinding M2 tool steel. The surface roughness values were generally lower for all three workpieces when using UAG.

(c) Aerospace alloys

Although there have been some instances were ultrasonic vibration was applied in turning of titanium alloys (Muhammad et al., 2012), published work on ultrasonic assisted grinding of titanium and nickel based aerospace alloys is limited. An ultrasonic machining unit for grinding of Ti-6Al-4V was developed by Nik et al. (2012) using mathematical modelling, FEM and genetic algorithms. The ultrasonic arrangement is shown in Fig. 2.2.34. The grinding trials were conducted using a Tyrolit (89A60K5AV217) wheel with the workpiece vibrated at a frequency of ~20.4 kHz in the longitudinal direction. UAG rendered reductions in normal and tangential forces by 13.5% and 14.2% respectively together with a 10% improvement in the surface roughness (Fig. 2.2.35). It was also stated that UAG could be carried out with higher wheel speed and depth of cut coupled with lower coolant consumption in comparison to conventional grinding, leading to a higher production rate and lower manufacturing cost.

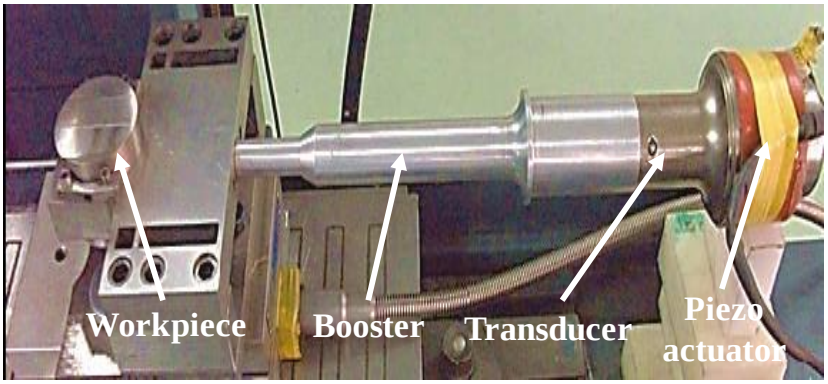


Fig. 2.2.34 Ultrasonic set up attached to the workpiece (Nik et al., 2012)

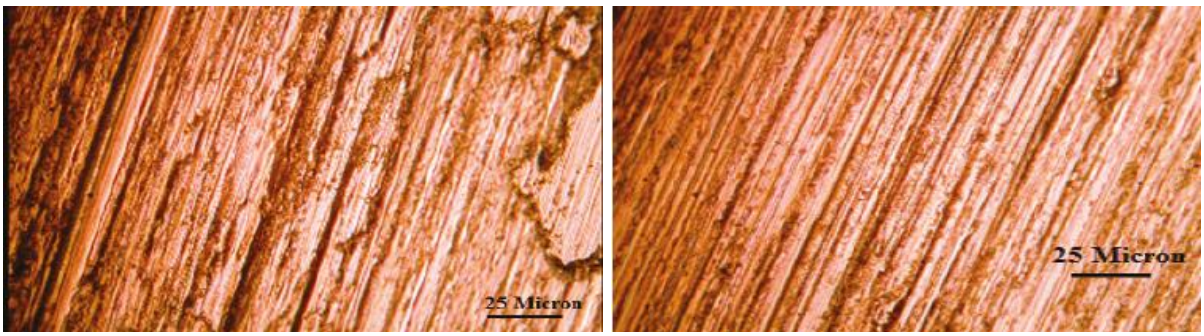


Fig. 2.2.35 Ground Ti-6Al-4V surfaces following dry grinding: (a) Without and (b) With ultrasonic assistance (Nik et al., 2012)

With regard to nickel based alloys, Abdullah et al. (2012) performed dry creep feed grinding and modelling research on Inconel 738LC superalloy under conventional and ultrasonic grinding conditions. An FE simulation of the grinding process and the kinematics of an abrasive grain along the cutting path with and without ultrasonic actuation were carried out. During the grinding trials the workpiece was vibrated in the feed direction with a frequency of 25 kHz and amplitude of ~1 µm. The kinemantic analysis showed that the motion of a single grain followed a continuous arc in conventional grinding, whereas it approximated a semi-sinusoidal curve when machining was assisted with vibration. The mechanism of chip formation obtained from FE modelling was found to be discontinuous under ultrasonic action, which corroborated the analytical results. The predicted vertical and horizontal grinding forces obtained with ultrasonic assistance were 42% and 38% lower respectively than those estimated in conventional grinding. The experimental results were in good agreement with the theoretical findings with reductions in vertical and horizontal forces by up to 27% and 22% respectively under hybrid conditions (Fig. 2.2.36).

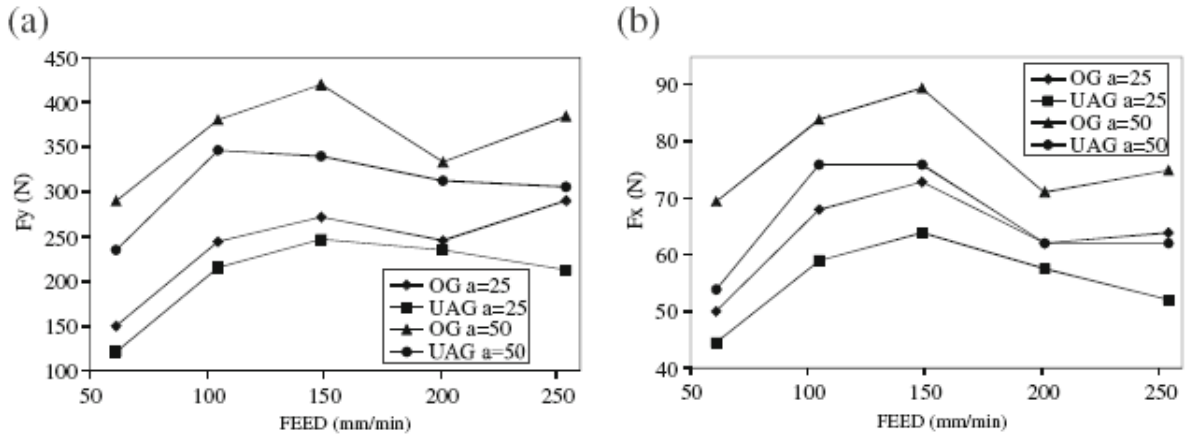


Fig. 2.2.36 Experimental grinding forces Vs feed rate at depths of cut of 25 and 50 µm: (a) Vertical forces (b) Horizontal forces (Abdullah et al., 2012)

(d) Aluminium workpieces

While grinding is not generally recommended for machining of aluminium, a recent paper has disclosed the effects of ultrasonic vibration when creep feed grinding Al 7075 with results compared with those obtained when UACFG of steel X210Cr12 (Abdullah et al., 2013). A 200 W sandwich Langevin type piezoelectric transducer was employed to transmit vibration to the workpiece in the feed direction while the grinding was carried out with alumina wheels at a wheel speed of 23.55 m/s, feed rates of 151 to 364 mm/min and depths of cut of 50 to 150µm. The maximum horizontal and vertical grinding forces reduced by up to 61% and 46% respectively when grinding with ultrasonic assistance and the workpiece surface was clean and burn-free. Similar reductions in force were also noted when grinding steel under hybrid mode (54% for F_h and 75% for F_v), see Fig. 2.2.37. When grinding without ultrasonic assistance, heavy burn was observed on the machined steel surfaces, which were absent on those subject to UAG.

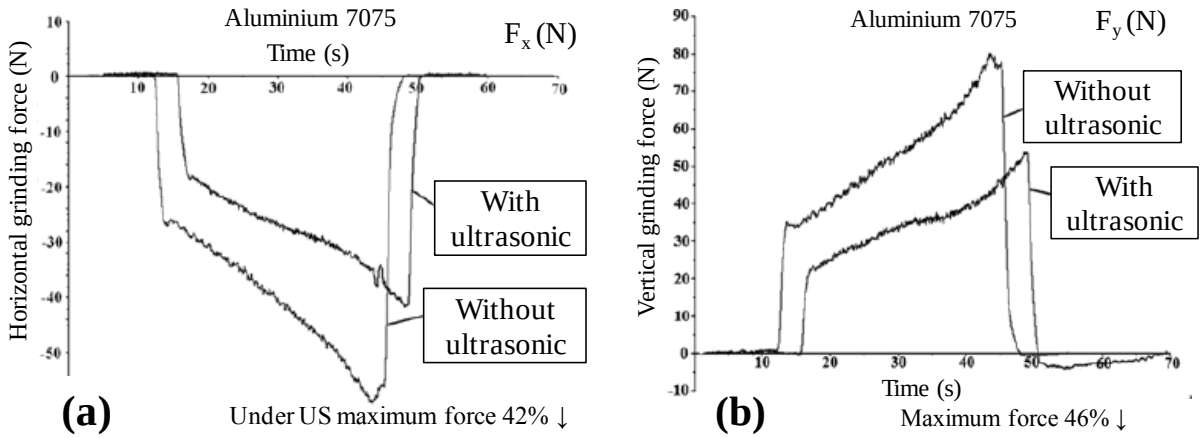


Fig. 2.2.37 Reduction in (a) Horizontal, (b) Vertical force when UAG (Abdullah et al., 2013)

2.2.3 Ultrasonic assisted dressing (UAD)

Dressing affects the performance of the grinding wheel by imparting the required wheel surface profile as well as suitable wheel topography (Tawakoli and Rasifard, 2011a). Dressing of a grinding wheel is carried out either with stationary or rotary dressers. The former type includes single-point, profile, multi-point diamond and dressing blades, whereas the latter may involve a profile roller, form roller or cup wheel. Published literature on ultrasonic assisted dressing details vibration superimposed on both stationary and roller dressers. Grinding forces typically decreased following ultrasonic assisted dressing compared with those obtained after conventional dressing (Tawakoli et al., 2008), however contradictory reports are available on the workpiece surface roughness recorded subsequent to dressing with and without ultrasonic actuation. It has been suggested that splintering and fracture of abrasive grains increases during dressing with ultrasonic actuation, which gives rise to a rougher wheel surface with fewer active cutting edges. This leads to a reduction in the grinding forces albeit at the cost of higher surface roughness on the ground workpieces. However, Jiao et al. (2006) reported that the surface finish was improved after an unstable initial grinding phase when a resin bonded SiC wheel was dressed with ultrasonic assistance. The effect of ultrasonic vibration on workpiece roughness depends on the grinding depth of cut with typically lower roughness values recorded when the depth of cut was higher than the amplitude of vibration.

As it is difficult to transmit an appropriate level of vibration to heavier and bulkier form rollers, compared with the stationary dressers, Tawakoli et al. (2011) developed a new form roller unit and employed it to dress cBN grinding wheels (Tawakoli and Rasifard, 2011b). As can be seen from Fig. 2.2.38, grinding forces decreased but workpiece roughness increased following ultrasonic assisted dressing; $A_{US} = 0$ denotes conventional dressing. Tawakoli et al. (2011) also showed that the radial wear of the form roller decreased when UAD was carried out in an up-mode, but increased during down-mode UAD, both in comparison to conventional dressing. In down-dressing, micro-splintering of the grits resulting from the mechanical load is the main wear mechanism of the dresser tool, where graphitisation of the dressing diamonds due to abrasive friction is the principal mechanism of wear during up-dressing. While ultrasonic assistance leads to an increase in the impacting load on the diamond grains, it also increases the coolant supply into the dressing contact zone, thereby lowering the coefficient of friction between the diamond grits on the dresser and the grains on the wheel surface. This reduces the generation of heat in the dressing zone and the propensity for graphitisation. It was concluded that ultrasonic assistance strengthened the principal

mechanism of diamond wear in up-dressing. While the conventional dressing of vitrified cBN wheels are usually carried out in down-dressing mode (i.e. $q_d > 0$), a comparable wheel topography can be obtained with ultrasonic assisted up-dressing (i.e. in the range $q_d < 0$), with much lower form roller wear.

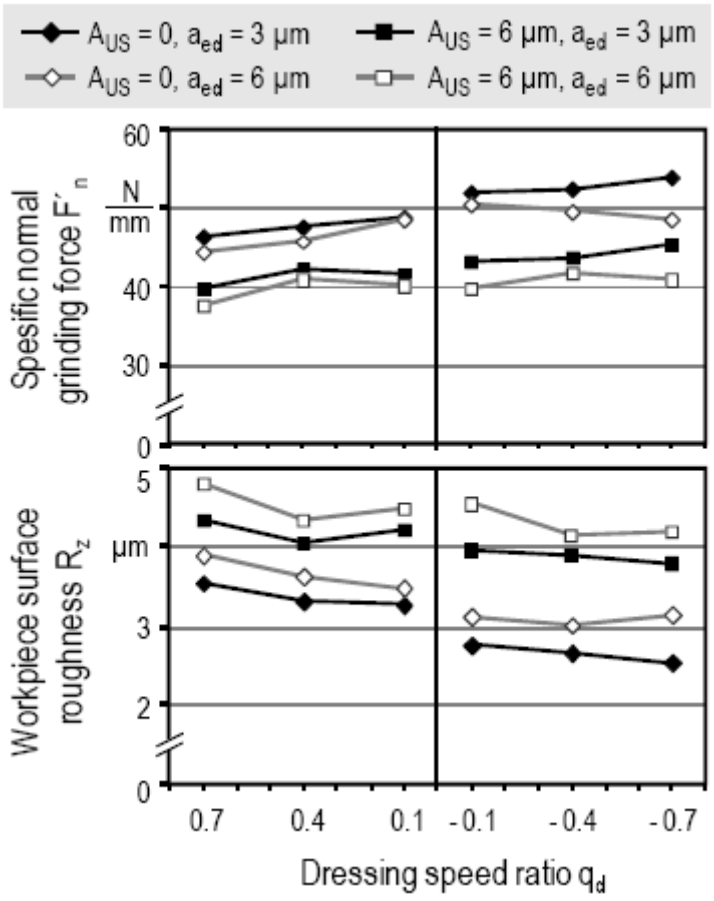


Fig. 2.2.38 Reduction in grinding forces and increase in workpiece roughness following ultrasonic assisted dressing with form roller, A_{US}: amplitude of vibration, a_{ed}: dressing depth of cut (Tawakoli et al., 2011)

2.3 Creep feed grinding (CFG)

2.3.1 Introduction

Grinding has traditionally been employed as a finishing operation in order to impart the desired surface finish and dimensional accuracy to components which have been processed by primary manufacturing processes, such as casting/forming, followed by subsequent machining operations such as turning, milling or broaching. Creep feed grinding (CFG) extends the application of grinding to encompass the preliminary stock removal as well as finishing operations (Andrew et al., 1985). Early references to CFG can be found in the

1960's stemming from collaborative work between the University of Bristol and Rolls Royce, where a study was carried out to find a way of removing large quantities of thermally sensitive, abrasive resistant material, more quickly and economically to closer tolerances than could be achieved with broaching, which was typically used at that time for complex shapes (Excell, 1995). In contrast to conventional grinding (known as pendulum or reciprocating grinding), creep feed grinding is essentially intended to remove most of the material in only one pass, however several passes may be employed when the depth of cut is large. Traditionally, the term 'creep' denotes the slow speed of the workpiece, typically in the range of 10-1000 mm/min while the high depth of cut is in the region of 1-10 mm or even larger, whereas in pendulum grinding, where values of between 5 to 25 m/min and 2 to 25 μm respectively are more typical. This produces a substantial reduction in cycle time (by ~60%) compared to reciprocating surface grinding (Anon., 1981). Figure 2.3.1 shows a comparison between pendulum and creep feed grinding in terms of the depth of cut and arc length. In the former type of grinding, the arc length is in the range of 1-3 mm, whereas for the latter case, the value lies between 10-30 mm.

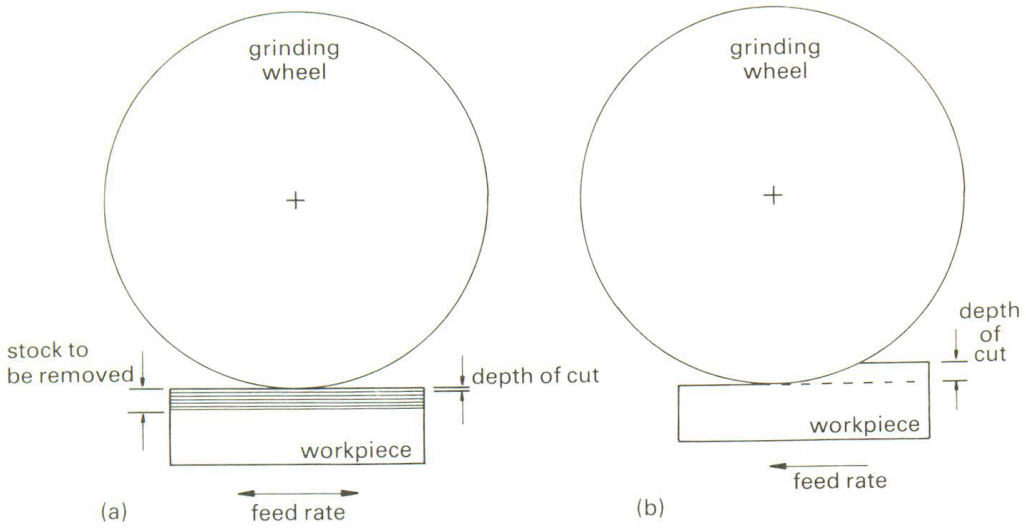


Fig. 2.3.1 Comparison between (a) Reciprocating surface grinding and (b) Creep feed grinding (Andrew et al., 1985)

Due to the longer length of contact, slow feed rate and heavy depth of cut in CFG, an extremely heavy-duty dynamically rigid machine with appropriate coolant application are required in order to prevent workpiece burn (see a typical example in Fig. 2.3.2) and damage to the surface integrity of final parts (Ye and Pearce, 1984). The design and location of the fluid delivery nozzles are one of the critical aspects of creep feed grinding. The nozzles must direct the flow of the coolant into the grinding zone to match the wheel's peripheral speed in

order to achieve optimum performance (Noaker, 1993). More recently, VIPER (Very Impressive Performance Extreme Removal) grinding has been developed using Programmable Coolant Nozzles (PCN) to inject high pressure fluid both circumferentially and radially around the grinding wheel (Scott, 2000).

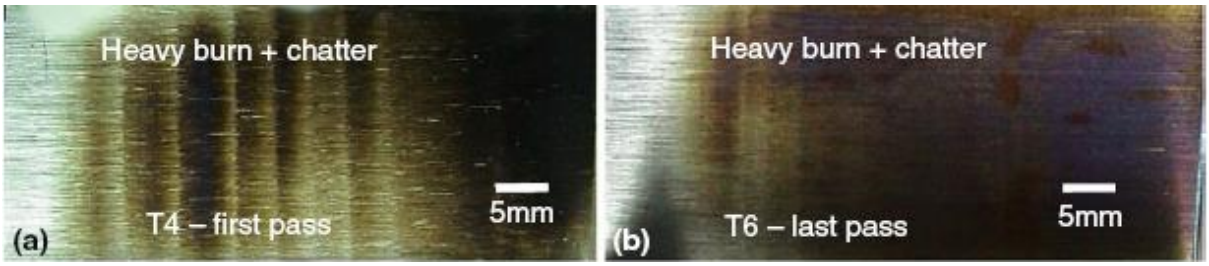


Fig. 2.3.2 Surface burn when creep feed grinding of burn-resistant titanium alloy (BuRTi) (Soo et al., 2011b)

The choice of grinding wheel is another important aspect in CFG. While the wheel hardness and structure number in pendulum grinding are typically G to J and 5 to 7 respectively, CFG uses softer wheels generally with hardness F and G and more open structure (structure number of 20 or higher). This helps in greater ingress of coolant/lubricant in the grinding zone and better retention of wheel form in profile grinding.

2.3.2 Mechanics

A schematic diagram of the grinding process is shown in Fig. 2.3.3, where the wheel diameter, depth of cut and maximum uncut chip thickness are denoted as D, a_e and h_m respectively. The peripheral speed of the wheel is represented as V_C and that of the workpiece is given as V_W. For $V_W << V_C$, the contact length (l_g) between the wheel and the work surface is expressed as:

$$l_g = \sqrt{a_e \times D} \quad \text{… 2.5 (Malkin, 1989)}$$

Considering a triangular cross-section of the chip, the maximum uncut chip thickness (h_m) can be derived as:

$$h_m = \left(\frac{3}{c \tan \alpha} \cdot \frac{V_W}{V_C} \cdot \sqrt{\frac{a_e}{D}} \right)^{1/2} \quad \text{… 2.6 (Hwang et al., 2000)}$$

where,

h_m: Undeformed chip thickness (mm)

c: Active cutting point density (number/mm^2)

α: Semi-included angle for the undeformed chip cross-section (degree)

V_C: Wheel velocity (m/s)

V_W: Table feed (mm/min)

a_e: Wheel depth of cut (mm)

D: Wheel diameter (mm)

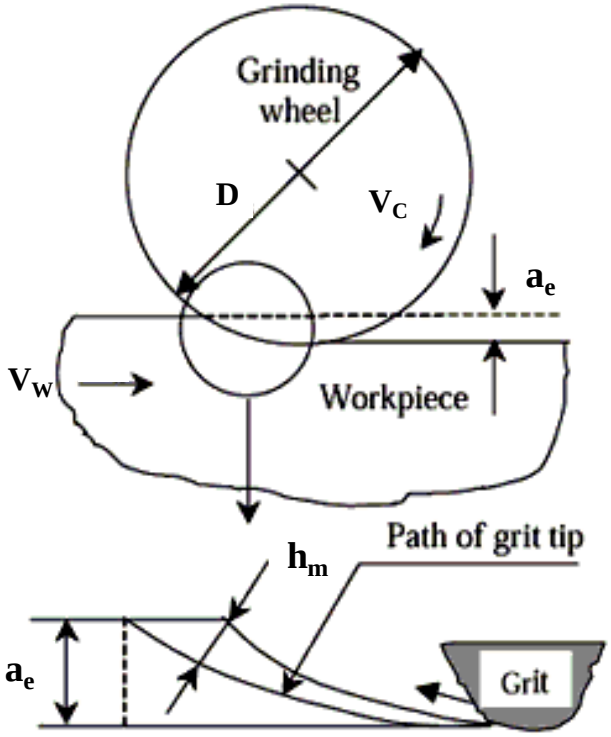


Fig. 2.3.3 Schematic diagram of grinding process showing different process variables (Bianchi et al., 2001)

The range of h_m, which is used within Rolls Royce when creep feed grinding of Inconel, lies between 0.25 to 1.5 µm with the upper limit of 1.5 µm for rough cut operations (Personal communication).

In creep feed grinding, the grinding forces are usually termed as vertical (F_v) and horizontal (F_h) forces, as opposed to the terms normal (F_n) and tangential (F_t) forces used in surface grinding. For small depths of cut and short arc length, $F_n \approx F_v$ and $F_t \approx F_h$, however this is not the case in creep feed grinding due to the much higher depth of cut and longer length of the arc.

The grinding power and specific energy are calculated according to the following equations:

Grinding power = Tangential force × wheel velocity … 2.7 (Malkin, 1989)

$$\text{Specific energy} = \frac{\text{Grinding power}}{\text{Material removal rate}} \quad \ldots 2.8 \text{ (Andrew et al., 1985)}$$

The specific energy in grinding is the result of rubbing, ploughing and shearing/micro-cutting actions. Typically, the value of specific energy in CFG is in the range of 10-1000 J/mm^3, whereas that in conventional grinding lies between 10-100 J/mm^3 (Andrew et al., 1985).

In order to predict the temperature generated in CFG, an approximate theoretical approach is undertaken by introducing a cooling term in Jaeger's (1942) moving heat source theory (Peters and Vansevenant, 1983, Andrew et al., 1985). The expression for workpiece temperature is shown in Eqn. 2.9.

$$T = \frac{2\kappa q}{\pi K V_w} f(X, L, H) \quad \ldots 2.9 \text{ (Andrew et al., 1985)}$$

where the non-dimensional parameters X, L and H are defined as follows:

$$X = \frac{V_w \chi}{2\kappa} \quad \ldots 2.10$$

$$L = \frac{V_w l}{2\kappa} \quad \ldots 2.11$$

$$H = \frac{2\kappa h}{K V_w} \quad \ldots 2.12$$

q: Heat flux applied by the source

κ: Thermal diffusivity of the workpiece material

K: Thermal conductivity of the workpiece material

h: Convective heat transfer coefficient

2.3.3 Applications

Traditionally creep feed grinding was developed to replace broaching operations in manufacturing fir tree root forms in turbine blades. Applications of CFG have grown to include the production of automotive steering racks, scissor blades, broaches, pump rotors, dies and handsaws etc. (Excell, 1995). Materials ground using CFG include steels, ceramics, tungsten carbides, nickel based superalloys and gamma titanium aluminides.

Morgan and Salter (1984) studied CFG of various steel workpieces with different hardness values ground with vitrified alumina wheels. The harder specimens exhibited better

surface finish but produced greater wheel blunting. The effectiveness of fluid supply conditions and wheel cleaning parameters in creep feed grinding of alloyed steels has been investigated by a number of researchers (Webster et al., 2002, Cameron et al., 2010). The wheel speed was found to influence the critical specific grinding power at burn. The cooling efficiency was improved by preventing the side flow/escape of coolant from the grinding zone. There appeared to be a limit to the critical flow rate, beyond which no measurable advantage was obtained in terms of MRR or specific energy.

Examples of ceramic materials that have been creep feed ground cover partially stabilized zirconia (PSZ) (Hooper and Morgan, 1989), Al-995 alumina (Liao and Sathyanarayanan, 1994), tungsten carbide (Abdullah et al., 2007) etc. General observations stemming from the research included an increase in normal force, specific energy and power with finer wheel grain size and higher abrasive concentration ((Liao and Sathyanarayanan, 1994), increased side corner and radial wheel wear as well as surface roughness with a rise in table feed but a drop in wheel speed etc (Abdullah et al., 2007). Figure 2.3.4 shows the variation in radial wheel wear measured (Δr) at different levels of cutting speed and feed rate.

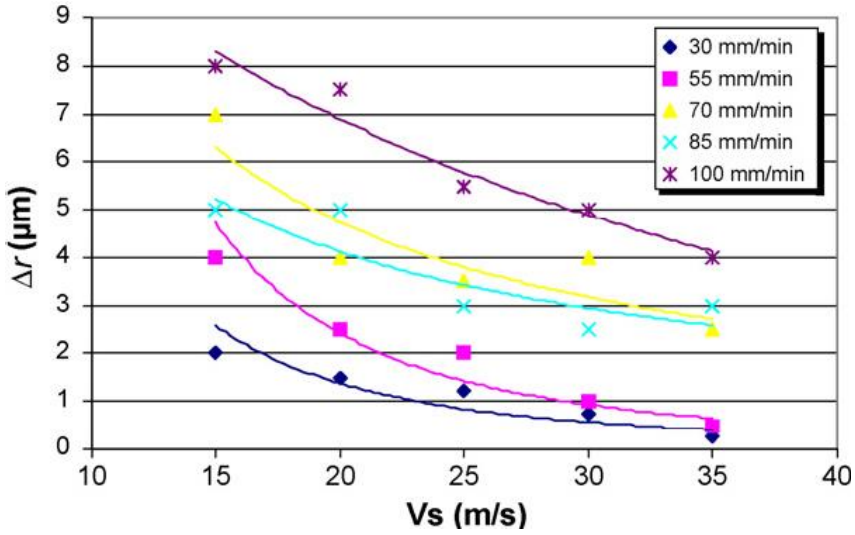


Fig. 2.3.4 Radial wheel wear measured (Δr) Vs cutting speed at different feed rates (Abdullah et al., 2007)

The major application of CFG is in the grinding aerospace alloys, such as Nimonic (Sunarto and Ichida, 2001), Rene (Vafaeesefat, 2009), Inconel (Abdullah et al., 2012) Udimet (Soo et al. 2002) etc. More recently, gamma titanium aluminide (Hood et al., 2007a) and burn-resistant titanium (BuRTi) alloys (Soo et al., 2011b) have been evaluated for CFG. Both conventional and superabrasive wheels were employed in grinding, however no major improvement was seen while using superabrasive wheels in terms of G-ratio (2 to 6). Typically, an increase in porosity of the wheel reduced grinding burn and cracks, albeit at the

cost of lower G-ratio and higher workpiece surface roughness. Cross-sections of machined specimens exhibited surface and sub-surface cracks when operating at higher depths of cut with bending of lamellae up to a depth of ~10 μm beneath the ground surface; a typical example is shown in Fig. 2.3.5 (Hood et al., 2007a).

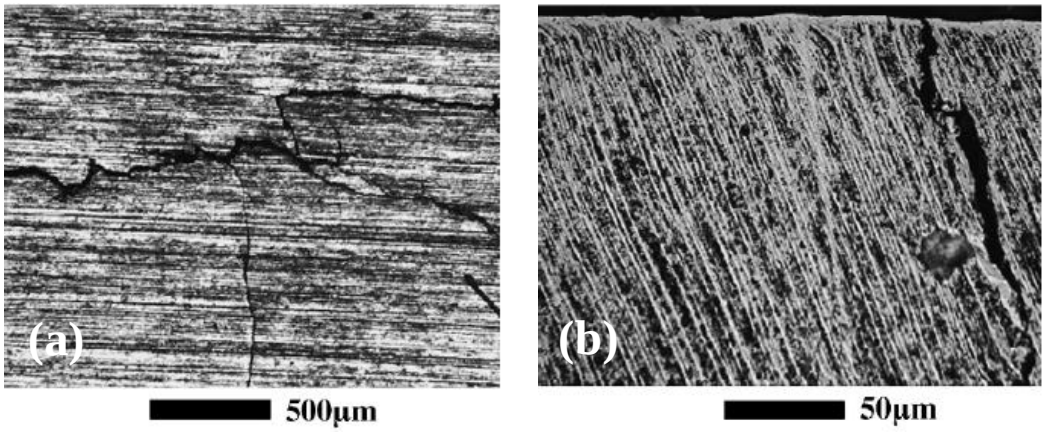


Fig. 2.3.5 (a) Crack on the machined surface, (b) Sub-surface crack shown on the cross-sectional view (Hood et al., 2007a)

2.3.4 Grinding wheel wear

The different types of grinding wheel wear are shown in Fig. 2.3.6, where 'A' denotes attritious wear while 'B' and 'C' represent grain fracture and bond fracture respectively (Malkin and Cook, 1971). Attritious wear is caused by various mechanisms such as rubbing of the abrasive particles against the work surface, gradual wear on the grits, minor chipping etc. This leads to flattening/dulling and generation of wear flats on the grits rendering a glazed appearance to the wheel when seen under a microscope. Typical examples of attritious wear are shown in Fig. 2.3.7 for single layer electroplated and brazed grinding wheels respectively. Fracture wear, in contrast, is the removal of the grits from the grinding wheel either by breakage within the grains or fracturing at the bond level. According to Yossifon and Rubenstein (1982), when grinding sticky materials like mild steel, three types of wear mechanism are prevalent, namely attritious wear, small-scale and large-scale adhesion.

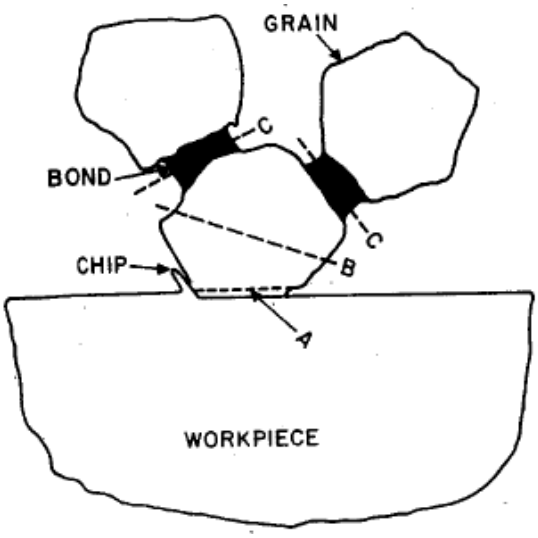


Fig. 2.3.6 Three types of wheel wear: A-Attritious wear, B-Grain fracture, C-Bond fracture (Malkin and Cook, 1971)

The wheel-workpiece-chip interactions in single-layer brazed and electroplated/galvanic grinding wheels are detailed by Ghosh and Chattopadhyay (2007) in Fig. 2.3.8. Due to the thickness of bond (~60-70% of the average grit height) the electroplated wheels are more prone to chip clogging/wheel loading. In contrast, the grains are more exposed in brazed wheels, thereby allowing greater chip accommodation, better penetration of coolant in the grinding zone and thus lower wheel loading. There are possibilities of wheel wear due to other interactions involving the chip-bond, chip-grit, chip-workpiece and bond-workpiece.

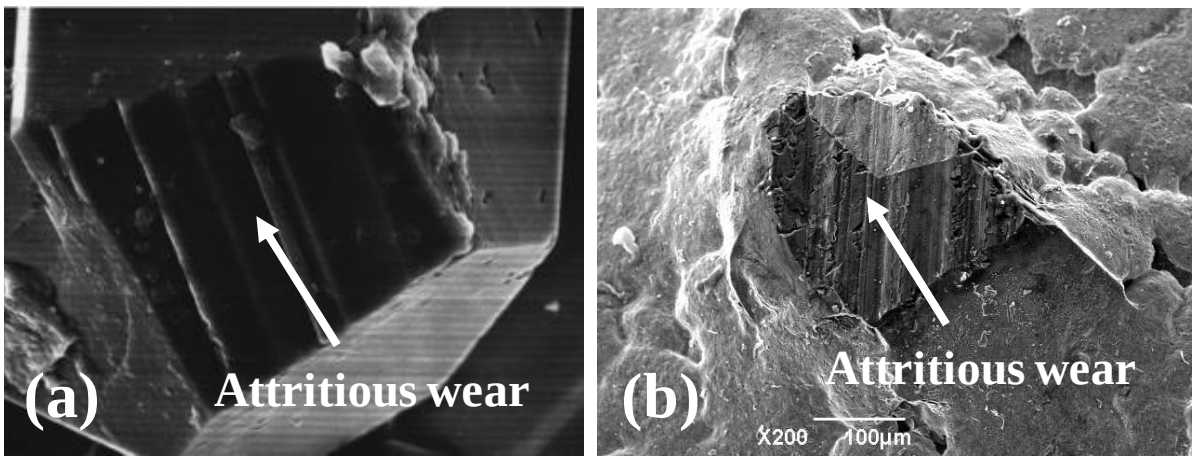


Fig. 2.3.7 Attritious wear on (a) An electroplated diamond grit (Hwang et al., 2000), (b) A brazed cBN grit (Bhaduri et al., 2011)

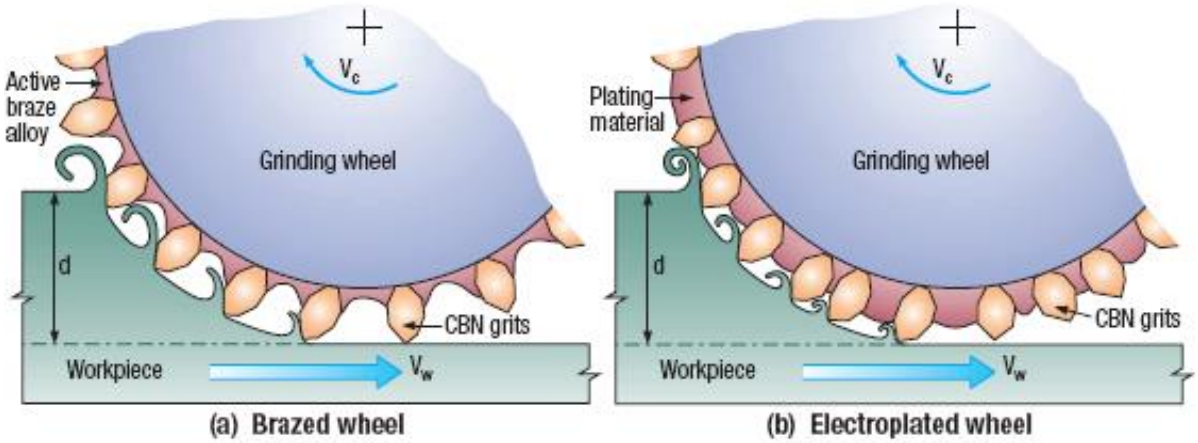


Fig. 2.3.8 Schematic diagram showing wheel-workpiece-chip interactions in: (a) Brazed wheel, (b) Electroplated wheel (Ghosh and Chattopadhyay, 2007)

The different grit/grain failures that can occur with electroplated wheels are shown in Fig. 2.3.9 (Bhaduri and Chattopadhyay, 2011). Grains can be pulled out of the nickel layer during grinding as the anchorage between the grit and the bond is purely mechanical and weak (Fig. 2.3.9(a)), as opposed to the strong chemical bond formed between the abrasive and the brazing alloy in brazed grinding wheels. The grains can also be fractured at the bond level (Fig. 2.3.9(b)), however this phenomenon is more common in brazed wheels due to the stress concentration at the interface of the grits and the bond. Monocrystalline grains used in galvanic wheels undergo breakage at cleavage planes above bond level, a typical example of which is shown in Fig. 2.3.9(c). Micro-fracturing of grits at the tip is depicted in Fig. 2.3.9(d) which exposes new active cutting points on the grains, leading to auto-sharpening of the grinding wheel.

Generally, grinding wheel wear is correlated with the calculation of G-ratio according to Eqn. 2.9.

$$\text{G - ratio} = \frac{\text{Volume of material removed from the workpiece}}{\text{Volume of material removed from the wheel}} \quad \ldots 2.13 \text{ (Hwang et al., 2000)}$$

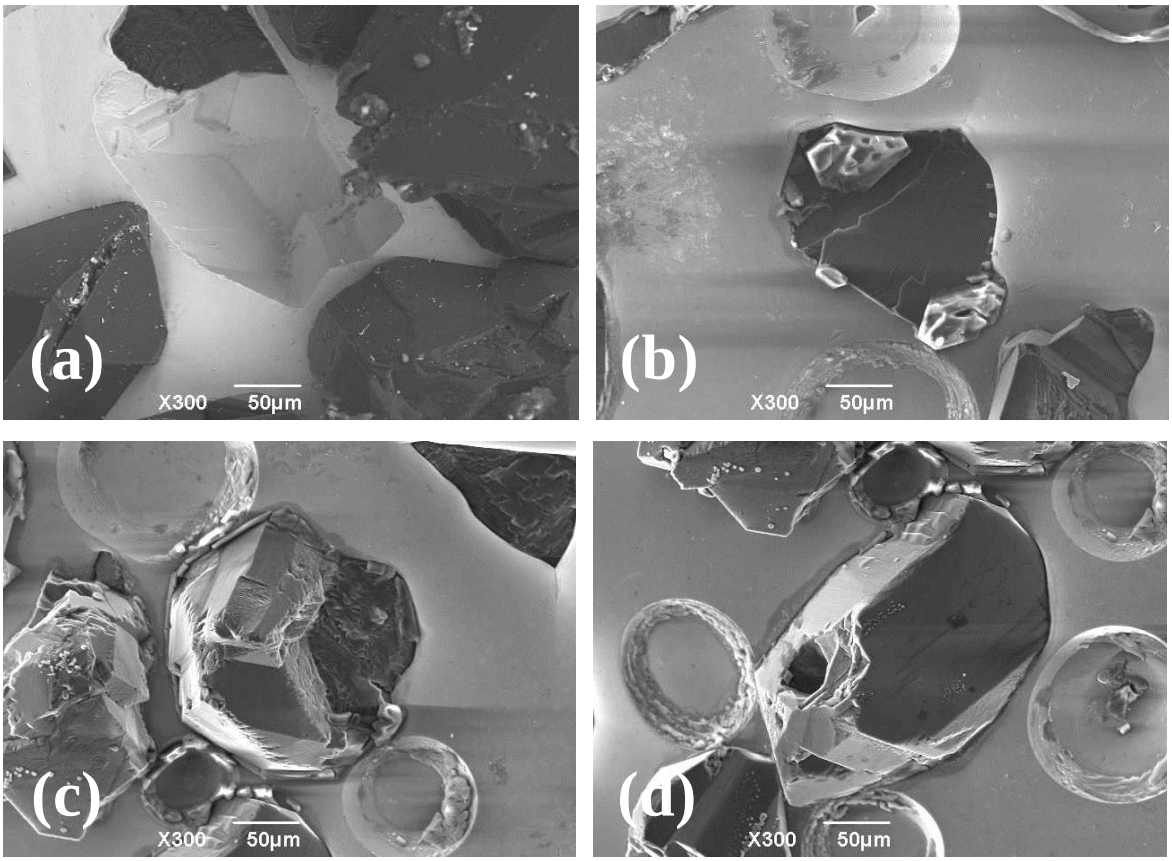


Fig. 2.3.9 Various grain failures in a single-layer electroplated wheel: (a) Grit pull-out, (b) Breakage at bond level, (c) Fracture above bond level, (d) Micro-fracture at the tip (Bhaduri and Chattopadhyay, 2011)

2.4 Nickel based superalloys

2.4.1 Introduction

The use of superalloys for turbosuperchargers and other components in aircraft turbine engines grew rapidly after the Second World War due to their excellent performance at elevated temperatures (>650°C), such as their ability to withstand loading at temperatures close to their melting points, resistance to mechanical degradation like fatigue, creep and rupture over an extended period of time, tolerance of severe operating environment in terms of resistance to oxidation and corrosion etc (Reed, 2006). First generation superalloys began to appear in the 1940's and depending on the major elements of the matrix, they were categorised as iron-based, cobalt-based or nickel-based superalloys. Nickel based alloys have emerged as the preferred choice for aeroengines and land based gas turbines, with the other types of superalloys having their specific application areas.

The earliest type of nickel based alloy was Nimonic 80 which contains 80% nickel and 20% chromium. This was subsequently modified to Nimonic 80A with the incorporation of

other alloying elements such as Ti, Al, Fe, C etc in order to improve grain boundary strengthening. Traditionally nickel based alloys were produced in wrought form, however since the late 1950's the demand for materials capable of withstanding higher operating temperature fostered the production of nickel alloys in cast form, of which the first was Inco 713C (Ezugwu et al., 1999). The early cast alloys had an equiaxed microstructure with non-directional grain boundaries, however they were more prone to fatigue and creep failures due to dislocations at the grain boundaries. Subsequent development of vacuum induction casting together with the introduction of directional solidification techniques rendered elimination of the transverse grain boundaries and improvement in creep-rupture strength. Alloy development led to the emergence of single crystal (SC) alloys in the late 1980's where the grain boundaries were completely absent (Caron and Khan, 1999). A comparison of microstructures for equiaxed, directionally solidified and single crystal superalloys is shown in Fig. 2.4.1.

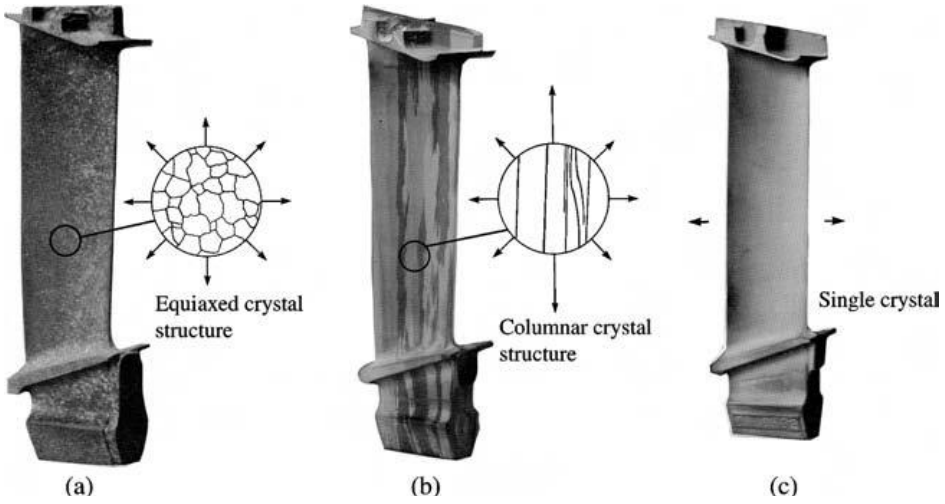


Fig. 2.4.1 Comparison of microstructures of (a) Eqiaxed, (b) Directionally solidified, (c) Single crystal superalloys (Rolls Royce plc., 1992)

2.4.2 Compositions

Nickel based superalloys are either solution strengthened, such alloys being used for burners and combustors in gas turbine engines, or precipitation strengthened, to render the alloy suitable for applications requiring high temperature strength. A common example of the former is Hastelloy X, while Inconel X-750 is a precipitation strengthened modification with three times higher yield strength than its solid-solution counterpart Inconel 600 (Bradley, 1988). Precipitation strengthened alloys contain aluminium and titanium phases (denoted as γ') in the form of Ni_3(Al, Ti) which precipitate during appropriate heat treatment and are

often coherent with the nickel matrix (known as γ phase). The nickel based alloys containing higher percentages of iron such as Inconel 718, have niobium as the primary strengthening precipitate and display a body-centred tetragonal ordered compound Ni_3Nb, known as γ''. Such alloys exhibit significantly better weldability than those containing γ' phases. The other phases present in nickel alloys are carbides and borides, known as grain boundary strengtheners, which combine with titanium, tantalum and hafnium and decompose in the form of $M_{23}C6$ and M_6C (where M stands for a metal atom) during processing or service (Reed, 2006). The high temperature creep and rupture strength of superalloys is due to the preferred segregation of carbides and borides along the γ-grain boundaries, thereby inhibiting grain boundary sliding. However single crystal superalloys are typically free from carbides and borides as they are redundant in the absence of grain boundaries.

First generation single crystal superalloys had significantly lower chromium content than polycrystalline alloys but greater amounts of refractory elements such as W, Ta and Mo in order to increase creep resistance. The addition of 3% rhenium provides increased temperature capability by ~31-36°C and additional improvement in creep strength (Erickson, 1995). These alloys are classified as second generation materials and include CMSX-4, PWA 1484 and René N5 etc. The operating temperature capability was further increased by ~30°C in third generation single crystal alloys, such as CMSX-10 and René N6, by increasing the Re content up to 6%, albeit at the cost of Cr content which varies in the range of 2 to 4.2% (Caron and Khan, 1999). The rise in Re% increases the likelihood of forming brittle topologically closed-packed (TCP) phases during exposure at elevated temperature, whereas a reduction in Cr percentage is detrimental to hot corrosion resistance. Therefore fourth generation single crystal alloys (e.g. MC-NG, EPM-102, TMS-162 etc), which have emerged since 2000, are characterised by the addition of small amounts of ruthenium in order to prevent the formation of undesirable TCP phases. The evolution of nickel based superalloys since the 1940's is presented in Fig. 2.4.2.

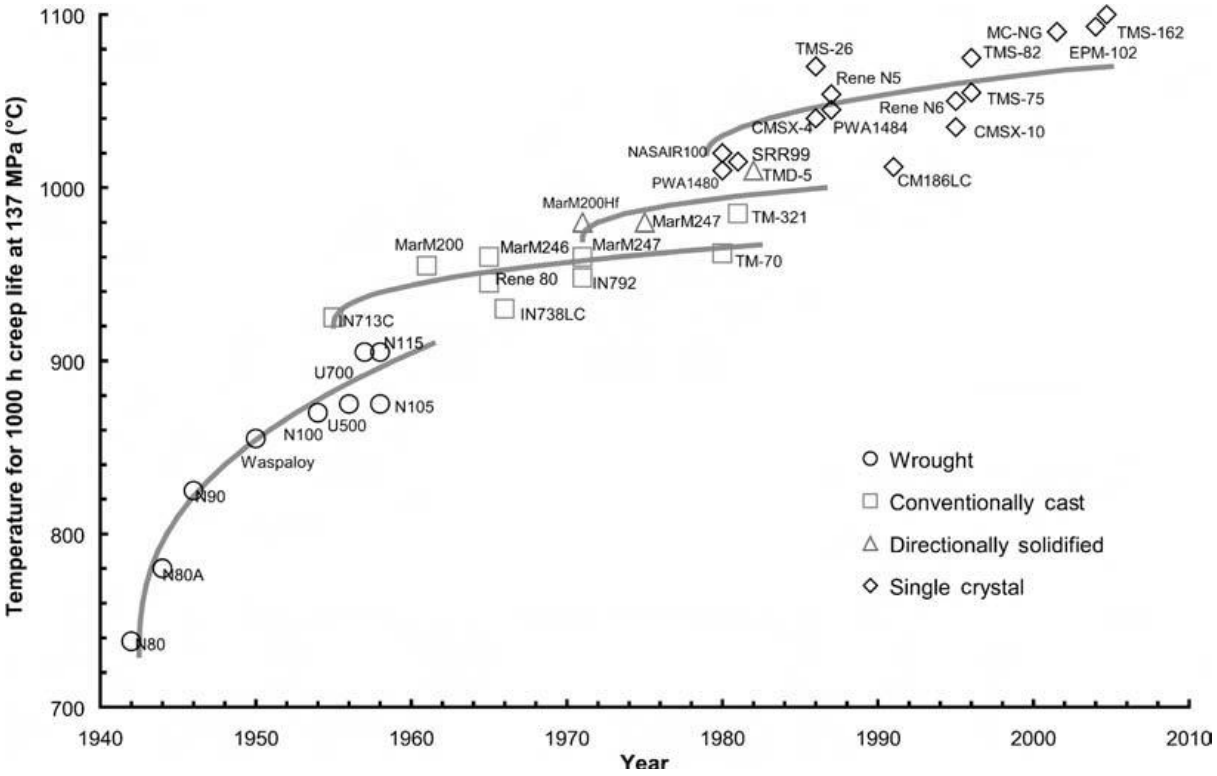


Fig. 2.4.2 Development of various nickel based superalloys over a period of ~70 years (Reed, 2006)

2.4.3 Applications

Early turbine blades were produced with extruded and forged nickel base superalloys, however since the 1970's, single crystal alloys, produced by investment casting methods, have replaced polycrystalline nickel alloys as the material for turbine blades. Wrought polycrystalline superalloys are used in the manufacture of turbine discs, which in a modern civil aircraft represent ~20% of the total weight of the turbofan (e.g. Rolls Royce Trent 800). Currently nickel based alloys account for some ~50% of the total aeroengine weight and despite predictions regarding the increase of nickel content up to ~60% (Bradley, 1988), it is unlikely that this percentage will escalate due to concurrent development in lighter titanium alloys, particularly gamma titanium aluminide which has higher temperature capability (up to ~800°C) than conventional Ti alloys and greater use of composites (Soo et al., 2011a). Figure 2.4.3 shows material usage in a typical aeroengine and the associated operating temperatures.

Applications of nickel based alloys are not solely limited to aeroengines or stationary gas turbines; they also encompass equipment for chemical and petrochemical plants, nuclear reactors, dentistry and prosthetic devices, space vehicles, metal processing systems, cryogenic applications etc.

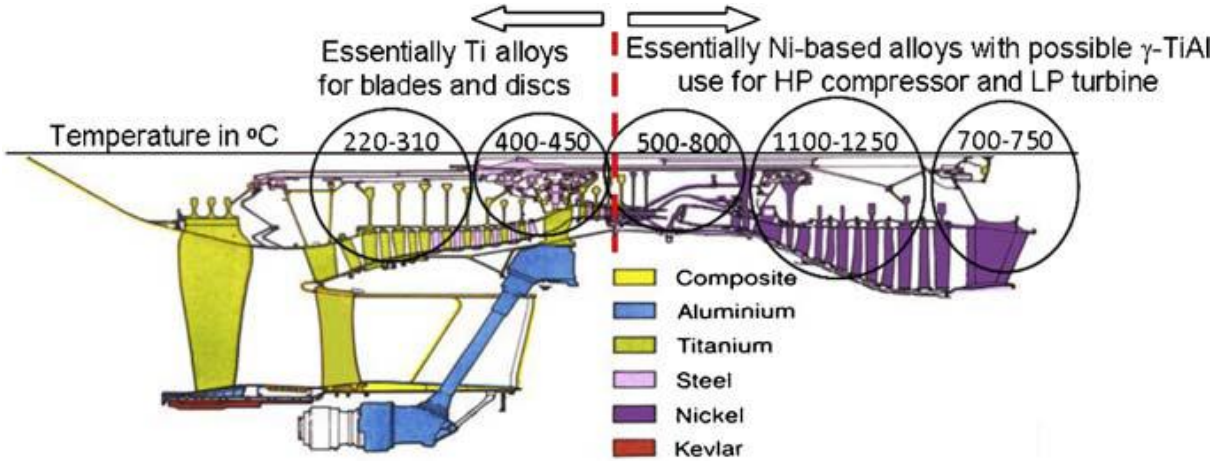


Fig. 2.4.3 Material usage and corresponding aeroengine temperatures (Soo et al., 2011a)

2.4.4 Grindability

The unique properties of nickel based superalloys, which have fostered their use in aerospace applications, makes machinability problematic. Nickel alloys are considered difficult-to-machine due to their retention of strength at high temperatures, work hardening, the presence of abrasive carbide particles in the matrix, chemical reactivity at elevated cutting temperatures etc (Ezugwu et al., 1999). Extensive research on conventional machining such as turning (Pawade et al., 2007), milling (Ng et al., 2000), drilling (Hood et al., 2011); non-conventional machining involving processes such as EDM/wire-EDM (Li et al., 2013) as well as hybrid high speed machining e.g. grinding/HSM and EDM/HSM (Aspinwall et al., 2001b) has been carried out in order to identify preferred operating parameters. On the grinding front, work on polycrystalline alloys such as Inconel is comprehensive; in contrast information on grinding of single crystal alloys is extremely limited.

Tso et al. (1995a) studied the grinding of Inconel 718 with conventional alumina, silicon carbide and superabrasive cBN wheels. The latter provided lower grinding forces and surface roughness, better dimensional accuracy and longer grinding wheel life than those obtained with the former two conventional wheels. Ming et al. (2001) correlated the visual colour change of the workpieces, grinding force ratio (F_n/F_t) and residual tensile stress levels with the occurrence of burn when grinding a directionally solidified nickel based alloy DZ4. The colour of the test-pieces appeared as yellow-black when the machining temperature exceeded 1100°C and was accomplished by a rapid increase in the force ratio. The metallic phases of the surface layer also altered along with the value of induced residual stress. Damage to workpiece surface integrity included the formation of white layers when grinding was carried out with a worn electroplated cBN wheel (Guo et al., 2007). Strong adhesion was also

observed between the abrasive particles and a K417 nickel based alloy when ground with an alumina wheel (Xu et al., 2003). Soo et al. (2002) reported on point grinding of turbine/compressor blade root forms with electroplated cBN form grinding tools, sometimes referred as grinding pins/points operating with high rotational speed (>50000 rpm). Figure 2.4.4 shows typical profiled grinding points and their operation in machining blade root slots.

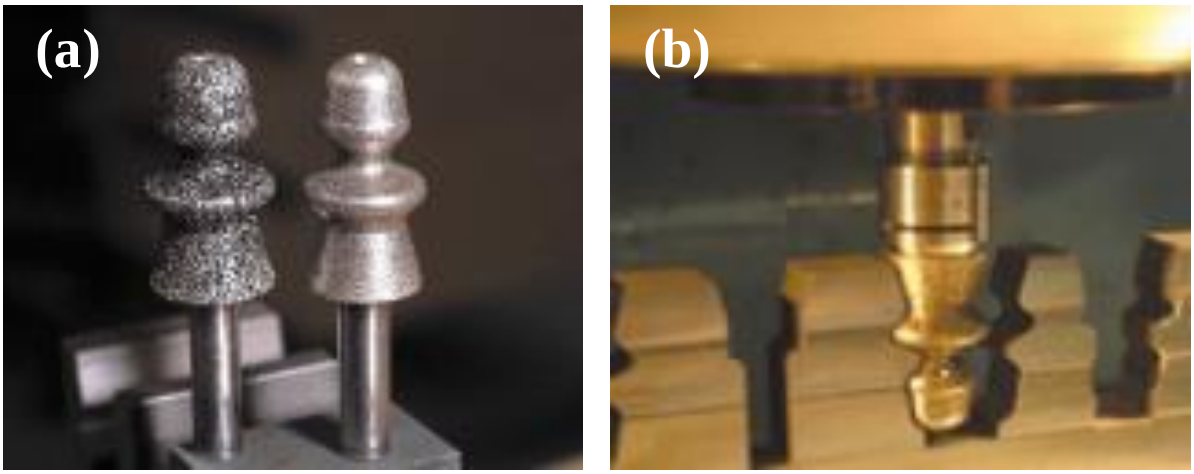


Fig. 2.4.4 (a) Profiled cBN grinding points, (b) Machining of one side of the blade root slot (Soo et al., 2002)

The work on point grinding of root forms was further extended by Aspinwall et al. (2007) when diamond D46 and cBN B46, B76, B91 electroplated tools were employed. The cBN wheels exhibited lower absolute wear in comparison to diamond however at the expense of greater workpiece surface roughness values. The wheel wear reduced with an increase in rotational speed or in other words cutting speed. There was no obvious wheel loading or consequent workpiece burn, however grits were pulled out at certain places from the surface of the grinding wheel. Typical grit pull out from a worn wheel is shown in Fig. 2.4.5.

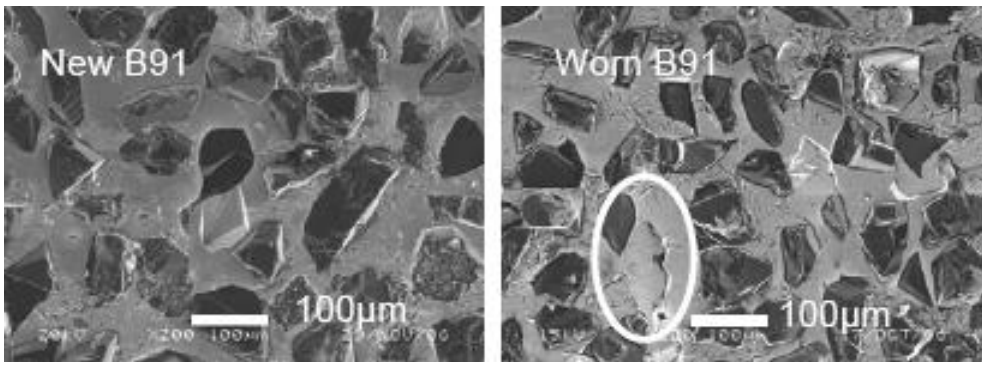


Fig. 2.4.5 SEM micrographs of grain pull out from a B91 cBN wheel (Aspinwall et al., 2007)

2.5 Gamma titanium aluminide intermetallic alloys

2.5.1 Introduction

Depending on composition and room temperature constituent phases, three groups of titanium alloy are available which are identified as α and near α, α/β and β alloys. Alloy Ti-6Al-4V is an α/β alloy, and is considered as 'the workhorse of the titanium industry' accounting for ~60% of the total titanium production (Boyer, 1996). Gamma titanium aluminide (γ-TiAl) is an intermetallic alloy and a potential candidate to replace some heavier nickel based superalloys (Clemens et al., 2003). Research and development of TiAl began in the mid 1950's (Cheng et al., 1999). It exhibits high strength at elevated temperatures (700 to 900°C) (Appel and Oehring, 2003), however low room temperature ductility and low fracture toughness of γ-TiAl are a major concern when considering machinabilty (Mantle and Aspinwall, 2001).

Initial development of γ-TiAl centred on alloys such as Ti-48Al-1V-0.3C, with deficiencies in strength and creep resistance. Second generation gamma alloys were developed in the late 1980's and consisted of Ti-(45-49 at.%)Al + (0.3-10 at.%)X, where X designated for alloying elements such as Cr and Nb. An instance of a second generation γ-TiAl is Ti-48Al-2Nb-2Cr, developed by General Electric (GE) (Loria, 2001). Third generation titanium aluminide alloys, developed in the mid-1990's, incorporated TiB_2 in order to prevent grain growth. These alloys were predominantly used for the aerospace applications; an example of this is Ti-45Al-2Nb-2Mn + 0.8 vol.% TiB_2 (45XD), developed by Howmet (Loria, 2001). The major phases in these alloys are γ-TiAl with ordered face-centred tetragonal $L1_0$ structure and α_2-Ti_3Al with ordered hexagonal $D0_{19}$ structure. With the application of different heat treatment procedures, a broad range of microstructures can be obtained, such as coarse near lamellar, equiaxed, duplex (DP) and fully lamellar (FL). Figure 2.5.1 shows the microstructures of a γ-TiAl based alloy of composition Ti-47Al-3.7(Nb, Cr, Mn, Si)-0.5B (at.%) following heat treatment at different temperatures (Apple et al., 2000). Typically, lamellar microstructures exhibit low tensile strength and ductility compared with the duplex microstructures due to their large grain sizes, lack of slip/twinning activity, and tendency for lamellae platelet separation coupled with reduced cleavage strength. Fracture in lamellar alloys occurs due to the delamination at lamellar interfaces and failure at the colony boundaries. Conversely, fracture in single phase and duplex alloys takes place by cleavage and grain boundary failure. The highest ductility occurs in the duplex structures in comparison to the lamellar microstructures which have lower ductility, lower tensile strength

but higher fracture toughness (20-35 MPa.m$^{1/2}$ compared with 10-16 MPa.m$^{1/2}$ of the duplex structures) (Sharman et al., 2001b).

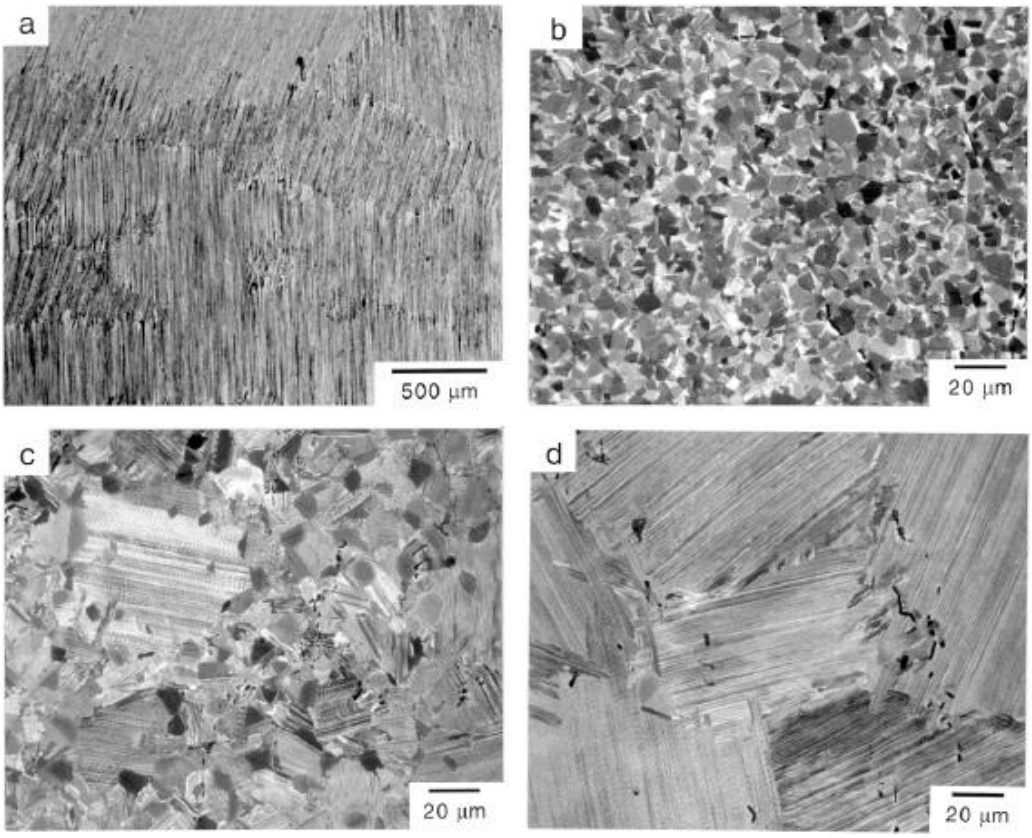


Fig. 2.5.1 Microstructures of Ti-47Al-3.7(Nb, Cr, Mn, Si)-0.5B (at.%): (a) Coarse near lamellar microstructure of the ingot, (b) Equiaxed, T = 1300°C, (c) Duplex, T = 1340°C, (d) Near-lamellar microstructure, T = 1360°C (Apple et al., 2000)

2.5.2 Properties

Compared with steel and aluminium alloys, gamma titanium aluminide has a much lower thermal conductivity (22 W/mK), however this is almost twice that of Inconel and three times higher than Ti-6Al-4V. This renders a better machinabilty of γ-TiAl with respect to Ti-6Al-4V, even though a major drawback of gamma alloys is their low room temperature ductility (<2% compared with ~20% of Ti-6Al-4V). The presence of carbon or silicon in the composition of gamma benefits its creep and high temperature performance, allowing operating temperature up to 800°C, compared with ~600-650°C with the earlier titanium alloys (Aspinwall et al., 2005). The potential of γ-TiAl as a replacement for nickel based superalloys in the aeroengine mainly stems from its much lower density, almost half that of Inconel 718. A comparison of the properties of γ-TiAl with those of the other materials is given in Table 2.5.1.

Table 2.5.1 Comparison of properties of γ-TiAl with other materials (Dimiduk, 1999, Hood, 2010, Sharman et al., 2001b)

	Units	Steels	Aluminium	Inconel 718	Ti-6Al-4V	γ-TiAl
Density	kg/m^3	7870	2700	8400	4430	3760
Young's modulus	GPa	195-200	69-79	180-214	110	150-175
Tensile strength	MPa	415-1750	90-600	1430	1035	672
Yield strength	MPa	205-1725	35-500	1190	965	548
Room temperature ductility	%	65	45	3-10	~20	2
Thermal conductivity	W/mK	50	230	11.3	7.5	22
Melting point	°C	1539	660	1455	1600	1460

2.5.3 Applications

The major thrust for the development of gamma titanium aluminide alloys has come from the aerospace and automobile industries. The typical target applications include blades and stators in the high pressure (HP) turbine compressor, low pressure (LP) turbine blades, inlet and outlet guide vanes and castings (Aspinwall et al., 2005). Studies have shown that it would be possible to reduce engine weight by 100 kg if γ-TiAl alloys were used in manufacturing of LP turbine blades in civil aircraft (Loretto, 1995). Over the past ~30 years, the worlds leading aeroengine manufacturers such as Rolls Royce, GE, Pratt & Whitney, have been active developing and evaluating γ-TiAl alloys, however the use of these alloys in commercial civil aircraft have been hindered by stringent safety requirements and the relatively high cost of production compared with the existing aerospace materials. In contrast, the uptake of γ-TiAl in the automotive sector has been faster and the applications include engine valves and turbochargers (Tetsui, 1999), see Fig. 2.5.2.

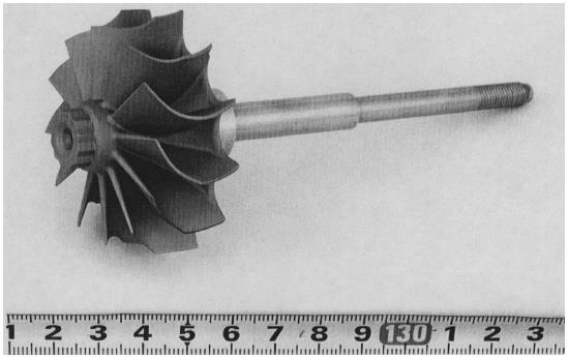


Fig. 2.5.2 A γ-TiAl made turbocharger for a passenger vehicle (Tetsui, 1999)

2.5.4 Grindability

The grinding of γ-TiAl produces fewer workpiece integrity problems in comparison to other machining processes (Aspinwall et al., 2005). Literature on grinding γ-TiAl includes reciprocating surface grinding (Bentley et al., 2001), speed stroke (Zeppenfeld, 2006), and creep feed grinding (Bentley and Aspinwall, 2000). A great deal of research work on machining of various gamma alloys has been undertaken at the University of Birmingham over the past ~25 years. The range of alloys tested encompasses Ti-48Al-2Mn-2Nb (48-2-2), Ti-45Al-2Mn-2Nb+0.8%TiB_2 XD^{TM} (45-2-2+0.8), and Ti-45Al-8Nb-0.2Cwt%. Work by Bentley and Aspinwall (2000) and Bentley et al. (2001) typically showed that grinding of γ-TiAl was able to produce surfaces without major microstructural alterations or the formation of cracks, pits, laps and heat affected zones (HAZ), albeit with significant work hardening up to a depth of ~10 μm below the machined surface. Workpiece surface roughness (R_a) values were generally between 1 to 2.5 μm with the occasional rise up to ~4.5 μm. More recently, extensive research was carried out by Hood et al. (2007a) on creep feed grinding of Ti-45Al-8Nb-0.2Cwt% with conventional SiC abrasives which compared results with the grindability of a burn resistant titanium alloy (BuRTi) of composition Ti-25V-15Cr-2Al-0.2Cwt% (Hood et al., 2007b). Grinding of γ-TiAl alloy was found to be easier than the BuRTi alloy with typically a 10 times higher G-ratio, 10% lower maximum power and 15% lower average workpiece surface roughness for the same operating parameter levels. The maximum specific energy and tangential force also reduced by 25% and 28% respectively when machining gamma. Crack-free surfaces were obtained when operating at lower wheel speeds and material removal rates as opposed to workpiece surface burn with extensive HAZ and cracking when grinding at higher levels of wheel speed and material removal rate. Sub-surface microhardness generally increased by 50-60$HK_{0.025}$ from the bulk value of 370$HK_{0.025}$ between 30-50 μm beneath the ground surface. Typical examples of cross-sections of machined γ-TiAl surfaces are shown in Fig. 2.5.3.

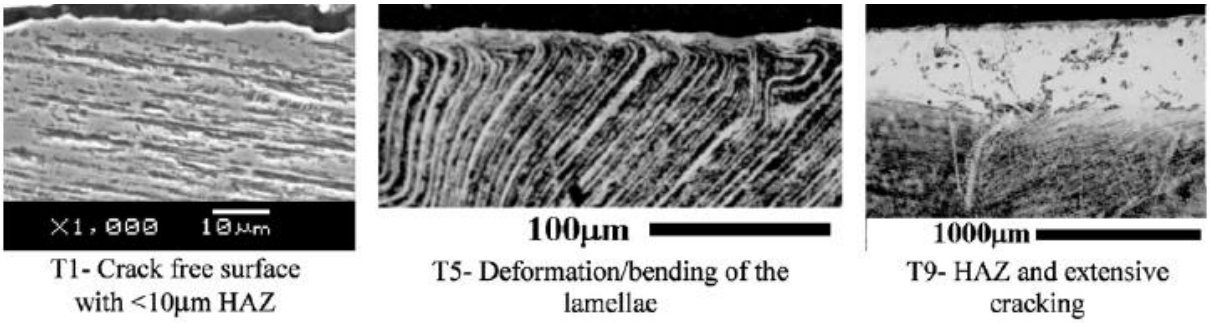


Fig. 2.5.3 Cross-sectional microstructures of γ-TiAl surfaces (Hood et al., 2007b)

2.6 Workpiece surface integrity

The concept of surface integrity in machining was first introduced by Field and Kahles (1964) and defined as the 'inherent or enhanced condition of a surface produced by machining processes or other surface generation operations'. A number of comprehensive reviews by Field and Kahles (1971) and Field et al. (1972) have specified three different levels of surface integrity data sets to study and evaluate the various metallurgical alterations occurring in the surface and sub-surface layers in material removal processes, see Table 2.6.1. Typical surface alterations include plastic deformation, micro-cracks, phase transformations, hardness variations, laps and tears relating to the formation of built-up edge, distribution of residual stress etc (Jawahir et al., 2011).

Table 2.6.1 Different levels of surface integrity (SI) data set (Field et al., 1972)

Minimum SI data set	**Standard SI data set**	**Extended SI data set**
• Surface finish • Microstructure (10× or less) • Microcracks • Macrocrack indications • Microstructure - Microcracks - Plastic deformation - Phase transformation - Intergranular attack - Pits, tears, laps, protrusions - Built-up edge - Melted and re-deposited layers - Selective etching • Microhardness	• Minimum SI data set • Fatigue test (screening) • Stress corrosion test • Residual stress and distortion	• Standard SI data set • Fatigue test (extended to • obtain design data) • Additional mechanical tests • Tensile • Stress rapture • Creep • Other specific tests (e.g., bearing performance, sliding friction evaluation, sealing properties of surface)

Extensive progress has been made in evaluating the surface integrity of machined components over the intervening decades, a detailed review of which was recently presented by M'Saoubi et al. (2008). Surface alterations due to the combination of machining operations, as in Hybrid processes, were reviewed by Lauwers (2011). Typical examples included crack formation, plastic deformation and material removal via brittle failure during vibration assisted machining, local softening in laser assisted machining and reduction in the thickness of the recast layer in abrasive wire-EDM (AWEDM) (Menzies and Koshy, 2008).

The assessment of surface integrity in respect of titanium alloys and nickel based superalloys is crucial due in part to the safety requirements associated with civil aircraft and land based power generation systems where these alloys constitute 70-80% of the total weight. Pusavec et al. (2011) evaluated the surface integrity of Inconel 718 via surface roughness and residual stress assessment when turning with carbide inserts under different environments such as dry, MQL (minimum quantity lubrication), cryogenic and cryo-MQL. Cryogenic machining produced smaller workpiece grain size and a reduction in plastic deformation on the work surface (up to ~1-2 μm beneath the surface) as opposed to ~5-10 μm of deformed layer obtained in dry and MQL machining. M'Saoubi et al. (2012) further studied surface integrity of Inconel 718 using optical and scanning electron microscopy, electron back scattered diffraction (EBSD), XRD, TEM and nano-indentation following finish turning with PcBN and PVD coated carbide tooling. EBSD data identified induced strain and pronounced recrystallisation when machining with worn cutting tools. Various surface and subsurface damage such as BUE, cracks, cavities, grooves, tearing and side flow were observed in high speed turning of Inconel 718 with whisker reinforced ceramic tools (Zhou et al., 2012), see Fig. 2.6.1. Machinability studies of next generation nickel based superalloys such as RR1000 were recently carried out by Soo et al. (2011a) when drilling and radius end milling with coated carbides. The machined sub-surface showed the presence of hardened layers to a depth of 100 μm with damage such as adhered chips, material drag etc together with moderate burring and occasional white layer formation.

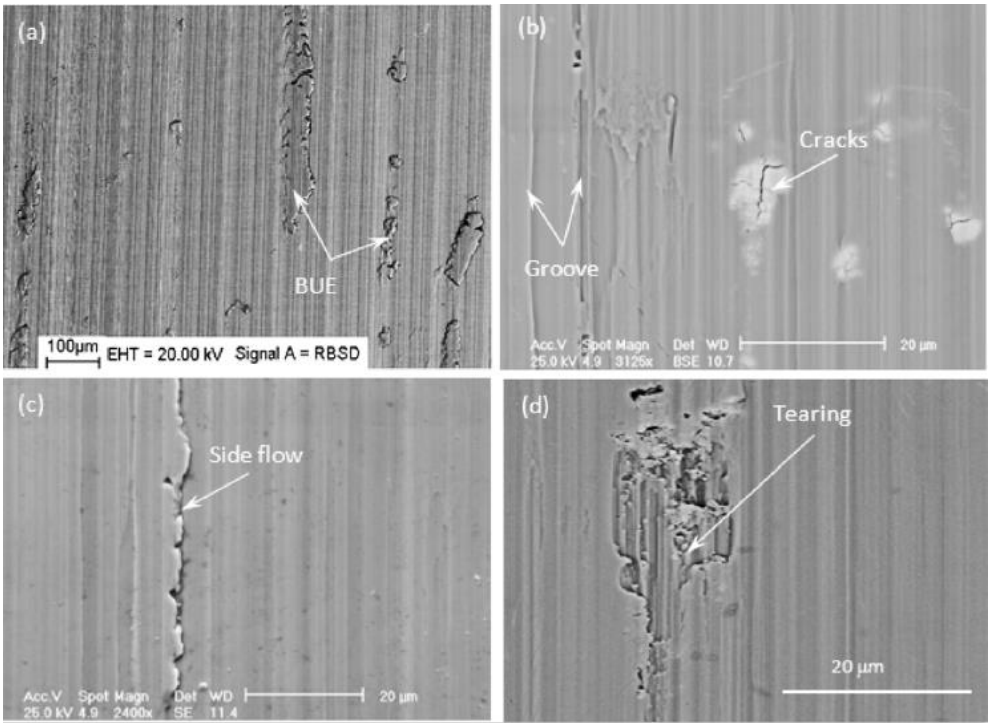


Fig. 2.6.1 Surface damages following machining: (a) BUE, (b) Grooves and cracks, (c) Side flow, (d) Tearing generated by broken carbide particles (Zhou et al., 2012)

On the titanium front, extensive work has been carried out on common alloys such as Ti-6Al-4V, Ti-6Al-2Sn-4Zr-2Mo etc, however research on more advanced alloys such as gamma-titanium aluminide and burn resistant titanium (BuRTi) is less comprehensive. High speed milled and creep feed ground BuRTi alloy exhibited material pull-out, smearing, crater formation, fractured carbides and carbide debonding on the machined surfaces, nevertheless there were no appreciable changes in the microstructures or microhardness values with either machining process (Novovic, 2003). Notable work on creep feed grinding and ball nose end milling of γ-TiAl alloys was carried out by Hood et al. (2007a and 2007b) and Hood et al. (2013) respectively. Fracture, material pull-out, and deformed lamellae were seen on the surfaces subject to milling, whereas creep feed ground surfaces were typically characterised by grinding burn and extensive cracking when machined with a heavy depth of cut.

With the growing acceptance of carbon fibre reinforced plastic (CFRP) laminates and CFRP/metallic stacks as replacements for aluminium alloys in aircraft wings and the fuselage along with engine components such as fan cases and fan blades, machining and consequent surface integrity evaluation of CFRP materials has been the focus of the research community since the late 1980's (König and Graβ, 1989). Despite the comparative lack of integrity data/descriptors compared with metallic alloys, reported surface integrity problems relating to machining of CFRP encompass fibre pull-out, breakage, fibre/matrix debonding, thermal degradation, fuzzing, spalling and delamination, see Fig. 2.6.2.

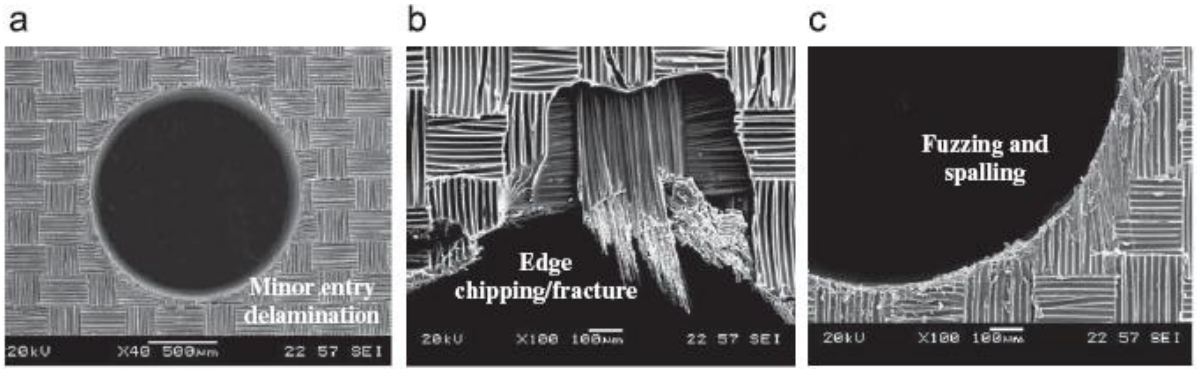


Fig. 2.6.2 Various surface damages when drilling CFRP: (a) Delamination, (b) Edge chipping/fracture, (c) Fuzzing and spalling (Shyha et al., 2009)

3. EXPERIMENTAL WORK

3.1 Workpiece materials

Three different aeroengine alloys were employed for the research which comprised two nickel based superalloys and a gamma titanium aluminide. The nickel based superalloys were Inconel 718 and CMSX-4 with the former produced by conventional cast-and-wrought ingot metallurgy while the latter was processed by investment casting. The Inconel 718 workpieces were solution treated and aged at 950-980°C for 1 hour and then air cooled, followed by precipitation treatment at 720°C for 8 hours with furnace cooling to 620°C and further precipitation treatment at 620°C for 8 hours prior to air cooling (Soo, 2003). In contrast, the CMSX-4 workpieces were directly taken from the cast ingots with no further solution treatment or ageing. The microstructures of both materials are shown in Fig. 3.1.1(a) and (b) respectively, while the nominal elemental compositions (% weight) are detailed in Table 3.1.1 (Reed, 2006).

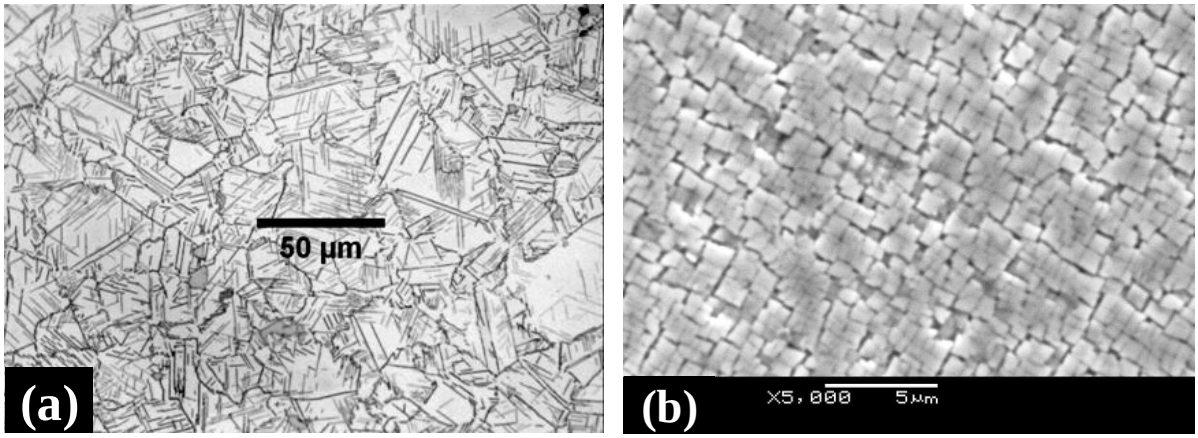


Figure 3.1.1 Microstructure of (a) Inconel 718, and (b) CMSX-4 workpiece material

Table 3.1.1 Elemental compositions (% weight) of nickel based superalloys under investigation

Alloys	Cr	Co	Mo	W	Al	Ti	Ta	Nb	Re	Fe	Hf	C	Ni
Inconel 718	19.0	-	3.0	-	0.5	0.9	-	5.1	-	18.5	-	0.04	Bal
CMSX-4	6.5	9.6	0.6	6.4	5.6	1.0	6.5	-	3.0	-	0.1	-	Bal

Energy dispersive spectroscopy (EDX) area mapping together with spot analysis was carried out in order to confirm the presence of different elements within the workpiece material. The EDX analysis on the microstructure of Inconel 718 material in Fig. 3.1.2

showed clusters of primary carbide particles of irregular shape, such as niobium carbide (spectrum 1) and titanium carbide (spectrum 2) were present within the nickel matrix.

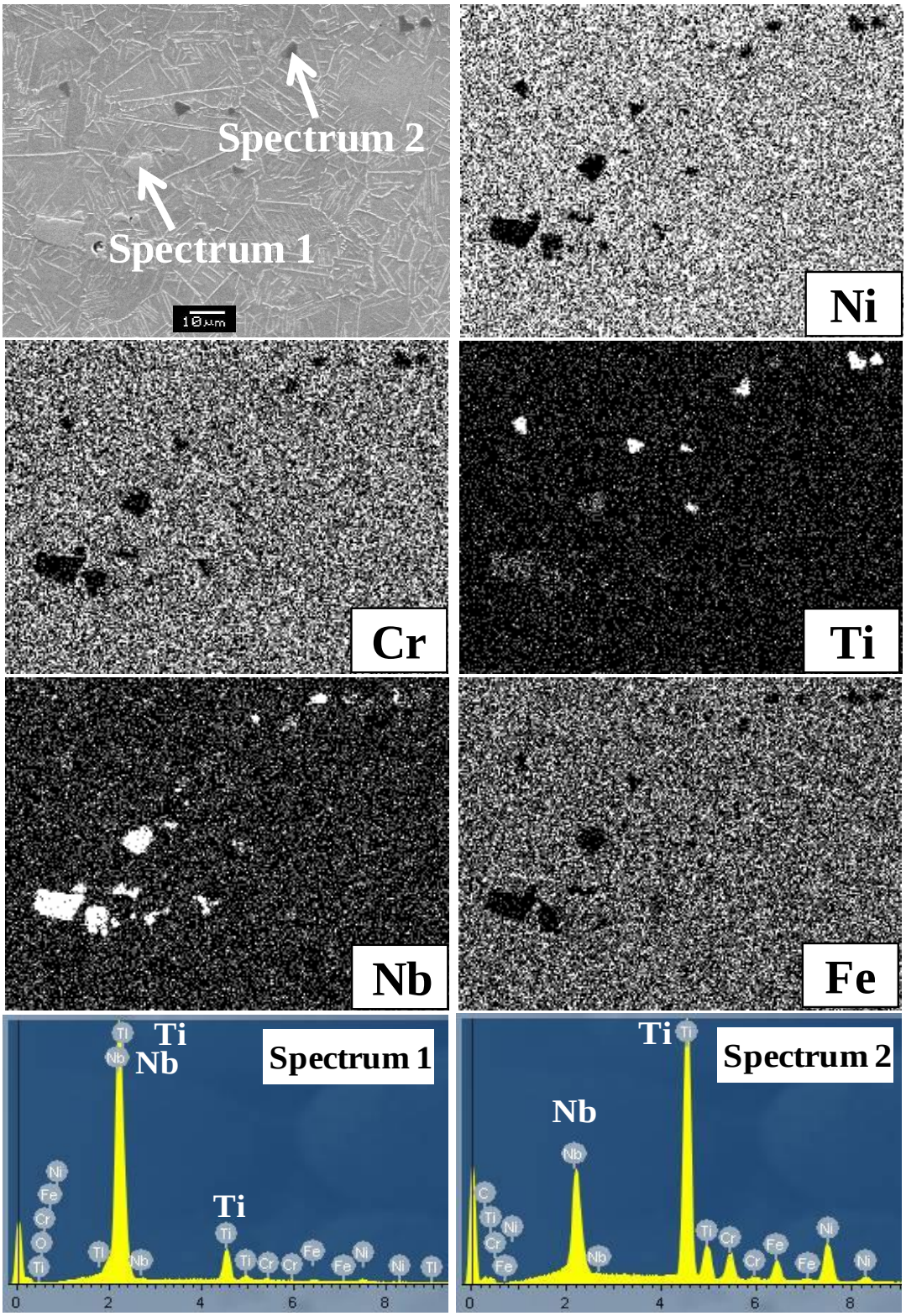


Fig. 3.1.2 EDX area mapping and spot analysis of etched Inconel 718 sample confirming the presence of different compositions

Rectangular workpiece test blocks for mainstream experiments were prepared using wire-EDM with dimensions of 110×50×10 mm and 110×55×7 mm for Inconel 718, whereas that of CMSX-4 was 70×50×5 mm.

The gamma titanium aluminide (γ-TiAl) used was a 45-2-2XD alloy with a nominal composition of 50Ti-45Al-2Mn-2Nb-1TiB_2 (%weight), which was produced by hot isostatic pressing (HIPing) at a temperature of 1480°C and pressure of 148 MPa for 4 hours and subsequently heat treated at a temperature of 1050°C-1080°C over 24 hours. Figure 3.1.3 shows the typical microstructure of the material together with corresponding EDX data. The material had a nearly fully lamellar structure with parallel plates of γ-TiAl and α_2-Ti_3Al (Clemens et al., 2003) and a colony size of ~100-130 μm. Spot EDX analysis showed that the needle like phases were primarily rich with Ti, whereas the bulk material generally exhibited the nominal composition, see Figs. 3.1.3(b) to (d).

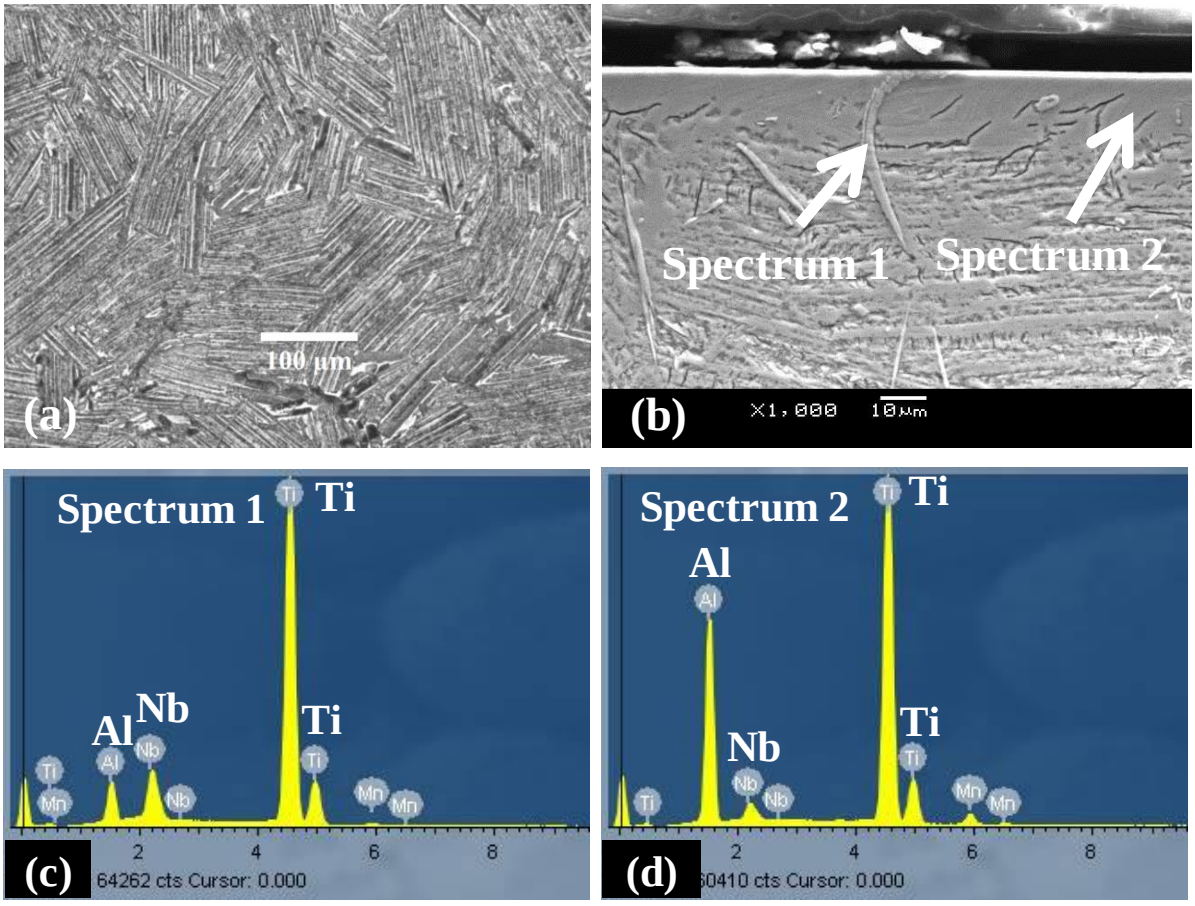


Fig. 3.1.3 (a) Microstructure of gamma titanium aluminide, (b) Regions for spot EDX analysis, (c) EDX data obtained for spectrum 1, (d) EDX data obtained for spectrum 2

3.2 Grinding wheels

Five different plain grinding wheels (all supplied by Saint-Gobain Abrasives) were utilised for the various phases of experimental work involving an electroplated superabrasive diamond and four vitrified bonded conventional abrasive (one silicon carbide and three alumina) products. All of the wheels were 220 mm in diameter with a bore diameter of 32 mm, while wheel widths varied from 15-25 mm. The silicon carbide (SiC) grinding wheel of specification GC601J45VKRNN, see Fig. 3.2.1(a), was employed for preliminary experiments on ultrasonic assisted grinding of Inconel 718 together with mainstream UAG tests on γ-TiAl as well as ultrasonic assisted dressing. The alumina (Al_2O_3) wheels included the VORTEX grade typically used in the VIPER grinding process (Hitchiner, 2007) and POROS2, which was designed for creep feed grinding operation of aerospace alloys, with both wheels having a porous and open structure. The VORTEX wheels were supplied with two different average grit sizes of ~250 µm (60 mesh) and ~180 µm (80 mesh) having specifications of IPA60EH20VTX and IPA80EH17VTX respectively, see Fig. 3.2.1(b), while only 60 mesh POROS2 wheels (25A601I74VPMCNN) as shown in Fig. 3.2.1(c) were evaluated.

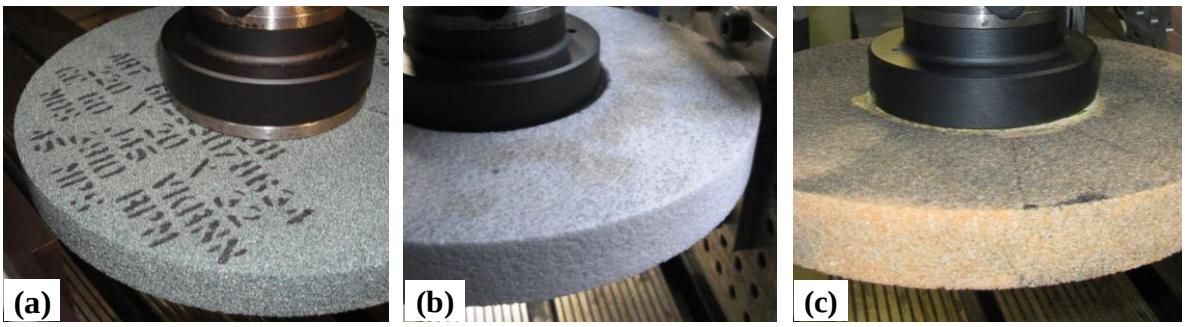


Fig. 3.2.1 Conventional abrasive wheels (a) SiC (GC601J45VKRNN), (b) VORTEX Al_2O_3 (IPA60EH20VTX), and (c) POROS2 (25A601I74VPMCNN)

The performance of the single layer electroplated diamond superabrasive wheel was assessed when ultrasonic assisted grinding γ-TiAl, see Fig. 3.2.2(a). The monocrystalline diamond grits had an average size of 252 µm (D252) which is equivalent to a 60/70 mesh size (Metzger, 1986), with the typical distribution of the grits detailed in Fig. 3.2.2(b). Table 3.2.1 shows a list of the wheels used in each test phase together with the corresponding workpiece materials.

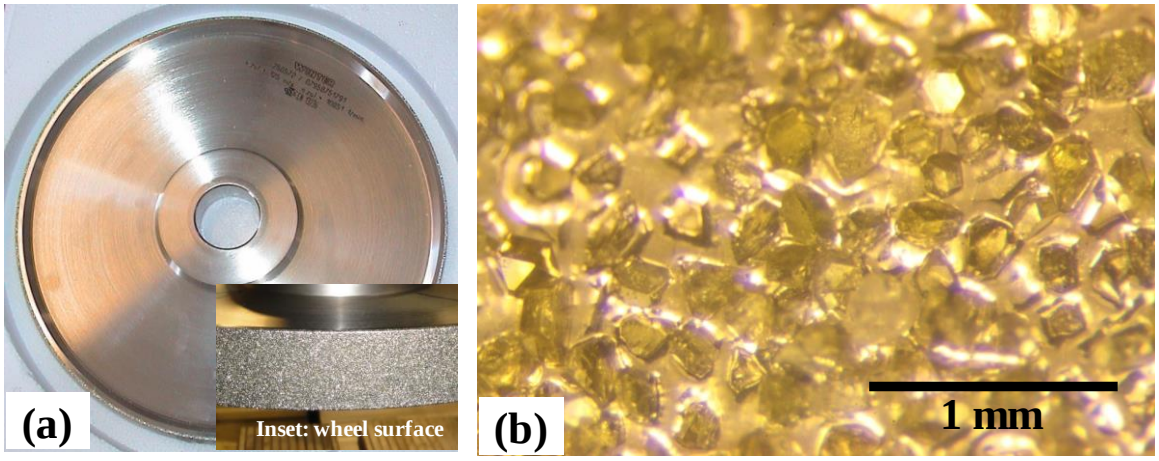


Fig. 3.2.2 (a) Electroplated diamond superabrasive wheel, (b) Distribution of diamond grits on the wheel surface

Table 3.2.1 Grinding wheels and corresponding workpiece materials employed in different experimental phases

Phases	Workpiece materials	Grinding wheels	Specifications of grinding wheels	Wheel width (mm)
1A	Inconel 718	SiC	GC601J45VKRNN	20
1B	Inconel 718	VORTEX 80 mesh	IPA80EH17VTX	15
1C	Inconel 718	SiC	GC601J45VKRNN	20
2A	Inconel 718	1. VORTEX 80 mesh 2. POROS2 3. VORTEX 60 mesh	1. IPA80EH17VTX 2. 25A601I74VPMCNN 3. IPA60EH20VTX	15 25 25
2B	Inconel 718	POROS2	25A601I74VPMCNN	25
2C	Inconel 718	VORTEX 60 mesh	IPA60EH20VTX	25
2D	CMSX-4	POROS2	25A601I74VPMCNN	25
2E	Inconel 718	POROS2	25A601I74VPMCNN	25
3A	γ-TiAl	SiC	GC601J45VKRNN	20
3B	γ-TiAl	Electroplated diamond	D252	20

3.3 Test and analysis equipment

3.3.1 Machine tool, wheel dressing and cooling/cleaning arrangement

All of the grinding and dressing trials were conducted on a Bridgeport FGC1000 flexible grinding centre, with a spindle speed range of 40-6000 rpm and power rating of 25 kW, see Figure 3.3.1. The grinding wheels were held using MST BT40 FMSB32-60 tool holders with associated blotters and flanges (Hood, 2010). The maximum travel along the X, Y and Z axes were 1020, 560 and 600 mm respectively with rapid feed rates of 43 m/min along X and Y as well as 30 m/min along the Z directions.



Fig. 3.3.1 Bridgeport FGC1000 flexible grinding centre

Dressing of conventional abrasive wheels was carried out prior to the start of each test in order to ensure similar initial wheel conditions. This was performed using a 105 mm diameter plain profile, hand set sintered diamond roller dresser (hydraulically driven) with an average grain size of ~800 µm and spacing of ~1.5 mm. The infeed rate of the dresser and dressing depth were 2 µm/rev and 50 µm respectively, while the grinding wheel speed was fixed at 15 m/s in order to maintain the ratio of dresser to wheel speed (q_d) at 0.8. The diamond roller dresser used is shown in Fig. 3.3.2(a). Two high pressure pumping systems were utilised for delivery of grinding fluid via laminar flow nozzles (with rectangular cross-section orifices) (Webster, 2007) for cooling and cleaning of the wheel during machining. The cooling nozzle (2×20 mm) was directed towards the grinding zone at an angle and distance of 20° and 170 mm respectively, while the cleaning nozzle (0.5×20 mm) was aimed along the periphery on the opposite side of the wheel, see Fig. 3.3.2(b). Fluid pressure for cooling ranged from 5-30 bar in order to match wheel velocity or increase the efficiency of fluid into the grinding zone. In contrast, the fluid pressure for cleaning was kept constant at 70 bar in all trials. The grinding fluid employed was a water-based synthetic oil product, Trim C270, with a concentration of 7-10 Vol%.

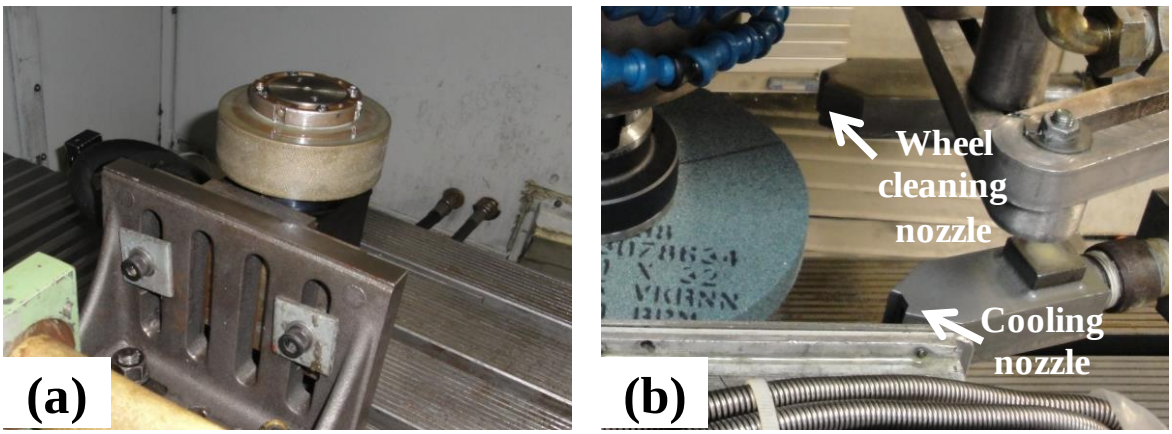


Fig. 3.3.2 (a) Diamond roller dresser, (b) Arrangement of cooling and cleaning jet nozzles

3.3.2 Ultrasonic vibration systems

Three different ultrasonic vibration systems were employed in the present work. Preliminary trials on UAG was carried out using a Flexiskills ultrasonic generator of 20 kHz frequency and 250 W power rating, capable of generating vibration along the longitudinal axis of the horn, see Fig. 3.3.3(a) and (b) for the generator and the transducer-booster-horn assembly, respectively.

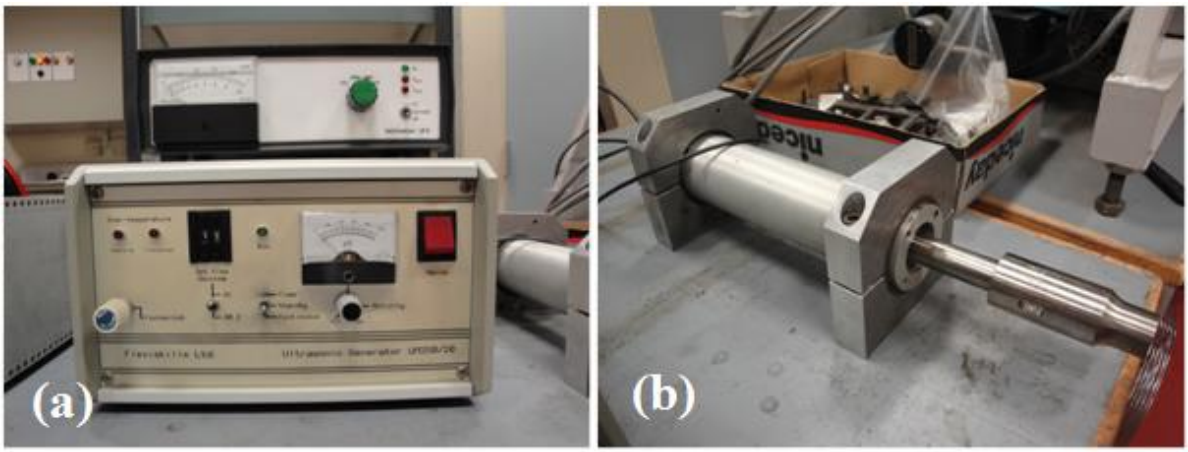


Fig. 3.3.3 (a) Flexiskills Ltd. 250 W ultrasonic generator, (b) 20 kHz ultrasonic transducer-booster-horn assembly

Following a survey of commercial ultrasonic equipment (see Appendix A2), an ultrasonic system was purchased from MP Interconsulting (MPI), Switzerland, and utilised for the mainstream experimental phases on UAG of nickel based superalloys and γ-TiAl. The ultrasonic system comprised of an advanced multi-frequency, multimodal, modulated (AMMM) ultrasonic generator of 20 kHz frequency and 1 kW maximum power, a high power ultrasonic transducer of 20 kHz starting frequency and 3 kW maximum power rating together with waveguide rod and connecting studs, a RS485-USB adapter associated with a LABVIEW-based software in order to tune/set the operating parameters of the generator. The transducer was a specially designed table/block sonotrode, manufactured at the Machining Research Group (MRG) laboratory according to the design provided by MP Interconsulting, see Fig. 3.3.4(a) and (b). The ultrasonic generator together with the sonotrode-booster-transducer assembly with a workpiece mounted is shown in Fig. 3.3.5.

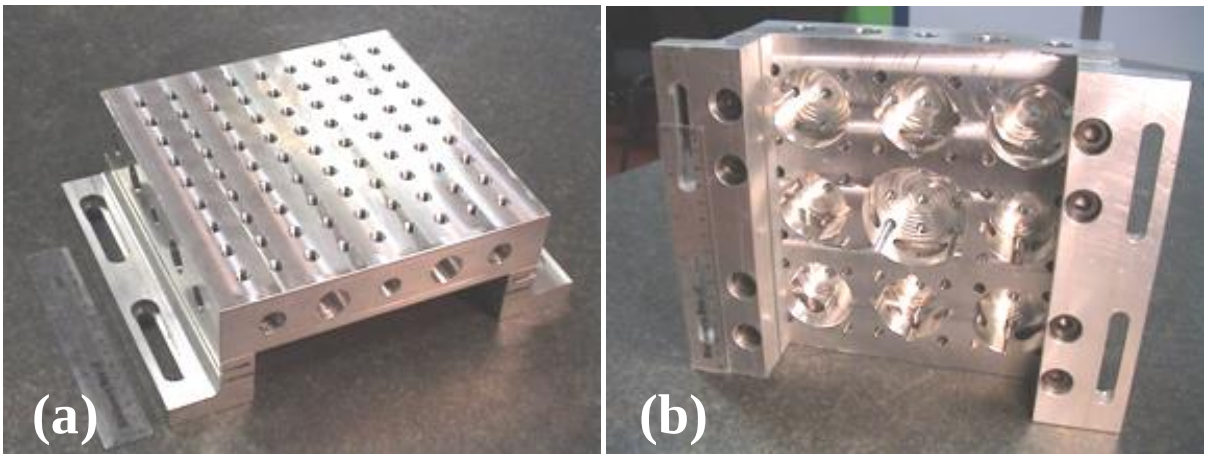


Fig. 3.3.4 (a) Top view of the table sonotrode, (b) Rear view

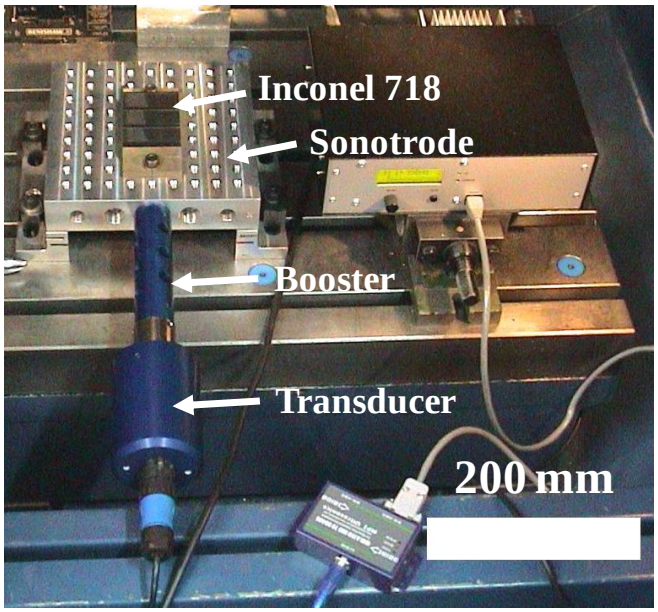


Fig. 3.3.5 Ultrasonic system with workpiece mounted on the table sonotrode

The ultrasonic generator was tuned using a LABVIEW based software in order to obtain the maximum possible amplitude on the sonotrode. There was no provision of varying the ultrasonic frequency of the transducer as it was operated at a fixed value of ~20 kHz. However, using a feedback loop system, the transducer was able to tune itself between 18 to 22 kHz in order to vibrate at the resonant (forced) frequency mode should there be a change in the load characteristics. Figure 3.3.6(a) shows the screenshot of a tuning curve obtained while vibrating the table sonotrode at an unloaded condition (i.e. no workpiece mounted on it) whereas Fig. 3.3.6(b) depicts that at a loaded situation. Further, there was no provision to obtain the exact amplitude of vibration from the generator; instead amplitude could be set on a

percentage scale ranging from 0 to 100%. The detail of measuring the actual amplitude of vibration is given in Appendix A3.

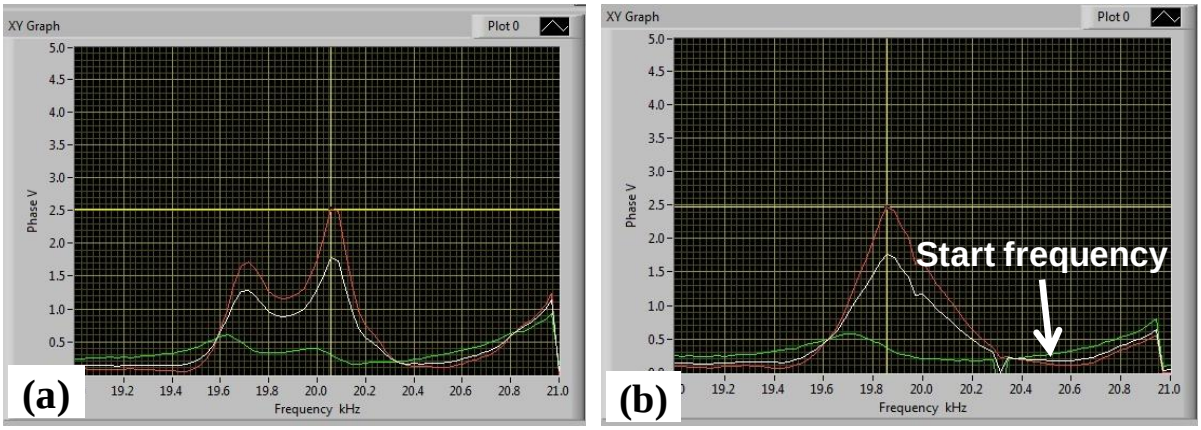


Fig. 3.3.6 Response curves during tuning of the transducer (a) Without load, (b) With load

All mainstream experimental trials on UAG involved a start frequency of 20.5 kHz while the amplitude was varied from 50% to 70%. Fig. 3.3.7 shows a screenshot of the operating parameters of the ultrasonic generator with the vibration active.

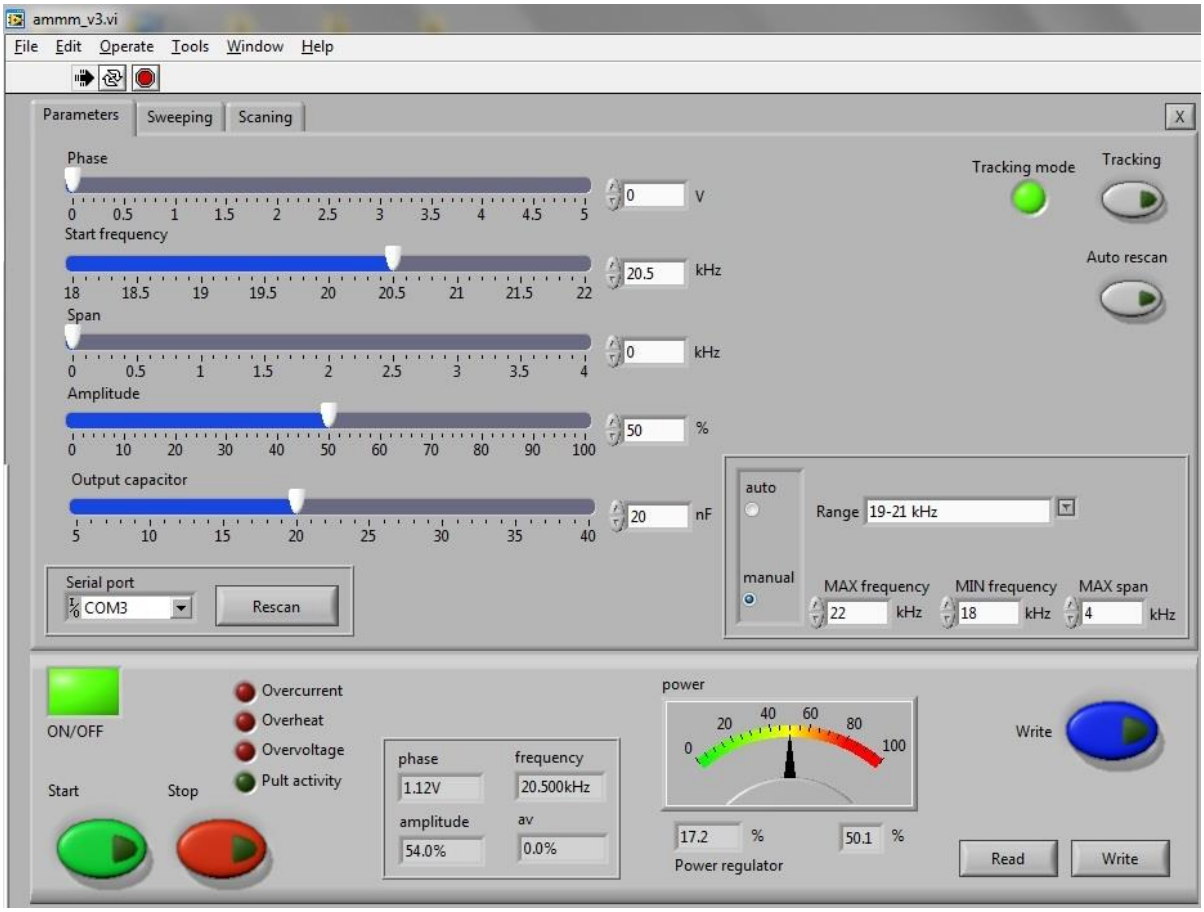


Fig. 3.3.7 Screenshot of ultrasonic parameter control settings in LABVIEW software

For a limited number of trials on ultrasonic assisted dressing, a Kerry 150 W ultrasonic generator connected to a transducer-booster-horn assembly vibrating axially with a frequency of 23 kHz and amplitude of 18.5 μm was utilised. The ultrasonic generator is shown in Fig. 3.3.8.



Fig. 3.3.8 Kerry 150 W ultrasonic generator

3.3.3 Grinding/dressing forces and power

Vertical, F_v (radial to the wheel surface) and horizontal, F_h (parallel to feed direction) grinding forces were measured using a Kistler 9257A 3-component piezoelectric platform dynamometer (resonant frequency of 2.3 kHz and a recommended operating frequency <760 Hz) coupled to 3 charge amplifiers and a PC running Kistler Dynoware software. The system was also utilised to measure the forces due to vibration of the table sonotrode (without grinding) and when ultrasonic assisted dressing.

While spindle power was monitored and displayed on the machine controller of the Bridgeport FGC1000 (Heidenhain), actual power drawn during grinding was recorded using a Field Instrumentation System (FIS) (model FIS 118, from Saint Gobain Abrasives), with a measuring range of 0-100 kW. The FIS unit was connected to the spindle current socket in the main power supply panel of Bridgeport machine, with power signals processed via software interfaced with the FIS instrument.

3.3.4 Radial wheel wear and G-ratio

In order to determine radial wheel wear and G-ratio, wheel diameters were measured before and after each grinding trial using a DEA Swift manual coordinate measuring machine (CMM) connected to a computer installed with Delcam Power Inspect software. The wheels

were assessed at 30 different points around the periphery, each at 5 different levels of the wheel width. The G-ratios were then calculated using Equation 3.1.

$$G - ratio = \frac{V_M}{V_R} \quad \ldots 3.1$$

where,

V_M: Volumetric material removed from the workpiece
V_R: Volumetric material removed from the grinding wheel

3.3.5 Surface roughness/topography

Both 2D surface roughness and 3D topographical profiles of the ground workpiece surfaces as well as graphite and resin replicas of the grinding wheels were recorded using a Taylor Hobson Form Talysurf 120L unit, see Fig. 3.3.9, with a vertical resolution of 10 nm, a stylus angle of 60° and a stylus tip radius of 2 µm. Cut-off and evaluation lengths of 0.8 and 8.0 mm respectively were used for 2D assessments while the transverse spacing distance was 6.13 µm for 3D analysis. R_a, R_t and R_z of the ground workpieces surfaces were recorded at three positions over the grinding track (start, middle and end) and presented individually in the graphs, however average values were taken into account for statistical analysis. On the other hand, the average of two 2D roughness data of the graphite replicating surfaces was shown in the graphs as well as considered for statistical analysis while assuming negligible wheel wear when grinding graphite. All 3D measurements were carried out only once due to time constraints.



Fig. 3.3.9 Photographic view of Taylor Hobson Form Talysurf 120L

As the surfaces of the resin replicas were direct representatives of a certain area on the grinding wheels, static cutting edge density (S_{ds}) was considered as the main surface parameter when analysing 3D topographies of the resin replicating surfaces.

3.3.6 Microhardness and microstructure analysis

Selected workpiece samples (Ni superalloys and γ-TiAl) were cut from the mid-region of the grinding tracks using wire-EDM. The specimens were then hot mounted in Buehler Epiomat equipment (Fig. 3.3.10(a)) using edge retentive bakelite, and subsequently ground and polished on a Buehler grinder-polisher (Fig. 3.3.10(b)) according to the procedures detailed in Tables 3.3.1 and 3.3.2 for the nickel based superalloys and γ-TiAl respectively.

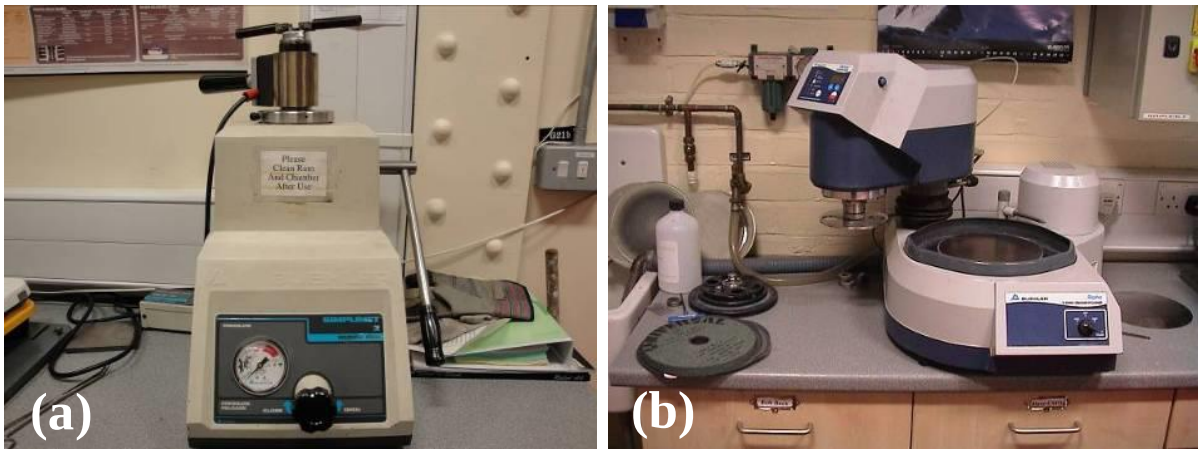


Fig. 3.3.10 (a) Buehler mould mounting equipment, (b) Buehler grinder-polisher

Table 3.3.1 Grinding and polishing conditions for Inconel 718 and CMSX-4 workpieces

Step No.	Base surface	Abrasive/Size	Load (lb)	Base speed (rpm)	Direction of rotation	Time (min)
1.	CARBIMET™ abrasive disc	SiC paper - P240 (water cooled)	5	240-300	Complimentary	10
2.	CARBIMET™ abrasive disc	SiC paper - P600 (water cooled)	5	120-150	Complimentary	5
3.	ULTRA-POL polishing cloth	6 µm METADI SUPREME diamond suspension	5	120-150	Complimentary	5
4.	TRIDENT polishing cloth	3 µm METADI SUPREME diamond suspension	5	120-150	Complimentary	5
5.	MICROCLOTH pad	~0.06 µm MASTERMET colloidal silica suspension	5	120-150	Contradictory	4

Table 3.3.2 Grinding and polishing conditions for γ-TiAl workpieces

Step No.	Base surface	Abrasive/Size	Load (lb)	Base speed (rpm)	Direction of rotation	Time (min)
1.	CARBIMET™ abrasive disc	SiC paper - P400 (water cooled)	6	240-300	Complimentary	10
2.	ULTRA-POL polishing cloth	9 µm METADI SUPREME diamond suspension	6	120-150	Contradictory	10
3.	MICROCLOTH pad	~0.06 µm MASTERMET colloidal silica suspension	6	120-150	Contradictory	10

Microhardness measurements of the ground workpieces (depth profile) were obtained using a Mitutoyo HM-124 microhardness tester (Fig. 3.3.11). A 25 g load and indent time of 15 s were used with three measurements taken, each set at 10 µm intervals from the ground surface until the bulk hardness was achieved. The average at each depth was calculated and plotted. Measurements were carried out in the transverse as well as the longitudinal feed direction. The centre point of indents was kept at a minimum distance of 30 µm from each other in order to avoid the influence of previous indents on the new reading.

For microstructural analysis, Inconel 718 samples were immersion etched using Kalling's reagent (a solution of 10 g cupric chloride, 50 ml hydrochloride acid and 50 ml ethanol) for 1 min. In contrast, the CMSX-4 specimens were electrolytic etched using a 10% orthophosphoric acid solution, while the γ-TiAl workpiecs were immersed in a solution of 2% hydrofluoric (HF) and 10% nitric acid (HNO_3) with balance water for 5 seconds.



Fig. 3.3.11 Mitutoyo HM-124 microhardness tester

3.3.7 Optical and scanning electron microscopy

Micrographs of the grinding wheel surfaces and workpiece subsurface microstructures were taken using an optical microscope connected to a digital camera (1.3 Megapixels) and where necessary, manipulated using Buelher Omnimet image processing software (Fig. 3.3.12(a)). High resolution scanning electron micrographs were taken using a JEOL 6060 scanning electron microscope (SEM) equipped with an OXFORD INCA energy dispersive X-ray (EDX) spectroscopy facility, see Fig. 3.3.12(b).

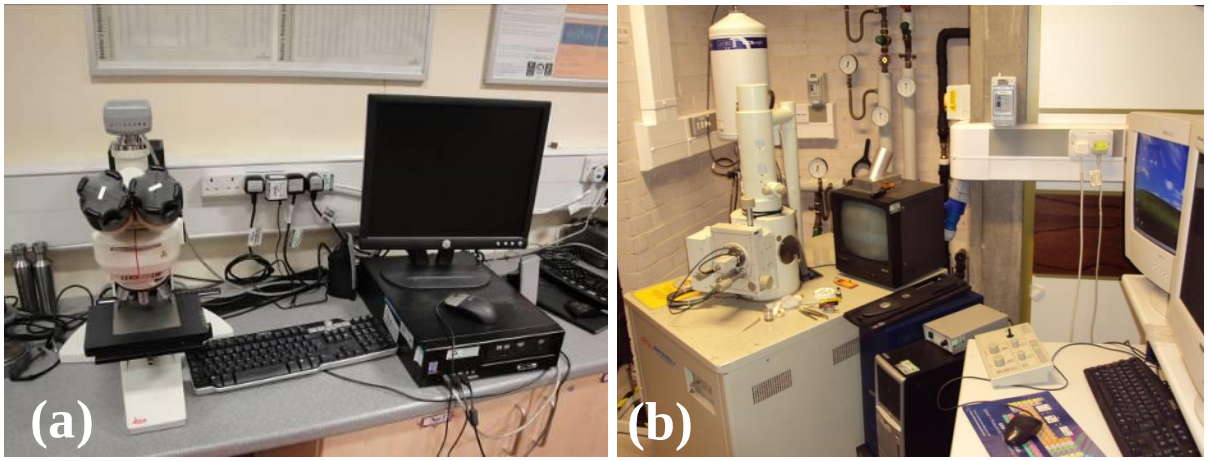


Fig. 3.3.12 (a) Leica DMLM microscope, (b) JEOL 6060 scanning electron microscope

3.4 Experimental procedure and test arrays

The present research was organised into three primary phases of experimental trials. Phase 1 involved initial assessment of different actuator/transducer systems when UAG of Inconel 718 together with a preliminary investigation on ultrasonic assisted dressing of SiC wheels. Phase 2 related to mainstream UAG experiments of both Inconel 718 and CMSX-4 while Phase 3 evaluated the performance of UAG when machining a γ-TiAl alloy. The experimental procedures and associated text arrays are detailed in the following sections.

3.4.1 Phase 1A: UAG experiments using Flexiskills ultrasonic system

Preliminary feasibility trials were carried out in order to assess the performance of the Flexiskills ultrasonic generator system under UAG conditions. A rectangular block of Inconel 718 measuring 50×50×25 mm was screw clamped at the end of a conical aluminium-bronze horn-booster-transducer assembly and vibrated at a frequency of 20 kHz in the longitudinal

direction. One side of the workpiece was placed in contact with the platform dynamometer; but was free to move along the axis of vibration (there was a micron size air-gap between the workpiece and the dynamometer prior to grinding), see Fig. 3.4.1.

Only two trials were performed using a vitrified bonded green silicon carbide wheel (GC601J45VKRNN) at a cutting velocity of 15 m/s together with a table feed and depth of cut of 150 mm/min and 0.05 mm respectively. The vertical (F_v) and horizontal (F_h) components of grinding force were measured with and without the ultrasonic assistance.

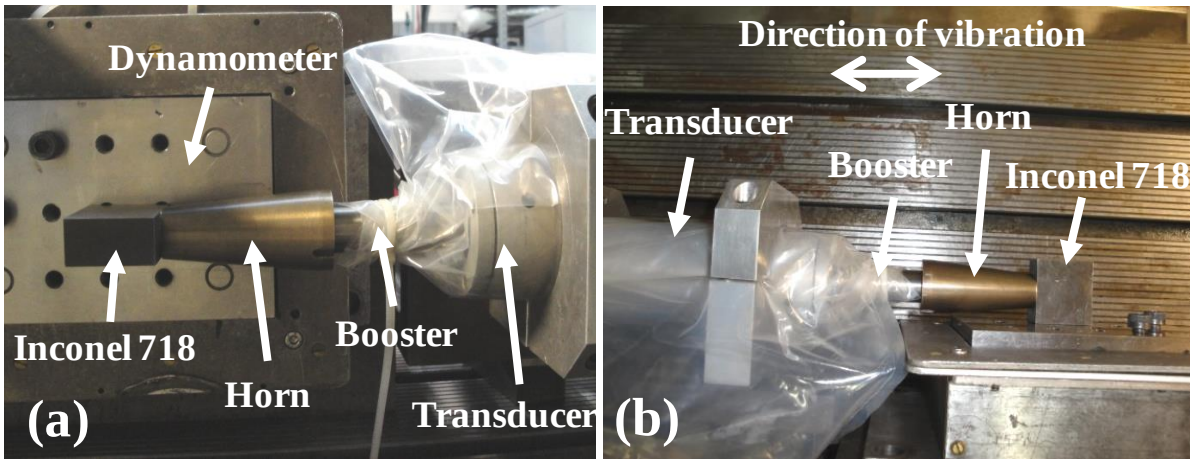


Fig. 3.4.1 On-machine configuration of workpiece-horn-booster-transducer assembly
(a) Front view, (b) Top view

3.4.2 Phase 1B: Initial UAG trials of Inconel 718 with a VORTEX 80 mesh wheel using the MPI ultrasonic system

Test in Phase 1B was carried out with a vitrified bonded VORTEX-80 mesh wheel (IPA80EH17VTX) at a constant wheel speed and table feed of 25 m/s and 200 mm/min respectively. The ultrasonic system from MPI was utilised with the Inconel 718 workpieces screw mounted on the table sonotrode and start frequency of vibration fixed at 20.5 kHz. Initial trials with amplitude of vibration varied at 20%, 30%, 40% and 50% was performed at a depth of cut of 0.5 mm together with corresponding experiments without vibration (Tests 1-6). Depth of cut in subsequent trials was increased to 1.0 mm (Tests 7-12) and 1.5 mm (Tests 13-14) when grinding either with vibration assistance at 50% amplitude or without vibration. Due to the presence of heavy depression marks towards the end of the grinding tracks in Tests 1-8, the influence of employing a dummy workpiece (resin) was investigated (Tests 9, 10, 13 and 14) to minimise the loss of fluid from the grinding zone at the exit location. All trials involved a single pass across the workpiece over a cut length of 55 mm except for Tests 11 and 12, which was extended to 100 mm. The parameters for each of the trials are detailed in

Table 3.4.1 with the corresponding experimental set-up shown in Fig. 3.4.2(a) and (b). The forces due purely to vibration (without load) and during grinding were recorded together with the measurement of radial wheel wear (except for Tests 1, 9, 10, 11 and 12). Surface parameters of the ground workpieces as well as graphite and resin replicas of the grinding wheel were recorded for evaluation of the workpiece surface quality in relation to the wheel surface topography when employed with and without ultrasonic assistance.

Table 3.4.1 List of trials carried out in Phase 1B

Test no.	**Depth of cut, a_e (mm)**	**Amplitude (%) (set from generator)**
1.	0.5	US OFF
2.		US ON-20%
3.		US ON-30%
4.		US OFF - repeat test
5.		US ON-40%
6.		US ON-50%
7.	1.0	US OFF
8.		US ON-50%
9.		US OFF-with dummy
10.		US ON-50%-with dummy
11.		US OFF-greater cut length
12.		US ON-50%-greater cut length
13.	1.5	US OFF-with dummy
14.		US ON-50%-with dummy

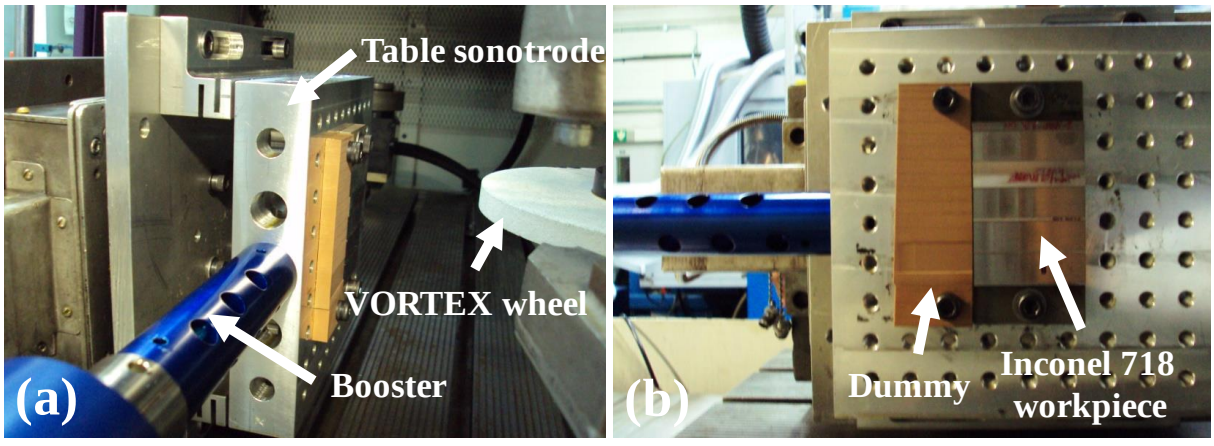


Fig. 3.4.2 (a) On-machine configuration of wheel-workpiece-sonotrode assembly, (b) Clamping arrangement of workpiece and dummy

3.4.3 Phase 1C: Initial experiments on ultrasonic assisted dressing

Limited tests were carried out to evaluate the viability and effect of ultrasonic assisted dressing on the performance of a green silicon carbide wheel. A polycrystalline diamond (PCD) insert (SNMA 120408) was brazed onto the end of a stepped aluminium-bronze horn, which was connected to a booster-transducer and vibrated axially at a frequency of 23 kHz and amplitude of 18.5 μm using a Kerry 150 W ultrasonic generator. The transducer-horn assembly was mounted on a Kistler platform dynamometer with dressing performed by feeding the PCD insert vertically across the peripheral face of the SiC wheel (single point dressing configuration), see Fig. 3.4.3. Four dressing experiments were undertaken to assess the influence of ultrasonic vibration (US OFF and US ON) and coolant (wet and dry) with wheel speed, feed and depth of cut constant at 20 m/s, 100 mm/min and 0.05 mm respectively. A single pass grinding operation on Inconel 718 (55 mm cut length) was performed following each dressing cycle at equivalent wheel speed of 20 m/s but with feed and depth of cut increased to 150 mm/min and 0.3 mm respectively, see Table 3.4.2. The measured responses were dressing and grinding forces and surface roughness parameters of the ground workpieces. The grinding force and workpiece roughness results were then compared with those recorded following conventional roller dressing.

Table 3.4.2 List of trials carried out in Phase 1C

Test no.	**Operations**	**Coolant**	**Vibration**	**Table feed, V_W (mm/min)**	**Depth of cut, a_e (mm)**
1.	Dressing cycle-1	ON	OFF	100	0.05
2.	Grinding pass-1	ON	OFF	150	0.3
3.	Dressing cycle-2	ON	ON	100	0.05
4.	Grinding pass-2	ON	OFF	150	0.3
5.	Dressing cycle-3	OFF	OFF	100	0.05
6.	Grinding pass-3	ON	OFF	150	0.3
7.	Dressing cycle-4	OFF	ON	100	0.05
8.	Grinding pass-4	ON	OFF	150	0.3

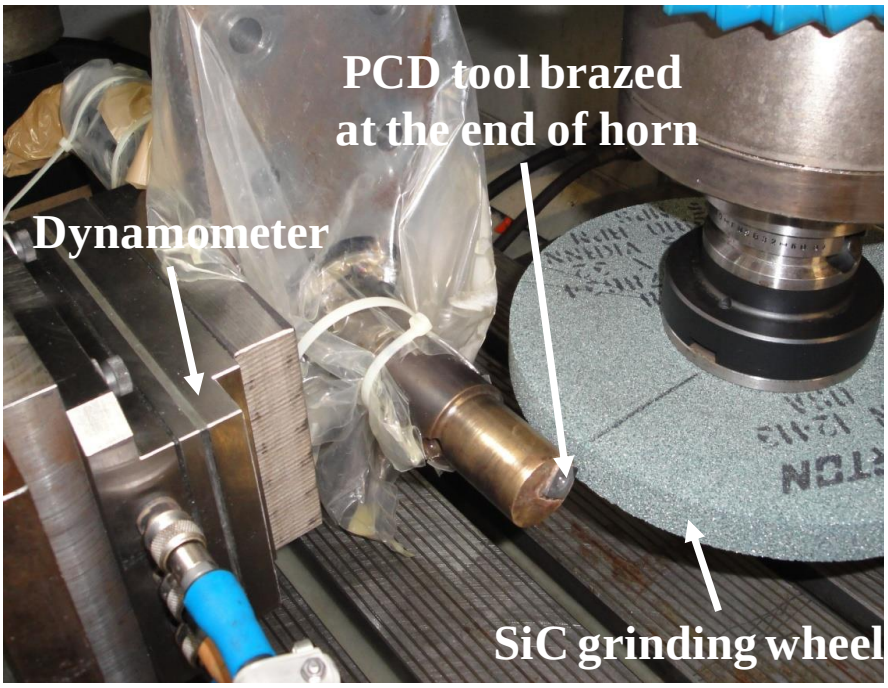


Fig. 3.4.3 On-machine configuration of wheel-dressing tool-dynamometer assembly

3.4.4 Phase 2A: Identification of process parameters for UAG of Inconel 718

Based on results from Phase 1B, extensive single pass grinding tests (without ultrasonic vibration) of Inconel 718 were undertaken to establish the effect of process parameters on machined surface topography/quality and identify appropriate operating conditions for mainstream UAG experiments. The majority of trials were performed using the VORTEX 80 mesh alumina wheel with a further two trials performed using an equivalent wheel having a larger grain size (VORTEX 60 mesh) and greater porosity (better ingress of coolant). Wheel speed was varied between 25 and 40 m/s, while two levels of table feed (200 and 400 mm/min) and depth of cut (1.0 and 1.5 mm) were employed with coolant pressure adjusted between 5 to ~28-30 bar. Following recommendations from Rolls Royce, an exploratory experiment involving an alternative alumina wheel (POROS2) was also undertaken at a wheel velocity of 40 m/s, table feed of 300 mm/min, depth of cut of 1.0 mm and fluid pressure of 28 bar. In general, tests were carried out (unless otherwise stated) with the workpiece clamped on the table sonotrode together with a resin dummy workpiece (placed at the exit) while the grinding wheel was dressed prior to each experiment according to the conditions outlined in Section 3.3.1. The detail of each trial is given in Table 3.4.3. In addition to operating parameters, other factors investigated included stiffness of the table sonotrode (Test 3), dressing infeed level (Tests 4 and 6), workpiece material (Test 7), effect of dummy workpiece (Test 9) and direction of the cooling nozzle (Test 10).

Table 3.4.3 List of trials carried out in Phase 2A

Test no.	Wheel velocity, V_C (m/s)	Table feed, V_W (mm/min)	Depth of cut, a_e (mm)	Undeform-ed chip thickness, h_m (µm)	Pressure of cutting fluid (bar)	Grinding wheel	Other variations in the process/remarks
1.	25	200	1.0	0.133	5	VORTEX 80 mesh	
2.					15		
3.					5		Workpiece mounted on dynamometer
4.					15		Dressing infeed: 1.5 µm/rev
5.							
6.							Dressing infeed: 1.5 µm/rev
7.							AISI 1040 steel workpiece
8.	30	200	1.0	0.111	15		
9.							No dummy workpiece
10.							Position of cooling nozzle changed to 20° from 0°
11.			1.5	0.167			
12.	35	200	1.0	0.095	15		
13.			1.5	0.143			
14.	40	200	1.0	0.083	15		
15.					20		
16.	30	200	1.0	0.111	20		
17.		400		0.222			
18.	40	400	1.0	0.167	25		
19.					25		
20.					20		
21.					28		
22.	30	200	1.0	0.111	20	VORTEX 60 mesh	
23.		400		0.111	25		
24.	40	300		0.125	28	POROS2	

3.4.5 Phase 2B and 2C: Evaluation of UAG on Inconel 718 using POROS2 and VORTEX 60 mesh wheels

Mainstream testing on the ultrasonic assisted grinding of Inconel 718 was aimed out with POROS2 (Phase 2B) and VORTEX 60 mesh (Phase 2C) alumina wheels with variations in wheel speed (30, 35 and 40 m/s), table feed (200, 250 and 300 mm/min) and operating condition (with and without vibration), while depth of cut was fixed at 1.0 mm based on

results from Phase 2A. An equivalent full factorial experimental array comprising 18 tests was utilised in both experimental phases and is shown in Table 3.4.4. All trials were performed in a down grinding mode without spark-out and involving a single pass of the workpiece (50 mm cut length). The respective experimental set-ups used in Phase 2B and 2C are shown in Figs. 3.4.4(a) and (b).

Table 3.4.4 Full factorial experimental array used in Phase 2B and 2C

Test no.	Wheel velocity, V_C (m/s)	Table feed, V_W (mm/min)	Condition of vibration
1.	30	200	OFF
2.		200	ON
3.		250	OFF
4.		250	ON
5.		300	OFF
6.		300	ON
7.	35	200	OFF
8.		200	ON
9.		250	OFF
10.		250	ON
11.		300	OFF
12.		300	ON
13.	40	200	OFF
14.		200	ON
15.		250	OFF
16.		250	ON
17.		300	OFF
18.		300	ON

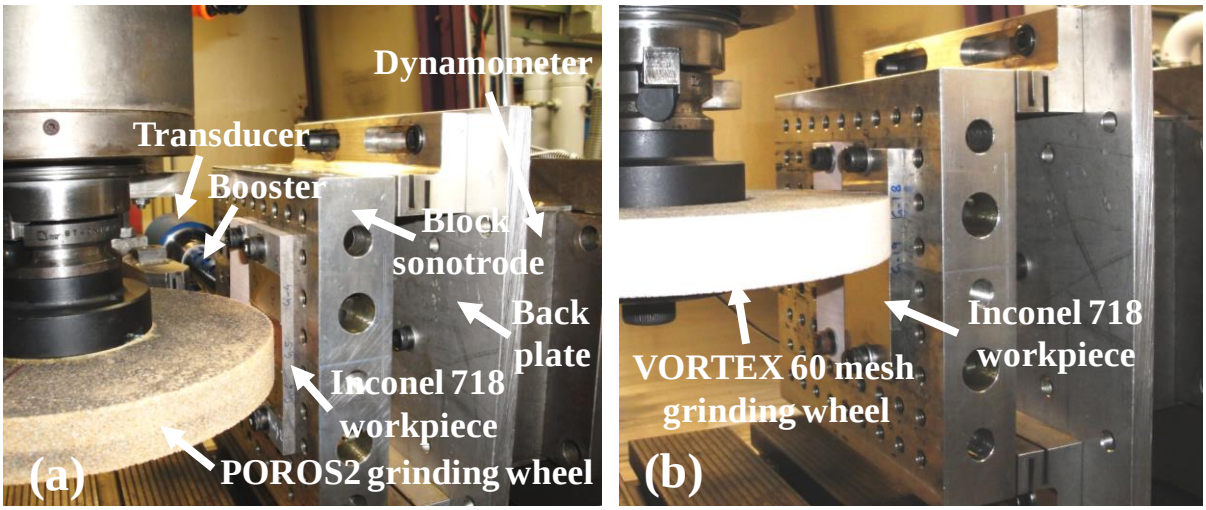


Fig. 3.4.4 Set-up for (a) Phase 2B, (b) Phase 2C

For trials involving US vibration, the workpiece (clamped on the table sonotrode and connected to MPI system) was actuated at a constant frequency of ~20.5 kHz, while the amplitude of vibration was set at 50% on the generator. The actual amplitude of the table sonotrode under zero-load condition (workpiece mounted but without grinding) and vibrating at the 50% setting was measured using a Laser Doppler Vibrometer (see Appendix A3). The maximum amplitude recorded was 4.2 μm with an average of 2 to 4 μm. The effects of ultrasonic vibration was evaluated with regard to grinding forces, radial wheel wear (G-ratio), workpiece surface roughness together with the microhardness and microstructure analysis and wheel surface topography. Statistical analysis (main effects and interaction plots together with the analysis of variance/ANOVA) on the measured responses was carried out using MINITAB 16 software.

3.4.6 Phase 2D: Assessment of UAG on CMSX-4 using POROS2 wheel

Work in this phase was designed to evaluate the performance of UAG for a cast CMSX-4 nickel based superalloy typically used in turbine blade applications. Due to the size of the workpiece material available, the sample blocks were held using a bespoke clamping assembly on the table sonotrode as shown in Figs. 3.4.5(a) and (b). A full factorial experimental array comprising three variable factors (two at two levels and one at four levels) which entailed a total of 16 tests as shown in Table 3.4.5. Table feeds up to 600 mm/min were evaluated, which were more representative of production parameters and material removal rates. Depth of cut was kept constant at 1.0 mm with all tests involving a single pass, carried out utilising the POROS2 alumina wheel based on comparative data from Phases 2B and 2C.

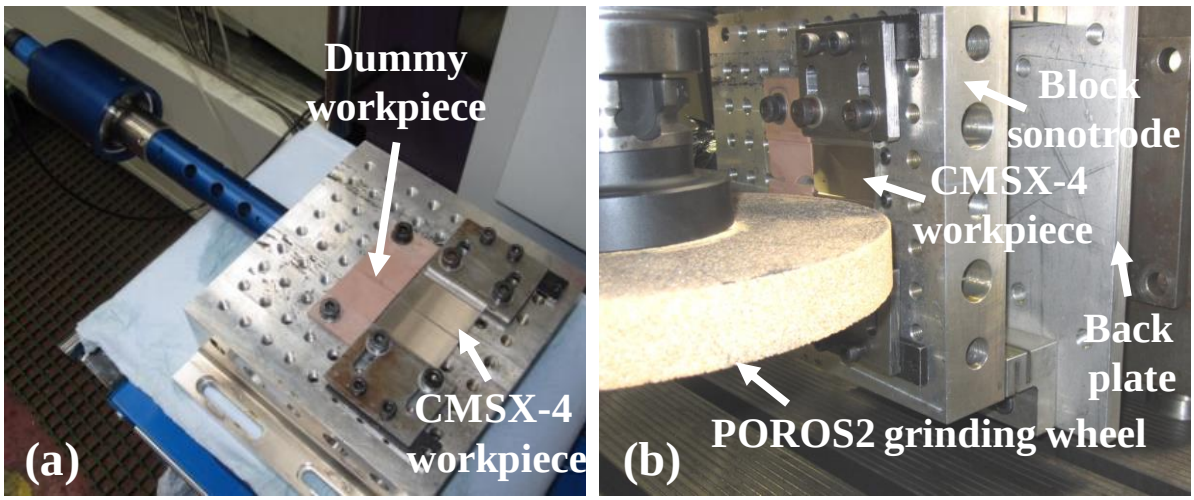


Fig. 3.4.5 (a) CMSX-4 workpiece clamped on to the block sonotrode
(b) On-machine configuration

Table 3.4.5 Full factorial experimental array used in Phase 2D

Test no.	Wheel velocity, V_C (m/s)	Table feed, V_W (mm/min)	Condition of vibration
1.	30	300	OFF
2.		300	ON
3.		400	OFF
4.		400	ON
5.		500	OFF
6.		500	ON
7.		600	OFF
8.		600	ON
9.	40	300	OFF
10.		300	ON
11.		400	OFF
12.		400	ON
13.		500	OFF
14.		500	ON
15.		600	OFF
16.		600	ON

3.4.7 Phase 2E: Effect of depth of cut and vibration amplitude when UAG of Inconel 718

Phase 2E was designed to assess the influence of varying amplitude of vibration and depth of cut on grinding forces, wheel wear, workpiece surface topography and quality and wheel surface characteristics. Trials were performed using a full factorial experimental array comprising 12 tests with variable factors including grinding condition (vibration OFF and ON), amplitude of vibration ('High' ~7-8 µm and 'Low' ~2-4 µm with details of amplitude measurement given in Appendix A3) and depth of cut (0.5, 1.0 and 1.5 mm) while keeping the wheel speed and table feed fixed at 30 m/s and 600 mm/min respectively. Table 3.4.6 details the experimental array undertaken in Phase 2E.

Table 3.4.6: Full factorial experimental array used in Phase 2E

Test no.	Depth of cut, a_e (mm)	Amplitude of vibration	Condition of vibration
1.	0.1	0	OFF
2.		High	ON
3.		0	OFF
4.		Low	ON
5.	0.5	0	OFF
6.		High	ON
7.		0	OFF
8.		Low	ON
9.	1.0	0	OFF
10.		High	ON
11.		0	OFF
12.		Low	ON

3.4.8 Phase 3A: Assessment of UAG on γ-TiAl using conventional SiC abrasive wheel

Phase 3A aimed to investigate the effects of ultrasonic vibration on grinding forces, wheel wear/G-ratio, workpiece surface quality/integrity and wheel surface topography when machining γ-TiAl. The selection of grinding parameters was predominantly based on previous work by Bentley and Aspinwall (1997a) and Hood et al. (2007a and 2007b) involving creep feed grinding of γ-TiAl with conventional silicon carbide (SiC) wheels. The current research considered the variation of cutting speed, table feed and grinding condition (each at two levels), while the depth of cut was fixed at 1.0 mm. The trials were carried out according to a full factorial experimental design comprising 8 tests, see Table 3.4.7. For tests with the ultrasonic vibration active, the 'Low' amplitude setting (average of 2-4 μm) was selected following results from Phase 2E. The experimental set-up is shown in Fig. 3.4.6.

Table 3.4.7: Full factorial experimental array used in Phase 3A

Test no.	Wheel velocity, V_C (m/s)	Table feed, V_W (mm/min)	Condition of vibration
1.	15	150	OFF
2.		150	ON
3.		600	OFF
4.		600	ON
5.	30	150	OFF
6.		150	ON
7.		600	OFF
8.		600	ON

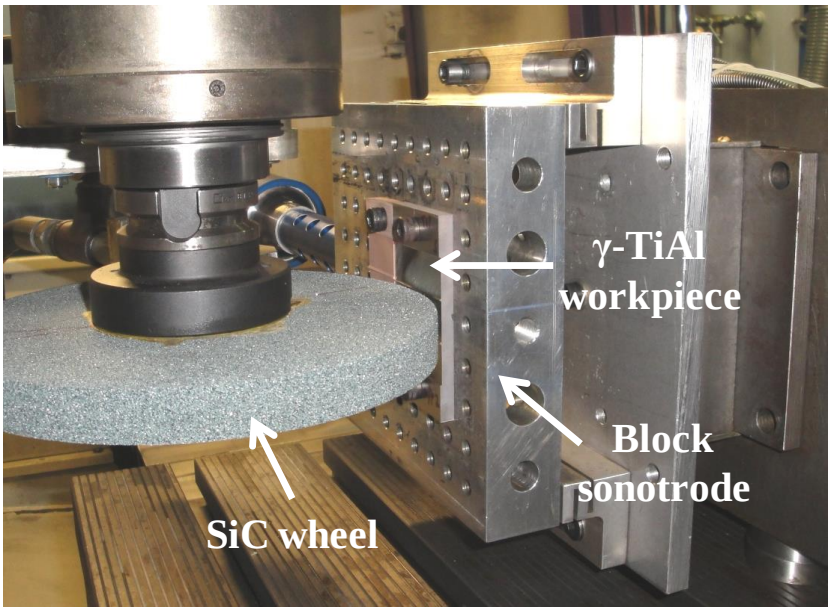


Fig. 3.4.6 Set-up for UAG of γ-TiAl trials with SiC wheel

3.4.9 Phase 3B: Investigation of UAG on γ-TiAl with electroplated diamond superabrasive wheel

The objective of Phase 3B work was to investigate the effects of ultrasonic vibration on the performance of a single layer electroplated diamond superabrasive wheel (D252) when creep feed grinding γ-TiAl. Unfortunately, only one electroplated superabrasive wheel was supplied by Saint-Gobain Abrasives due to the high cost and extended lead time for manufacture. A series of 4 tests alternatively between standard and ultrasonic assisted grinding at a wheel speed, table feed and depth of cut of 30 m/s, 150 mm/min and 1.0 mm were initially performed. Two additional tests (with and without ultrasonic vibration) were subsequently conducted at increased cutting speed of 40 m/s and table feed of 600 mm/min. No further tests were possible due to limited availability of workpiece material. The sequence of tests is detailed in Table 3.4.8 with the corresponding experimental set-up shown in Fig. 3.4.7.

Table 3.4.8 Full factorial experimental array used in Phase 3B

Test no.	Wheel velocity, V_C (m/s)	Table feed, V_W (mm/min)	Condition of vibration
1.	30	150	OFF
2.			ON
3.			OFF
4.			ON
5.	40	600	OFF
6.			ON

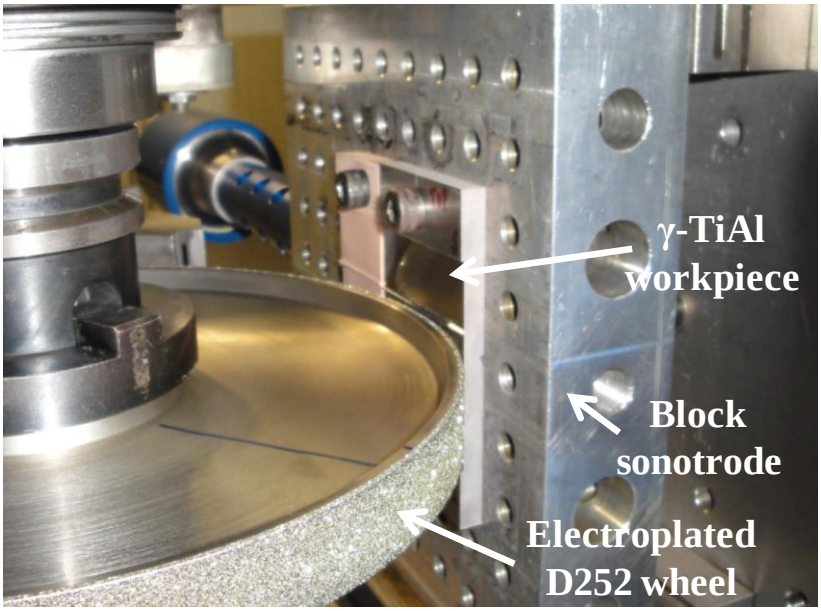


Fig. 3.4.7 Set-up for UAG of γ-TiAl with electroplated D252 diamond wheel

4. RESULTS AND DISCUSSION

4.1 Initial trial experiments on ultrasonic assisted grinding and dressing

4.1.1 Phase 1A: UAG experiments using Flexiskills ultrasonic system

Table 4.1.1 details the operating conditions and the related average vertical (F_v) and horizontal (F_h) force data recorded during grinding Inconel 718. The corresponding force profiles are shown in Fig. 4.1.1.

Table 4.1.1 Grinding forces recorded without and with ultrasonic assistance

Trial No.	Grinding parameters			Ultrasonic vibration	F_v (N)	F_h (N)
	V_C (m/s)	V_W (mm/min)	a_e (mm)			
1.	15	150	0.05	OFF	74.09	8.21
2.				ON	100.89	7.72

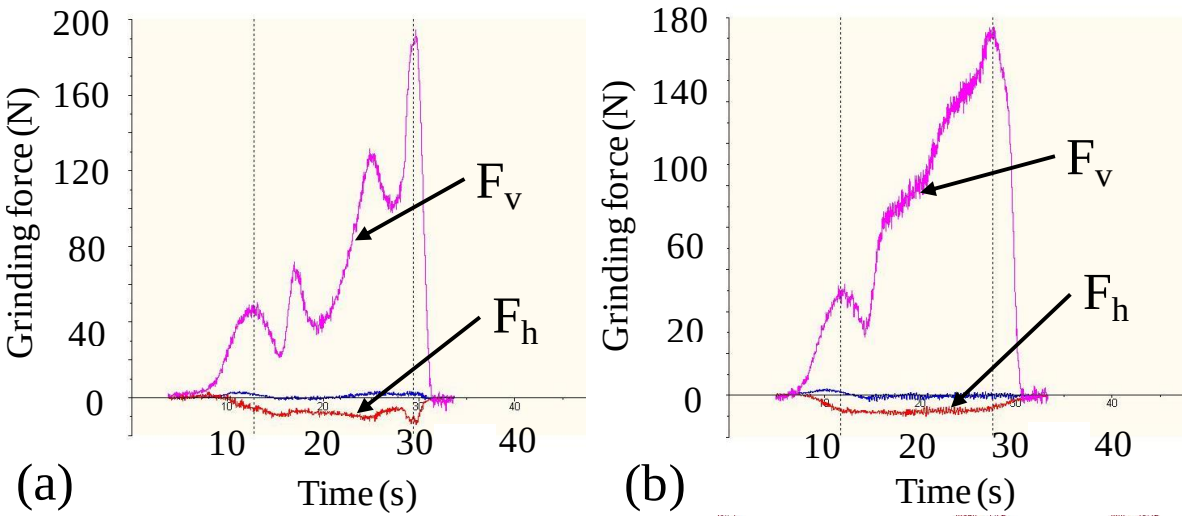


Fig. 4.1.1 Force traces when grinding (a) Without and (b) With ultrasonic vibration

Higher average vertical grinding force (F_v) was obtained when grinding was employed with ultrasonic vibration, although the maximum value of F_v was greater in the conventional mode. The corresponding vertical force profile in conventional grinding displayed several steep 'spikes' which were generally absent in the force trace recorded during UAG. The horizontal grinding forces (F_h) recorded with and without the assistance of vibration were

comparable, although a sudden 'spike' towards the end of the cut was observed in conventional grinding.

The experimental set-up encountered several limitations which prevented its use for further detailed study on UAG. They were:

- It was difficult to transmit an adequate/consistent ultrasonic vibration to the workpiece by using the conical horn.
- There was ingress of cutting fluid into the transducer sleeve despite attempts were made at shielding using plastic sheeting.
- There was problem regarding the fixation/repeat mounting of the workpiece at the end of the horn.
- It was not possible to assess the amplitude of vibration from the analogue output of ultrasonic generator.

4.1.2 Phase 1B: Initial UAG trials of Inconel 718 with a VORTEX 80 mesh wheel using the MPI ultrasonic system

The forces generated due to ultrasonic vibration (i.e. under zero grinding load condition) recorded at different amplitude settings of the ultrasonic generator are shown in Figure 4.1.2. The vertical (F_v) and horizontal force (F_h) components generally increased with amplitude, with the largest F_v doubling from ~150 N to ~300 N as the amplitude level was varied from 20 to 50%.

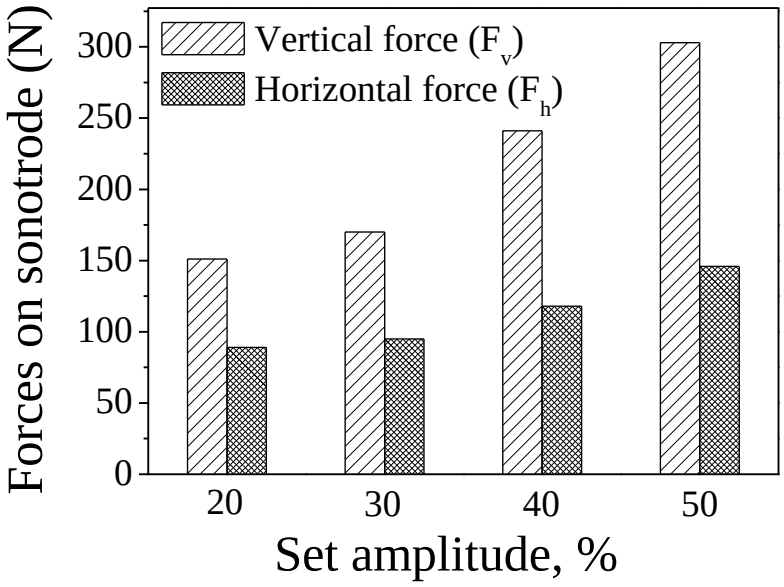


Fig. 4.1.2 Forces due to ultrasonic vibration (zero load) at varying amplitude levels

The maximum forces recorded during various grinding conditions are shown in Fig. 4.1.3 while radial wheel wear and G-ratio for selected trials are detailed in Fig. 4.1.4.

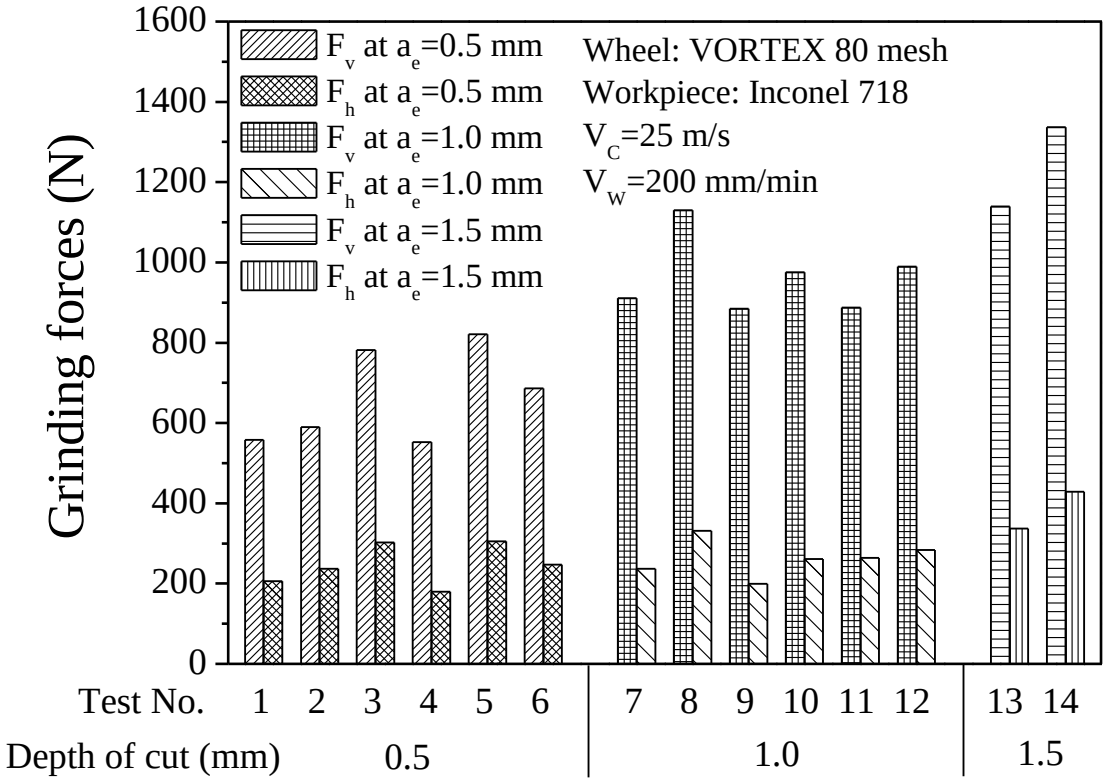


Fig. 4.1.3 Maximum forces recorded during grinding of Inconel 718

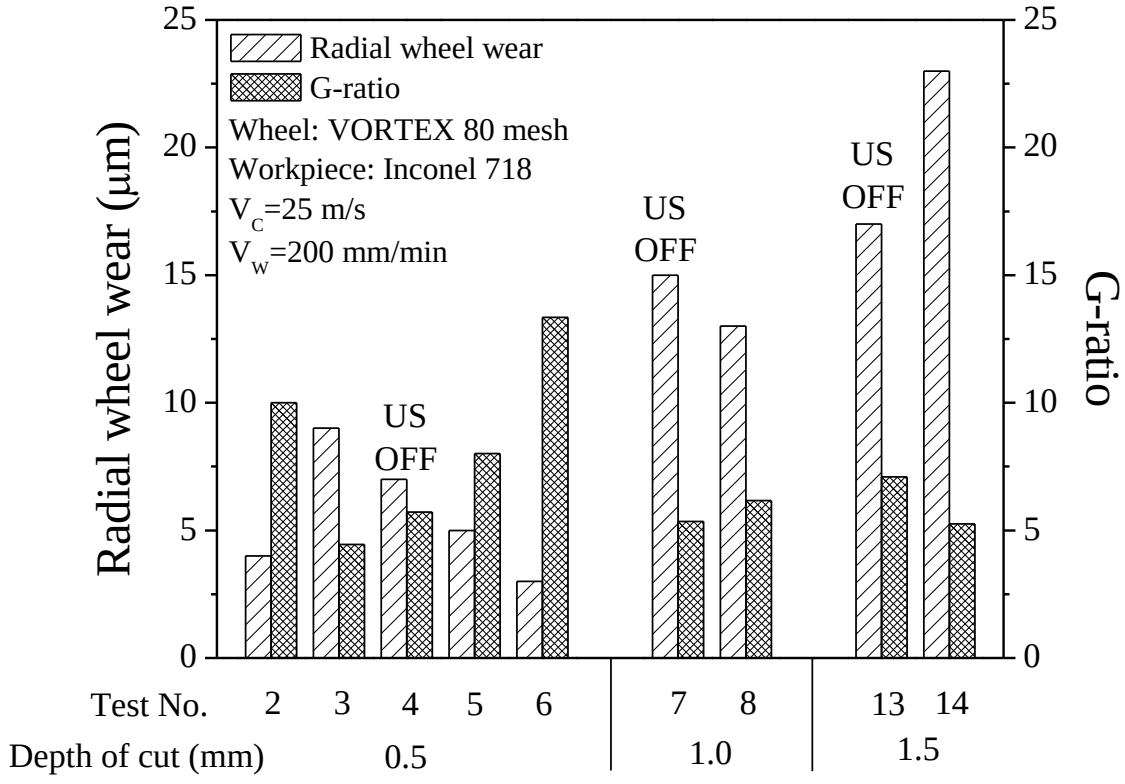


Fig. 4.1.4 Radial wheel wear and corresponding G-ratio of VORTEX 80 mesh wheel

With the exception of Test 3, radial wheel wear generally decreased (with corresponding increase in G-ratio) when employing ultrasonic assistance at a depth of cut of 0.5 mm, while the trend was reversed as depth of cut was increased to 1.5 mm (Tests 13 and 14). A decrease in radial wheel wear and an increase in G-ratio generally corresponded with an increase in surface roughness values of the ground workpieces.

Figures 4.1.5(a) and (b) show images of selected surfaces ground at a depth of cut of 0.5 mm. Single depression/trough marks varying in depth from ~45 to 90 µm (measured using Taylor Hobson Form Talysurf and a typical profile shown in Fig. 4.1.6) were visible towards the end of grinding track machined at a depth of cut of 0.5 mm (Tests 1 to 6), irrespective of the grinding conditions. As depth of cut was increased to 1.0 mm, multiple depressions formed in both trials with and without ultrasonic vibration (Tests 7 and 8), see Fig. 4.1.7(a). The use of a dummy workpiece when grinding at a depth of cut of 1 mm (Tests 9 and 10) eliminated the deformation, which suggests a possible loss of coolant at the exit of cut, although the depression reappeared on the machined surface (at a greater frequency with depths up to ~140 µm) as depth of cut was further increased to 1.5 mm, with the dummy plate providing no discernable benefit, see Fig. 4.1.7(b).

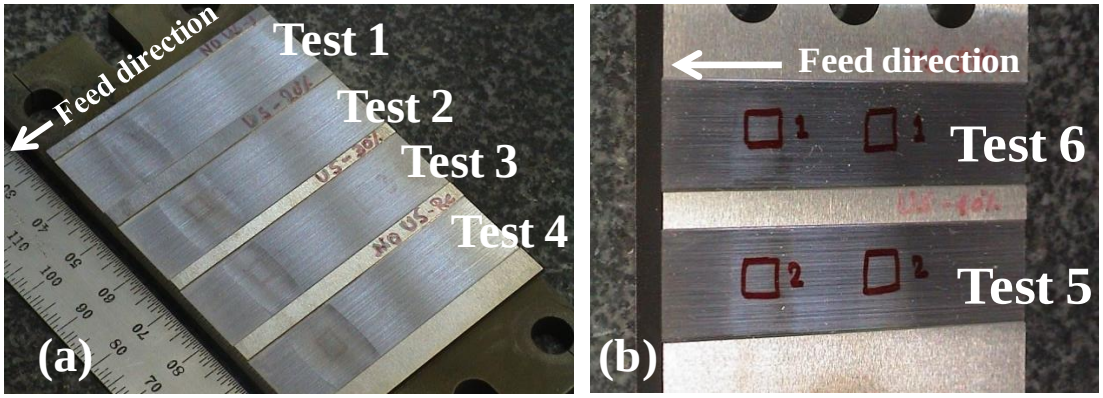


Fig. 4.1.5 Images of workpiece surfaces ground at a depth of cut of 0.5 mm

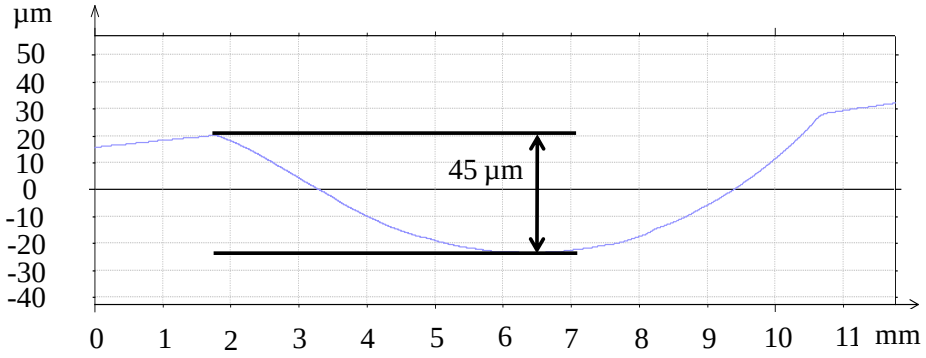


Fig. 4.1.6 A typical 2D surface profile showing the depth of deformation

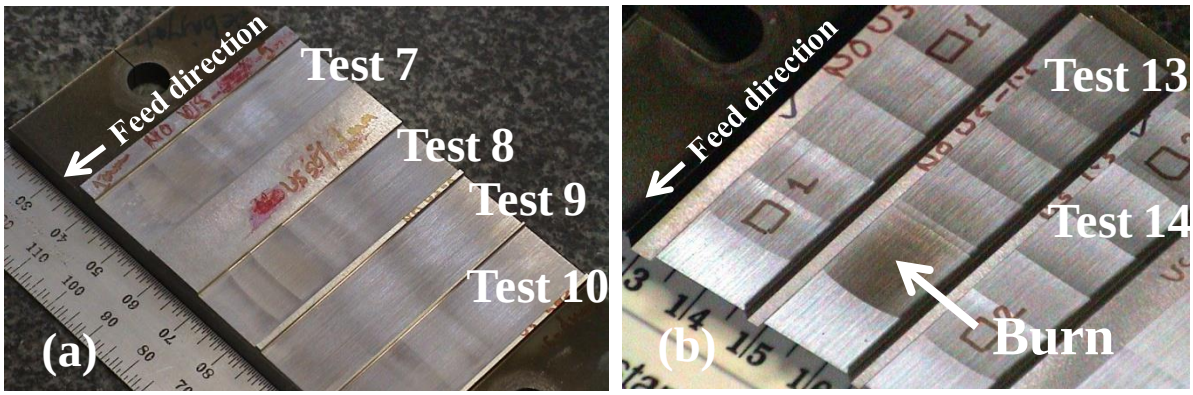


Fig. 4.1.7 Images of workpiece surfaces ground at depths of cut of (a) 1.0 mm and (b) 1.5 mm

Figure 4.1.8 shows SEM micrographs of the ground surfaces near the start and end of the track in Test 7. The former appeared to be smoother and generally free of any major defects while the latter, which was within the depression zone, was characterised by smearing, adhered material, deeper groves etc. This corresponded to 2D roughness measurements (R_a) which showed that surface quality typically deteriorated towards the end of the ground surface (by an average of ~40 to 50%). The introduction of the dummy workpiece however (Tests 9 and 10) led to a substantial improvement in average surface roughness across the machined track (16 to 35% reduction in R_a) compared to the associated experiments without the dummy plate (Tests 7 and 8).

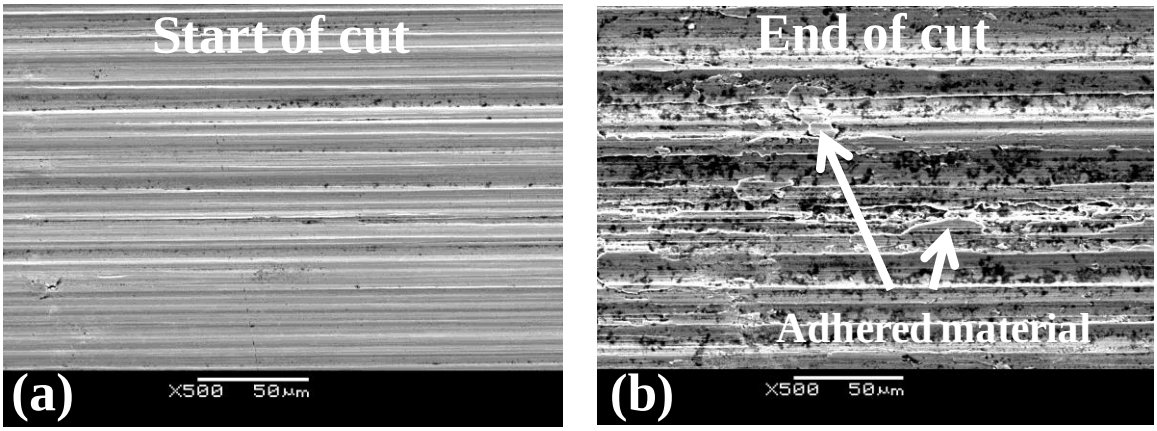


Fig. 4.1.8 SEM micrographs of Inconel 718 workpiece ground at a depth of cut of 1.0 mm without vibration (Test 7) at (a) Start of cut, (b) End of cut

4.1.3 Phase 1C: Initial experiments on ultrasonic assisted dressing

4.1.3.1 Dressing and grinding forces

The maximum and average forces recorded when dressing of the vitrified bonded SiC wheel are presented in Figs. 4.1.9 and 4.1.10 respectively. A 27 to 40% reduction in maximum vertical force (F_v) together with a 22 to 50% drop in maximum horizontal force (F_h) were observed when operating with ultrasonic vibration. Conversely, the influence of ultrasonic vibration on average dressing forces was marginal. A marked difference however was evident between wet and dry environments, with average vertical force levels almost doubling when dressing was performed without coolant. This was possibly due to the greater interaction/contact between the dislodged/fragmented grits that were not flushed away, with those on the wheel surface.

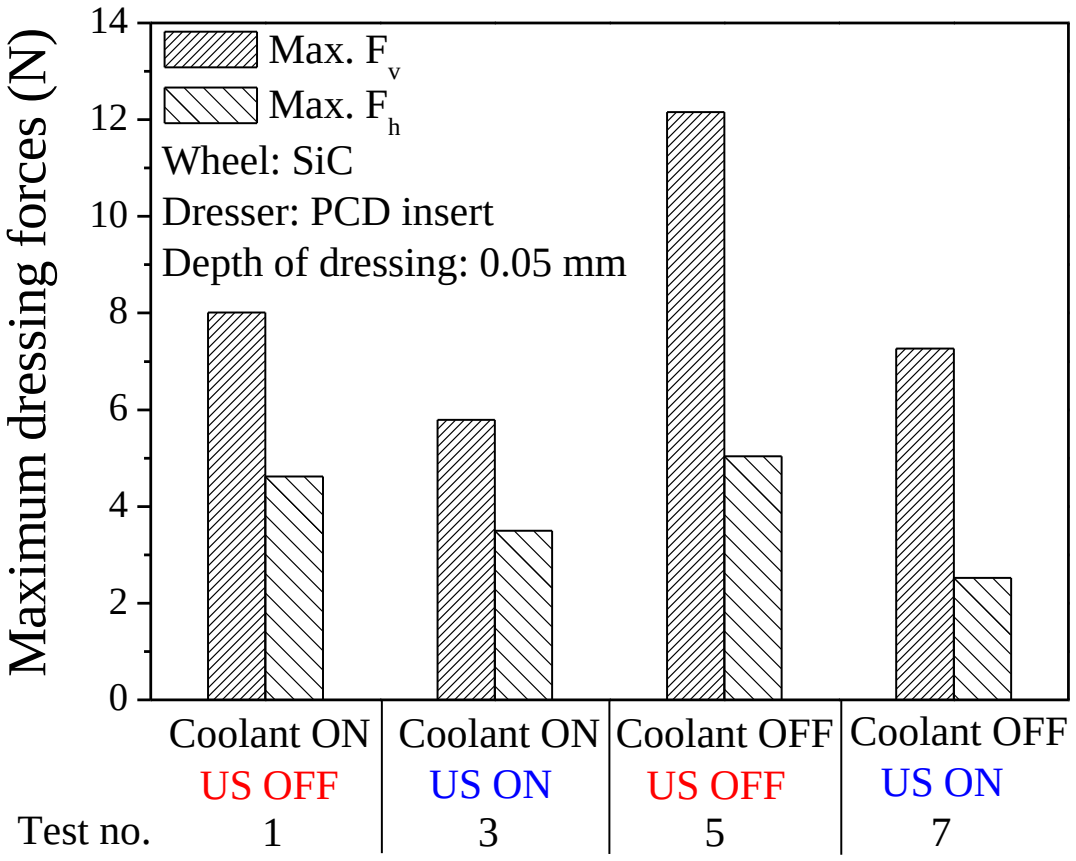


Fig. 4.1.9 Maximum dressing forces recorded when dressing with single point PCD insert

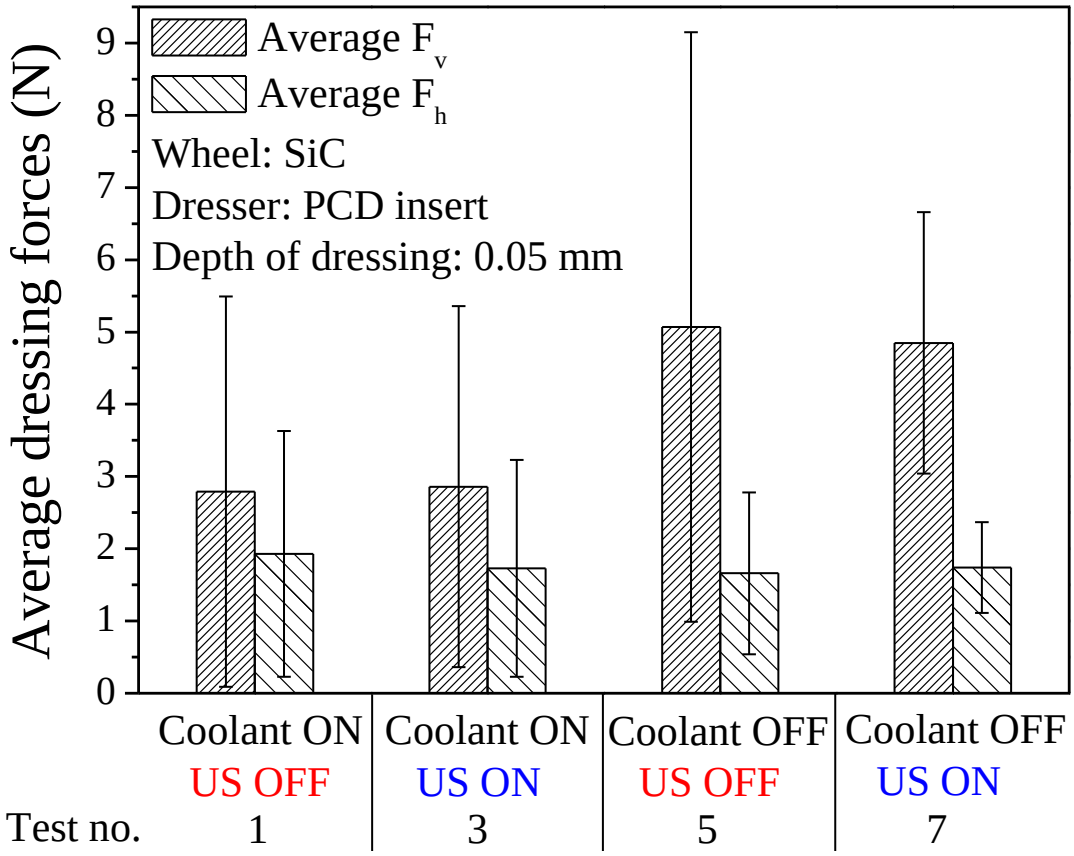


Fig. 4.1.10 Average dressing forces recorded when dressing with single point PCD insert

Average forces recorded when grinding Inconel 718 following various dressing regimes are shown in Fig. 4.1.11. The wheel prepared by roller dressing typically resulted in 15 to 35% lower vertical grinding forces than those dressed via the single point configuration. When comparing the performance of conventional single point against ultrasonic assisted dressed wheels, the latter exhibited a ~10% reduction in average grinding forces when machining wet, with a further drop in vertical forces of up to ~20% when operating under dry conditions.

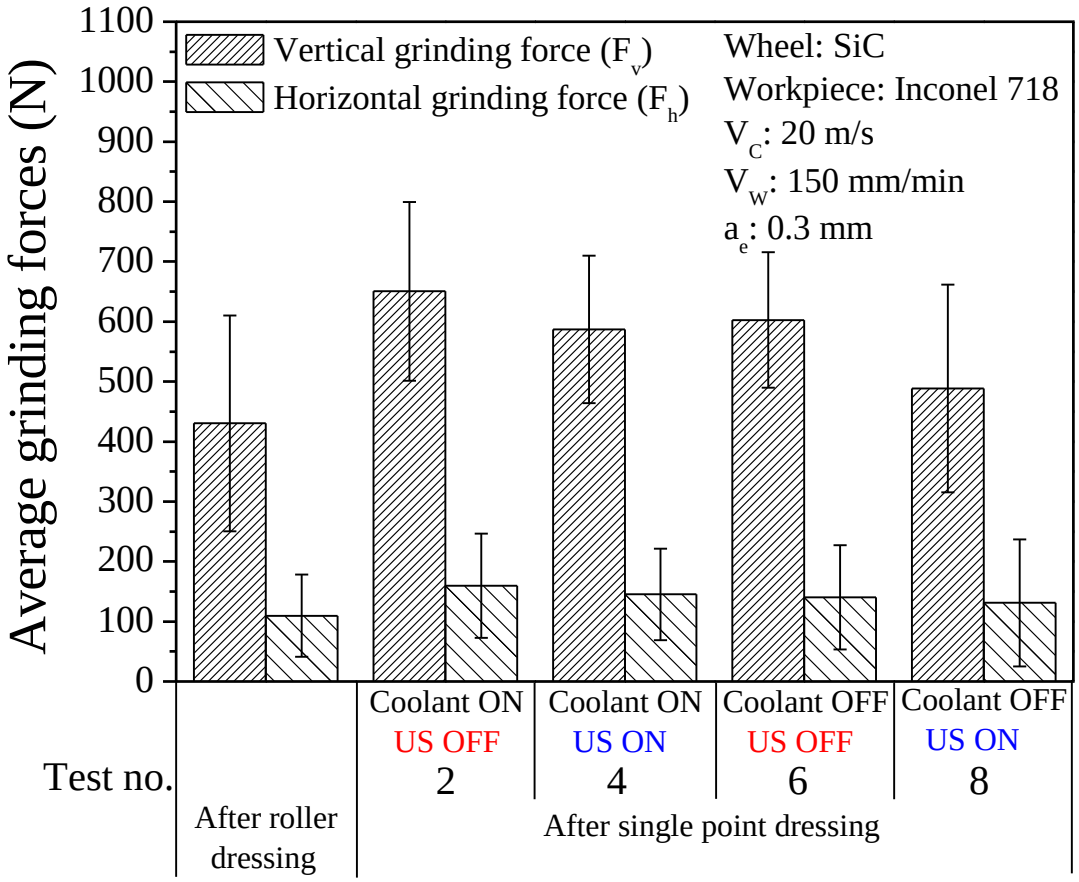


Fig. 4.1.11 Average grinding forces following dressing with roller dresser and single point PCD dressing tool

4.1.3.2 Workpiece surface topography and quality

Figure 4.1.12 shows the 2D roughness parameters of the workpiece surfaces following grinding in each test. The roughness levels (R_a, R_t and R_z) were typically two times higher when utilising the roller dressed wheel as opposed to tests employing wheel prepared by single point dressing. This was due to the presence of lower number of active cutting points on the wheel surface following roller dressing. There was a marginal reduction in the surface roughness values of the workpiece when ground by an ultrasonically dressed wheel compared to a non-ultrasonically dressed wheel. The typical examples of optical micrographs of ground surfaces, shown in Fig. 4.1.13, exhibited several 'surging' marks towards the end of grinding tracks, which was particularly severe when grinding with a conventionally dressed (without ultrasonic vibration) wheel.

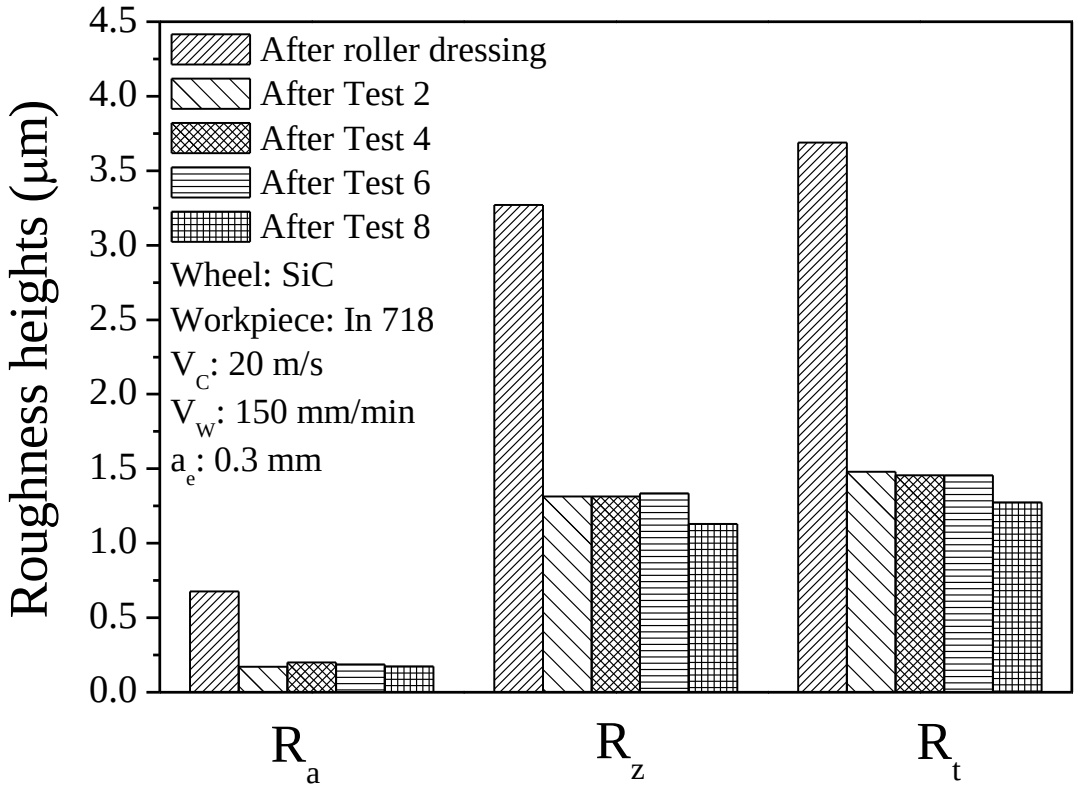


Fig. 4.1.12 Influence of dressing operation on ground workpiece surface roughness

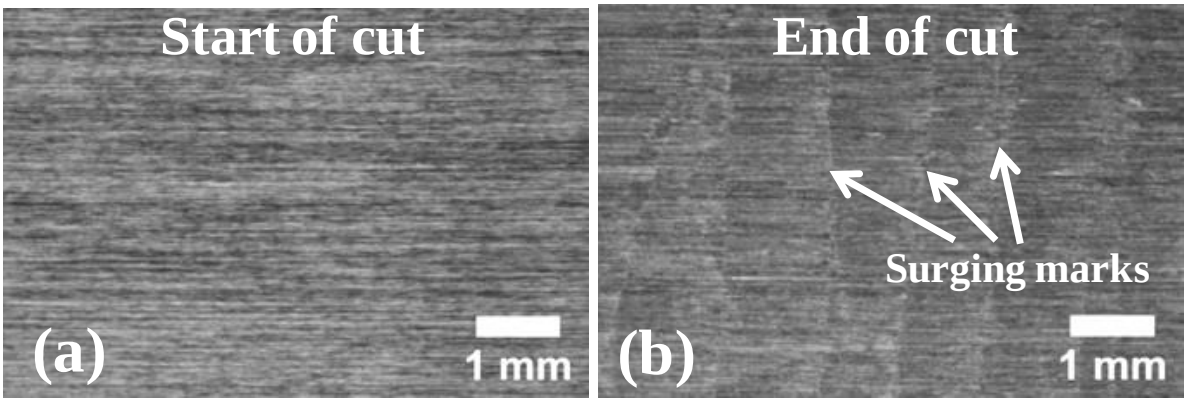


Fig. 4.1.13 Optical micrographs of ground surfaces following conventional dressing (without ultrasonic vibration) under dry environment (a) Start of cut, (b) End of cut

The SEM micrographs in Figs. 4.1.14(a) and (b) showed smearing/adhesion of material on the ground workpiece surfaces following conventional dressing. Conversely, surfaces ground with an ultrasonically dressed wheel exhibited much smoother appearance with lower levels of smeared material, see Figs. 4.1.14(c) and (d).

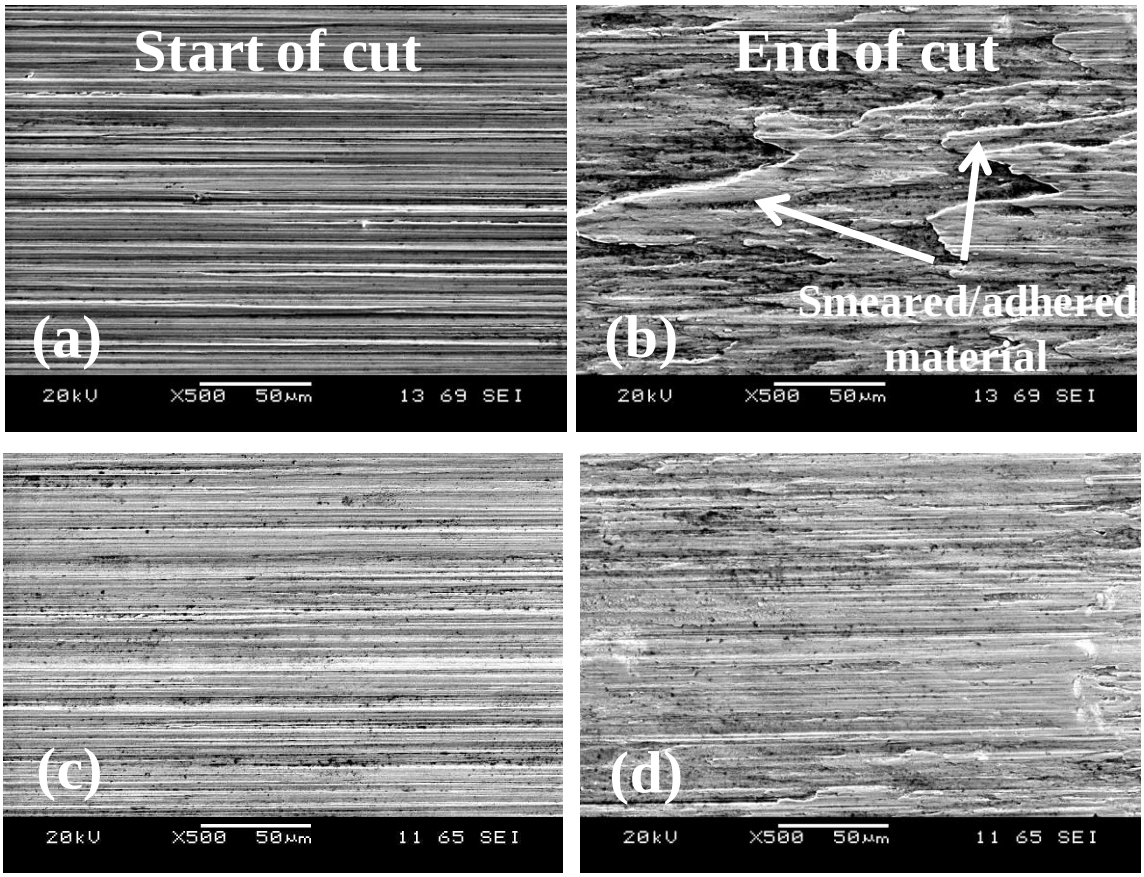


Fig. 4.1.14 SEM micrographs of ground surfaces following (a) and (b) conventional dressing under wet environment, (c) and (d) Ultrasonic assisted dressing under wet environment

4.1.3.3 Wear of PCD insert and wheel condition following grinding

The PCD insert employed for single point dressing exhibited wear (~0.3 mm) at its tip following the completion of all trials, see Fig. 4.1.15. Additionally, no significant difference in the appearance of the ultrasonically and non-ultrasonically dressed SiC wheel was noted when observed under the optical microscope, see Fig. 4.1.16. Following single point dry dressing, the wheel was clogged with dislodged/broken grits/debris, which was however flushed away after cleaned with a jet of coolant before subsequent grinding.

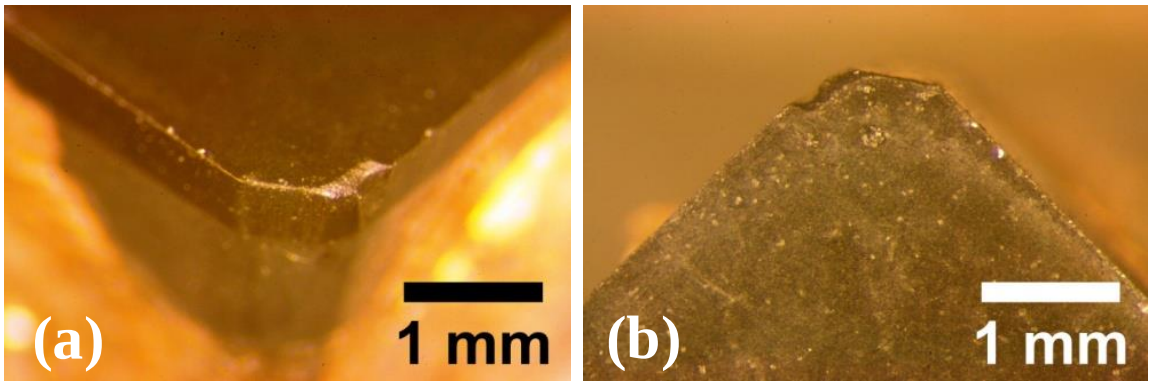


Fig. 4.1.15 Wear of PCD insert following dressing

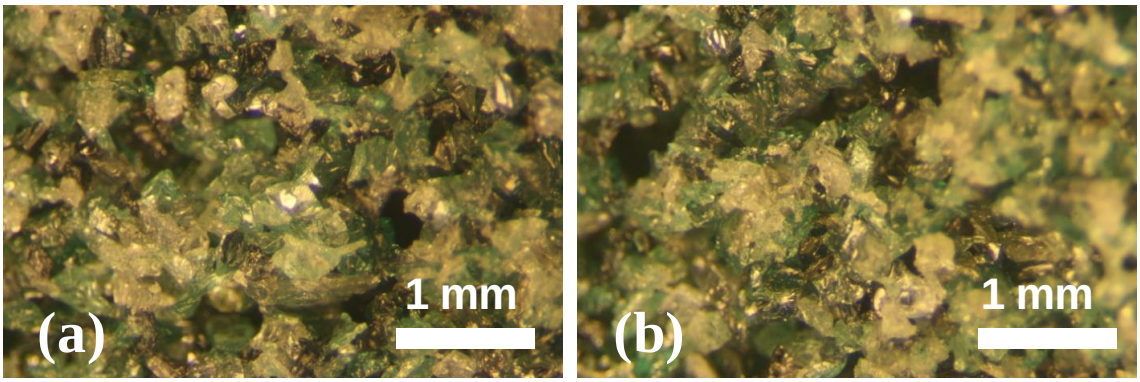


Fig. 4.1.16 Condition of grinding wheel surface following (a) Wet conventional dressing (Test 1), (b) Wet ultrasonic assisted dressing (Test 3)

4.2 Ultrasonic assisted grinding of nickel based superalloys

4.2.1 Phase 2A: Identification of process parameters for UAG of Inconel 718

Extended grinding trials were performed involving variation of key process parameters in order to identify appropriate operating windows to prevent formation of surface defects observed in Phase 1B.

Two depression marks were observed on the workpiece surface towards the end of grinding track in Test 1, possibly due to the use of a very low coolant pressure (5 bar) which was insufficient for creep feed grinding. An increase in fluid pressure up to 15 bar reduced the number of depression signs in Test 2, see Fig. 4.2.1(a). The stiffness of the table sonotrode did not appear to be the reason for the deformed regions as such surface defects could not be eliminated when the workpiece was directly mounted on the dynamometer (Test 3). CFG following dressing with a reduced infeed rate (1.5 µm/rev) also exhibited three depression signs with greater depths (Test 4). An increased dressing infeed of 2.0 µm/rev rendered indentation marks with lower depths in the subsequent grinding trial (Test 5). A repeat trial of Test 4 again showed heavy depression mark on the work surface (Test 6), see Fig. 4.2.1(b). Therefore a dressing indeed rate of 2.0 µm/rev appeared to more appropriate than 1.5 µm/rev in regard to the depression depth. No signs of indentation were observed when grinding a AISI 1040 steel workpiece (Test 7) with the equivalent cutting and dressing conditions employed in Test 5. This was possibly due to the easy-to-grind property of AISI 1040 in comparison to Inconel 718.

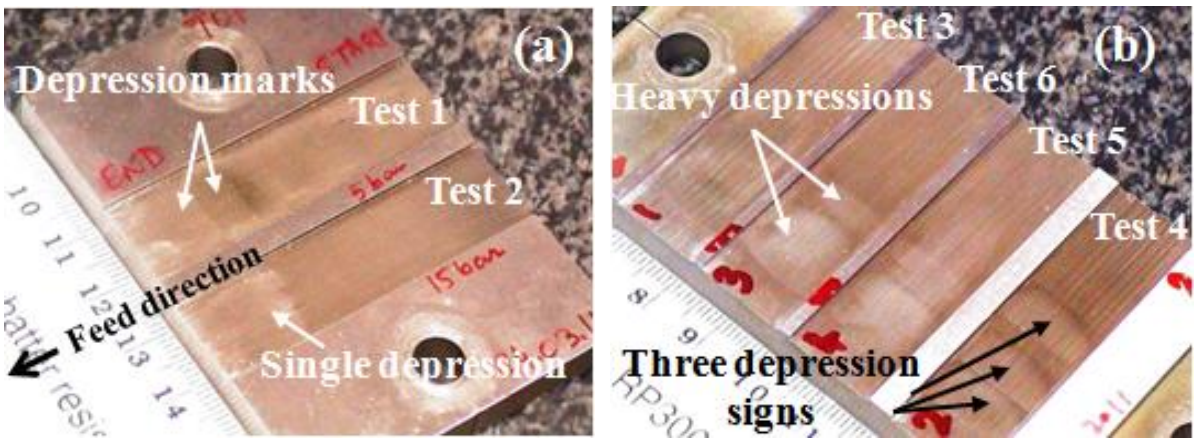


Fig. 4.2.1 Ground Inconel 718 workpieces showing depression marks at various operating conditions: (a) Tests 1 and 2, (b) Tests 3 to 6

The depression marks on the ground Inconel 718 workpieces disappeared when the cutting speed was increased to 30 m/s together with the use of a dummy plate (Test 8), possibly due to reductions in the undeformed chip thickness and loss of coolant from the grinding zone. The absence of the dummy workpiece again resulted in the formation of heavy deformation signs (Test 9), see Fig. 4.2.2(a). This established the necessity of employing a dummy specimen at the grinding exit in order to prevent the escape of fluid from the cutting zone. The subsequent grinding trial (Test 10) confirmed that the position of coolant nozzle had an influence on eliminating surface damages as no indentation marks were observed when the nozzle was placed at 20° from the point of first wheel/workpiece contact (compared to the previous tests when the nozzle was positioned at 0°). While keeping the other parameters unchanged from Test 10, an increase in depth of cut to 1.5 mm resulted in three depression regions with large depths (Test 11), see Fig. 4.2.2(b). This could possibly be due to the level of coolant pressure which appeared to be insufficient for machining with a high a_e (1.5 mm).

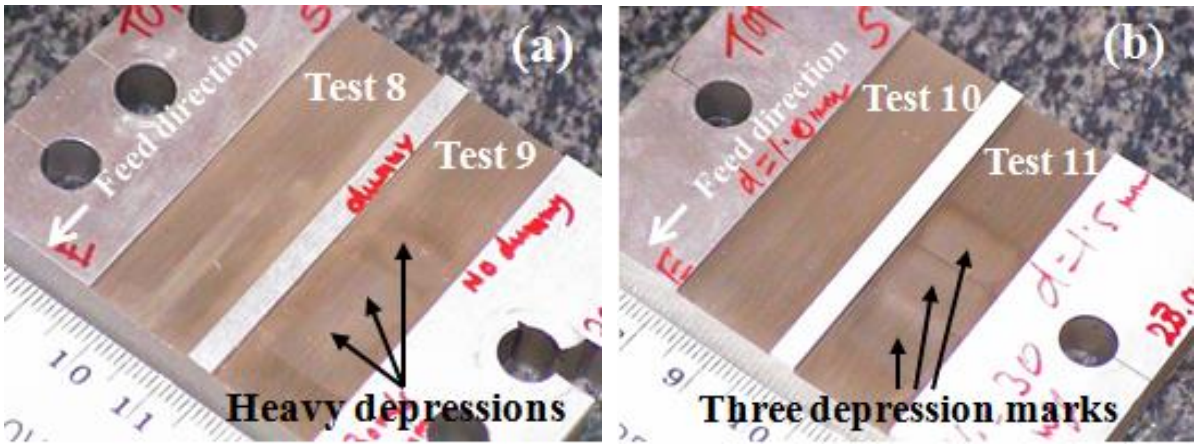


Fig. 4.2.2 Ground Inconel 718 workpieces showing depression marks as well as damage-free surfaces in: (a) Tests 8 and 9, (b) Tests 10 and 11

The surface defects were eliminated with an increase in wheel speed to 35 m/s and reduction in depth of cut to 1.0 mm in Test 12. An increase in depth of cut to 1.5 mm while the wheel speed unchanged again resulted in heavy indentation signs (Test 13), see Fig. 4.2.3(a). This suggested that a higher wheel speed but a depth of cut limited to 1.0 mm were favourable for damage-free machining. A further increase in cutting speed to 40 m/s however resulted in a single indented region with large depth (Test 14), possibly due to the mismatch of wheel velocity with the velocity of cutting fluid at a pressure of 15 bar. Test 15 produced defect-free ground surface when the coolant pressure was raised to 20 bar, suggesting that comparable velocities of the wheel and the cutting fluid were achieved, see Fig. 4.2.3(a). This was further rechecked with a reduced wheel velocity (30 m/s) at an equivalent fluid pressure (20 bar) and no depression signs were observed (Test 16), see Fig. 4.2.3(b). Therefore it was inferred that a cutting speed of 30 to 40 m/s was suitable for producing damage-free specimens with an associated coolant pressure of ~20 bar.

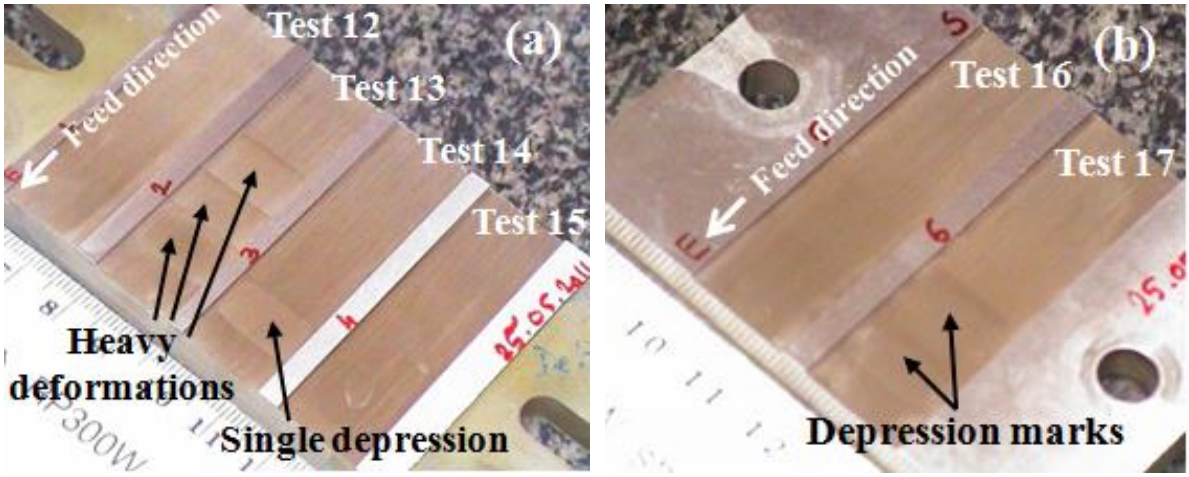


Fig. 4.2.3 Ground Inconel 718 workpieces showing depression marks as well as damage-free surfaces in: (a) Tests 12 to 15, (b) Tests 16 and 17

While comparing with Test 16, Test 17 indicated that a 20 bar coolant pressure was inadequate to produce deformation-free surfaces when the table feed was increased to 400 mm/min when keeping the wheel speed and depth of cut unchanged (30 m/s and 1.0 mm respectively), see Fig. 4.2.3(b). The subsequent two tests (Tests 18 and 19) with increased wheel velocity (40 m/s) and fluid pressure (25 bar) but constant table feed (400 mm/min) could not eliminate the depression marks as well. A reduced coolant pressure of 20 bar (Test 20) even worsened the surface features with indentations all over the machined track together with grinding burn. Workpiece surface characteristics were comparatively improved with minor signs of deformation and burn when the fluid pressure was raised to ~28 bar (Test 21), see Fig. 4.2.4(a).

The deformed regions on the work surface were eliminated when the VORTEX 60 mesh wheel (with a larger grain size and greater porosity compared to VORTEX 80 mesh wheel) was utilised in Test 22 while keeping other operating conditions similar to Test 16. Therefore it was inferred that the VORTEX 60 mesh wheel rendered better ingress of cutting fluid into the grinding zone, thereby reducing the surface defects. An increase in table feed to 400 mm/min however again produced minor depression marks on the workpiece surface (Test 23), although a higher coolant pressure was utilised (25 bar), see Fig. 4.2.4(b). This necessitated further increase in fluid pressure to 28 bar when moderate to high table feeds (300 to 400 mm/min) were employed. No signs of deformation were observed in Test 24 when an alternative alumina wheel (POROS2) with an equivalent grain size and porosity of VORTEX 60 mesh wheel was utilised at a V_C and V_W of 40 m/s and 300 mm/min respectively together with a cutting fluid pressure of ~28 bar, see Fig. 4.2.4(b).

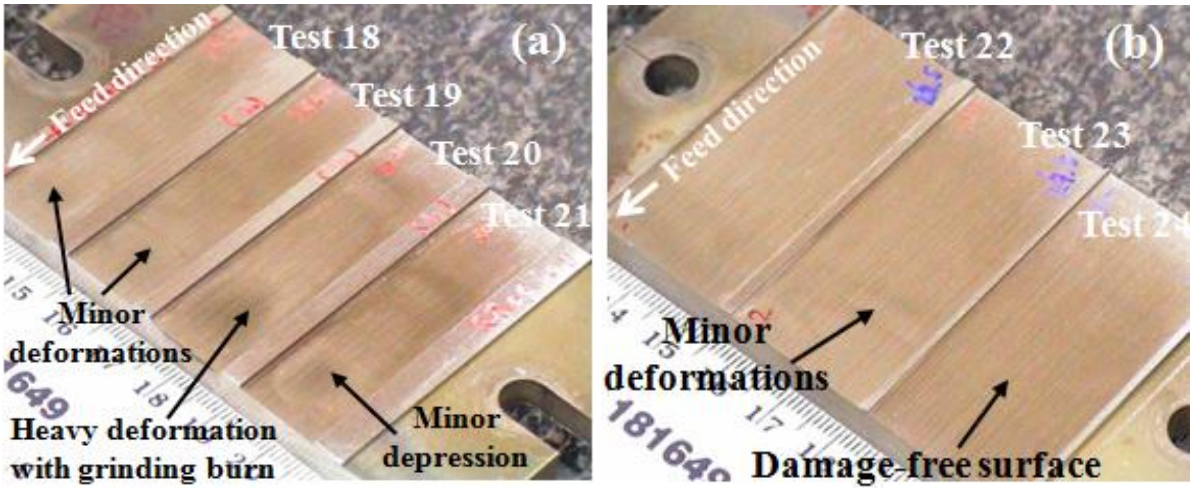


Fig. 4.2.4 Ground Inconel 718 workpieces showing depression marks as well as damage-free surfaces in: (a) Tests 18 to 21, (b) Tests 22 to 24

The onset of depression marks/grinding burn was also observed from the recorded force graphs. Each spike on the vertical grinding force (F_v) profile corresponded to the formation of a depression on the ground tracks. An example is detailed in Fig. 4.2.5(a) for Test 11 (with a high depth of cut of 1.5 mm and low coolant pressure of 15 bar) where three spikes were observed in the F_v and F_h force traces. Conversely, the force profile recorded in Test 21 (with a moderate depth of cut of 1.0 mm and higher coolant pressure of 28 bar) exhibited only one spike, which corresponded to a single depression mark on the ground surface, see Fig. 4.2.5(b).

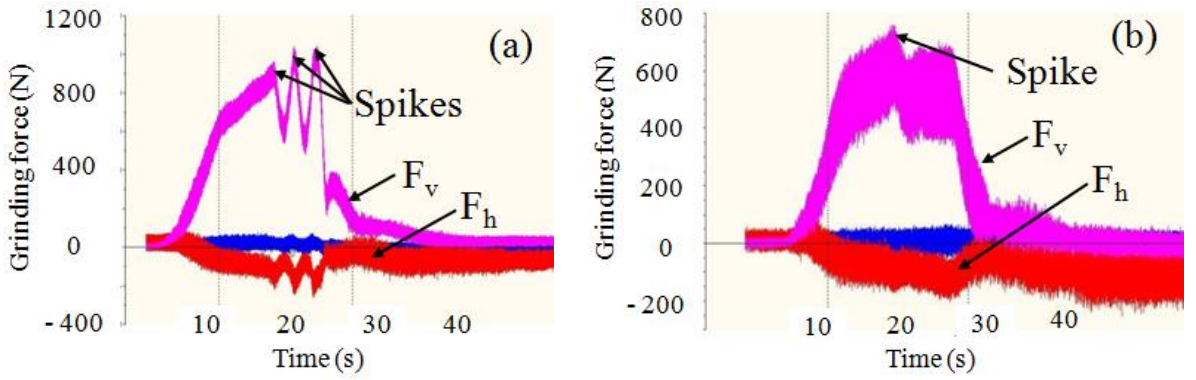


Fig. 4.2.5 Grinding force graphs obtained in (a) Test 11: V_C=30 m/s, V_W=200 mm/min, a_e=1.5 mm, Pressure=15 bar (b) Test 21: V_C=40 m/s, V_W=400 mm/min, a_e=1.0 mm, Pressure=28 bar

A summary of the results from experiments is detailed below:

- An increase in wheel velocity (V_C) from 25 to 30 m/s eliminated the depression marks at a cutting fluid pressure of 15 bar. This was due to a reduction in undeformed chip thickness as well as matching of wheel velocity with the velocity of cutting fluid (Webster, 2007). Similarly, the fluid pressure was increased to 28 bar when V_C was raised to 40 m/s.
- Heavy depressions were obtained in all tests employing higher depth of cut (1.5 mm), irrespective of the other operating conditions, due to insufficient ingress of coolant into the grinding zone.
- Depressions on the workpiece were also evident at the higher table feed of 400 mm/min. However, at 300 mm/min feed no surface anomalies were observed when grinding with the POROS2 wheel.
- A dummy workpiece was always required in order to restrict the escape of cutting fluid from the grinding zone.
- Grinding wheels with larger grit size and higher porosity offered more efficient transfer of cutting fluid to the grinding zone.

4.2.2 Phase 2B: Evaluation of UAG on Inconel 718 using POROS2 wheel

4.2.2.1 Grinding forces

The vertical (F_v) and horizontal (F_h) forces obtained when grinding Inconel 718 with and without ultrasonic vibration using an open structured alumina wheel (POROS2) are shown in Fig. 4.2.6.

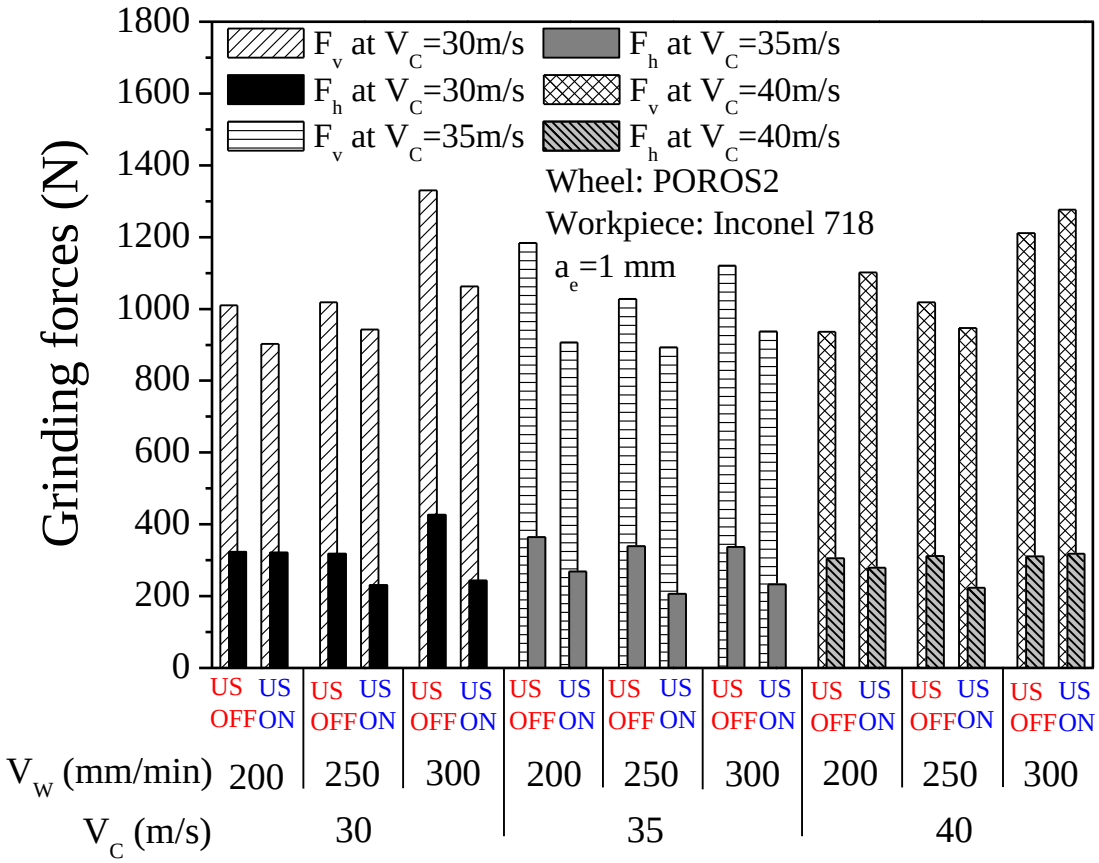


Fig. 4.2.6 Vertical (F_v) and horizontal (F_h) forces under different grinding conditions

In general, both force components decreased when operating with ultrasonic vibration while no clear trends were observed with respect to variation in wheel speed and table feed. A similar reduction in the grinding forces (~25%) was also observed by Azarhoushang and Tawakoli (2012) when ultrasonic assisted grinding 100Cr6 steel using vitrified and resin bonded cBN grinding wheels. It was postulated that the ultrasonic actuation induced multiple-impact interactions between the grits and workpiece material during grinding as well as between the grits and chips, thereby reducing the contact time and length, which essentially resulted in a discontinuous cutting process. The intermittent contact between the wheel and workpiece also facilitated improved ingress of cutting fluid, which decreased friction and

consequently grinding forces. Additionally incidence of 'sticking' friction (as well as the coefficient of friction) most likely decreased due to the vibration and higher sliding speed in UAG compared to conventional grinding (Tawakoli and Azarhoushang, 2008).

Figures 4.2.7 and 4.2.8 detail the main effects and interaction plots for both vertical and horizontal grinding forces respectively. The intermediate level of wheel speed and table feed typically resulted in the lowest grinding forces. The associated analysis of variance (ANOVA) showed that table feed, vibration condition and interaction between wheel speed and vibration condition (V_C × Vib) were statistically significant with regard to vertical forces, each having percentage contribution ratios (PCR's) of 37.68%, 14.55% and 17.81% respectively, see Table 4.2.1. In contrast, vibration condition was the sole variable affecting horizontal grinding forces with a relatively high PCR of 52.83%, despite considerable interactions between factors observed in Fig. 4.2.8.

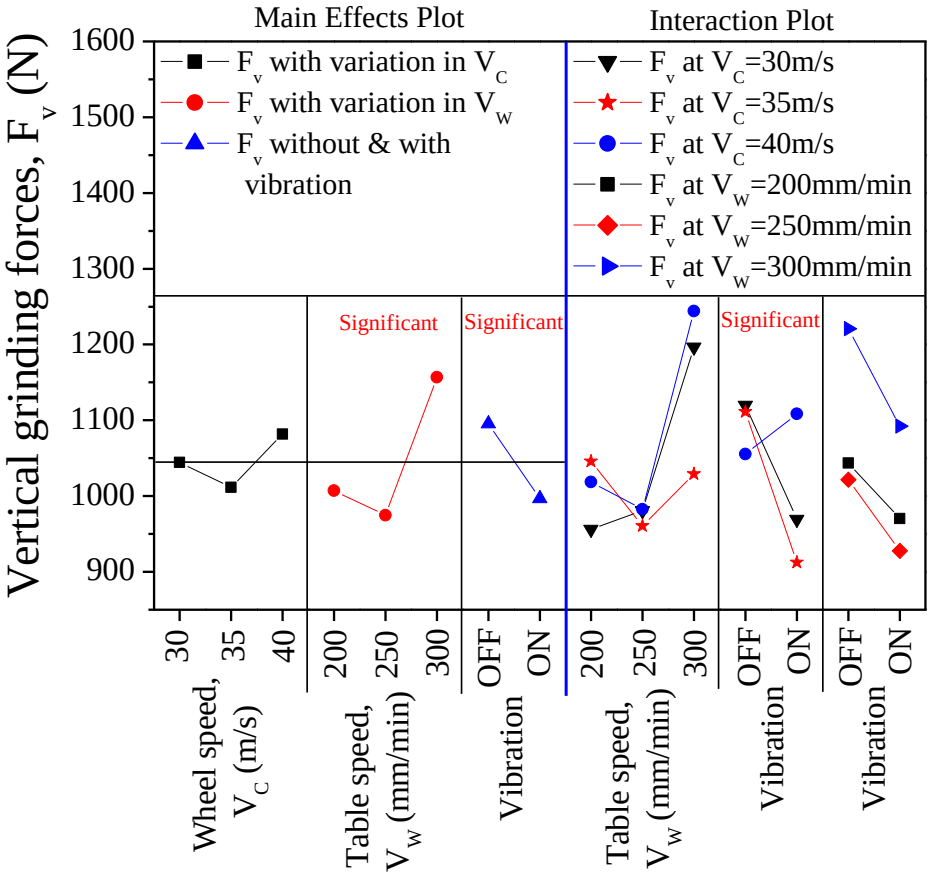


Fig. 4.2.7 Main effects and interaction plots for vertical grinding force

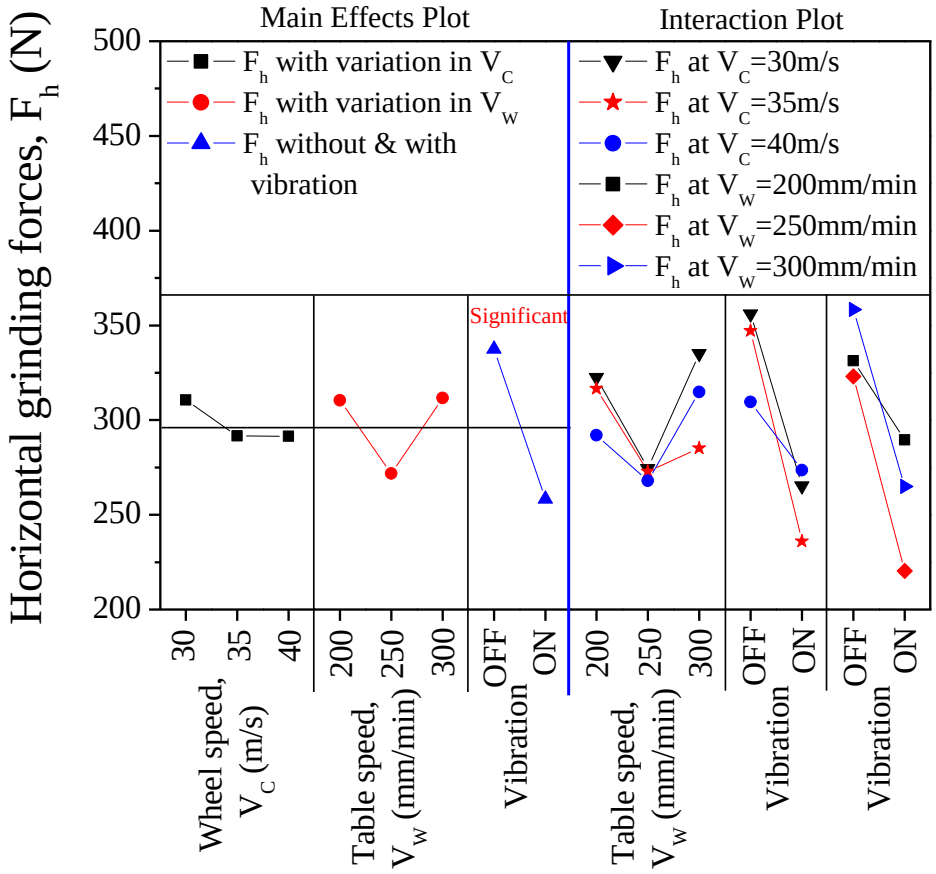


Fig. 4.2.8 Main effects and interaction plots for horizontal grinding force

Table 4.2.1 Percentage contribution ratios of factors with respect to different response measures (Phase 2B)

Factors	**Percentage contribution ratios (PCR's)**								
	F_v	**F_h**	**G-ratio**	**W/P R_a**	**W/P S_a**	**Graphite R_a**	**Graphite S_a**	**Resin replica S_a**	**Resin replica S_{ds}**
Wheel speed (V_C)	4.92	2.74	10.47	20.14*	14.49	0.25	0.75	25.56	40.83*
Table feed (V_W)	37.68*	11.55	17.24*	21.23*	15.68	31.63*	56.52*	4.45	10.48
Vibration (Vib)	14.55*	52.83*	0.13	1.99	6.09	1.58	4.14	2.97	2.97
V_C×V_W	15.08	4.02	59.31*	4.65	11.22	1.26	8.52	33.95	28.08
V_C×Vib	17.81*	8.46	5.54	15.28	18.76	11.69*	2.76	9.72	1.56
V_W×Vib	0.79	6.02	1.99	19.34*	14.46	28.37*	12.06	8.73	10.21
V_C×V_W×Vib	9.18	14.38	5.32	17.34	19.33	25.22*	15.25	14.62	5.88
* Statistically significant factors at the 5% level									

Figure 4.2.9 shows example of the typical force traces recorded when grinding without and with ultrasonic vibration. The former was generally characterised by a steep/rapid rise in vertical forces, with the majority displaying a sharp 'spike' towards the end of the cut, see Fig. 4.2.9(a), which coincided with the onset of depressions as well as some limited burning

on the workpiece surfaces, especially when operating at higher grinding parameters (e.g. Vc=40 m/s and Vw=250 mm/min). This was possibly due to the higher grinding temperatures and greater loading of the grinding wheel (Ming et al., 2001). In contrast, no sudden surges in force signals were evident with a gradual rise over the in-cut duration when operating in ultrasonic assisted mode, see Fig. 4.2.9(b).

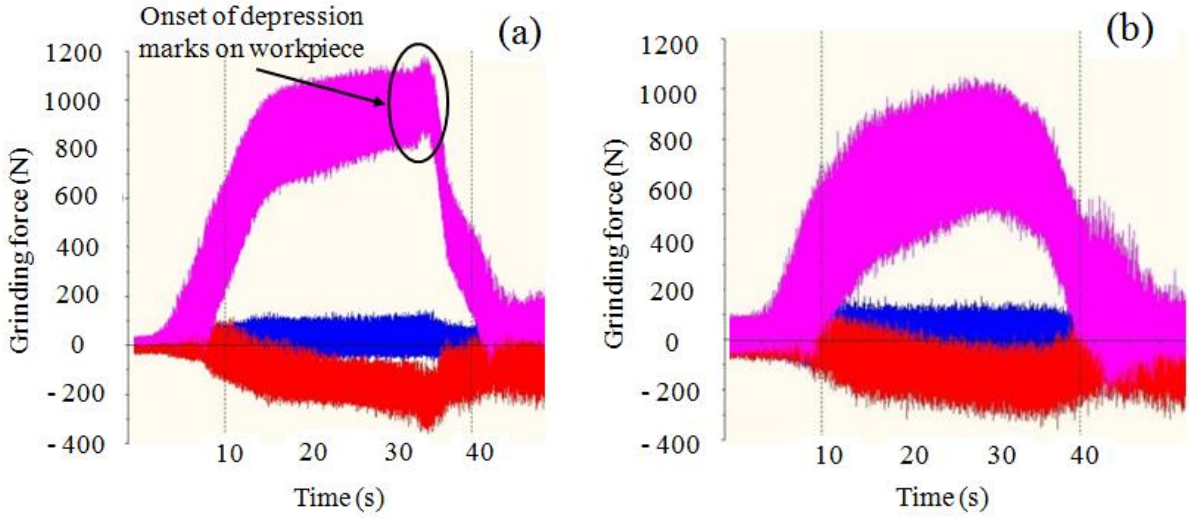


Fig. 4.2.9 Typical force traces when grinding at V_C=35 m/s, V_W=200 mm/min, a_e=1 mm, (a) Without and (b) With ultrasonic vibration

4.2.2.2 Radial wheel wear and G-ratio

The effects of operating parameters on radial wheel wear (RWW) and G-ratio are shown in Figure 4.2.10. Typically RWW decreased with increasing table speed when machining under conventional CFG mode, which was attributed to the shorter contact time between the wheel and workpiece at higher feeds. No such trend however was observed with regard to variation in wheel speed as well as when employing ultrasonic vibration. The main effects plot detailed in Fig. 4.2.11 showed that G-ratio increased (~40%) with a rise in V_C from 30 to 35 m/s, which was probably due to a reduction in the undeformed chip thickness and subsequent grinding forces. Corresponding ANOVA calculations however highlighted that table feed was the only significant factor affecting G-ratio (PCR of 17.24%), although interaction between wheel speed and table feed ($V_C \times V_W$) had the greatest influence at a PCR of 59.31%, see Table 4.2.1.

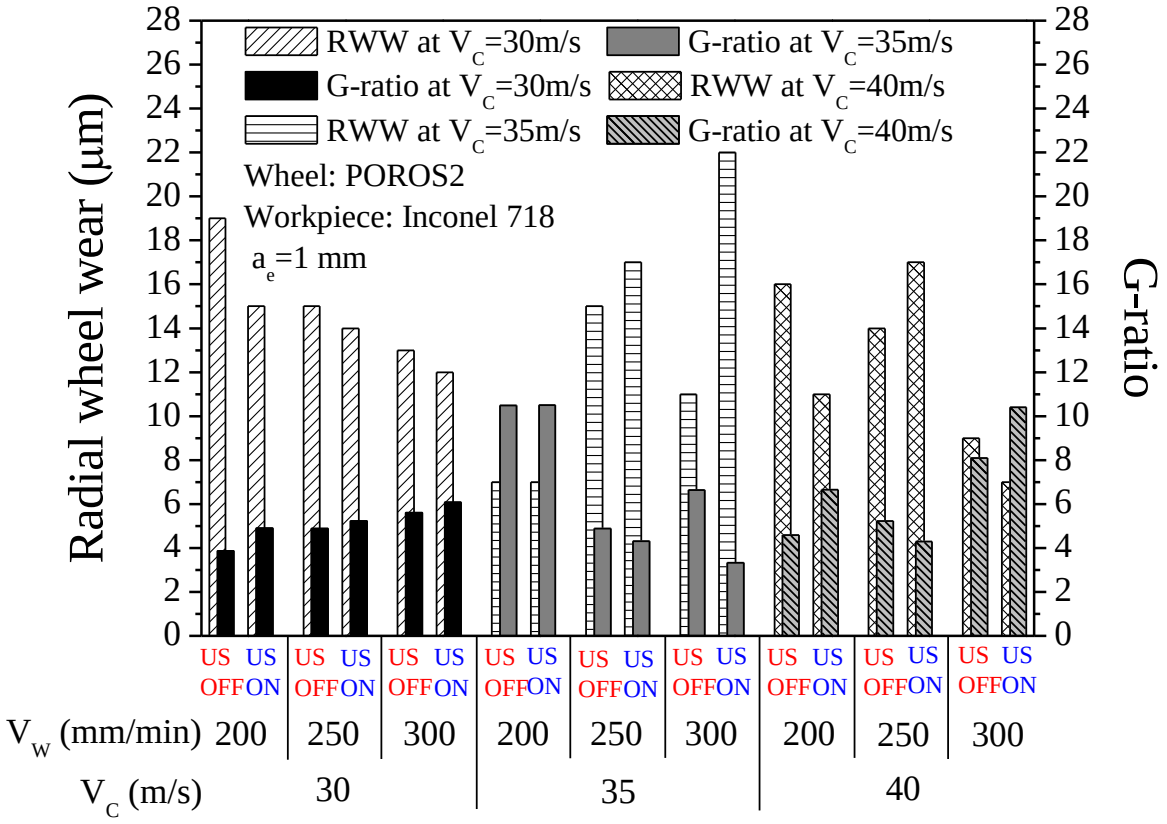


Fig. 4.2.10 Radial wheel wear and G-ratio under different grinding conditions

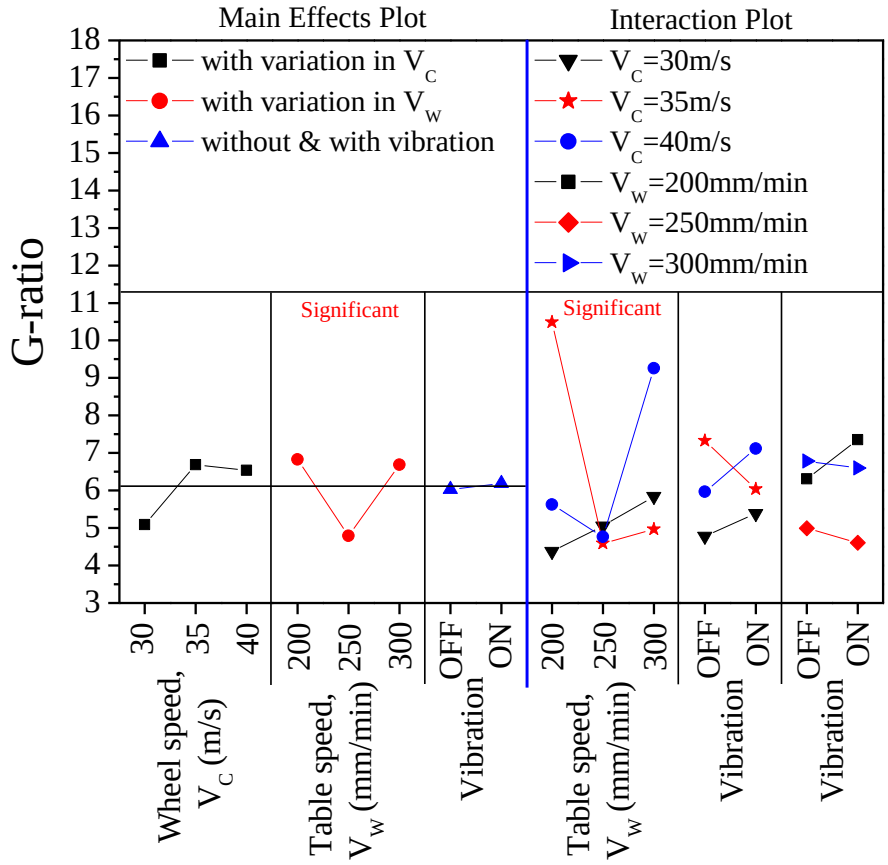


Fig. 4.2.11 Main effects and interaction plots for wheel G-ratio

While not statistically significant, wheel G-ratio was seen to improve by between 7 to 45% in 5 of the 9 trials (Tests 2, 4, 6, 14, 18) involving the hybrid configuration (UAG mode), although it was also found to decrease in 3 of the remaining 4 experiments (Tests 10, 12, 16). Compared to conventional grinding, ultrasonic oscillation along the Z-direction (radial to the wheel surface) caused steeper angles as well as larger depths of grit indentation into the workpiece surface, thus exposing the abrasive particles to higher mechanical loads (Spur and Holl, 1997). The high frequency, cyclic loading on the cutting edges (Uhlmann, 1998) resulted in micro-splintering of the grits as well as fracture of the associated bonds leading to higher wheel wear (lower G-ratio) in 3 out of 9 of the grinding trials.

4.2.2.3 Workpiece surface topography and quality

Figure 4.2.12 details sample images of workpieces machined at different parameters while Fig. 4.2.13 shows representative 3D topographies of the workpiece surfaces ground with and without ultrasonic assistance. The majority of tests produced damage/burn free surfaces, although minor depressions were observed towards the end of cut on surfaces machined at intermediate/high wheel speeds (V_C=35 m/s, V_W=200 mm/min and V_C=40 m/s, V_W=250 mm/min) without ultrasonic vibration. In contrast, none of the workpieces ground with ultrasonic assistance exhibited any signs of surface indentations.

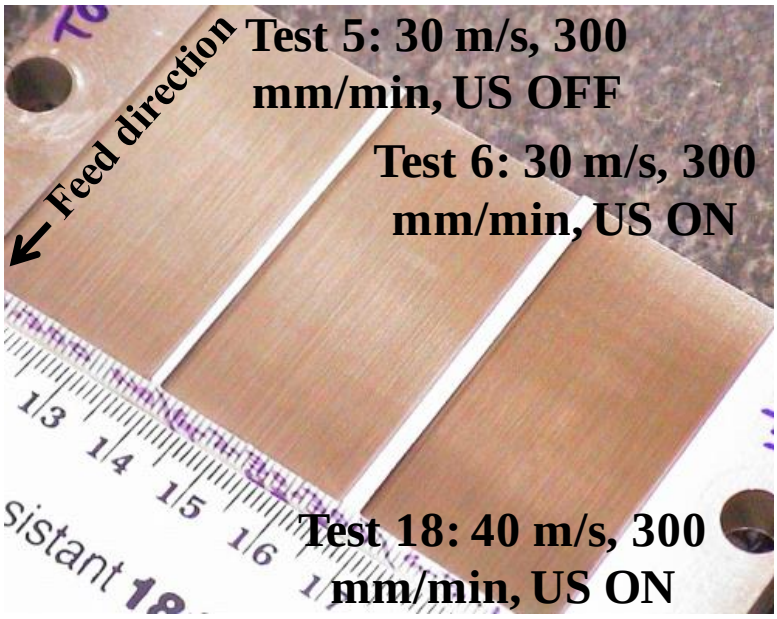


Fig. 4.2.12 Images of Inconel 718 workpiece surfaces ground at different operating conditions

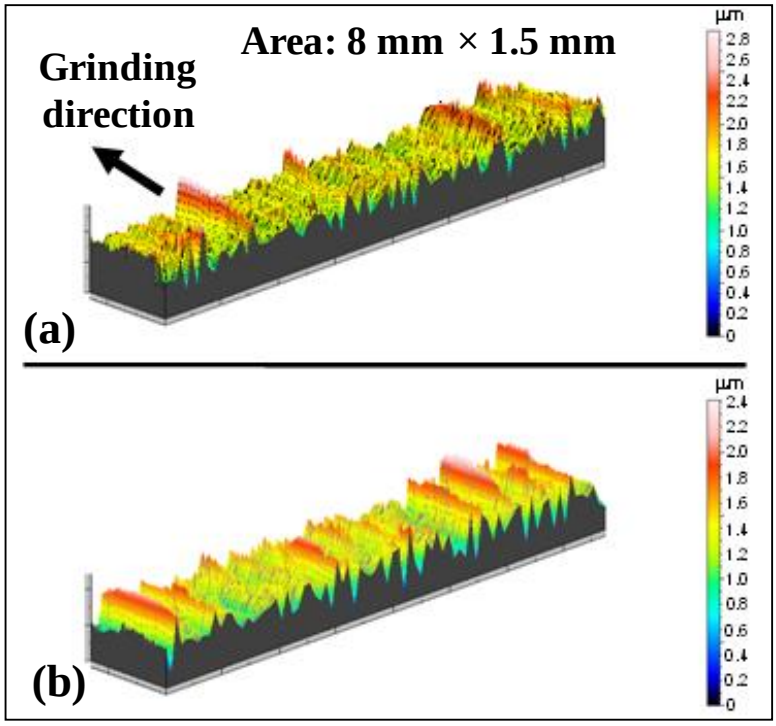


Fig. 4.2.13 Representative 3D topographies of ground surfaces produced
(a) With ultrasonics and (b) Without ultrasonics

Figure 4.2.14 details the surface roughness (R_a) measured at three locations of the ground track for all tests. With the exception of Test 5, the surface roughness typically varied between 0.5-0.75 µm, irrespective of machining conditions.

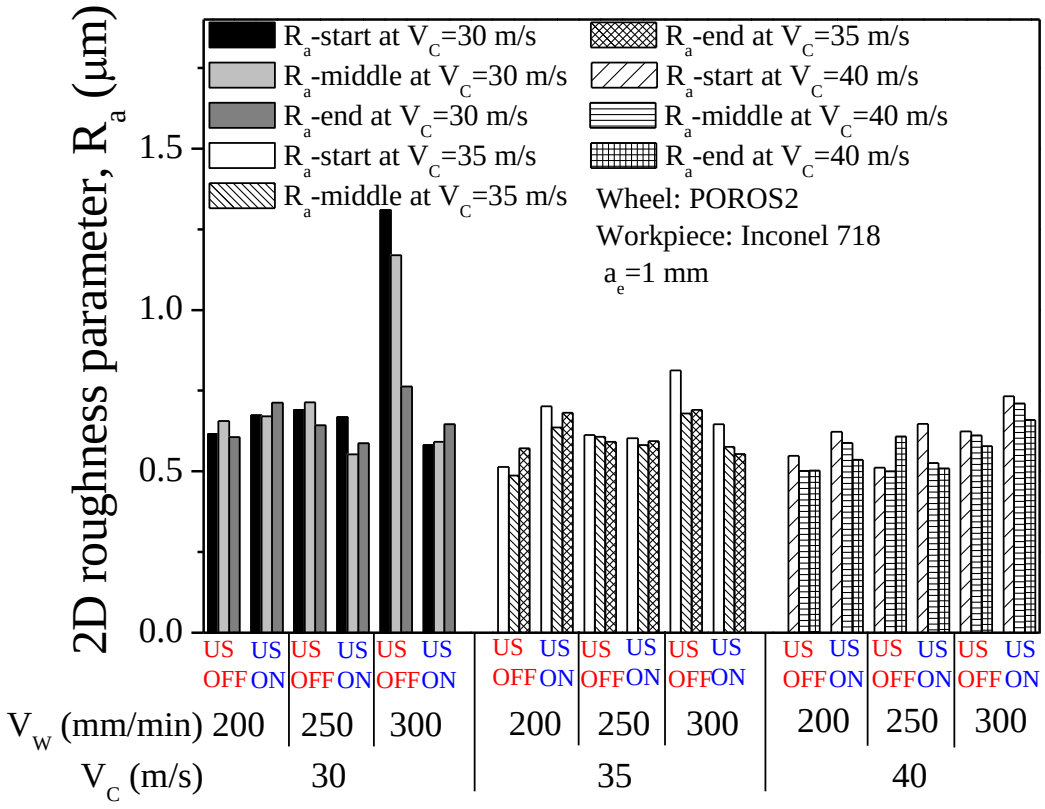


Fig. 4.2.14 Surface roughness (R_a) of ground Inconel 718 workpiece surfaces

The associated main effects plot shown in Fig. 4.2.15 indicated that mean R_a generally decreased as V_C increased from 30 to 40 m/s due to a reduction in contact time of grits with the work surface. The opposite trend however was observed in terms of V_W rising from 200 to 300 mm/min, which was likely the result of increasing undeformed chip thickness. Similar observations were also reported by Tso (1995a) when grinding Inconel 718 using different wheels including white alumina, green SiC and cBN. In addition, both V_C and V_W were statistically significant parameters affecting R_a with comparable PCR's of 20.14% and 21.23% respectively. While vibration condition did not have a substantial influence on R_a based on the ANOVA calculations, its interaction with table feed (V_W × Vib) was a significant factor (at the 5% level) with a PCR of 19.34%.

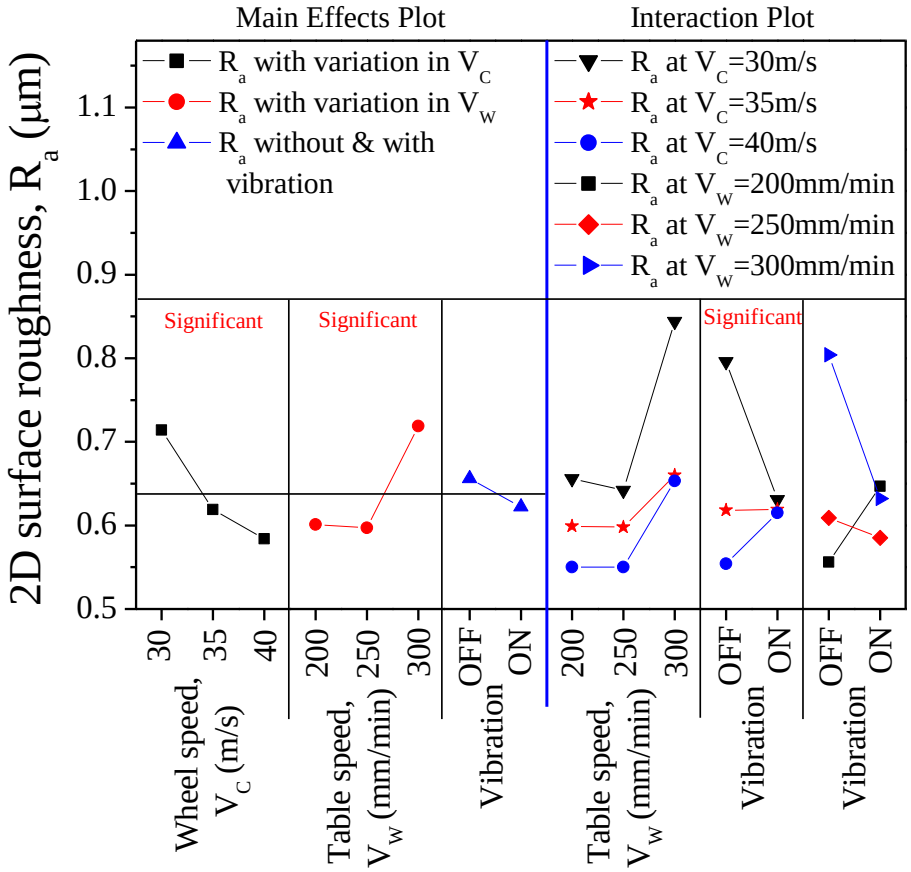


Fig. 4.2.15 Main effects and interaction plots for 2D surface roughness (R_a) of ground workpieces

Figure 4.2.16 details the 3D surface topographical parameters (S_a, S_t and S_z) for all tests. The average area surface roughness (S_a) was generally lower when employing US vibration except for tests at the highest parameters (Test 16: V_C=40 m/s, V_W=250 mm/min and Test 18: V_C=40 m/s, V_W= 300 mm/min). Conversely, peak to peak (S_t) and 10-point average roughness (S_z) parameters were typically higher with surfaces machined under US assisted

mode. This was thought to be due to the vibration along the Z-axis of the sonotrode (i.e. in a direction radial to the wheel surface). Furthermore, vibration assisted grinding typically generated surfaces with higher/more positive skewness (6 out of 9 tests), which are preferable for applications requiring high bearing ratios (Azarhoushang and Tawakoli, 2011).

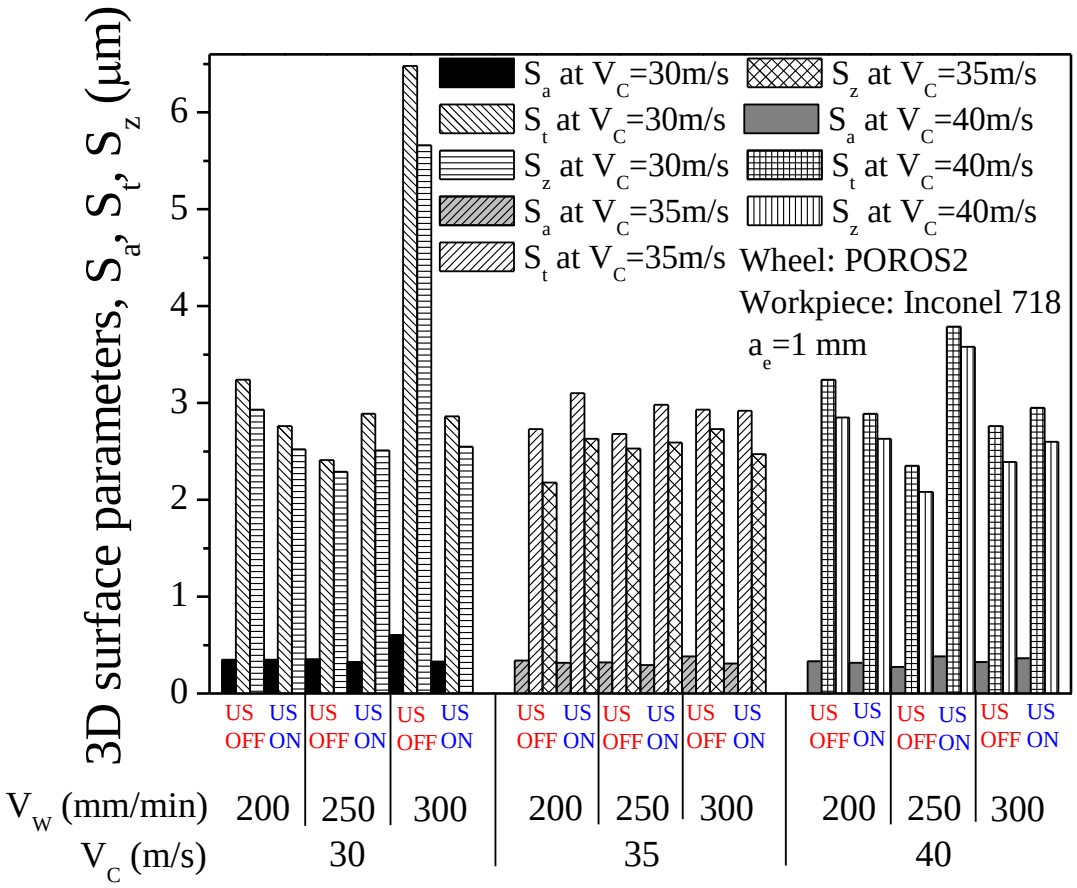


Fig. 4.2.16 3D topographical parameters of ground Inconel 718 workpiece surfaces

Although not shown here, the trends of the main effects plot for S_a with respect to the individual variable parameter levels were similar to those observed for R_a, although none of the factors and interactions were found to be significant at the 5% level, see Table 4.2.1.

The SEM images in Fig. 4.2.17 of ground surfaces from several tests reveals typical grooves and ridges produced by the interactions of abrasives with the workpiece (Xu et al., 2003) along with the presence of side flow (SF) and smearing of material, which was particularly evident towards the end of the cut. Unlike surfaces produced in turning of Inconel 718 using PcBN (M'Saoubi et al., 2012), all of the ground workpieces were generally free of macro/micro-cracking or surface tearing, although the occasional formation of micro-cavities was seen on several of the machined samples, similar to that shown in Fig. 4.2.18.

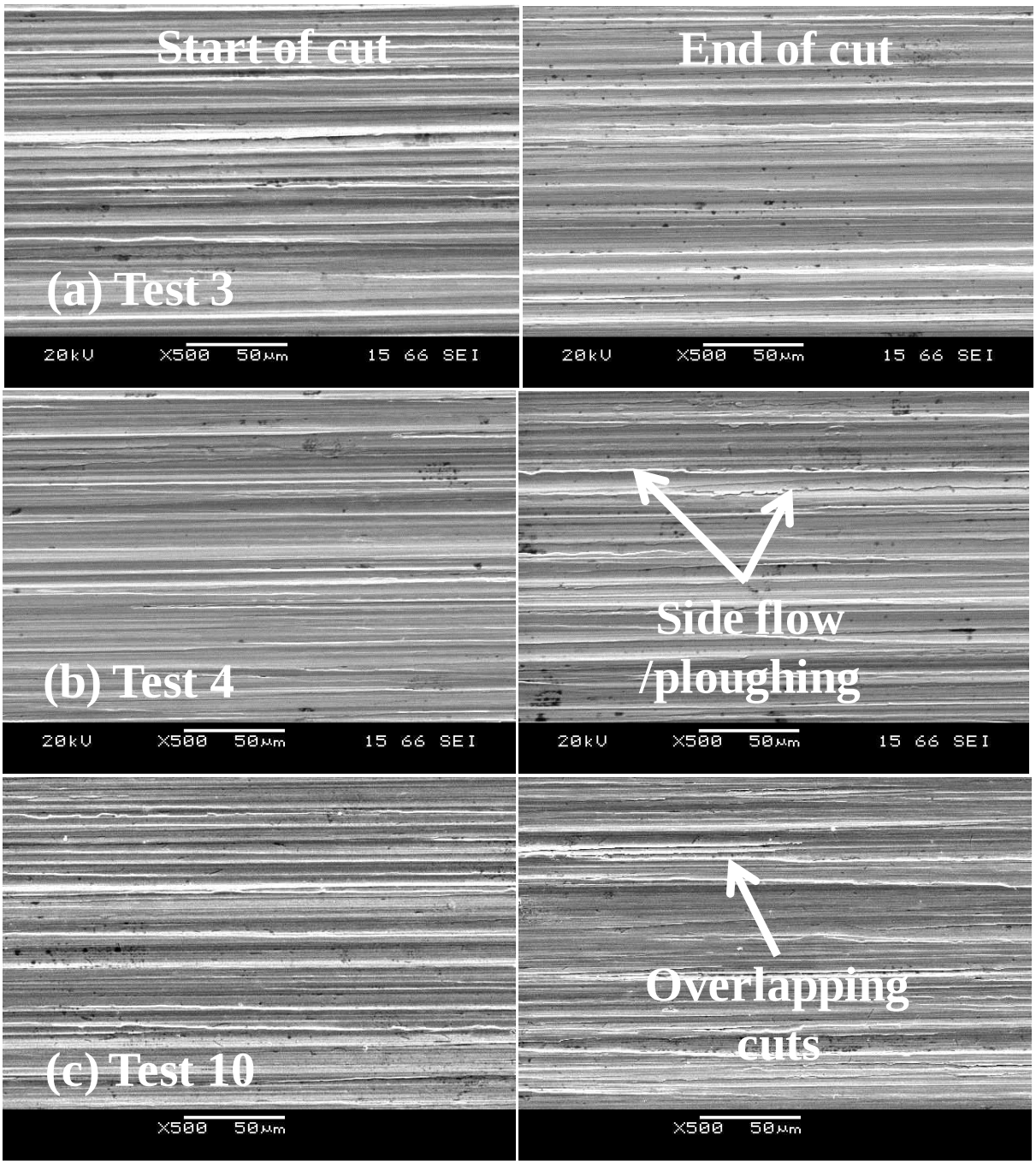


Fig. 4.2.17 SEM micrographs of ground workpiece surfaces (a) Test 3: V_C=30 m/s, V_W=250 mm/min, US OFF, (b) Test 4: V_C=30 m/s, V_W=250 mm/min, US ON, (c) Test 10: V_C=35 m/s, V_W=250 mm/min, US ON

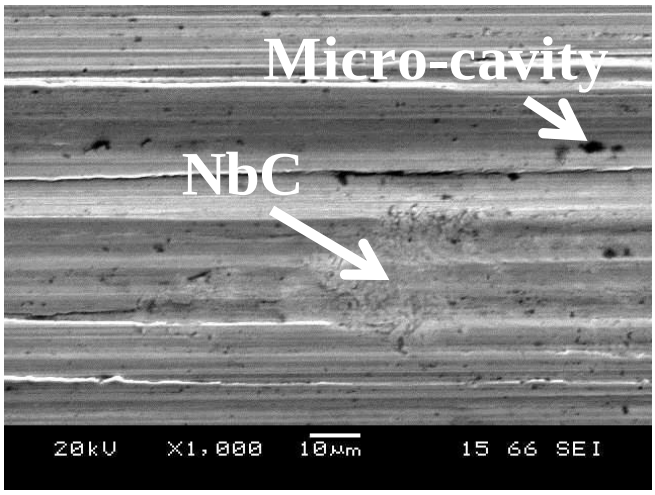


Fig. 4.2.18 Presence of NbC on the ground surface

An exposed niobium carbide (NbC) particle was also observed (confirmed by energy dispersive spectroscopy/EDX), while there were no signs of loss/breakage of carbides at the vicinity of NbC/TiC enriched regions. When operating with ultrasonic vibration, greater levels of smearing and side flow/ploughing of the workpiece material were observed on the majority of samples analysed (Fig. 4.2.17(b) and (c)), suggesting that increased plastic deformation occurred (Spur and Holl, 1996, Uhlmann, 1998). Additionally, the higher incidence of overlapping grit marks (compared to conventional CFG), as seen in Fig. 4.2.17(c), was thought to be due to lateral movement of the grains (Tawakoli et al., 2009a) along the transverse feed direction under the action of multi-modal vibration (X, Y and Z) of the table sonotrode.

4.2.2.4 Grinding wheel surface evaluation

Typical 3D topographies of wheel surfaces measured from graphite replicas (negative) following grinding with and without ultrasonic assistance are shown in Fig 4.2.19(a) and (b) respectively. The 2D and 3D surface parameters (R_a and S_a) of the graphite replicas in Fig 4.2.20 showed that both responses generally increased with a rise in table feed from 200 to 300 mm/min, irrespective of the other operating conditions. The trend was similar to that observed from the equivalent 2D roughness parameters of the ground workpiece surfaces. Following activation of US vibration, S_a of the graphite replicas/wheel surface decreased in most cases (6 out of 9 trials) compared to plain grinding (although R_a reduced in 5 out of 9 tests) suggesting greater uniformity of the grit heights. This was most likely caused by the 'conditioning effect' as a result of the component of vibration radial to the wheel surface.

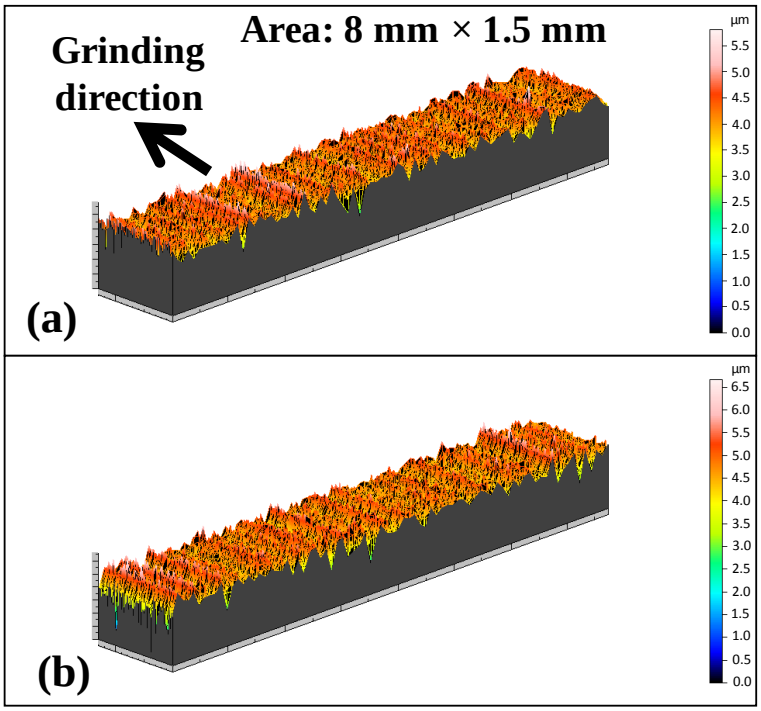


Fig. 4.2.19 Typical 3D topographies of wheel surfaces measured from graphite replicas (negative) following grinding (a) With ultrasonics and (b) Without ultrasonics

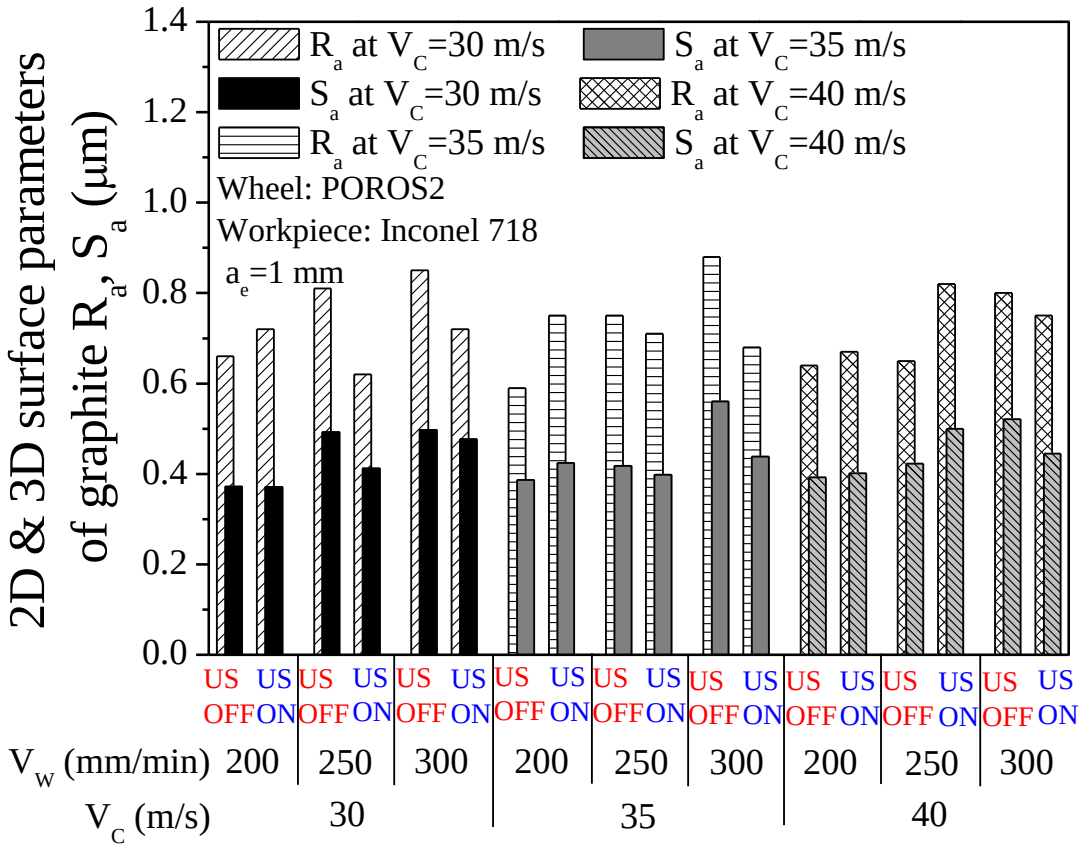


Fig. 4.2.20 Surface topography parameters (2D and 3D) from graphite (negative) replicas of the grinding wheel

The associated main effects plot for graphite R_a, see Fig. 4.2.21, exhibited that table feed had a significant influence with a PCR of 31.63%. Although the sole effects of both wheel speed and vibration condition were negligible on graphite R_a (with PCR's of 0.25% and 1.58% respectively), their interaction (V_C × Vib) had a significant influence at 5% level with a PCR of 11.69%. The interaction of table feed and vibration (V_W × Vib) was also a significant factor for R_a of the graphite replicating surfaces with a PCR of 28.37%.

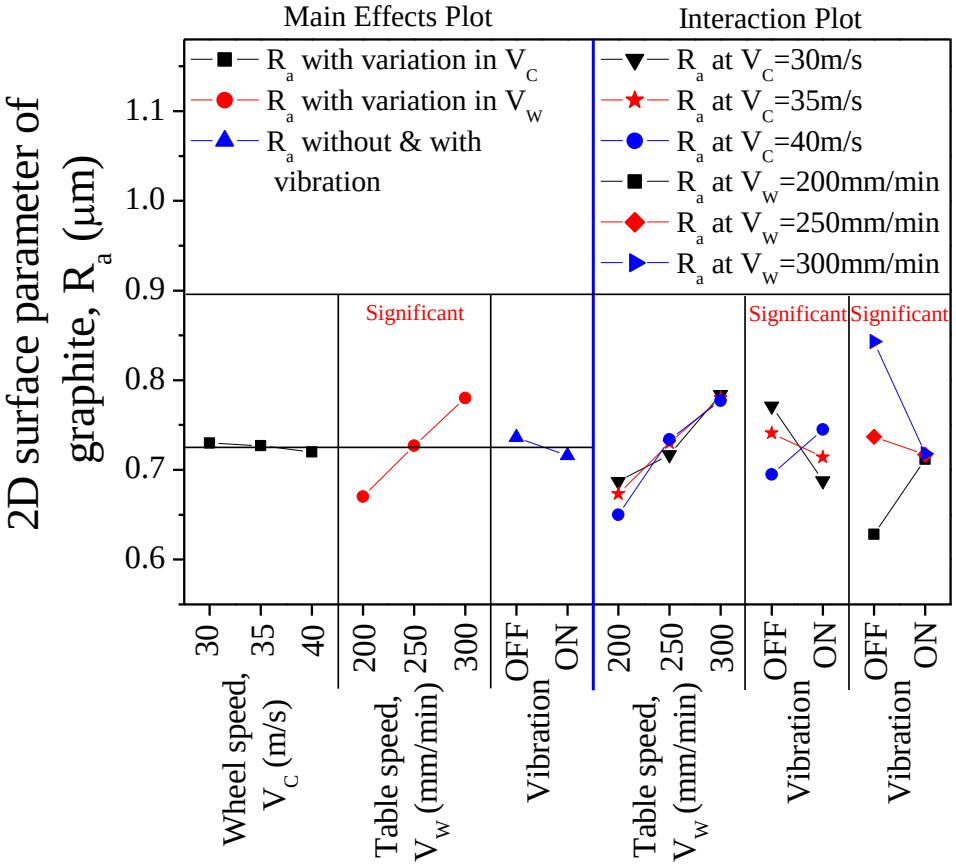


Fig. 4.2.21 Main effects and interaction plots for 2D surface roughness (R_a) of graphite (negative) replicas of the grinding wheel

While not shown here, the main effects and interaction plot for S_a of the graphite replicas followed the similar trend with regard to the individual operating conditions, although only table feed a significant influence on S_a with a PCR of 56.52%.

Typical 3D topographies of the grinding wheel surfaces measured from resin (positive) replicas following grinding with and without ultrasonic vibration are shown in Figs. 4.2.22(a) and (b), while the S_a and S_{ds} parameters are detailed in Fig. 4.2.23. S_a generally decreased with a reduction in wheel speed from 30 to 40 m/s with the trend being similar to that of workpiece R_a with the variation in V_C, thereby indicating that a greater uniformity in grit heights resulted in lower work surface roughness. In contrast, no such trend was apparent for resin S_a with the variation in table feed. With the assistance of ultrasonic vibration, S_a of the

resin replicas typically increased (6 out of 9 tests) compared to those obtained following conventional CFG. The density of peaks (S_{ds}) of the resin replicas also generally increased in 6 out of 9 trials involving vibration with the exception of Tests 4, 10 and 16.

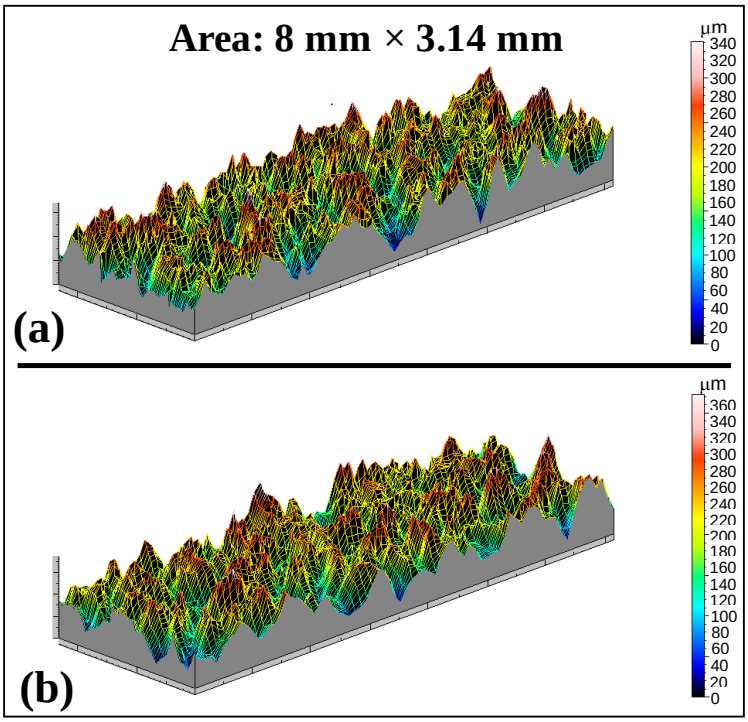


Fig. 4.2.22 Typical 3D topographies of wheel surfaces measured from resin replicas (positive) following grinding; (a) With ultrasonics (b) Without ultrasonics

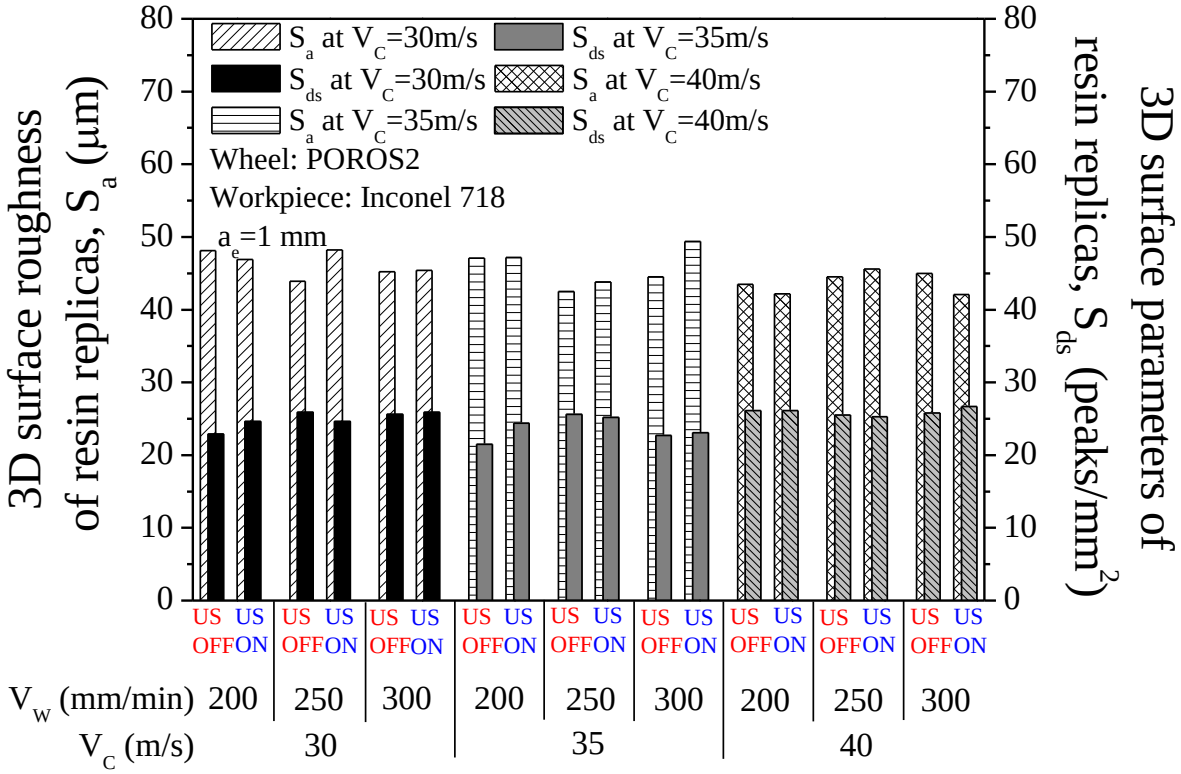


Fig. 4.2.23 3D topographical parameters of resin (positive) replicas of the grinding wheel

The main effects an interaction plots for graphite S_a obtained from ANOVA, see Fig. 4.2.24, showed that none of the operating parameters were statistically significant at 5% level, although wheel speed and an interaction of wheel speed and table feed ($V_C \times V_W$) had relatively high PCR's of 25.56% and 33.95% respectively, see Table 4.2.1.

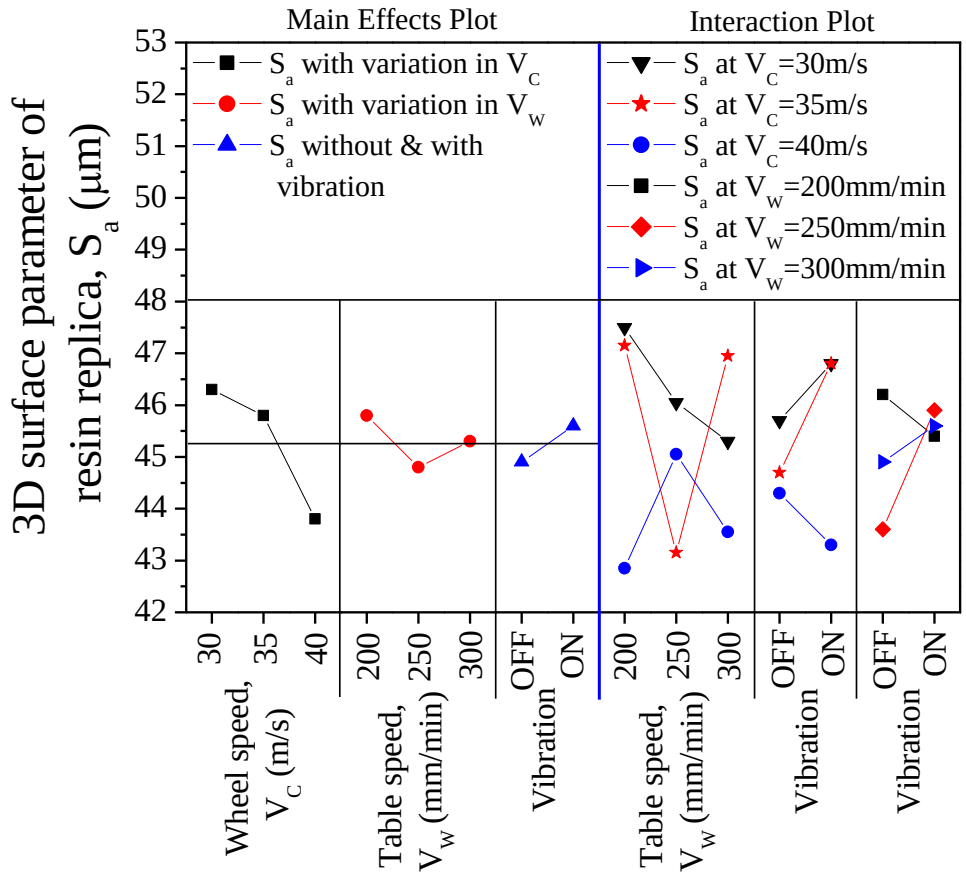


Fig. 4.2.24 Main effects and interaction plots for 3D surface parameter (S_a) of resin (positive) replicas of the grinding wheel

Figure 4.2.25 details the main effects and interaction plots for S_{ds} parameter of the resin replicating surfaces. Although no particular trend in the variation of S_{ds} was observed with the change in wheel speed, the factor was statistically significant with a PCR of 40.83%. While vibration had only a PCR of 2.97% on S_{ds}, it typically resulted in higher S_{ds} values of resin replicating surfaces compared to those measured following conventional CFG. A decrease in wheel S_{ds} is generally allied to a rise in workpiece surface roughness, and vice versa (Butler et al., 2002). This was in line with the results detailed in Figs. 4.2.15 and 4.2.25 where an increase in S_{ds} (under vibration) corresponded to a lower workpiece surface roughness. The reason could be attributed to a greater number of active cutting points per grain (due to grit fracture) generated with use of US vibration. Butler et al. (2002) further suggested that a decrease in S_{ds} value signalled loss of grain sharpness, implying that wheels became sharper when using ultrasonic assisted grinding.

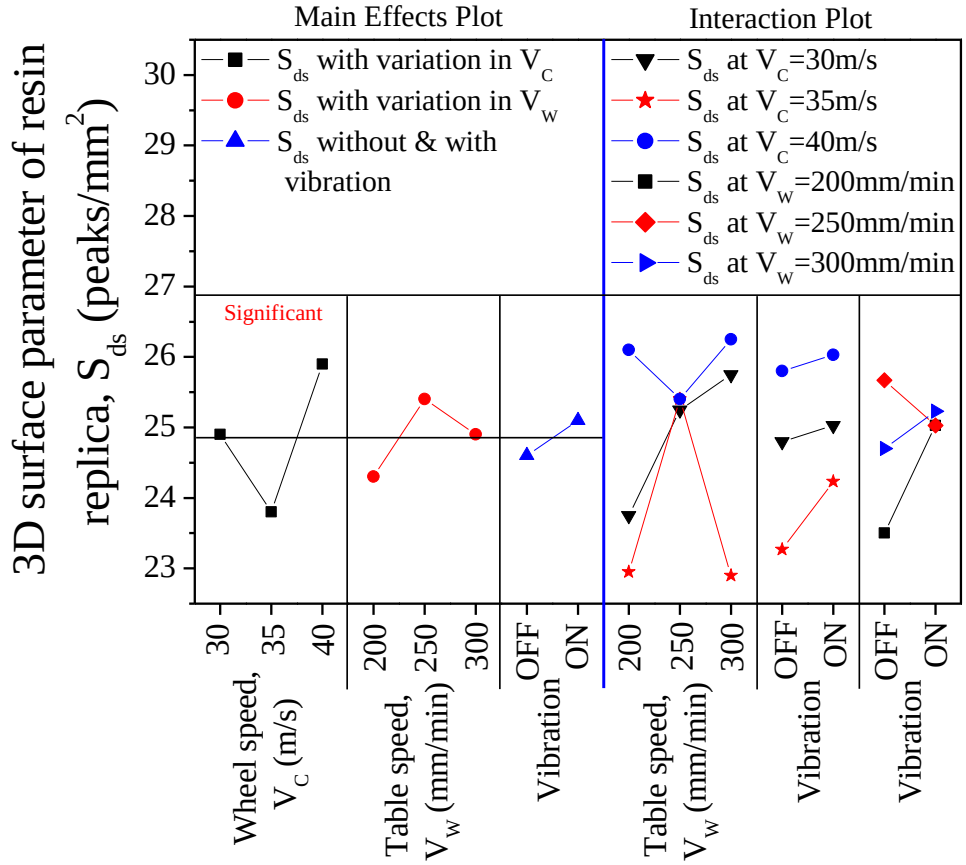


Fig. 4.2.25 Main effects and interaction plots for 3D surface parameter (S_{ds}) of resin (positive) replicas of the grinding wheel

The SEM micrographs of wheel resin replicas, see Figures 4.2.26(a), (b) and (c), revealed that the active grit density on the wheel surface was higher following roller dressing in comparison to those following grinding with and without ultrasonic assistance. While comparing Figs. 4.2.26(b) and (c), it was observed that greater amount of voids/pores were generated in between the grains when grinding was employed with ultrasonic vibration. This could possibly be due to higher micro-splintering of alumina grains under the action of vibration (Uhlmann, 1998), leading to more grit/bond fracture and a consequent rise in the S_{ds} parameter of the wheel surfaces (as evident from Fig. 4.2.25).

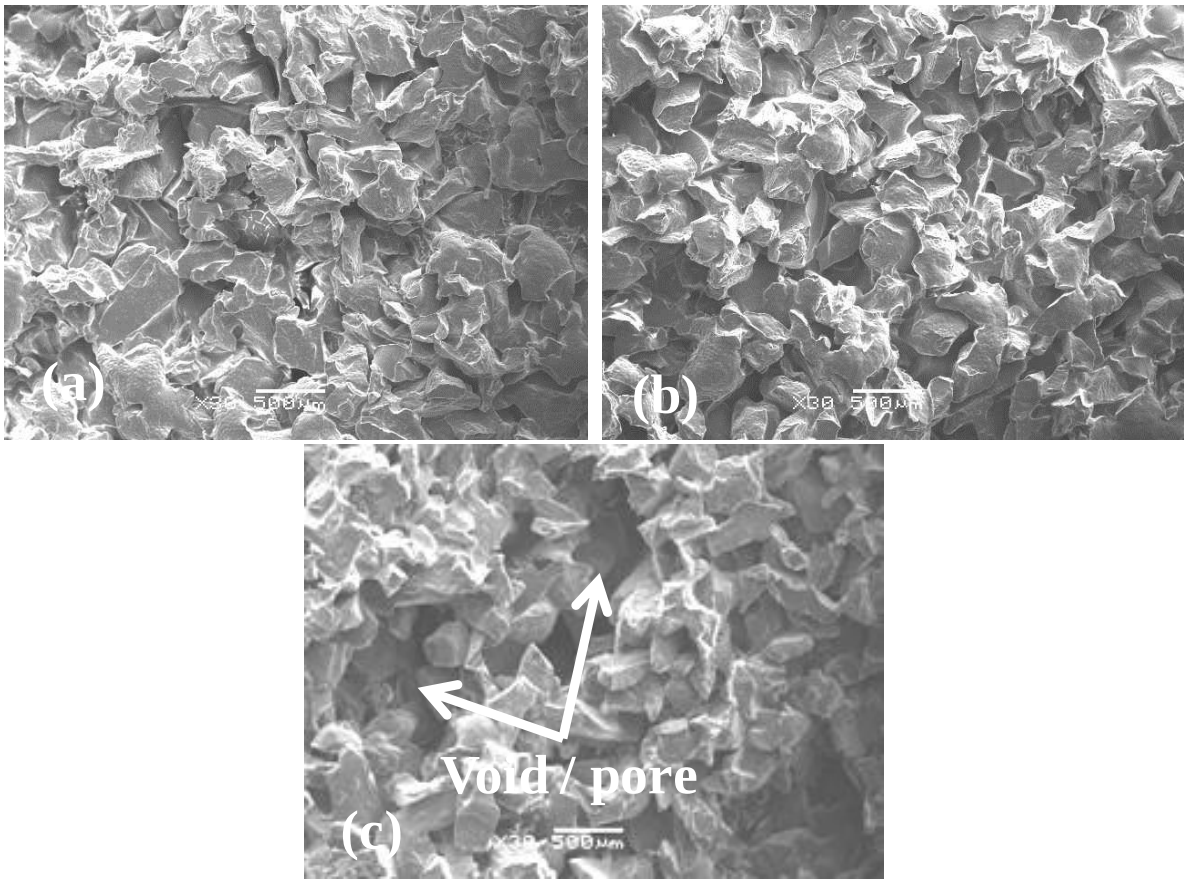


Fig. 4.2.26 SEM micrographs of selected wheel surface resin replicas following (a) Roller dressing, (b) Test 5:V_C=30 m/s, V_W=300 mm/min, US OFF, (c) Test 6:V_C=30 m/s, V_W=300 mm/min, US ON

4.2.2.5 Microhardness and workpiece microstructure

The microhardness depth profiles of selected Inconel 718 samples in the transverse and longitudinal feed planes when grinding with a table feed of 200 mm/min are shown in Figs. 4.2.27 and 4.2.28 respectively. In general, a hardened layer with a maximum of ~515 $HK_{0.025}$ (15% above bulk hardness) and extending to a depth of up to 300 µm was observed, with no appreciable difference between both directions. This observation was in agreement with that reported by Devillez et al. (2011), where workpiece hardening at the surface was in a range of 510-525 $HV_{0.1}$ with a gradual decrease to bulk values (430-440 $HV_{0.1}$) at about 250 µm beneath the machined surface. In general, the workpiece sub-surface microhardness was found to be ~5-10% higher when machining under UAG mode, which was probably due to greater plastic deformation (Xu et al., 2002), as a result of the greater mechanical impact of the grits on the work surface under the action of vibration (Ulhmann, 1998) in the radial wheel direction (multi-modal characteristic of the transducer system).

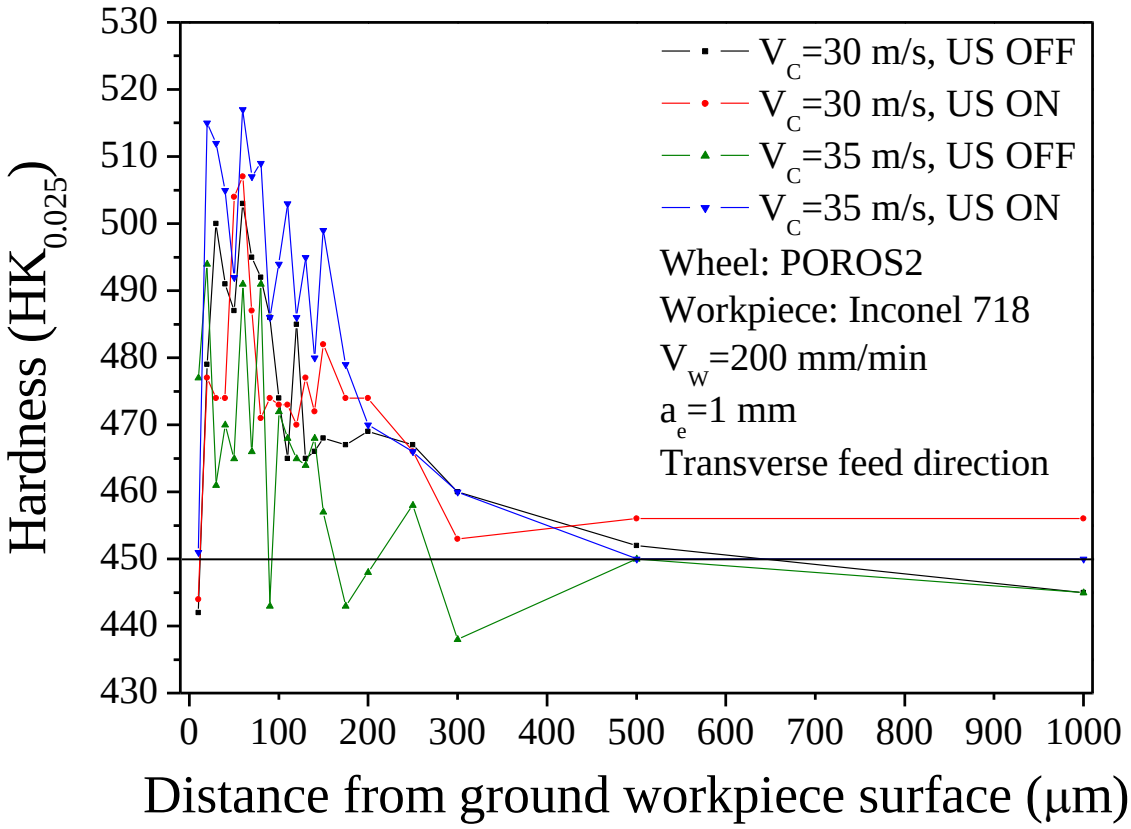


Fig. 4.2.27 Microhardness depth profile of Inconel 718 samples ground at V_W=200 mm/min; measurements taken along transverse feed direction

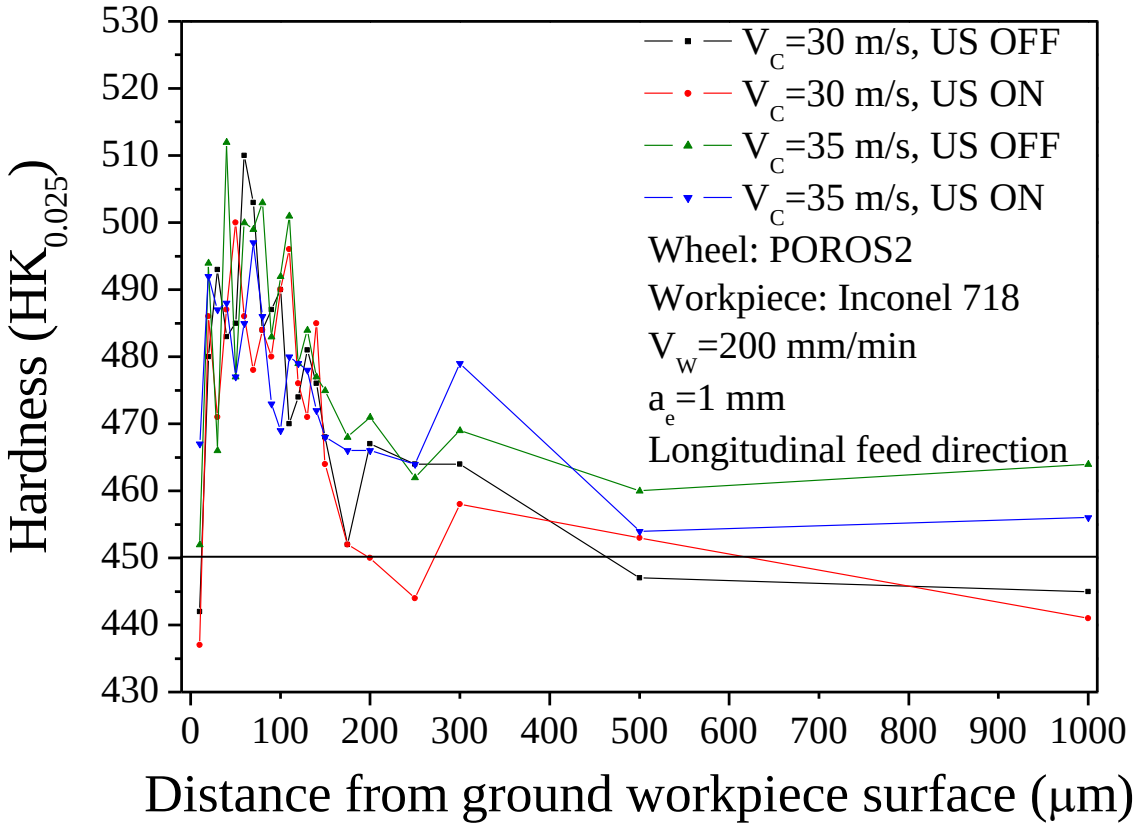


Fig. 4.2.28 Microhardness depth profile of Inconel 718 samples ground at V_W=200 mm/min; measurements taken along longitudinal feed direction

Elongation of grain boundaries up to 5-10 µm beneath the machined surface along the feed direction were observed at all grinding conditions, similar to that shown in Fig. 4.2.29. Yao et al. (2013) also reported comparable results when surface grinding of Inconel 718. In addition, none of the test specimens evaluated showed any signs of cracks, tears, laps, folds or breakage of carbide particles. This suggests that the operating conditions used were appropriate for producing defect-free surfaces.

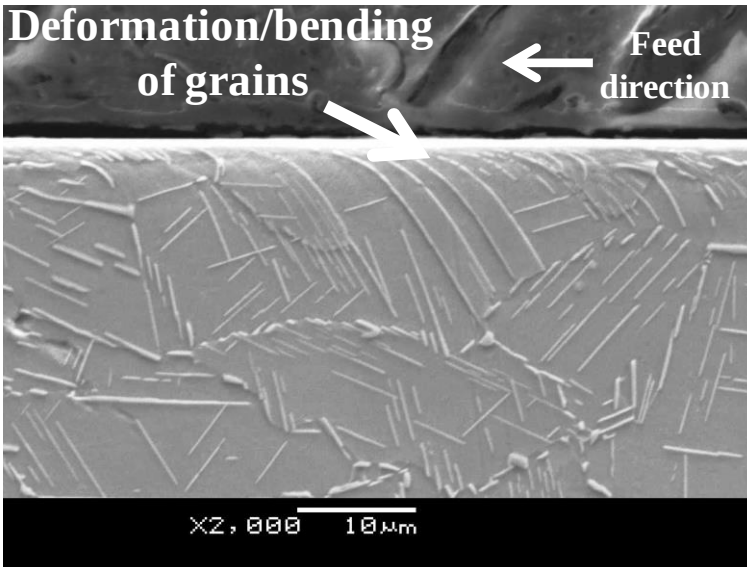


Fig. 4.2.29 Microstructure of Inconel 718 on longitudinal feed plane showing deformation/bending of grains (Test 7)

In contrast to the longitudinal feed plane, grit marks were apparent on cross-sectional SEM micrographs, taken perpendicular to the feed direction, see Fig. 4.2.30, despite lower levels of sub-surface grain deformation. The use of ultrasonic vibration however did not result in any significant variation of the workpiece microstructure.

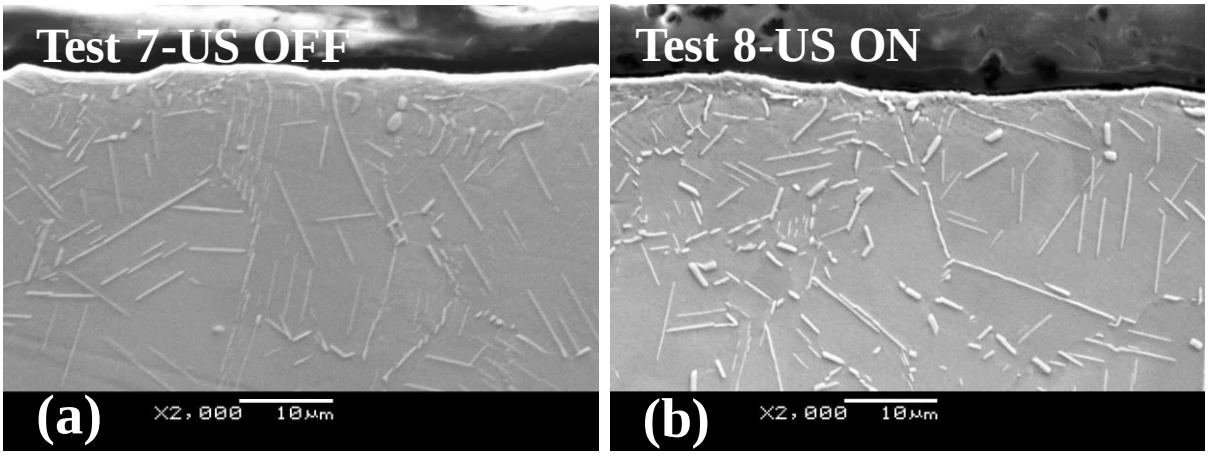


Fig. 4.2.30 Microstructures of Inconel 718 on transverse feed plane ground at V_C = 35 m/s, V_W = 200 mm/min, d = 1.0 mm, (a) US OFF, (b) US ON

The key results obtained from Phase 2B are summarised below:

- The use of ultrasonic vibration generally resulted in reductions in F_v and F_h by up to 23% and 43% respectively.
- Wheel G-ratio was improved by between 7 to 45% in 5 of the 9 trials, however decreased in 3 of the remaining 4 experiments when operated with the hybrid configuration.
- The majority of the ground surfaces were free from depression marks/grinding burn.
- Greater side flow/ploughing was observed with the workpieces ground ultrasonically in comparison to conventional creep feed ground specimens. Furthermore, greater numbers of overlapping grit marks were visible on surfaces subject to UAG.
- Sub-surface microhardness generally increased by ~5-10% when the workpieces were actuated with ultrasonic vibration.
- There were only marginal differences in the microstructures of specimens ground with and without ultrasonic assistance. Additionally, no cracks, tears, laps, folds or breakage of carbide particles were seen on any of the specimens evaluated.

4.2.3 Phase 2C: Evaluation of UAG on Inconel 718 using VORTEX 60 mesh wheel

4.2.3.1 Grinding forces

The grinding forces (F_v and F_h) recorded when CFG of Inconel 718 workpieces with and without ultrasonic assistance using the VORTEX 60 mesh alumina wheel are shown in Fig. 4.2.31.

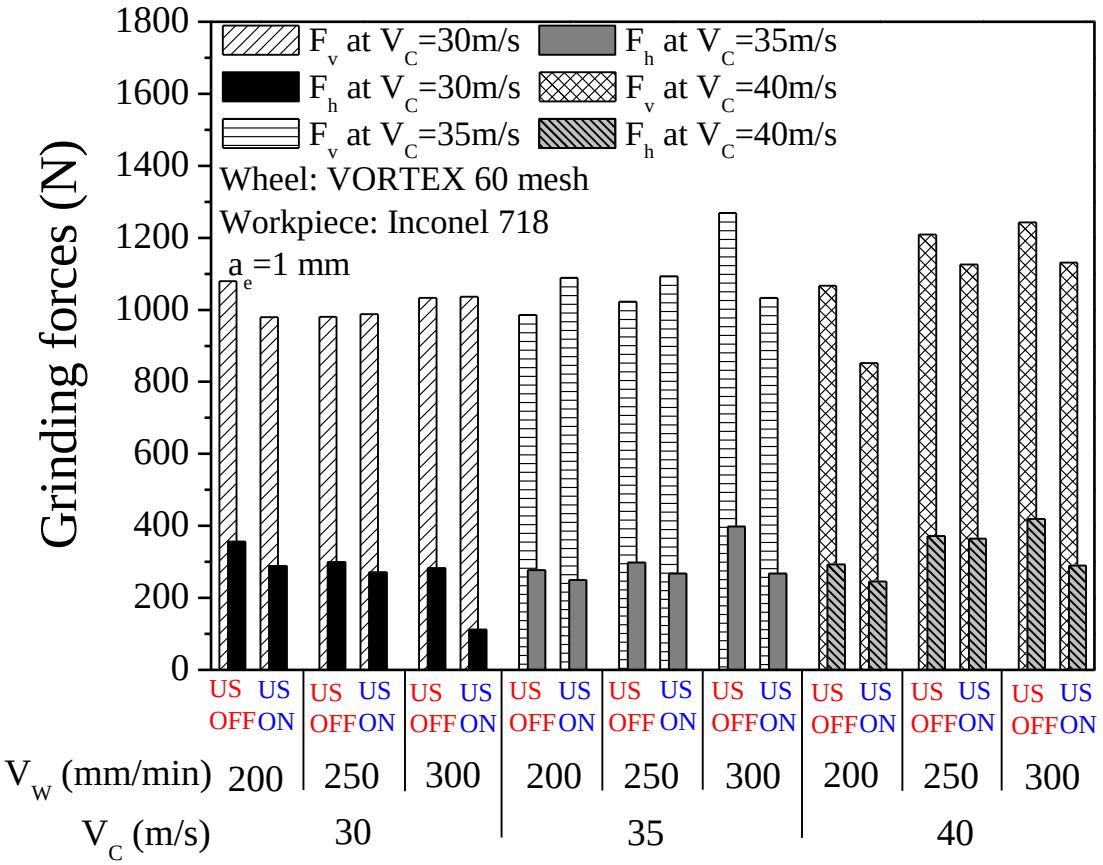


Fig. 4.2.31 Vertical (F_v) and horizontal (F_h) forces under different grinding conditions

The vertical and horizontal forces varied between ~950 to 1150 N and ~200 to 375 N respectively when conventional CFG, which were comparable to those obtained in the Phase 2B. With the assistance of ultrasonic vibration F_v decreased in 5 out of 9 tests by up to ~20%, whereas F_h reduced by ~10-30% (maximum reduction by ~60% in Test 6) in all tests involving UAG. Comparable reductions by up to 27% and 22% respectively in the vertical and horizontal grinding forces were reported by Abdullah et al. (2012) when ultrasonic assisted creep feed grinding of Inconel 728LC. The reduction in forces under hybrid mode was possibly a cumulative effect of discreet machining passes (Peng et al., 2012b), which resulted in reduction in friction, crushing of material by 'microhammering effect', decrease in

strength of material under the influence of ultrasound, better flushing of the grinding swarf and greater ingress of coolant/cutting fluid into the grinding zone (Heisel et al., 2011). The associated main effects and interaction plots for both F_v and F_h, shown in Figures 4.2.32 and 4.2.33 respectively, together with the corresponding PCR's in Table 4.2.2 showed that vibration had a significant influence on the horizontal component of forces (PCR of 27.94%), while its effect on F_v was relatively low (PCR of 9.76%) and statistically insignificant at 5% level.

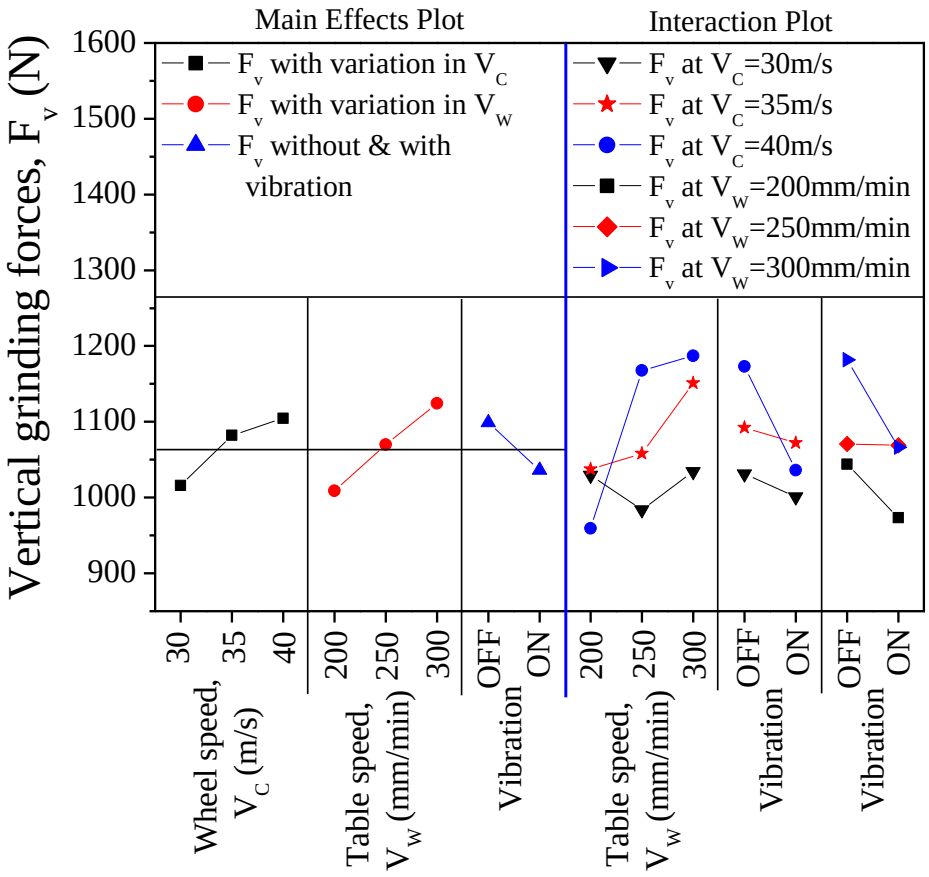


Fig. 4.2.32 Main effects and interaction plots for vertical grinding force

Figures 4.2.32 and 4.2.33 further showed that both F_v and F_h increased with a rise in wheel speed from 30 to 40 m/s, possibly due to the increase in rubbing and ploughing components of the grinding forces at a faster wheel speed such as 40 m/s (Hwang et al., 2000). Similar observation was also reported by Burrows et al. (2000) when superabrasive point grinding of Inconel 718 and Udimet 720. While F_v increased with an increase in table feed, F_h did not show a particular trend in this occasion. The drop in F_h at the highest level of table feed (300 mm/min) could be due to the reduction in contact time between the abrasive grains and workpiece leading to a decrease in grinding zone temperature (Kohli et al., 1995, Malkin and Guo, 2007).

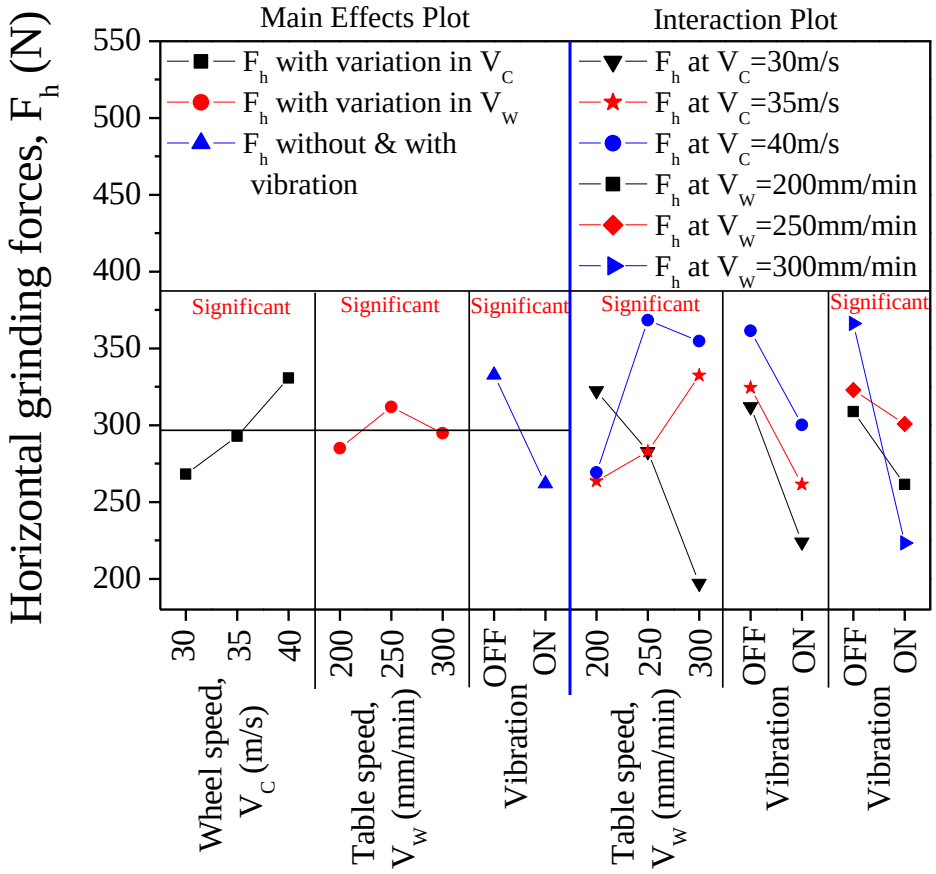


Fig. 4.2.33 Main effects and interaction effects plots for horizontal grinding force

Table 4.2.2 Percentage contribution ratios of factors with respect to different response measures (Phase 2C)

Factors	Percentage contribution ratios (PCR's)								
	F_v	**F_h**	**G-ratio**	**W/P R_a**	**W/P S_a**	**Graphite R_a**	**Graphite S_a**	**Resin replica S_a**	**Resin replica S_{ds}**
Wheel speed (V_C)	14.13	14.80*	9.57	39.08	19.00	3.22	8.58	27.95*	24.27
Table feed (V_W)	22.19	2.73*	19.57	6.27	5.58	14.99	10.52	7.83	14.42
Vibration (Vib)	9.76	27.94*	9.33	4.61	10.22	0.79	6.35	2.07	5.01
V_C×Vw	23.00	38.16*	13.27	15.69	18.77	33.79	56.61	46.91*	30.28
V_C×Vib	6.93	0.84	7.25	19.52	3.46	9.32	1.41	1.42	2.91
V_W×Vib	5.44	15.03*	17.79	4.22	36.59	28.00*	11.82	7.17	5.21
V_C×V_W×Vib	18.55	0.50	23.21	9.60	5.96	9.88	4.77	6.65	17.90
* Statistically significant factors at the 5% level									

ANOVA analysis showed that both wheel speed and table feed had significant effects on F_h, despite the low value of PCR of V_W (2.73%). The interactions between wheel speed and table feed (V_C × V_W) as well as table feed and vibration condition (V_W × Vib) were statistically significant with regard to F_h with PCR's of 38.16% and 15.03% respectively,

whereas none of them had significant influences on F_v despite moderate PCR's of 23.00% and 5.44% for ($V_C \times V_W$) and ($V_W \times$ Vib) respectively, see Table 4.2.2.

4.2.3.2 Radial wheel wear and G-ratio

Figure 4.2.34 details radial wheel wear and the corresponding G-ratio of the VORTEX 60 mesh wheel. RWW varied from 12 to 27 μm (with an exception of Test 15 where a wheel wear of ~6 μm was measured). A much lower wheel wear of ~2-10 μm was reported by Azizi et al. (2009) following grinding of Inconel 738 with a vitrified cBN wheel. The G-ratio of the VORTEX 60 mesh wheel was within ~3 to 6 (with the exception of Test 15 where a G-ratio of ~12 was obtained); the values marginally differed from those recorded for the POROS2 wheel in Phase 2B. A much higher G-ratio of ~15-30 was observed by Neslušan (2009) when using a VORTEX 60 J17 V wheel when grinding a nickel based superalloy. Wheel wear increased (G-ratio decreased) in 6 out of 9 tests when grinding was employed with ultrasonic assistance. This was possibly the result of higher micro-fracturing of the abrasive grains under the high mechanical load/impact imposed by the vibration (Peng et al., 2012b).

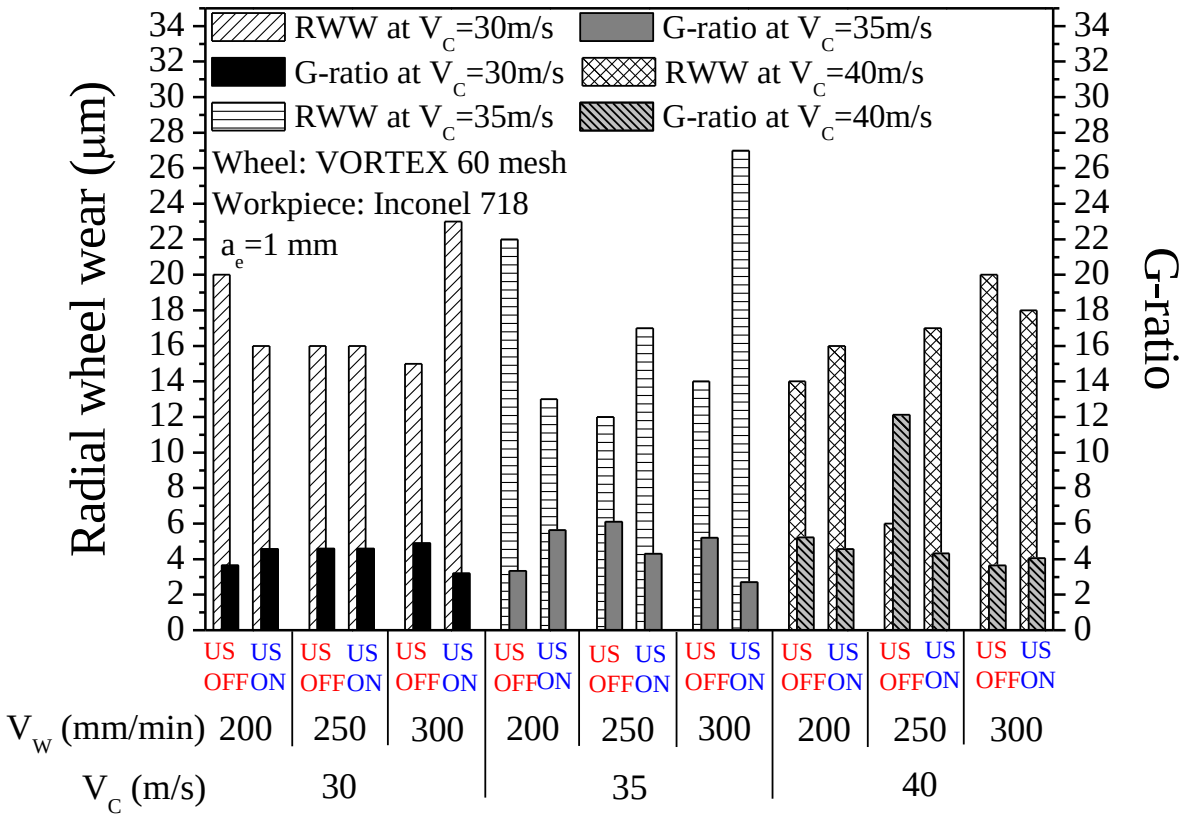


Fig. 4.2.34 Radial wheel wear and G-ratio under different grinding conditions

The main effects and interaction plots for G-ratio in Fig. 4.2.35 showed that it increased with an increase in wheel speed irrespective of other operating conditions. This could possibly be due to the reduction in number of grits in contact with the work surface per rotation of the wheel leading to a decrease in wheel wear. G-ratio also increased with a rise in table feed up to 250 mm/min, however dropped subsequently at a table feed of 300 mm/min. Table 4.2.2 shows that amongst all parameters, an interaction between V_C, V_W and vibration condition ($V_C \times V_W \times$ Vib) had the maximum PCR on G-ratio (23.21%), however it was not statistically significant. This was followed by the sole effect of V_W (19.57%), the interaction between V_W and vibration (17.79%) and that between V_C and V_W (13.27%). The main effects of V_C and vibration on G-ratio were rather lower (9.57% and 9.33% respectively). None of the parameters was found to be statistically significant at 5% level with regard to G-ratio.

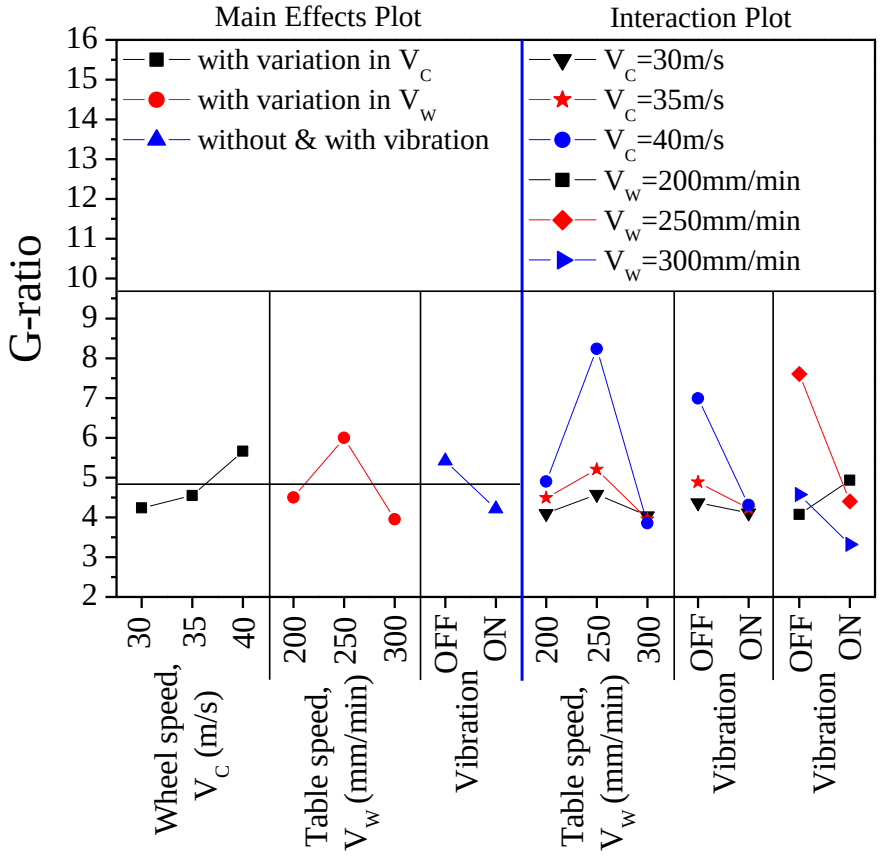


Fig. 4.2.35 Main effects and interaction plots for wheel G-ratio

4.2.3.3 Workpiece surface topography and quality

The images of workpiece surfaces ground at different parameters are shown in Fig. 4.2.36. Although VORTEX wheels were said to have naturally occurring high porosity for the purpose of absorbing copious quantities of coolant (Anon, 2005), some depression marks with

depths of ~90 to 150 μm were observed towards the end of grinding tracks in 4 out of 9 conventional CFG trials, which were indications of grinding burn (Andrew et al., 1985). However no burn, depression or chatter marks were observed on any of the workpieces ground with ultrasonic assistance.



Fig. 4.2.36 Images of Inconel 718 workpiece surfaces ground at different operating conditions

The workpiece 2D surface roughness data recorded at three locations of the ground track, detailed in Figure 4.2.37, shows that R_a typically decreased from the start to the end of the machined slots due to the generation of wear flats on the grains with the progress of grinding. With the incidence of depressions/grinding burns, a 'spike' in the R_a value was observed towards the end of cut length (shown by arrow marks in Fig. 4.2.37). The associated main effects plot shown in Fig. 4.2.38 displayed that average R_a typically decreased with increasing cutting speed from 30 to 40 m/s, however it increased with a rise in table feed from 200 to 300 mm/min. This observation was in agreement with work by Vashista and Paul (2008) where surface roughness reduced with a decrease in depth of cut as well as table speed while it increased with a reduction in wheel velocity when high speed grinding AISI 1060 steel. The PCR of V_C for R_a was 39.08%, although that of V_W was much lower (6.27%) while none of the parameters had significant effects on R_a, see Table 4.2.2. The interaction between V_C and V_W had a PCR of 15.69%, although it was statistically insignificant.

The 3D surface parameters of the ground workpieces are shown in Fig. A4.1 in Appendix A4. Although not shown here, the main effects plot for S_a exhibited similar trends to those observed for R_a with the variations in wheel speed and table feed. The PCR of V_C for S_a was comparatively lower (19%) than that for R_a, whereas V_W and the interaction between V_C and V_W ($V_C \times V_W$) exhibited comparable PCR's of 5.58% and 18.77% respectively, although none of the factors were statistically significant.

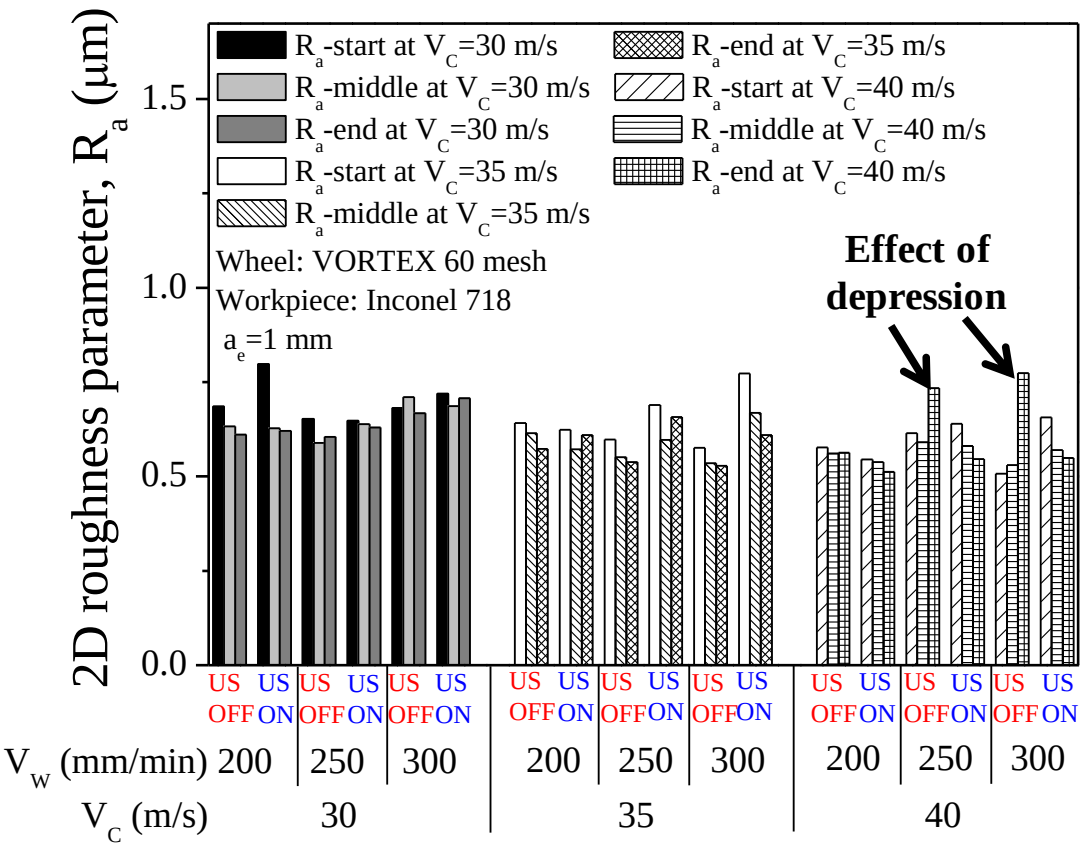


Fig. 4.2.37 2D roughness parameter (R_a) of ground Inconel 718 workpiece surfaces

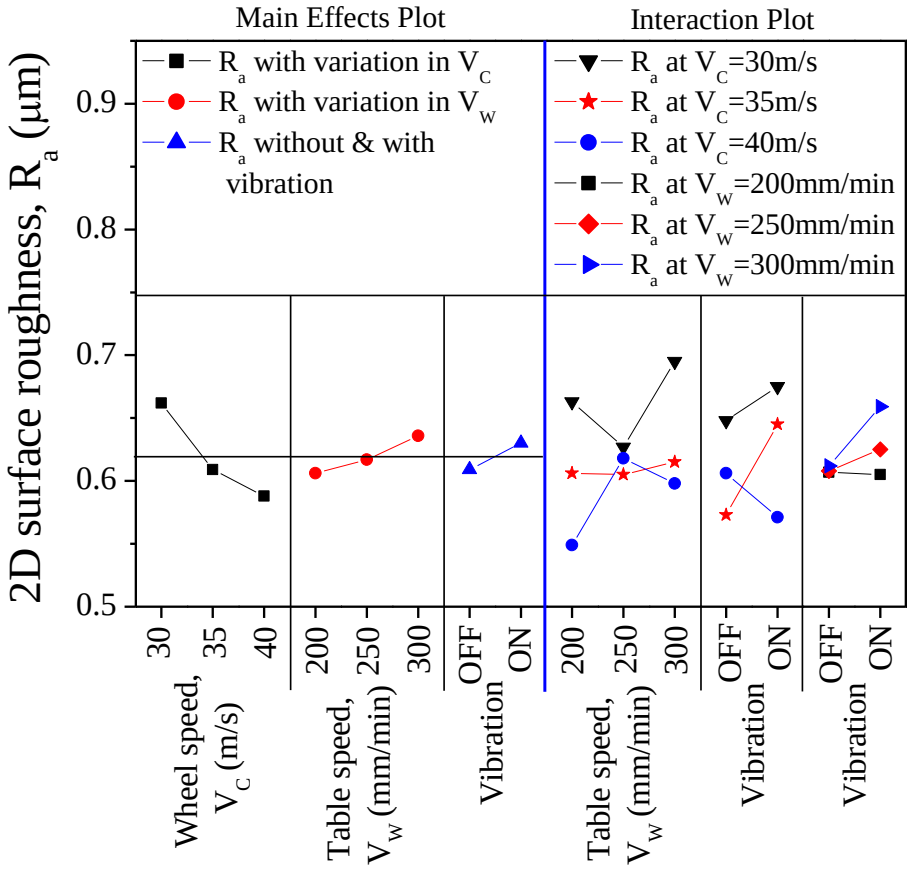


Fig. 4.2.38 Main effects and interaction plots for 2D roughness (R_a) of ground workpieces

Figure 4.2.37 and Fig. A4.1 further showed that mean R_a and S_a of the workpiece surfaces increased in 6 out of 9 trials involving ultrasonic vibration in comparison to conventionally ground specimens. The other 2D and 3D surface parameters such as R_t, R_z, S_t, S_z, S_p and S_v also typically increased when UAG. The PCR's of vibration condition and its interactions with wheel speed and table feed (V_C × Vib and V_W × Vib) for R_a were 4.61%, 19.52% and 4.22% respectively, while those for S_a were 10.22%, 3.46% and 36.59% respectively, although none of these factors were statistically significant at 5% level.

The SEM micrographs of the machined workpieces shown in Fig. 4.2.39 revealed that the conventionally ground surfaces were characterised with typical grooving marks in the feed direction, see Fig. 4.2.39(a). Tso (1995b) reported similar rubbing traces on the work surfaces parallel to the grinding direction while machining Inconel 718. Conversely, extensive plastic deformation due to the generation of high grinding zone temperature, was observed on the deformed/burnt regions on the ground surfaces (Tests 1, 11, 15 and 17), see Fig. 4.2.39(b).

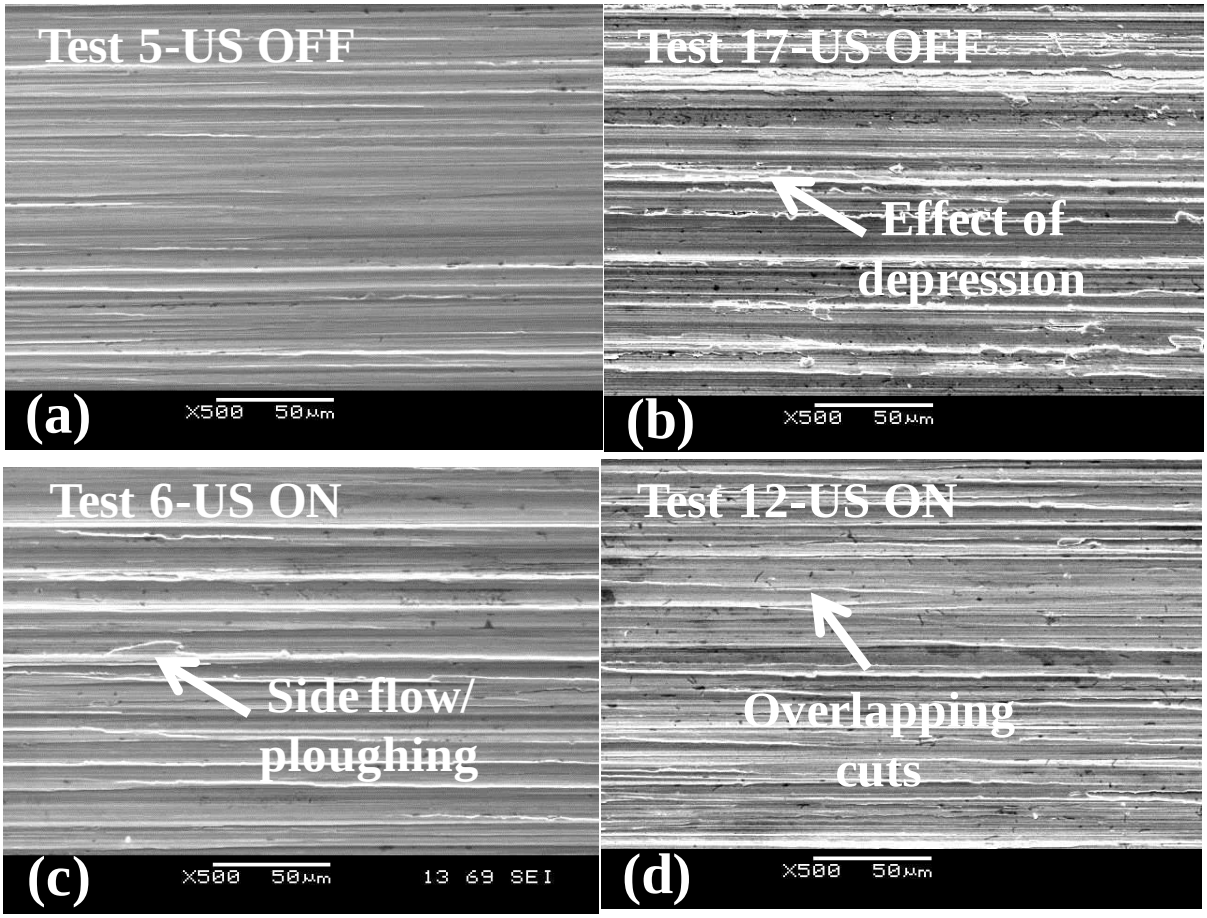


Fig. 4.2.39 SEM micrographs of ground workpiece surfaces (a) Test 5: V_C=30 m/s, V_W=300 mm/min, US OFF, (b) Test 17: V_C=40 m/s, V_W=300 mm/min, US OFF, (c) Test 6: V_C=30 m/s, V_W=300 mm/min, US ON, (d) Test 12: V_C=35 m/s, V_W=300 mm/min, US ON

The ultrasonic assisted ground surfaces exhibited a greater degree of side flow compared to the burn-free conventionally machined specimens, see Fig. 4.2.39(c). This suggested that higher plastic deformation (Spur and Holl, 1996) occurred due to intensive mechanical impacts when operating with ultrasonic vibration (Uhlmann, 1998). The ultrasonically machined specimens also typically exhibited overlapping grit marks throughout the ground slots, see Fig. 4.2.39(d), which were possibly due to the lateral shifts of the abrasive grains under the multi-modal vibration characteristic of the table sonotrode (Azarhoushang and Tawakoli, 2011).

4.2.3.4 Grinding wheel surface evaluation

The R_a and S_a values measured from the graphite replicas of the post-grinding wheel surfaces and the associated main effects and interaction plots for R_a are shown in Figs. 4.2.40 and 4.2.41 respectively.

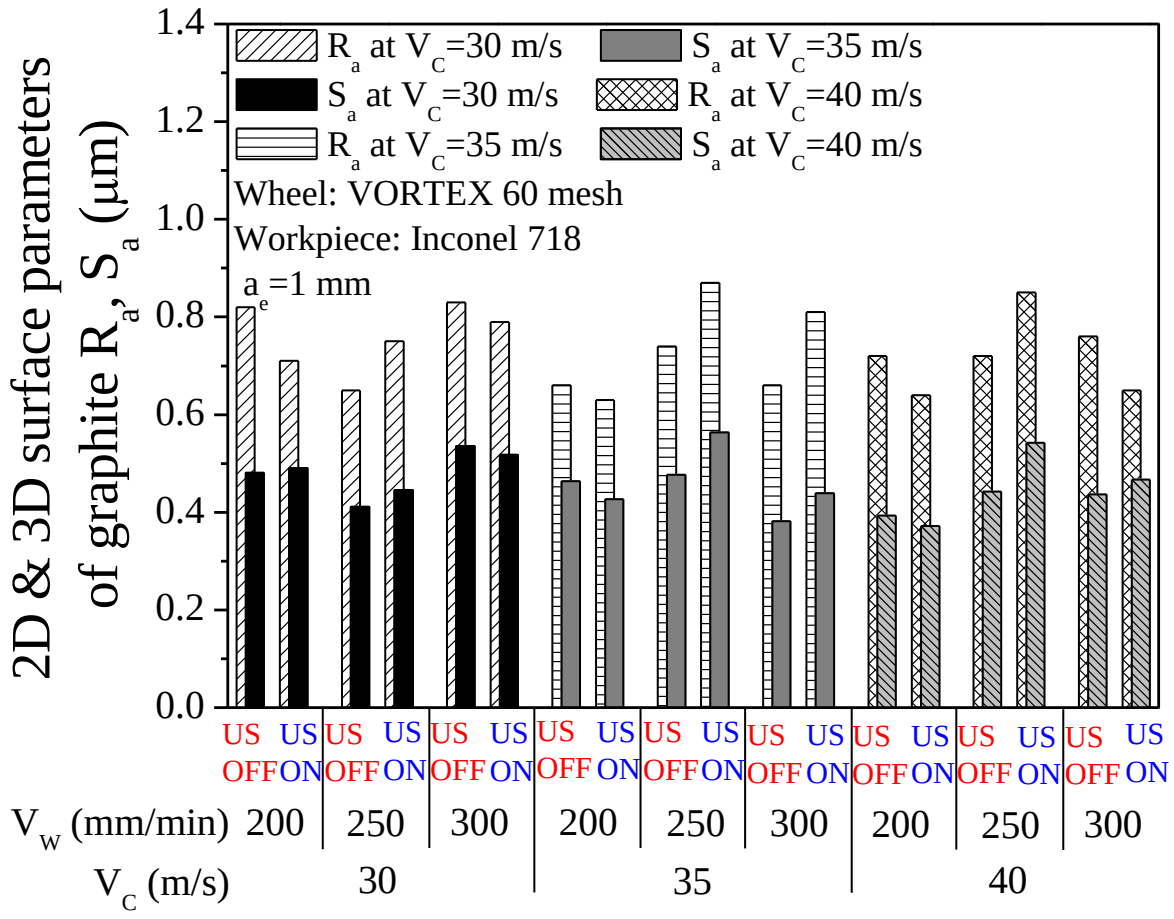


Fig. 4.2.40 2D and 3D surface parameters of graphite (negative) replicas of grinding wheel

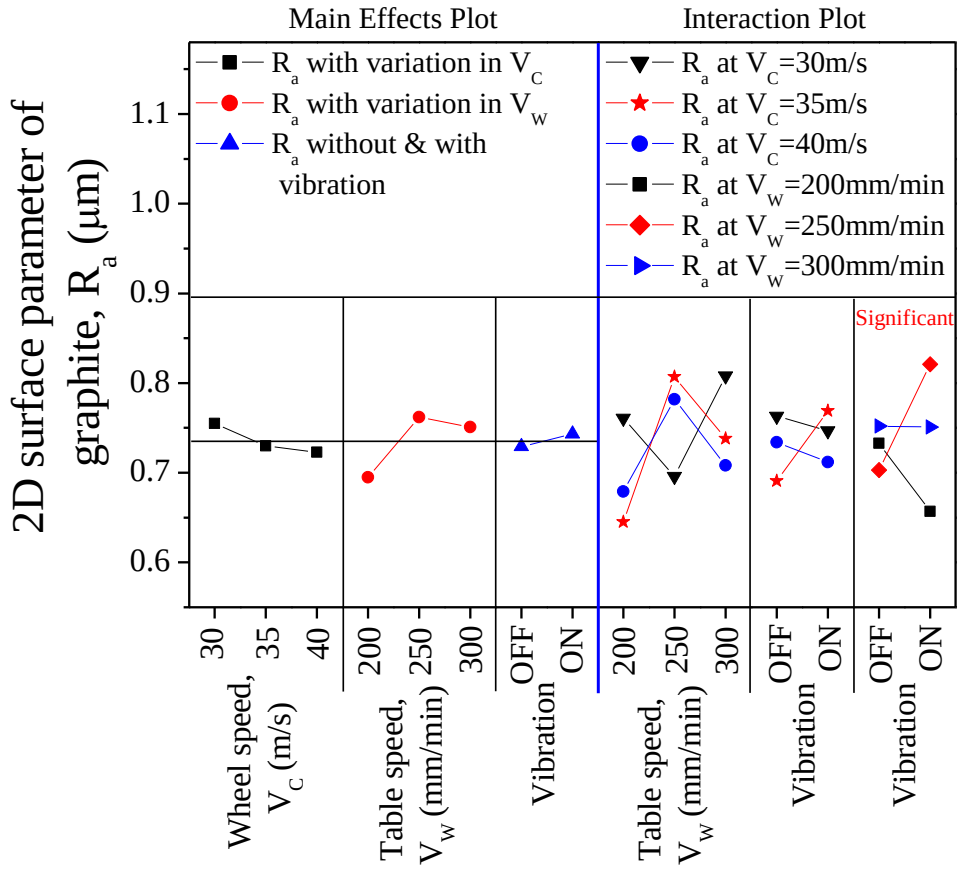


Fig. 4.2.41 Main effects and interaction plots for 2D surface roughness (R_a) of graphite (negative) replicas of the grinding wheel

Graphite surface roughness typically decreased with an increase in wheel speed from 30 to 40 m/s. This observation was in agreement with the roughness data recorded from the ground workpiece surfaces. Both R_a and S_a of the graphite blocks also generally increased with an increase in table feed from 200 to 250 mm/min, however decreased subsequently with a further rise in V_W up to 300 mm/min. The reason could possibly be due to the generation of wear flats on the abrasive grains at a higher table feed, which was evidenced by a lower G-ratio (higher wheel wear) obtained at 300 mm/min. Both V_C and V_W exhibited low PCR's for R_a (3.22% and 14.99%) and S_a (8.58% and 10.52%) and none of them were statistically significant, however their interaction ($V_C \times V_W$) showed comparatively higher PCR's (33.79% for R_a and 56.61% for S_a) although the effects were statistically insignificant.

Figure 4.2.41 further showed that graphite surface R_a typically increased when grinding was carried out with ultrasonic assistance, the trend being similar to that obtained with the workpiece R_a. The main effects plot for graphite S_a (not shown here) also followed the similar course as that of R_a. Although the sole effects of vibration on R_a and S_a were insignificant (with PCR's of 0.79% and 6.35% respectively), its interaction with table feed ($V_W \times$ Vib) was statistically significant for R_a together with a PCR of 28%, see Table 4.2.2.

The 3D topographical parameters of the resin replicas are detailed in Fig. 4.2.42 and the related main effects and interaction plots for resin S_a and S_{ds} are shown in Figs. 4.2.43 and 4.2.44 respectively. Both S_a and S_{ds} of resin surfaces typically decreased when operating with ultrasonic vibration, which indicated a difference in the grain protrusions as well as generation of larger pores per unit area on the wheel surface caused by the grit fractures under the action of high mechanical impacts imparted by the US vibration. In contrast, none of the parameters showed any particular trends with the variations in V_C and V_W, although ANOVA analysis showed that the sole effect of VC and an interaction between V_C and V_W ($V_C \times V_W$) had significant influences on resin S_a with PCR's of 46.91% and 27.95% respectively. The same factors also had comparable PCR's for resin surface S_{ds} (30.28% and 24.27% respectively), although none of them was statistically significant, see Table 4.2.2.

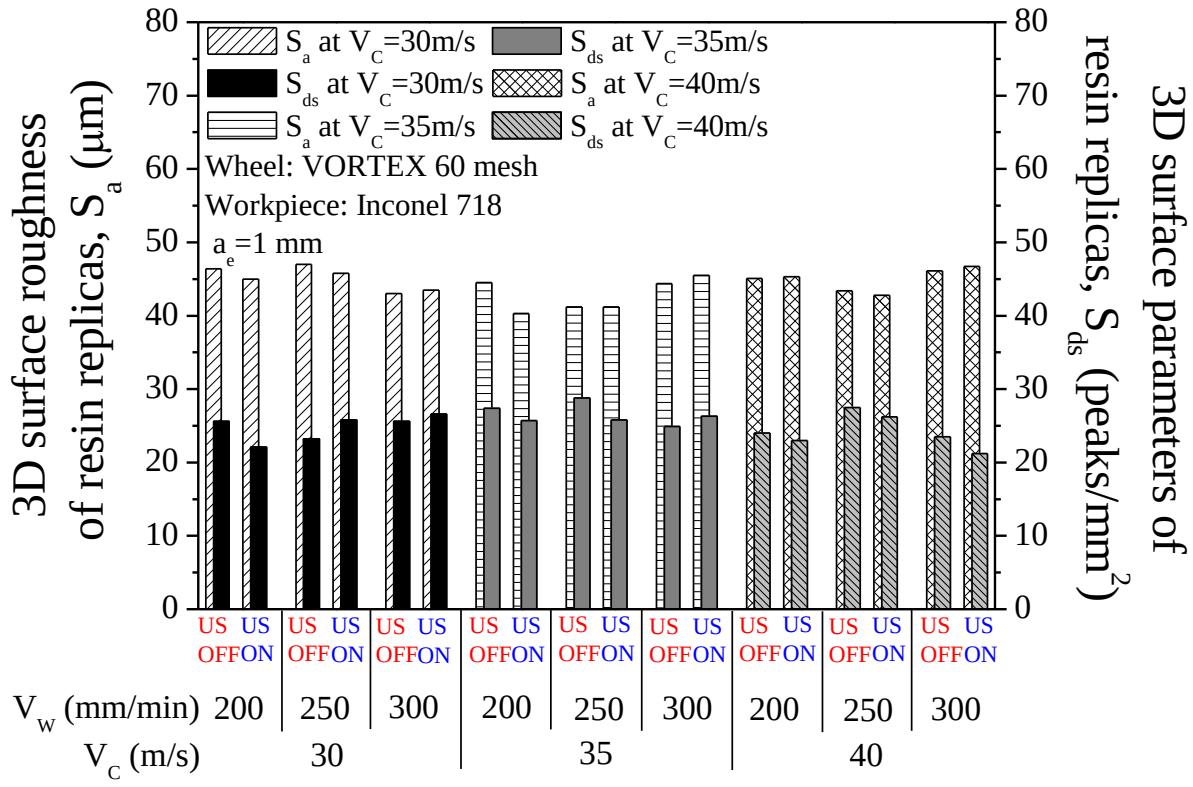


Fig. 4.2.42 3D topographical parameters of resin (positive) replicas of VORTEX wheel

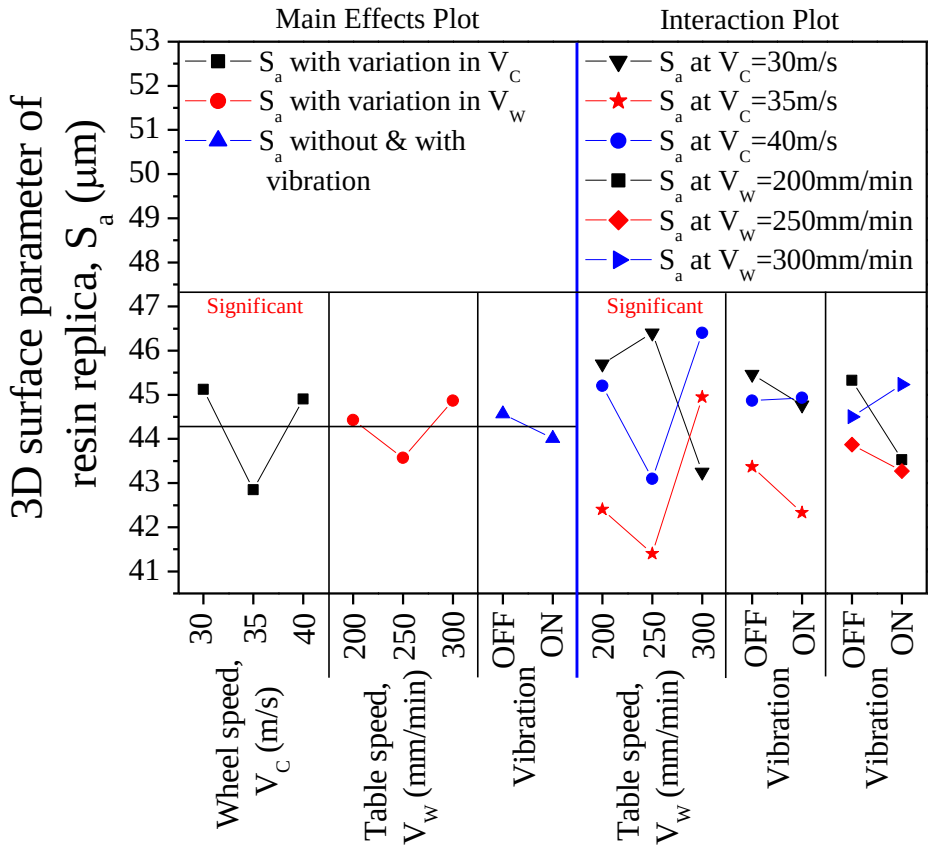


Fig. 4.2.43 Main effects and interaction plots for 3D surface parameter (S_a) of resin (positive) replicas of the VORTEX wheel

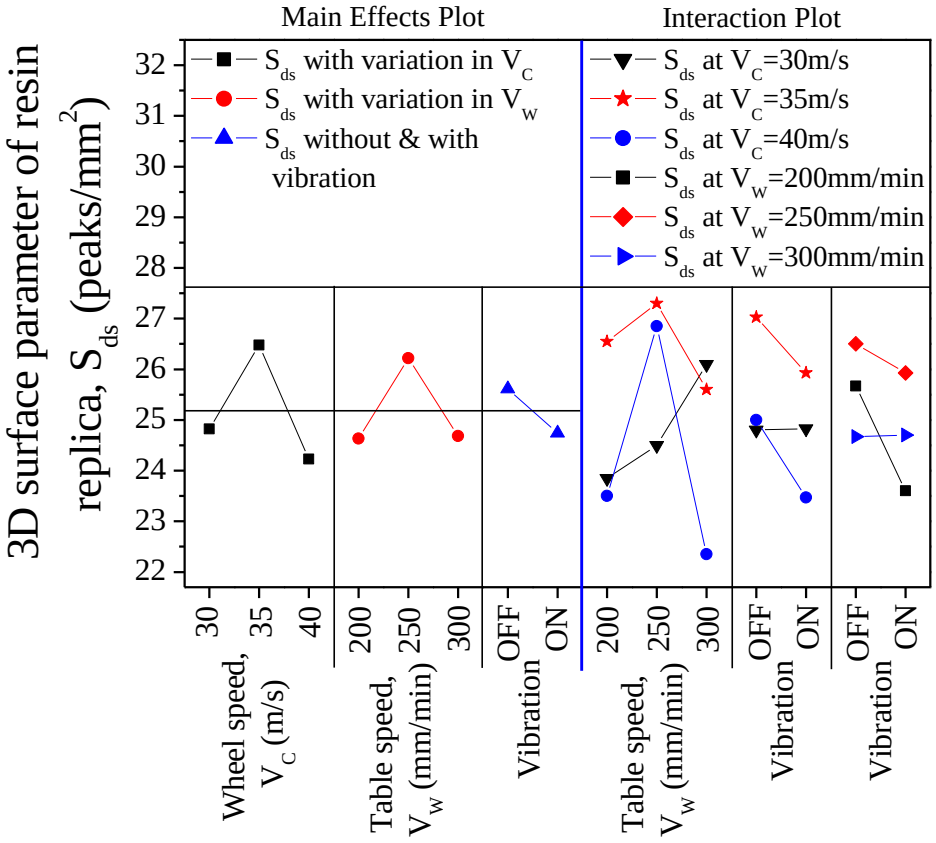


Fig. 4.2.44 Main effects and interaction effects plots for 3D surface parameter (S_{ds}) of resin (positive) replicas of the VORTEX wheel

Figure 4.2.45(a) shows typical surface of a VORTEX wheel (Anon., 2005). The SEM micrographs of the resin replicas (Fig. 4.2.45(b) to (d)) in the present study marginally differed from the one shown in Fig. 4.2.45(a). The wheel surfaces subject to UAG generally exhibited larger voids/pores in between the grains (Fig. 4.2.45(d)) compared to those observed following conventional grinding (Fig. 4.2.45(b) and (c)). This could possibly be one of the reasons of higher workpiece roughness recorded following UAG.

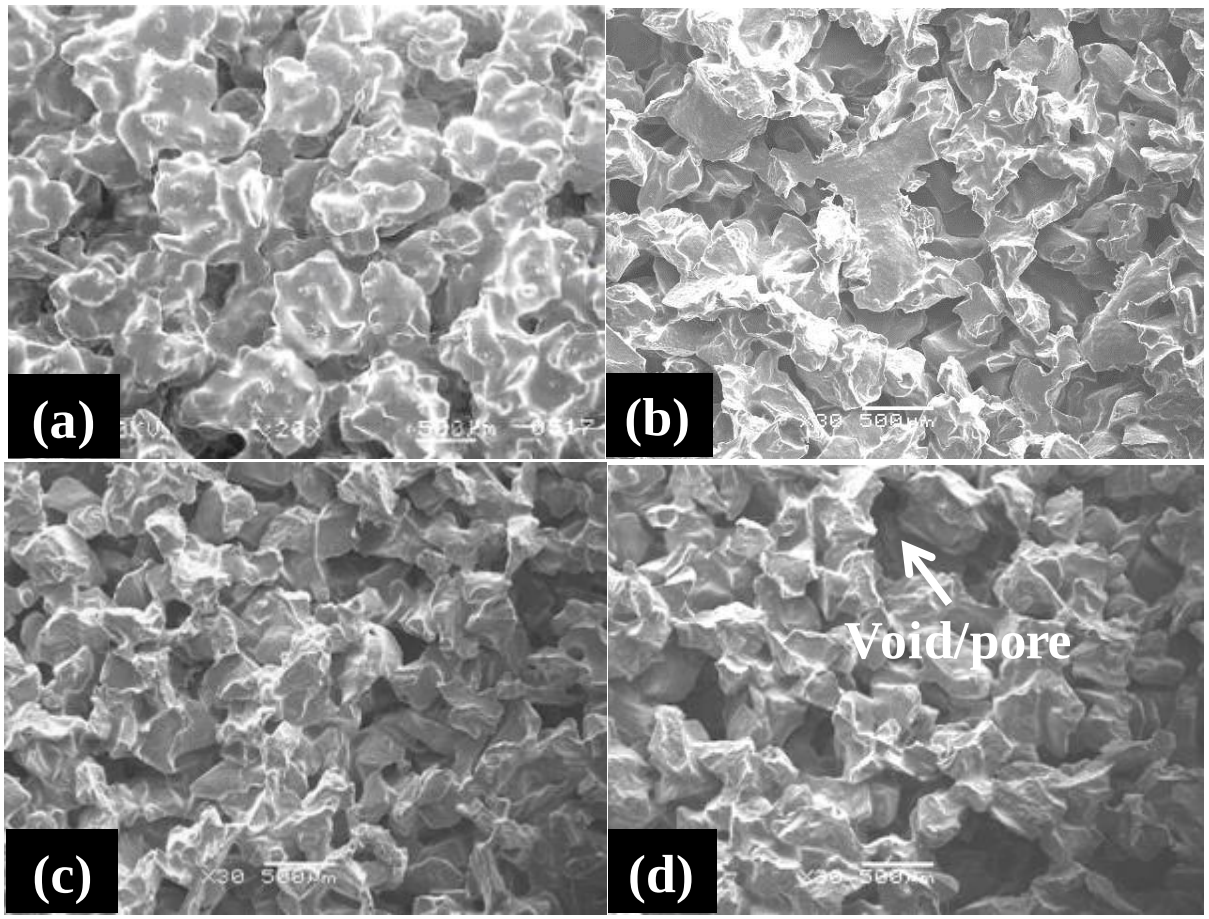


Fig. 4.2.45 SEM micrographs of (a) VORTEX wheel surface (Anon. 2005), (b) wheel resin replicas taken after Test 13: V_C=40 m/s, V_W=200 mm/min, US OFF, (c) Test 17: V_C=40 m/s, V_W=300 mm/min, US OFF, (d) Test 18: V_C=40 m/s, V_W=300 mm/min, US ON

4.2.3.5 Microhardness and workpiece microstructure

The microhardness depth profiles of selected Inconel 718 samples in the transverse as well as longitudinal feed planes when grinding at a table feed of 200 mm/min are shown in Figs. 4.2.46 and 4.2.47 respectively (microhardness depth profiles of specimens ground at a table feed of 300 mm/min are shown in Figs. A4.2 and A4.3 in Appendix A4). Sub-surface microhardness typically increased up to a range of ~500-520 $HK_{0.025}$ from a depth of 10 μm to ~200 μm beneath the machined surface until the bulk hardness was achieved (450 $HK_{0.025}$).

This observation was similar to that in Phase 2B when utilising the POROS2 wheel. There was a marginal difference in the microhardness values recorded along the transverse and longitudinal feed planes. With the application of vibration in grinding, sub-surface microhardness typically increased by 6-8% in comparison to conventionally ground specimens, possibly due to the higher plastic deformation caused by the greater mechanical impact under ultrasonic mode. Nerubai (1987) described that the superimposition of ultrasonic vibration during compression and tension of difficult-to-deform material resulted in a reduction in their resistance to plastic deformation, yield point and strength owing to the formation of additional damages within their crystal structures.

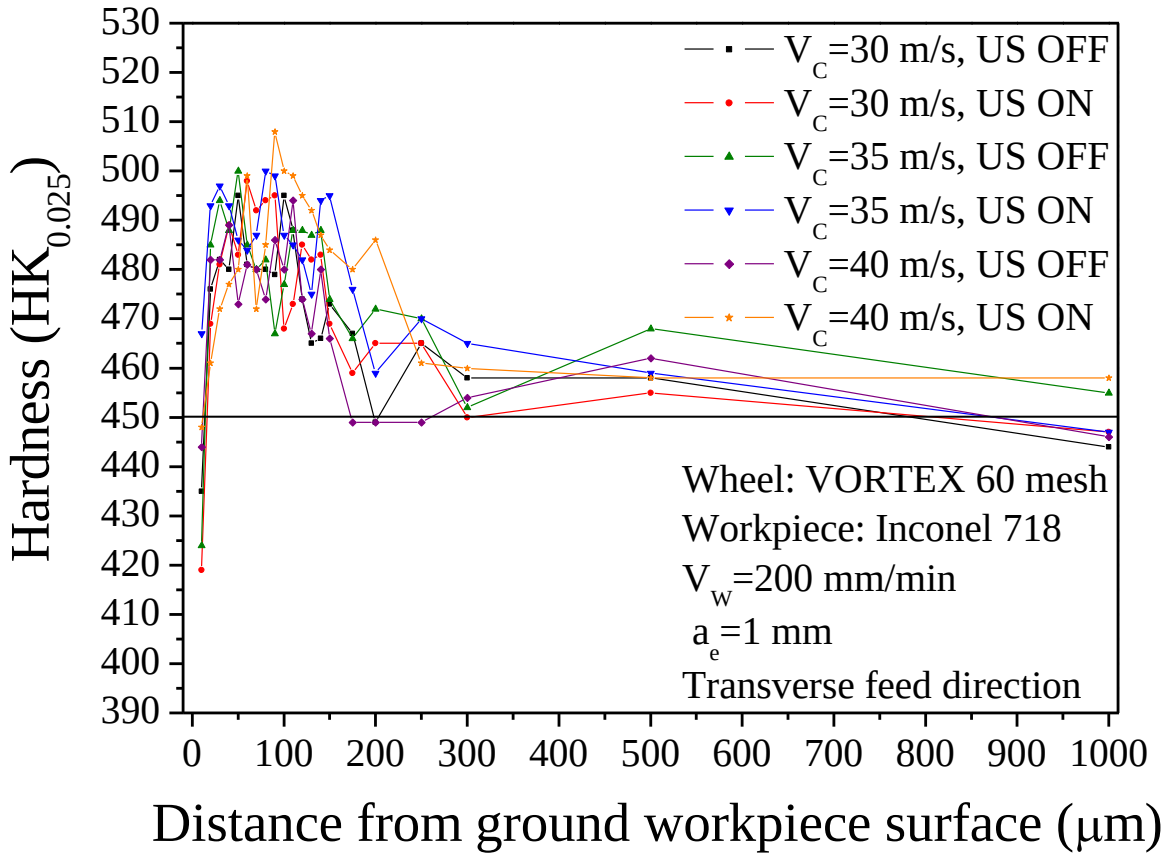


Fig. 4.2.46 Microhardness depth profile of Inconel 718 samples ground at V_W=200 mm/min; measurements taken in transverse feed direction

The SEM micrographs of the microstructures of ground Inconel 718 specimens showed typical trace marks of the abrasive particles on the work surface in the transverse feed plane, see Fig. 4.2.48(a). In contrast, elongation of grains along the feed direction was apparent on the longitudinal feed plane, see Fig. 4.2.48(b). The machined surfaces were typically free from any macro or micro cracks, tears, laps, folds etc. There were also no signs of interior cracks within the NbC particles. Despite the higher mechanical load imposed on the

workpiece surfaces by the abrasive grains under the operation of ultrasonic vibration (Uhlmann, 1998), the material did not appear to have any significant variation in the microstructure following UAG.

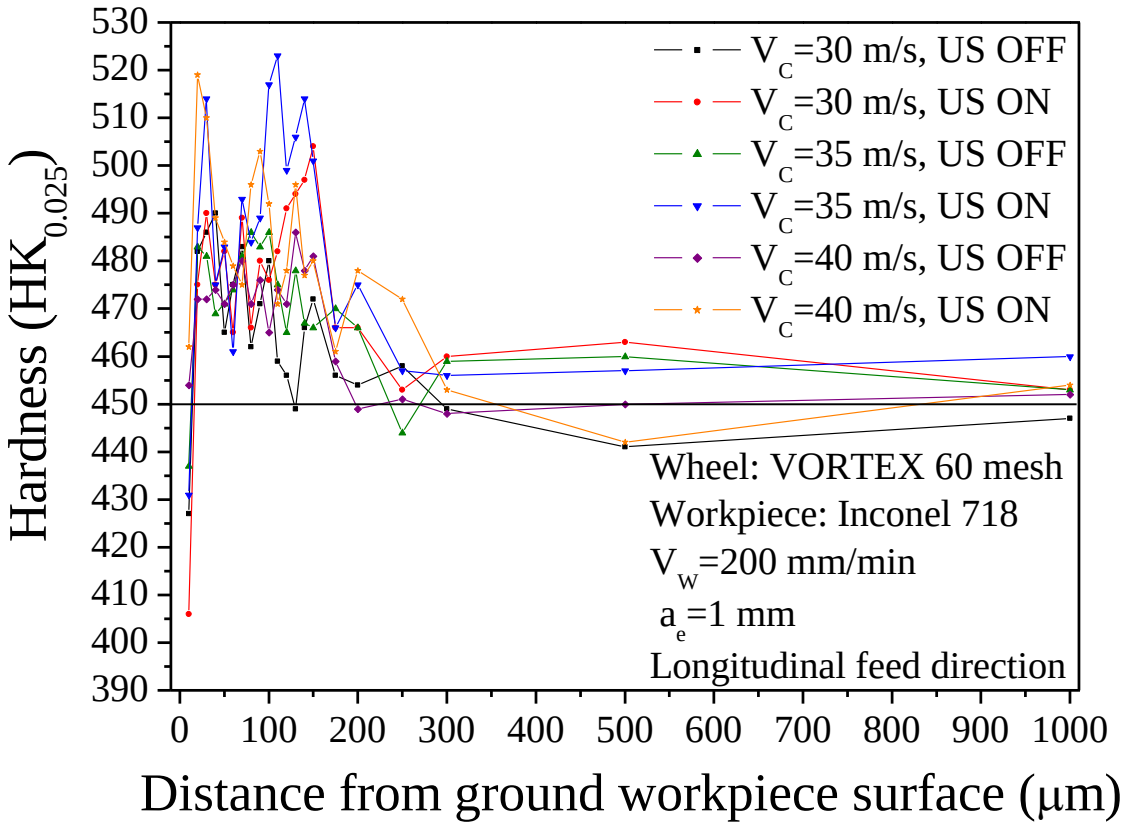


Fig. 4.2.47 Microhardness depth profile of Inconel 718 samples ground at V_W=200 mm/min; measurements taken in longitudinal feed direction

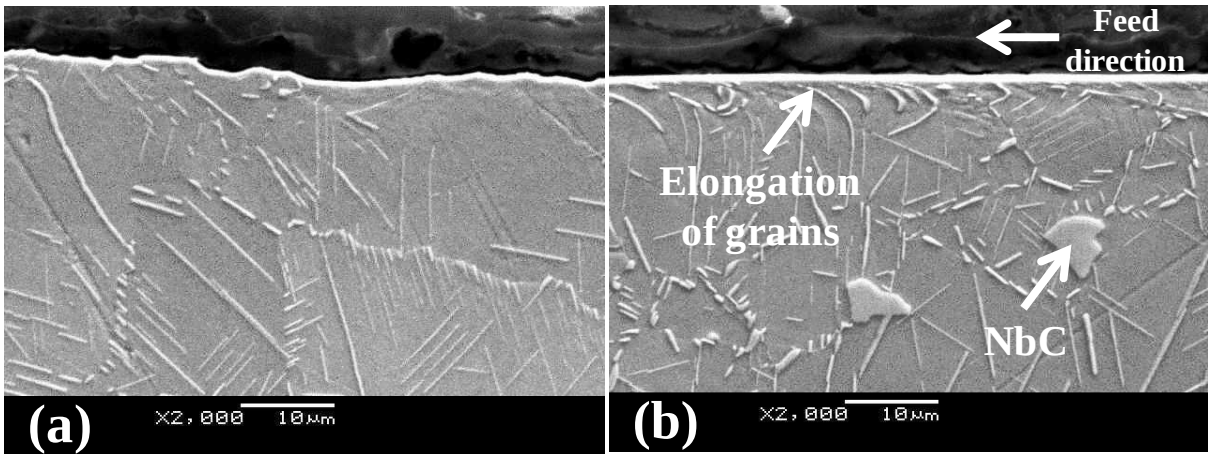


Fig. 4.2.48 SEM micrographs of microstructures of Inconel 718 on (a) Transverse feed plane, (b) Longitudinal feed plane; ground at V_C = 40 m/s, V_W = 300 mm/min, d = 1.0 mm, US ON

The major findings from Phase 2C are summarised as:

- The employment of ultrasonic vibration resulted in reductions in F_v in 5 out of 9 tests by up to ~20%, whereas F_h decreased in all of experiments. The maximum reduction in F_h was ~60% however it typically decreased by ~10-30% in the majority of trials subject to vibration.
- Radial wheel wear typically varied between 12-27 μm with the corresponding G-ratio varying between ~3 to 6. Wheel wear generally increased (with a maximum reduction in G-ratio by ~60%) when grinding was employed with ultrasonic assistance.
- In general, both R_a and S_a of the ground surfaces increased (by up to ~25% and ~49% respectively) in trials involving ultrasonic actuation. Greater amounts of plastic deformation and consequent side flow/ploughing were observed on specimens subject to vibration.
- Reductions in S_a and S_{ds} of the resin replicating surfaces together with larger voids/pores in between the grains were observed following UAG.
- With the assistance of US vibration, sub-surface microhardness typically increased by 6-8%.
- There was no difference in the microstructures of the specimens ground with and without ultrasonic assistance.

4.2.4 Phase 2D: Assessment of UAG on CMSX-4 using POROS2 wheel

4.2.4.1 Grinding forces

Figure 4.2.49 shows the vertical and horizontal forces obtained when grinding CMSX-4 with and without the assistance of ultrasonic vibration.

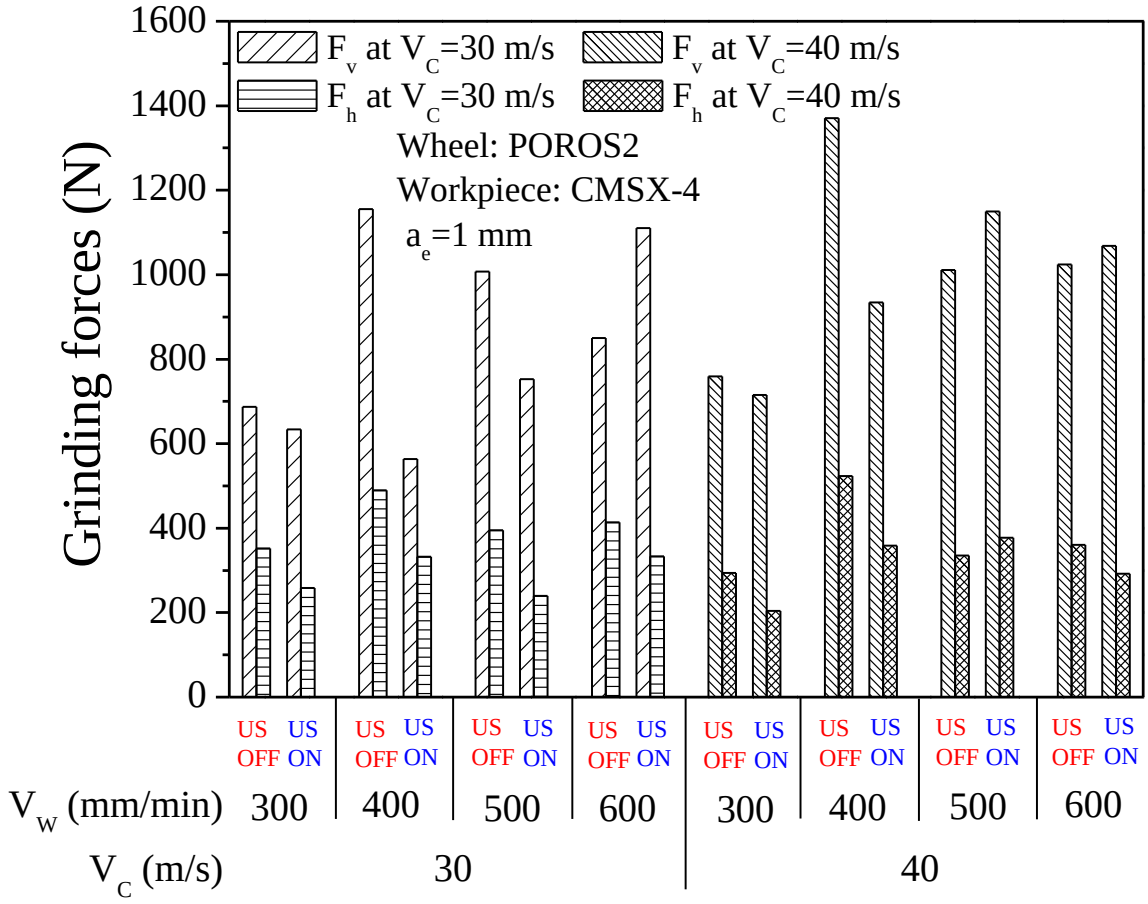


Fig. 4.2.49 Vertical (F_v) and horizontal (F_h) forces under different grinding conditions

Both F_v and F_h typically decreased (by up to 51% and 39% respectively) in the majority of tests involving ultrasonic vibration compared to conventional CFG. This was possibly due to the alternate engagement and disengagement of the individual cutting edges with the work surface during UAG resulting in an intermittent cutting action of the abrasives as well as reduction in contact time between the workpiece and the abrasive grains, leading to a decrease in frictional forces (Spur and Holl, 1996) under the hybrid mode. This also contributed to a reduction in the thermal load on the grits as well as smaller average chip thicknesses when grinding with ultrasonic assistance (Spur and Holl, 1997, Uhlmann, 1998).

The main effects and interaction plots for F_v and F_h are shown in Figs. 4.2.50 and 4.2.51 respectively. The associated ANOVA analysis showed that vibration had a significant effect on horizontal component of grinding force with a PCR of 35.66% whereas it was statistically insignificant for F_v with a PCR of only 7.21%.

Figure 4.2.50 further showed that F_v generally increased with an increase in wheel speed from 30 to 40 m/s over the range of table speeds tested. This observation was similar to that by Hwang et al. (2000), who reported an escalation of vertical grinding force when using a faster wheel speed due to the increase in sliding length per unit volume of the material removed. This resulted in generation of wear flats, thereby increasing the rubbing and ploughing components of F_v. Vertical grinding force also typically increased with an increase in table feed due to an increase in undeformed chip thickness. Analysis of variance showed that both V_C and V_W and an interaction between V_W and vibration condition ($V_W \times$ Vib) had significant influences on F_v with PCR's of 13.31%, 36.09% and 31.36% respectively, see Table 4.2.3.

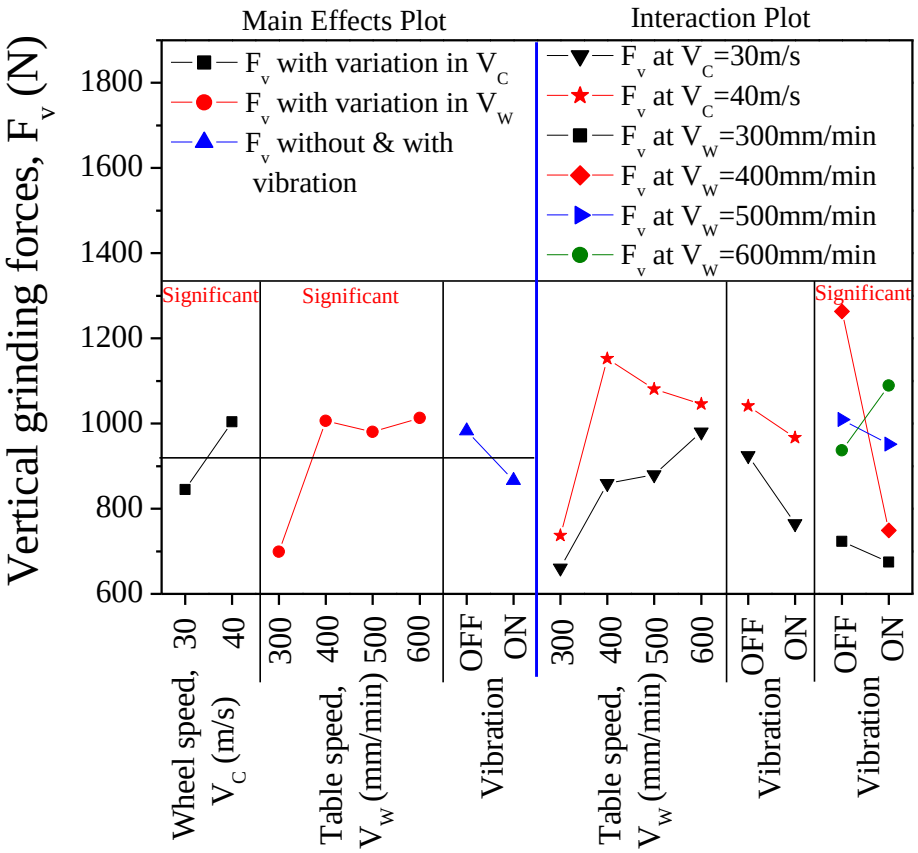


Fig. 4.2.50 Main effects and interaction plots for vertical grinding force

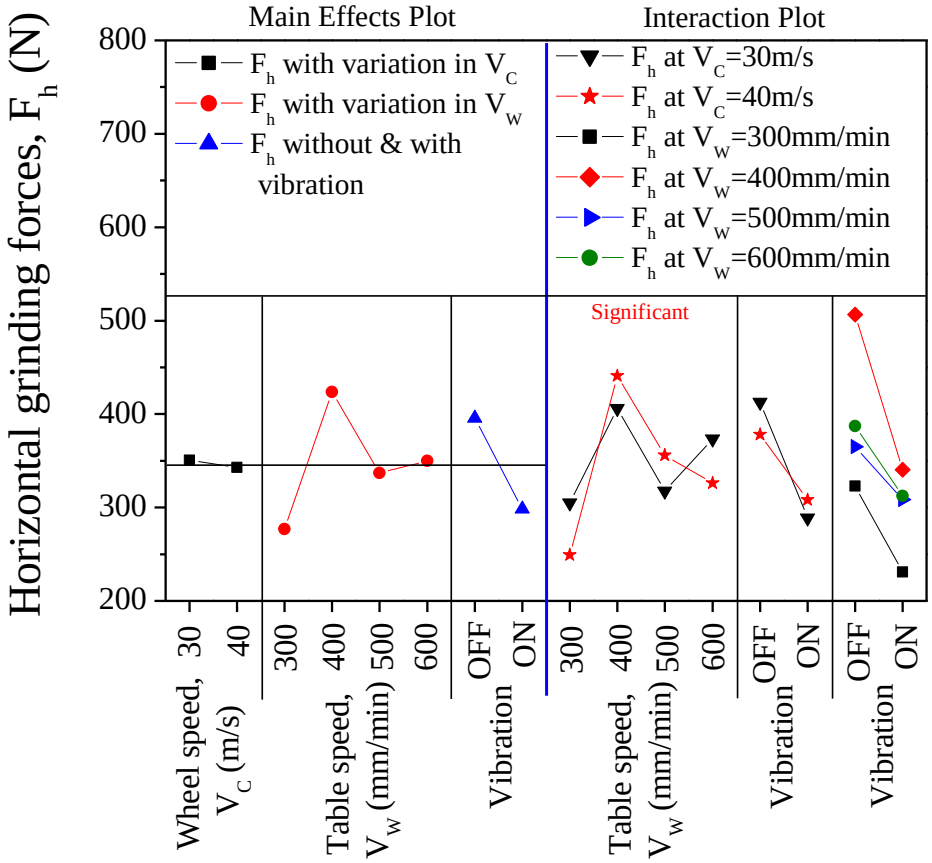


Fig. 4.2.51 Main effects and interaction plots for horizontal grinding force

Table 4.2.3 Percentage contribution ratios of factors with respect to different response measures (Phase 2D)

Factors	**Percentage contribution ratios (PCR's)**								
	F_v	**F_h**	**G-ratio**	**W/P R_a**	**W/P S_a**	**Graphite R_a**	**Graphite S_a**	**Resin replica S_a**	**Resin replica S_{ds}**
Wheel speed (V_C)	13.31*	0.21	0.81	36.00*	0.70	14.58*	0.10	1.03	0.68
Table feed (V_W)	36.09*	40.97	17.01	7.50	40.30*	39.34*	23.15*	18.57*	47.84
Vibration (Vib)	7.21	35.66*	0.92	21.00*	20.30*	20.61*	9.10*	12.45*	7.23
V_C×Vw	4.63	7.42	57.21*	13.30	15.50	1.54	20.21*	31.75*	10.43
V_C×Vib	0.95	2.80	0.34	2.40	12.10*	0.53	0.22	17.87*	3.73
V_W×Vib	31.36*	6.54	9.41	6.50	4.70	20.30*	41.72*	1.13	17.01
V_C×V_W×Vib	6.45	6.39	14.30	13.30	6.40	3.10	5.50	17.20*	13.08
* Statistically significant factors at the 5% level									

Figure 4.2.51 showed that F_h marginally decreased with an increase in cutting speed from 30 to 40 m/s, however did not show any particular trend with a rise in table feed. Although the contribution of V_W for F_h (PCR of 40.97%) was the maximum amongst all factors, its effect on F_h was not significant at 5% level.

4.2.4.2 Radial wheel wear and G-ratio

Figure 4.2.52 details the radial wheel wear and G-ratio of the POROS2 wheel when grinding CMSX-4. G-ratio varied from ~4 to 6 in conventional CFG. Liu et al. (2007) reported wheel G-ratio within ~1 to 3 when grinding CMSX-4 with alumina based wheels (60E and 60F) at wheel speeds of 35-55 m/s, a table speed of 1500 mm/min and a depth of cut of 2 mm.

Wheel wear decreased (G-ratio improved by 6 to 25%) in 4 out of 8 trials involving ultrasonic vibration (Tests 2, 4, 10 and 14), although it increased (G-ratio decreased by 7 to 39%) in other four tests utilising hybrid configuration. The higher wheel wear was possibly due to the effect of ultrasonic oscillation radial to the wheel surface resulting in greater mechanical loads (Spur and Holl, 1997) on the abrasive grains leading to micro-splintering and fracture of the grains and the associated bond. The main effects and interaction plots for G-ratio, shown in Fig. 4.2.53, indicated that the factor 'vibration condition' was not 'significant' with a very low PCR of 0.92% only. An interaction of table feed and vibration condition (V_W × Vib) had a relatively higher PCR of 9.41%, although it was statistically insignificant, see Table 4.2.3.

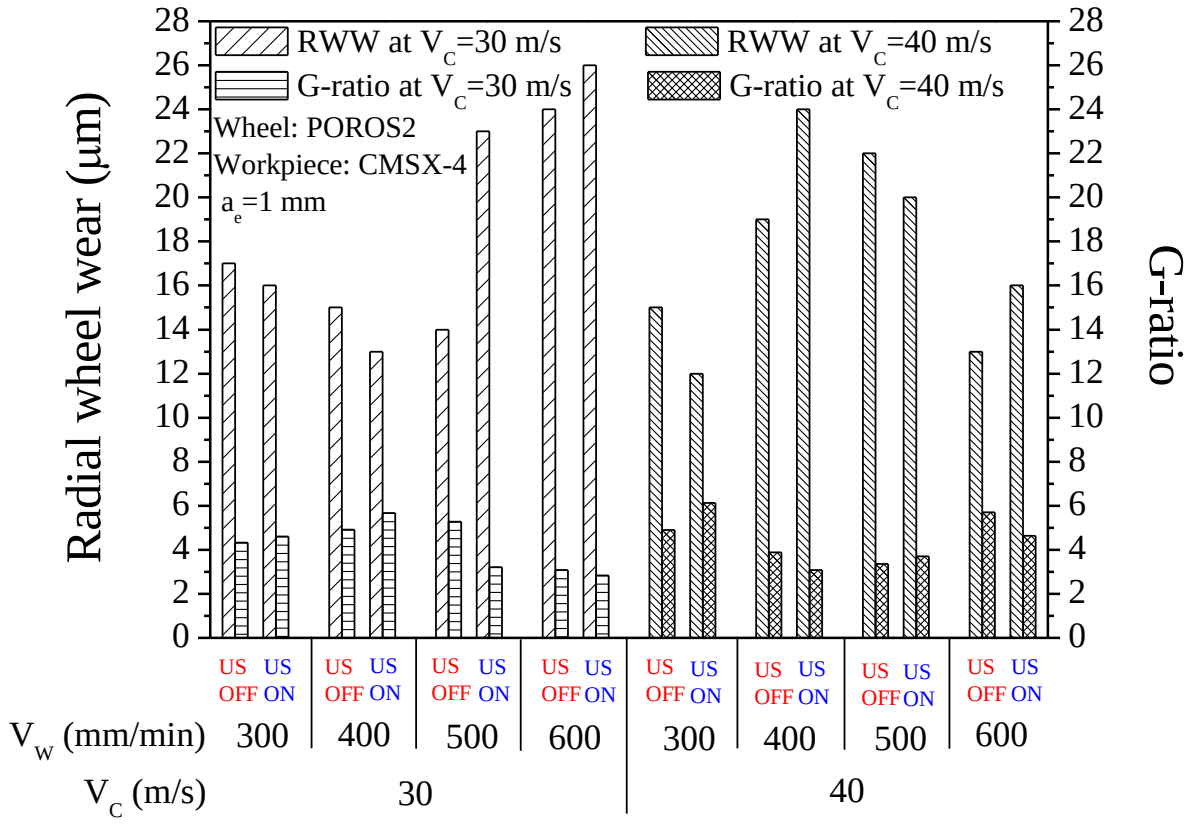


Fig. 4.2.52 Radial wheel wear and G-ratio of the POROS2 wheel when grinding CMSX-4 under different operating conditions

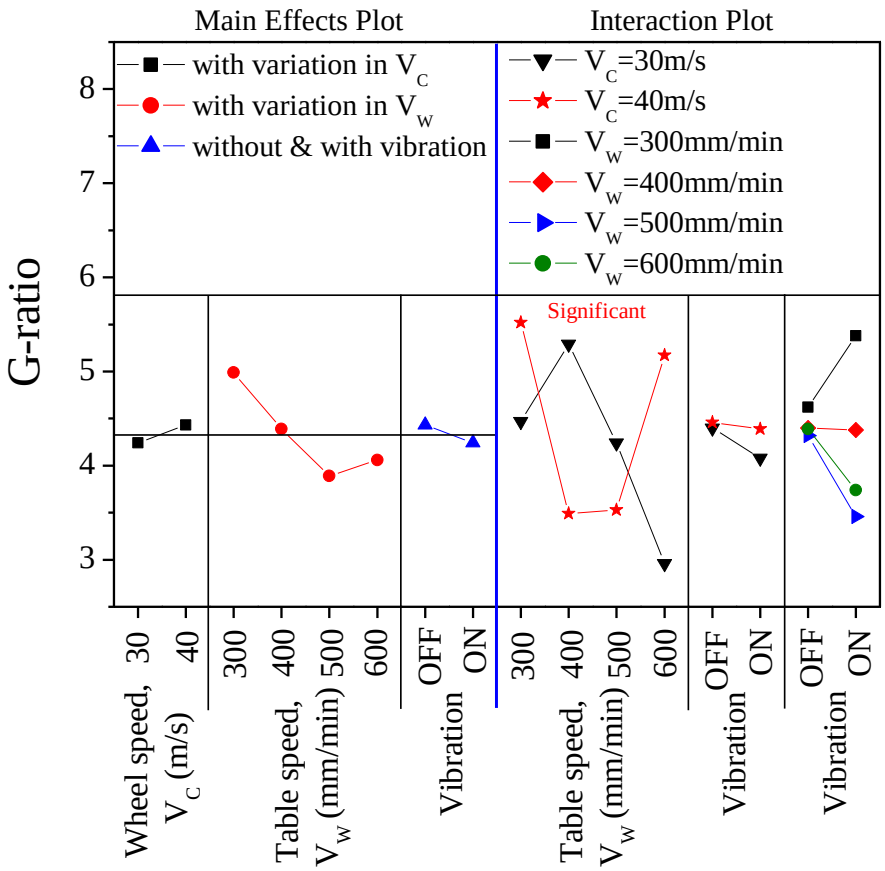


Fig. 4.2.53 Main effects and interaction plots for wheel G-ratio

Wheel G-ratio increased with an increase in wheel speed but decreased with a rise in table speed up to 500 mm/min. Although the sole effects of V_C and V_W on G-ratio were statistically insignificant, their interaction ($V_C \times V_W$) had a significant influence with a PCR of 57.21%, see Table 4.2.3.

4.2.4.3 Workpiece surface topography and quality

Figure 4.2.54(a) and (b) show surfaces ground with and without ultrasonic assistance at grinding conditions of V_C=30m/s, V_W=400mm/min and V_C=40m/s, V_W=300mm/min respectively. None of the ground specimens exhibited any signs of burn, depressions or chatter marks; irrespective of operating conditions/parameters. The 2D (R_a) and 3D surface parameters (S_a, S_t, S_z) of the ground workpieces are detailed in Fig. 4.2.55 and 4.2.56 respectively. Both R_a and S_a typically decreased with an increase in wheel speed due to the reduction of number of grits in contact with the work surface, however they increased with a rise in table feed because of higher undeformed chip thickness.

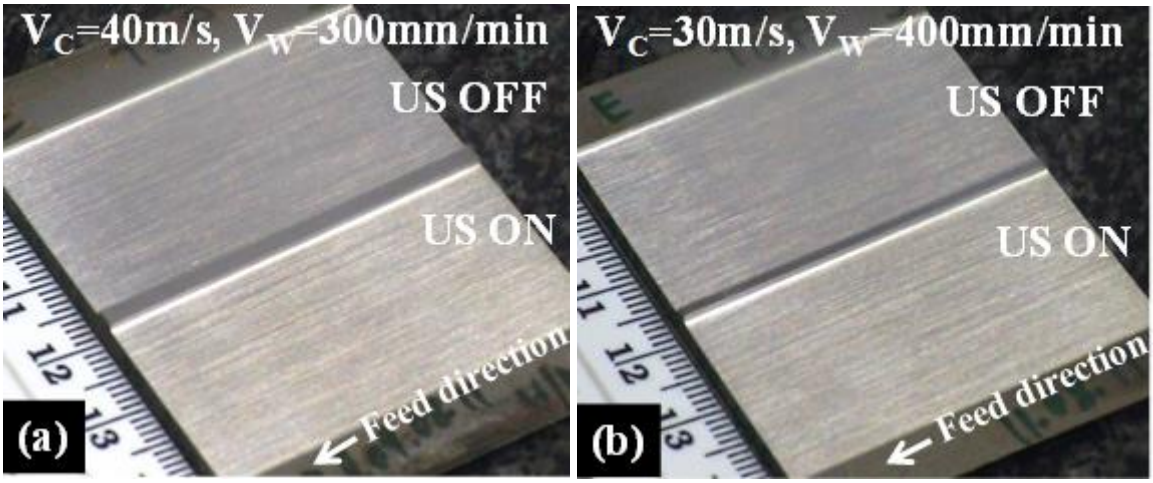


Fig. 4.2.54 Images of CMSX-4 workpiece surfaces ground at different operating conditions

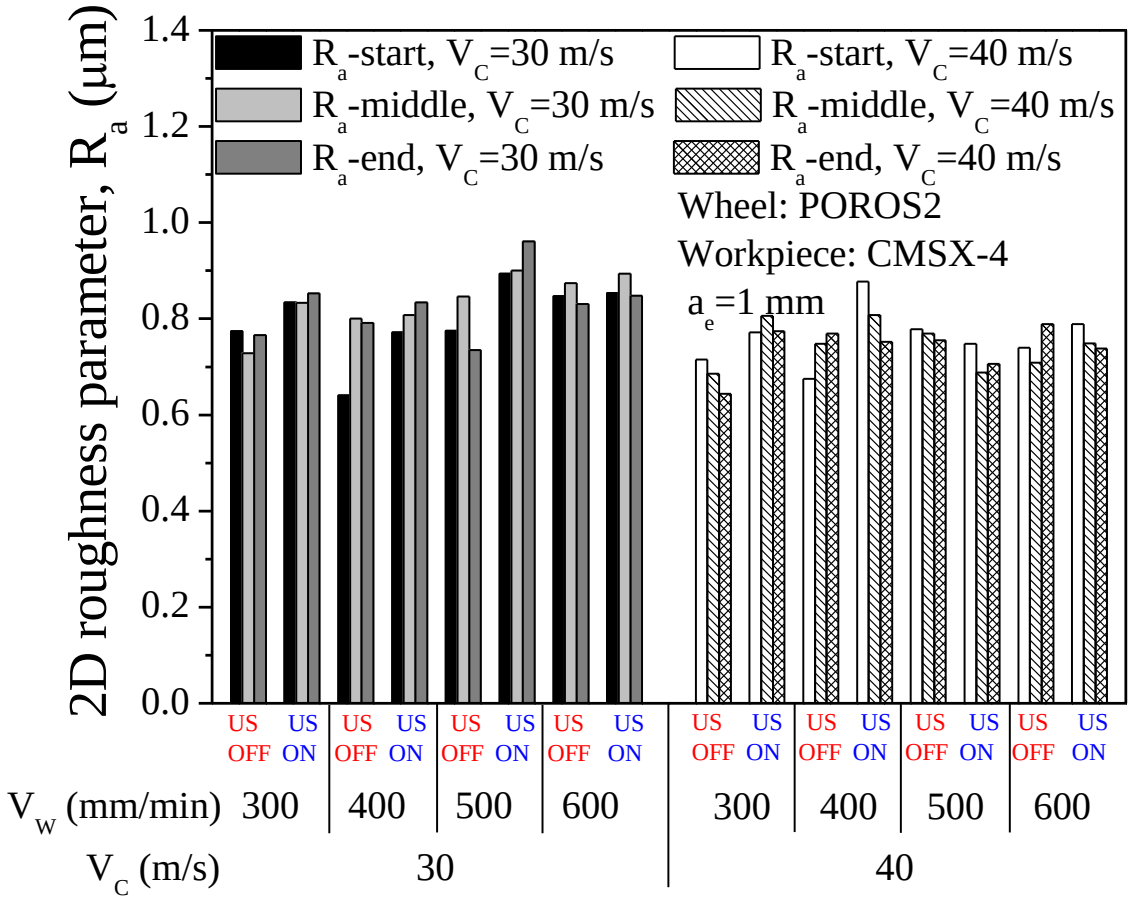


Fig. 4.2.55 2D roughness parameter (R_a) of ground CMSX-4 workpiece surfaces

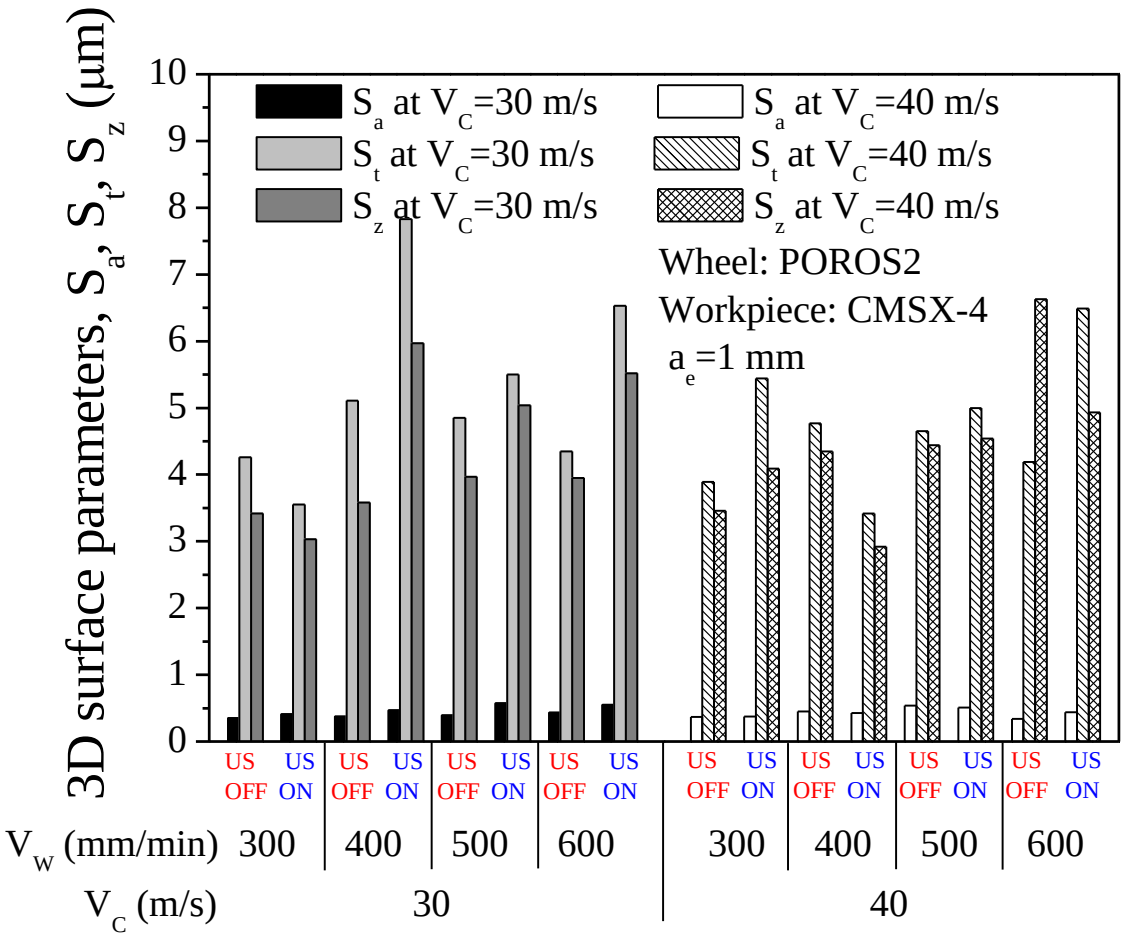


Fig. 4.2.56 3D topographical parameters of ground CMSX-4 workpiece surfaces

Fig. 4.2.56 further reveals that S_t and S_z typically increased in 6 and 5 out of 8 tests, respectively, associated with ultrasonic vibration. This could be due to the effect of the vibration component in the Z-direction (i.e. perpendicular to the work surface), which resulted in a greater penetration of the grits into the work surface. A consequent effect of this was reflected on the S_p, S_v and skewness parameters of the ground surfaces. Both S_p and S_v increased in 6 out of 8 trials, whereas surfaces with higher/more negative skewness were obtained when grinding under UAG mode.

The main effects and interaction plots for R_a, shown in Fig. 4.2.57, and the associated ANOVA analysis indicated that wheel speed had a significant effect on R_a with a PCR of 36%, see Table 4.2.3, however it was insignificant for S_a (not shown here) with a negligible PCR of 0.70% only. Conversely, table feed was statistically significant for S_a (PCR of 40.30%) but not for R_a (PCR of 7.50%). A general trend also showed that workpiece surface roughness increased when grinding with ultrasonic assistance. Vibration had significant contributions to both R_a and S_a with comparable PCR's of 21% and 20.30% respectively. This was possibly due to the higher plastic deformation induced by the greater mechanical impact

under the action of vibration. The SEM micrographs of ultrasonic assisted ground surfaces also corroborated this observation where greater side flow/ploughing, smearing of material together with overlapping cut/grit marks are seen, see Fig. 4.2.58(c) to (f). Conversely, conventionally ground specimens exhibited typical grit marks in the feed direction, see Fig. 4.2.58(a) and (b). This observation was similar to those obtained for the machined Inconel 718 surfaces in the previous phases (Phase 2B and 2C).

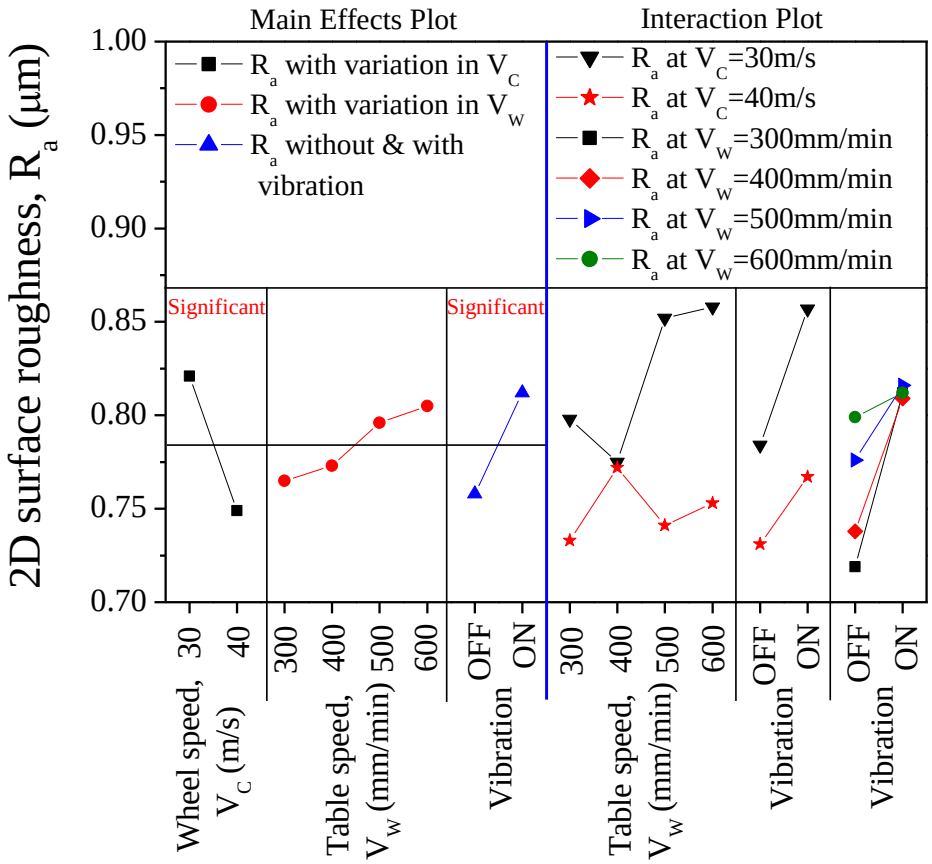


Fig. 4.2.57 Main effects and interaction plots for 2D surface roughness (R_a) of ground CMSX-4 workpieces

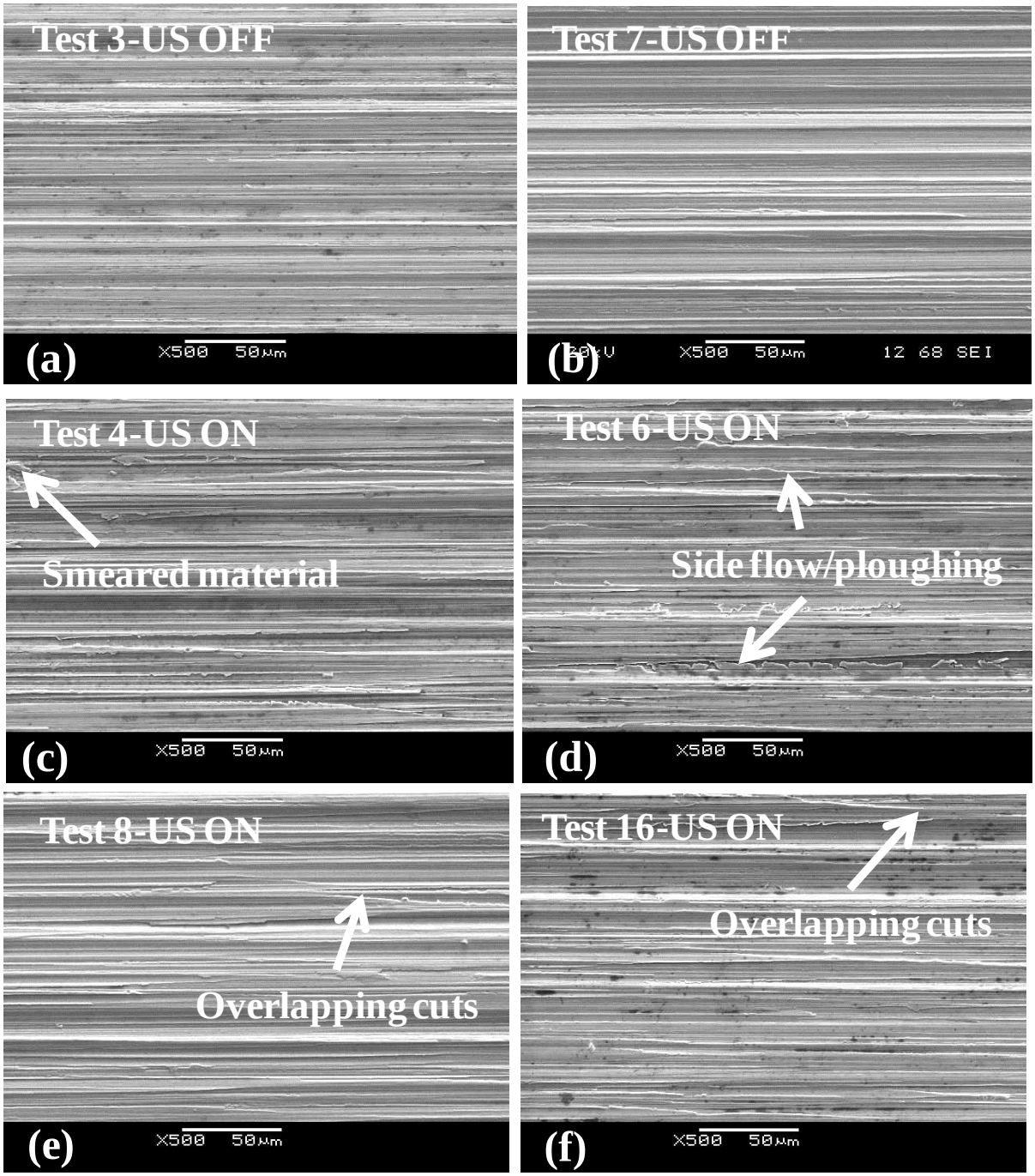


Fig. 4.2.58 SEM micrographs of ground workpiece surfaces (a) Test 3: V_C=30 m/s, V_W=400 mm/min, US OFF, (b) Test 7: V_C=30 m/s, V_W=600 mm/min, US OFF, (c) Test 4: V_C=30 m/s, V_W=400 mm/min, US ON, (d) Test 6: V_C=30 m/s, V_W=500 mm/min, US ON, (e) Test 8: V_C=30 m/s, V_W=600 mm/min, US ON, (f) Test 16: V_C=40 m/s, V_W=600 mm/min, US ON

4.2.4.4 Grinding wheel surface evaluation

Figure 4.2.59 details the 2D and 3D surface parameters (R_a and S_a) of the graphite replicas of the POROS2 wheel. Both R_a and S_a typically increased when grinding was carried out with the assistance of vibration. This observation was in agreement with the higher surface

roughness values obtained for the ground CMSX-4 specimens subject to vibration. The higher average roughness of the post-grinding wheel surface could be attributed to the greater mechanical impact and the consequent micro-splintering of alumina grits as well as the associated bond caused by the radial component of vibration (along Z-direction).

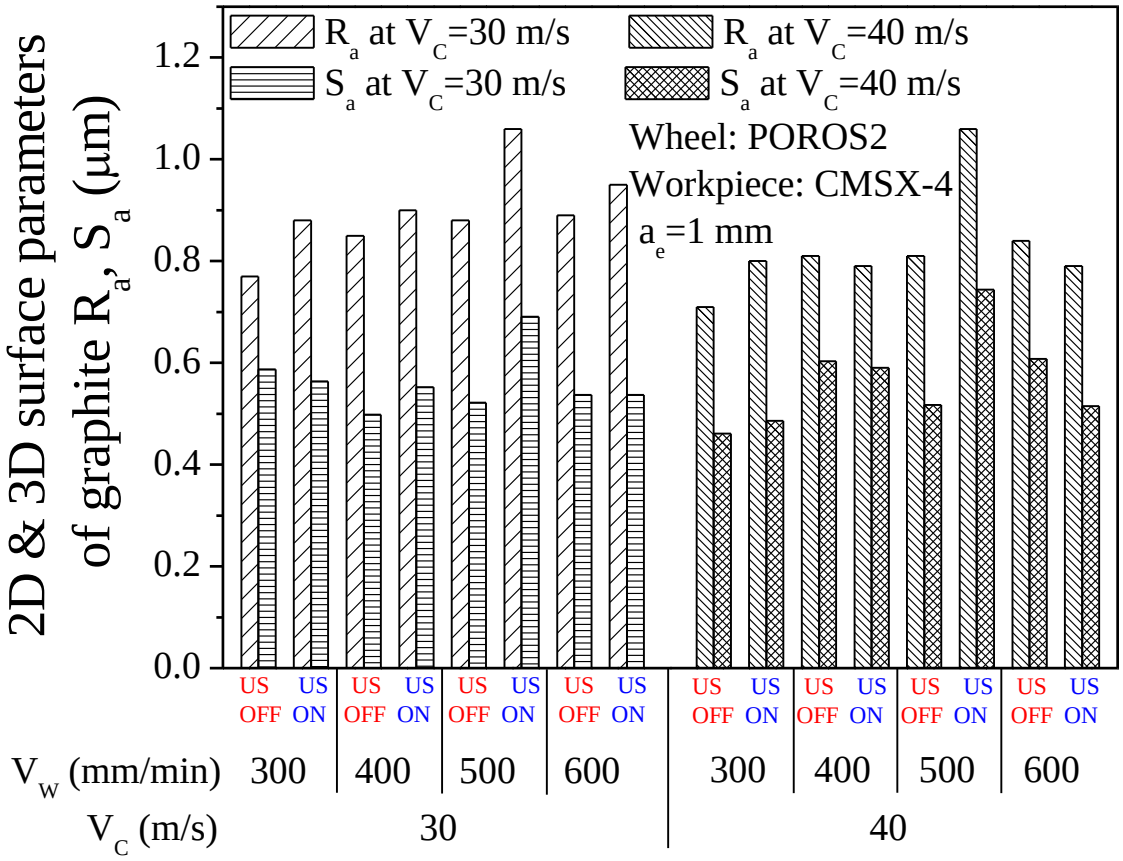


Fig. 4.2.59 2D and 3D surface parameters of graphite (negative) replicas of grinding wheel

Figure 4.2.60 shows the main effects and interaction plot for R_a. Both R_a and S_a (although the main effects plot for S_a not shown here) were significantly influenced by the sole effect of vibration, with respective PCR's of 20.61% and 9.10%, as well as an interaction between table feed and vibration (V_W × Vib), with PCR's of 20.30% and 41.72% respectively, see Table 4.2.3.

Figure 4.2.60 further revealed that graphite surface roughness (R_a) typically decreased with an increase in wheel speed irrespective of other operating conditions, however R_a increased with an increase in table feed from 300 to 500 mm/min and dropped subsequently at a table feed of 600 mm/min. Similar trend was also obtained with S_a of the graphite replicas. The fall in R_a and S_a at the table feed of 600 mm/min could possibly be due to the loss of grain sharpness. The observation can be supported by the higher vertical force data recorded at 600 mm/min (see Fig. 4.2.50). While comparing Fig. 4.2.57 with Fig. 4.2.60, it can be

inferred that loss of grain sharpness at a faster table feed could not produce lower workpiece roughness as increased side flow/ploughing and overlapping grit marks were always prevalent on the surfaces subject to ultrasonic vibration.

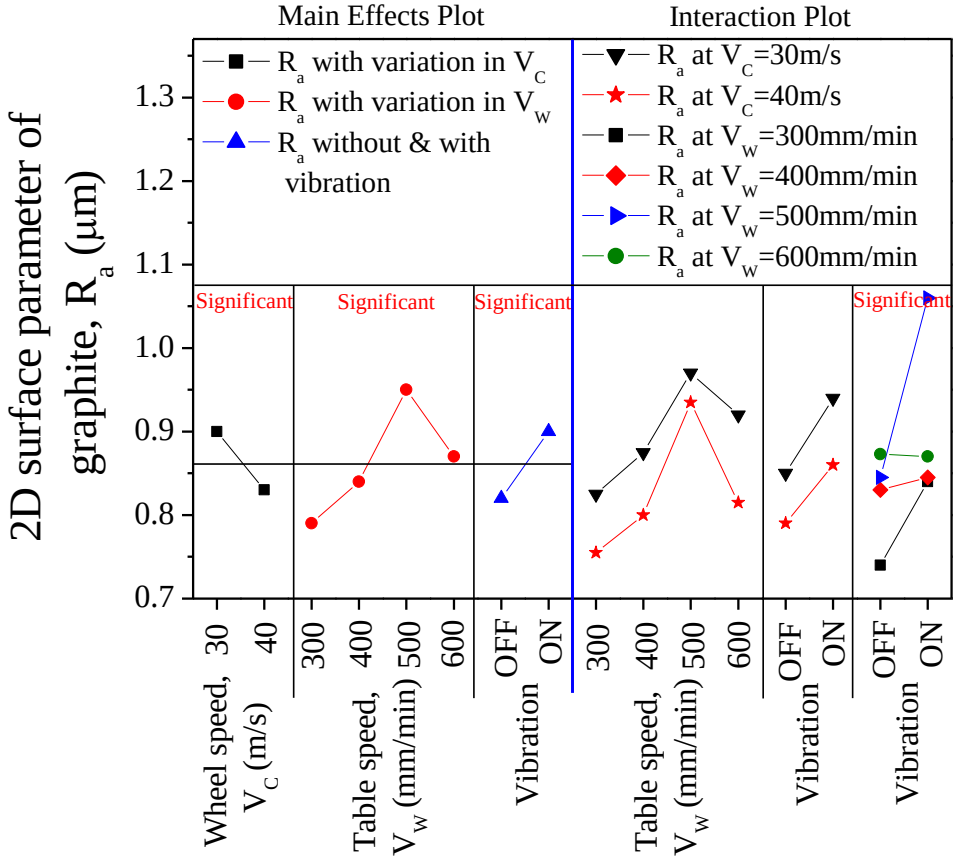


Fig. 4.2.60 Main effects and interaction plots for 2D surface roughness (R_a) of graphite (negative) replicas of the POROS2 wheel

Both wheel speed and table feed had significant influences on graphite R_a (PCR's of 14.58% and 39.34% respectively), although only table feed was statistically significant for S_a of the replicating surfaces (PCR of 23.15%). An interaction between wheel speed and table feed ($V_C \times V_W$) also had significant contribution to graphite S_a (PCR of 20.21%), see Table 4.2.3.

Figure 4.2.61 details the S_a and S_{ds} parameters obtained from the topographical measurements of the resin replicas. Resin surface S_a typically decreased (6 out of 9 tests) while S_{ds} generally increased (7 out of 9 trials) when grinding with vibration assistance. This suggested that the wheel had undergone 'conditioning effect' under the action of vibration together with an increase in active cutting point density (Butler et al., 2002). The main effects and interaction plots for S_a, shown in Fig. 4.2.62, indicated that the effect of vibration was statistically significant with a PCR of 12.45%.

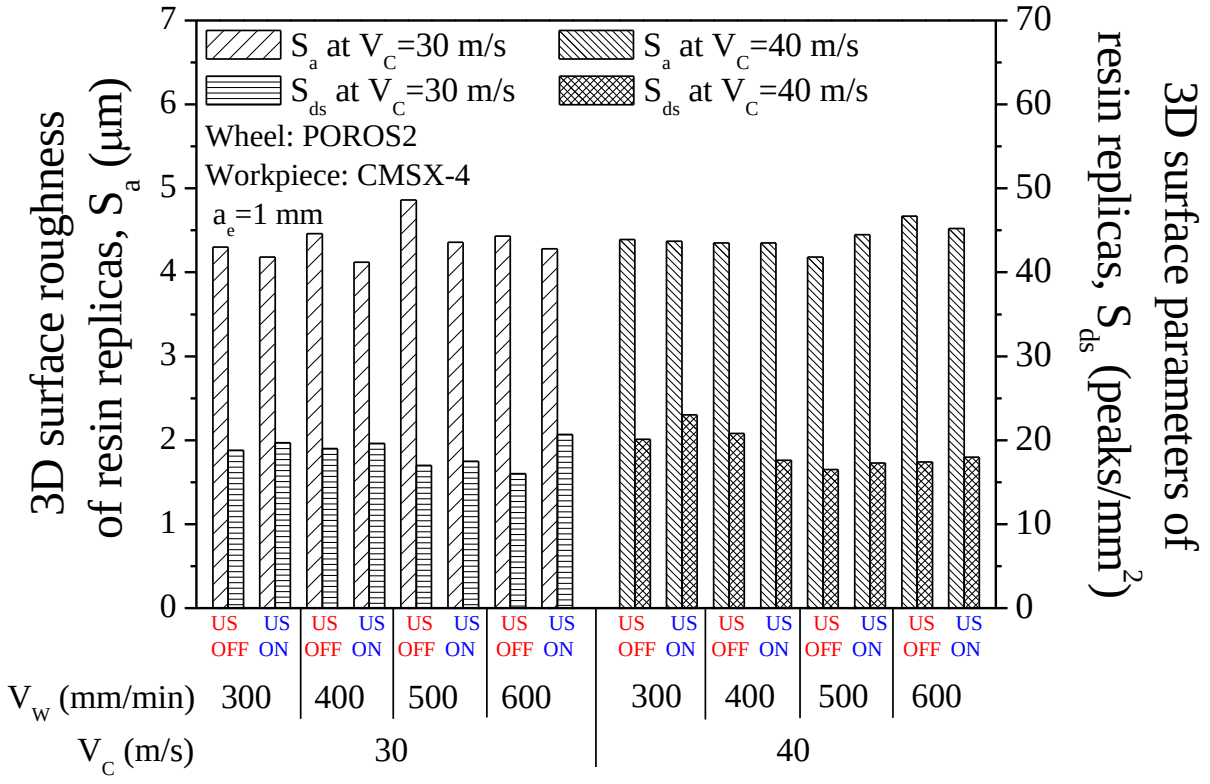


Fig. 4.2.61 3D topographical parameters of resin (positive) replicas of grinding wheel

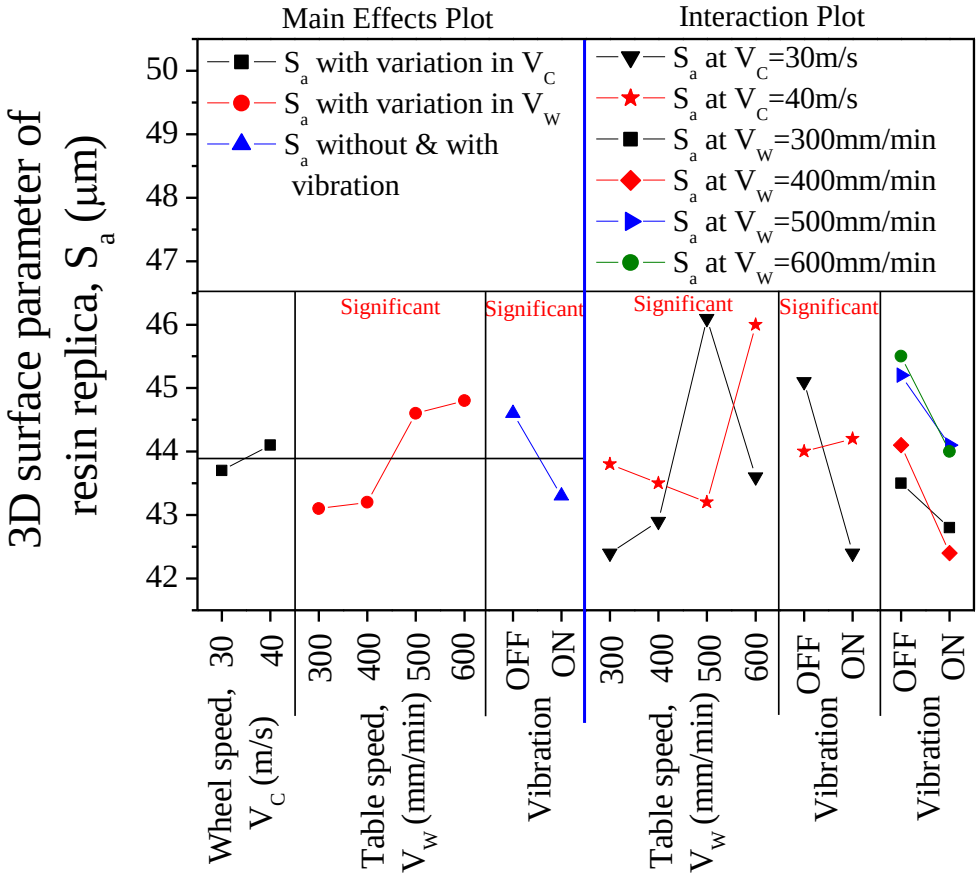


Fig. 4.2.62 Main effects and interaction plots for 3D surface parameter (S_a) of resin (positive) replicas of the POROS2 wheel

Figure 4.2.62 further showed that wheel S_a marginally increased with a rise in wheel speed but it significantly escalated with an increase in table feed. This was possibly due to a greater degree of wheel wear and consequent loss in the uniformity of grain protrusions at a faster table feed. The PCR's of table feed and an interaction between wheel speed and table feed ($V_C \times V_W$) for wheel S_a were 18.57% and 31.75% respectively with both factors statistically significant.

Figure 4.2.63 details the main effects and interaction plots for wheel S_{ds} parameter. Wheel S_{ds} marginally increased when a faster wheel speed of 40 m/s was used, although it typically decreased with an increase in table feed (with the exception at a V_W of 600 mm/min). Despite considerably high PCR of table feed (47.84%), it was statistically insignificant for S_{ds} parameter. The interactions between wheel speed and table feed ($V_C \times V_W$) and between table feed and vibration ($V_W \times$ Vib) also had moderate PCR's (10.43% and 17.01% respectively), although none of them were significant at 5% level.

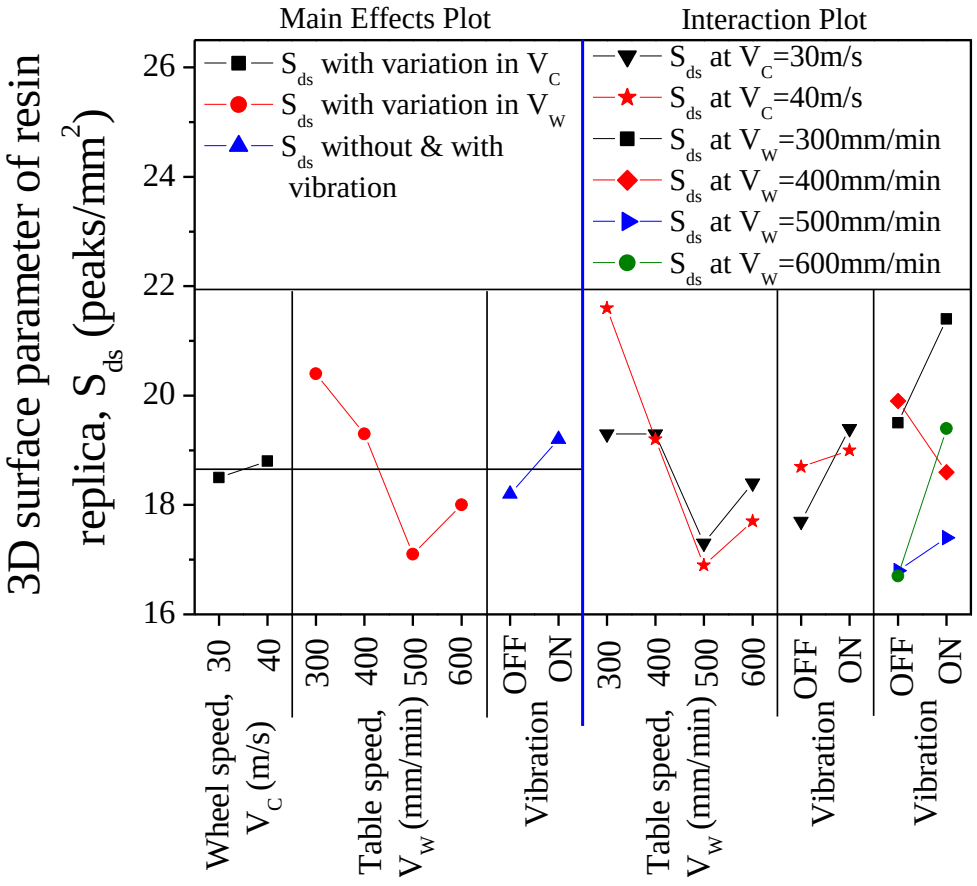


Fig. 4.2.63 Main effects and interaction plots for 3D surface parameter (S_{ds}) of resin (positive) replicas of the POROS2 wheel

The SEM micrographs of selected resin replicas in Fig. 4.2.64 showed larger voids/pores in between the abrasive particles when subject to US vibration, compared to those observed

following conventional CFG. This suggested that greater grit/bond fracture occurred under the hybrid mode, which possibly resulted in a higher wheel wear and increased workpiece surface roughness typically seen when operating with ultrasonic assistance.

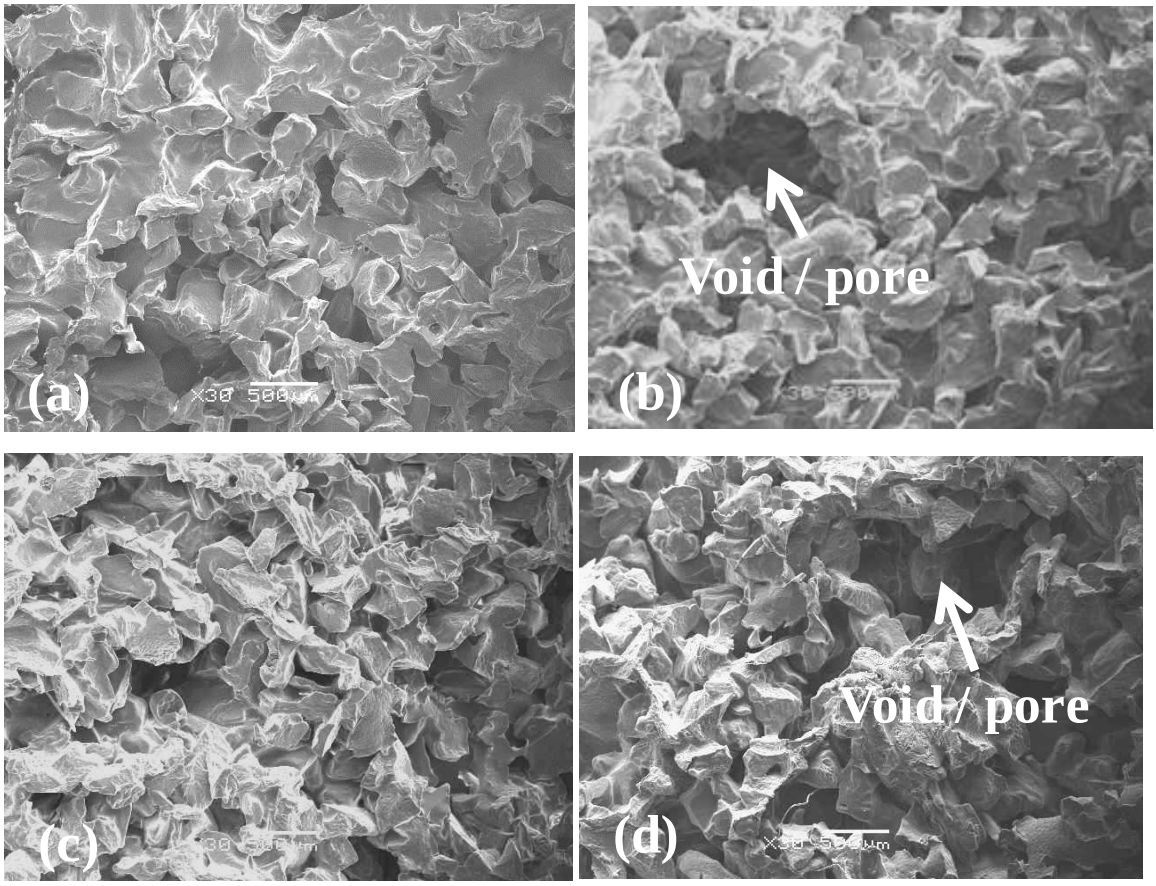


Fig. 4.2.64 SEM micrographs of POROS2 wheel resin replicas taken after (a) Test 11: V_C=30 m/s, V_W=300 mm/min, US OFF, (b) Test 2: V_C=30 m/s, V_W=300 mm/min, US ON, (c) Test 7: V_C=30 m/s, V_W=600 mm/min, US OFF, (d) Test 10: V_C=40 m/s, V_W=300 mm/min, US ON

4.2.4.5 Microhardness and workpiece microstructure

Figures 4.2.65 and 4.2.66 show the microhardness depth profiles of selected CMSX-4 samples ground at a wheel speed of 40 m/s. The other microhardness depth profiles of specimens ground at a V_C of 30 m/s are shown in Figs. A5.1 and A5.2 in Appendix A5. Although there exists a competition between thermal softening and work hardening when the workpiece material is subjected to high grinding temperature as well as large grinding pressure (Ding et al., 2010a), the rate of thermal softening behaviour is always much greater when machining nickel based superalloys than that of the work hardening effects in the process of the plastic deformation and alteration of sub-surface microstructure (Hood et al., 2007b). However Figs. 4.2.65 and 4.2.66 apparently showed no sign of soft region but a

hardened layer from a depth of 10 µm below the machined surface up to a depth of ~140 to 150 µm irrespective of operating conditions, suggesting that workpiece burning was avoided. The bulk hardness (~390$HK_{0.025}$) was achieved at a depth of ~200 to 250 µm beneath the ground surface. The microhardness was marginally higher by up to ~6% when measured in the longitudinal feed plane compared to that measured in the transverse feed plane. This was possibly due to the deformation of γ' phase under the action of cutting points/grits in the table feed direction, see Fig. 4.2.67.

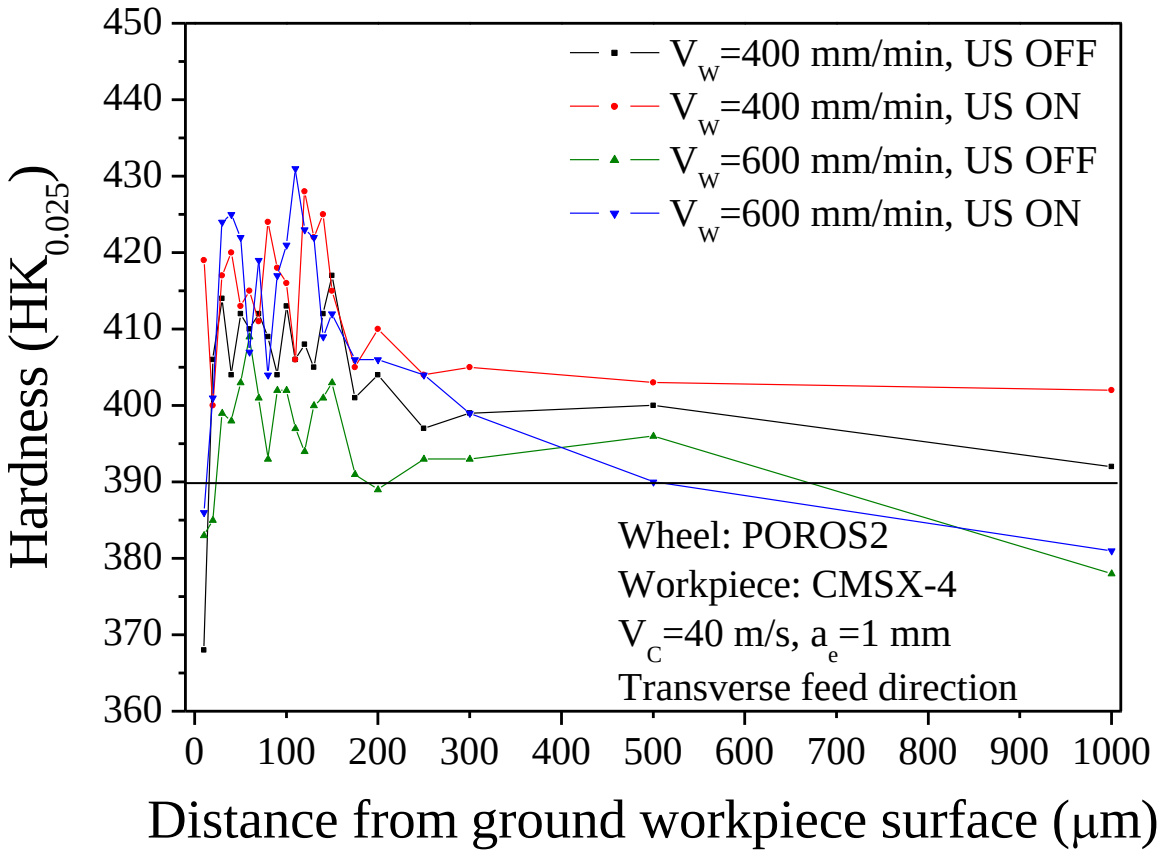


Fig. 4.2.65 Microhardness depth profile of CMSX-4 samples ground at V_C=40m/s; measurements taken in the transverse feed direction

With the assistance of ultrasonic vibration, sub-surface microhardness typically increased by ~5-10% compared to those ground with conventional CFG. This could be attributed to the greater plastic deformation occurred during machining with vibration assistance, which was also evident from the SEM micrographs of ground workpieces, see Fig. 4.2.58. The maximum average microhardness was recorded as 444$HK_{0.025}$ when UAG at a cutting speed and feed rate of 40 m/s and 600 mm/min respectively, which was 13% higher than the bulk hardness value (~390$HK_{0.05}$).

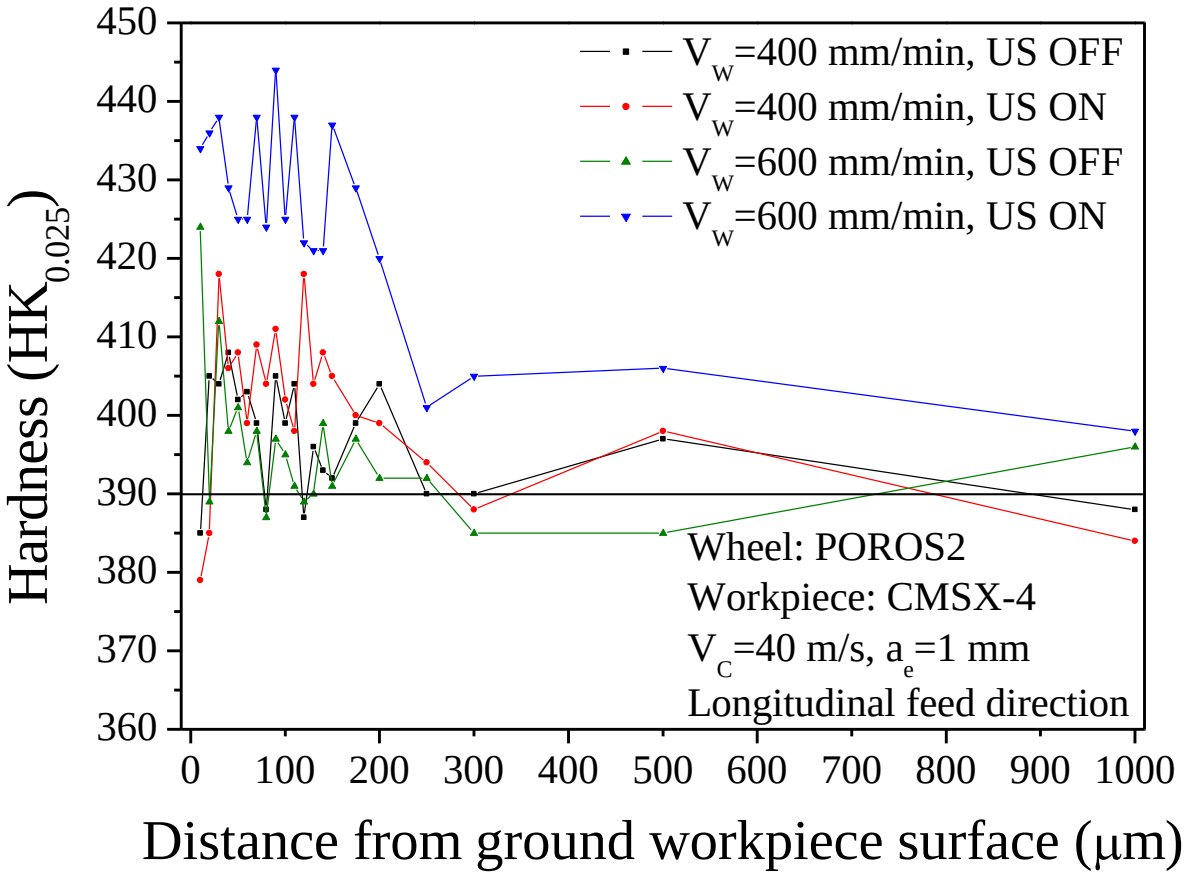


Fig. 4.2.66 Microhardness depth profile of CMSX-4 samples ground at V_C=40m/s; measurements taken along longitudinal feed direction

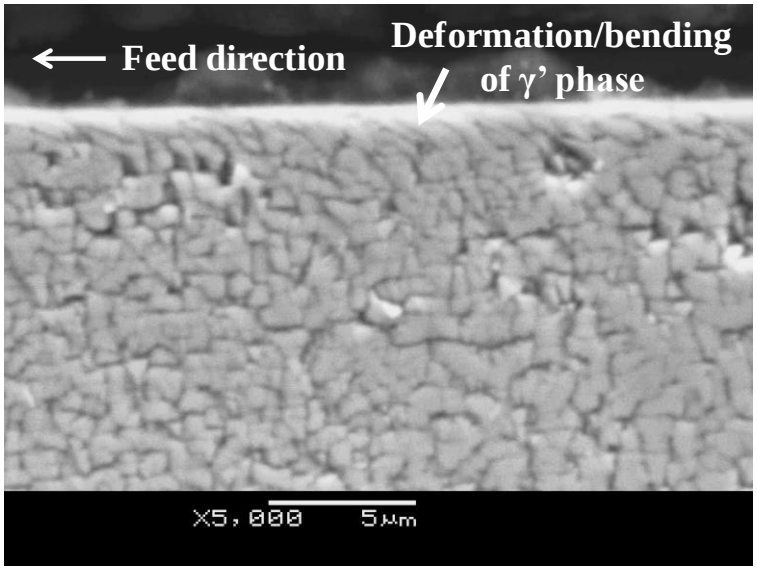


Fig. 4.2.67 Microstructure of CMSX-4 on longitudinal feed plane showing deformation/bending of γ' phase

The optical micrographs of the microstructures of selected CMSX-4 samples ground without and with ultrasonic assistance are shown in Fig. 4.2.68(a) and (b) respectively. No

discerning change in the microstructure was observed between the specimens ground conventionally or under hybrid mode.

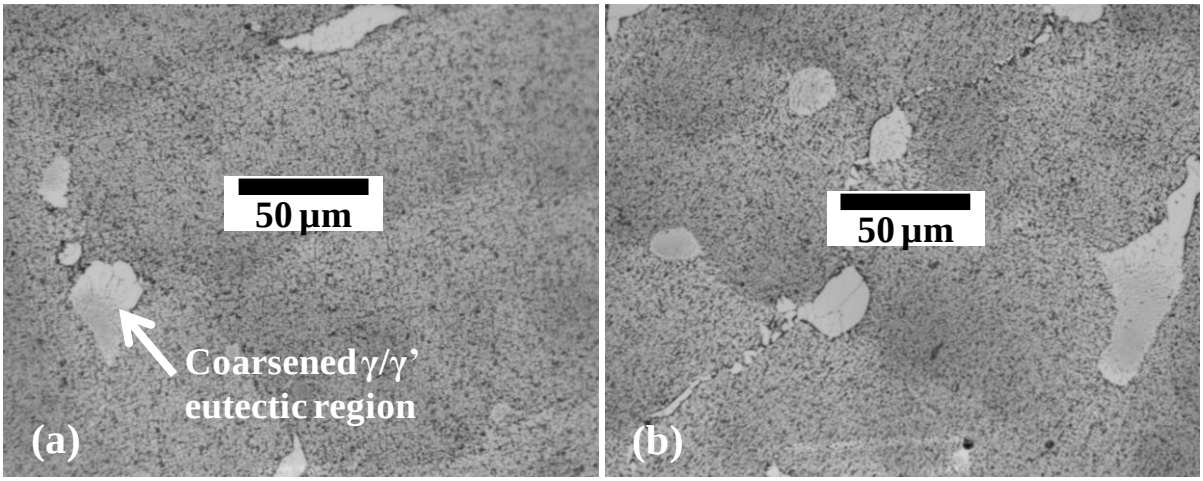


Fig. 4.2.68 Microstructures of CMSX-4 on transverse feed plane ground at V_C = 30 m/s, V_W = 400 mm/min, d = 1.0 mm, (a) US OFF, (b) US ON

Typical grit marks were observed when the microstructures were evaluated on the transverse feed plane, see Fig. 4.2.69, in contrast to when viewed on the longitudinal feed plane, see Fig. 4.2.67, although deformation of cuboidal γ' phases can be seen beneath the machined surface in the latter case. None of ground specimens showed any signs of white layer formation, cracks, tears, laps, folds etc, which suggested that the operating parameters were suitable for a defect-free machining of CMSX-4.

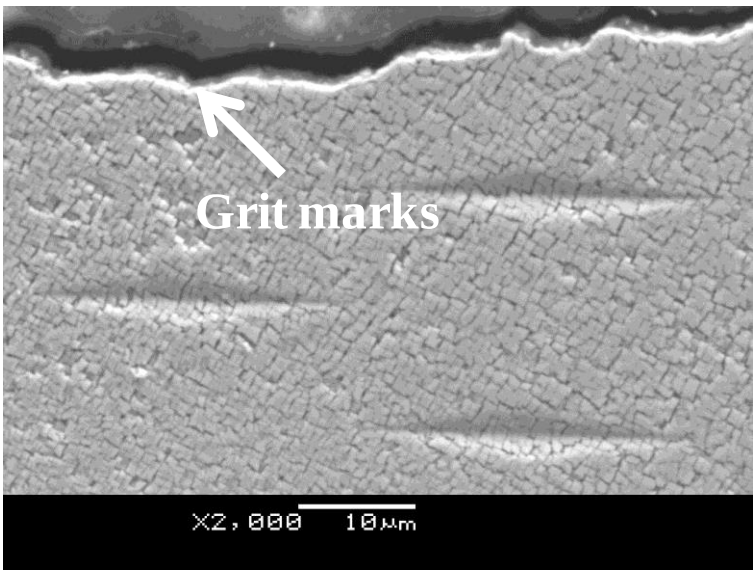


Fig. 4.2.69 Microstructure of CMSX-4 on transverse feed plane showing typical grit marks

The key observations from the Phase 2D trials are as follows:

- Vertical and horizontal grinding forces decreased by up to 51% and 39%, respectively, when UAG of CMSX-4. Higher wheel wear (7-39% lower G-ratio) was also observed in some tests involving vibration.
- The R_a and S_a of ground workpieces typically increased (by up to ~15% and 28% respectively) when grinding was employed with vibration. Additionally greater plastic deformation, side flow/ploughing, smearing of material and overlapping cuts were observed on the surfaces subject to vibration.
- Sub-surface microhardness generally increased from a depth of 10 µm below the ground surface up to a depth of 140 to 150 µm until reaching the bulk hardness (~390$HK_{0.025}$) at a depth of ~200 to 250 µm. With the assistance of ultrasonic vibration, sub-surface microhardness typically increased by ~5-10% in comparison to specimens CFG without vibration.
- The microstructure of CMSX-4 showed a high volume fraction of strengthening ordered γ' phase particles homogenously distributed in the continuous γ matrix of nickel based austenitic phase. Deformation/bending of γ' phase was observed in the longitudinal feed plane with a depth of deformation of ~5 µm. No white layer formation, or any cracks/tearing was seen in any of the specimens assessed.

4.2.5 Phase 2E: Effect of depth of cut and vibration amplitude when UAG of Inconel 718

4.2.5.1 Grinding forces and power

The forces recorded when grinding Inconel 718 with varying amplitude of vibration and wheel depth of cut using conventional and hybrid configurations are shown in Fig. 4.2.70.

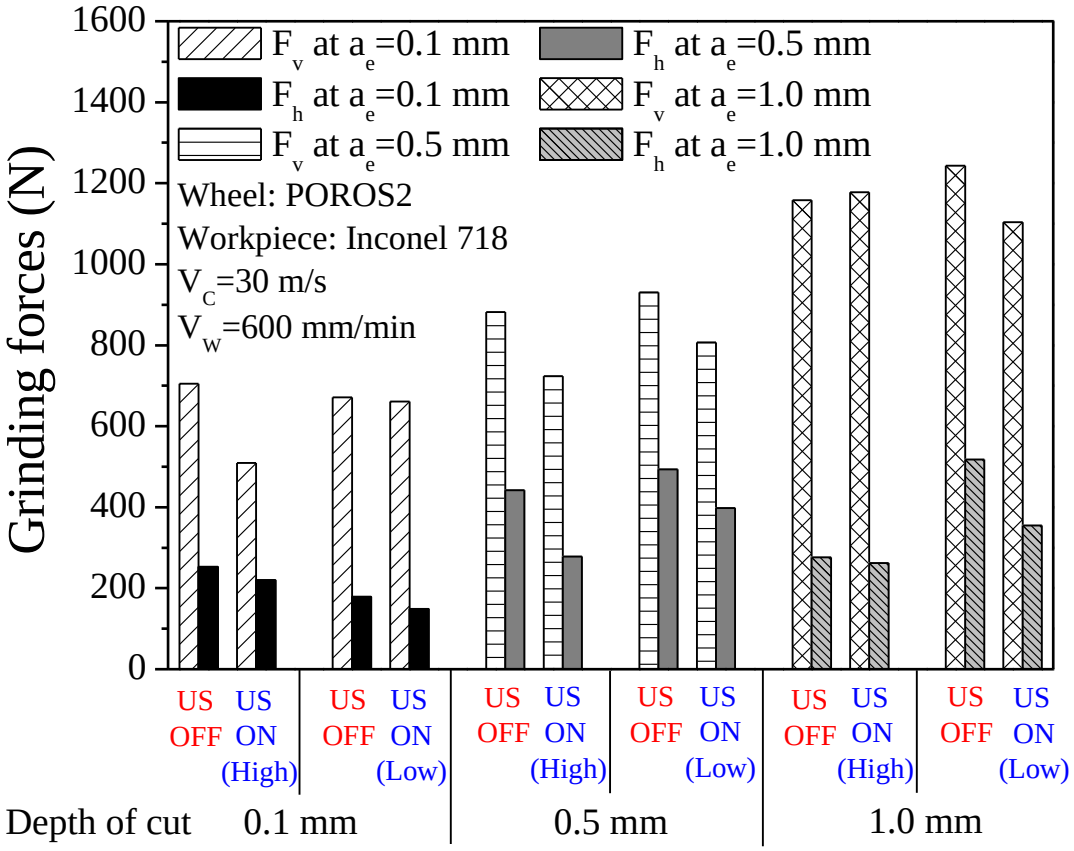


Fig. 4.2.70 Vertical (F_v) and horizontal (F_h) forces under different grinding conditions

Both vertical and horizontal force components typically increased with an increment in depth of cut from 0.1 to 1.0 mm due to an increase in the undeformed chip thickness as well as chip length (with the exception of Tests 9 and 10, where F_h decreased at a depth of cut of 1.0 mm compared to that recorded at an a_e of 0.5 mm). The majority of tests involving ultrasonic vibration exhibited reductions in F_v and F_h by up to 28% and 37% respectively. According to Uhlmann and Sammler (2010), the ultrasonic amplitude must be greater than the uncut chip thickness in order to ensure that the contact between tool and workpiece is intermittently broken by the vibration. The uncut chip thickness, in the present study, was calculated as ~0.33 µm at a depth of cut of 1 mm, whereas the amplitude of vibration at the 'Low' setting was ~2 to 4 µm. Therefore the decrease in force levels during UAG can

possibly be related to a reduction of thermal load on the abrasive grits, caused by the discontinuous cutting action of the grains (Uhlmann, 1998). The anticipated lower temperatures most likely resulted in decreased localised welding/adhesion between the high asperities of the work surfaces, grits and loaded material within pores of the wheel (Yossifon and Rubenstein, 1982), thereby lowering frictional forces. The main effects and interaction plots for F_v, shown in Fig. 4.2.71, indicated that reduction in vertical force was typically higher when operating with the 'High' amplitude setting compared to the 'Low' amplitude mode. Similar trend was also observed for the horizontal grinding force (the main effects and interaction plots for F_h is shown in Fig. A6.1 in Appendix A6). The engagement of more active grits during cutting with the lower vibration amplitude could be a possible reason (this was also evident from the SEM micrographs of the wheel replicas shown in Section 4.2.5.4).

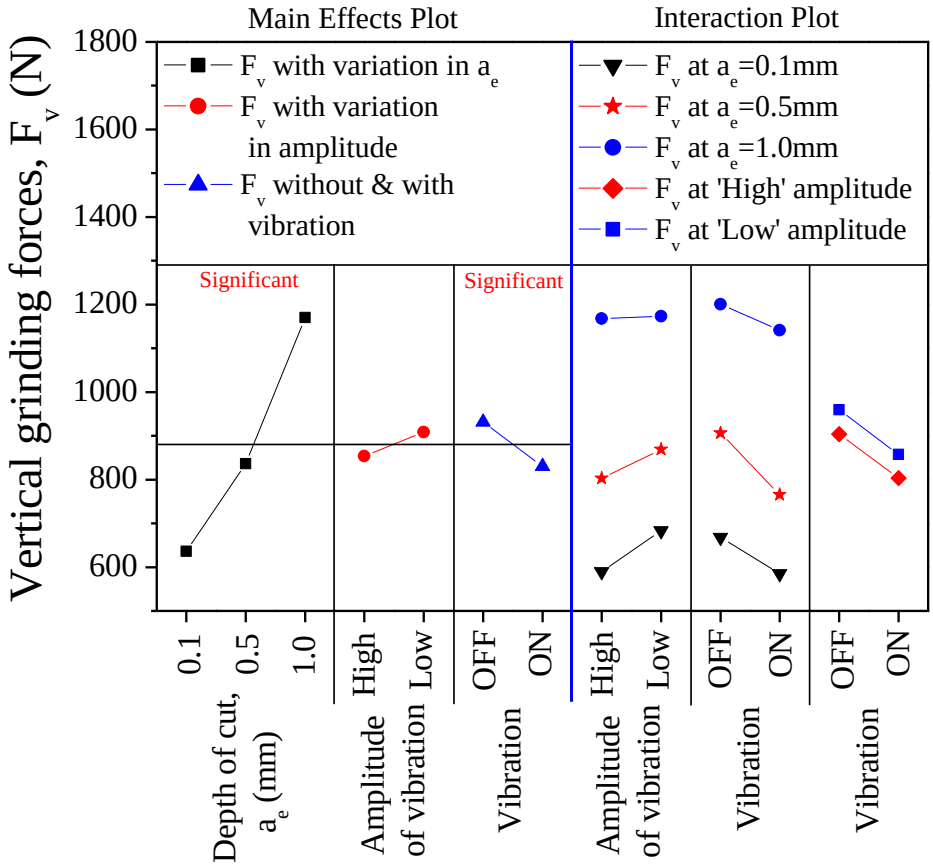


Fig. 4.2.71 Main effects and interaction plots for vertical grinding force

Both F_v and F_h were significantly influenced by depth of cut (PCR's of 91.07% and 54.96% respectively), while the contribution of vibration for F_v was relatively lower (4.80%), although it was statistically significant. Conversely, vibration condition and amplitude had comparatively higher PCR's for F_h (12.81% and 13.33% respectively) although they were not significant at 5% level, see Table 4.2.4.

Table 4.2.4 Percentage contribution ratios of factors with respect to different response measures (Phase 2E)

Factors	Percentage contribution ratios (PCR's)								
	F_v	**F_h**	**G-ratio**	**W/P R_a**	**W/P S_a**	**Graphite R_a**	**Graphite S_a**	**Resin replica S_a**	**Resin replica S_{ds}**
Depth of cut (a_e)	91.07*	54.96*	55.82*	22.09	20.84*	50.85	57.66*	31.29	19.66
Amplitude (Amp)	1.41	13.33	1.41	25.00*	55.17*	18.32	28.90*	20.53	1.72
Vibration (Vib)	4.80*	12.81	22.17*	0.44	6.17	4.22	4.70*	1.70	42.99*
ae×Amp	0.63	8.51	1.95	10.82	3.93	10.65	1.01	11.69	13.76
ae×Vib	0.52	2.99	8.41	6.15	9.35	6.57	0.32	6.95	2.68
Amp×Vib	0.00	2.60	3.70	21.13	0.67	5.29	1.34	9.91	1.04
ae×Amp×Vib	1.58	4.80	6.58	14.30	3.93	4.10	6.10	17.92	18.13
* Statistically significant factors at the 5% level									

The grinding power and the corresponding force levels measured when conventional and ultrasonic assisted grinding (with 'Low and 'High' amplitude of vibration settings) at fixed levels of V_C, V_W and a_e are shown in Figs. 4.2.72 and 4.2.73 respectively. Peak power decreased by ~5 to 6% when operating with ultrasonic assistance compared to conventional CFG. This was also supported by the corresponding force graph where ~5 to 25% reduction in F_v and F_h were observed under hybrid configuration. The peak power was also marginally lower when a 'High' amplitude setting was used compared to that obtained with the 'Low' amplitude.

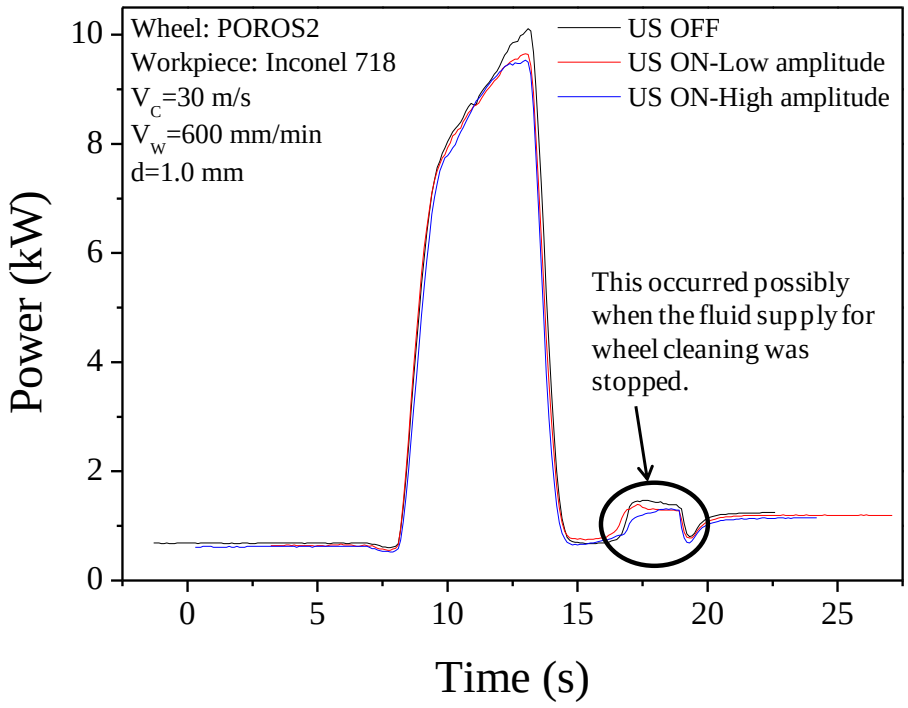


Fig. 4.2.72 Grinding power measured under conventional and ultrasonic assisted conditions

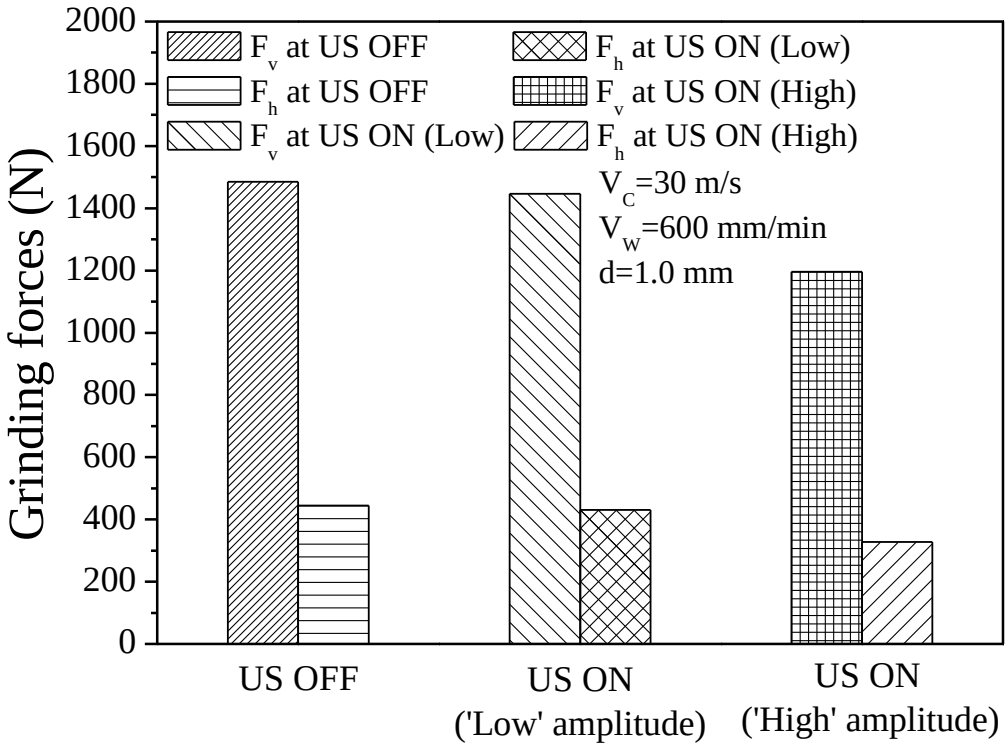


Fig. 4.2.73 Grinding forces measured when conventional and ultrasonic assisted grinding with varying amplitude of vibration

4.2.5.2 Radial wheel wear and G-ratio

The effects of depth of cut and amplitude of vibration on radial wheel wear and G-ratio are shown in Fig. 4.2.74. Wheel wear was found to be almost negligible (2 to 3μm) at a depth of cut of 0.1 mm when grinding was carried out without vibration. In general, radial wheel wear increased as depth of cut was varied from 0.1 to 1.0 mm. However, the main effects and interaction plots for wheel G-ratio in Fig. 4.2.75 similarly showed an increase with a rise in depth of cut, due to a greater percentage gain in volume of material removed than that of radial wheel wear. Table 4.2.4 showed that G-ratio was significantly influenced by depth of cut with a PCR of 55.82%.

When ultrasonic actuation was employed, wheel G-ratio reduced by 30 to 60% in 5 out of 6 tests. It was also observed that the ‘Low’ amplitude setting rendered marginally lower G-ratio than that obtained with the ‘High’ amplitude level. This can be explained from the lower force values obtained with the ‘High’ amplitude setting, which led to lower wheel wear (higher G-ratio). Although vibration condition had a significant influence on wheel G-ratio with a PCR of 22.17%, amplitude of vibration exhibited an insignificant effect with a PCR of 1.41% only. None of the interactions between the factors were statistically significant either, see Table 4.2.4.

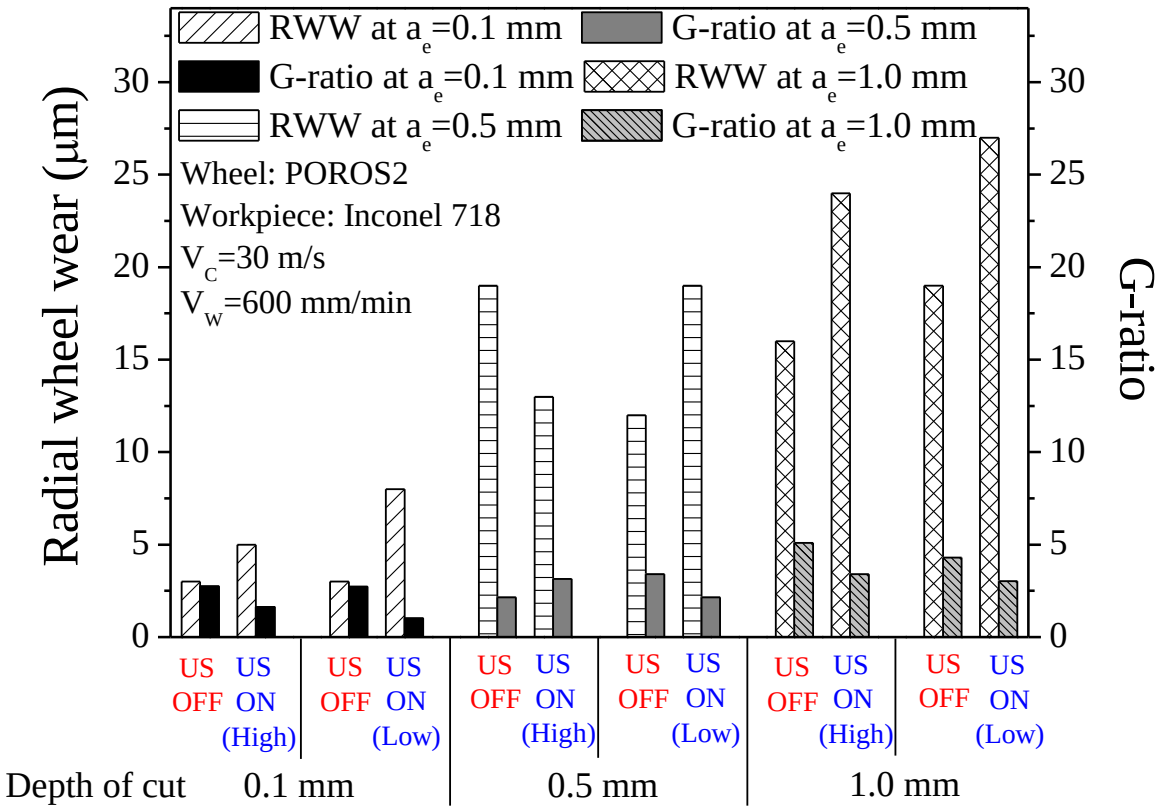


Fig. 4.2.74 Radial wheel wear and G-ratio under different grinding conditions

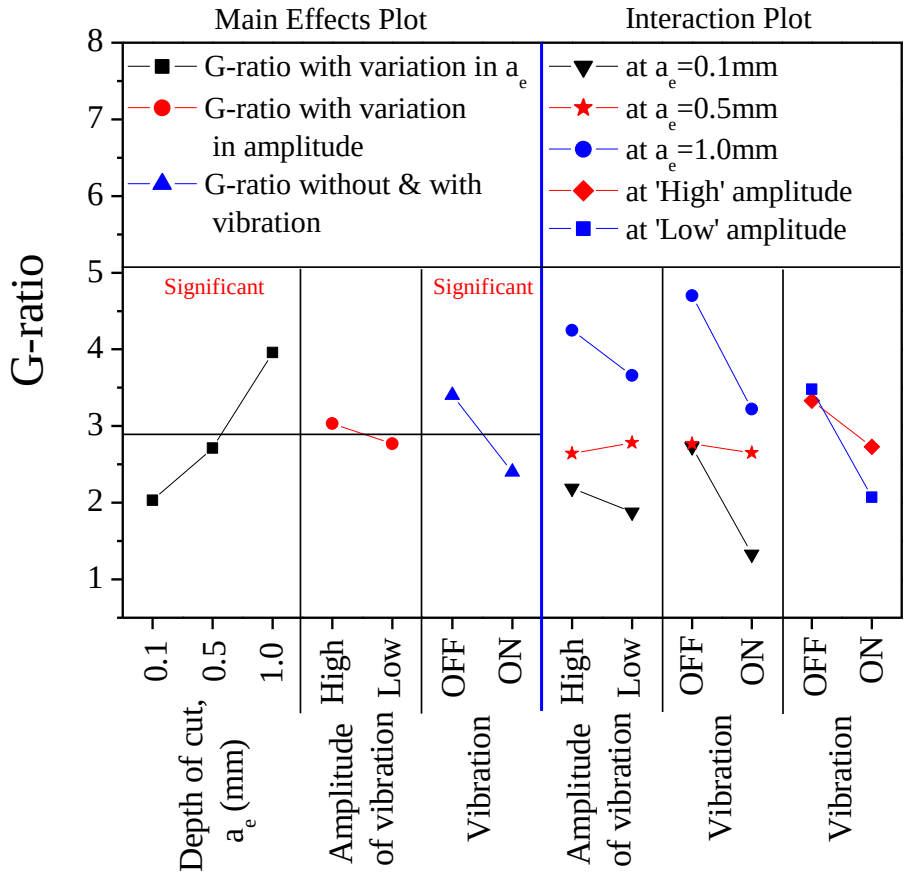


Fig. 4.2.75 Main effects and interaction plots for wheel G-ratio

4.2.5.3 Workpiece surface topography and quality

The images of Inconel 718 workpieces ground at different operating conditions are shown in Fig. 4.2.76. All machined surfaces were free from any indentation marks/deformed regions and grinding burn. Figures 4.2.77 and 4.2.78 detail 2D roughness (R_a) and 3D topographical parameters (S_a, S_t, S_z) respectively of the ground surfaces. R_a generally decreased from the start to the end of cut due to generation of wear flats on the grits as grinding progressed. However, no significant variation in R_a was observed with change in a_e from 0.1 to 1.0mm.

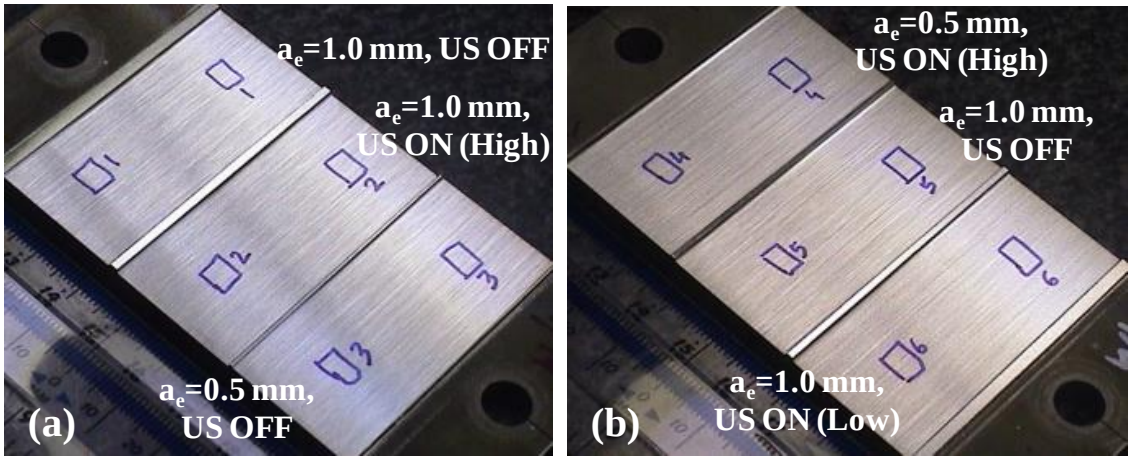


Fig. 4.2.76 Images of Inconel 718 workpiece surfaces ground at different operating conditions

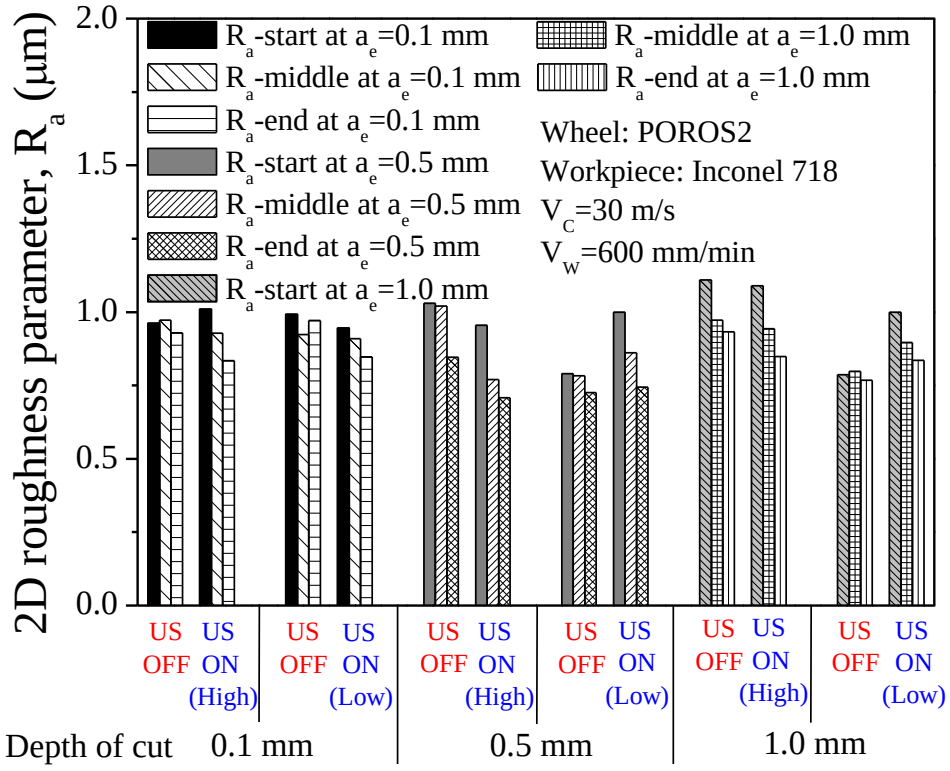


Fig. 4.2.77 Surface roughness (R_a) of ground Inconel 718 workpieces

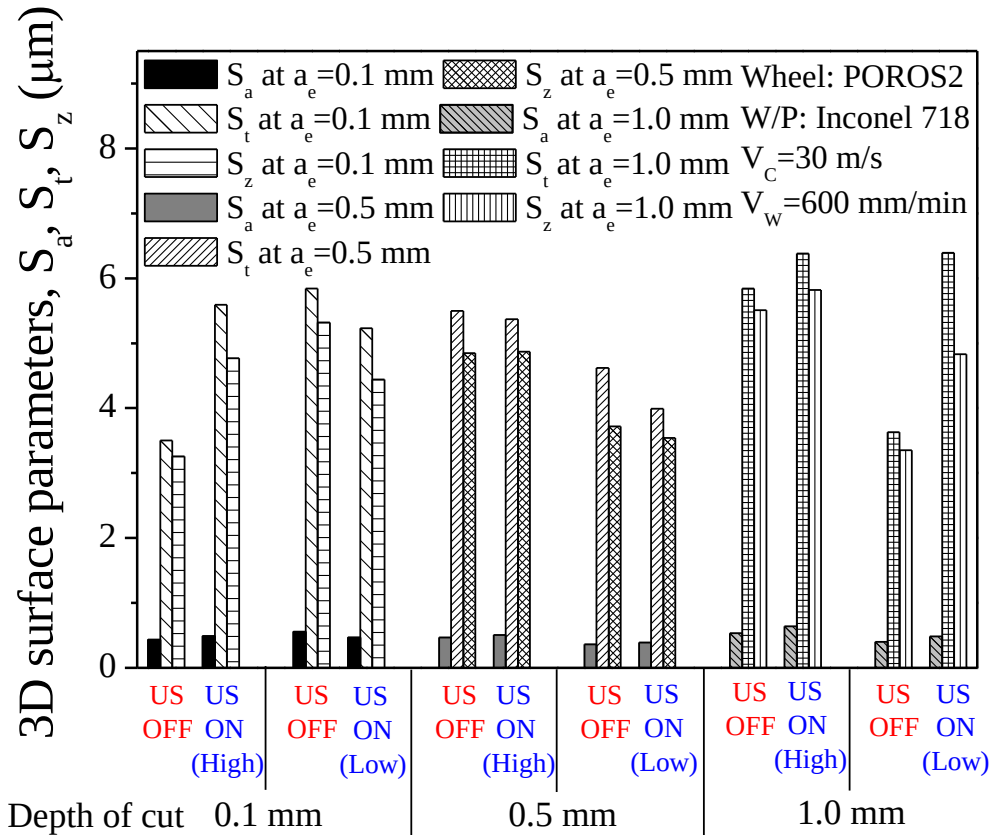


Fig. 4.2.78 3D topographical parameters of ground Inconel 718 workpiece surfaces

Both R_a and S_a of the ground workpieces typically increased with the assistance of US vibration in comparison to those obtained without vibration. This was possibly the result of increased smearing and side flow/ploughing of the workpiece material when operating with vibration (seen from the SEM micrographs in Fig. 4.2.79(c) and (d)), which was caused by lateral movement of the grits under multi-modal ultrasonic actuation (Tawakoli et al., 2009a). The data also suggests greater plastic deformation (Spur and Holl, 1996) of the workpiece material. In contrast, some pull-out of the material was observed when grinding was employed without vibration (Fig. 4.2.79(b)), which was absent on the surfaces subject to US actuation. The majority of tests also showed that the maximum depth of valley S_v, of the ground surfaces was generally higher in the hybrid mode in comparison to those obtained in conventional CFG. This was thought to be due to the action of vibration along the Z-axis of the table sonotrode, i.e. in a direction radial/normal to the wheel surface. The main effects plot relating to workpiece surface roughness (Figs. A6.2 and A6.3 in Appendix A6) showed that the vibration setting with 'High' amplitude resulted in higher R_a and S_a in comparison to those obtained with the 'Low' amplitude setting, suggesting that the latter led to greater numbers of active cutting points/grits in contact with the work surface. This also explains the reason for higher grinding forces obtained with the latter setting in comparison to those obtained with the former. The ANOVA showed that variation in amplitude of vibration (High and Low) had

a significant effect on the R_a and S_a of ground workpiece surfaces (25% and 55.17% respectively), see Table 4.2.4.

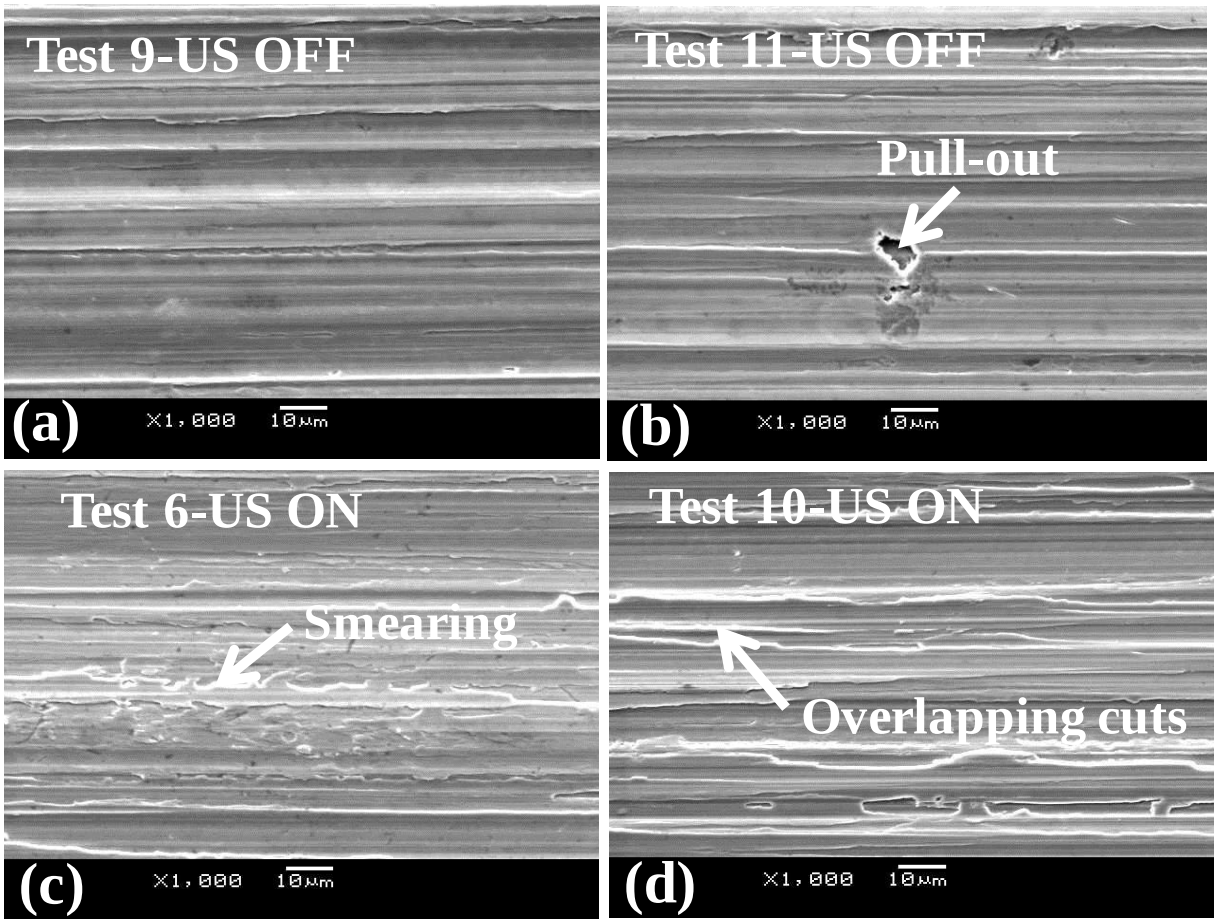


Fig. 4.2.79 SEM micrographs of ground workpiece surfaces (a) Test 9: V_C=30 m/s, V_W=300 mm/min, US OFF, (b) Test 17: V_C=40 m/s, V_W=300 mm/min, US OFF, (c) Test 6: V_C=30 m/s, V_W=300 mm/min, US ON, (d) Test 12: V_C=35 m/s, V_W=300 mm/min, US ON

4.2.5.4 Grinding wheel surface evaluation

The average 2D and 3D surface parameters (R_a and S_a) of the graphite blocks are represented in Fig. 4.2.80. The S_a and density of peaks (S_{ds}) obtained from the resin replicas are shown in Fig. 4.2.81. Both the R_a and S_a of the graphite replicas were generally lower when grinding was performed with ultrasonic vibration in comparison to plain grinding, which suggested greater uniformity of the resulting grit heights. The 'Low' amplitude vibration setting resulted in lower R_a and S_a values of the graphite replicas in comparison to those obtained with the 'High' amplitude setting.

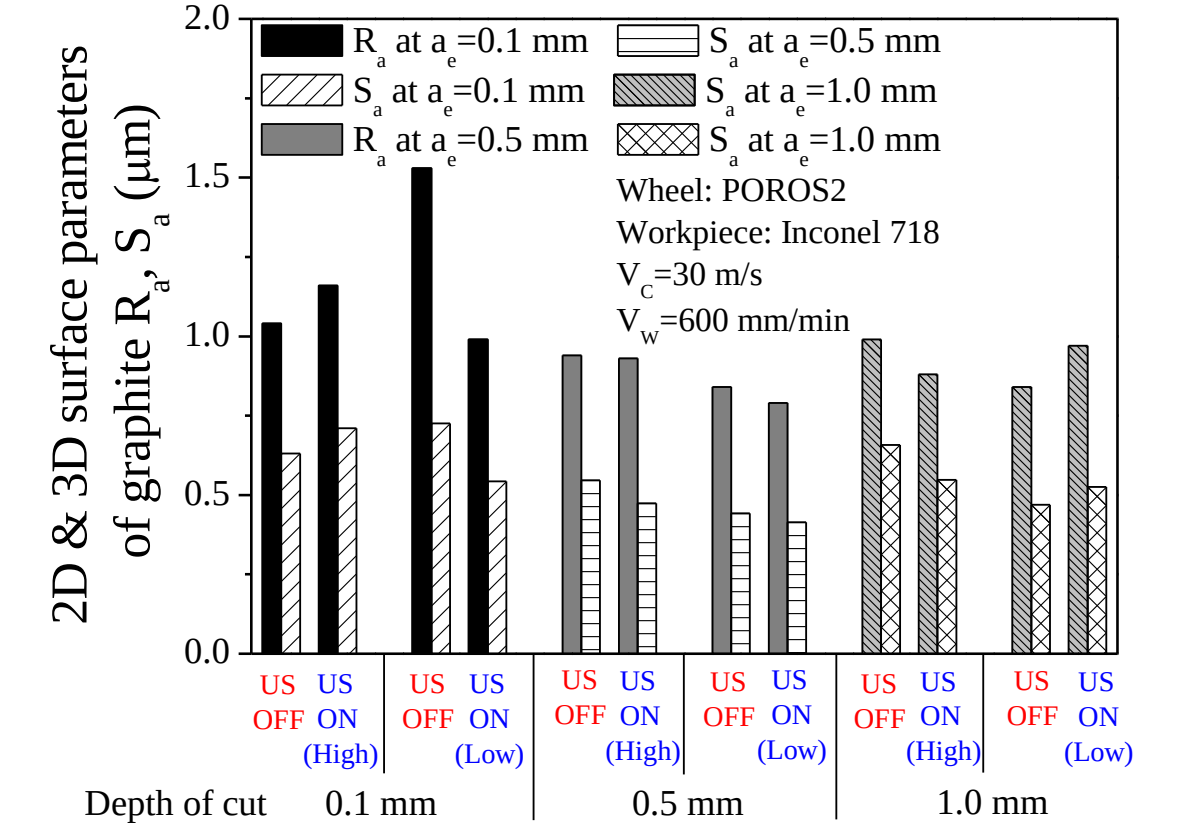


Fig. 4.2.80 Surface topography parameters (2D and 3D) from graphite (negative) replicas of the grinding wheel

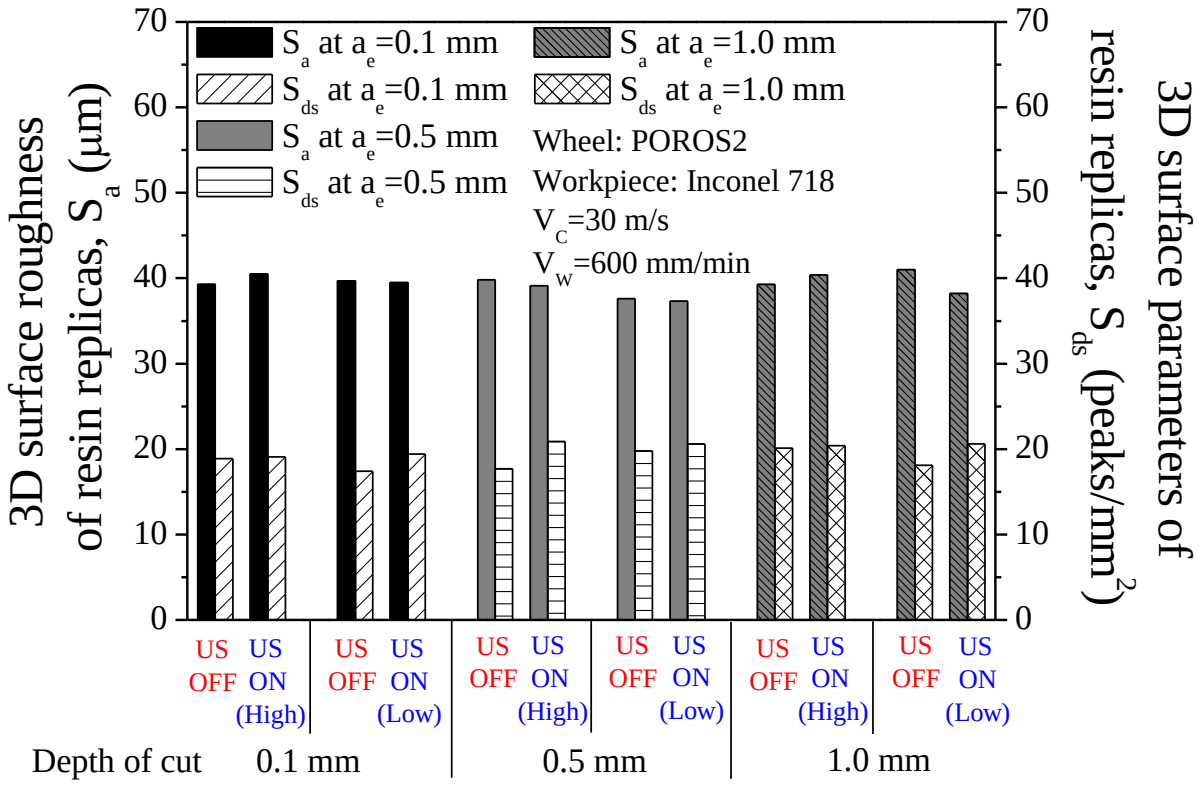


Fig. 4.2.81 3D topographical parameters of resin (positive) replicas of grinding wheel

The main effects plot (Figs A6.4 in Appendix A6) and the related statistical analysis for graphite R_a showed that depth of cut had the highest contributions on R_a as well as S_a (although the main effects plot for S_a not shown here) with PCR's of 50.9% and 57.7% respectively, followed by amplitude of vibration (18.3 and 28.9% respectively), although these factors were not statistically significant for R_a. Conversely, both factors had a significant effect on the S_a of graphite replicas, see Table 4.2.4. The assistance of ultrasonic vibration also had a statistically significant contribution on S_a of graphite surfaces (4.7%).

The wheel surface S_a typically decreased while S_{ds} increased when grinding was assisted with ultrasonic actuation. This was attributed to the greater number of active cutting points per grain (due to grit fracture) generated with use of US vibration. The factor 'vibration' had the most significant contribution to S_{ds} of resin replicas (42.99%) followed by depth of cut (19.66%), however the latter was statistically insignificant. The S_a of wheel surface was primarily influenced by depth of cut (31.29%), succeeded by the variation in vibration amplitude (20.53%), however both effects were not statistically significant.

The SEM micrographs of resin replicas, taken after roller dressing and grinding, revealed many sharp active cutting points following dressing, see Fig. 4.2.82(a), whereas grit flattening can be observed on the wheel surface succeeding conventional grinding, see Fig. 4.2.82(b). The surfaces of the wheel subject to US vibration showed that more voids/pores were generated in between grains (Figs. 4.2.82(c) and (d)); suggesting more grit/bond fracture due to vibration. This could be a possible reason for the lower G-ratio values measured under hybrid operation. Furthermore, larger voids/pores were observed on the wheel surface following grinding involving the 'High' amplitude mode (Fig. 4.2.82(c)), which corresponded with lower grinding forces but higher workpiece surface roughness as opposed to those obtained with the 'Low' amplitude setting.

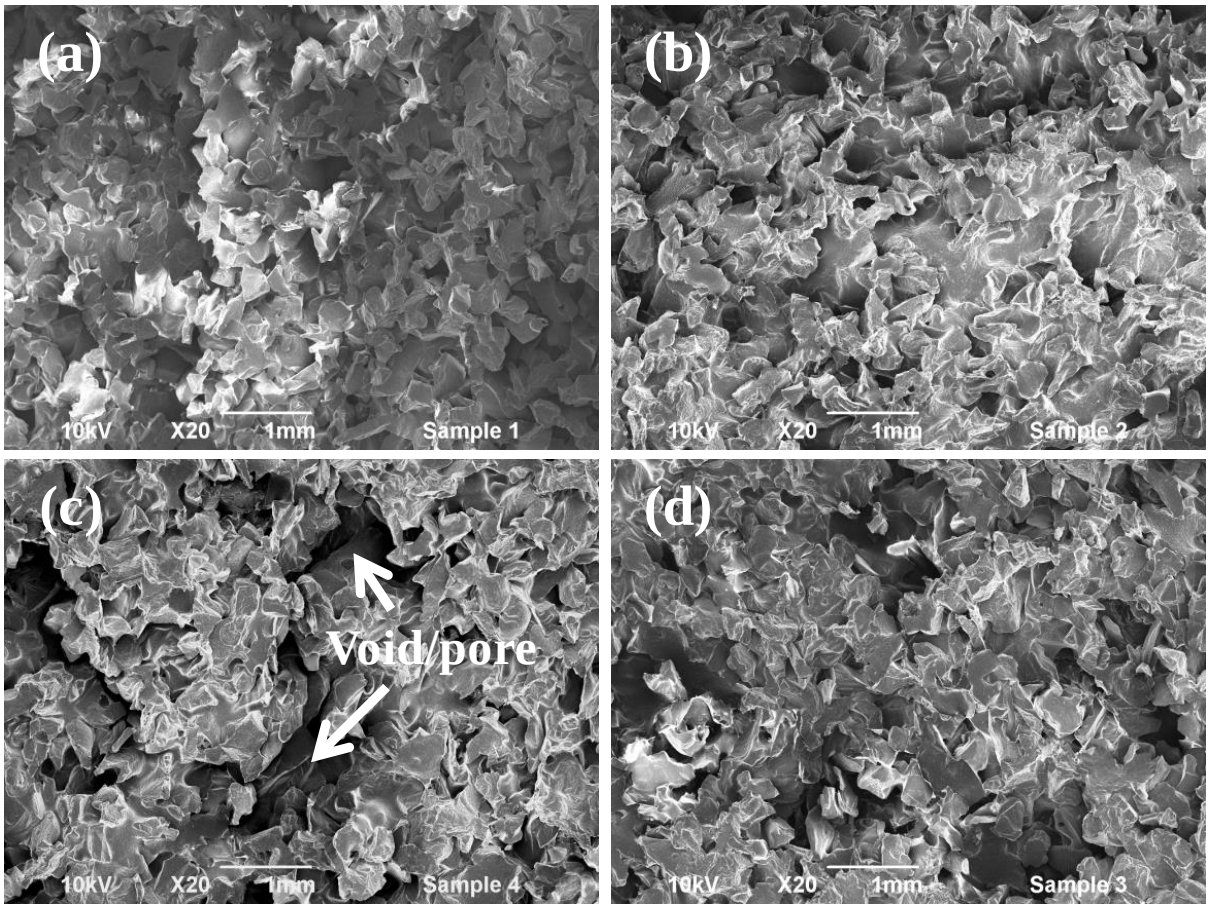


Fig. 4.2.82 SEM micrographs of POROS2 wheel surface following: (a) Roller dressing, (b) Grinding without vibration, (c) With vibration at 'High' amplitude, (d) With vibration at 'Low' amplitude

4.2.5.5 Microhardness and workpiece microstructure

Figures 4.2.83 and 4.2.84 show the microhardness depth profiles in the transverse feed plane of selected Inconel 718 samples ground at depths of cut of 1.0 mm and 0.5 mm respectively. The other microhardness depth profiles are shown in Figs. A6.5 to A6.8 in Appendix A6. Similar to Phase 2B and 2C, sub-surface microhardness typically increased up to ~490 to 525 $HK_{0.025}$ from a depth of 10 μm to ~200 μm beneath the machined surface until the bulk hardness was attained (~450 $HK_{0.025}$). This was possibly due to the plastic deformation of the material caused by the elongation of grains in the feed direction under the action of grit motion, see Fig. 4.2.85. The application of vibration further increased the sub-surface microhardness by ~6 to 10% due to the greater plastic flow of the material (Panin et al., 2004).

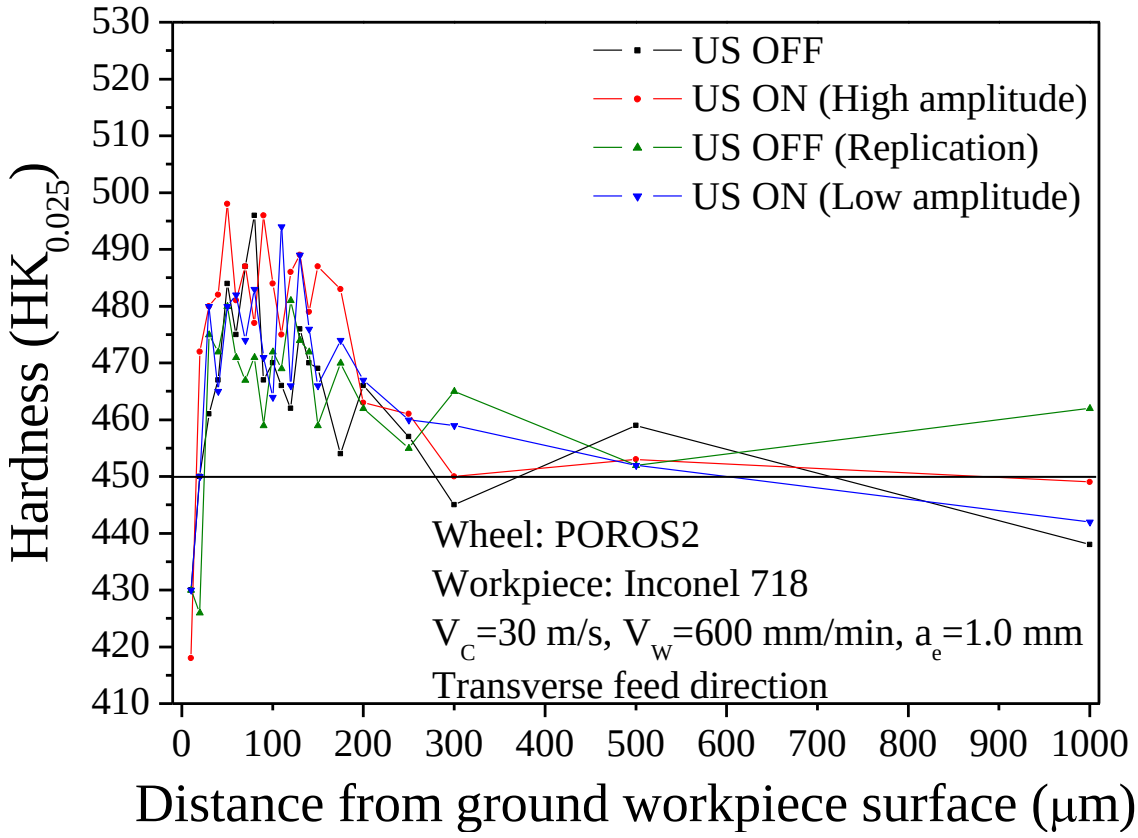


Fig. 4.2.83 Microhardness depth profile of Inconel 718 samples ground at a_e=1.0 mm; measurements taken in the transverse feed plane

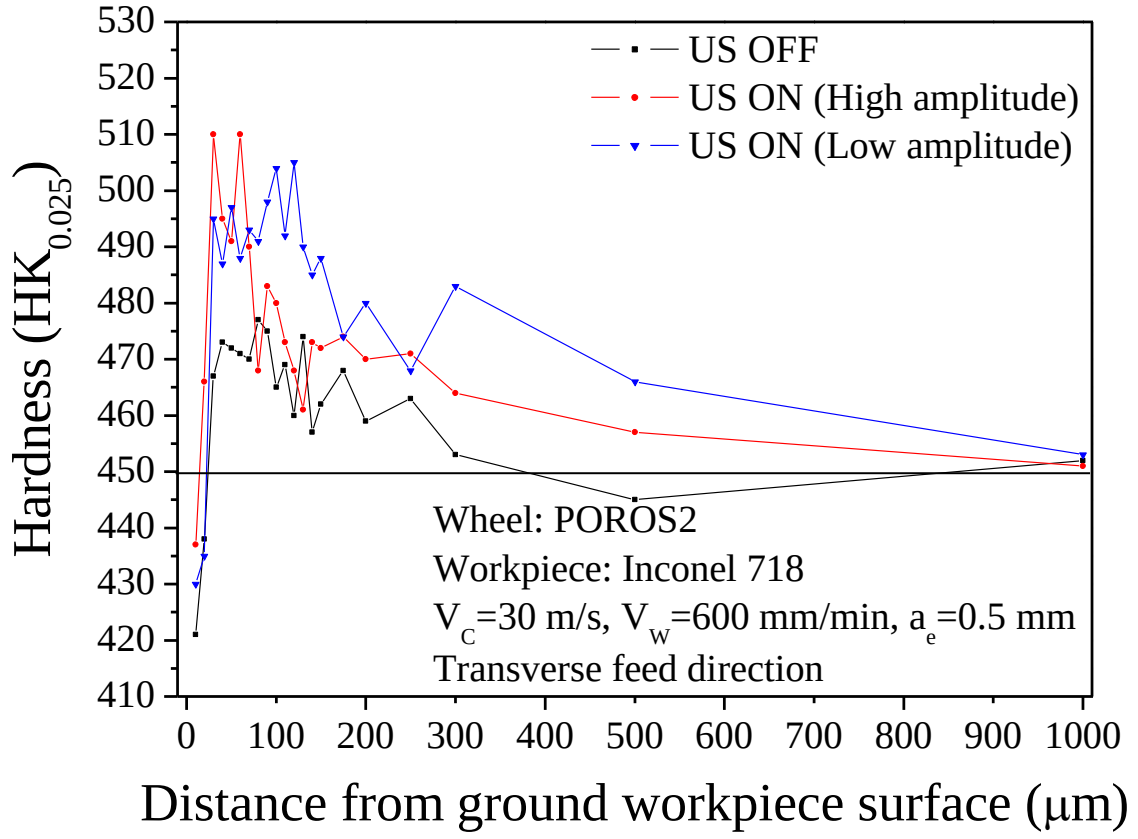


Fig. 4.2.84 Microhardness depth profile of Inconel 718 samples ground at a_e=0.5 mm; measurements taken in the transverse feed plane

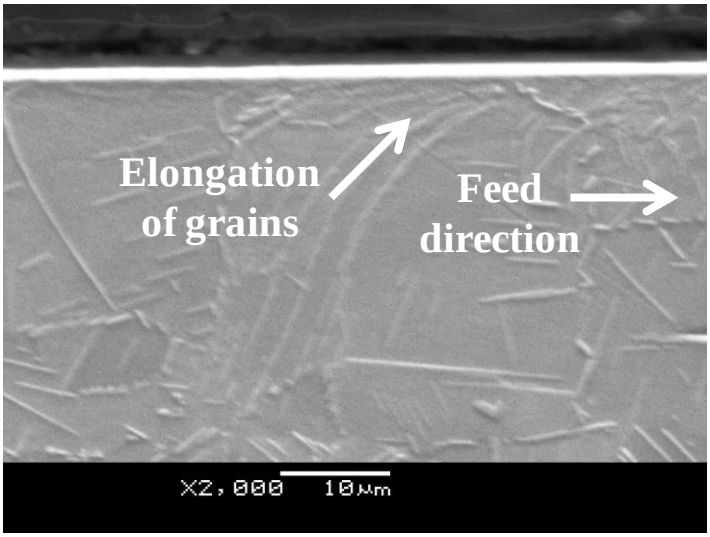


Fig. 4.2.85 Microstructure of Inconel 718 on longitudinal feed plane showing elongation/deformation of grains

The microstructure of the material beneath the machined surface in the transverse feed plane showed distinctive abrasive grain marks, see Fig. 4.2.86, which were not apparent when viewed on the transverse feed direction (Fig. 4.2.85). The grain sizes typically varied from 5 to 15 µm with the presence of niobium carbide (NbC) within the nickel matrix. The assiatnce of ultrasonic vibration however did not significantly alter the material microstructure.

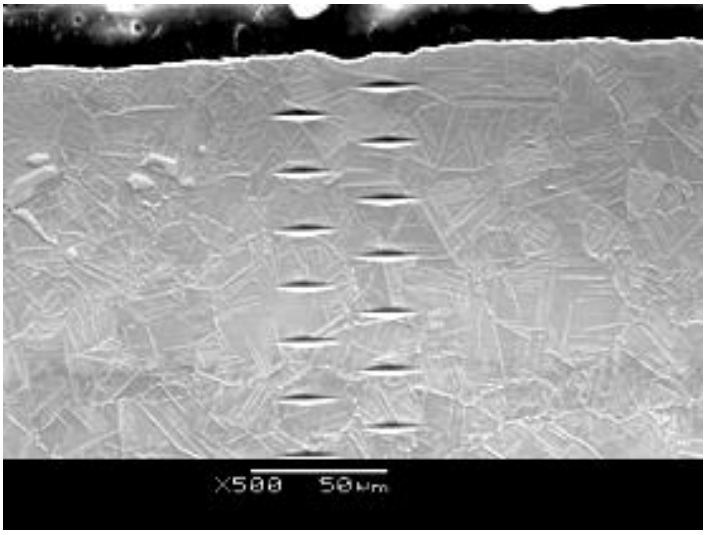


Fig. 4.2.86 Microstructure of Inconel 718 on transverse feed plane showing typical grit marks

The key results obtained from Phase 2E are appended below:

- The application of ultrasonic vibration resulted in reductions in F_v and F_h by up to 28% and 37% respectively, but increased wheel wear (30-60% lower G-ratio).
- Peak power decreased by ~5-6% when grinding with US vibration.
- An increase in amplitude of vibration produced lower grinding forces (up to 30% for F_v and 43% for F_h) but higher workpiece surface roughness (up to 24%).
- Ultrasonic vibration typically resulted in an increase in the active cutting point density of the resin replicas. Furthermore, a 'High' amplitude of vibration produced greater voids/pores on the wheel surface, which resulted in lower grinding forces but higher surface roughness in comparison to those obtained when grinding was carried out with 'Low' amplitude settings.
- Sub-surface microhardness generally increased up to ~490-525 $HK_{0.025}$ from a depth of 10 μm to ~200 μm underneath the machined surface, which was further increased by ~6-10% with the application of vibration.

4.3 Ultrasonic assisted grinding of gamma titanium aluminide (γ-TiAl) intermetallic alloys

4.3.1 Phase 3A: Assessment of UAG on γ-TiAl using conventional SiC abrasive wheel

4.3.1.1 Grinding forces

The vertical (F_v) and horizontal (F_h) grinding forces obtained when operating with and without ultrasonic vibration are shown in Fig. 4.3.1. The maximum F_v varied from ~1450 to 2300 N, which were comparable to those reported by Bentley and Aspinwall (1997a) and Hood et al. (2007b) when creep grinding γ-TiAl at similar process parameters.

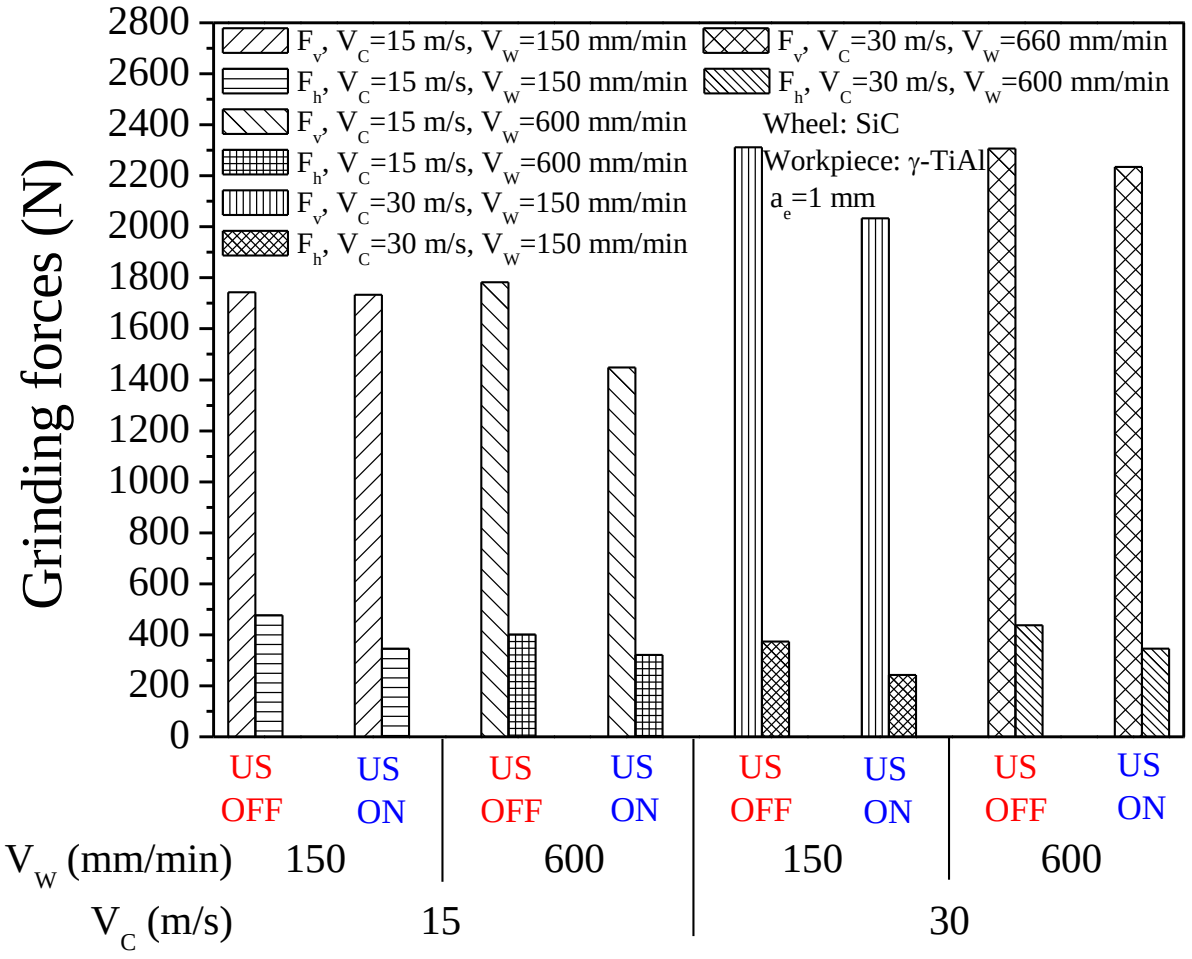


Fig. 4.3.1 Vertical (F_v) and horizontal (F_h) forces under different grinding conditions

The main effects plots for vertical forces in Fig. 4.3.2 showed an increasing trend with wheel speed rising from 15 to 30 m/s, which was in line with previous work by Hood et al.

(2007a and 2007b). This was attributed to an increase in the sliding length per unit volume of material removed when grinding at faster wheel speeds (Malkin, 1989), which resulted in greater attritious wear and dulling of the abrasive grits leading to higher rubbing and ploughing. A similar explanation was also detailed by Andrew et al. (1985) when grinding nickel based superalloys with conventional abrasive wheels. Evidence of greater rubbing and ploughing at higher wheel speed due to attritious wear on the grits was observed from SEM micrographs of the ground workpiece surfaces in Figure 4.3.3. Significantly more side flow/ploughing of the material was clearly visible in the sample from Test 5 machined at 30 m/s, see Fig. 4.3.3(b). Use of UAG generally led to lower vertical forces while variation in table feed from 150 to 600 mm/min appeared to have minimal influence.

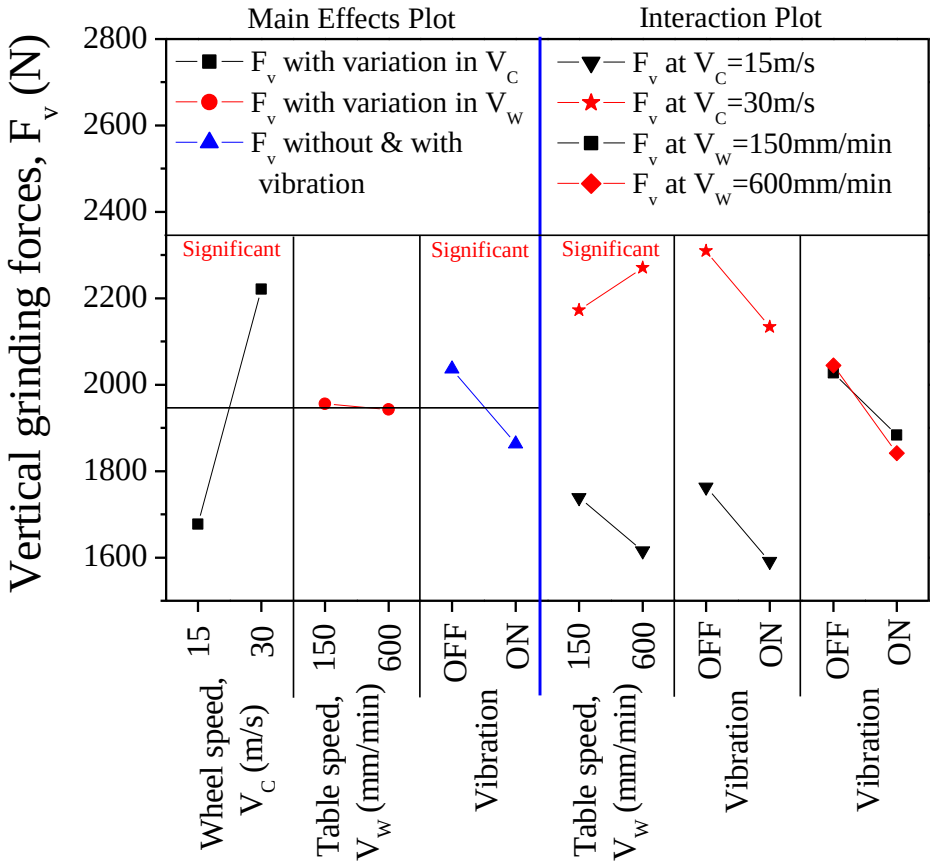


Fig. 4.3.2 Main effects and interaction effects plots for vertical grinding force

Corresponding ANOVA calculations also indicated that wheel speed was the principal significant factor affecting F_v with an overwhelming PCR of 83.02%, see Table 4.3.1. Although statistically significant, both vibration condition and interaction between wheel speed and table feed ($V_C \times V_W$) had relatively low PCR's of 8.43% and 3.42% respectively.

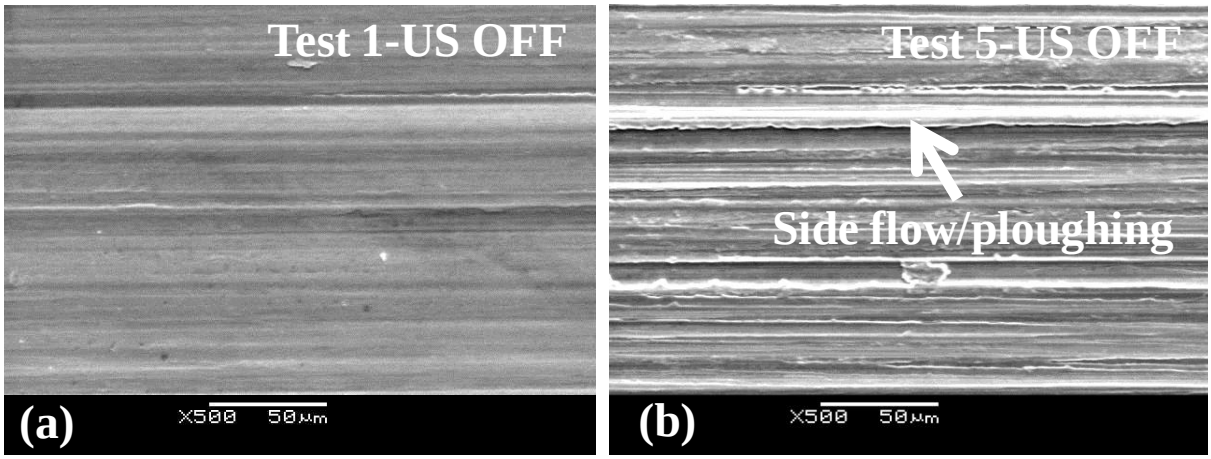


Fig. 4.3.3 SEM micrographs of ground γ-TiAl surface at (a) Test 1: V_C = 15 m/s, V_W = 150 mm/min, d = 1.0 mm, US OFF, (b) Test 5: V_C = 30 m/s, V_W = 150 mm/min, d = 1.0 mm, US OFF

Table 4.3.1 Percentage contribution ratios of factors with respect to different response measures (Phase 3A)

Factors	**Percentage contribution ratios (PCR's)**							
	F_v	**F_h**	**G-ratio**	**W/P R_a**	**W/P S_a**	**Graphite S_a**	**Resin replica S_a**	**Resin replica S_{ds}**
Wheel speed (V_C)	83.02*	7.17*	49.33*	76.61*	61.10*	8.82	0.02	0.01
Table feed (V_W)	0.04	1.44*	4.43	4.48	25.76*	54.55*	75.15*	81.19*
Vibration (Vib)	8.43*	64.52*	20.85*	8.72*	0.50*	11.74	0.39	1.12
V_C×Vw	3.42*	23.95*	14.08	3.64	12.59*	4.23	8.35	17.09*
V_C×Vib	0.01	0.04	8.72	5.90	0.01	15.08	9.87	0.18
V_W×Vib	0.23	2.82*	0.01	0.08	0.02	4.88	2.67	0.00
V_C×V_W×Vib	4.84	0.06	2.59	0.57	0.01	0.70	3.55	0.40
* Statistically significant factors at the 5% level								

The main effects plots for tangential grinding force (F_h), see Fig. 4.3.4, showed that it decreased with an increase in wheel speed and use of ultrasonic vibration. Conversely, F_h increased at higher table feed, although all three variables were found to have a significant effect with vibration condition having the largest PCR of 64.52%, see Table 4.3.1. In addition, the interactions between table feed versus both wheel speed and vibration also had a major influence on F_h.

The application of ultrasonic actuation generally led to reductions in both onventi and horizontal components of grinding force by up to 19% and 35% respectively. Similar results were also reported by Nik et al. (2012) when grinding Ti-6Al-4V alloy with a vitrified bonded alumina wheel, with F_v and F_h decreasing by 13.5% and 14.2% respectively under wet

conditions. This was attributed to the generation of impact loads between the grits and workpiece surfaces, which provided a self-sharpening action for abrasive grains, and a consequent reduction in grinding forces.

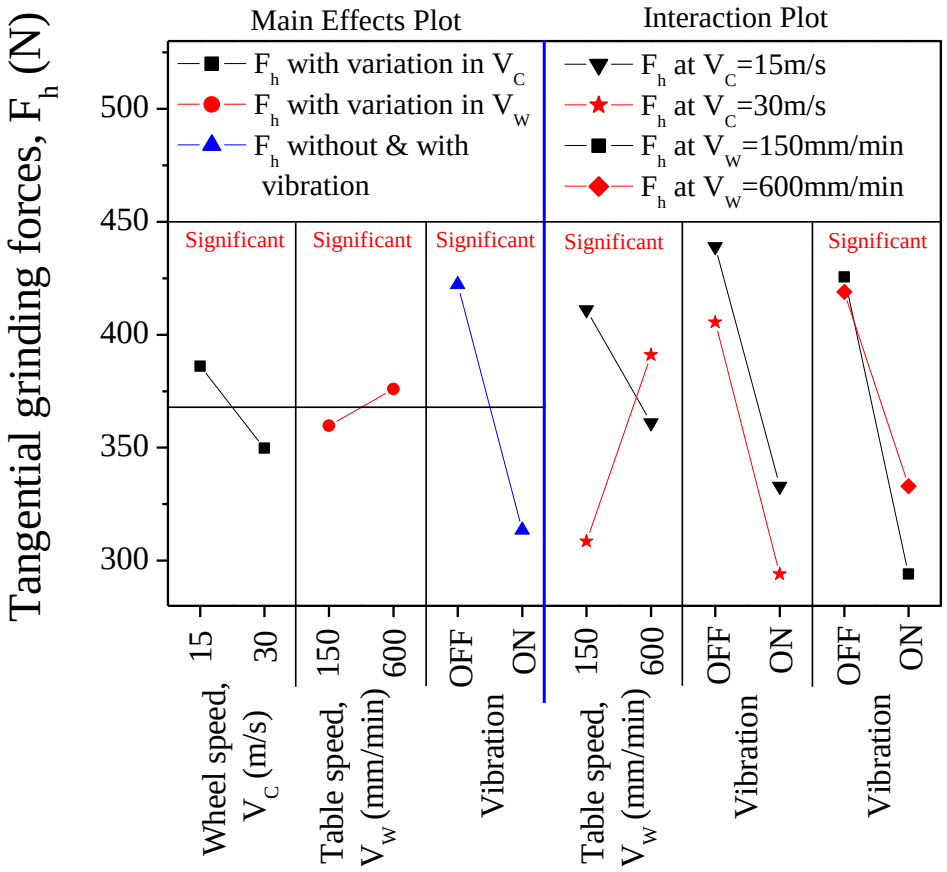


Fig. 4.3.4 Main effects and interaction plots for horizontal grinding force

4.3.1.2 Radial wheel wear and G-ratio

The radial wheel wear measured following each grinding pass and corresponding G-ratio are presented in Fig. 4.3.5. The wheel G-ratio varied from 3.19 to 7.99 depending on the test conditions, which were considerably lower than that reported by Bentley and Aspinwall (1997b), where values greater than 40 were recorded when surface grinding γ-TiAl intermetallic with vitrified bonded SiC wheels. However the results of the current work were similar to those of Hood (2010) who detailed G-ratios of 5 to 10 when creep feed grinding Ti–45Al–8Nb–0.2C wt% with conventional SiC abrasive wheels. The values of G-ratio were also comparable to those found when grinding nickel based superalloys with vitrified alumina wheels in previously outlined Phase 2B experiments. In general, RWW increased with both wheel speed and table feed while use of UAG mode reduced wheel wear. This was most

likely due to an increase in attritious wear at a higher cutting speed coupled with larger undeformed chip thickness at a higher table feed leading to greater frictional forces.

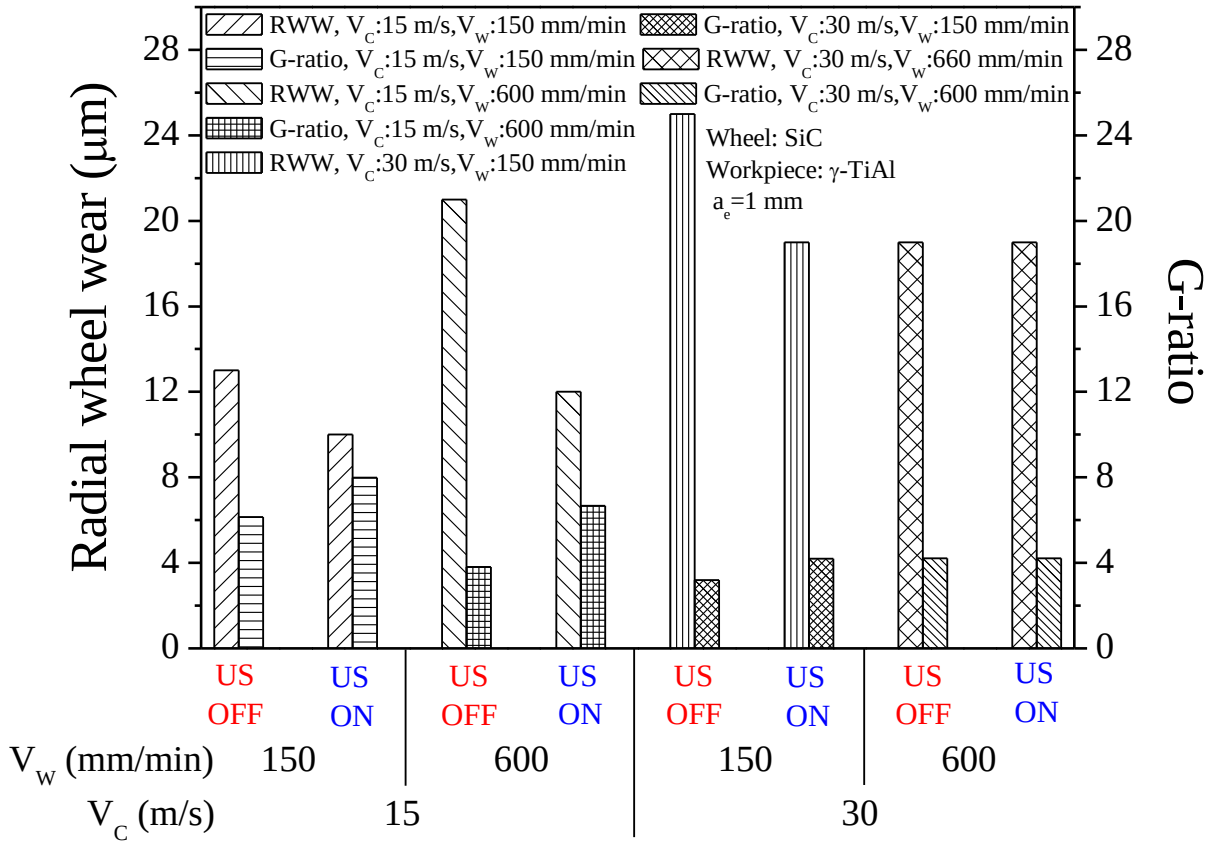


Fig. 4.3.5 Radial wheel wear and G-ratio under different grinding conditions

The benefit of improved G-ratio (~30 to 75% increase) when operating with ultrasonic assistance was probably due to a reduction in thermal load as described by Tawakoli et al. (2009b). However, this was in contrast with results obtained when grinding nickel based superalloys using vitrified alumina wheels, where G-ratio was typically found to decrease following UAG. A possible reason for this is lower specific weight of γ-TiAl compared to nickel based superalloys (Bentley and Aspinwall, 2000), resulting in more effective transmission of vibration to the workpiece. Figure 4.3.6 details the main effects and interaction plots for G-ratio, with wheel speed and vibration found to have a major influence with PCR's of 49.33% and 20.85% respectively. None of the factor interactions however were statistically significant, despite ($V_C \times V_W$) having a PCR of 14.08%.

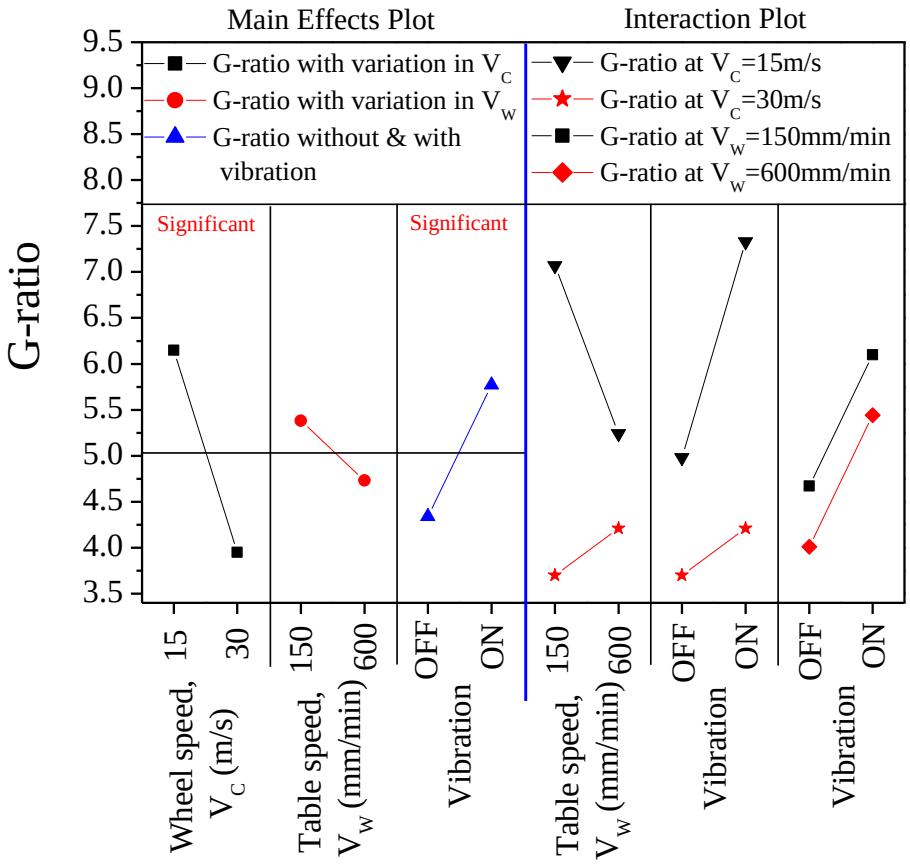


Fig. 4.3.6 Main effects and interaction effects plots for wheel G-ratio

4.3.1.3 Workpiece surface topography and quality

Figure 4.3.7 shows sample photographs of γ-TiAl surfaces ground with and without ultrasonic assistance. Minor burn and serration marks were observed when grinding at V_C=30 m/s, V_W=150 mm/min and ultrasonic vibration OFF, which was likely due to the generation of high temperatures when operating at the highest wheel speed (30 m/s). This however was a substantial improvement over results by Hood et al. (2007a and 2007b) who reported heavy workpiece burn and extensive crack formation following CFG of a Ti–45Al–8Nb–0.2C wt% material, albeit at relatively low pressure of 7 bar. The use of increased pressure (~28 bar) most probably led to greater penetration of fluid into the grinding zone in the current experiments. No workpiece burning was visible in any of the trials involving ultrasonic actuation, which suggests a reduction in thermal load/grinding temperature. The use of hybrid configuration also improved evacuation of chips from the cut zone (Tsuboi et al., 2012), thereby decreasing damage on the work surfaces. An analysis of SEM images taken on the ground surfaces revealed some evidence of surface fracture and redeposited material on workpieces produced under conventional CFG conditions, see Figs. 4.3.8(a) and (b). Similar defects were also observed by Sharman et al. (2001b) when finish turning of a γ-TiAl. No

such damage however was apparent on any of the workpieces subject to UAG, although greater amounts of plastic deformation, side flow/ploughing of material and overlapping grit marks were evident as detailed in Figs. 4.3.8(c) and (d). The higher plastic deformation was thought to be due to a change in material removal mechanism from a fracture based regime in conventional grinding to a ductile mode in ultrasonic assisted grinding (Gao et al., 2009). In contrast, the greater incidence of overlapping grit marks were possibly caused by the lateral movement of the grits (Tawakoli et al., 2009a) under multi-modal ultrasonic actuation of the table sonotrode.

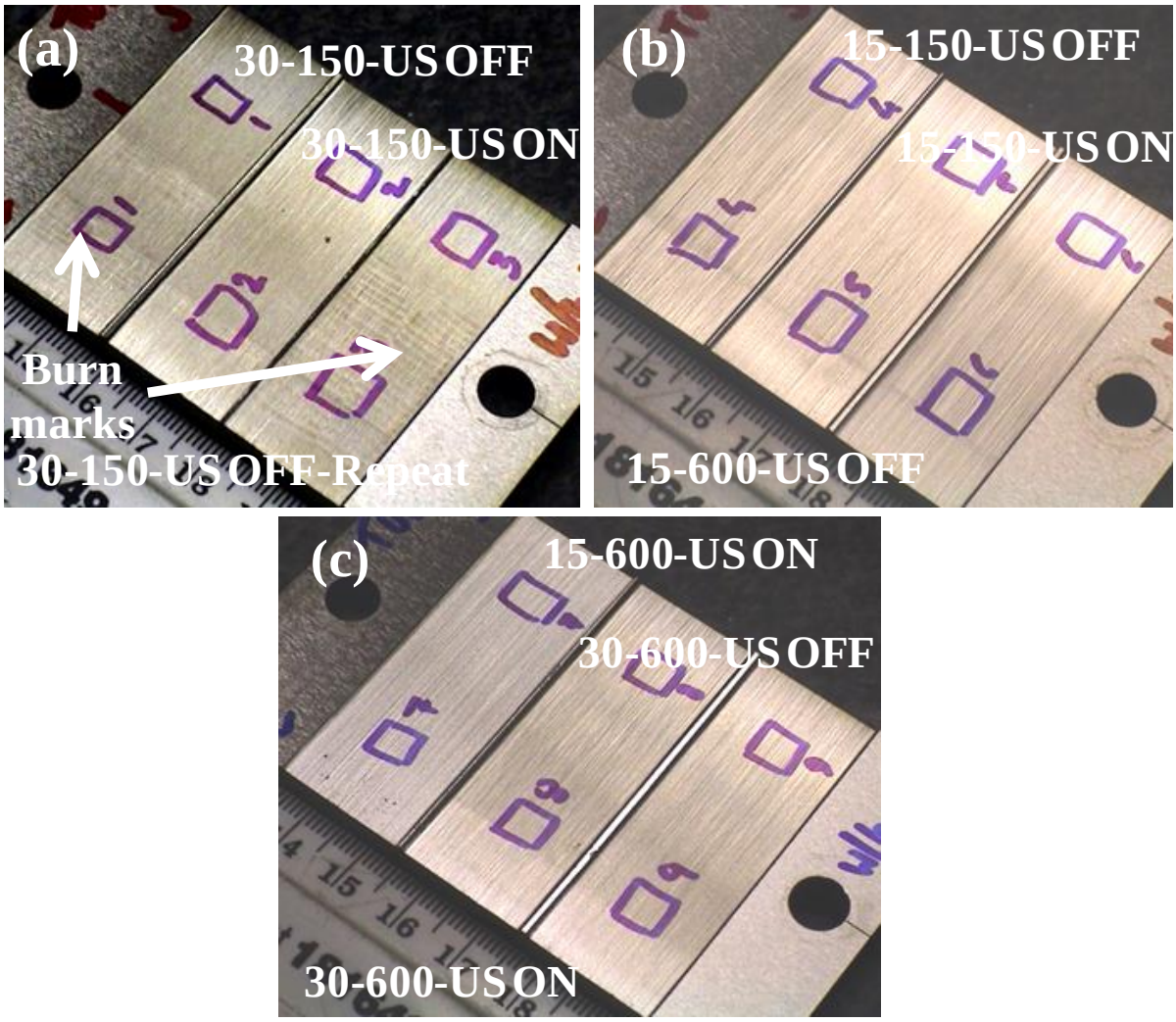


Fig. 4.3.7 Photographic views of ground γ-TiAl workpiece surfaces

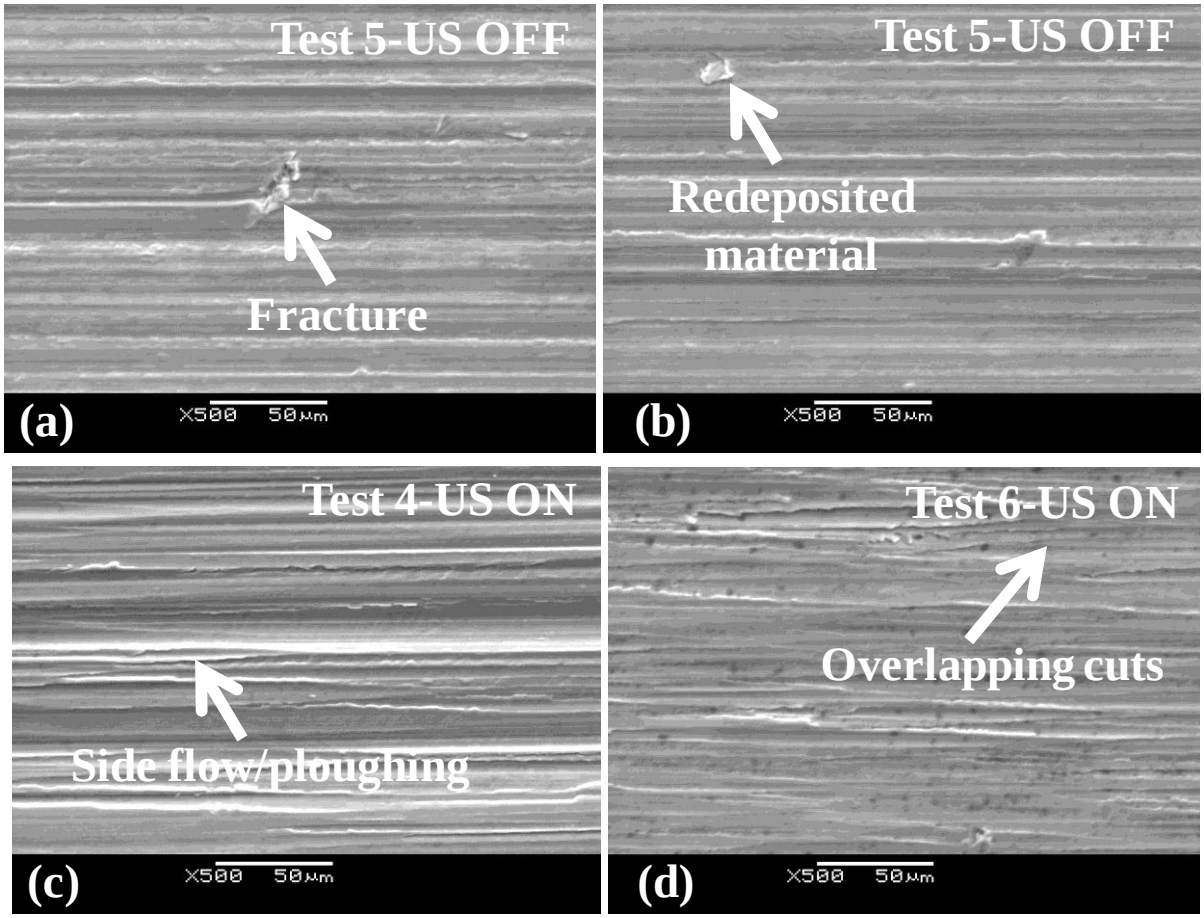


Fig. 4.3.8 SEM micrographs of ground γ-TiAl surface at (a) and (b) Test 5: V_C = 15 m/s, V_W = 150 mm/min, d = 1.0 mm, US OFF, (c) Test 4: V_C = 15 m/s, V_W = 600 mm/min, d = 1.0 mm, US ON, (d) Test 6: V_C = 30 m/s, V_W = 150 mm/min, d = 1.0 mm, US ON

2D surface roughness (R_a) values recorded at the start, middle and end of grinding tracks on the ground workpieces are shown in Fig. 4.3.9, while 3D surface parameters (S_a, S_t and S_z) are detailed in Fig. 4.3.10. Average values of R_a varied in a range of 1.56 to 2.01 µm, which were comparable to those reported by Hood et al. (2007b). Bentley et al. (2001) measured R_a values typically within ~1.0 to 2.5 µm while reciprocating surface grinding of a γ-TiAl alloy. However in some other work by Bentley and Aspinwall (1997a and 1997b), much lower surface roughness within 0.2 to 1.2 µm and 0.6 to 1.4 µm respectively were recorded.

While comparing between Figs. 4.3.9 and 4.3.10, it was observed that S_a of the ground surfaces were much lower than the corresponding R_a data. This was due to the fact that S_a provides information about an area on the surface, whereas R_a signals a line information. Both parameters (R_a and S_a) followed comparable trends with respect to the operating conditions as observed from the main effects and interaction plots for R_a, see Fig. 4.3.11 (main effects plots for S_a not shown).

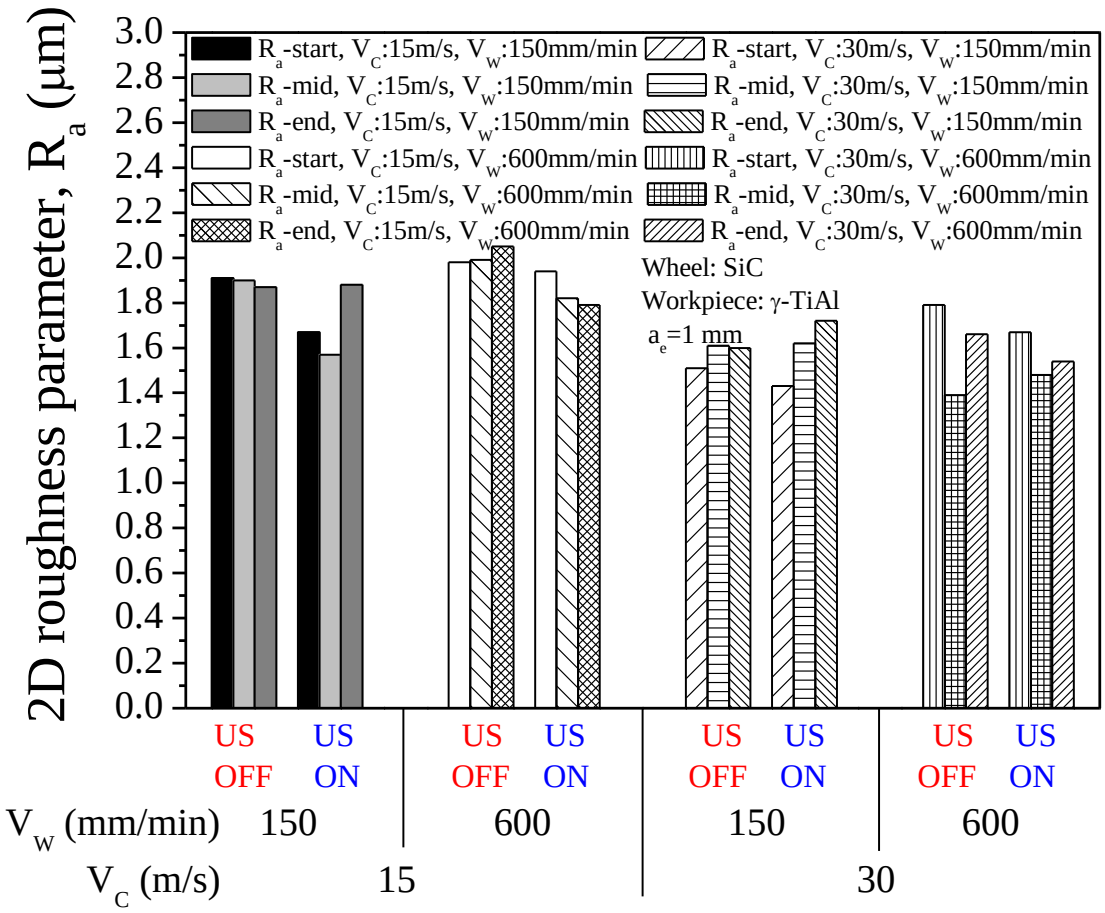


Fig. 4.3.9 2D roughness parameter (R_a) of ground γ-TiAl workpiece surfaces

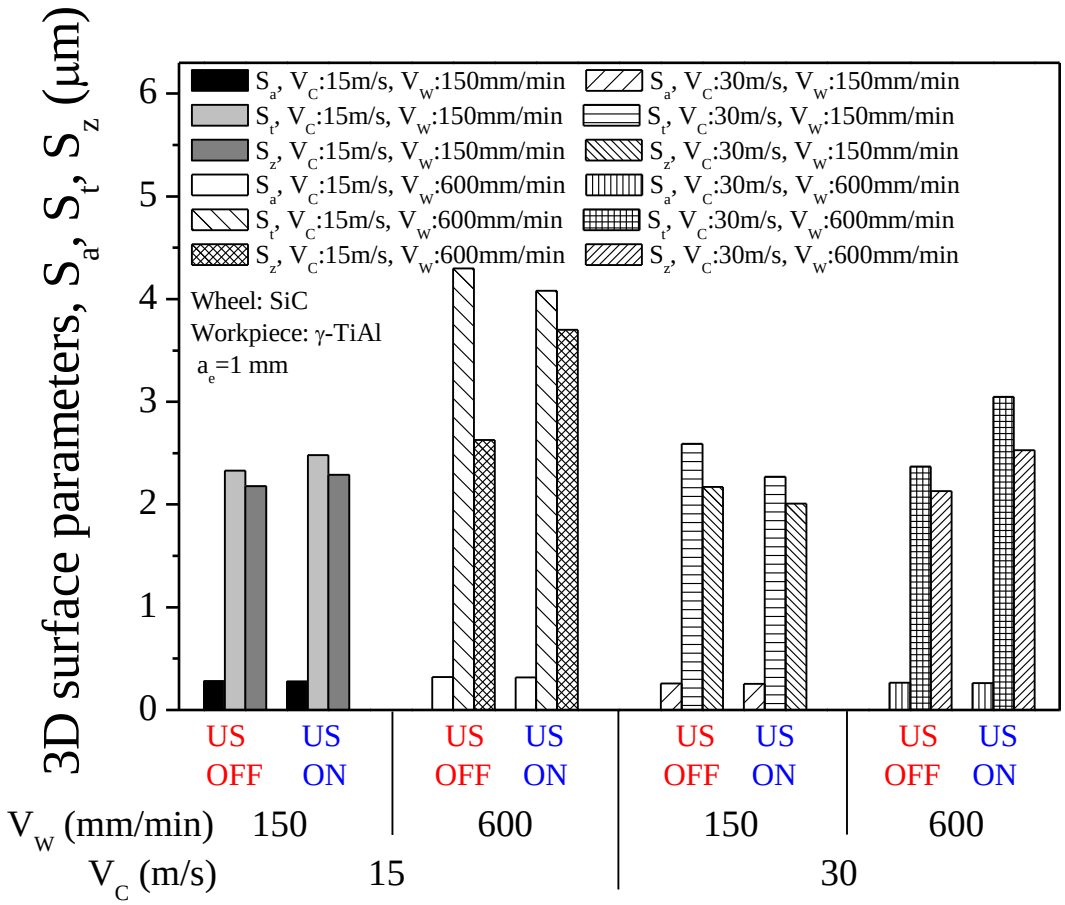


Fig. 4.3.10 3D topographical parameters of ground γ-TiAl workpiece surfaces

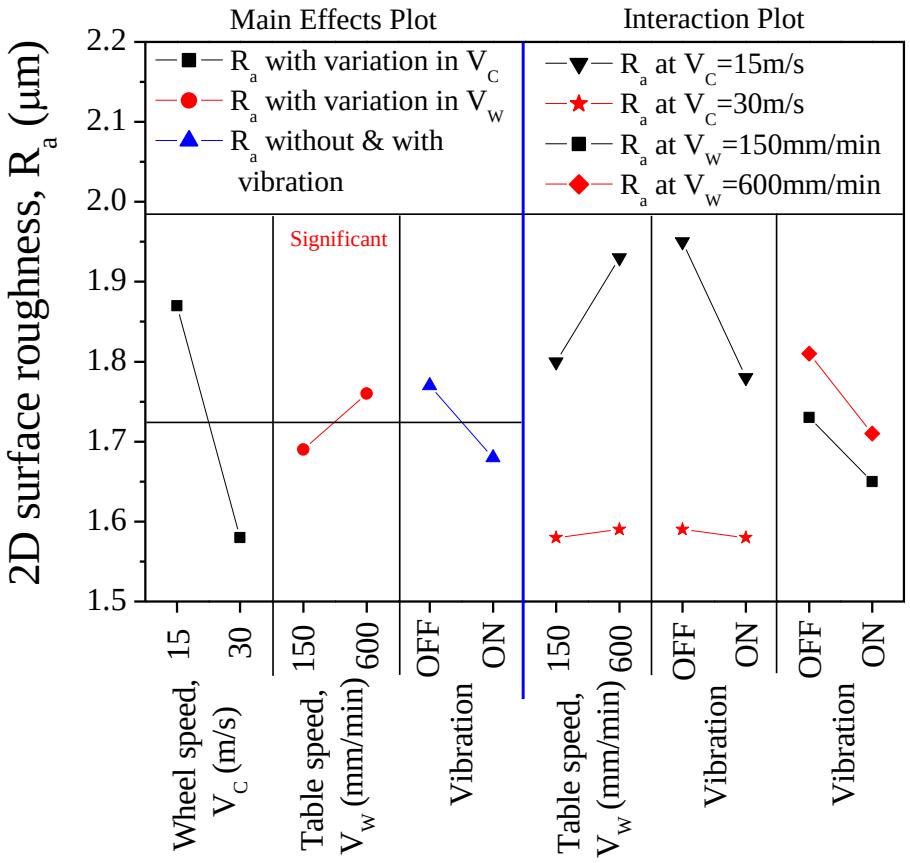


Fig. 4.3.11 Main effects and interaction plots for 2D surface roughness (R_a) of ground γ-TiAl workpieces

Both R_a and S_a the ground surfaces increased with an increase in table feed from 150 to 600 mm/min due to an increase in undeformed chip thickness (h_m), however they decreased with a rise in cutting speed from 15 to 30 m/s due to a lowering of the number of grits in contact with the work surface. Both surface parameters typically decreased (~3-10% reduction in R_a) when ultrasonic vibration was utilised in comparison to those obtained when conventional CFG. This was in contrast with the previous observations when UAG of Inconel 718 and CMSX-4, although both materials exhibited greater plastic deformation under hybrid mode. This could be attributed to the lamellar microstructure of γ-TiAl as opposed to the polycrystalline (e.g. Inconel 718) or equiaxed (e.g. as-cast CMSX-4) structures of nickel alloys, together with higher rapid fatigue crack growth rate, lower fracture toughness and impact resistance of γ-TiAl (Materials Properties Handbook, 1994) compared to the nickel based superalloys, which resulted in easier material removal from the gamma workpieces under the impact-loading action of ultrasonic vibration.

Table 4.3.1 showed that wheel speed had the highest contributions on both R_a and S_a of the ground workpieces (76.61% and 61.10% respectively), with both effects statistically significant. Table feed had a significant effect on S_a (25.76%) although its effect on R_a was

statistically insignificant with a PCR of only 4.48%. The PCR of vibration condition for R_a was 8.72%, although it was only 0.50% for S_a, with the former being statistically significant. An interaction between V_C and V_W had a significant contribution on workpiece S_a (PCR of 12.62%).

In contrast to the trend exhibited by R_a, the other 2D roughness parameters such as R_t and R_z typically increased when grinding with hybrid configuration. S_t and S_z parameters were also found to increase in 2 out of 4 and 3 out of 4 tests respectively under ultrasonic mode. This was most likely due to the effect of the component of vibration in the Z-axis (i.e. perpendicular to the work surface), which resulted in greater penetrations of the abrasive grains into the work surface. A consequence of this was reflected on the S_v values of the ground surfaces, which were found to increase in 3 out of 4 tests when operating with vibration. Additionally, all surfaces subject to vibration exhibited higher negative skewness values.

4.3.1.4 Grinding wheel surface evaluation

The 3D surface parameters (S_a, S_t and S_z) of the graphite replicas of the SiC wheel are shown in Fig. 4.3.12. The S_a of the graphite replicas decreased in 3 out of 4 tests when grinding was assisted with US vibration. This indicated a greater uniformity in the grit heights under hybrid mode due to micro-breakage at the tip of the grits under the action of vibration. Similar trend was observed for the S_z values of graphite surfaces which decreased in 3 out of 4 trials subject to ultrasonic assistance. Although not shown here, S_p decreased in all tests while S_v reduced in 3 out of 4 cases involving UAG. The consequence of the greater uniformity in the abrasive grain heights directly reflected on the workpiece surface roughness data which were also found to decrease with ultrasonic assistance.

The main effects and interaction plots for S_a of the graphite surfaces in Fig. 4.3.13 showed similar trends to those obtained for ground workpieces. Graphite S_a typically decreased with an increase in wheel speed from 15 to 30 m/s due to the reduction in contact time at a faster wheel speed, whereas it increased with an increase in table feed from 150 to 600 mm/min due to a rise in the undeformed chip thickness. Table feed had the maximum influence on graphite S_a with a PCR of 54.55%, which was statistically significant as well. A combination of V_C and vibration condition (V_C × Vib) had the next highest PCR (15.08%), followed by the sole effect of vibration (11.74%), however both factors were statistically insignificant. Wheel speed contributed to a relatively small PCR of 8.82% for the graphite surface S_a, see Table 4.3.1.

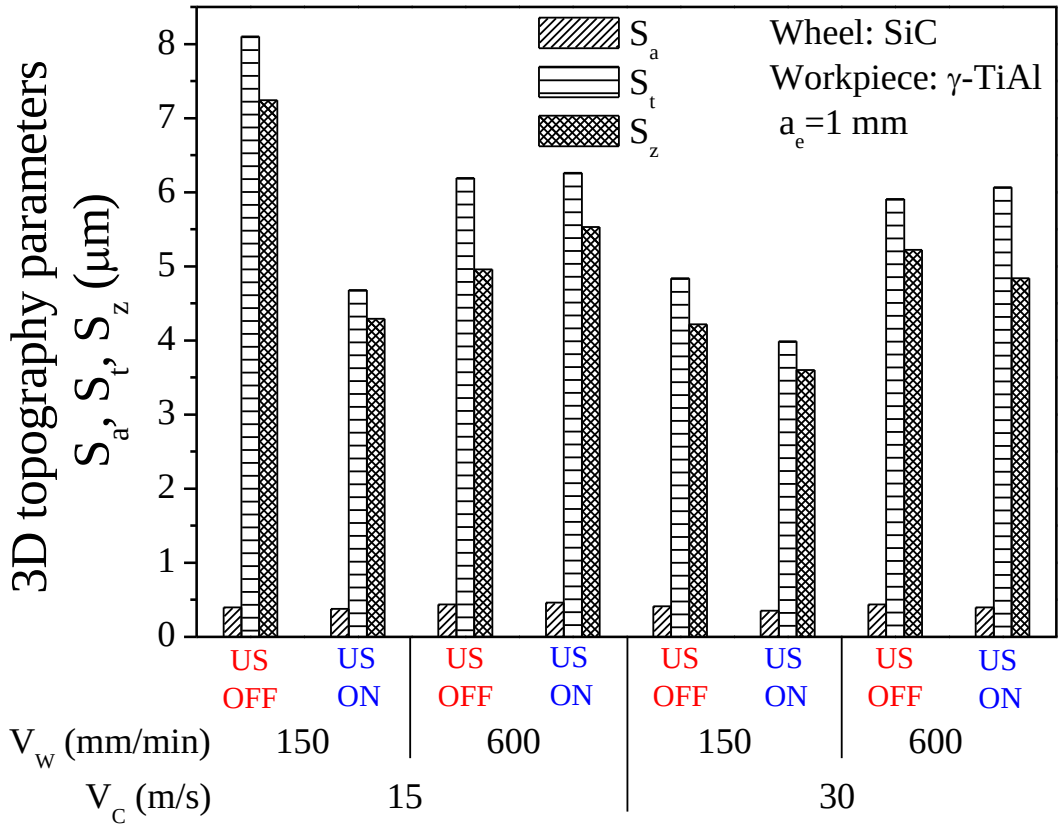


Fig. 4.3.12 3D surface parameters of graphite (negative) replicas of SiC wheel

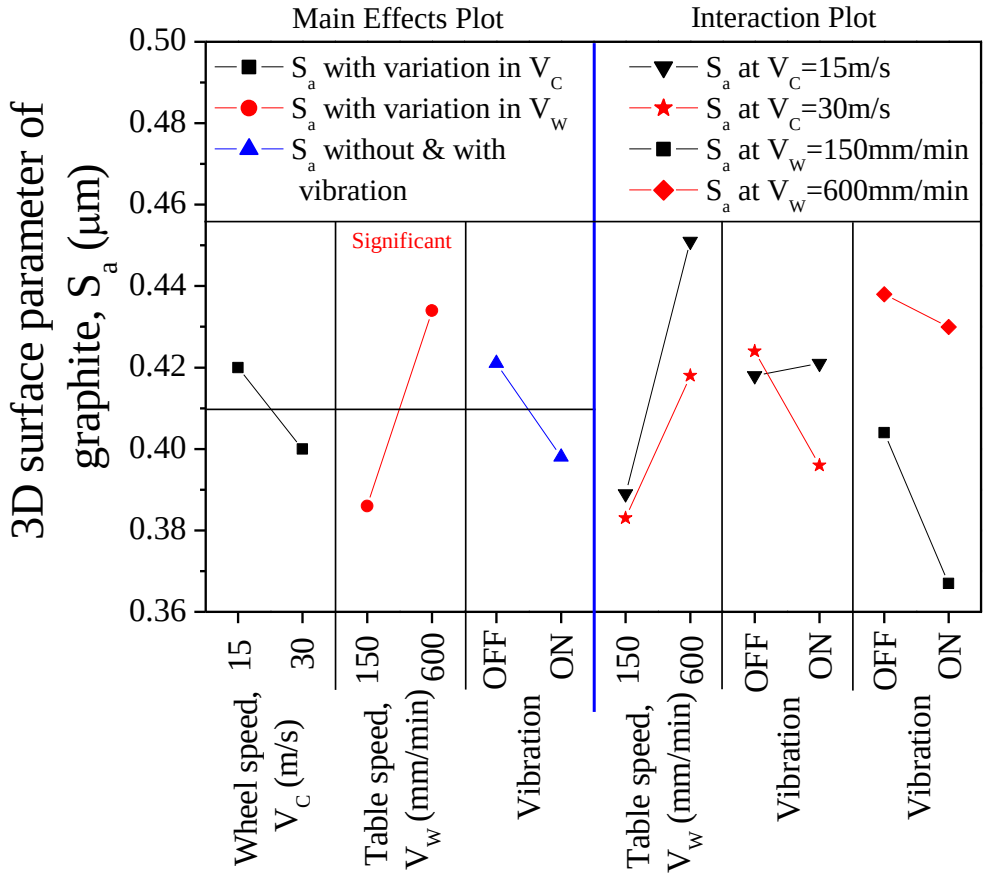


Fig. 4.3.13 Main effects and interaction plots for 3D surface roughness (S_a) of graphite (negative) replicas of the SiC wheel

While considering the 3D surface parameters (S_a and S_{ds}) of the resin (positive) replicas of the grinding wheel, shown in Fig. 4.3.14, it was observed that both parameters generally decreased and increased respectively with a rise in V_W. With the increase in table feed, the grains became duller, which in turn resulted in a lower S_a of the wheel surface. In contrast, the variations in S_a and S_{ds} were marginal with a rise in the cutting speed. The main effects and interaction plots for wheel S_a and S_{ds} are shown in Figs. 4.3.15 and 4.3.16 respectively. Both surface parameters were found to decrease following UAG in comparison to onventional CFG. This observation was in contrast with the previous results obtained for UAG of nickel based alloys where an increase in S_{ds} value was typically observed under hybrid configuration. This was possibly due to the different wear mechanism of vitrified SiC wheel from that of porous vitrified alumina wheels under the action of vibration. Furthermore, the ductile regime material removal mechanism of γ-TiAl in UAG might also have influenced the wear pattern of the SiC grains.

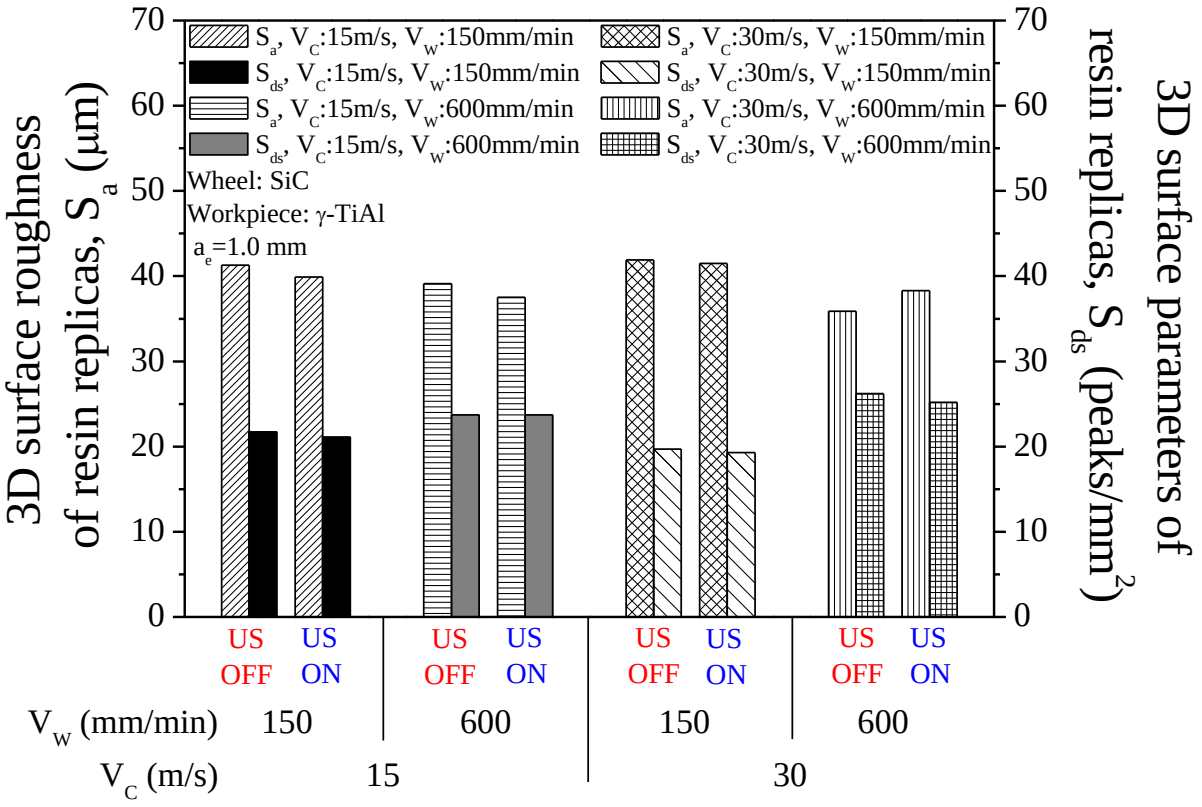


Fig. 4.3.14 3D topographical parameters of resin (positive) replicas of SiC wheel

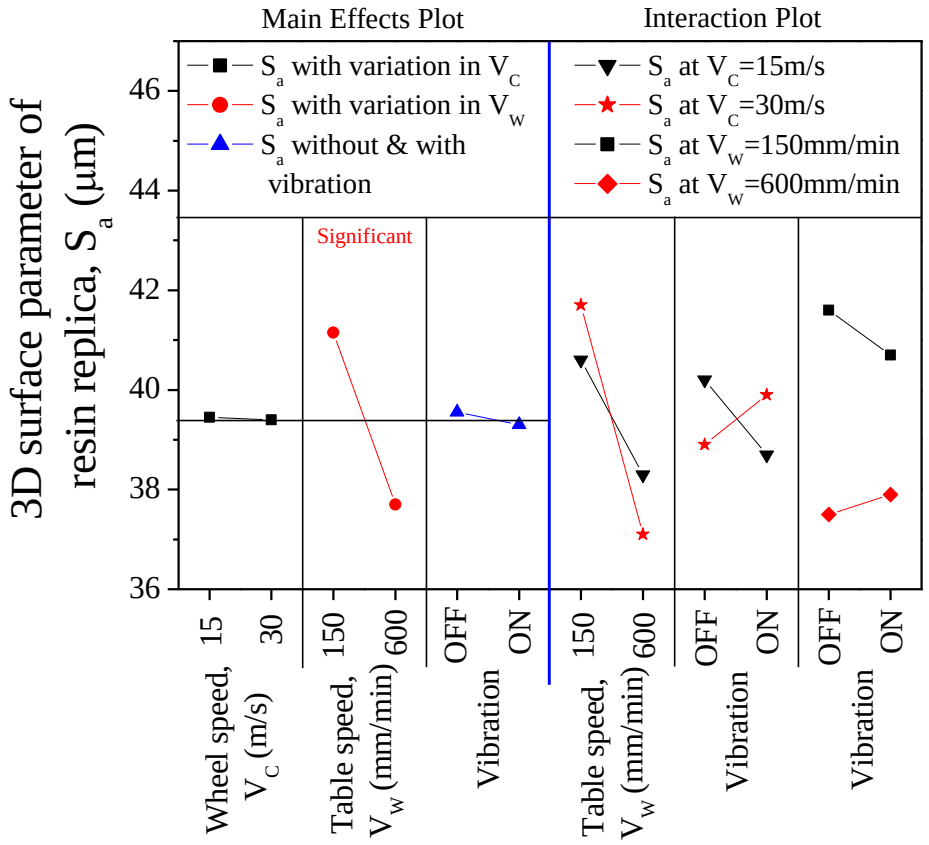


Fig. 4.3.15 Main effects and interaction plots for 3D surface parameter (S_a) of resin (positive) replicas of the SiC wheel

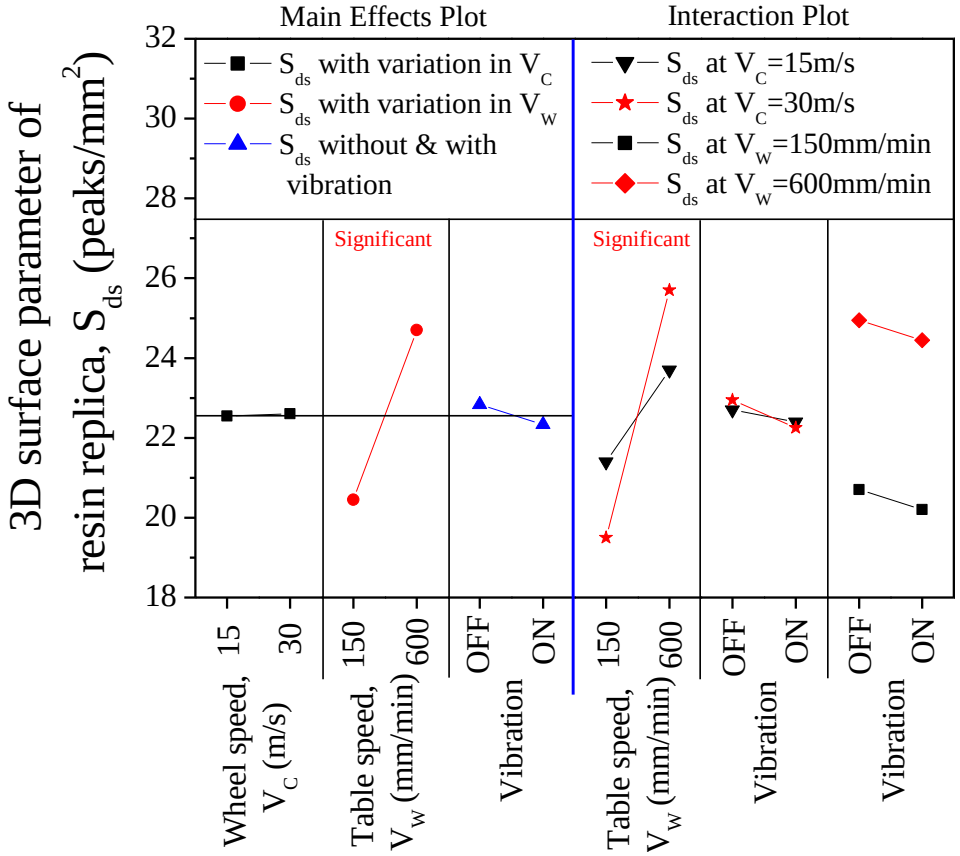


Fig. 4.3.16 Main effects and interaction plots for 3D surface parameter (S_{ds}) of resin (positive) replicas of the SiC wheel

The statistical analysis showed that table feed had significant effects on both S_a and S_{ds} parameters of the wheel surface (PCR's of 75.15 and 81.19% respectively). Additionally, the interaction between wheel speed versus table feed ($V_C \times V_W$) and vibration condition ($V_C \times$ Vib) had PCR's of 8.35% and 9.87% respectively for wheel S_a, however none of the factors were statistically significant. Conversely, wheel S_{ds} was significantly affected by an interaction between wheel speed and table feed ($V_C \times V_W$) with PCR of 17.09%.

A comparison among different wheel surfaces following roller dressing and grinding with and without ultrasonic assistance is shown in Fig. 4.3.17. Large voids/loss of grits can be seen on the wheel surface following conventional CFG, which could be attributed to a higher wheel wear (lower G-ratio) seen in Fig. 4.3.6. The wheel surface appeared to be more or less uniform when operating under UAG mode with minor loss of grains. This could possibly be the reason for lower workpiece S_a measured following UAG. However the grits underwent micro-fracture along the cleavage planes due to the mechanical impact imparted by the vibration, see Fig. 4.3.17(d).

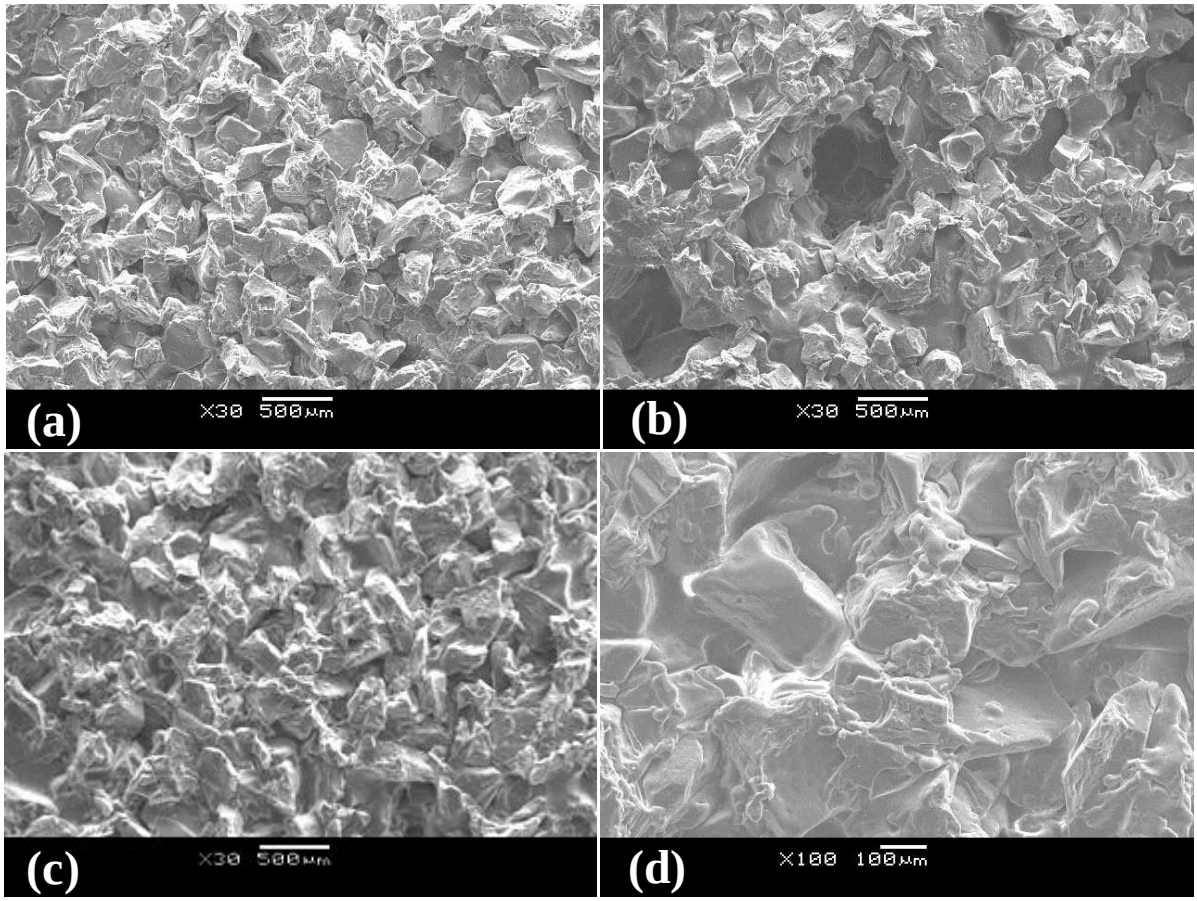


Fig. 4.3.17 SEM micrographs of selected wheel surface resin replicas: (a) After roller dressing, (b) Grinding at V_C=30 m/s, V_W=150 mm/min, US OFF, (c) Grinding at V_C=30 m/s, V_W=150 mm/min, US ON, (d) Micro-fracture at cleavage planes of grains subject to vibration

4.3.1.5 Microhardness and workpiece microstructure

Microhardness depth profiles in the transverse and longitudinal feed planes of selected γ-TiAl specimens ground at a cutting speed of 30 m/s are shown in Fig. 4.3.18 and 4.3.19 respectively. The rest of the microhardness data are detailed in Figs. A7.1 and A7.2 in Appendix A7.

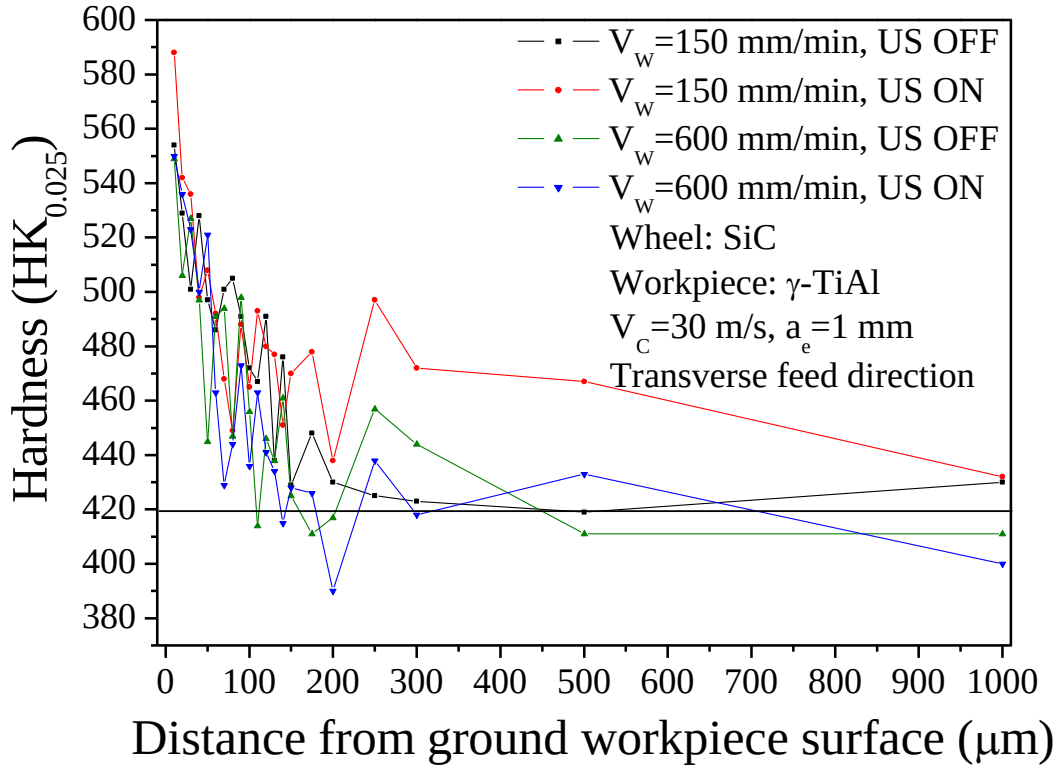


Fig. 4.3.18 Microhardness depth profile of γ-TiAl samples ground at V_C=30m/s; measurements taken in the transverse feed direction

Sub-surface microhardness typically were the maximum (~545 to 585$HK_{0.025}$) at a depth of 10 μm below the machined surface due to the greater rubbing and plastic deformation during machining, which then gradually decreased up to a depth of ~200-300 μm. Similar trend for the microhardness profile was reported by Bentley et al. (2001) when reciprocating surface grinding of a Ti-45Al-2Mn-2Nb-0.8%vol.TiB_2 XD^{TM} intermetallic alloy with SiC wheels. The occasional rise in the microhardness beyond a depth of 200 μm was probably due to the presence of Ti-rich needle-like phases at the site of indentation. Zhang et al. (1995) reported a rise in microhardness of up to ~700 $HV_{0.025}$ following creep feed grinding of a Ti-45Al-2Mn-2Nb-0.8%vol.TiB_2 XD^{TM} γ-TiAl with SiC, cBN and diamond wheels, which subsequently reduced to the bulk hardness level at ~100 μm depth below the surface. An increase in microhardness by up to 200HK above the bulk hardness (400HK) up to a depth of

50-100 μm was observed by Bentley et al. (1999) when using the aforementioned gamma alloy for surface grinding. Hood et al. (2007a and 2007b) also observed a maximum microhardness of ~550$HK_{0.025}$ and ~600 $HK_{0.025}$, respectively, following creep feed grinding of a Ti-45Al-8Nb-0.2C γ-TiAl intermetallic using SiC wheels.

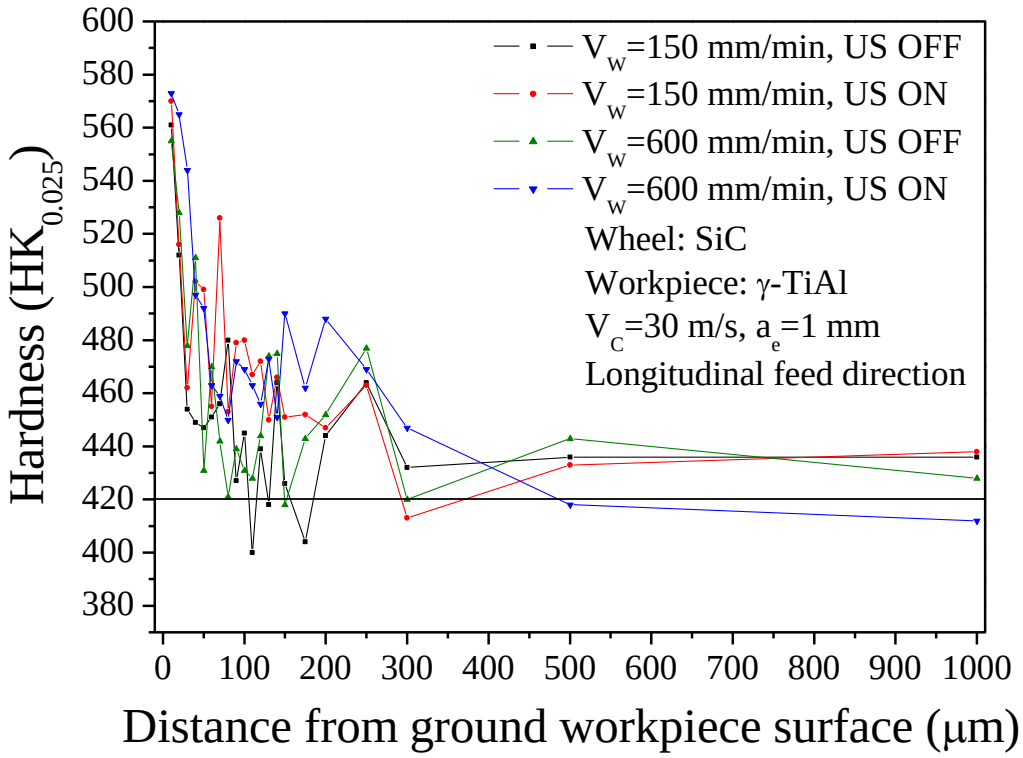


Fig. 4.3.19 Microhardness depth profile of γ-TiAl samples ground at V_C=30m/s; measurements taken in the longitudinal feed direction

With the assistance of ultrasonic vibration, sub-surface microhardness typically increased by ~6-8% compared to onventional CFG. According to Bentley et al. (2001), a greater probability of grit fracture produces lower tangential forces as well as restricts the amount of heat entering the workpiece. The surface hardness is therefore expected to increase due to the strain hardening capacity of the gamma alloy. Similar explanation could also be provided for the higher hardness obtained with ultrasonic assistance in the current experiments, where micro-fracturing of the grits was evident from the surface topography data of the graphite replicas. The increased sub-surface microhardness for the ultrasonically machined samples could also possibly be a consequence of the change in the material removal mechanism from fracture regime to ductile regime (Gao et al., 2009). The gamma alloy was thought to be undergone a mechanically activated brittle to ductile transition (BDT) under the action of vibration, which facilitated in stress relaxation through plastic deformation rather than through brittle failure. This was also evident from the SEM micrographs where greater plastic

deformation, ploughing/side flow and smearing of material were observed on the surfaces subject to vibration (Figs. 4.3.8(c) and (d)). In contrast, the lower sub-surface hardness values obtained for the conventionally ground workpieces was probably a function of the increased thermal energy entered into the workpiece (Bentley et al., 2001).

A typical deformation/bending of lamellae on the longitudinal feed plane of the workpiece following grinding in the table feed direction is shown in Fig. 4.3.20. The depth of deformation was up to ~15 μm beneath the machind surface. This was possibly the results of the surface drag, where lamellae that were originally perpendicular to the surface deformed almost parallel to the work surface under the cutting action of the abrasive grains. This indicated strain at high temperature, possibly >500°C according to Mantle and Aspinwall (1997). A deformed layer up to ~25 μm under the machined surface was also observed by Sharman et al. (2001b) when finish turning a Ti-45Al-2Mn-2Nb+0.8vol.%TiB_2 XD^{TM} gamma alloy.

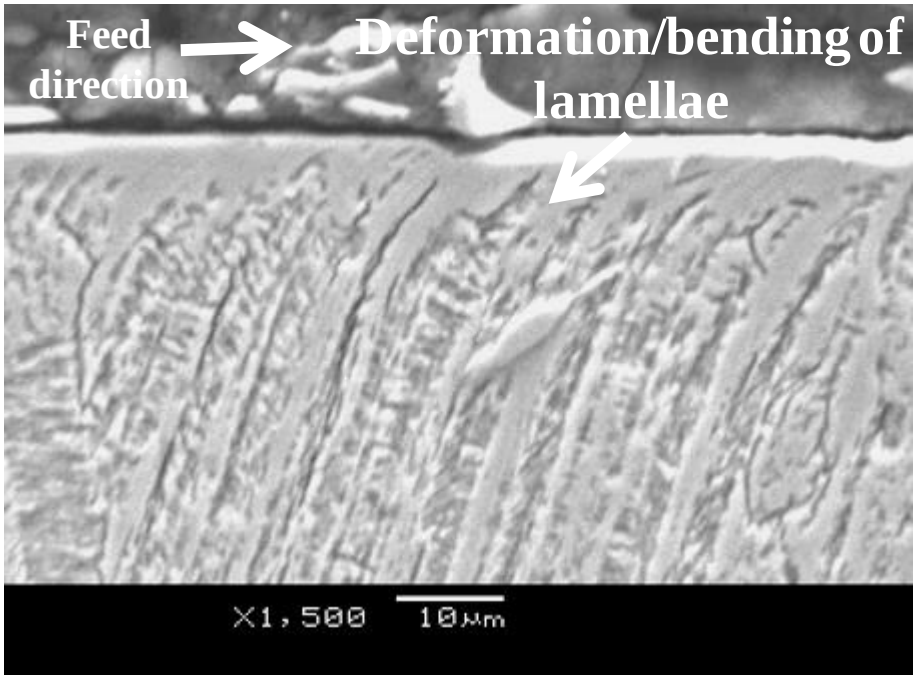


Fig. 4.3.20 SEM micrograph of the microstructure of γ-TiAl in the longitudinal feed plane showing deformation/bending of lamellae (ground at V_C = 15 m/s, V_W = 150 mm/min, d = 1.0 mm, US ON)

Unlike the observation on the longitudinal feed planes, the bending of lamellae was not apparent on the transverse feed planes as seen from the SEM micrographs of the selected γ-TiAl microstructures in Fig. 4.3.21, although Zhang et al. (1995) exhibited examples of deformed layer on the transverse cross-section following creep feed grinding of γ-TiAl. Figures 4.3.21(a) and (b) show the typical grit marks on the transverse plane, which were

however absent on the longitudinal plane. The cross-sections of the machined surfaces were mostly free from cracks, laps, folds or heat affected zone, although minor pull-out of material was observed on the machined surface cross-section in Test 7. This observation was in agreement with the findings by Bentley et al. (1999), however it was in contrast to the study by Hood et al. (2007a and 2007b) and Hood (2010), where extensive cracking, fracture/pull-out and smearing of material were reported when creep feed grinding γ-TiAl and burnt-resistant titanium (BuRTi) alloys. The application of ultrasonic vibration did not significantly alter the material microstructures possibly due to generation of low to moderate temperatures during UAG.

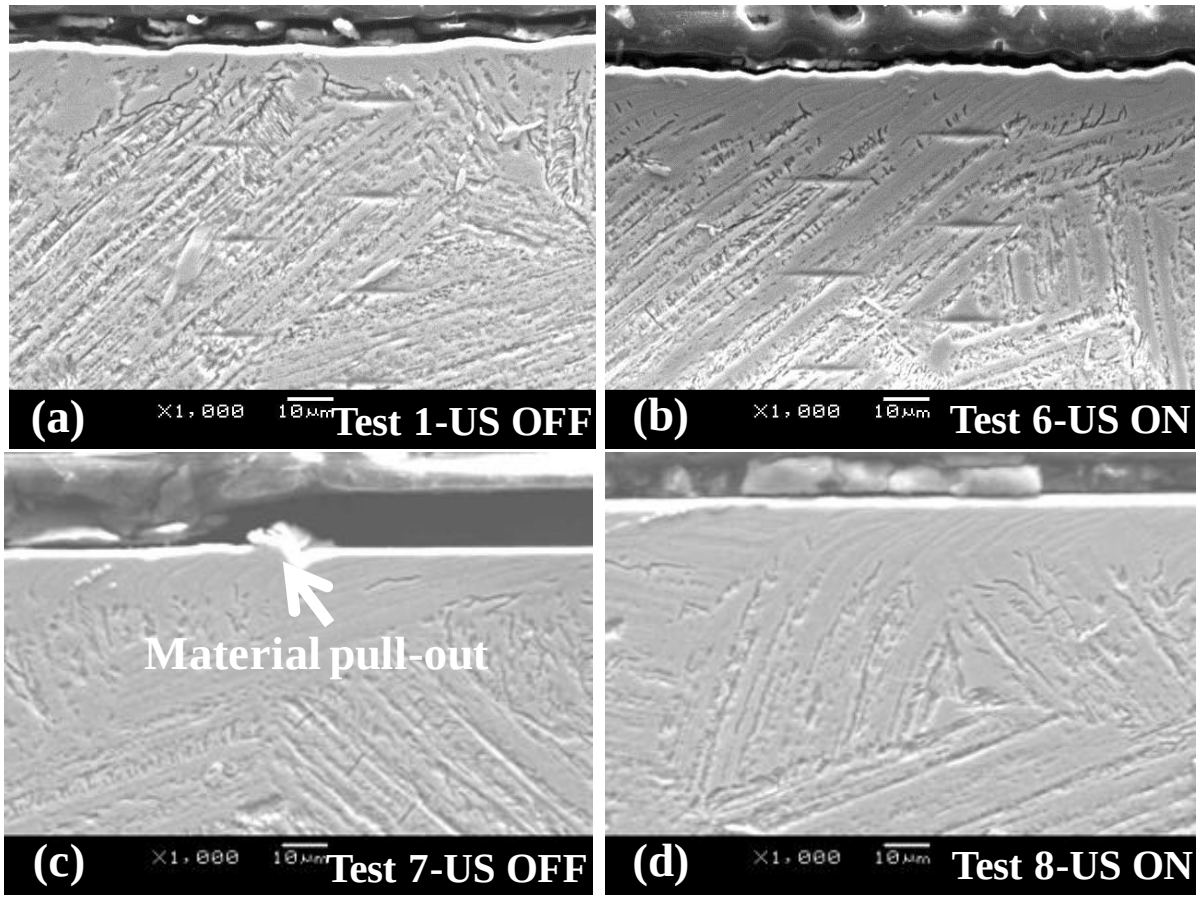


Fig. 4.3.21 Microstructures of γ-TiAl samples on (a), (b) Transverse feed planes, (c), (d) Longitudinal feed planes

The main observations from Phase 3A trials were:

- The assistance of ultrasonic actuation to the workpiece produced reductions in both F_v and F_h by up to 19% and 35% respectively.

- G-ratio varied from 3.19 to 7.99 with the maximum level recorded at the lowest V_C (15 m/s) and V_W (150 mm/min) under conventional CFG mode, which was further enhanced by ~30-75% (except Test 8) when UAG.
- Both R_a and S_a of the ground surfaces typically decreased (~3-10% reduction in R_a) with the application of vibration.
- The S_a of the graphite replicas decreased in 3 out of 4 tests when grinding with US vibration. The S_a and S_{ds} of the resin replicas also generally decreased following UAG in comparison to conventional CFG.
- Sub-surface microhardness was typically at its maximum (~580 $HK_{0.025}$) at a depth of 10 µm below the machined surface, which then gradually decreased to the bulk hardness (~420 $HK_{0.025}$) at a depth of ~200-300 µm. With ultrasonic assistance, sub-surface microhardness typically increased by ~ 6-8%.
- Cross-sectional microstructures in the longitudinal feed plane showed typical deformation/bending of lamellae with a depth of deformation up to ~15 µm beneath the machined surface. Ground surfaces were mainly free from cracks, laps, folds or heat affected zone with little or no material pull-out. The application of ultrasonic vibration did not significantly alter material microstructure.

4.3.2 Phase 3B: Investigation of UAG on γ-TiAl with electroplated diamond superabrasive wheel

4.3.2.1 Grinding forces

Figure 4.3.22 details the vertical (F_v) and horizontal (F_h) grinding forces obtained with and without ultrasonic vibration when grinding a γ-TiAl with an electroplated diamond (D252) wheel.

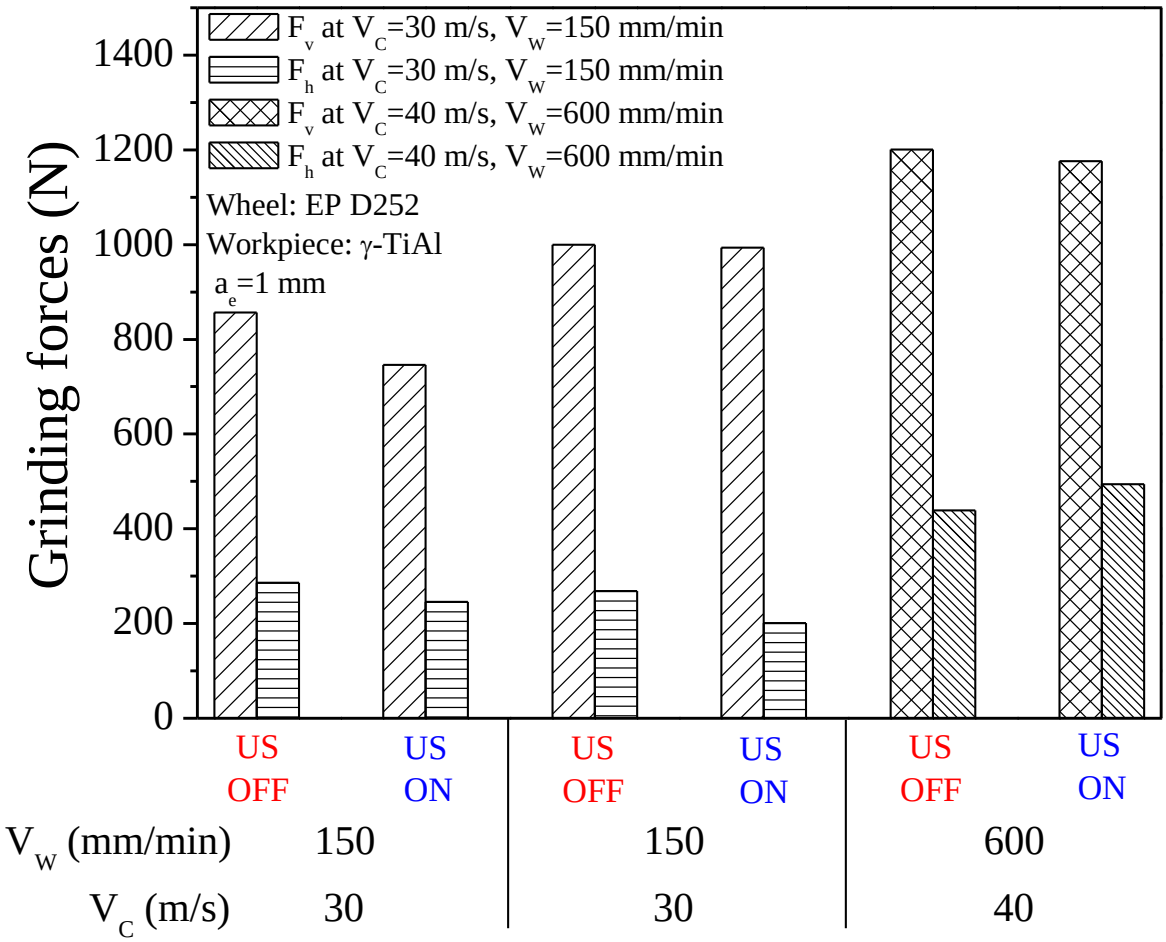


Fig. 4.3.22 Vertical (F_v) and horizontal (F_h) forces under different grinding conditions

In the initial stage of grinding with a single layer wheel, the grits with higher protrusions from the nickel bond surface prevent those with smaller protrusions from participating in cutting action. This results in lower number of grits taking part in micro-cutting, which however increases as greater number of grits become active due to micro/macro-fracture with the progression of grinding (Changyong et al., 2010), leading to an increase in the force levels from the previous to the successive passes. Therefore the grinding process can be divided into

two stages, such as an early unsteady period and a subsequent steady phase (Ding et al., 2010b). Similar observations was also made by Chattopadhyay et al. (1991) where normal forces increased from the 1st to ~10th pass and reached the steady state subsequently when grinding aluminium oxide and cast iron workpieces with monolayer brazed diamond wheels. However in the present study, the vertical force did not appear to reach its steady state when grinding was carried out conventionally. Unfortunately further tests were not possible due to a limited availability of the workpieces. When grinding was carried out without ultrasonic actuation, F_v increased from 857 to 1201 N as the grinding progressed from the 1st to 3rd and 3rd to 5th pass. Soo et al. (2011b) reported a mean normal force of ~1600 N when grinding a burn-resistant titanium (BuRTi) material with vitrified bonded diamond (D91) wheels. The increase in force values from the 1st to 3rd pass was due to micro/macro fracture of abrasive grains and participation of more grits in micro-cutting action. However an increase in undeformed chip thickness (Ding et al., 2010a) at a higher level of table feed (600 mm/min) also played an important role for increasing F_v from the 3rd to 5th pass. Although the normal forces were expected to increase from the 1st to 2nd, 3rd to 4th and 5th to 6th passes due to grain fracture, they were always lower when the grinding was employed with vibration (2nd, 4th and 6th pass). Ghosh and Chattopadhyay (2007) highlighted the different mechanisms of grit failures in single layer electroplated wheels such as grain pull-out, breakage at the bond level as well as above the bond level and micro-fracture at the tip. It was observed previously that an increase in normal force could be either due to attritious wear (Hwang et al., 2000) or fracture at the bond level (Bhaduri and Chattopadhyay, 2010). The reduction in force under the vibrating mode was possibly due to micro-breakage of the grits and thereby preserving the grit sharpness under hybrid configuration. The maximum reduction in F_v was by 13% from the 1st to 2nd pass, whereas that in F_h was by ~25% from the 3rd to 4th pass. F_h was found to marginally increase from the 5th to 6th pass due possibly to an increase in frictional force between a greater number of grits with the work surface.

4.3.2.2 Radial wheel wear and G-ratio

The initial high radial wheel wear (~7 μm) obtained with the electroplated wheel in the 1st pass was due to a 'running-in' wear of the over-protruded grits (Fig. 4.3.23). Wheel wear decreased to only ~2 μm in the 3rd pass as the majority of the highly protruded grits had already undergone micro-fracture above the bond level. The increase in wheel wear in the 5th pass (~3 μm) was the result of using a faster wheel speed (40 m/s) and a consequent generation of higher temperature. The radial wheel wear however remained almost negligible

(~1 µm) when grinding was operated with ultrasonic vibration. This could be attributed to the micro-conditioning effect fostered by the component of vibration along the Z-direction (radial to the wheel surface). This resulted in micro-fracture on the grit tips instead of creating wear flats. This was also evidenced by the reduction of force levels under hybrid grinding conditions, which indicated that the grains retained their sharpness under the action of vibration.

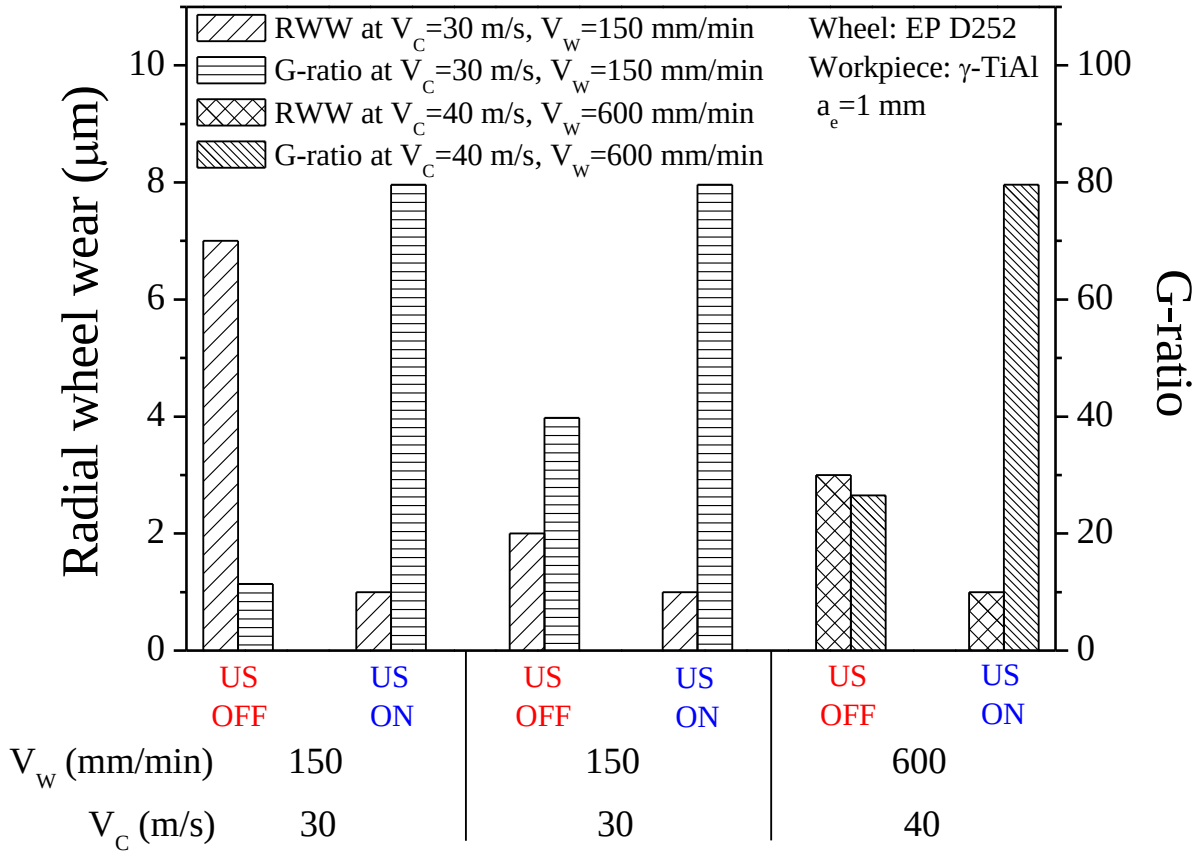


Fig. 4.3.23 Radial wheel wear and G-ratio under different grinding conditions

While comparing with the G-ratios obtained with the silicon carbide wheel (~3 to 8) in Phase 3A, it was observed that the EP diamond wheel always exhibited much higher G-ratios, in a range of ~11-80. G-ratios varied within ~11 to 40 in conventional CFG, whereas it remained almost constant at a value of ~80 under hybrid configuration. The maximum increase in G-ratio with the EP wheel (39.80) was by ~550% with respect to that obtained with the SiC wheel (6.14) when grinding was carried out conventionally. Under vibrating mode, maximum G-ratios recorded with the electroplated and SiC wheels were 79.60 and 7.99 respectively (an increase by ~900%).

The G-ratios obtained for vitrified diamond wheels in a previous sturdy were between 2 to 6, whereas cBN wheels exhibited much higher G-ratios between 7 to 286 when grinding a burn-resistant titanium (BuRTi) alloy (Soo et al., 2011b). However this observation was in contrast to the findings of Liu et al. (2007) where electroplated diamond wheels exhibited much less loading and attritious wear compared to cBN wheels while grinding nickel based superalloys. A study on the grinding of silicon nitride with single layer diamond wheels showed that the wear mechanism was primarily dominated by attritious wear with little evidence of fracture or grain pull-out (Hwang et al., 2000). Similar observation was also reported by Liu et al. (2007) and Guo et al. (2007). In the present research, however, attritious wear was negligible when the wheel was viewed under the microscope following each grinding pass. In contrast, the grains appeared to have undergone cleavage fractures on the grit tips and/or on the different faces of the grits (Sunarto and Ichida, 2001). Figure 4.3.24 (a) and (b) show the wheel surfaces after 1st and 2nd pass respectively. A possible wear flat is shown in Figure 4.3.24 (a), however wheel surfaces typically exhibited minor attritious wear. There were also apparently no visible evidence for loaded chips and/or adhered material at the tip of the grits or inter-grit spaces.

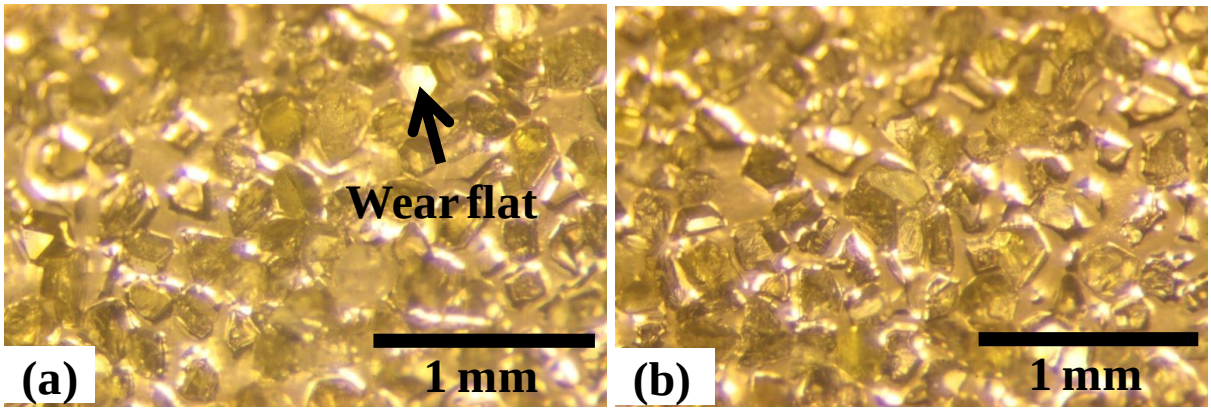


Fig. 4.3.24 Optical micrographs of wheel surfaces following grinding at (a)V_C=30 m/s, V_W=150 mm/min, US OFF, (b) V_C=30 m/s, V_W=150 mm/min, US ON

4.3.2.3 Workpiece surface topography and quality

The images of the γ-TiAl workpiece surfaces ground with the EP diamond wheel are shown in Fig. 4.3.25. No apparent surface cracks or grinding burn/chatter was visible on any of the ground specimens. This observation was in contrast with that obtained by Hood (2010) and Soo et al. (2011b). This could be probably attributed to a higher coolant pressure (~28-30

bar) used in the current work compared to that utilised in the previous studies (7 bar), thereby ensuring better ingress of cutting fluid into the grinding zone.

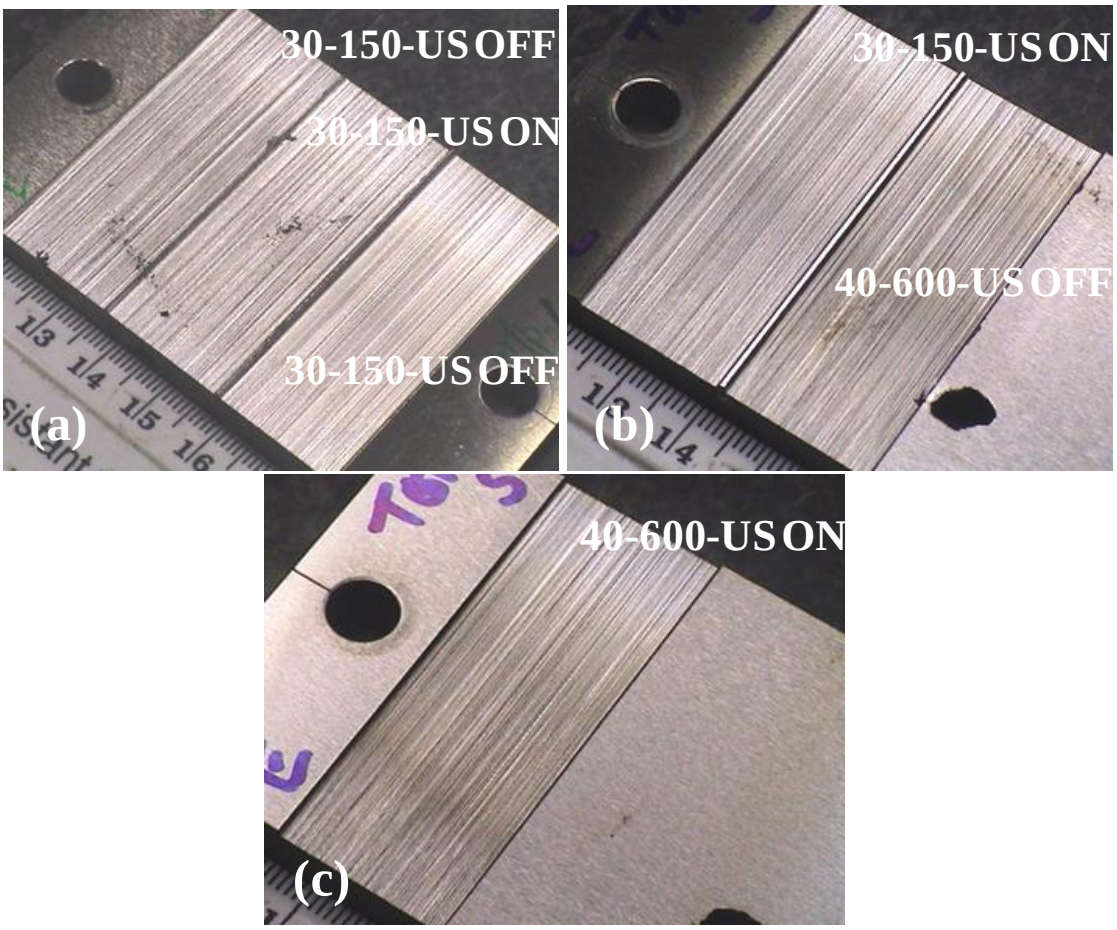


Fig. 4.3.25 Images of the ground γ-TiAl workpiece surfaces

The 2D and 3D workpiece surface parameters are detailed in Figs. 4.3.26 and 4.3.27 respectively. Typically R_a and S_a of the ground surfaces decreased gradually from the 1st to 4th pass due to the engagement of greater number of grits in cutting. However both parameters increased in the 5th pass due to an increase in the table feed and a consequent rise in the undeformed chip thickness. However, R_a and S_a subsequently decreased in the 6th pass due to micro-splintering of grits caused by vibration. The R_a of the ground surfaces (~4 to 6 µm) was much higher than that (0.97-1.65 µm) reported by Soo et al. (2011b). This could be attributed to a difference in the grit densities and average grain sizes used in the previous and present studies. The R_t and R_z parameters followed the same trends as that of R_a. Although S_t and S_z decreased from the 1st to 2nd pass, they increased from the 3rd to 4th and 5th to 6th passes. This could be due to the effect of the radial component of vibration (along Z-direction). Typically S_p and S_v (not shown here) also exhibited the same trends as S_t and S_z. While comparing between the γ-TiAl surfaces ground with the SiC and EP diamond wheels, the latter produced higher R_a and S_a due to a lower grain packing density on the wheel surface.

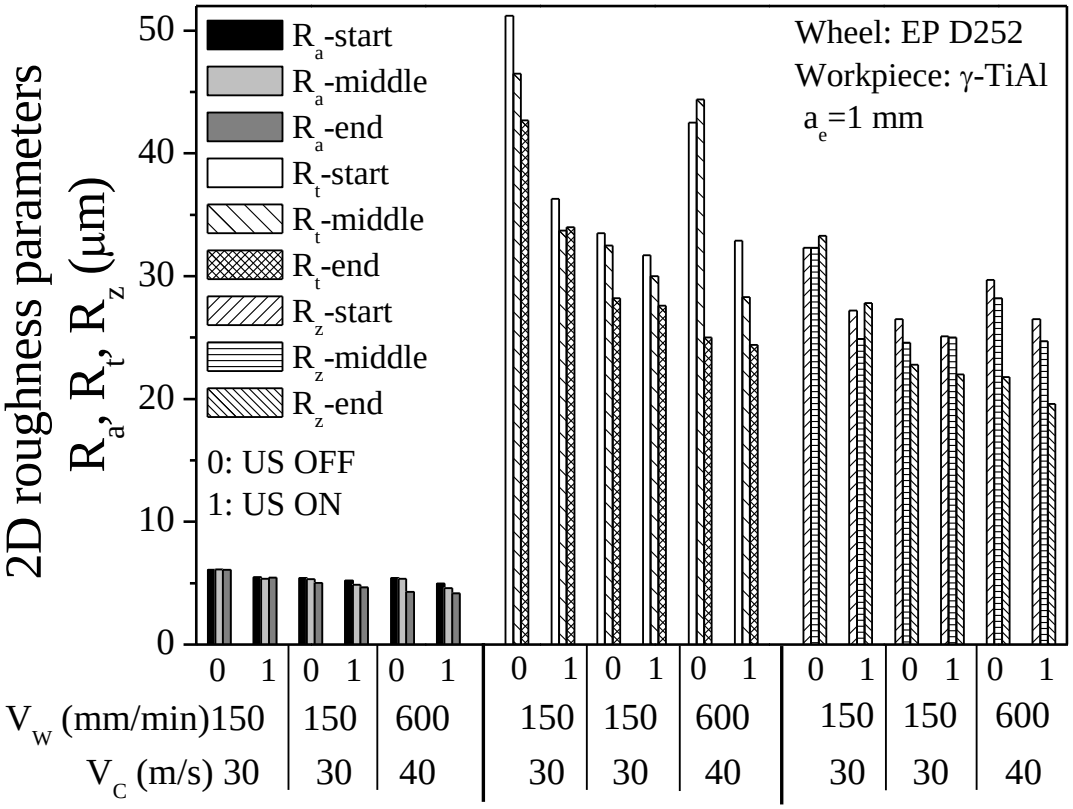


Fig. 4.3.26 Surface roughness parameter (R_a) of ground γ-TiAl workpiece surfaces

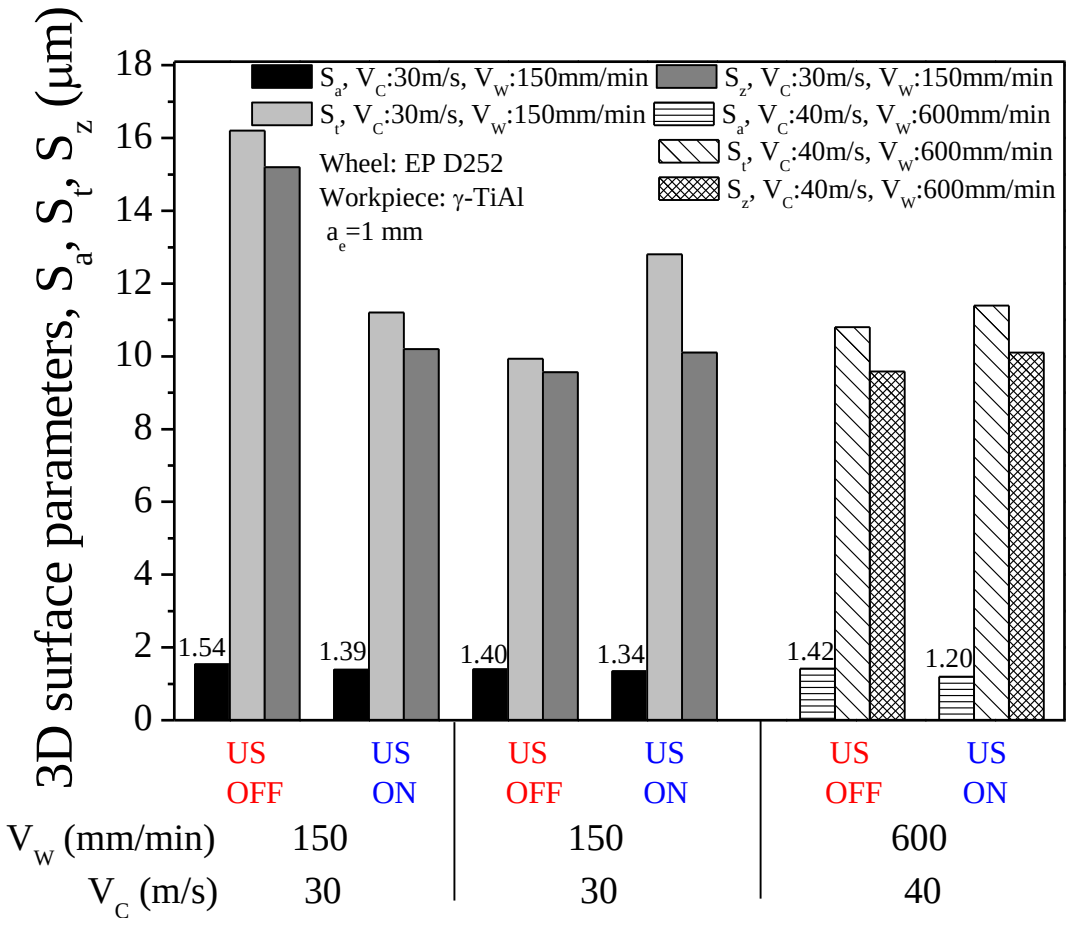


Fig. 4.3.27 3D topographical parameters of ground γ-TiAl workpiece surfaces

The rapid running-in wear of the grinding wheel and the reductions in R_a and S_a from the 1st to 3rd pass were evident from the corresponding SEM micrographs of the ground surfaces, see Fig. 4.3.28(a) and (b). The former micrograph revealed deep characteristic striations and scratches along the grinding direction due to a fewer number of grits engaged in cutting/shearing in Test 1, which according to Hwang et al. (2000), was an indication of extensive ductile flow of the material. Teicher et al. (2008) also reported that the chips produced during grinding of Ti-6Al-4V alloy with monolayer brazed diamond wheels were ductile and contained small, deformed chips together with long, sheared, and leafy chips. In contrast, the ground surface in Fig. 4.3.28(b) (Test 3) showed smoother, much shallower grooves with some fine gouges and very fine striations along the grinding direction.

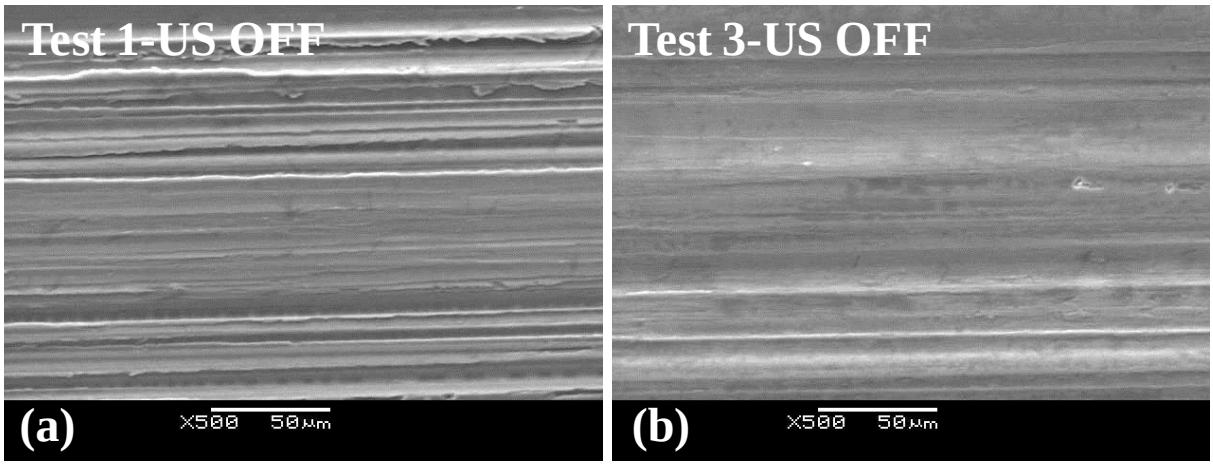


Fig. 4.3.28 SEM micrographs of ground γ-TiAl surface at (a) Test 1: V_C = 30 m/s, V_W = 150 mm/min, d = 1.0 mm, US OFF, (b) Test 3: V_C = 30 m/s, V_W = 150 mm/min, d = 1.0 mm, US OFF

With the assistance of vibration, the material appeared to be more plastically deformed as higher side flow/ploughing can be seen in the corresponding SEM micrographs, see Fig. 4.3.29(a). Similar to the observations in the previous phases, the ultrasonic assisted ground surfaces exhibited greater amount of overlapping grit marks, see Fig. 4.3.29(b). The ground surface in Test 5 became smoother along with a fewer striation marks, see Fig. 4.3.29(c). In contradiction to the expectation, the ultrasonically ground surface in Test 6 revealed deep striations as well as side flow of the material, see Fig. 4.3.29(d). This observation was in agreement with Zheng and Xu (2006) who reported the existence of many tiny scratches and plastic flow at the bottom of the grooves when ultrasonic assisted creep feed grinding of alumina ceramics. It can be inferred that ultrasonic vibration resulted in a change in the mechanical properties of the material (Azarhoushang and Tawakoli, 2012) and thereby transforming the material removal mechanism from fracture regime in conventional grinding

to ductile regime in hybrid grinding (Gao et al., 2009). The potential of vertical elliptic ultrasonic assisted grinding for ductile cutting of brittle materials like polysilicon was also identified by Peng et al. (2012b).

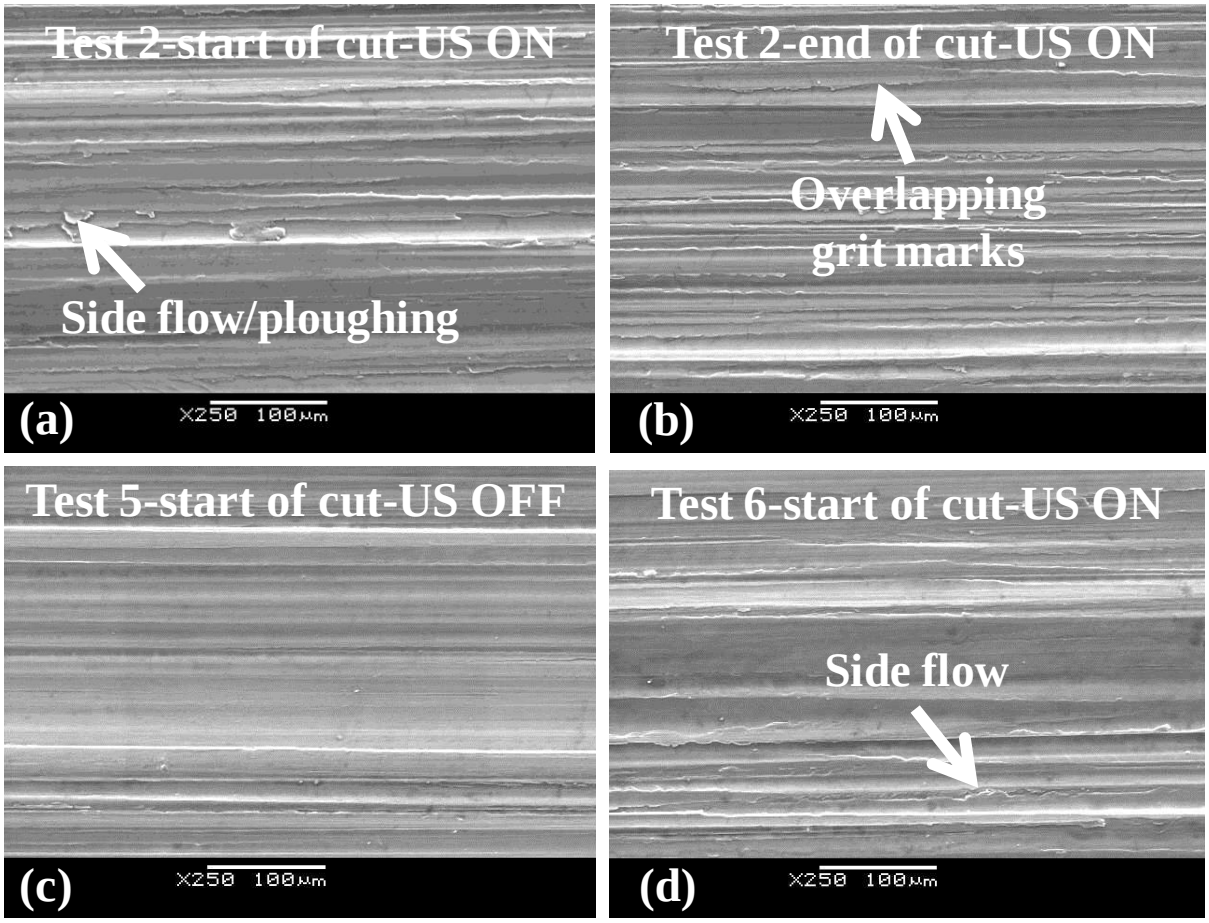


Fig. 4.3.29 SEM micrographs of ground γ-TiAl surface at (a) and (b) Test 2: V_C = 30 m/s, V_W = 150 mm/min, d = 1.0 mm, US ON, (c) Test 5: V_C = 40 m/s, V_W = 600 mm/min, d = 1.0 mm, US OFF, (d) Test 6: V_C = 40 m/s, V_W = 600 mm/min, d = 1.0 mm, US ON

4.3.2.4 Grinding wheel surface evaluation

S_a of the graphite replicas followed the same trend of workpiece R_a and S_a. Figure 4.3.30 shows that S_a of the graphite replicas decreased gradually from the 1st to 4th pass, however increased in the 5th pass and subsequently decreased in the 6th pass. A decrease in S_a from the 1st to 4th pass indicated breakage/fracture of the over-protruded grits and participation of more number grits in grinding. The increase in S_a in the 5th pass was in line with the workpiece surface roughness data. This was due to an increase in table speed from 150 to 600 mm/min and a corresponding rise in the undeformed chip thickness. S_a of graphite surfaces however decreased in the 6th pass confirming the 'conditioning effect' of vibration on the grits, thereby imparting greater uniformity on the grit heights.

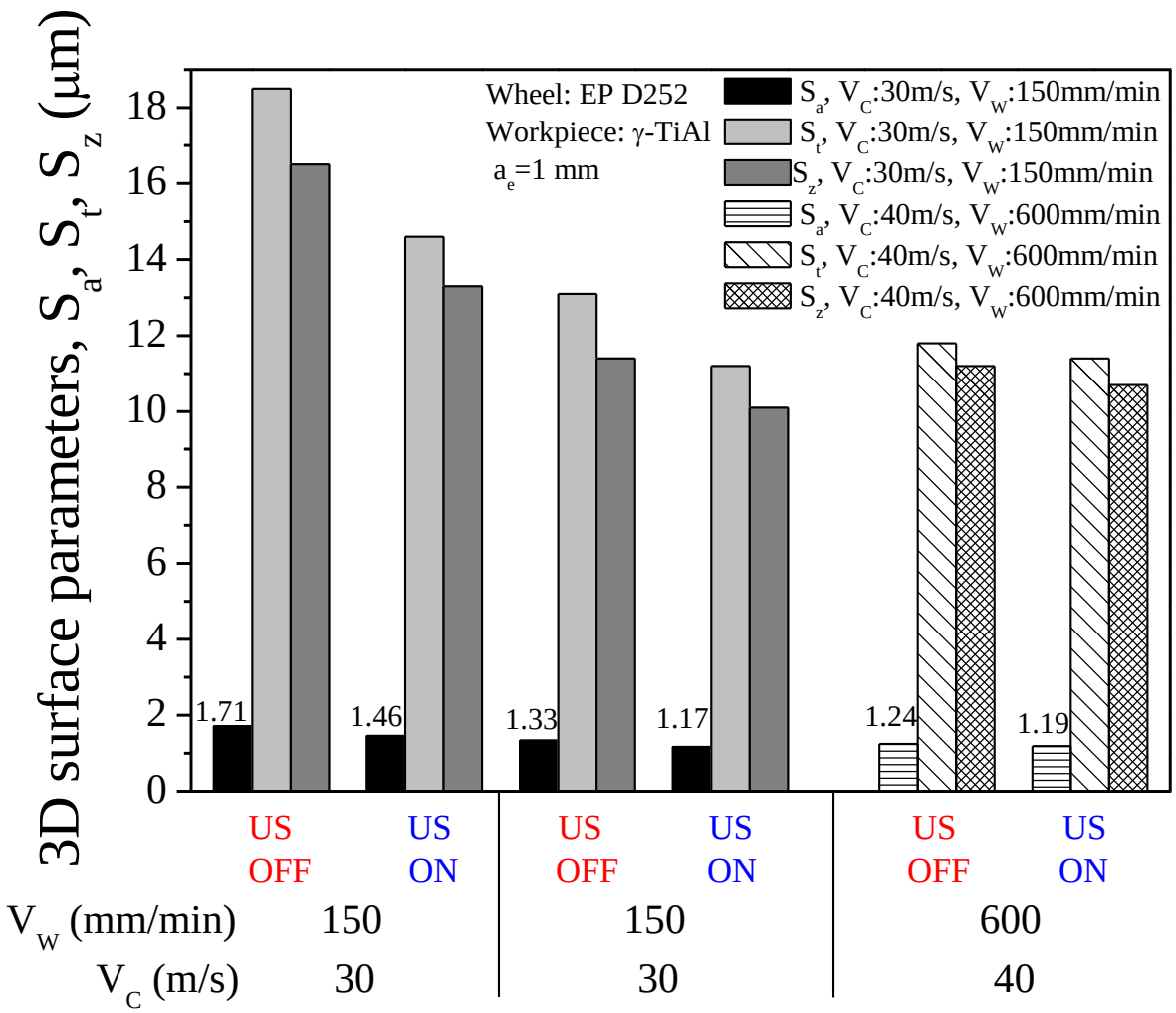


Fig. 4.3.30 2D and 3D surface parameters of graphite (negative) replicas of EP D252 wheel

4.3.2.5 Microhardness and workpiece microstructure

Figures 4.3.31 and 4.3.32 show microhardness depth profile of the ground workpieces after 1st & 2nd and 5th & 6th passes respectively. Microhardness increased by ~30-60% within 10-20 μm beneath the machined surface, which then gradually reduced to the bulk hardness value at a depth of ~100 μm. The other microhardness depth profiles are presented in Figs. 8.1 to 8.4 in Appendix A8. The higher hardness below the ground surface was attributed to greater mechanical working/ploughing in the presence of high vertical grinding force (Soo et al., 2011b). Initially ultrasonically ground samples exhibited lower sub-surface microhardness than the conventionally ground specimens. This was due to the lower vertical force in the 2nd pass in comparison to that in the 1st pass. However sub-surface microhardness was ~16% higher following the 6th pass than that after the 5th pass. This was attributed to the higher mechanical load imparted by ultrasonic vibration and consequent plastic deformation of the workpiece surface.

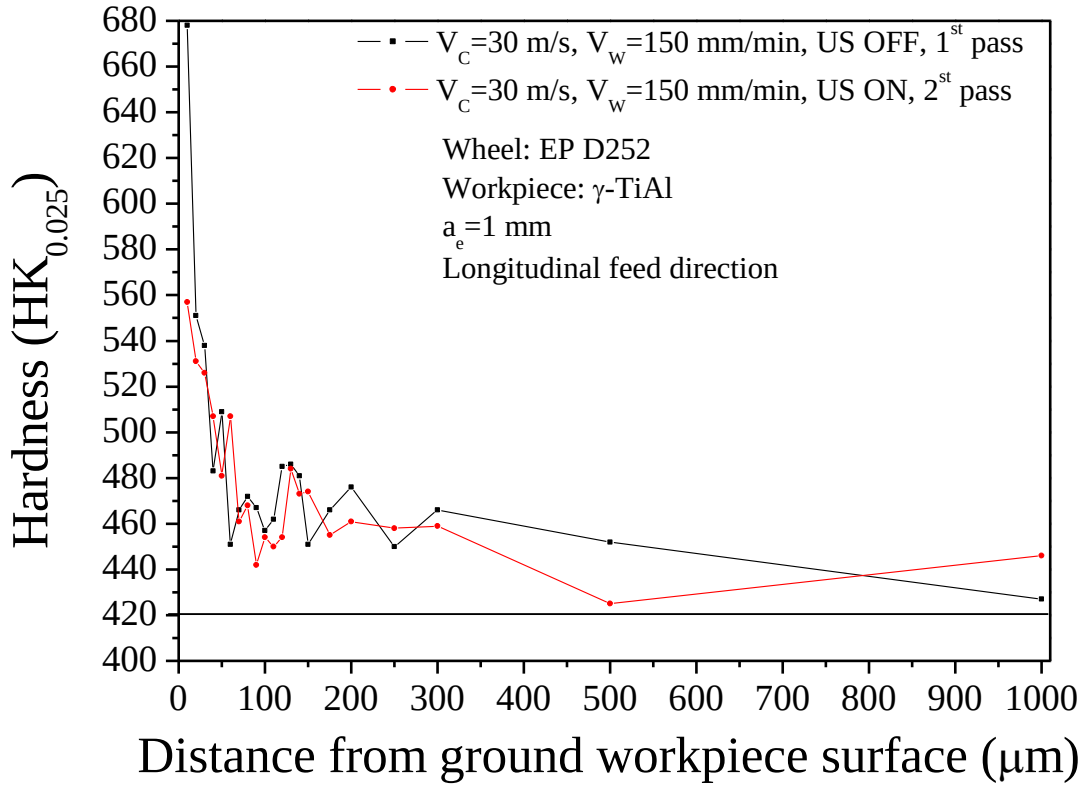


Fig. 4.3.31 Microhardness depth profile of γ-TiAl samples after 1st and 2nd pass; measurements taken in the longitudinal feed direction

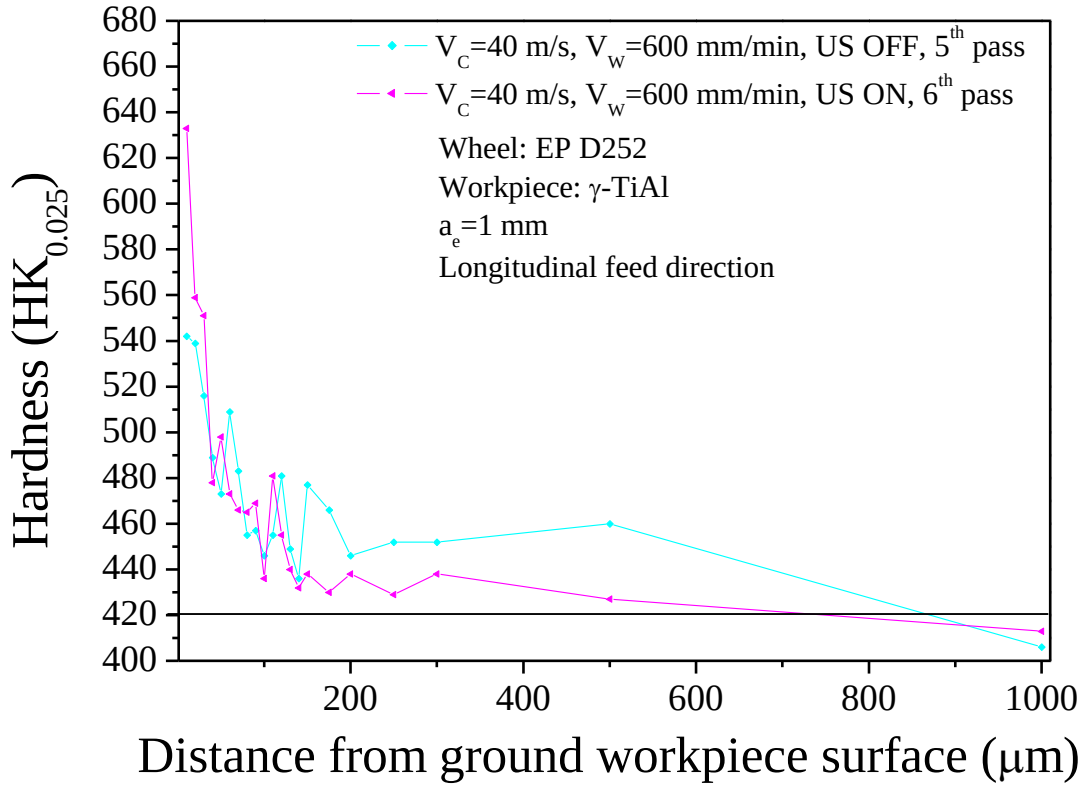


Fig. 4.3.32 Microhardness depth profile of γ-TiAl samples after 5th and 6th pass; measurements taken in the longitudinal feed direction

The microstructure of the γ-TiAl specimens in the transverse feed plane showed typical grit marks, see Fig. 4.3.33. The depth and width of the indentation marks generally reduced from the 1st to the 6th pass, due to the fracture of grains and an increase in the active cutting points on the single layer wheel surface with the progress of grinding, see Fig. A8.5 in Appendix A8. The microstructures taken on the longitudinal feed plane showed deformation of lamellae up to ~20-25 µm below the machined surface, see Fig. 4.3.34. The cross-sectional microstructures generally did not reveal any tears, laps, fractures or loss of grains.

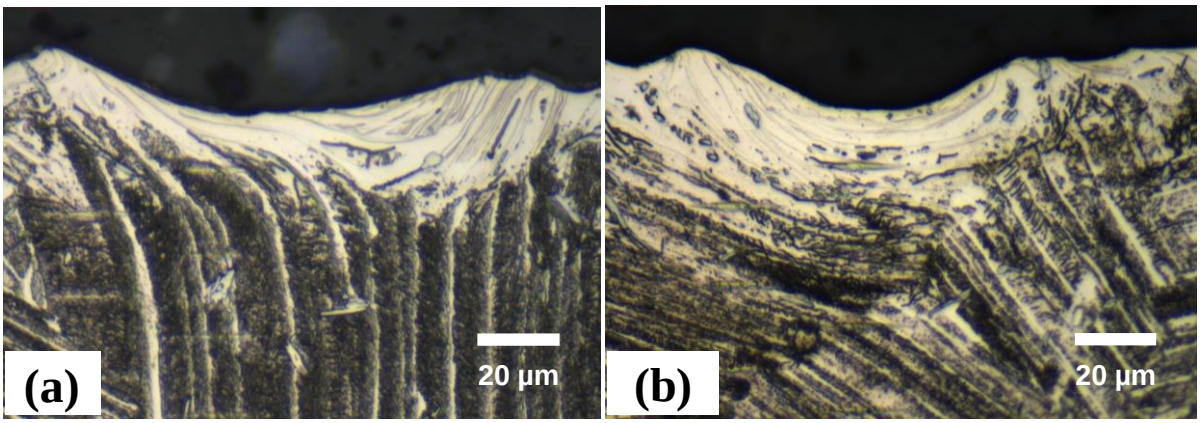


Fig. 4.3.33 Microstructure of γ-TiAl on the transverse feed plane: (a) After 1st pass, (b) After 6th pass

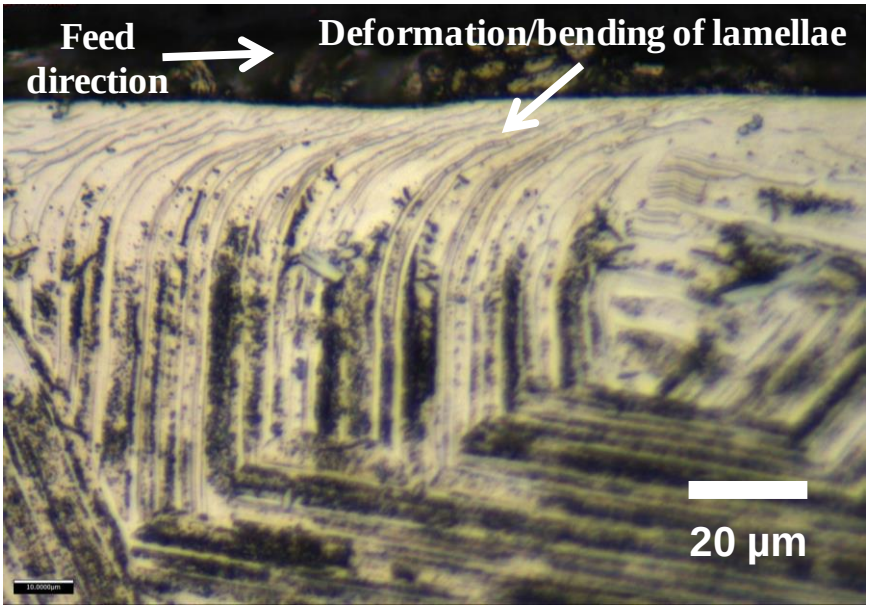


Fig. 4.3.34 Microstructure of γ-TiAl on the longitudinal feed plane showing deformation/bending of lamellae

The key results from Phase 3B are given below:

- Forces F_v and F_h generally reduced when grinding with ultrasonic vibration with maximum reduction in F_v by 13% from the 1st to 2nd pass, and that in F_h by ~25% from the 3rd to 4th pass.
- Radial wheel wear remained almost negligible (~1 µm) when operating with ultrasonic assistance. The corresponding G-ratios for conventional CFG varied from ~11-40 whereas it remained almost constant at ~80 with UAG.
- The R_a and S_a of the ground surfaces gradually decreased from the 1st to 4th pass, however they increased in the 5th pass but decreased again in the 6th pass.
- Sub-surface microhardness increased by ~30-60% within 10-20 µm beneath the machined surface, which then gradually reduced to the bulk hardness value at a depth of ~100 µm. Initially sub-surface microhardness of the ultrasonically ground specimens was lower than that of the conventionally ground samples, however the former increased by ~16% following the 6th pass.
- The microstructures in the longitudinal feed plane showed deformation of lamellae up to ~20-25 µm below the machined surface but were free from other defects such as tears, laps, fractures or loss of grains etc.

5. CONCLUSIONS

The key observations stemming from the literature review and experimental work on ultrasonic assisted grinding and dressing are summarised below. Overall conclusions are then presented correlating the results with the scientific explanation.

5.1 Literature review on ultrasonic assisted grinding

- In the majority of past studies, ultrasonic vibration was applied using piezoelectric devices, a few papers were found where magnetostrictive devices were used to generate ultrasonic vibration.
- When US vibration was applied to the grinding wheel/tool, vibration was applied axially to the wheel/tool. In contrast, ultrasonic actuation of workpieces utilised vibration either in the feed or cross-feed directions. In some cases, vibration was simultaneously employed in two mutually perpendicular directions with the resulting motion following an elliptical path. A minority of papers also discussed the application of vibration to the cutting fluid for improved cleaning of grinding wheels.
- The typical range of frequency was 20 to 25 kHz, with the amplitude of vibration 0.5 to 32 μm. The majority of papers did not disclose details of ultrasonic power.
- The body of research on UAG to date mainly focussed on the surface grinding of ceramics, however other workpiece materials such as glass and various grades of steel (stainless, plain carbon, alloyed etc.) were also subject to US vibration. Limited information was found on ultrasonic assisted grinding of advanced aerospace materials such as nickel based superalloys or γ-TiAl.
- The superimposition of ultrasonic vibration in grinding resulted in an intermittent cutting action of the grits, thereby reducing the thermal load but increasing the mechanical impact. This led to reductions in both normal and tangential grinding forces by ~30-50%, specific grinding energy decreased by ~10-30%, surface roughness decreased by ~30-50%. In a minority of papers an increase in workpiece R_a was reported due to higher wheel wear resulting from the micro-splintering of grits under the action of vibration.
- Ultrasonic assisted grinding is capable of producing intricate and complex shapes, mirror surface finish, micro-fabrication of parts and dry grinding of soft steel.

5.2 Experimental work

5.2.1 Phase 1A: UAG experiments using Flexiskills ultrasonic system

- Higher vertical grinding force (F_v) was obtained with the application of vibration during grinding; however the force due purely to vibration was not subtracted from the total grinding force.
- It was difficult to transmit an adequate/consistent ultrasonic vibration to the workpiece by employing the 250 W Flexiskills ultrasonic generator using a conical horn.
- There was ingress of cutting fluid into the transducer sleeve despite attempts to shield the transducer using plastic sheets.
- There were problems regarding the fixation/repeat mounting of the workpiece at the end of the horn.
- It was not possible to assess the amplitude of vibration from the analogue output of the ultrasonic generator.

5.2.2 Phase 1B: Initial UAG trials of Inconel 718 with a VORTEX 80 mesh wheel using the MPI ultrasonic system

- The radial wheel wear generally decreased and G-ratio increased when the grinding was carried out at a_e of 0.5 mm with ultrasonic assistance; however the reverse trend was observed when a_e increased to 1.5 mm.
- A single depression/trough mark (45-90 μm deep) appeared on each of the grinding tracks when a_e was 0.5 mm irrespective of vibration assistance.
- The number of depression marks increased to two or three when a_e increased to 1.0 mm. With a further increase in a_e up to 1.5 mm, the depression marks (with a depth up to 140 μm) appeared over most of the grinding track.
- Deformation was eliminated by using a dummy workpiece when grinding was performed at an a_e of 1.0 mm; however it again occurred from the start of grinding when a_e was set at 1.5 mm.
- The ground surfaces exhibited a much smoother appearance at the beginning of the grinding track, which however worsened towards the end of cut.
- The majority of 2D profiles showed an increase in R_a, R_t and R_z from the beginning to the end of the grinding tracks. There was no typical trend in R_a of the workpieces following

grinding at an a_e of 0.5 mm with and without the assistance of vibration, although higher R_t and R_z were observed when the amplitude was set at 40 and 50%. All 2D parameters (R_a, R_t and R_z) were found to be lower when grinding was conducted at a depth of cut of 1.5 mm under hybrid operation. Surface roughness R_a was marginally higher when grinding was employed with vibration but without a dummy workpiece at an a_e of 1.0 mm. Introduction of the dummy workpiece reduced R_a by 16-35%.

5.2.3 Phase 1C: Initial experiments on ultrasonic assisted dressing

- A 27 to 40% reduction in maximum vertical force (F_v) and 22 to 50% reduction in maximum horizontal force (F_h) were observed when dressing was assisted with ultrasonic vibration. However, there were marginal differences in the average dressing forces obtained with or without ultrasonic vibration.
- Reductions in vertical and horizontal grinding forces by up to 13% and 12% respectively were observed when grinding Inconel 718 following ultrasonic assisted dressing. In contrast, when dressing was carried out in dry condition, the subsequent grinding operations exhibited marginal differences in forces with the ultrasonically and non-ultrasonically dressed wheel.
- There was a marginal reduction in the surface roughness of the workpieces ground with an ultrasonically dressed wheel compared to a non-ultrasonically dressed wheel.
- There were several surging marks on the ground workpieces towards the end of the grinding tracks.
- No significant difference in the appearance of the ultrasonically and non-ultrasonically dressed GC wheel was noted when observed under an optical microscope.

5.2.4 Phase 2A: Identification of process parameters for UAG of Inconel 718

- An increase in V_C from 25 to 30 m/s eliminated the depression marks at a cutting fluid pressure of 15 bar.
- Heavy depressions were obtained in all tests employing higher a_e (1.5 mm).
- Depressions were also observed at a higher V_W of 400 mm/min. However, at 300 mm/min no depressions were observed with the POROS2 wheel.
- A dummy workpiece was required in order to restrict the escape of cutting fluid from the grinding zone.

- Grinding wheels with larger grit size and higher porosity appeared to offer more efficient transfer of cutting fluid into the grinding zone.
- **The optimum operating parameters for a depression-mark-free grinding were identified as V_C and V_W of 30 to 40 m/s and 200 to 300 mm/min, respectively, together with a fixed a_e of 1.0 mm and cutting fluid pressure of ~28-30 bar.**

5.2.5 Phase 2B: Evaluation of UAG on Inconel 718 using POROS2 wheel

- Grinding force typically increased with an increase of V_W from 200 to 300 mm/min.
- **The use of ultrasonic assisted operation generally resulted in reductions in F_v and F_h by up to 23% and 43% respectively.**
- Wheel G-ratio was improved by between 7 to 45% in 5 of the 9 trials, however decreased in 3 of the remaining 4 experiments when operated with the hybrid configuration.
- The majority of the ground surfaces were free from depression marks/grinding burn, however little depressions were observed towards the end of cut on the non-ultrasonically ground surfaces when machined at severe cutting conditions such as V_C=35 m/s, V_W=200 mm/min and V_C=40 m/s, V_W=250 mm/min. The ultrasonically ground surfaces, however, did not show any sign of indentation marks.
- **Greater side flow/ploughing was observed with the workpieces ground ultrasonically in comparison to conventional creep feed ground specimens. Furthermore, greater numbers of overlapping grit marks were visible on surfaces subject to UAG.**
- US vibration generally led to an increase in the number of active cutting points on the grinding wheel. This subsequently resulted in a decrease of corresponding average workpiece surface roughness (S_a) by up to 45%.
- Sub-surface microhardness typically increased from a depth of 10 µm below the machined surface up to a depth of 140 to 150 µm until the bulk hardness (~450 $HK_{0.025}$) was achieved at a depth of ~175 to 200 µm. **Sub-surface microhardness generally increased by ~5-10% when the workpieces were actuated with ultrasonic vibration.**
- There were only marginal differences in the microstructures of specimens ground with and without ultrasonic assistance. Additionally, no cracks, tears, laps, folds or breakage of carbide particles were seen on any of the specimens evaluated.

5.2.6 Phase 2C: Evaluation of UAG on Inconel 718 using VORTEX 60 mesh wheel

- The employment of ultrasonic vibration resulted in reductions in F_v in 5 out of 9 tests by up to ~20%, whereas F_h decreased in all of experiments. **The maximum reduction in F_h was ~60% however it typically decreased by ~10-30% in the majority of trials subject to vibration.**
- Radial wheel wear varied between 12-27 μm (with an exception of Test 15 where a wheel wear of ~6 μm was measured) with the corresponding G-ratio varying between ~3 to 6 (G-ratio was ~12 in Test 15).
- Radial wear increased (with a maximum reduction in G-ratio by ~60%) in 6 out of 9 tests when grinding was employed with ultrasonic assistance.
- The ground workpiece surfaces were typically free from depression marks (except Tests 1 and 15) and grinding burn.
- Both R_a and S_a of the ground surfaces increased (by up to ~25% and ~49% respectively) in 6 out of 9 trials involving ultrasonic actuation. Greater amounts of plastic deformation and consequent side flow/ploughing were observed on specimens subject to vibration.
- The R_a and S_a measured on graphite replicas of the grinding wheel increased when operating with ultrasonic assistance.
- Reductions in S_a and S_{ds} of the resin replicating surfaces together with larger voids/pores in between the grains were observed following UAG.
- Sub-surface microhardness generally increased up to ~500-520 $HK_{0.025}$ from a depth of 10 to ~200 μm beneath the machined surface until the bulk hardness was achieved (~450 $HK_{0.025}$). **With the assistance of US vibration, sub-surface microhardness typically increased by 6-8%.**
- There was no difference in the microstructures of the specimens ground with and without ultrasonic assistance.

5.2.7 Phase 2D: Assessment of UAG on CMSX-4 using POROS2 wheel

- **Reductions in F_v and F_h by up to 51% and 39%, respectively, were observed when UAG of CMSX-4 together with greater wheel wear (7-39% lower G-ratio) in some tests.**
- The R_a and S_a of ground workpieces typically increased (by up to ~15% and 28% respectively) when grinding was employed with vibration. Additionally greater plastic

deformation, side flow/ploughing, smearing of material and overlapping cuts were observed on the surfaces subject to vibration.

- Three-dimensional topographic measurement of grinding wheel surface replicas indicated that US vibration led to an increase in the number of active cutting points on the wheel, together with a difference in the grit heights as well as larger voids/pores in between the grains.
- Sub-surface microhardness generally increased from a depth of 10 µm below the ground surface up to a depth of 140 to 150 µm until reaching the bulk hardness (~390$HK_{0.025}$) at a depth of ~200 to 250 µm. **With the assistance of ultrasonic vibration, sub-surface microhardness typically increased by ~5-10% in comparison to specimens CFG without vibration.**
- The microstructure of CMSX-4 showed a high volume fraction of strengthening ordered γ' phase particles homogenously distributed in the continuous γ matrix of nickel based austenitic phase. Deformation/bending of γ' phase was observed in the longitudinal feed plane with a depth of deformation of ~5 µm. **No white layer formation, or any cracks/tearing was seen in any of the specimens assessed.**

5.2.8 Phase 2E: Effect of depth of cut and vibration amplitude when UAG of Inconel 718

- **The application of ultrasonic vibration resulted in reductions in F_v and F_h by up to 28% and 37% respectively, but increased wheel wear (30-60% lower G-ratio).**
- Peak power decreased by ~5-6% when grinding with US vibration.
- **An increase in amplitude of vibration produced lower grinding forces (up to 30% for F_v and 43% for F_h) but higher workpiece surface roughness (up to 24%).**
- US vibration typically resulted in an increase in the S_{ds} parameter of the resin replicas. Furthermore, a 'High' amplitude of vibration produced more voids/pores on the wheel surface, which resulted in lower grinding forces but higher surface roughness in comparison to those obtained when grinding was carried out with 'Low' amplitude settings.
- Sub-surface microhardness generally increased up to ~490-525 $HK_{0.025}$ from a depth of 10 µm to ~200 µm underneath the machined surface, which was further increased by ~6-10% with the application of vibration.

5.2.9 Phase 3A: Assessment of UAG on γ-TiAl using conventional SiC abrasive wheel

- Vertical grinding force (F_v) increased with an increase in V_C from 15 to 30 m/s, however marginally reduced with an increase in V_W from 150 to 600 mm/min. **The assistance of ultrasonic actuation to the workpiece produced reductions in both F_v and F_h by up to 19% and 35% respectively.**
- G-ratio varied from 3.19 to 7.99 with the maximum level recorded at the lowest V_C (15 m/s) and V_W (150 mm/min) under conventional CFG mode, which was further enhanced by ~30-75% (except Test 8) when UAG.
- Burn/serration marks were observed on the workpieces conventionally ground with a V_C and V_W of 30 m/s and 150 mm/min respectively, which were however eliminated with ultrasonic assistance. There was some evidence of surface fracturing, redeposited material etc on the non-ultrasonically ground surfaces; however such defects were absent on the workpieces subject to ultrasonic vibration, although greater plastic deformation, side flow/ploughing of material and overlapping grit marks were observed in the latter case.
- The R_a and S_a of the ground surfaces increased with an increase in V_W from 150 to 600 mm/min, however they decreased with an increase in V_C from 15 to 30 m/s. **With UAG, both parameters typically decreased (~3-10% reduction in R_a), although R_t, R_z, S_t and S_z generally increased under ultrasonic mode.**
- The S_a of the graphite replicas typically decreased with an increase in V_C but increased with a rise in V_W. S_a decreased in 3 out of 4 tests when grinding with US vibration.
- The S_a and S_{ds} of the resin replicas generally decreased and increased respectively with an increase in V_W. In contrast, the variations in S_a and S_{ds} were marginal with a rise in V_C. Both surface parameters decreased following UAG in comparison to conventional CFG.
- Sub-surface microhardness was typically at its maximum (~580 $HK_{0.025}$) at a depth of 10 µm below the machined surface, which then gradually decreased to the bulk hardness (~420 $HK_{0.025}$) at a depth of ~200-300 µm. **With ultrasonic assistance, sub-surface microhardness typically increased by ~ 6-8%.**
- Cross-sectional microstructures in the longitudinal feed plane showed typical deformation/bending of lamellae with a depth of deformation up to ~15 µm beneath the machined surface. **Ground surfaces were mainly free from cracks, laps, folds or heat affected zone with little or no material pull-out observed in Test 7. The application of ultrasonic vibration did not significantly alter material microstructure.**

5.2.10 Phase 3B: Investigation of UAG on γ-TiAl with electroplated diamond superabrasive wheel

- With conventional CFG, F_v increased from 857 to 1201 N with the progression of grinding from the 1st to 3rd and 3rd to 5th pass. Forces F_v and F_h generally reduced when grinding with ultrasonic vibration. **The maximum reduction in F_v was 13% from the 1st to 2nd pass, whereas that in F_h was ~25% from the 3rd to 4th pass.**
- Radial wheel wear was initially high (~7 µm) in the 1st pass however this decreased to ~2 µm in the 3rd pass, followed by an increase (~3 µm) in the 5th pass involving a faster V_C (40 m/s) and V_W (600 mm/min). **Wheel wear however remained almost negligible (~1 µm) when operating with ultrasonic assistance. The corresponding G-ratios for conventional CFG varied from ~11-40 whereas it remained almost constant at ~80 with UAG.**
- No apparent surface cracks or grinding burn/chatter was visible on any of the ground specimens.
- The R_a and S_a of the ground surfaces gradually decreased from the 1st to 4th pass, however they increased in the 5th pass but decreased again in the 6th pass.
- The S_a of the graphite replicas followed a similar trend as the workpiece R_a and S_a.
- Sub-surface microhardness increased by ~30-60% within 10-20 µm beneath the machined surface, which then gradually reduced to the bulk hardness value at a depth of ~100 µm. Initially sub-surface microhardness of the ultrasonically ground specimens was lower than that of the conventionally ground samples, however the former increased by ~16% following the 6th pass.
- The microstructures in the longitudinal feed plane showed deformation of lamellae up to ~20-25 µm below the machined surface but were free from other defects such as tears, laps, fractures or loss of grains etc.

5.3 Overall conclusions

5.3.1 UAG of Inconel 718 and CMSX-4

- The use of ultrasonic assisted operation on nickel based superalloys typically resulted in reduction of both vertical and horizontal grinding forces. This was due to the intermittent cutting action of the abrasive grains leading to a decrease in frictional force as well as thermal load on the grits. The radial wheel wear however increased (G-ratio decreased by

up to ~30-60%) in the majority of trials subject to US vibration due to greater micro-splintering of grits under the action of vibration.

- In terms of surface quality of the ground workpieces, both materials typically exhibited higher surface roughness when subject to ultrasonic vibration. The material was more plastically deformed due to the additional mechanical impact imparted by vibration which in turn resulted in greater smearing, side flow and ploughing. The multi-modal characteristics of ultrasonic generator also rendered overlapping grit marks on the work surface leading to higher surface roughness.
- Three-dimensional topographic measurements of grinding wheel surface replicas indicated that roughness parameters of the graphite (negative) surfaces typically decreased when grinding was conducted with US assistance, suggesting uniformity in grit heights resulted from the micro-conditioning effect of vibration. In contrast, S_t and S_v values were generally higher with vibration. Ultrasonic assistance also generally led to an increase in the number of active cutting points on the wheel, indicating that the wheel became sharper under the action of vibration.
- A higher amplitude of vibration (~7-8 μm) typically produced lower grinding forces, but higher wheel wear as well as higher surface roughness of the ground workpieces in comparison to those subject to a low amplitude (~2-4 μm) of vibration.
- With the assistance of ultrasonic vibration, sub-surface microhardness generally increased by ~5-10% due to the higher plastic deformation, in comparison with conventional CFG. Ground surfaces were typically free from cracks, tears, laps, folds or loss of grains. No distinguishing variation in the microstructures of the specimens ground with and without ultrasonic assistance was observed.

5.3.2 UAG of γ-TiAl

- Gamma titanium aluminide exhibited more promising results in ultrasonic assisted grinding compared to those observed with nickel based superalloys. The size and weight (density) of the workpiece materials had a significant effect on the amplitude of vibration transferred to the workpiece-sonotrode assembly. The densities of Inconel 718 and CMSX-4 are 8100 and 8690 kg/m^3 respectively, whereas that of γ-TiAl is 3800 kg/m^3. The amplitude of vibration transmitted to the γ-TiAl workpieces was greater in comparison to those measured for the nickel based alloys, although workpieces of comparable sizes from both materials were utilised. This was reflected in the force, radial wheel wear and surface roughness data recorded for γ-TiAl. The vertical and horizontal

grinding forces generally decreased (by up to 19% and 35% in Phase 3A and 13% and 25% in Phase 3B) under the ultrasonic mode together with a reduction in wheel wear (higher G-ratio) in the majority of trials subject to vibration. The effect was more prominent with the superabrasive wheel when a 600% increase in G-ratio was obtained with the hybrid configuration. The maximum increase in G-ratio with the superabrasive wheel (39.80) was ~550% with respect to that obtained with the conventional SiC wheel (6.14) when grinding was carried out conventionally. Under vibrating mode, maximum G-ratios obtained with the electroplated and SiC wheels were 79.60 and 7.99 respectively (an increase of ~900%).

- The roughness of the ground γ-TiAl workpieces subject to vibration typically decreased compared with conventional CFG. Similar to nickel based superalloys, UAG machined γ-TiAl surfaces displayed greater smearing, side flow/ploughing and overlapping grit marks. This was thought to be due to a change in material removal mechanism of γ-TiAl from brittle fracture to ductile regime with the assistance of vibration. The higher plastic deformation of the material during UAG also led to an increase of the sub-surface microhardness (by ~6-8%) with no major alteration of the microstructure.
- The primary advantage of employing ultrasonic vibration in CFG was the reduction in grinding forces for both nickel based superalloys and γ-TiAl, with superior performance observed in the latter in terms of lower radial wheel wear and workpiece surface roughness. While surface defects in the majority of conventional CFG trials were found to be minimal, US assisted grinding typically produced damage-free surfaces.
- While comparing the performance of the different grinding wheels employed in machining of nickel alloys and γ-TiAl, the open structured POROS2 wheel exhibited improved performance when UAG of Inconel 718 in terms of wheel wear and workpiece roughness compared to the VORTEX wheel (which utilises extruded grains). This was due to the better ingress of cutting fluid into the grinding zone and wheel pores resulting in a reduction in temperature and improved wheel cleaning. Conversely, silicon carbide wheels are typically recommended for grinding γ-TiAl. The performance of UAG further enhanced when using a single layer electroplated diamond wheel with a ~900% increase in G-ratio in comparison to the conventional SiC wheel.

6. RECOMMENDATIONS FOR FUTURE WORK

Based on results from the experimental work, the following aspects have been identified for further investigation:

- Evaluation of the effects of ultrasonic vibration and establishment of preferred operating parameter windows when creep feed grinding of alternative wrought and cast nickel based superalloys.

- Further in-depth study on UAG of Ti-45-45-2-XD γ-TiAl alloy as limited numbers of trial were carried out in the present research. The results could be compared with those when UAG of a conventional α/β-Ti-alloy such as Ti-6Al-4V.

- Evaluation of the effects of US vibration when CFG of recently developed but difficult-to-machine burnt-resistant Ti alloys (BuRTi) and compare the results with those obtained when UAG of γ-TiAl alloy.

- Further in-depth investigation involving UAG of γ-TiAl using vitrified as well as single layer superabrasive wheels of varying grit size, hardness and porosity.

- Evaluation of the influence of increased ultrasonic generator power (>1 kW) and greater amplitude of vibration (>10 μm) on grinding forces, wheel wear and workpiece surface integrity when UAG of nickel based superalloys and γ-TiAl.

- Measurement of grinding temperature when UAG of advanced aerospace alloys.

- Assessment of workpiece residual stress following UAG.

- Evaluation and comparison of workpiece fatigue performance following conventional CFG and UAG.

7. REFERENCES

Abdullah A., Farhadi A., Pak A., 2012. Ultrasonic-assisted dry creep-feed up-grinding of superalloy Inconel738LC, Experimental Mechanics 52, 843-853.

Abdullah A., Pak A., Farahi M., Barzegari M., 2007. Profile wear of resin-bonded nickel-coated diamond wheel and roughness in creep-feed grinding of cemented tungsten carbide, Journal of Materials Processing Technology 183, 165-168.

Abdullah A., Sotoodezadeh M., Abedini R., Fartashvand V., 2013. Experimental study on ultrasonic use in dry creep-feed up-grinding of Aluminum 7075 and Steel X210Cr12, International Journal of Precision Engineering and Manufacturing 14(2), 191-198.

Andrew C., Howes T.D., Pearce T.R.A., 1985. Creep feed grinding. Industrial Press inc. New York, USA. ISBN 0-8311-1167-4.

Anon, 1963. Ultrasonic vibrations help grinding, Steel The Metalworking Weekly 152, 56-58.

Anon, 1981. Creep-feed grinding cuts cycle time 60%, Grinding, Manufacturing Engineering, 68-70.

Anon, 2005. High porosity grinding wheels increase productivity and avoid burning, Aircraft Engineering and Aerospace Technology, 168-169.

Appel F., Brossmann U., Christoph U., Eggert S., Janschek P., Lorenz U., Müllauer J., Oehring M., Paul J.D.H., 2000. Recent progress in the development of gamma titanium aluminide alloys, Advanced Engineering Materials 2(11), 699-720.

Apple F., Oehring M., 2003. γ-Titanium aluminide alloys: Alloy design and properties, Titanium and Titanium Alloys: Fundamentals and Applications, 89-152, Wiley-VCH GmbH & Co., Germany. ISBN 3-527-30534-3.

Aspinwall D.K., Dewes R.C., Burrows J.M., Paul M.A., 2001b. Hybrid high speed machining (HSM): System design and experimental results for grinding/HSM and EDM/HSM, Annals of CIRP 50(1), 145-148.

Aspinwall D.K., Dewes R.C., Mantle A.L., 2005. The machining of γ-TiAl intermetallic alloys, Annals of CIRP 54, 99-104.

Aspinwall D.K., Kasuga Y., Mantle A.L., 2001a. The use of ultrasonic machining for the production of holes in γ-TiAl, Proceedings of the 13th International Symposium for Electromachining (ISEM XIII), Bilbao, Spain, 925-937.

Aspinwall D.K., Soo S.L., Curtis D.T., Mantle A.L., 2007. Profiled superabrasive grinding wheels for the machining of a nickel based superalloy, Annals of CIRP 56(1), 335-338.

Astashev V.K., Andrianov N.A., Kozochkin M.P., Kolik L.V., Krupenin V.L., Solis-Pinargote N.V., 2009. On the Implementation of Ultrasonic Technology, Journal of Machinery Manufacture and Reliability 38(6), 566-571.

Azarhoushang B., Akbari J., 2007. Ultrasonic-assisted drilling of Inconel 738-LC, International Journal of Machine Tools and Manufacture 47, 1027-1033.

Azarhoushang B., Tawakoli T., 2011. Development of a novel ultrasonic unit for grinding of ceramic matrix composites, International Journal of Advanced Manufacturing Technology 57, 945-955.

Azarhoushang B., Tawakoli T., 2012. Developing a special block sonotrode for ultrasonic-assisted grinding process, International Journal of Mechatronics and Manufacturing Systems 5(2), 165-176.

Azizi A., Rezaei S.M., Rahimi A., 2009. Study on the rotary cup dressing of CBN grinding wheel and the grinding performance, International Journal of Advanced Manufacturing Technology 47(9-12), 1053-1063.

Babitsky V.I., Kalashnikov A.N., Meadows A., Wijesundara A.A.H.P., 2003. Ultrasonically assisted turning of aviation materials, Journal of Materials Processing Technology 132, 157-167.

Babitsky V.I., Mitrofanov A.V., Silberschmidt V.V., 2004. Ultrasonically assisted turning of aviation materials: simulations and experimental study, Ultrasonics 42, 81-86.

Balamuth L., 1945. Method of abrading, British patent 602801.

Balamuth L., 1966. Ultrasonic assistance to conventional metal removal, Ultrasonics 4(3), 125-130.

Barker K., Kaliszer H., Rowe G.W., 1967-68. Topography and mechanical properties of ground metal surfaces, Proceedings of Institution of Mechanical Engineers 182, 195-204.

Bentley S.A., Aspinwall D.K., 1997a. The identification of significant operating parameters when conventional abrasive creep feed grinding a gamma titanium aluminide intermetallic. Proceedings of the Forth International Charles Parsons Turbine Conference, Advances in Turbine Materials, Design and Manufacturing, Newcastle Upon Tyne, UK, 474-488.

Bentley S.A., Aspinwall D.K., 1997b. A comparison of the grinding of IMI318 titanium alloy and a gamma titanium aluminide intermetallic. Proceedings of the 32nd MATADOR Conference, Manchester, UK, 331-336.

Bentley S.A., Aspinwall D.K., 2000. Creep feed grinding of γ-TiAl. Proceedings of the 33rd MATADOR Conference, Manchester, UK, 439-446.

Bentley S.A., Goh N.P., Aspinwall D.K., 2001. Reciprocating surface grinding of a gamma titanium aluminide intermetallic alloy, Journal of Materials Processing Technology 118, 22-28.

Bentley S.A., Lim S.Z., Aspinwall D.K., 1999. The effect of wheel dressing parameters on the surface integrity of a surface ground gamma titanium aluminide intermetallic alloy, Intermetallics and Superalloys, Proceedings of the EUROMAT '99, Vol. 10, 216-221.

Bhaduri D., Chattopadhyay A.K., 2010. Study on the role of PVD TiN coating in improving the performance of electroplated monolayer superabrasive wheel, Surface and Coatings Technology 205, 658-667.

Bhaduri D., Chattopadhyay A.K., 2011. Influence of grinding parameters and substrate bias voltage in dry surface grinding with TiN-coated single layer galvanic cBN wheel, Materials and Manufacturing Processes 26(8), 982-990.

Bhaduri D., Kumar R., Chattopadhyay A.K., 2011. On the grindability of low-carbon steel under dry, cryogenic and neat oil environments with monolayer brazed cBN and alumina wheels, International Journal of Advanced Manufacturing Technology 57, 927-943.

Bianchi E.C., Silva E.J., Silva C.E. Jr., Aguiar P.R., Valarelli I.D., Monici R.D., 2001. Advanced ceramics: Evaluation of the mechanism of stock removal and ground surface quality, Journal of the Brazilian Society of Mechanical Sciences 23(1), 9-22.

Boyer R.R., 1996. An overview on the use of titanium in the aerospace industry, Materials Science and Engineering A213, 103-114.

Bradley E.F., 1988. Superalloys: A Technical Guide, (Consulting Editor), ASM International, Ohio, USA. ISBN 0-87170-327.

Brecher C., Schug R., Weber A., Wenzel C., Hannig S., 2010. New systematic and time-saving procedure to design cup grinding wheels for the application of ultrasonic-assisted grinding, International Journal of Advanced Manufacturing Technology 47, 153-159.

Brehl D.E., Dow T.A., 2008. Review on vibration-assisted machining, Precision Engineering 32, 153-172.

Buckley J.T., Freeman M.K., 1970. Ultrasonic tube drawing, Ultrasonics, 8(3), 152-158.

Burrows J.M., Dewes R.C., Aspinwall D.K., 2000. Grinding of Inconel 718 and Udimet 720 using superabrasive grinding points mounted on a high speed machining centre. Proceedings of the 33rd MATADOR Conference, Manchester, UK, 447-452.

Butler D.L., Blunt L.A., See B.K., Webster J.A., Stout K.J., 2002. The characterisation of grinding wheels using 3D surface measurement techniques, Journal of Materials Processing Technology 127, 234-237.

Cameron A., Bauer R., Warkentin A., 2010. An investigation of the effects of wheel-cleaning parameters in creep-feed grinding, International Journal of Machine Tools and Manufacture 50, 126-130.

Caron P., Khan T., 1999. Evolution of Ni-based superalloys for single crystal gas turbine blade applications, Aerospace Science Technology 3, 513-523.

Chang S.S.F., Bone G.M., 2004. Burr size reduction in drilling by ultrasonic assistance, International Journal of Robotics Computer-Integrated Manufacturing 21, 442-450.

Changyong Y., Jiuhua X., Wenfeng D., Zhenzhen C., Yucan F., 2010. Dimension accuracy and surface integrity of creep feed ground titanium alloy with monolayer brazed CBN shaped wheels, Chinese Journal of Aeronautics 23, 585-590.

Chattopadhyay A.K., Chollet L., Hintermann H.E., 1991. On performance of brazed bonded monolayer diamond grinding wheel, Annals of CIRP 40(1), 347-350.

Chen H., Tang J., Zhou W., 2013. An experimental study of the effects of ultrasonic vibration on grinding surface roughness of C45 carbon steel, International Journal of Advanced Manufacturing Technology 68, 2095-2098.

Chen T.T., Hu D., Loretto M.H., Jones I.P., 1999. γ-TiAL alloy development, Intermetallic and Superalloys, EUROMAT 99, Vol. 10, 246-250, Wiley-VCH GmbH, Germany. ISBN 3-527-30192-5.

Chen Y-F, Lin Y-C, 2009. Surface modifications of Al–Zn–Mg alloy using combined EDM with ultrasonic machining and addition of TiC particles into the dielectric, Journal of Materials Processing Technology 209, 4343-4350.

Churi N.J., Pei Z.J., Treadwell C., 2006. Rotary ultrasonic machining of titanium alloy: effects of machining variables, Machining Science and Technology 10(3), 301-321.

Churi N.J., Pei Z.J., Treadwell C., 2007. Rotary ultrasonic machining of titanium alloy (Ti-6Al-4V): effects of tool variables, International Journal of Precision Technology 1(1), 85-96.

Clemens H., Appel F., Bartels A., Baur H., Gerling R., Güther V., Kestler H., 2003. Processing and application of engineering γ-TiAl based alloys, Proceedings of the 10th World Conference on Titanium, Ti-2003: Science and Technology, Hamburg, Germany, 2123-2136.

Colwell L.V., 1956. The effects of high-frequency vibrations in grinding, Transactions of the ASME 78, 837-845.

Denkena B., Friemuth T., Reichstein M., 2003. Potentials of different process kinematics in micro grinding, Annals of CIRP 52(1), 463-466.

Devillez A., Le Coz G., Dominiak S., Dudzinski D., 2011. Dry machining of Inconel 718, workpiece surface integrity, Journal of Materials Processing Technology 211, 1590-1598.

Dimiduk D.M., 1999. Gamma titanium aluminide alloys - an assessment within the competition of aerospace structural materials, Materials Science and Engineering A 263, 281-288.

Ding W., Xu J., Chen Z., Su H., Fu Y., 2010a. Grindability and surface integrity of cast nickel-based superalloy in creep feed grinding with brazed CBN abrasive wheels, Chinese Journal of Aeronautics 23, 501-510.

Ding W., Xu J., Chen Z., Su H., Fu Y., 2010b. Wear behavior and mechanism of single-layer brazed CBN abrasive wheels during creep-feed grinding cast nickel-based superalloy, International Journal of Advanced Manufacturing Technology 51,541-550.

Doutsu T., Yanagimoto H., Take Y., Koga S., 1996. Grooving of zirconia ceramics by ultrasonic vibration machining, Proceedings of the 3rd International Conference on Progress of Cutting and Grinding, Osaka, Japan, 587-592.

Erickson G.L., 1995. A new, third-generation, single-crystal, casting superalloy, JOM, The Journal of The Minerals, Metals and Materials Society 47(4), 36-39.

Enache St., Opran C., Stoica G., Strâjescu E., 1990. The study of EDM with forced vibration of tool-electrode, Annals of ClRP 39(1), 167-170.

Excell M., 1995. Grinding process creeps forward, Grinding, Metalworking Production, 67-70.

Ezugwu E.O., Wang Z.M., Machado A.R., 1999. The machinability of nickel-based alloys: a review, Journal of Materials Processing Technology 86, 1-16.

Field M., Kahles J.F., 1964. The surface integrity of machined and ground high strength steels, DMIC Report 210, 54-77.

Field M., Kahles J.F., 1971. Review of surface integrity of machined components, Annals of CIRP 20(2), 153-163.

Field M., Kahles J.F., Cammett J.T., 1972. A review of measuring methods for surface integrity, Annals of CIRP 21(2), 219-238.

Gao G.F., Zhao B., Xiang D.H., Kong Q.H., 2009. Research on the surface characteristics in ultrasonic grinding nano-zirconia ceramics, Journal of Materials Processing Technology 209, 32-37.

Ghosh A., Chattopadhyay A.K., 2007. On grit-failure of an indigenously developed single layer brazed CBN wheel, Industrial Diamond Review 67(1), 59-64.

Ghosh A., Mallik A.K., 1985. Manufacturing Science. Affiliated East-West Press Private Limited, New Delhi. ISBN 81-85095-85-X.

Graff K.F., 1975. Macrosonics in industry: 5. Ultrasonic machining, Ultrasonics 13(3), 103-109.

Guo C., Shi Z., Attia H., McIntosh D., 2007. Power and wheel wear for grinding nickel alloy with plated CBN wheels, Annals of CIRP 56(1), 343-346.

Guo Z.N., Lee T.C., Yue T.M., Lau W. S., 1997a. A study of ultrasonic-aided wire electrical discharge machining, Journal of Materials Processing Technology 63, 823-828.

Guo Z.N., Lee T.C., Yue T.M., Lau W. S., 1997b. Study on the machining mechanism of WEDM with ultrasonic vibration of the wire, Journal of Materials Processing Technology 69, 212-221.

Hanasaki S., Fujiwara J., Wada T., 1996. Vibratory cut-off grinding, Proceedings of the 3rd International Conference on Progress of Cutting and Grinding, Osaka, Japan, 450-455.

Hara K., Isobe H., Kyusojin A., Okada M., 2008. Study on mirror surface grinding of die steel by using ultrasonically assisted diamond tools, International Journal of Abrasive Technology, 1(3/4), 265-273.

Heisel U., Eisseler R., Eber R., Wallaschek J., Twiefel J., Huang M., 2011. Ultrasonic-assisted machining of stone, Production Engineering Research Development 5, 587-594.

Hitchiner, M., 2007. Grinding in the aerospace industry. Proceedings of Advances in Absrasive Technology X, ISAAT. Michigan, USA, 491-497.

Hood R., 2010. The machinability of a gamma titanium aluminide intermetallic. PhD Thesis, University of Birmingham, UK.

Hood R., Aspinwall D.K., Sage C., Voice W., 2013. High speed ball nose end milling of γ-TiAl alloys, Intermetallics 32, 284-291.

Hood R., Aspinwall D.K., Voice W., 2007a. Creep feed grinding of a gamma titanium aluminide intermetallic alloy using SiC abrasives, Journal of Materials Processing Technology 191, 210-214.

Hood R., Lechner F., Aspinwall D.K., Voice W., 2007b. Creep feed grinding of gamma titanium aluminide and burn resistant titanium alloys using SiC abrasive, International Journal of Machine Tools and Manufacture 47, 1486-1492.

Hood R., Soo S.L., Aspinwall D.K., Andrews P., Sage C., 2011. Twist drilling of Haynes 282 superalloy, Procedia Engineering 19, 150-155.

Hooper R.M., Morgan J.E., 1989. Wear processes in the diamond grinding of zirconia ceramics, Wear 130, 353-356.

Hsu C.Y., Lin Y.Y., Lee W.S., Lo S.P., 2008. Machining characteristics of Inconel 718 using ultrasonic and high temperature-aided cutting, Journal of Materials Processing Technology 198, 359-365.

Hwang T.W., Evans C.J., Whitenton E.P., Malkin S., 2000. High speed grinding of silicon nitride with electroplated diamond wheels. Part 1. Wear and wheel life, Transactions of the ASME, Journal of Manufacturing Science and Engineering 122, 32-41.

Ismail M.F., Yanagi K., Isobe H., 2011. Characterization of geometrical properties of electroplated diamond tools and estimation of its grinding performance, Wear 271, 559-564.

Jadoun R.S., Kumar P., Mishra B.K., 2009. Taguchi's optimization of process parameters for production accuracy in ultrasonic drilling of engineering ceramics, Production Engineering Research and Development 3, 243-253.

Jaeger J.C., 1942. Moving sources of heat and the temperature at sliding contacts, Proceeding Royal Society of New South Wales 76, 203-224.

Jawahir I.S., Brinksmeier E., M'Saoubi R., Aspinwall D.K., Outeiro J.C., Meyer D., Umbrello D., Jayal A.D., 2011. Surface integrity in material removal processes: Recent advances, Annals of CIRP 60, 603-626.

Jiao F., Zhao B., Zhu X.S., Fan Q.T., 2006. Ultrasonic dressing of grinding wheel and its influence on grinding quality, Key Engineering Materials 304-305, 62-65.

Jimma T., Kasuga Y., Iwaki N., Miyazawa O., Mori E., Ito K., Hatano H., 1998. An application of ultrasonic vibration to the deep drawing process, Journal of Materials Processing Technology 80-81, 406-412.

Jin M., Murakawa M., 2001. Development of a practical ultrasonic vibration cutting tool system, Journal of Materials Processing Technology 113, 342-347.

Jixian Y., Yonghong Z., Sumei Y., Libin H., 1996. Ultrasonic vibration grinding experiment for ceramic deep hole, Proceedings of the 3rd International Conference on Progress of Cutting and Grinding, Osaka, Japan, 605-609.

Kaliszer H., Limb M., 1968. Application of ultrasonic technique in grinding processes. International Journal Machine Tool Design and Research 8, 189-201.

Kazantsev V.F., 1966. Improving the output and accuracy of ultrasonic machining, Machines and Tooling 37(4), 33-39.

Khairy A.B.E., 1990. Assessment of some dynamic parameters for the ultrasonic machining process, Wear 137, 187-198.

Klocke F., Rübenach O., 2000. Ultrasonic-assisted diamond turning of glass and steel, Industrial Diamond Review 3, 227-239.

Kohli S., Guo C., Malkin S., 1995. Energy partition to the workpiece for grinding with aluminium oxide and CBN abrasive wheels, Transactions of the ASME, Journal of Engineering for Industry 117, 160-168.

König W., Graβ P., 1989. Quality definition and assessment in drilling of fibre reinforced thermosets, Annals of CIRP 38(1), 119-124.

Kozak, J., Rajurkar, K.P., 2000. Hybrid machining process evaluation and development, Proceedings of the 2nd International Conference on Machining and Measurements of Sculptured Surfaces, Krakow, Poland, 501-536.

Kremer D., Ghabrial S.M., Moisan A., 1981. The state of the art of ultrasonic machining, Annals of CIRP 30, 107-110.

Kremer D., Lebrun J.L., Hosari B., Moisan A., 1989. Effects of ultrasonic vibrations on the performances in EDM, Annals of ClRP 38(1), 199-202.

Kremer D., Lhiaubet C., Moisan A., 1991. A study of the effect of synchronizing ultrasonic vibrations with pulses in EDM, Annals of CIRP 40(1), 211-214.

Lauwers B., 2011. Surface integrity in hybrid machining processes, Procedia Engineering 19, 241-251.

Legge P., 1966. Machining without abrasive slurry, Ultrasonics 4, 157-162.

Li L., Guo Y.B., Wei X.T., Li W., 2011. Surface integrity characteristics in wire-EDM of inconel 718 at different discharge energy, Procedia CIRP 6, 220-225.

Liang Z., Wang X., Wu Y., Xie L., Liu Z., Zhao W., 2012. An investigation on wear mechanism of resin-bonded diamond wheel in Elliptical Ultrasonic Assisted Grinding (EUAG) of monocrystal sapphire, Journal of Materials Processing Technology 212, 868-876.

Liang Z., Wu Y., Wang X., Zhao W., 2010. A new two-dimensional ultrasonic assisted grinding (2D-UAG) method and its fundamental performance in monocrystal silicon machining, International Journal of Machine Tools and Manufacture 50, 728-736.

Liao T.W., Sathyanarayanan G., 1994. On the study of creep feed grinding of alumina, International Journal of Machine Tools and Manufacture 34(2), 257-276.

Liao Y.S., Chen Y.C., Lin H.M., 2007. Feasibility study of the ultrasonic vibration assisted drilling of Inconel superalloy, International Journal of Machine Tools and Manufacture 47, 1988-1996.

Lin Y.C., Yan B.H., Chang Y.S., 2000. Machining characteristics of titanium alloy (Ti-6Al-4V) using a combination process of EDM with USM, Journal of Materials Processing Technology 104, 171-177.

Liu Q., Chen X., Gindy N., 2007. Assessment of Al_2O_3 and superabrasive wheels in nickel-based alloy grinding, International Journal of Advanced Manufacturing Technology 33, 940-951.

Loria E.A., 2001. Quo vadis gamma titanium aluminide, Intermetallics 9, 997-1001.

Loretto M.H., 1995. Intremetallics in turbines and compressors for aeroengines, Proceedings of the 3rd International Charles Parsons Turbine Conference on Materials Engineering in Turbine and Compressor, Newcastle Upon Tyne, UK, 25-27.

Malkin S., 1989. Grinding technology: Theory and applications of machining with abrasives. Society of Manufacturing Engineers, Michigan, USA. ISBN 0-87263-480-9.

Malkin S., Cook N.H., 1971. The wear of grinding wheels, Part 1. Attritious wear, Transactions of the ASME, Journal of Engineering for Industry 93, 1120-1128.

Malkin S., Guo C., 2007. Thermal analysis of grinding, Annals of CIRP 56(2), 760-782.

Mantle A.L., Aspinwall D.K., 1997. Surface integrity and fatigue life of turned gamma titanium aluminide, Journal of Materials Processing Technology 72, 413-420.

Mantle A.L., Aspinwall D.K., 2001. Surface integrity of a high speed milled gamma titanium aluminide, Journal of Materials Processing Technology 118, 143-150.

Materials Properties Handbook: Titanium Alloys, ASM International, Ohio, USA. ISBN-10: 0-87170-481-1.

Menzies I., Koshy P., 2008. Assessment of abrasion-assisted material removal in wire EDM, Annals of CIRP 57(1), 195-198.

Metzger J.L., 1986. Superabrasive grinding. Butterworths, Kent, UK. ISBN 0-408-01586-1.

Ming C., Xiaotian L., Fanghong S., Yucheng X., Bingyuan X., 2001. Studies on the grinding characteristics of directionally solidified nickel-based superalloy, Journal of Materials Processing Technology 116, 165-169.

Morgan J.E., Salter N.D., 1984. The creep-feed grinding of hard and soft steels, Transactions of the ASME, Journal of Engineering for Industry 106, 229-232.

Moriwaki T., Shamoto E., 1991. Ultra precision diamond turning of stainless steel by applying ultrasonic vibration, Annals of CIPR 40(1), 559-562.

Moriwaki T., Shamoto E., Eguchi D., 1996. Vibration assisted micro-machining of alloyed steel, Proceedings of the 3rd International Conference on Progress of Cutting and Grinding, Osaka, Japan, 251-255.

M'Saoubi R., Larsson T., Outeiro J., Guo Y., Suslov S., Saldana C., Chandrasekar S., 2012. Surface integrity analysis of machined Inconel 718 over multiple length scales, Annals of CIRP 61(1), 99-102.

M'Saoubi R., Outerio J.C., Chandrasekaran H., Dillon Jr. O.W., Jawahir I.S., 2008. A review of surface integrity in machining and its impact on functional performance and life of machined products. International Journal of Sustainable Manufacturing 1(1-2), 203-236.

Muhammad R., Ahmed N., Roy A., Silberschmidt V.V., 2012. Numerical modelling of vibration-assisted turning of Ti-15333, Procedia CIRP 1, 364-369.

Nakagawa T., Suzuki K., Uematsu T., Kimura M., Yoshida Kogyo K.K., 1988. Development of a new turning centre for grinding ceramic materials, Annals of CIRP 37, 319-322.

Neppiras E.A., 1956. What is ultrasonic machining, Metalworking Production 100, 1283-1288.

Neppiras E.A., 1964, Ultrasonic machining and forming, Ultrasonics 2(4), 167-173.

Neppiras E.A., 1972. Macrosonics in industry: 1. Introduction, Ultrasonics 10(1), 9-13.

Neppiras E.A., Foskett R.D., 1957. Ultrasonic machining - II, Operating conditions and performance of ultrasonic drills, Philips. Technical Review 18(12), 368-379.

Nerubai M.S., 1987. Effect of ultrasonic vibrations on the mechanical properties of difficult-to-deform materials, Metal Science and Heat Treatment 29(4), 254-258.

Neslušan M., 2009. Grinding of Ni-based alloys with grinding wheels of high porosity, Advances in Production Engineering and Management 4(1-2), 29-36.

Neugebauer R., Stoll A., 2004. Ultrasonic application in drilling, Journal of Materials Processing Technology 149, 633-639.

Ng E-G, Lee D.W., Dewes R.C., Aspinwall D.K., 2000. Experimental evaluation of cutter orientation when ball nose end milling Inconel 718™, Journal of Manufacturing Processes 2(2), 108-115.

Nik M.G., Movahhedy M.R., Akbari J., 2012. Ultrasonic-assisted grinding of Ti6Al4V alloy, Procedia CIRP 1, 370-375.

Nishimura G., Jimbo Y., Shimakawa S., 1954. Ultrasonic machining (Part 1), Journal of the Faculty of Engineering, University of Tokyo, 24(3), 65-100.

Nomura M., Wu Y., Kuriyagawa T., 2007. Investigation of internal ultrasonically assisted grinding of small holes: effect of ultrasonic vibration in truing and dressing of small CBN grinding wheel, Journal of Mechanical Science and Technology 21, 1605-1611.

Novovic D., Aspinwall D.K., Dewes R.C., Voice W., Bowen P., 2003. The surface integrity of a burn resistant titanium alloy (Ti-25V-15Cr-2Al-0.2C wt%) after high speed milling and creep feed grinding, Proceedings of the 10th World Conference on Titanium - Ti-2003: Science and Technology, 2817-2824, Wiley-VCH GmbH & Co., Germany. ISBN 3-52730-306-5.

Onikura H., Ohnish O., Take Y., 2000. Fabrication of micro carbide tools by ultrasonic vibration grinding, Annals of CIRP 49(1), 257-260.

Panin A.V., Klimenov V.A., Pochivalov Y.I., Son A.A., Kazachenok M.S., 2004. The effect of ultrasonic treatment on mechanical behavior of titanium and steel specimens, Theoretical and Applied Fracture Mechanics 41, 163-172.

Pawade R.S., Joshi S.S., Brahmankar P.K., Rahman M., 2007. An investigation of cutting forces and surface damage in high-speed turning of Inconel 718, Journal of Materials Processing Technology 192-193, 139-146.

Peng Y., Liang Z., Wu Y., Guo Y., Wang C., 2012a. Characteristics of chip generation by vertical elliptic ultrasonic vibration-assisted grinding of brittle materials, International Journal of Advanced Manufacturing Technology 62, 563-568.

Peng Y., Liang Z., Wu Y., Guo Y., Wang C., 2012b. Effect of vibration on surface and tool wear in ultrasonic vibration-assisted scratching of brittle materials, International Journal of Advanced Manufacturing Technology 59, 67-72.

Peng Y., Wu Y.B., Liang Z.Q., Guo Y.B., Lin X., 2011. An experimental study of ultrasonic vibration-assisted grinding of polysilicon using two-dimensional vertical workpiece vibration, International Journal of Advanced Manufacturing Technology 54, 941-947.

Pentland E.W., Ektermanis J.A., 1965. Improving ultrasonic machining rates - some feasibility studies, Journal of Engineering for Industry, Transactions of the ASME 87(Series B), 39-46.

Personal communication with Dr. Donka Novovic, Manufacturing Engineering Specialist - Machining, Rolls-Royce plc, Derby, 2011.

Peters J, Vansevenant E., 1983. A thermal model covering pendulum grinding and creep feed grinding, Annals of CIRP 32(1), 491-494.

Pujana J., Rivero A., Celaya A., López de Lacalle L.N., 2009. Analysis of ultrasonic-assisted drilling of Ti6Al4V, International Journal of Machine Tools and Manufacture 49, 500-508.

Pusavec F., Hamdi H., Kopac J., Jawahir I.S., 2011. Surface integrity in cryogenic machining of nickel based alloy-Inconel 718, Journal of Materials Processing Technology 211, 773-783.

Qin N., Pei Z.J., Treadwell C., Guo D.M., 2009. Physics-based predictive cutting force model in ultrasonic vibration assisted grinding for Ti drilling, Transactions of the ASME, Journal of Manufacturing Science and Engineering 131, 041011-1-9.

Qu W., Wang K., Miller M.H., Huang Y., Chandra A., 2000. Using vibration-assisted grinding to reduce subsurface damage, Precision Engineering 24, 329-337.

Rajurkar K.P., Zhu D., McGeough J.A., Kozak J., De Silva A., 1999. New developments in Elctro-chemical machining, Annals of CIRP 48(2), 569-579.

Reed R.C., 2006. The Superalloys: Fundamentals and Appllications. Cambridge University Press, New York, USA. ISBN 13 978-0-521-85904-2.

Rolls Royce plc, 1992. The Jet Engine, 4th Edn, The Technical Publications Department, Derby, UK.

Rozenberg L.D., Kazantsev V.F., Makarov L.O., Yakhimovich D.F., 1964. Ultrasonic Cutting, Consultants Bureau, New York.

Rübenach O., 2003. From process innovation to product innovation-ultrasonic assisted diamond turning of optical glass, Industrial Diamond Review 3, 40-49.

Sakamoto H., Kajiwara K., Shimizu S., Ohmori S., 2006. Mechanism of improvement effect of ultrasonically activated coolant on finished surface roughness in cylindrical grinding, JSME International Journal (Series C) 49(2), 346-352.

Scott J., 2000. Future requirements for abrasive processes in the aerospace industry, 'Grinding beyond 2000', Technical meeting, Institute of Grinding Technology, 1-11.

Sharman A.R.C., Aspinwall D.K., Dewes R.C., Bowen P., 2001b. Workpiece surface integrity considerations when finish turning gamma titanium aluminide, Wear 249, 473-481.

Sharman A.R.C., Li X.P., Rahman M., Bowen P., Dewes R.C., Aspinwall D.K., 2001a. Ultrasonic assisted turning of gamma titanium aluminide, Proceedings of the 13th International Symposium for Electromachining (ISEM XIII), Bilbao, Spain, 939-951.

Shaw M.C., 1956. Ultrasonic grinding, Microtechnic 10(6), 257-265.

Shyha I.S., Aspinwall D.K., Soo S.L., Bradley S., 2009. Drill geometry and operating effects when cutting small diameter holes in CFRP, International Journal of Machine Tools and Manufacture 49, 1008-1014.

Singh R., Khamba J.S., 2006. Ultrasonic machining of titanium and its alloys: A review, Journal of Materials Processing Technology 173, 125-135.

Skelton R.C., 1969. Effect of ultrasonic vibration on the turning process, International Journal Machine Tool Design and Research 9, 363-374.

Spur G., Holl S.-E., 1996. Ultrasonic assisted grinding of ceramics, Journal of Materials Processing Technology 62, 287-293.

Spur G., Holl S.-E., 1997. Material removal mechanisms during ultrasonic assisted grinding, Production Engineering IV/2, 9-14.

Soo S.L., 2003. 3D Modelling when high speed end milling Inconel 718 superalloy. PhD Thesis, University of Birmingham, UK.

Soo S.L., Hood R., Aspinwall D.K., Voice W.E., Sage C., 2011a. Machinability and surface integrity of RR1000 nickel based superalloy, Annals of CIRP 60, 89-92.

Soo S.L., Hood R., Lannette M., Aspinwall D.K., Voice W.E., 2011b. Creep feed grinding of burn-resistant titanium (BuRTi) using superabrasive wheels, International Journal of Advanced Manufacturing Technology 53, 1019-1026.

Soo S.L., Ng E.G., Dewes R.C., Aspinwall D.K., Burrows J.M., 2002. Point grinding of nickel-based superalloys, Industrial Diamond Review 2, 109-116.

Sunarto, Ichida Y., 2001. Creep feed profile grinding of Ni-based superalloys with ultrafine-polycrystalline cBN abrasive grits, Precision Engineering 25, 274-283.

Suzuki K., Nakabayashi H., Uematsu T., Mishiro S., 1992. A method for making grooves with sharp corners on a green ceramic body using a tool with biaxial ultrasonic vibration, Ceramic Transactions 26 (ACers), 225-230.

Suzuki K., Tochinai H., Uematsu T., Mishiro S., *submitted by Nakagawa T.*, 1993. A new grinding method for ceramics using a biaxially vibrated nonrotational ultrasonic tool. Annals of CIRP 42, 375-378.

Suzuki K., Uematsu T., Asano S., \ánase T., Nakagawa T., 1988. Advances in grinding ceramics and WC, Industrial Diamond Review 6, 278-282.

Takeyama H., Kato S., 1991. Burrless drilling by means of ultrasonic vibration, Annals of CIRP 40(1), 83-86.

Tawakoli T., Azarhoushang B., 2008. Influence of ultrasonic vibrations on dry grinding of soft steel, International Journal of Machine Tools and Manufacture 48, 1585-1591.

Tawakoli T., Azarhoushang B., Rabiey M., 2009a. Ultrasonic assisted grinding of soft steel, Industrial Diamond Review 1, 40-44.

Tawakoli T., Azarhoushang B., Rabiey M., 2009b. Ultrasonic assisted dry grinding of 42CrMo4, International Journal of Advanced Manufacturing Technology 42, 883-891.

Tawakoli T., Azarhoushang B., Rabiey M., 2009c. Grinding of soft steel with assistance of ultrasonic vibrations, Key Engineering Materials 389-390, 271-276.

Tawakoli T., Rasifard A., 2011a. Dressing of grinding wheels, Machining with Abrasives (Ed. Jackson M.J., Davim J.P.), Springer, USA. ISBN 978-1-4419-7301-6.

Tawakoli T., Rasifard A., 2011b. Ultrasonic assisted dressing of CBN grinding wheels with form rollers, International Journal of Mechatronics and Manufacturing Systems 4(6), 473-331.

Tawakoli T., Rasifard A., Azarhoushang B., 2008. Dressing of CBN grinding wheels with ultrasonic assistance, International Journal of Mechatronics and Manufacturing Systems 1(4), 321-331.

Tawakoli T., Rasifard A., Azarhoushang B., 2011. New developments in ultrasonic-assisted grinding and dressing, 4th International Multi-Conference on Engineering and Technological Innovation (IMETI 2011), Orlando, Florida, USA, 210-214.

Tawakoli T., Westkämper E., Azarhoushang B., 2009d. Effects of vibration-assisted grinding on wear behaviour of vitrified bond Al_2O_3 wheel, Advanced Materials Research 76-78, 21-26.

Teicher U., Künanz K., Ghosh A., Chattopadhyay A.B., 2008. Performance of diamond and CBN single-layered grinding wheels in grinding titanium, Materials and Manufacturing Processes 23, 224-227.

Tetsui T., 1999. Gamma Ti aluminides for non-aerospace applications, Current Opinion in Solid State and Materials Science 4, 243-248.

Thoe T.B., Aspinwall D.K., 1996. Ultrasonic machining of silicon nitride and synthetic ruby using SYNDITE PCD microdrill tools, Industrial Diamond Review 4, 120-124.

Thoe T.B., Aspinwall D.K., Killey N., 1999. Combined ultrasonic and electrical discharge machining of ceramic coated nickel alloy, Journal of Materials Processing Technology 92-93, 323-328.

Thoe T.B., Aspinwall D.K., Wise M.L.H., 1995. The effect of operating parameters when ultrasonic contour machining, 12th Annual Conference of the Irish Manufacturing Committee (IMC-12), Cork, Ireland, 305-312.

Thoe T.B., Aspinwall D.K., Wise M.L.H., 1998. Review on ultrasonic machining, International Journal of Machine Tools and Manufacture 38, 239-255.

Tsiakoumis V., Batako A.D., 2012. Vibration assisted surface grinding of mild and hardened steel: performance of a novel vibrating jig design, Proceedings of the 37th MATADOR Conference, Manchester, UK, 185-188.

Tso P.-L., 1995a. Study on the grinding of Inconel 718, Journal of Materials Processing Technology 55, 421-426.

Tso P.-L., 1995b. An investigation of chip types in grinding, Journal of Materials Processing Technology 53, 521-532.

Tsuboi R., Kakinuma Y., Aoyama T., Ogawa H., Hamada S., 2012. Ultrasonic vibration and cavitation-aided micromachining of hard and brittle materials, Procedia CIRP 1, 359-363.

Uhlmann E., *Submitted by G. Spur*, 1998. Surface formation in creep feed grinding of advanced ceramics with and without ultrasonic assistance, Annals of CIRP 47, 249-252.

Uhlmann E., Sammler C., 2010. Influence of coolant conditions in ultrasonic assisted grinding of high performance ceramics, Production Engineering Research and Development 4, 581-587.

Vafaeesefat A., 2009. Optimum creep feed grinding process conditions for Rene 80 supper alloy using neural network, International Journal of Precision Engineering and Manufacturing 10(3), 5-11.

Vashista M., Paul S., 2008. Study of the effect of process parameters in high-speed grinding on surface integrity by Barkhausen noise analysis, Proceedings of the Institution of Mechanical Engineers, Part B: Journal of Engineering Manufacture 222, 1625-1637.

Vogt B., 2002. Ultrasonic technology revolutionises the machining of brittle-hard materials, Industrial Diamond Review 4, 242-245.

Webster J.A., 2007. Improving surface integrity and economics of grinding by optimum coolant application, with consideration of abrasive tool and process regime. Proceedings of the Institution of Mechanical Engineers, Part B: Journal of Engineering Manufacture 221(12), 1665-1675.

Webster J., Brinksmeier E., Heinzel C., Wittmann M., Thoens K., 2002. Assessment of grinding fluid effectiveness in continuous-dress creep feed grinding, Annals of CIRP 51(1), 235-240.

Wood R.W., Loomis A.L., 1927. The physical and biological effects of high-frequency sound-waves of great intensity, Philosophical Magazine and Journal of Science 7th Series, 4 (22), 417-436.

Wu Y., Fan Y., Kato M., 2006. A feasibility study of microscale fabrication by ultrasonic-shoe centerless grinding, Precision Engineering 30, 201-210.

Wu Y., Fan Y., Kato M., Kuriyagawa T., Syoji K., Tachibana T., 2004b. Development of an ultrasonic elliptic-vibration shoe centerlessgrinding technique, Journal of Materials Processing Technology 155-156, 1780-1787.

Wu Y., Kondo T., Kato M., 2005. A new centerless grinding technique using a surface grinder, Journal of Materials Processing Technology 162-163, 709-717.

Wu Y.B., Nomura M., Feng Z.J., Kato M., 2004a. Modeling of grinding force in constant-depth-of-cut ultarasonically assisted grinding, Materials Science Forum 471-472, 101-106.

Wu Y., Yokoyama S., Sato T., Lin W., Tachibana T., 2009. Development of a new rotary ultrasonic spindle for precision ultrasonically assisted grinding, International Journal of Machine Tools and Manufacture 49, 933-938.

Xu X., Yu Y., Huang H., 2003. Mechanisms of abrasive wear in the grinding of titanium (TC4) and nickel (K417) alloys, Wear 255, 1421-1426.

Xu X.P., Yu Y.Q., Xu H.J., 2002. Effects of grinding temperatures on the surface integrity of a nickel-based superalloy, Journal of Materials Processing Technology 129, 359-363.

Xu W., Wu Y., Sato T., Lin W., 2010. Effects of process parameters on workpiece roundness in tangential-feed centerless grinding using a surface grinder, Journal of Materials Processing Technology 210, 759-766.

Yan Y., Zhao B., Junli L., 2009. Ultraprecision surface finishing of nano-ZrO_2 ceramics using two-dimensional ultrasonic assisted grinding, International Journal of Advanced Manufacturing Technology 43, 462-467.

Yan Y., Zhao B., Wu Y., Liu C., Zhu X., 2006. Study on material removal mechanism of fine-crystalline ZrO_2 ceramics under two-dimensional ultrasonic grinding, Materials Science Forum 532-533, 532-535.

Yao C.F., Jin Q.C., Huang X.C., Wu D.X., Ren J.X., Zhang D.H., 2013. Research on surface integrity of grinding Inconel 718, International Journal of Advanced Manufacturing Technology 65, 1019-1030.

Ye N.E., Pearce T.R.A., 1984. A comparison of oil and water as grinding fluids in the creep feed grinding process, Proceedings of the Institution of Mechanical Engineers 198B(14), 229-237.

Yossifon, S., Rubenstein C., 1982. Wheel wear when grinding workpieces exhibiting high adhesion, International Journal of Machine Tool Design and Research 22, 159-176.

Zhang C.M., Zhang De Y., Ma X.J., 2010. Effects of ultrasonic vibration on machining accuracy in drilling, Advanced Materials Research 102-104, 521-524.

Zhang H., Mantle A., Wise M.L.H., 1995. Investigation of surface and sub-surface damage of γ-titanium aluminide after creep feed grinding, Proceedings of the 8th World Conference on Titanium, Titanium ’95: Science and Technology, Birmingham, UK, 497-503.

Zhang H.L., Zhang J.H., 2009. Separate critical condition for ultrasonic vibration assisted grinding, Journal of Shanghai University 13(5), 391-395.

Zhang L.B., Wang L.J., Liu X.Y., Zhao H.W., Wang X., Luo H.Y., 2001. Mechanical model for predicting thrust and torque in vibration drilling fibre-reinforced composite materials, International Journal of Machine Tools and Manufacture 41, 641-657.

Zhang Q.H., Wu C.L., Sun J.L., Jia Z.X., 2000. The mechanism of material removal in ultrasonic drilling of engineering ceramics, Proceedings of the Institution of Mechanical Engineers, Part B: Journal of Engineering Manufacture 214, 805-810.

Zhao B., Wu Y., Liu C.S., Gao A.H., Zhu X.S., 2006a. The study on ductile removal mechanism of ultrasonic vibration grinding of nano-ZrO_2 ceramics, Key Engineering Materials 304-305, 171-175.

Zhao B., Yan Y.Y., Wu Y., Jiao F., Liu C.S., 2006b. Study on motion model of abrasive particle and surface formation mechanics under two dimensional ultrasonic grinding, Key Engineering Materials 315-316, 314-318.

Zheng Jian-xin, Xu Jia-wen, 2006. Experimental research on the ground surface quality of creep feed ultrasonic grinding ceramics (Al_2O_3), Chinese Journal of Aeronautics 19(4), 359-365.

Zhixin J., Jianhua Z., Xing A., 1997. Study on a new kind of combined machining technology of ultrasonic machining and electrical discharge machining, International Journal of Machine Tools and Manufacture 37(2), 193-199.

Zhong, Z.W., Yang, H.B., 2004. Development of a vibration device for grinding with microvibration, Materials and Manufacturing Processes 19(6), 1121-1132.

Zhou J.M., Bushlya V., Stahl J.E., 2012. An investigation of surface damage in the high speed turning of Inconel 718 with use of whisker reinforced ceramic tools, Journal of Materials Processing Technology 212, 372-384.

A. APPENDICES

Appendix A1: Collaborators contact details

The project was conducted in collaboration with Rolls Royce plc, Saint-Gobain Abrasives, Hardinge-Bridgeport and Element Six Ltd. The contact persons for the respective industrial collaborators are given in Table A1.1.

Table A1.1 Industrial collaborators' contacts

Company	**Contact details**
Rolls Royce plc	Dr. Donka Novovic Manufacturing Engineering Specialist - Machining Global Manufacturing Process Owner for Grinding Rolls-Royce plc Wilmore Road, PCF-32, Derby DE24 9BD, UK.
Saint-Gobain Abrasives	Dr. Stefan Bohr Director Product Management and Business Development Superabrasives Industrial Europe Saint-Gobain Diamantwerkzeuge GmbH & Co. KG Schützenwall 13-17 D-22844 Norderstedt, Germany. Mr. David Balshaw National Sales Manager Key Accounts Engineered Markets Saint Gobain Abrasives UK Ltd Doxey Road, Stafford. ST16 1EA, UK.
Hardinge-Bridgeport	Mr. David Martin Mr. Chris Waterhouse Applications Manager Hardinge Machine Tools Ltd. Whiteacres Cambridge Road Leicester LE8 6BD, UK.
Element Six Ltd.	Dr. Peter Harden Manager: Market Support Centre Element Six Ltd., Shannon, Co Clare, Republic of Ireland.

Appendix A2: Survey of commercial ultrasonic equipment suppliers

A survey of commercial ultrasonic equipment suppliers was carried out. Several of the companies were contacted for quotations for an ultrasonic system including transducer, generator, booster and horn/sonotrode capable of accommodating workpieces of varying size; with specifications of ~3 kW peak power, 1.5 kW mean power with corresponding frequency of vibration in the range of 20-40 kHz and an amplitude range of 10-50 μm. The quotations/responses received from different companies are listed in Table A2.1.

Table A2.1 List of the companies contacted and the respective quotations received

Sr. No.	Suppliers	Response/Quotation
1.	MP Interconsulting, Switzerland	Formal quotation was received, € 10k.
2.	Tamark Engineering Ltd., UK	No response was received.
3.	Flexiskills Ltd., UK	£5k, in addition to the cost of a couple of test baseplate sonotrodes.
4.	Hielscher Ultrasonics GmbH, Germany	~ € 49k estimated cost.

Appendix A3: Measurement of amplitude of vibration

The actual amplitude of the table sonotrode under zero-load condition (workpiece mounted but without grinding) and vibrating at different percentage settings (0-70%) from the generator was measured using a Polytech OFV 3001 Laser Doppler Vibrometer coupled to an OFV 303 sensor head at the University of Glasgow, see Figs. A3.1(a) and (b) for Y and Z-axis measurement arrangements respectively. In order to obtain a distribution of vibration amplitude along Z-direction, 64 measurements were carried out over the top surface area of the sonotrode, see Fig. A3.1(c); bar graph as well as contour plot of the amplitudes are shown in Figs. A3.1(d) and (e) respectively.

The table sonotrode exhibited a multi-modal vibration characteristic in all 3 axes. The maximum amplitude recorded was ~4.2 µm and the average amplitude varied from ~2 to 4 µm, which however did not match with the expected level and therefore different settings on the ultrasonic generator were tested in order to increase the level of amplitude. Due to the limited availability of the Laser Doppler Vibrometer, a mechanical amplitude-meter of model YP0901B (manufacturer: Hangzhou Success Ultrasonic Equipment Co. Ltd.) having a sensitivity of 1 µm was utilised to measure the amplitude of vibration. The set-up for amplitude measurement is shown in Fig. A3.2(a). With a new generator setting, it was possible to increase the maximum level of amplitude up to ~7-8 µm. The evidence is given in the Figs. A3.2(b) and (c), where the former represents the reading of the amplitude-meter before switching on the ultrasonic generator while the latter showing the same after turning it on. An amplitude of 2-4 µm was termed as a ‘Low’ amplitude setting while that in a range of 7-8 µm was denoted as a ‘High’ amplitude mode. These two settings were used in Phase 2E when the effects of the amplitude of vibration on measured responses were evaluated.

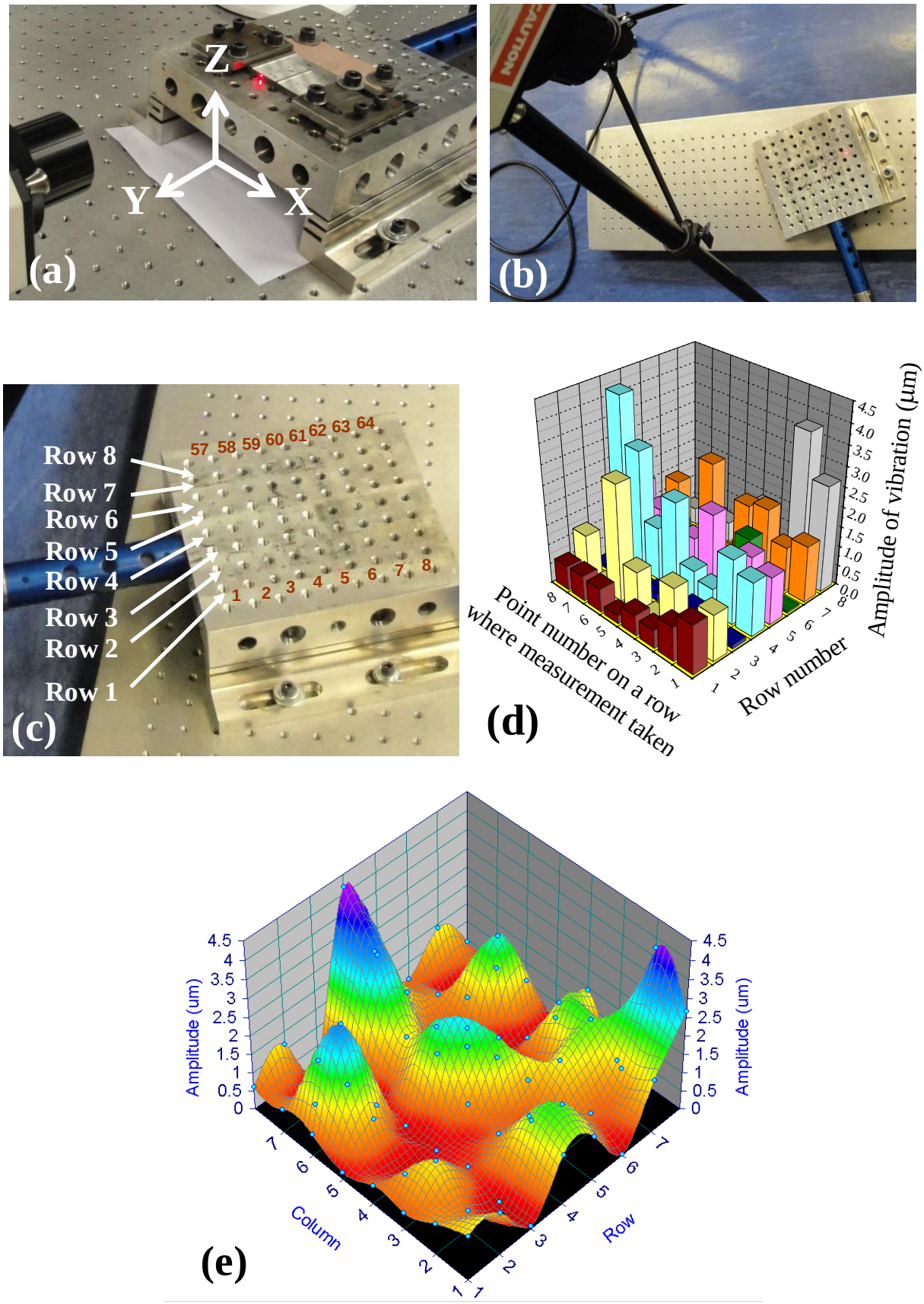


Fig. A3.1 (a) Set-up for measuring the amplitude of vibration using Laser Doppler vibrometer along Y-axis, (b) Z-axis, (c) Locations for measuring vibration amplitude along Z-axis, (d) Bar graph and (e) Contour plot of amplitude of vibration along Z-axis

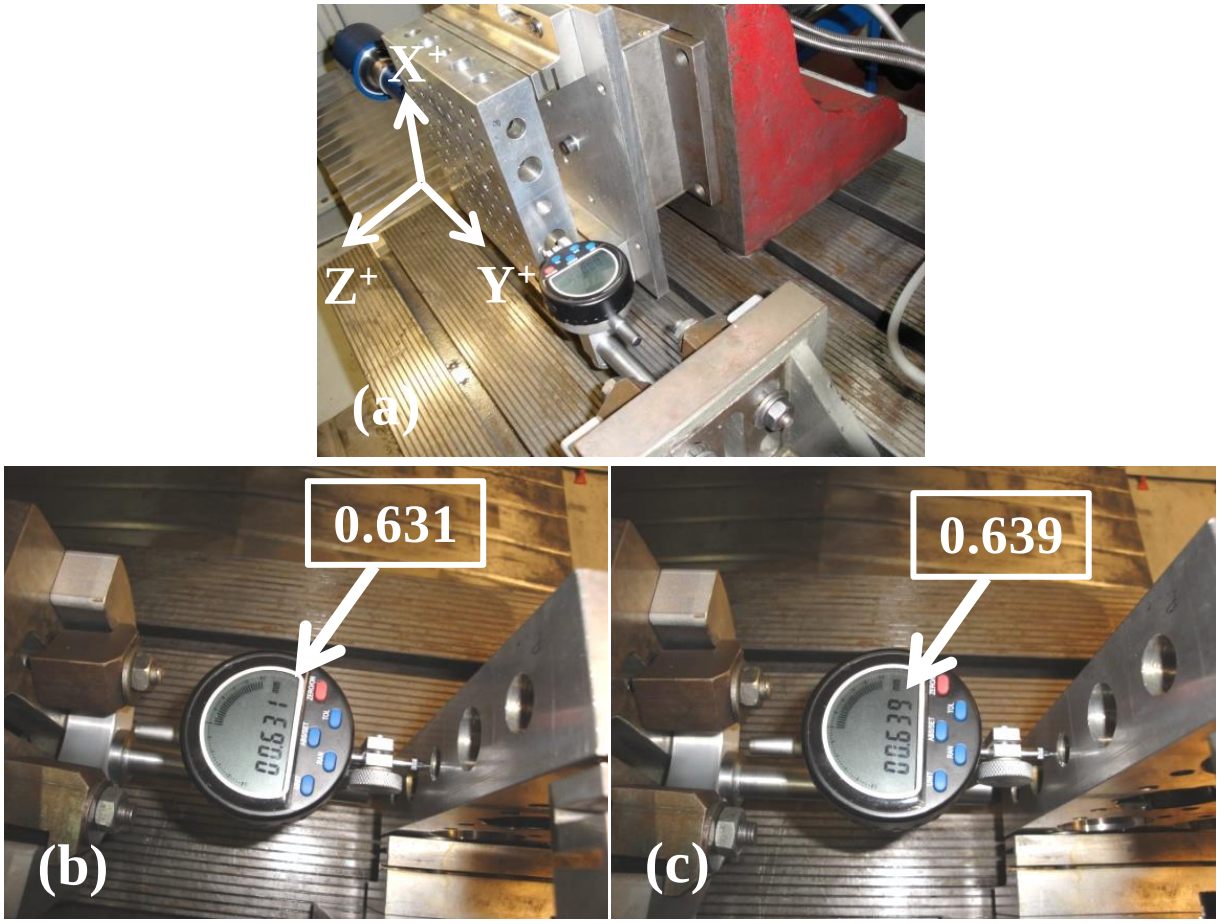


Fig. A3.2 (a) Set-up for measuring the amplitude of vibration using a mechanical amplitude-meter along Y-axis, (b) Reading taken before ultrasonics ON, (c) Reading taken after ultrasonics ON

The force due to vibration increased with the rise in the amplitude. The forces recorded in all 3 axes (X, Y and Z) under a 'no-load condition' of the ultrasonic generator (i.e. without grinding) with the 'High' and 'Low' amplitude settings are presented in Figs. A3.3(a) and (b) respectively. A 'High' amplitude setting produced higher vibration forces compared to that obtained with the 'Low' amplitude setting. Vertical component of forces typically increased from a 0% amplitude setting up to 60-70% and then either saturated or dropped, indicating that the maximum amplitude could be attained at a setting of 70% from the generator.

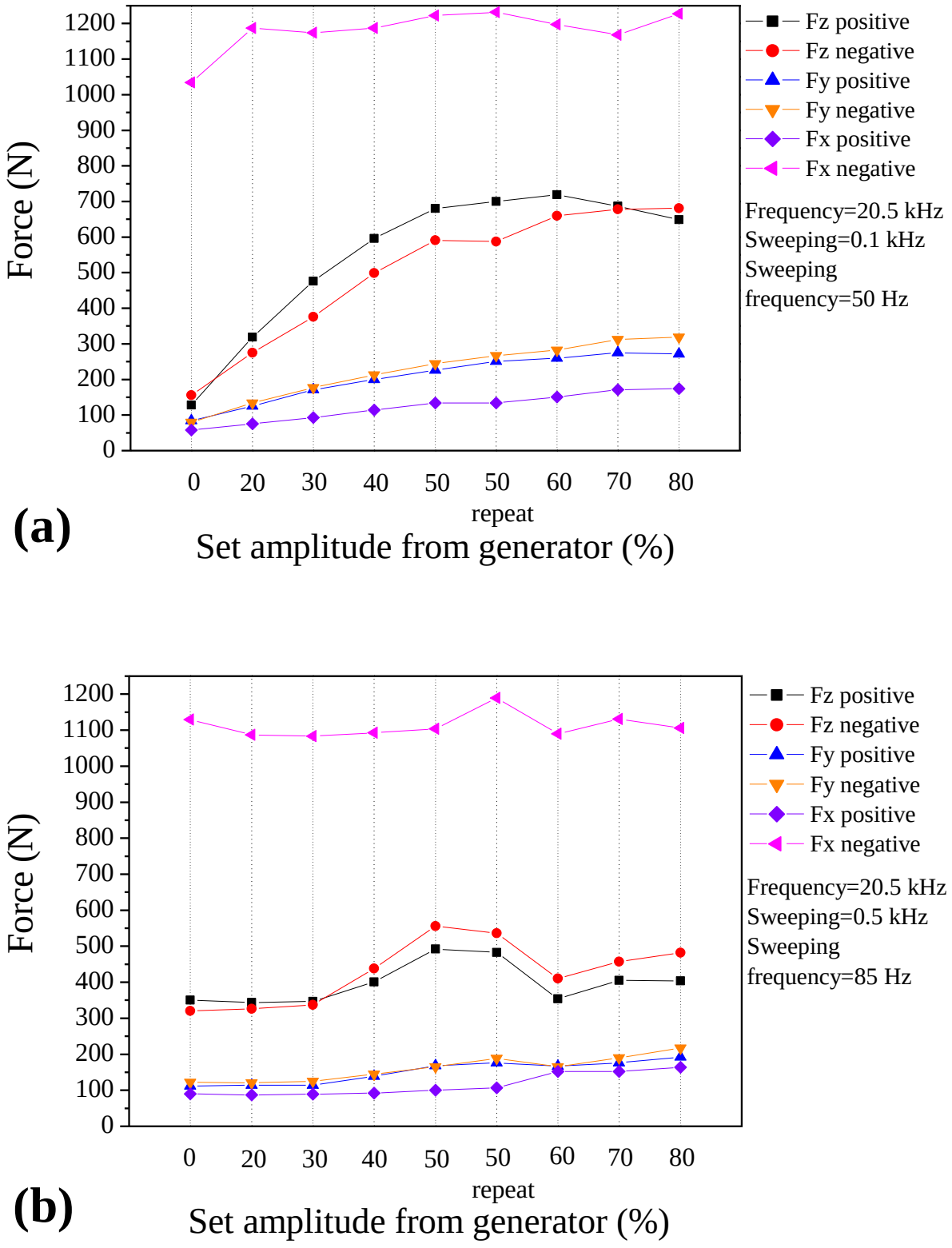


Fig. A3.3 Force graphs obtained at ultrasonic generator settings for (a) 'High' amplitude, (b) 'Low' amplitude

Appendix A4: Evaluation of UAG on Inconel 718 using VORTEX 60 mesh wheel

- **3D surface parameters of Inconel 718 workpieces ground using VORTEX 60 mesh wheel**

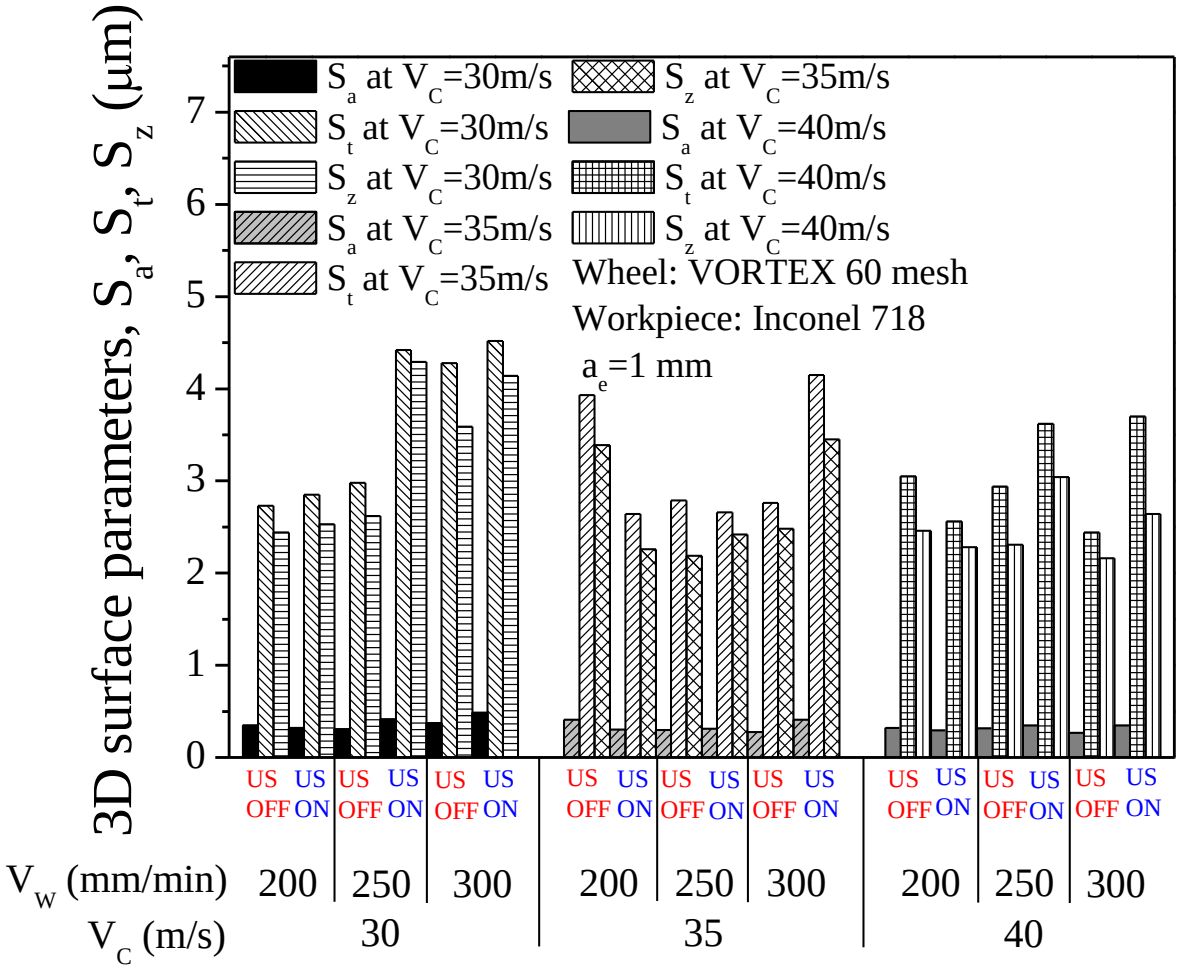


Fig. A4.1 3D topographical parameters of ground Inconel 718workpiece surfaces

- **Microhardness depth profiles of selected Inconel 718 workpieces ground at a table feed of 300 mm/min using VORTEX 60 mesh wheel**

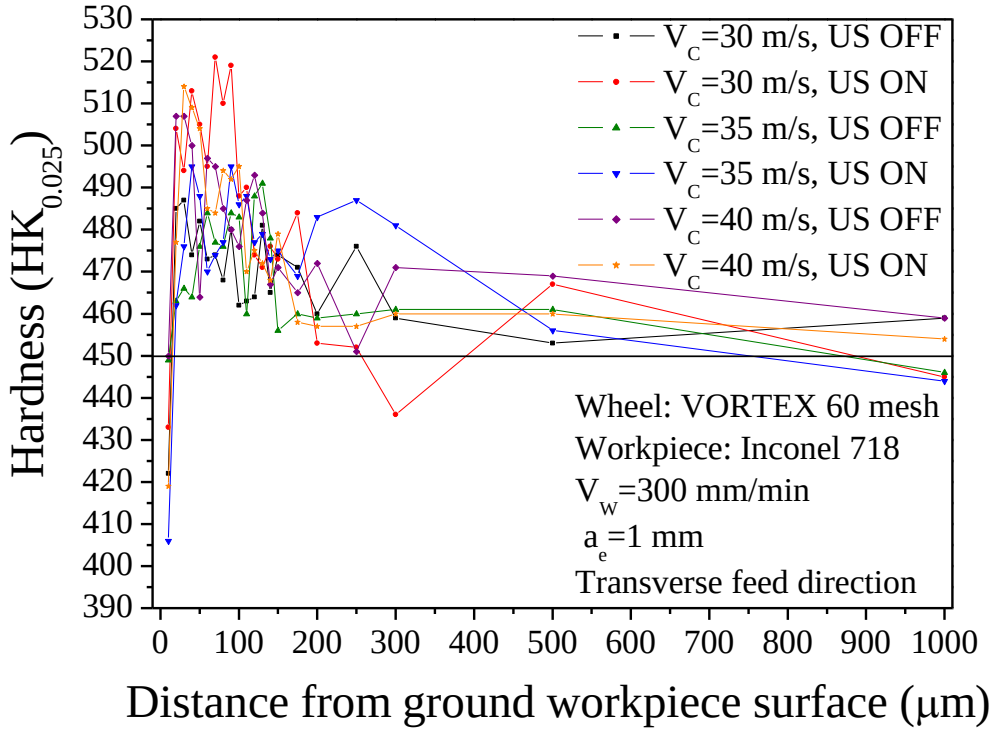


Fig. A4.2 Microhardness depth profile of Inconel 718 samples ground at V_W=300 mm/min; measurements taken in the transverse feed direction

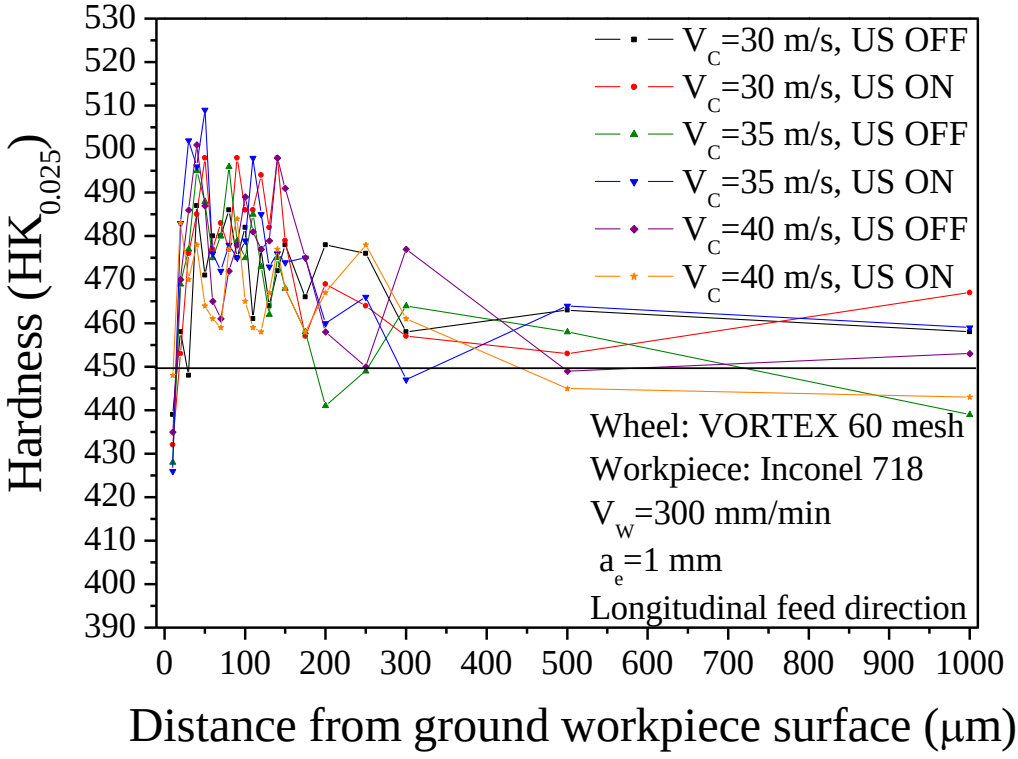


Fig. A4.3 Microhardness depth profile of Inconel 718 samples ground at V_W= 300 mm/min; measurements taken in the longitudinal feed direction

Appendix A5: Assessment of UAG on CMSX-4 using POROS2 wheel

- **Microhardness depth profiles of selected CMSX-4 workpieces ground at a wheel speed of 30 m/s using the POROS2 wheel**

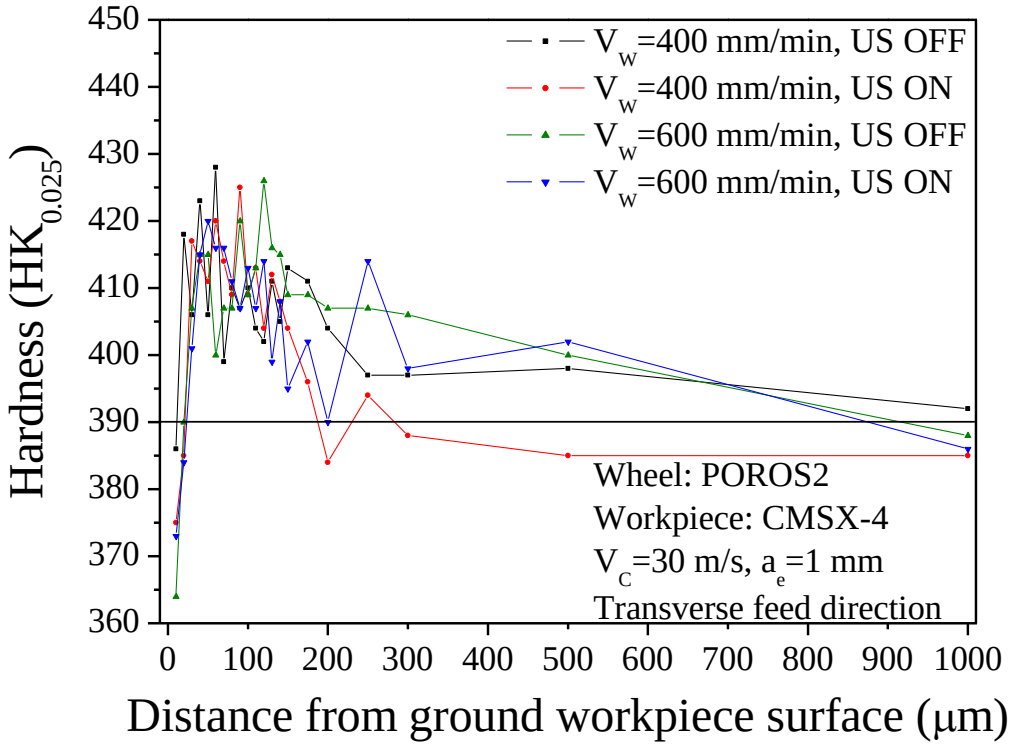


Fig. A5.1 Microhardness depth profiles of CMSX-4 samples ground at V_C=30m/s; measurements taken in the transverse feed direction

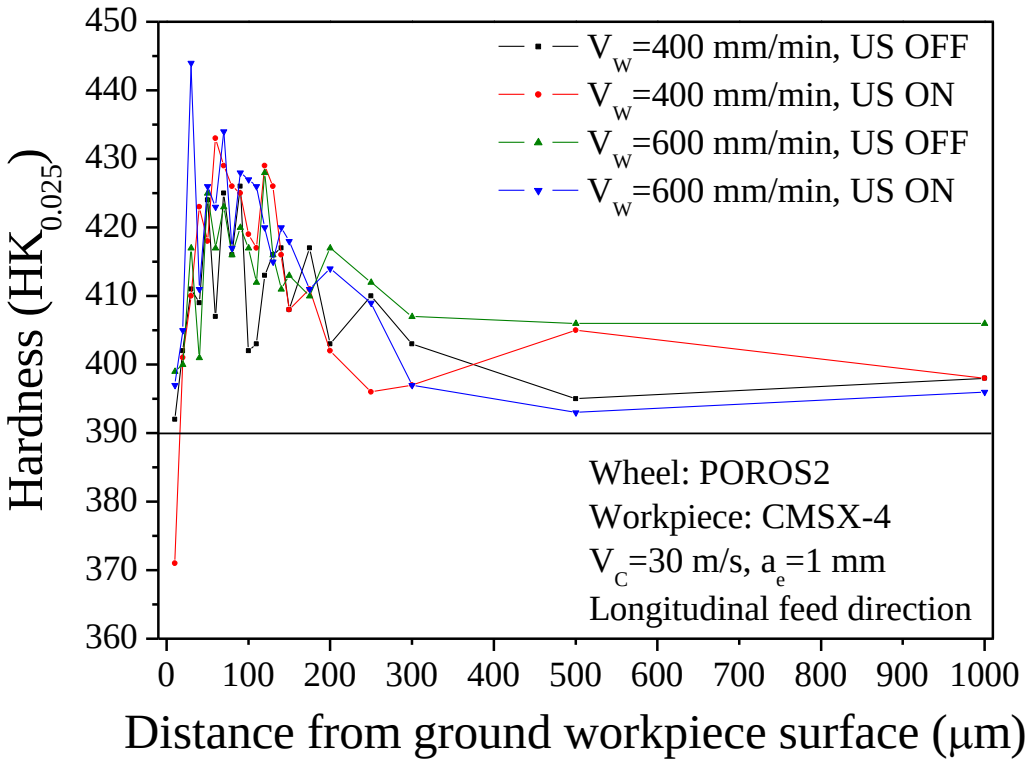


Fig. A5.2 Microhardness depth profiles of CMSX-4 samples ground at V_C=30m/s; measurements taken in the longitudinal feed direction

Appendix A6: Effect of depth of cut and vibration amplitude when UAG of Inconel 718

- **Main effects and interaction plots for horizontal force (F_h) when grinding Inconel 718 using POROS2 wheel**

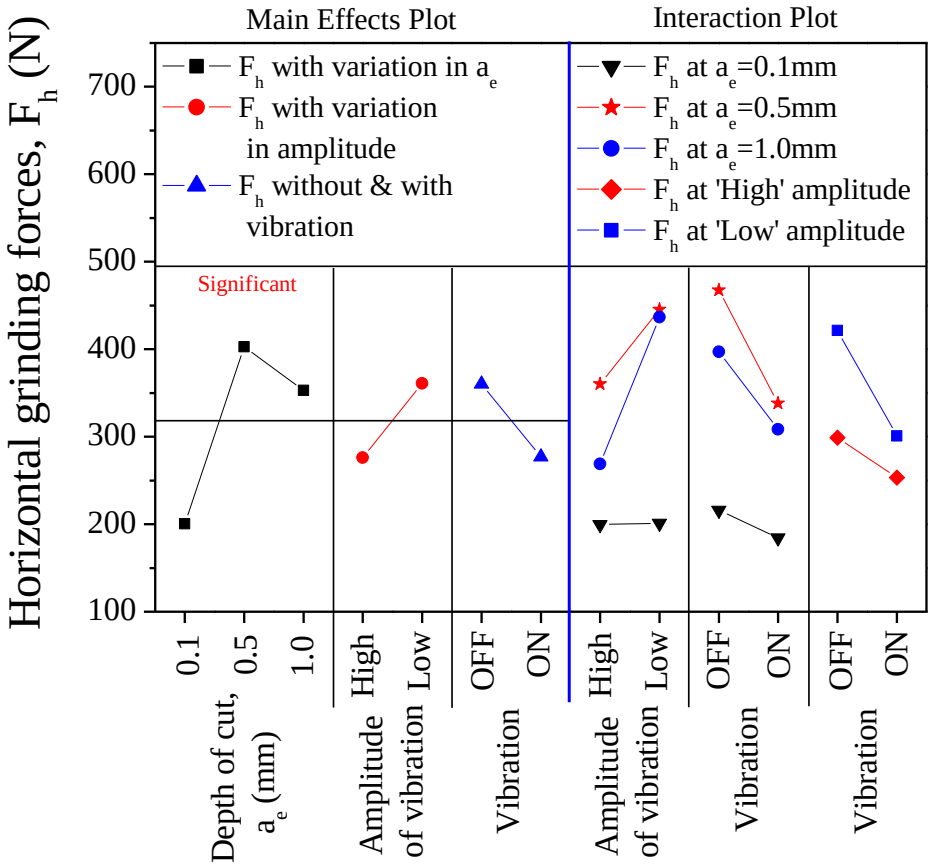


Fig. A6.1 Main effects and interaction plots for horizontal grinding force

- **Main effects and interaction plots for 2D surface roughness (R_a) of ground Inconel 718 workpieces**

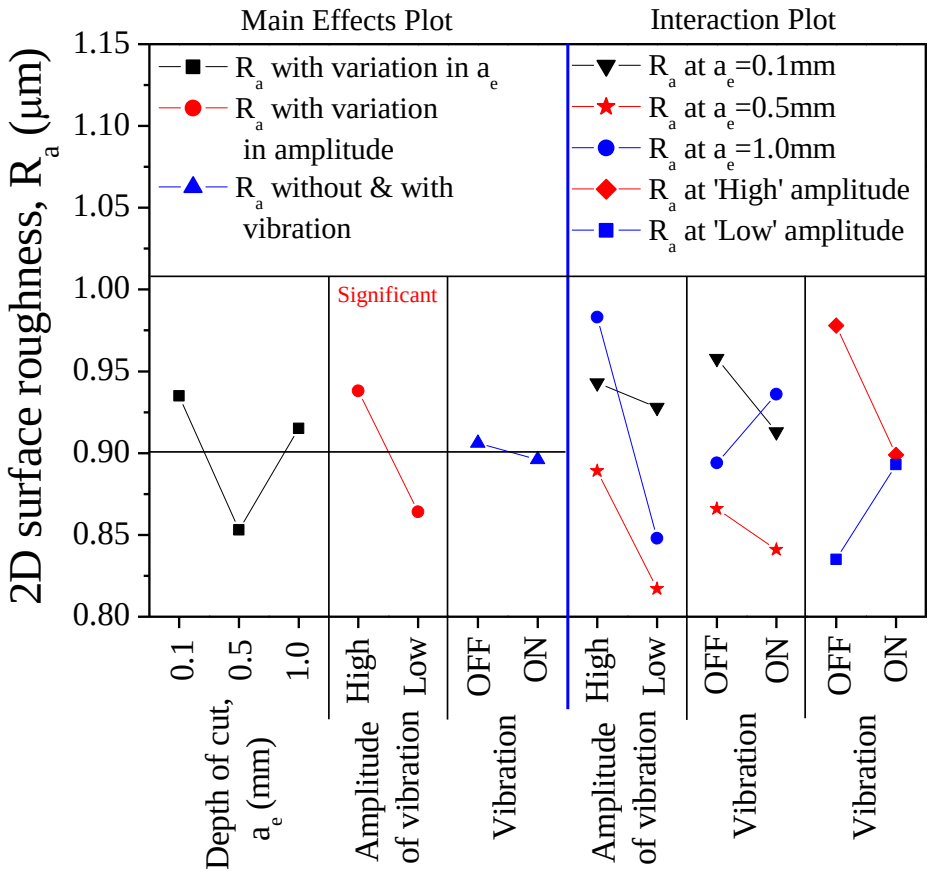


Fig. A6.2 Main effects and interaction plots for 2D surface roughness (R_a) of ground Inconel 718 workpieces

- **Main effects and interaction plots for 3D surface parameter (S_a) of ground Inconel 718 workpieces**

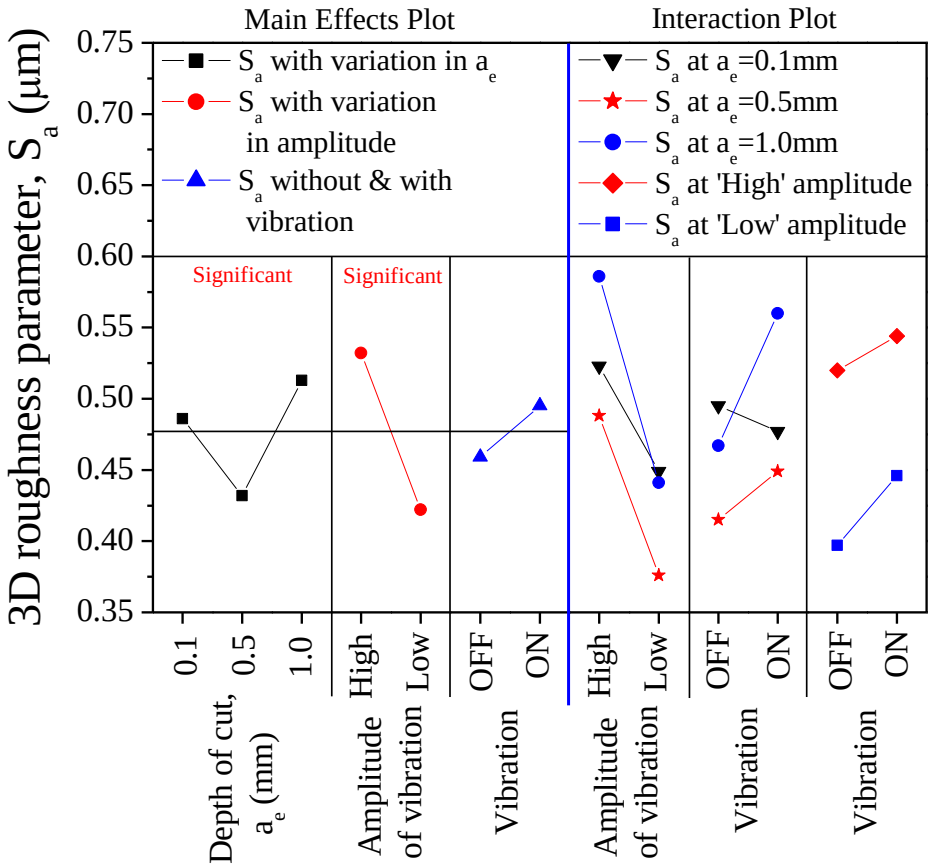


Fig. A6.3 Main effects and interaction plots for 3D surface roughness (S_a) of ground Inconel 718 workpieces

- **Main effects and interaction plots for 2D surface roughness (R_a) of graphite (negative) replicas of the POROS2 wheel**

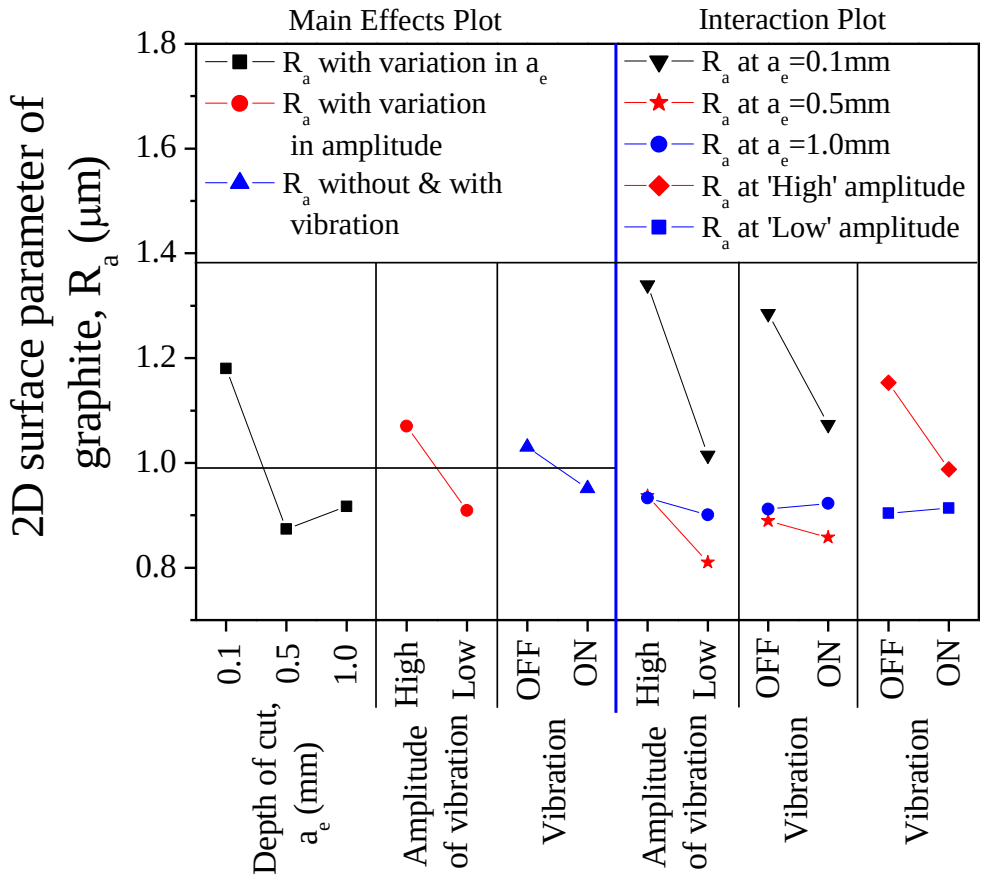


Fig. A6.4 Main effects and interaction plots for 2D surface roughness (R_a) of graphite (negative) replicas of the POROS2 wheel

- **Microhardness depth profiles of selected Inconel 718 workpieces ground at different depths of cut using the POROS2 wheel**

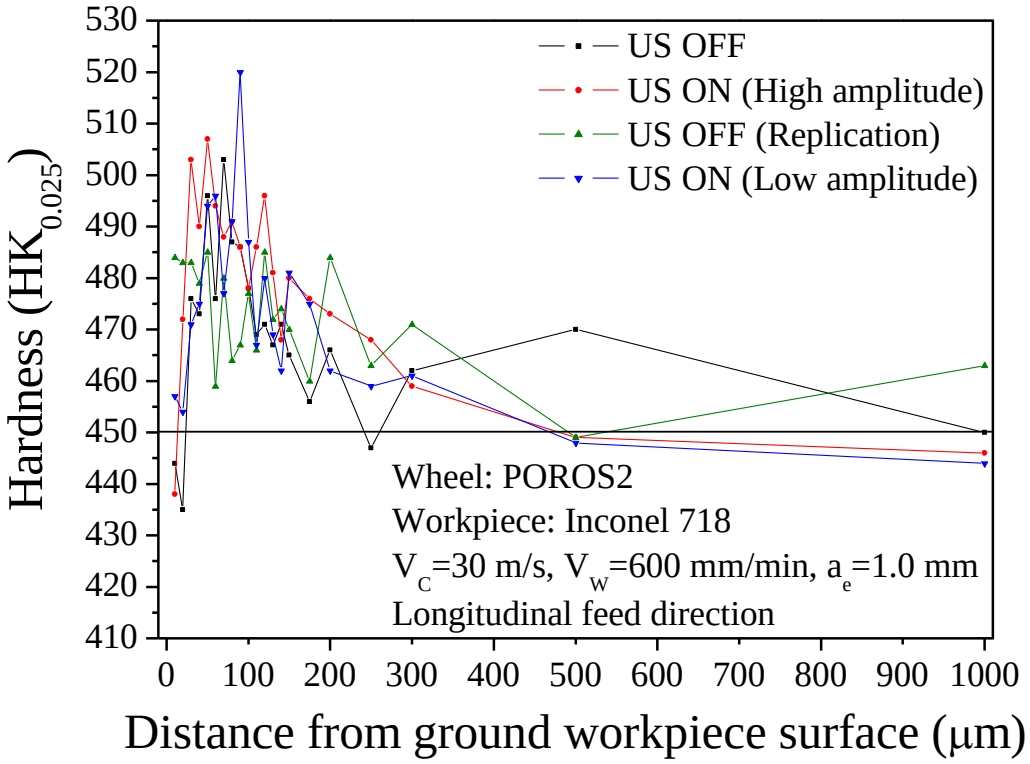


Fig. A6.5 Microhardness depth profile of Inconel 718 samples ground at a_e=1.0 mm; measurements taken in the longitudinal feed direction

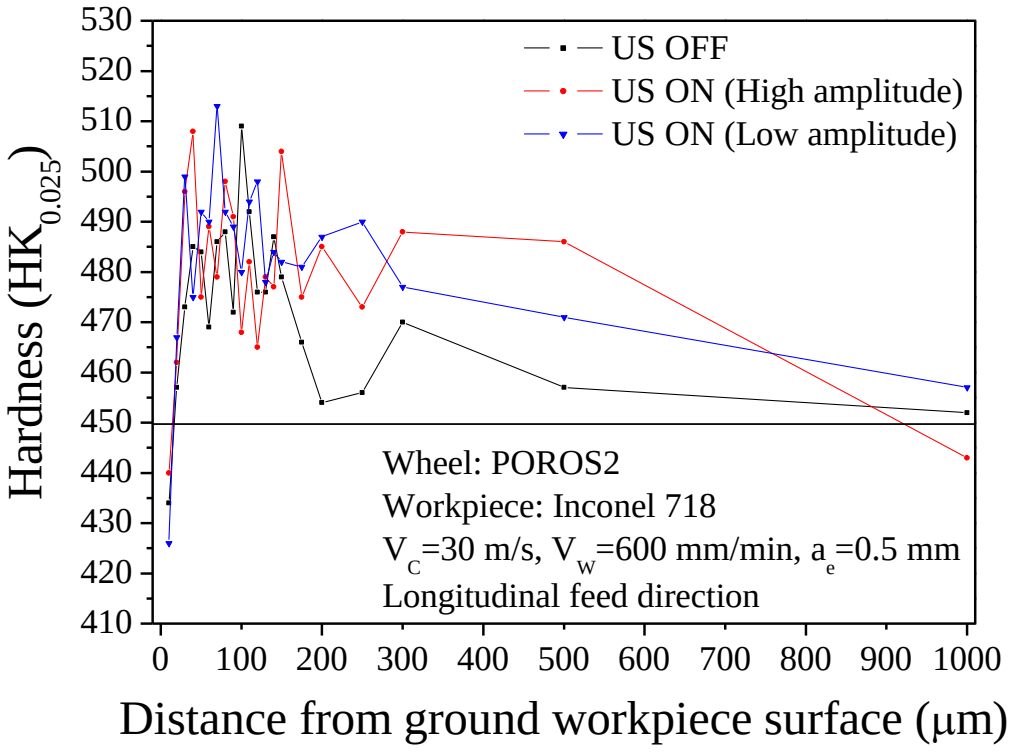


Fig. A6.6 Microhardness depth profile of Inconel 718 samples ground at a_e=0.5 mm; measurements taken in the longitudinal feed direction

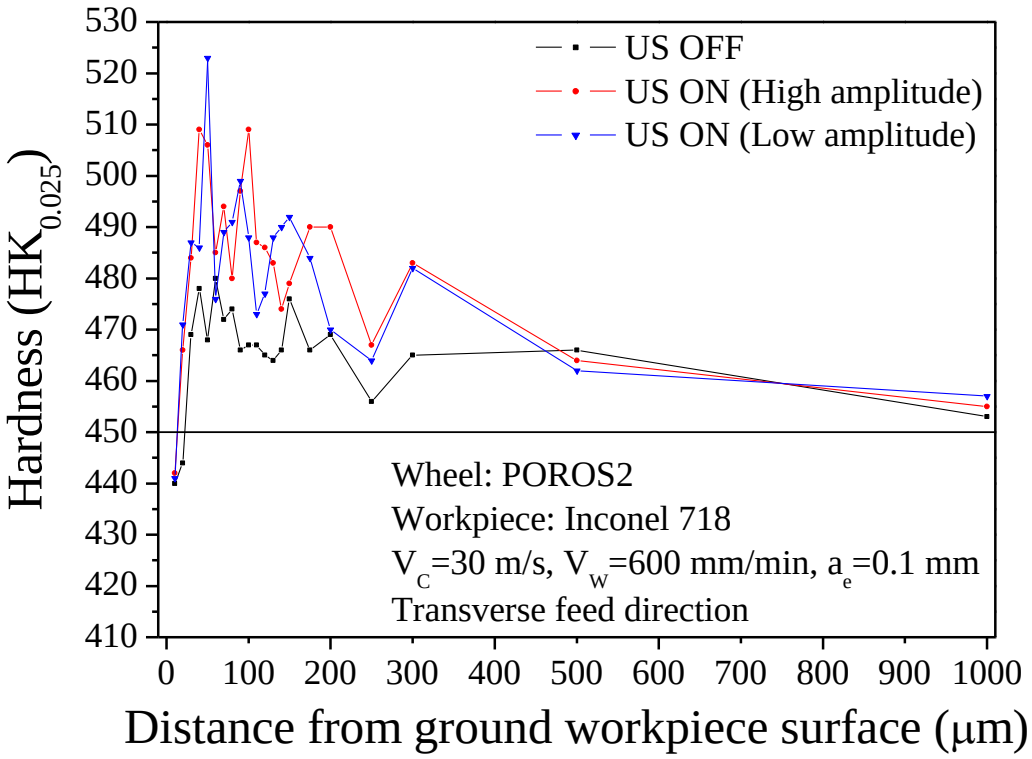


Fig. A6.7 Microhardness depth profile of Inconel 718 samples ground at a_e=0.1 mm; measurements taken in the transverse feed direction

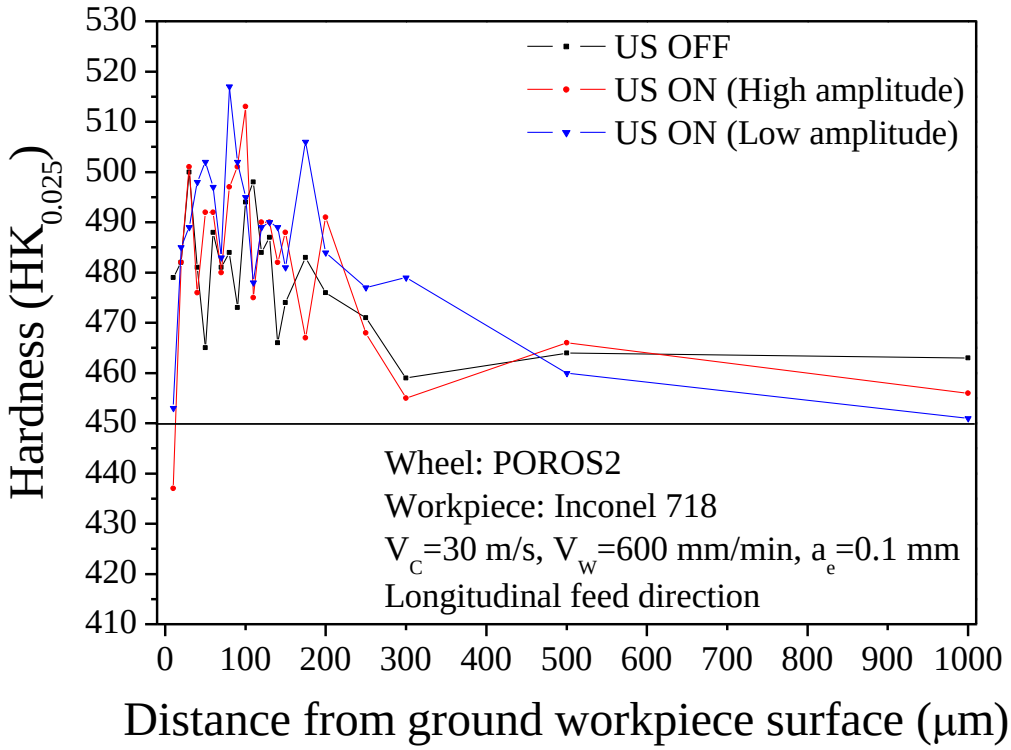


Fig. A6.8 Microhardness depth profile of Inconel 718 samples ground at a_e=0.1 mm; measurements taken in the longitudinal feed direction

Appendix A7: Assessment of UAG on γ-TiAl using conventional SiC abrasive wheel

- **Microhardness depth profiles of selected γ-TiAl workpieces ground at a cutting speed of 15 m/s using the conventional SiC wheel**

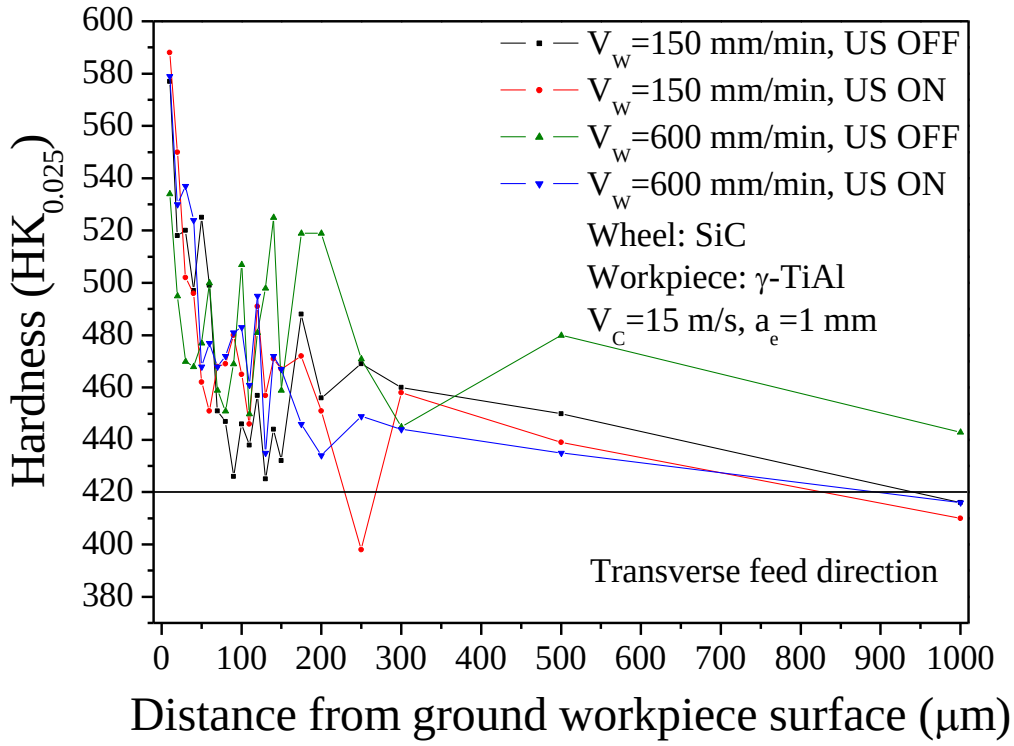


Fig. A7.1 Microhardness depth profile of γ-TiAl samples ground at V_C=15m/s; measurements taken in the transverse feed direction

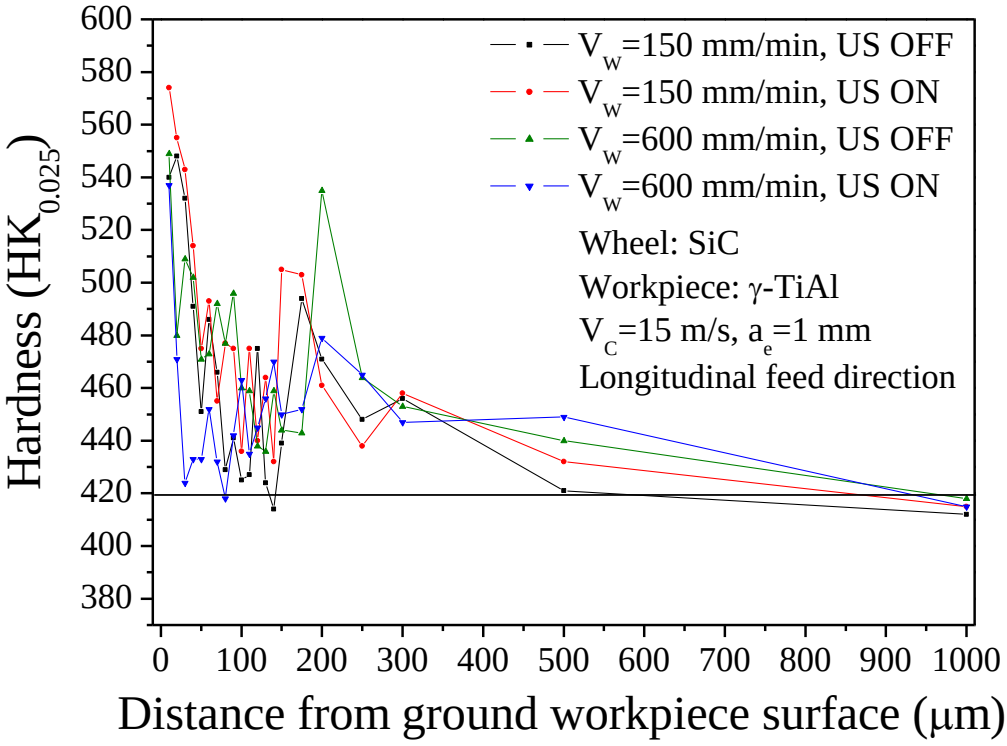


Fig. A7.2 Microhardness depth profile of γ-TiAl samples ground at V_C=15m/s; measurements taken along longitudinal feed direction

Appendix A8: Investigation of UAG on γ-TiAl with electroplated diamond superabrasive wheel

- **Microhardness depth profiles of selected γ-TiAl workpieces ground with the single layer electroplated diamond superabrasive wheel**

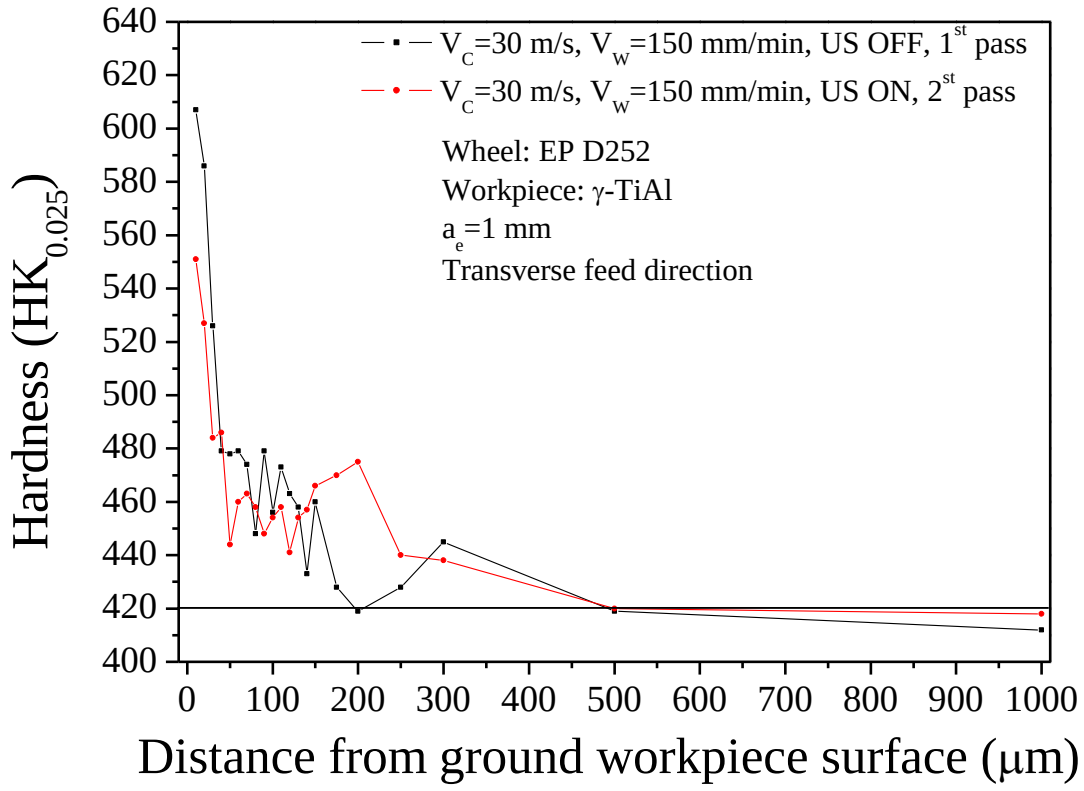


Fig. A8.1 Microhardness depth profile of γ-TiAl samples after 1st and 2nd pass; measurements taken in the transverse feed plane

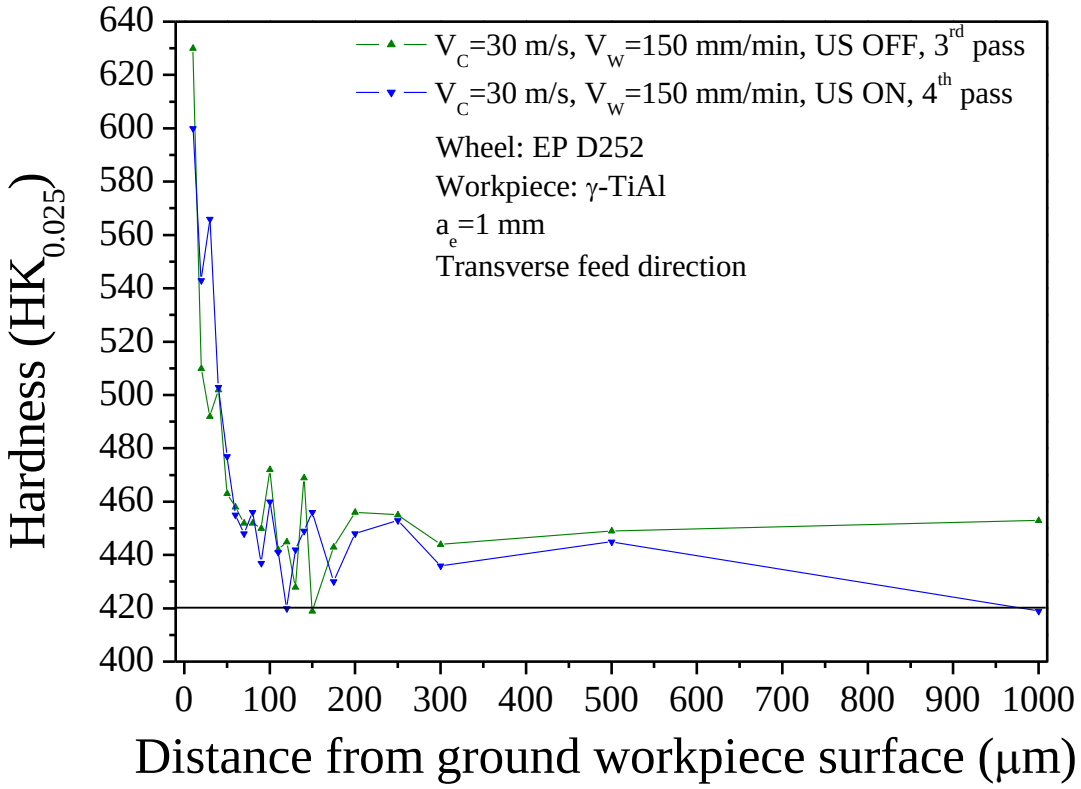


Fig. A8.2 Microhardness depth profile of γ-TiAl samples after 3rd and 4th pass; measurements taken in the transverse feed plane

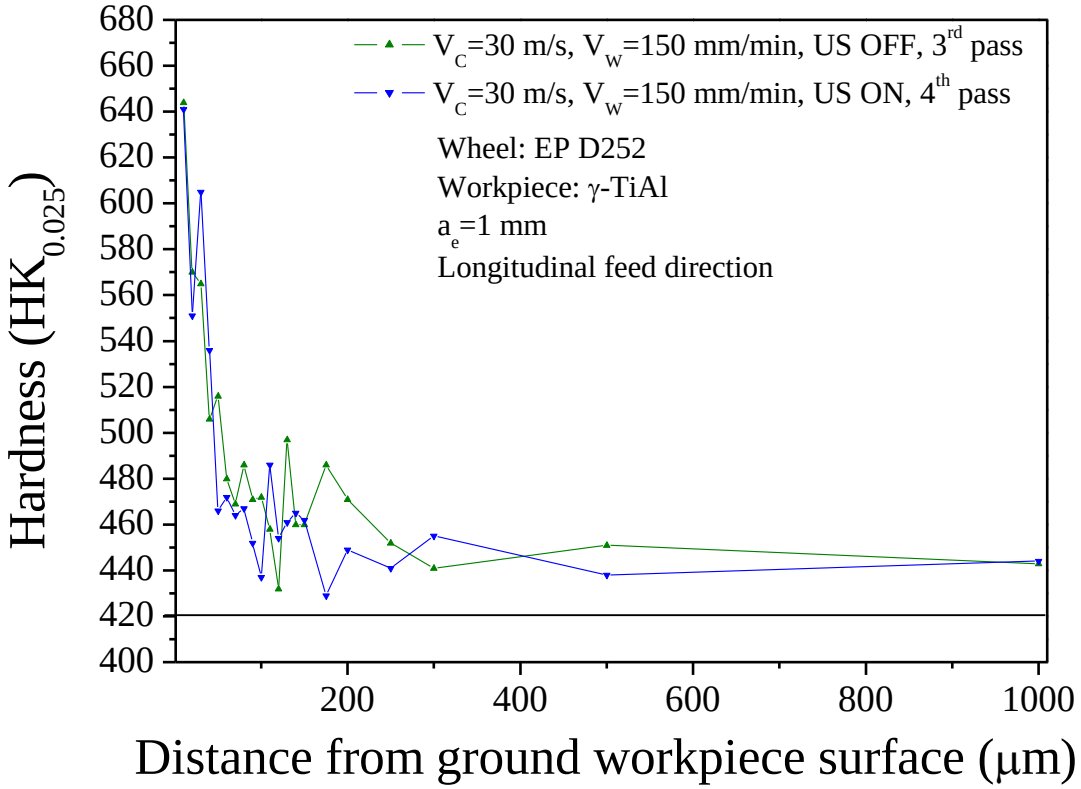


Fig. A8.3 Microhardness depth profile of γ-TiAl samples after 3rd and 4th pass; measurements taken in the longitudinal feed plane

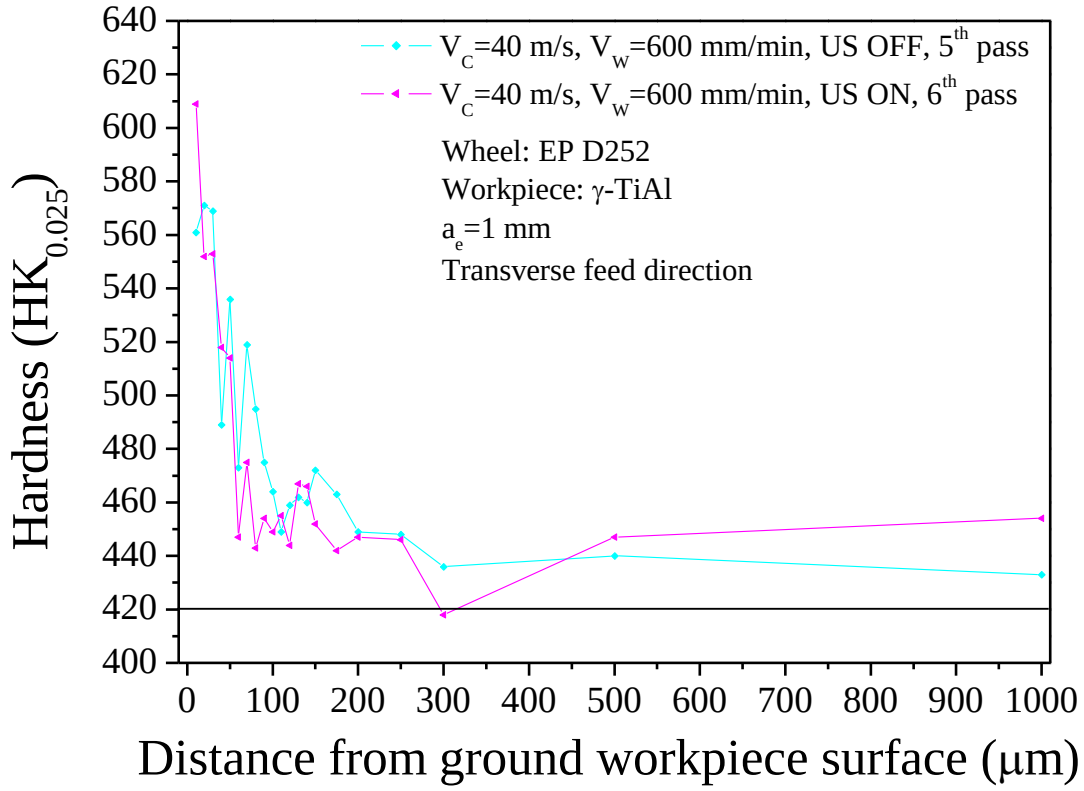
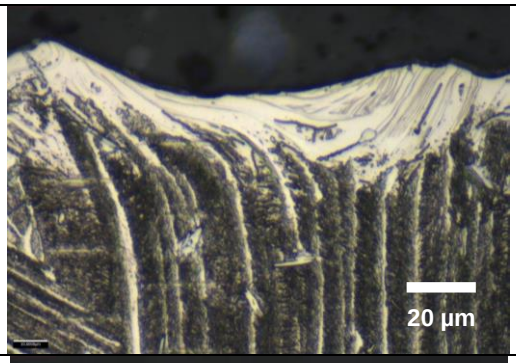
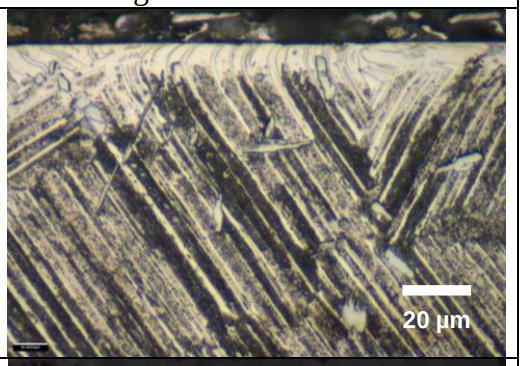
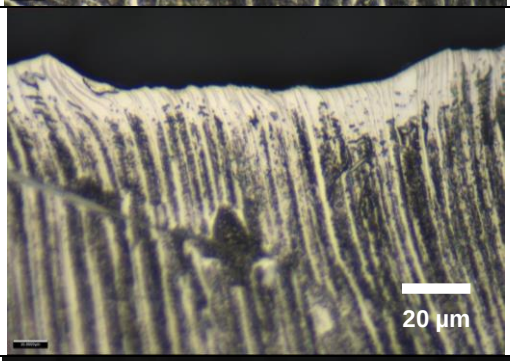
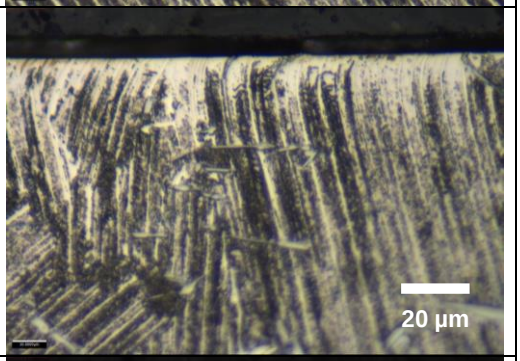
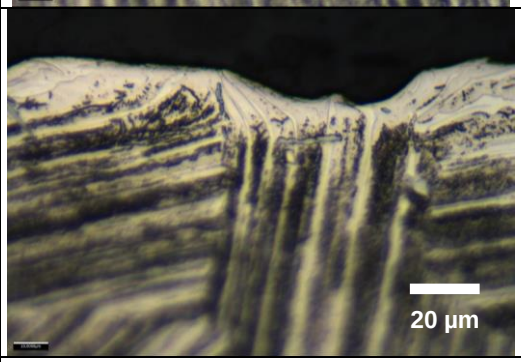
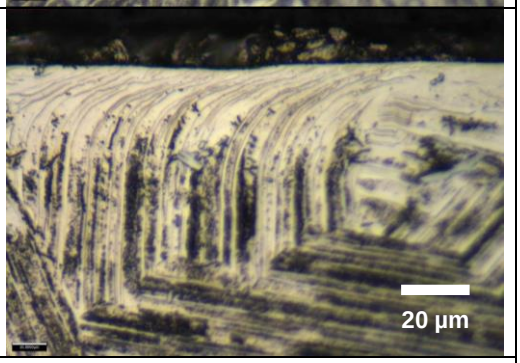
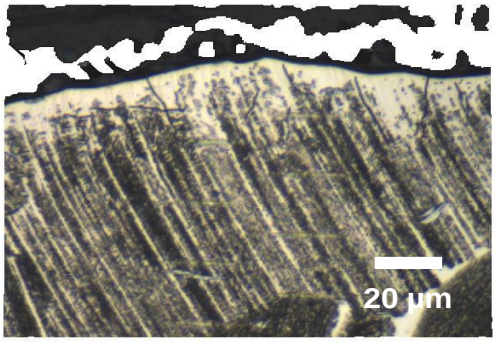
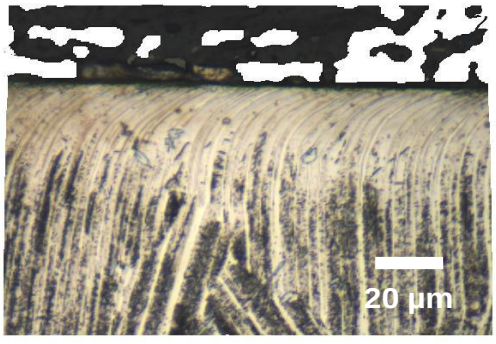
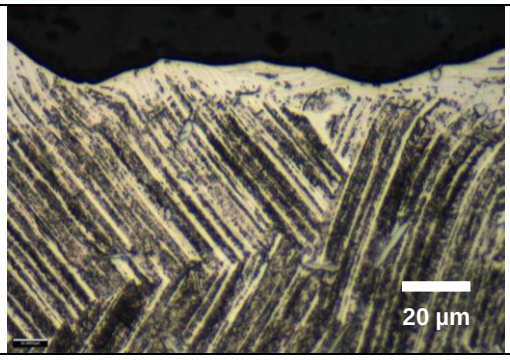
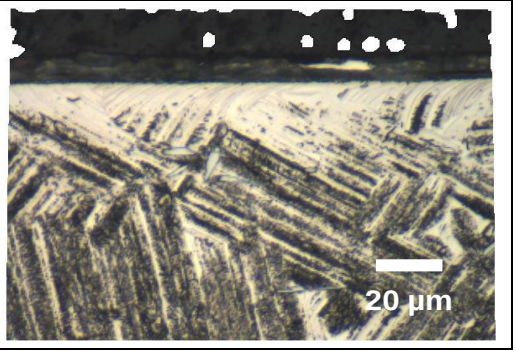


Fig. A8.4 Microhardness depth profile of γ-TiAl samples after 5th and 6th pass; measurements taken in the transverse feed plane

- **Cross-sectional microstructures of γ-TiAl specimens**

	Transverse feed direction	Longitudinal feed direction
(1) V_C=30m/s V_W=150 mm/min US OFF		
(2) V_C=30m/s V_W=150 mm/min US ON		
(3) V_C=30m/s V_W=150 mm/min US OFF		
(4) V_C=30m/s V_W=150 mm/min US ON		
(5) V_C=40m/s V_W=600 mm/min US OFF		

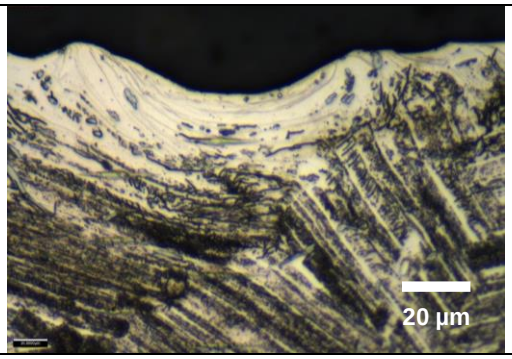
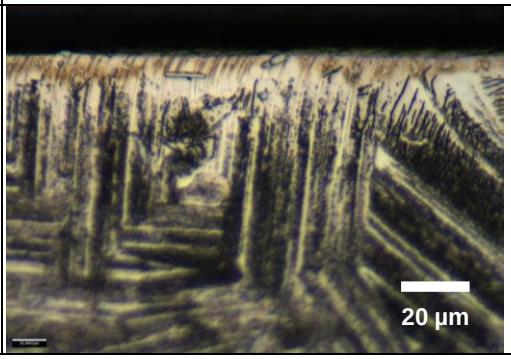
(6) V_C=40m/s V_W=600 mm/min US ON		

Fig. A8.5 Optical micrographs of the γ-TiAl microstructures taken in the transverse and longitudinal feed planes